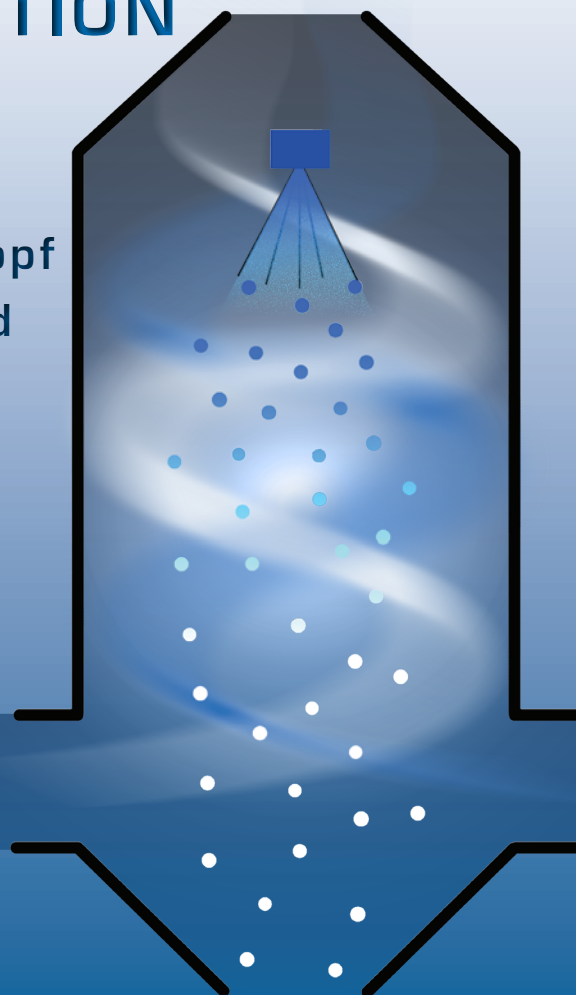


MULTIPHASE FLOWS

with DROPLETS
and PARTICLES

SECOND EDITION

Clayton T. Crowe
John D. Schwarzkopf
Martin Sommerfeld
Yutaka Tsuji



CRC Press
Taylor & Francis Group

MULTIPHASE FLOWS

with **DROPLETS**
and **PARTICLES**

SECOND EDITION

This page intentionally left blank

MULTIPHASE FLOWS

*with DROPLETS
and PARTICLES*

SECOND EDITION

Clayton T. Crowe

Washington State University, Pullman, USA

John D. Schwarzkopf

Washington State University, Richland, USA

Martin Sommerfeld

Martin Luther University, Germany

Yutaka Tsuji

Osaka University, Japan



CRC Press

Taylor & Francis Group
Boca Raton London New York

CRC Press is an imprint of the
Taylor & Francis Group, an **informa** business

CRC Press
Taylor & Francis Group
6000 Broken Sound Parkway NW, Suite 300
Boca Raton, FL 33487-2742

© 2012 by Taylor & Francis Group, LLC
CRC Press is an imprint of Taylor & Francis Group, an Informa business

No claim to original U.S. Government works
Version Date: 20110713

International Standard Book Number-13: 978-1-4398-4051-1 (eBook - PDF)

This book contains information obtained from authentic and highly regarded sources. Reasonable efforts have been made to publish reliable data and information, but the author and publisher cannot assume responsibility for the validity of all materials or the consequences of their use. The authors and publishers have attempted to trace the copyright holders of all material reproduced in this publication and apologize to copyright holders if permission to publish in this form has not been obtained. If any copyright material has not been acknowledged please write and let us know so we may rectify in any future reprint.

Except as permitted under U.S. Copyright Law, no part of this book may be reprinted, reproduced, transmitted, or utilized in any form by any electronic, mechanical, or other means, now known or hereafter invented, including photocopying, microfilming, and recording, or in any information storage or retrieval system, without written permission from the publishers.

For permission to photocopy or use material electronically from this work, please access www.copyright.com (<http://www.copyright.com/>) or contact the Copyright Clearance Center, Inc. (CCC), 222 Rosewood Drive, Danvers, MA 01923, 978-750-8400. CCC is a not-for-profit organization that provides licenses and registration for a variety of users. For organizations that have been granted a photocopy license by the CCC, a separate system of payment has been arranged.

Trademark Notice: Product or corporate names may be trademarks or registered trademarks, and are used only for identification and explanation without intent to infringe.

Visit the Taylor & Francis Web site at
<http://www.taylorandfrancis.com>

and the CRC Press Web site at
<http://www.crcpress.com>

....

Dedicated to
Ezra and Jeannette
and
Megumi
and
Rebecca, Ryan, Zackary and Michael

This page intentionally left blank

Contents

Preface	xiii
1 Introduction	1
1.1 Industrial applications	4
1.1.1 Spray drying	4
1.1.2 Pollution control	5
1.1.3 Transport systems	6
1.1.4 Fluidized beds	10
1.1.5 Manufacturing and material processing	11
1.2 Energy conversion and propulsion	14
1.2.1 Pulverized-coal-fired furnaces	14
1.2.2 Solid propellant rocket	14
1.3 Fire suppression and control	15
1.4 Summary	15
2 Properties of Dispersed Phase Flows	17
2.1 Concept of a continuum	17
2.2 Density and volume fraction	19
2.3 Particle or droplet spacing	21
2.4 Response times	24
2.5 Stokes number	25
2.6 Dilute versus dense flows	26
2.7 Phase coupling	29
2.7.1 Mass coupling	30
2.7.2 Momentum coupling	33
2.7.3 Energy coupling	34
2.8 Properties of an equilibrium mixture	35
2.9 Summary	36
2.10 Exercises	36
3 Size Distribution	39
3.1 Discrete size distributions	39
3.2 Continuous size distributions	41
3.3 Statistical parameters	42

3.3.1	Mode	43
3.3.2	Mean	43
3.3.3	Variance	43
3.3.4	Median	43
3.3.5	Sauter mean diameter	44
3.4	Frequently used size distributions	44
3.4.1	Log-normal distribution	44
3.4.2	Rosin-Rammler distribution	47
3.4.3	Log-hyperbolic distribution	49
3.5	Summary	51
3.6	Exercises	51
4	Particle-Fluid Interaction	57
4.1	Single-particle equations	57
4.1.1	Continuity equation	58
4.1.2	Translational momentum equation	59
4.1.3	Angular momentum equation	59
4.1.4	Energy equation	60
4.2	Mass coupling	60
4.2.1	Evaporation or condensation	60
4.2.2	Mass transfer from slurry droplets	63
4.2.3	Combustion	65
4.3	Linear momentum coupling	67
4.3.1	Particle drag forces	67
4.3.2	Particle lift forces	96
4.3.3	Equation summary	100
4.3.4	Body forces	100
4.3.5	Rotational momentum coupling	102
4.4	Energy coupling	103
4.4.1	Convective heat transfer	104
4.4.2	Transient term	107
4.4.3	Radiative heat transfer	108
4.4.4	Dielectric heating	110
4.5	Summary	110
4.6	Exercises	110
5	Particle-Particle Interaction	119
5.1	Particle-particle interaction	119
5.1.1	Hard sphere model	120
5.1.2	Soft sphere model (DSEM)	124
5.1.3	Hard sphere simulation of a soft sphere model	132
5.1.4	Cohesive force	133
5.1.5	van der Waals forces	135
5.1.6	Solid particle agglomeration	137
5.1.7	Fluid forces on approaching particles	137

5.2	Particle-wall interaction	139
5.2.1	Momentum and energy exchange at walls	140
5.2.2	Irregular bouncing	149
5.2.3	Erosion	151
5.3	Summary	152
5.4	Exercises	153
6	Continuous Phase Equations	157
6.1	Averaging procedures	158
6.1.1	Time averaging	158
6.1.2	Volume averaging	160
6.1.3	Ensemble averaging	162
6.2	Volume averaging	163
6.3	Property flux through a particle cloud	167
6.4	Volume-averaged conservation equations	169
6.4.1	Quasi-one-dimensional flow	169
6.4.2	Continuity equation	169
6.4.3	Momentum equation	173
6.4.4	Energy equation	181
6.5	Equation summary	191
6.6	Summary	191
6.7	Exercises	192
7	Turbulence	199
7.1	Review of turbulence in single-phase flow	199
7.1.1	General features of turbulence	199
7.1.2	Modeling single-phase turbulence	201
7.2	Turbulence modulation by particles	202
7.3	Review of modulation models	207
7.3.1	Empirical Models	208
7.3.2	Turbulence models with dusty-gas equations	209
7.3.3	Point particle models	211
7.3.4	Models based on volume averaging	211
7.4	Basic test case for turbulence models	212
7.5	Volume-averaged turbulence models	214
7.5.1	Defining volume-averaged turbulence	215
7.5.2	Turbulence kinetic energy equation	216
7.5.3	Turbulence dissipation equation	217
7.5.4	Turbulence Reynolds stress equation	222
7.6	Application to experimental results	226
7.7	Summary	230
7.8	Exercises	232

8 Droplet-Particle Cloud Equations	235
8.1 Discrete Element Method (DEM)	238
8.2 Discrete Parcel Method (DPM)	239
8.2.1 Non-dense flows	240
8.2.2 Dense flows	253
8.3 Two-fluid model	254
8.4 PDF models	257
8.5 Summary	258
9 Numerical Modeling	259
9.1 Complete Numerical Simulation	260
9.2 DNS models	261
9.2.1 Model formulation and solution procedure	261
9.2.2 Application to particle-laden flows	262
9.2.3 Current status	264
9.3 LES models	264
9.3.1 Model formulation	264
9.3.2 Application to particle-laden flows	265
9.4 VANS numerical models	267
9.4.1 Boundary conditions	276
9.4.2 Numerical solution procedures	276
9.4.3 Application examples	285
9.5 Summary	290
10 Experimental Methods	291
10.1 Sampling methods	294
10.1.1 Imaging methods, microscopy	295
10.1.2 Sieving analysis	296
10.1.3 Sedimentation methods	299
10.1.4 Electrical sensing zone method (Coulter principle)	306
10.1.5 Optical analysis	308
10.2 Integral methods	308
10.2.1 Light attenuation	309
10.2.2 Laser-diffraction method	310
10.2.3 Cross-correlation techniques	314
10.3 Local measurement techniques	317
10.3.1 Isokinetic sampling	318
10.3.2 Optical fiber probes	322
10.3.3 Scattering intensity measurements	324
10.3.4 Laser-Doppler anemometry	335
10.3.5 Phase-Doppler anemometry	347
10.3.6 Imaging techniques	367
10.4 Summary	377
10.5 Exercises	378

A Single-Particle Equations	381
A.1 Reynolds transport theorem	381
A.2 Mass conservation	386
A.3 Momentum conservation	387
A.3.1 Linear momentum	387
A.3.2 Moment of momentum	391
A.4 Energy conservation	393
A.4.1 Heat transfer to particle	396
A.4.2 Work rate of particles on surroundings	396
B Volume Averaging	401
B.1 Volume average of the gradient operation	402
B.2 Volume averaging of the time derivative	406
C Volume-Averaged Equations	409
C.1 Continuity equation	409
C.2 Momentum equation	411
C.3 Energy equation	414
C.3.1 Thermal energy equation	415
C.3.2 Mechanical energy equation	419
C.3.3 Total energy equation	424
D Turbulence Equations	425
D.1 Turbulence energy	426
D.1.1 Continuity and momentum equations	427
D.1.2 Mechanical energy equation	427
D.1.3 Turbulence energy equation	432
D.2 Turbulence dissipation	435
D.2.1 Volume averaging	436
D.2.2 The dissipation transport equation	443
D.3 Reynolds stress	446
D.3.1 Volume-averaged momentum equations	446
D.3.2 Volume average for the Reynolds stress	447
D.3.3 Reynolds stress equation	451
E Brownian Motion	455
References	461
Nomenclature	483

This page intentionally left blank

Preface

Since the publication of the first edition of *Multiphase Flow with Droplets and Particles* in 1998 there have been important advances in the science and technology of dispersed phase flows. The intent of the second edition is to include these advances while retaining the organized, pedagogical approach of the first edition. The primary change is the introduction of a new chapter, Chapter 7, on the effect of the dispersed phase particles on the turbulence of the carrier phase. The other chapters have been modified and revised to reflect the new material. Chapter 4 has been updated to include the new information on particle drag and heat transfer. In Chapter 6, a reassessment of the volume-averaged conservation equations has been made with respect to the general applicability of the “two-fluid” concept. Chapter 8, on the equations for the dispersed phase, has been completely rewritten to include the current techniques for modeling dilute and dense flows. Chapter 9, on numerical modeling, has also been rewritten to include DNS and LES as well as volume-averaged equations for the $k - \varepsilon$ and Reynolds stress models. The exercises have been expanded and a solution manual is available to support the use of the book in an instructional environment.

The first edition of *Multiphase Flow with Droplets and Particles* included a FORTRAN computer program for the multiphase flow of particles in a quasi-one-dimensional duct based on the conservative variable approach. This has not been included in the second edition. Should anyone want the description of the model and the program, they can contact the senior author (CTC) directly.

Several books on or relating to dispersed phase flows have appeared since 1998. In 2006 Michaelides published *Particles, Bubbles, and Drops: Their Motion, Heat and Mass Transfer*, which is an extension of the classic work, *Bubbles, Drops and Particles* (Clift, Grace and Weber, 1978). Michaelides’ book provides an excellent resource on particle-fluid interactions. Also, in 2006, the *Multiphase Flow Handbook* appeared, which has several chapters devoted to dispersed phase flows. In 2007, *Computational Methods for Multiphase Flows* was published by Prosperetti and Tryggvason. This book reviews various numerical techniques such as immersed-boundary, lattice-Boltzmann and boundary-integral methods for detailed analysis of fluid-particle flow systems. Finally in 2009, Brennen published *Fundamentals of Multiphase Flow*,

which gives an excellent background on fundamentals and focuses primarily on bubbly flows.

Authors

Clayton T. Crowe is Professor Emeritus at Washington State University (WSU) in Pullman, WA, retiring from the university in 2001. He received his Ph.D. from the University of Michigan in Ann Arbor, MI, in 1962. For seven years he worked in the rocket industry, before joining the Department of Mechanical Engineering of WSU in 1969. He is the primary author of *Engineering Fluid Mechanics* currently in its 9th edition, coauthor of *Multiphase Flow of Droplets and Particles* (1998), and editor of the *Multiphase Flow Handbook* (2006). He received the ASME Fluids Engineering Award in 1995 and the International Prize for Multiphase Flows in 2001. In 2009 ASME recognized Professor Crowe for his contributions to the Society, and in 2010 he received the WSU Emeritus Society Award for Excellence.

John D. Schwarzkopf is currently a staff scientist in the X-Theoretical Design (XTD) Division of the Los Alamos National Laboratory in Los Alamos, NM. He received his Ph.D. in mechanical engineering from Washington State University in 2008. His graduate work addressed turbulence modulation in particle-laden flows. Prior to receiving his Ph.D., he worked in the electronics cooling industry for seven years; he is the coauthor on a patent in this area. Currently he is involved with code development and validation.

Martin Sommerfeld is currently Professor of Mechanical Process Engineering at the Martin-Luther University of Halle-Wittenberg in Germany. He received his Dipl.-Ing. degree in 1981 and his Dr.-Ing. degree in 1984 from the University of Aachen, Germany. Before his promotion to professor at Martin-Luther University he led a research group on two-phase flow at the University of Erlangen in Germany. He has performed detailed experimental studies of multiphase flows utilizing advanced digital image analyses and phase-Doppler anemometry. In 1997 he received the DECHEMA Award for his contributions to multiphase flow measurements, modeling, and numerical predictions. His current activities include development of models for flow around agglomerates, experimental analysis with modern optical instrumentation, and direct numerical simulation.

Yutaka Tsuji retired from Osaka University, Japan, in 2007. After receiving his DE from Osaka University in 1974, he directed his attention to numerical analysis and measurements of fluid-solid flows. He has been the recipient of several prestigious awards, such as the JSME Metal in 1992 and the AIChE Thomas Baron Award in 1999, honoring his contributions to the field. Since retirement he has become the managing director of the Hosokawa Powder Technology Foundation promoting powder and particle technology. He is also the editor-in-chief for the *KONA Powder and Particle Journal*.

Acknowledgments

Professor Crowe acknowledges the ideas and insights provided by his students and colleagues over the many years he was actively involved with multiphase flow studies and activities. He is particularly thankful for the support of the Owen Science Library at Washington State University in providing accessibility to the literature through electronic access and interlibrary loans. He acknowledges the continuous love and support of his wife, Jeannette, two incredible sons, Kevin and Chad (and Brenda), and two remarkable step-daughters, Marcia and Mary Ann, and their families.

Dr. Schwarzkopf acknowledges the contributions of his teachers and colleagues. He is thankful for support provided by Los Alamos National Laboratory. He is also indebted to his family and friends for their continued support and encouragement.

Professor Tsuji acknowledges the assistance and contributing research of former students in his laboratory. These people include: Dr. Toshitsugu Tanaka, Professor at Osaka University, Japan; Dr. Toshihiro Kawaguchi, Associate Professor of Kansai University, Japan, and Dr. Takuya Tsuji, Associate Professor at Osaka University.

Clayton T. Crowe
John D. Schwarzkopf
Martin Sommerfeld
Yutaka Tsuji

This page intentionally left blank

Chapter 1

Introduction

The flow of particles and droplets in fluids is a subcategory of multicomponent, multiphase flows. The flow of multicomponent, multiphase mixtures covers a wide spectrum of flow conditions and applications. A *component* is a chemical species such as nitrogen, oxygen, water or Freon. A *phase* refers to the solid, liquid or vapor state of the matter. Examples of single and multicomponent, multiphase flows are provided in Table 1.1.

	Single component	Multicomponent
Single-phase	Water flow Nitrogen flow	Air flow Flow of emulsions
Multiphase	Steam-water flow Freon-Freon vapor flow	Air-water flow Slurry flow

Table 1.1. Examples of single and multicomponent, multiphase flows.

The flow of air, which is composed of a mixture of gases (nitrogen, oxygen, etc.), is the best example of a single-phase multicomponent flow. It is common practice to treat these types of flows as the flow of a single component with a viscosity and thermal conductivity which represents the mixture. Such an approach is practical unless the major constituents of the component gases have significantly different molecular weights. In this case the momentum associated with the diffusional velocities may be important. Also, the multicomponent nature of air will be important at high temperatures where dissociation occurs, or at very low temperatures where some species may condense out.

The flow of mixtures of liquids is also an important industrial application. For example, water is sometimes used to flush oil from a well which gives rise to a multicomponent single-phase flow. If the two liquids are miscible, then

the mixture will be treated as a single-phase with modified properties. If the liquids are immiscible, then the liquid cannot be regarded as homogeneous and treatment of the flow problem becomes much more complex. In this situation one may have “globs” of oil in the water or for high oil content, globs of water carried by the oil. The mixtures of two liquids are generally referred to as emulsions.

Single-component, multiphase flows are typically the flow of a liquid with its vapor. The most common example is steam-water flows which are found in a wide variety of industries. Another example of single-component, multiphase flows are refrigerants in a refrigeration system.

The flow of fluids of a single phase has occupied the attention of scientists and engineers for many years. The equations for the motion and thermal properties of single-phase fluids are well accepted (Navier-Stokes equations) and closed-form solutions for specific cases are well documented. The major difficulty is the modeling and quantification of turbulence and its influence on mass, momentum and energy transfer. The state-of-the art for multiphase flows is considerably more primitive in that the correct formulation of the governing equations is still subject to debate. For this reason, the study of multiphase flows represents a challenging and potentially fruitful area of endeavor for the scientist or engineer.

Gas-liquid flows	Bubbly flows Separated flows Gas-droplet flows
Gas-solid flows	Gas-particle flows Pneumatic transport Fluidized beds
Liquid-solid flows	Slurry flows Hydrotransport Sediment transport
Three-phase flows	Bubbles in a slurry flow Droplets/particles in gaseous flows

Table 1.2. Categories and examples of multiphase flows.

Multiphase flows can be subdivided into four categories: gas-liquid, gas-solid, liquid-solid and three-phase flows. Examples of these four categories are shown in Table 1.2. A gas-liquid flow can assume several different configurations. For example, the motion of bubbles in a liquid in which the liquid is the continuous phase is a gas-liquid flow. On the other hand, the motion of liquid droplets in a gas is also a gas-liquid flow. In this case, the gas is the continuous phase. Also, a separated flow in which the liquid moves along the bottom of a pipe and the gas along the top is also a gas-liquid flow. In this situation both phases are continuous. The first two examples, bubbles in

a liquid and droplets in a gas, are known as dispersed phase flows since one phase is dispersed and the other is continuous. By definition, one can pass from one point to another in the continuous phase while remaining in the same medium. One cannot pass from one droplet to another without going through the gas.

Gas-solid flows are usually considered to be a gas with suspended solid particles. This category includes pneumatic transport as well as fluidized beds. Another example of a gas-solid flow would be the motion of particles down a chute or inclined plane. These are known as granular flows. Particle-particle and particle-wall interactions are much more important than the forces due to the interstitial gas. If the particles become motionless, the problem reduces to flow through a porous medium in which the viscous force on the particle surfaces is the primary mechanism affecting the gas flow. An example is a pebble-bed heat exchanger. It is not appropriate to refer to flow in a porous medium as a gas-solid flow since the solid phase is not in motion. Gas-solid flow is another example of a dispersed phase flow since the particles constitute the dispersed phase and the gas is the continuous phase.

Liquid-solid flows consist of flows in which solid particles are carried by the liquid and are referred to as slurry flows. Slurry flows cover a wide spectrum of applications from the transport of coals and ores to the flow of mud. These flows can also be classified as dispersed phase flows and are the focus of considerable interest in engineering research. Once again it is not appropriate to refer to the motion of liquid through a porous medium as a liquid-solid flow since the solid phase is not in motion.

Three-phase flows are also encountered in engineering problems. For example, bubbles in a slurry flow gives rise to the presence of three phases flowing together. There is little work reported in the literature on three-phase flows.

The subject of this book is the flow of particles or droplets in a fluid, specifically the flow of particles and/or droplets in a conveying gas as well as particles in a conveying liquid. The other area of dispersed phase flows, namely, bubbly flows, will not be addressed here.

The flow of particles and droplets in fluids has a wide application in industrial processes. The removal of particulate material from exhaust gases is essential to the control of pollutants generated by power plants fired by fossil fuels. The efficient combustion of droplets and coal particles in a furnace depends on the interaction of particles or droplets with air. The generation of many food products depends on the drying of liquid droplets to powders in high temperature gas streams. The transport of powders in pipes is common to many chemical and processing industries.

For many years, the design of systems with particle/droplet flows was based primarily on empiricism. However, more sophisticated measurement techniques have led to improved process control and evaluation of fundamental parameters. Increased computational capability has enabled the development of numerical models that can be used to complement engineering system design. The improved understanding of this is a rapidly growing field of tech-

nology which will have far-reaching benefits in upgrading the operation and efficiency of current processes and in supporting the development of new and innovative approaches.

A current status of multiphase flow technology in industrial applications can be found in the *Multiphase Flow Handbook* (Crowe, 2006).

1.1 Industrial applications

The objective of this book is to provide a background in this important area of fluid mechanics to assist those new to the field and to provide a resource to those actively involved in the design and development of multiphase systems. In this chapter, examples of multiphase flows in industrial and energy conversion processes are outlined to illustrate the wide application of this technology.

1.1.1 Spray drying

Many products such as foods, detergents and pharmaceuticals are produced through spray drying (Masters, 1972). This is a process in which a liquid material is atomized, subjected to hot gases and dried into the form of a powder. The general configuration of a counter current flow spray dryer is shown in Figure 1.1. A slurry or concentrated mixture is introduced at the top of the dryer and atomized into droplets. Hot gases are fed into the bottom with a swirl component and move upward through the dryer. The droplets are dried as they fall through the hot rising gases to form a powder which is collected at the bottom and removed as the final product.

Accumulation of the dried product on the wall is to be avoided because of uncontrolled drying and the possibility of fire. Also, in the case of food production, the product cannot become too hot to avoid altering the taste.

The gas-droplet (particle) flow within the dryer is very complex. The swirling motion of the gases transports the particles toward the wall which may lead to impingement and accumulation. The temperature distribution in the dryer will depend on the local concentration of the droplets as they fall through the dryer. High local concentrations will depress the local gas temperature and lead to less effective drying. The result may be a non-uniformly dried product reducing product quality.

Even though spray drying technology has been continuously improved through the years, it is still difficult to scale up models to prototype operation. It is also difficult to determine, without actual testing, how modifying the design of a conventional dryer will affect performance. There have been significant progress (Verdurmen et al., 2004) in the development of numerical and analytic tools that adequately simulate the gas-droplet flow field in the dryer. Such models or analyses could be effectively used to improve the efficiency of current designs, predict off-design performance and serve as a tool for scale-up of promising bench-scale designs to prototype operation.

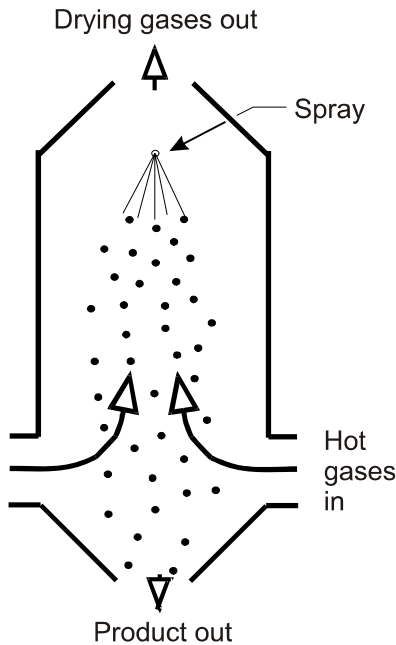


Figure 1.1: Counter-current flow spray dryer.

1.1.2 Pollution control

The removal of particles and droplets from industrial effluents is a very important application of gas-particle and droplet flows (Jorgensen and Johnsen, 1981). Several devices are used to separate particles or droplets from gases. If the particles are sufficiently large (greater than 50 microns), a settling chamber can be used in which the condensed phase simply drops out of the flowing gas and is collected. For smaller particles (~ 5 microns), the cyclone separator shown in Figure 1.2 is used. The gas-particle flow enters the device in a tangential direction as shown. The resulting vortex motion in the separator causes the particles to migrate toward the wall due to centrifugal acceleration and then fall toward the bottom where they are removed. The gases converge toward the center and form a vortex flow which exits through the top. The performance of the cyclone is quantified by the “cut size” which is the particle diameter above which all the particles are collected. Years of experience in cyclone design have resulted in “standard” designs that, under normal operating conditions, have predictable performance. Numerical modeling or other approaches are needed to design cyclones for special applications such as hot-gas clean up.

The particles issuing from power plants operating with fossil fuels are on the order of a micron in diameter. In these applications, the electrostatic

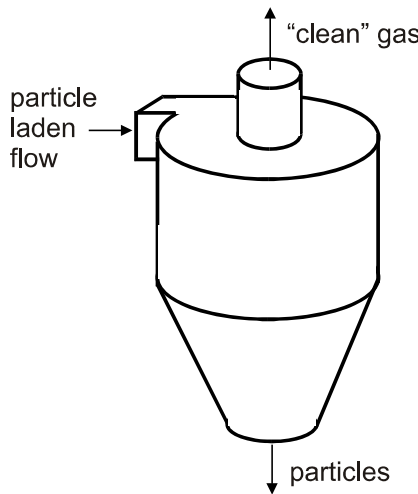


Figure 1.2: Cyclone separator.

precipitator is generally used. The top view of a conventional electrostatic precipitator is shown in Figure 1.3. The high voltage applied to the wires creates a corona with charged ions. These ions travel along the electric lines of force to the particles and accumulate on the particles. The resulting charged particles are moved toward the wall by Coulomb forces and deposited on the wall. Periodically the plates are vibrated (rapped) and the particles fall into a collection bin. The fluid mechanics of the electrostatic precipitator is quite complex. The particle-fluid interaction obviously influences the particle concentration and the charge density. These, in turn, affect the electric field. Flow turbulence is also introduced by the structural ribs in the system. Electrostatic precipitators are still designed using empirical formulas because of the complexity of the fluid-particle-electrical field interactions.

Another pollution control device is the wet gas scrubber which is designed to remove particulate as well as gaseous pollutants. Scrubbers come in many configurations but the venturi scrubber shown in Figure 1.4 represents a simple design. Droplets are introduced upstream of the venturi and the particles are collected on the droplets. The droplets, being much larger than the particles, can be more easily separated from the flow. Sulfur dioxide can also be removed by using droplets mixed with lime. The sulfur dioxide is absorbed on the surface of the droplets. These droplets are collected, the sulfur products are removed and the droplets are reused in the scrubber.

1.1.3 Transport systems

Materials can be transported by either gases or liquids, depending on the specific application. The transport of materials by air is known as pneumatic

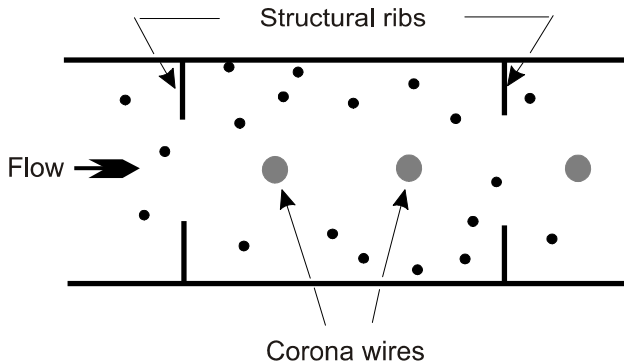


Figure 1.3: Electrostatic precipitator.

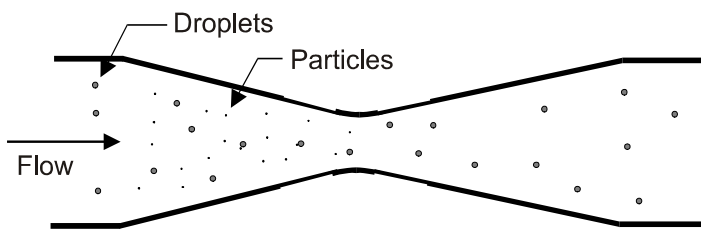


Figure 1.4: Venturi scrubber.

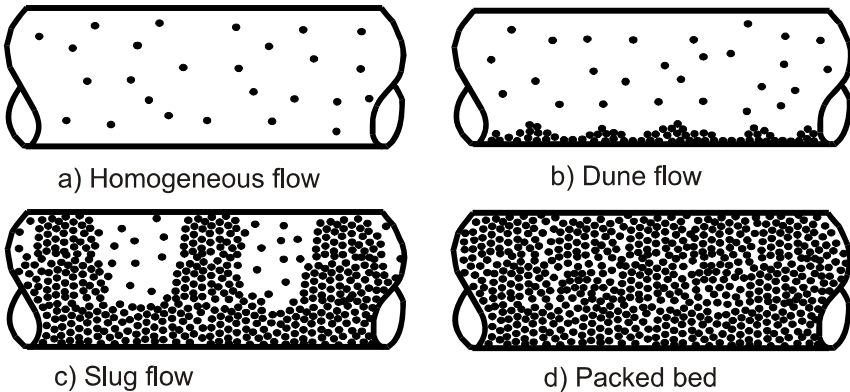


Figure 1.5: Horizontal pneumatic transport.

transport. The movement of materials by liquids (usually water) is slurry transport.

Pneumatic transport

Pneumatic transport is used widely in industry for the transport of cement, grains, metal powders, ores, coal, etc. (Klinzing, 1981; Cheremisinoff and Cheremisinoff, 1984). The major advantage over a conveyor belt is continuous operation, flexibility of location and the possibility to tap into the pipe at arbitrary locations. Pneumatic transport has been used in industry for many years for the transport of solid materials. It has been particularly useful in layouts where obstacles prohibit straight-line transport or systems which require tapping the line at arbitrary locations.

Flow patterns will depend on many factors, such as solids loading, Reynolds number and particle properties. Vertical pneumatic transport corresponds to gas flow velocities exceeding the fast fluidization velocity. The following regimes, illustrated in Figure 1.5, have been identified for horizontal, gas-particle flows. In homogeneous flow, the gas velocity is sufficiently high that the particles are well mixed and maintained in a nearly homogeneous state by turbulent mixing as illustrated in Figure 1.5a. As the gas velocity is reduced, the particles begin to settle out and collect on the bottom of the pipe as shown in Figure 1.5b. The velocity at which deposition begins to occur in the pipe is called “the saltation velocity.” After a layer builds up, ripples begin to form due to the gas flow. These ripples resemble “dunes.” As powder continues to fill the pipe, there are alternate regions where particles have settled and where they are still in suspension as shown in Figure 1.5c. This is called slug flow. Finally, at even lower gas velocities, the powder completely fills the pipe and the flow of gas represents flow through a packed bed depicted by Figure 1.5d. At this point, pneumatic transport ceases to exist.

Pneumatic conveying systems are generally designated as dilute, or dense-phase transport. Dilute-phase transport is represented by Figure 1.5a. These systems normally operate on low pressure differences with low solids loading and high velocity (higher than the saltation velocity). Dense-phase transport is represented by Figure 1.5c in which the pressure drop and solids loading are higher. The lower velocity leads to less material degradation and line erosion.

Many studies on pressure drop in pneumatic transport have been reported. There are considerable discrepancies in the data. Extensive experience with the design, installation and operation of pneumatic transport systems has given rise to design criteria which ensure a functional system. In dense-phase transport, the pressure drop is proportional to the square of the length of the slug, so various schemes have been devised to achieve this end. Still, there are situations where extensive experience is insufficient. One such case is the transport of wet particles. Little information is available on the tendency of these particles to accumulate on the wall or in bends, and plug the pipe. Even more fundamental, there is essentially no information on the head loss associated with the conveying of wet solids.

Slurry transport

The transport of particles in liquids is identified as slurry flow (Shook and Roco, 1991). The term “hydrotransport” is sometimes used for the transport of large particles like rock or chunks of coal. The flow of mud is regarded as a slurry flow. Considerable effort has also been devoted to the development of coal-water slurries which could be substituted for fuel oils.

Slurries are classified as homogeneous, heterogeneous, moving bed or stationary bed. Homogeneous slurries normally consist of small particles which are kept in suspension by the turbulence of the carrier fluid. On the other hand, heterogeneous slurries are generally composed of coarse particles which tend to settle on the bottom of the pipe. The velocity at which the particles settle out is the deposition velocity which is equivalent to the saltation velocity in pneumatic transport. Of course no slurry flow will be completely homogeneous. The rule of thumb is that the slurry is homogeneous if the variation in particle concentration from the top to bottom of the pipe is less than 20 percent. There are no well-established rules which predict whether a slurry will be homogeneous or not. The moving bed regime occurs when the particles settle on the bottom of the pipe and move along as a bed. In this case, the flow rate is considerably reduced because the bed moves more slowly than the fluid above the bed. Finally, when the particles fill the duct and no further motion is possible the flow configuration becomes a stationary bed. The flow is now analogous to the flow through a porous medium.

The fluid mechanics of the liquid-solid flows is complex because of the particle-particle and fluid-particle interaction. Usually the homogeneous slurry is treated as a single-phase fluid with modified properties which depend on solids loading. The various correlations for head loss which have been developed for slurry flows can only be used with confidence for slurries with

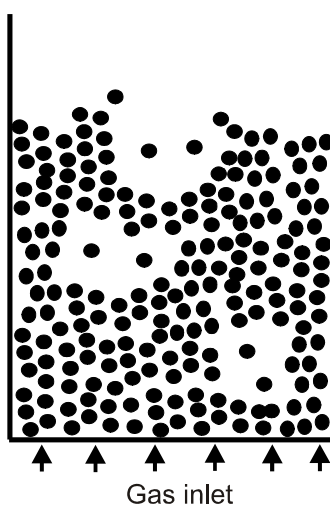


Figure 1.6: Fluidized bed.

properties identical to those for which the correlations have been obtained. Extrapolation of the correlations to other slurries may lead to significant errors in pressure drop predictions.

A comprehensive review of slurry flows is given by Hu in Chapter 4 of the *Multiphase Flow Handbook* [Crowe, C.T. (ed.), 2006].

1.1.4 Fluidized beds

The fluidized bed is also another example of an important industrial operation involving multiphase flows. A fluidized bed consists of a vertical cylinder containing particles where gas is introduced through holes (distributor) in the bottom of the cylinder as shown in Figure 1.6. The gas rising through the bed suspends the particles. At a given flow rate “bubbles,” which are regions of low particle density, appear and rise through the bed which intensifies mixing within the bed. Fluidized beds are used for many chemical processes such as coal gasification, combustion, liquefaction as well as the disposal of organic, biological and toxic wastes.

Currently the design and operation of a fluidized bed is the result of many years of experience in building, modifying and testing to achieve the best performance possible. The mechanics of the multiphase flow in a fluidized bed has been, and continues to be, a challenge to the scientist and practicing engineer. Some have chosen to treat this flow as a fluid with a modified viscosity and thermal conductivity. Others have approached the problem using the discrete particle approach in which the motion of each particle is considered. The former approach depends on developing relationships for the transport

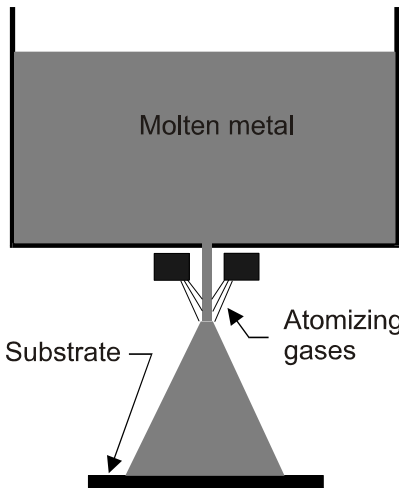


Figure 1.7: Spray forming process.

properties of the particulate phase. The latter approach requires extensive computer capability to include sufficient particles to simulate the system.

Even though the numerical models for multiphase flow in a fluidized bed appear promising, there are still many issues that have to be included such as the cohesiveness of particles, the sticking probability of a wet particle as well as particle-wall interaction.

1.1.5 Manufacturing and material processing

The flow of droplets and particles in gases is important to many manufacturing and material processing techniques, a few of which are described next.

Spray forming

An important process in the manufacturing industry is spray forming or spray casting. This is a process in which molten metals are atomized into fine droplets, transported by a carrier gas and deposited on a substrate as shown in Figure 1.7. This casting technique has several advantages. The rapid solidification of the small metal droplets gives rise to a fine grain structure and improved material properties of the deposited material. Also, by moving the substrate it is possible to produce a shape close to the final product, which minimizes material waste.

The importance of gas-particle flow is evident in spray forming. The state of the droplet upon impact with the substrate is important. A completely solidified droplet will have to be remelted to form a homogeneous deposit. A liquid droplet may splatter complicating the deposition pattern. Also, the

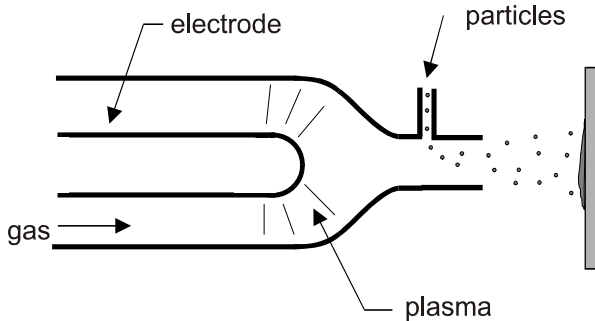


Figure 1.8: Plasma coating.

energy associated with the latent heat of the droplet will have to be conducted through the substrate which may slow the cooling of the material on the surface. The cooling rate of the droplets depends on the droplet size and the local temperature in the spray. Droplets on the edge of the spray will cool faster than those near the core. The understanding and ability to predict the thermal behavior of the droplets in the spray is important to the continued development of the spray casting process.

Plasma spray coating

Another important area of gas-particle flows in manufacturing is plasma coating. The typical plasma torch consists of a chamber where a plasma is produced by an RF or DC source. Particles, introduced into the plasma flow, are melted and convected toward the substrate as shown in Figure 1.8. The heat transfer and drag on a particle in a plasma is fundamental to the operation of the torch. At present the plasma torch is designed primarily by experience. The improvement of efficiency, operation in off-design conditions and scale-up will be dependent on improved multiphase flow models for particles in a plasma.

Abrasive water-jet cutting

The rapid and accurate cutting of various materials through the use of high velocity water jets with entrained abrasive materials is another application of multiphase flows. A typical abrasive water jet is shown in Figure 1.9. Water issues through a small orifice from a high pressure source. Some systems operate at 60,000 psi with jet velocities of 3000 ft/sec. The material is moved while the jet remains stationary to cut out the desired shapes. The inclusion of an abrasive material (usually garnet) in the jet enables cutting of hard materials such as concrete or glass. The effectiveness of the abrasive water jet depends on the speed with which the abrasive material impacts the surface.

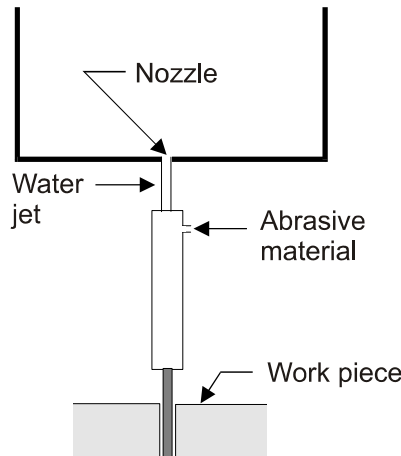


Figure 1.9: Abrasive water jet cutting.

The abrasive material is accelerated by the drag of the fluid which is an intriguing multiphase flow problem.

Synthesis of nanophase materials

An emerging area of multiphase flow applications in materials processing is the generation of nanophase materials. These materials have grain sizes of the order of 5 to 50 nanometers and can be produced by the compaction of noncrystalline material. One approach that has been investigated to produce nanoclusters is gas phase synthesis. One technique is the injection of precursors into diffusion or premixed flames. The resulting particles are from 1 to 500 nanometers in diameter. The wide range of sizes results from the lack of control of the steep thermal gradients. Another approach is with thermal reactors in which precursors are introduced into the furnace in the form of an aerosol. Chemical reactions occur as the multiphase mixture passes through the furnace. The control of particle size is highly dependent on the regulation of temperature and flow velocity. This represents an important application of multiphase flows in which thermal coupling between the gaseous and particulate phases is important. Spray pyrolysis is also being used in connection with furnace reactors in which a precursor is atomized and convected through the furnace. The solvent evaporates and reaction occurs between the particles to form the material. This approach is promising because of the possibility of making multicomponent materials. It is important in this approach to control the temperature as well as the time of the particles in the furnace. This is a challenging problem in multiphase flow technology.

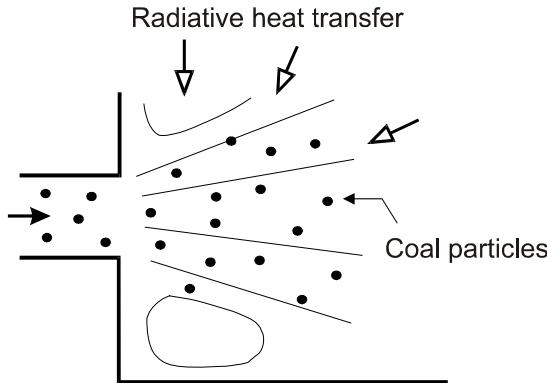


Figure 1.10: Corner-fired furnace with pulverized coal.

1.2 Energy conversion and propulsion

There are many examples of droplet/particle flows in energy conversion and propulsion systems ranging from coal-fired or oil-fired furnaces to rocket propulsion.

1.2.1 Pulverized-coal-fired furnaces

Furnaces fired by pulverized coal operate by blowing a coal particle-air mixture from the corner of a furnace as shown in Figure 1.10. The corner-fired furnace produces a swirling flow in the furnace which enhances mixing. When the particles enter the furnace, the radiative heat transfer heats the particles, and the volatiles (mostly methane) are released. These gases serve as the primary fuel for combustion. Ultimately, the remaining char burns but at a lower rate. Obviously the effective mixing of the volatiles and the gas is important for efficient combustion with minimum pollutant production. The gas-particle flow in the furnace is very complex because of the interaction of heat transfer, combustion and particle dynamics.

1.2.2 Solid propellant rocket

An example of a gas-particle flow in a propulsion system is the solid propellant rocket shown in Figure 1.11. The fuel of solid propellant rocket can be aluminum powder. When the aluminum burns, small alumina droplets about a micron in diameter are produced and convected out the nozzle in the exhaust gases. The presence of these particles lowers the specific impulse of the rocket. The principles of gas-particle flows are used to design nozzles to achieve the best specific impulse possible within the design constraints of the system.

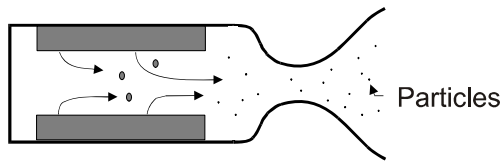


Figure 1.11: Solid propellant rocket motor.

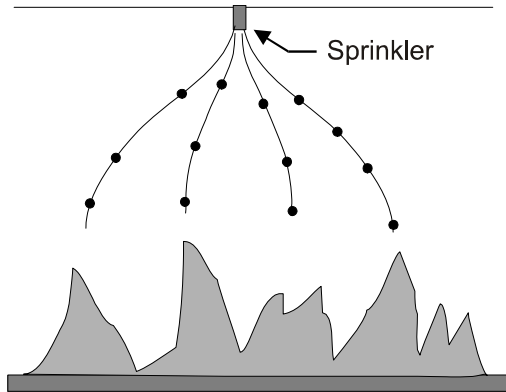


Figure 1.12: Ceiling sprinkler fire suppression system.

1.3 Fire suppression and control

Fire suppression systems in buildings usually consist of nozzles located in ceilings that are activated in the event of a fire as shown in Figure 1.12. Usually the high temperatures produced by the fire melt wax in the nozzle which allows the water to flow. The suppression systems are designed to deliver the amount of water flux per unit area (required delivery density) to extinguish the fire. This design criterion is generally established by experiment. The phenomena associated with the spray are very complex. As the droplets are projected toward the fire, they are evaporated by the hot gases and may not penetrate to the location of the fire. The evaporating droplets will cool the gases and reduce the radiative feed back to the flame. Modeling fire suppression by droplets is an active area of research.

1.4 Summary

There are many other applications of the flow of particles and droplets in fluids which have not been addressed here. Those discussed above illustrate the technological significance of this important area of fluid mechanics.

The objective of this book is to present the fundamental concepts and

approaches to address fluid particle flows. Chapter 2 provides important definitions to characterize the flow. The various parameters used to define particle and droplet size are presented in Chapter 3. The interaction between the fluid and the particle and droplet phase are addressed in Chapter 4. The equations describing particle-particle and particle-wall interactions are discussed in Chapter 5. The volume-averaged form of the continuous phase equations are presented in Chapter 6. Turbulence in fluid-particle flows is addressed in Chapter 7. The equations for particle clouds are presented and discussed in Chapter 8. The concepts important to numerical modeling and examples are provided in Chapter 9 and, finally Chapter 10 describes measurement techniques for fluid-particle systems.

Chapter 2

Properties of Dispersed Phase Flows

Dispersed phase flows are flows in which one phase, the dispersed phase, is not materially connected. These include gas-droplet, gas-particle and liquid-particle flows in which the particles and droplets constitute the dispersed phase. Bubbles in a bubbly flow also represent the dispersed phase. The objective of this chapter is to introduce definitions of dispersed phase flows which apply specifically to particle or droplet flows.

2.1 Concept of a continuum

The concept of the *continuum* is important in the development of equations for multiphase flows. A fluid is regarded as consisting of continuous matter for which properties such as density and velocity vary continuously from point to point. This idea is important in the development of the differential forms of the conservation equations in which their derivation depends on taking limits as the length, area or volume approaches zero.

To further understand the concept of the continuum, consider a gas consisting of individual molecules as shown in Figure 2.1. The density for the gas is defined as the mass per unit volume. The sampling volume ΔV in Figure 2.1a contains molecules with a total mass of ΔM so the density is

$$\rho \simeq \frac{\Delta M}{\Delta V}$$

A very small volume on the dimensions of the intermolecular spacing would contain very few molecules. As an example, if the sampling volume contained initially only one molecule and expanded to include two molecules, the density would essentially double. However, as the volume is increased further the variations become progressively smaller as shown in Figure 2.1b. Finally

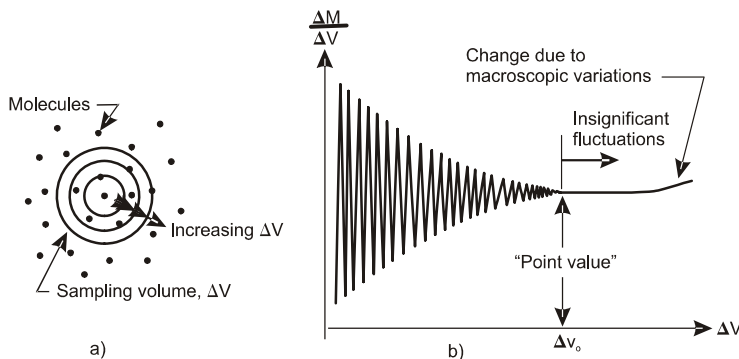


Figure 2.1: The variation of molecular mass per unit volume of mixture with size of sampling volume.

a volume is reached, ΔV_o , in which the variations become insignificant and a “point value” for the density can be defined. The volume ΔV_o will be designated as the “point” volume. According to probability theory (Poisson distribution), the fluctuations will be less than 1% for a volume containing 10^5 molecules. As the volume is increased further, the density will change according to macroscopic variations such as shock waves, spatial density gradients or other macroscopic features. The local density is then defined as

$$\rho = \lim_{\Delta V \rightarrow \Delta V_o} \frac{\Delta M}{\Delta V} \quad (2.1)$$

If the dimension of the point volume is much less than the dimensions of the flow system, the continuum assumption is justified. The size of the point volume can be assessed by using Avogadro’s number, 6.02×10^{23} , which is the number of molecules per gm-mole of material. For any ideal gas at 273 K and 101 kPa the volume occupied by 1 gm-mole is $22.4 \times 10^{-3} \text{ m}^3$ so the volume per molecule is $3.72 \times 10^{-26} \text{ m}^3$. The cube root of this number is the mean molecular spacing which is $3.3 \times 10^{-9} \text{ m}$ or approximately 10 times the molecular diameter of nitrogen. The sampling volume needed to contain 10^5 molecules is $3.72 \times 10^{-21} \text{ m}^3$ which corresponds to a cube with side of approximately $0.15 \mu\text{m}$.

The size of the sampling volume for a liquid to maintain insignificant variations is much smaller than that for a gas. For example, the size of a volume containing 10^5 molecules in water is $1.5 \times 10^{-2} \mu\text{m}$ which is much smaller than a typical particle diameter. Thus the concept of a continuum applies to much smaller particles in a liquid-particle flow.

The application of the Navier-Stokes equations to analyze the flow around a particle with diameter D would require that $V_o^{1/3} \ll D$ because the Navier-

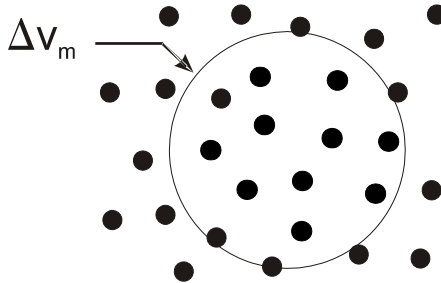


Figure 2.2: Particles in a mixture sampling volume.

Stokes equations were developed for a continuum. Another requirement for the assumption of a continuum in a gas flow is the magnitude of the Knudsen number which is the ratio of the mean free path, λ , to the particle diameter D , namely

$$Kn = \frac{\lambda}{D} \quad (2.2)$$

In order to define transport properties, such as viscosity and thermal conductivity, the Knudsen number must be less than 10^{-3} . For nitrogen at standard conditions, $\lambda = 10^{-7}$ m so the Knudsen number for a $10 \mu\text{m}$ particle would be 10^{-2} which suggests the use of the standard approach for analyzing the flow around a particle of this size would be open to question. These issues are discussed in Section 4.3 in Chapter 4.

2.2 Density and volume fraction

In order to define properties of dispersed phase flows, consider the dispersed phase elements enclosed by the mixture sampling volume, ΔV_m shown in Figure 2.2. The *number density* is defined as the number of particles per unit volume

$$n \simeq \frac{\Delta N}{\Delta V_m}$$

where ΔN is the number of particles. Using the same arguments as above for molecules in a sampling volume, the mixture sampling volume must contain a sufficient number of dispersed phase elements to ensure insignificant variations and provide a continuous change in properties from point to point. Defining this volume as ΔV_{mo} the number density is

$$n = \lim_{\Delta V \rightarrow \Delta V_{mo}} \frac{\Delta N}{\Delta V} \quad (2.3)$$

The *volume fraction* of the dispersed phase is defined as

$$\alpha_d = \lim_{\Delta V \rightarrow \Delta V_{mo}} \frac{\Delta V_d}{\Delta V} \quad (2.4)$$

where ΔV_d is the volume of the dispersed phase in the volume. Equivalently, the volume fraction of the continuous phase is

$$\alpha_c = \lim_{\Delta V \rightarrow \Delta V_{mo}} \frac{\Delta V_c}{\Delta V} \quad (2.5)$$

where ΔV_c is the volume of the continuous phase in the volume. This volume fraction is sometimes referred to as the *void fraction*. By definition, the sum of the volume fractions must be unity.

$$\alpha_d + \alpha_c = 1 \quad (2.6)$$

The *bulk density* (or *apparent density*) of the dispersed phase is the mass of the dispersed phase per unit volume of mixture or, in terms of a limit, is defined as

$$\bar{\rho}_d = \lim_{\Delta V \rightarrow \Delta V_{mo}} \frac{\Delta M_d}{\Delta V} \quad (2.7)$$

where ΔM_d is the mass of the dispersed phase. If all the particles in a volume have the same mass, m , the bulk density is related to the number density by

$$\bar{\rho}_d = nm$$

The corresponding definition for the bulk density of the continuous phase is obvious.

The sum of the bulk densities for the dispersed and continuous phases is the mixture density,

$$\bar{\rho}_d + \bar{\rho}_c = \rho_m. \quad (2.8)$$

The bulk density can be related to the volume fraction and material density. The mass associated with the dispersed phase can be written as

$$\Delta M_d = \rho_d \Delta V_d \quad (2.9)$$

where ρ_d is the material, or actual, density of the dispersed phase material. For example, if the dispersed phase were water droplets, this would be the density of the water. Substituting Equation 2.9 into Equation 2.7 gives

$$\bar{\rho}_d = \lim_{\Delta V \rightarrow \Delta V_{mo}} \frac{\rho_d \Delta V_d}{\Delta V} = \rho_d \lim_{\Delta V \rightarrow \Delta V_{mo}} \frac{\Delta V_d}{\Delta V} = \rho_d \alpha_d \quad (2.10)$$

Correspondingly, the bulk density of the continuous phase is

$$\bar{\rho}_c = \rho_c \alpha_c \quad (2.11)$$

so an alternate expression for the mixture density is

$$\rho_m = \alpha_c \rho_c + \alpha_d \rho_d \quad (2.12)$$

Another parameter important to the definition of dispersed phase flows is the dispersed phase *mass concentration* or

$$C = \frac{\bar{\rho}_d}{\bar{\rho}_c} \quad (2.13)$$

which is the ratio of the mass of the dispersed phase to that of the continuous phase in a mixture. This parameter will sometimes be referred to as the particle or droplet mass ratio. The ratio of mass flux of the dispersed phase to that of the continuous phase is the *loading*,

$$z = \frac{\dot{m}_d}{\dot{m}_c} = \frac{\bar{\rho}_d v}{\bar{\rho}_c u} \quad (2.14)$$

where v and u are the velocities of the dispersed and continuous phases, respectively. This is the “local” loading or the mass flux ratio at a local region in the flow. The total loading is the ratio of the overall mass flow rate of the dispersed phase flow to the overall mass flow rate of the continuous phase,

$$Z = \frac{\dot{M}_d}{\dot{M}_c} \quad (2.15)$$

For example, if droplets were sprayed into a gas flow, then z would be the local mass flux ratio which would vary throughout the spray and would be zero outside the spray envelope. The overall loading, Z , would be the ratio of total liquid mass flow rate supplied to the atomizer to the total gas flow rate. Obviously, the total loading can be indicative of the magnitude of the local loading in the flow field.

2.3 Particle or droplet spacing

The mechanics of a dispersed phase flow depends significantly on the average distance between the dispersed phase elements. This information is important to determine if a particle or droplet can be treated as an isolated element.

Consider the elements in Figure 2.3 that are enclosed in cubes with side ℓ which is the distance between element centers. The volume fraction of the dispersed phase is

$$\alpha_d = \frac{\pi D^3}{6\ell^3} \quad (2.16)$$

If the particles were in contact in this configuration, the volume fraction of the dispersed phase would be $\pi/6^1$.

The particle or droplet spacing is related to the volume fraction by

$$\frac{\ell}{D} = \left(\frac{\pi}{6\alpha_d} \right)^{\frac{1}{3}} \quad (2.17)$$

¹This lattice arrangement does not represent the maximum volume fraction for uniform-size spheres.

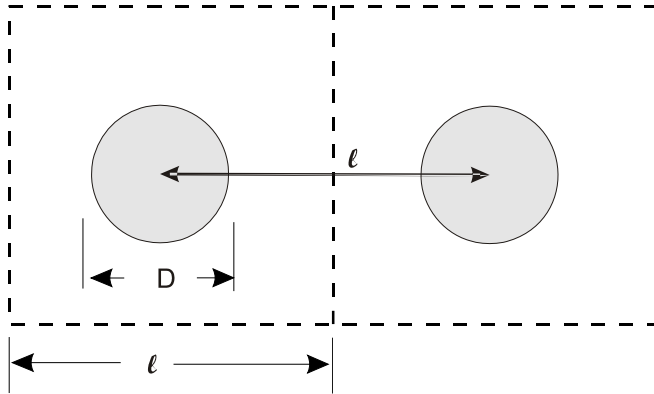


Figure 2.3: Interparticle spacing.

For a dispersed volume fraction of 10%, the spacing is 1.7 which would suggest that the dispersed phase elements are too close to be treated as isolated. That is, the mass, momentum and heat transfer for each element are influenced by the neighboring elements.

This equation can also be used to assess the size of the mixture sampling volume required to have insignificant variations of the mixture properties. The dimension of the sampling volume, $\Delta\ell_m$, with ΔN particles is

$$\frac{\ell_m}{D} = \left(\frac{\pi\Delta N}{6\alpha_d}\right)^{\frac{1}{3}} \quad (2.18)$$

With $\Delta N = 10^5$ to maintain fluctuations of less than 1%

$$\frac{\ell_m}{D} = 37\alpha_d^{-1/3} \quad (2.19)$$

Thus, for a field with 100 μm particles with a volume fraction of 0.01, the size of the sampling volume would be about 17 mm.

The volume fraction of the dispersed phase can be also expressed in terms of the dispersed phase mass concentration and material density ratio. The dispersed phase volume fraction is given by

$$\alpha_d = \frac{\bar{\rho}_d}{\rho_d} = \frac{\bar{\rho}_d}{\bar{\rho}_c} \frac{\bar{\rho}_c}{\rho_c} \frac{\rho_c}{\rho_d}$$

This equation can be written as

$$\alpha_d = C\alpha_c \frac{\rho_c}{\rho_d} \quad (2.20)$$

Using the relationship $\alpha_c = 1 - \alpha_d$ in Equation 2.20 yields

$$\alpha_d = \frac{\kappa}{1 + \kappa} \quad (2.21)$$

where $\kappa = C\rho_c/\rho_d$. Thus the distance between elements in a dispersed phase flow can be expressed as

$$\frac{\ell}{D} = \left(\frac{\pi}{6} \frac{1+\kappa}{\kappa}\right)^{\frac{1}{3}} \quad (2.22)$$

For most gas-particle and gas-droplet flows the ratio of material densities, ρ_c/ρ_d , is of the order of 10^{-3} so the interparticle spacing for flows with a mass ratio of unity is

$$\frac{\ell}{D} \sim 10$$

In this case, individual particles or droplets could be treated as isolated droplets with little influence of the neighboring elements on the drag or heat transfer rate. However, in fluidized beds, the mass ratio is large and the particles may be located less than 3 diameters apart so the particles cannot be treated as isolated. For slurry flow, the material density ratio can be the order of unity and the particle spacing is insufficient to treat the particles as isolated elements.

Example: A sand-water slurry has a concentration of 0.3. Find the particle volume fraction and the interparticle spacing.

Solution: The density ratio of sand to water is $2500/1000 = 2.5$. The value of κ is $0.3 \times 2.5 = 0.75$. Thus, the particle volume fraction is

$$\alpha_d = \frac{\kappa}{1 + \kappa} = 0.43$$

and the spacing ratio is

$$\frac{\ell}{D} = \left(\frac{\pi}{6} \frac{1+\kappa}{\kappa}\right)^{\frac{1}{3}} = 1.07$$

This value must be regarded as an estimate since the particle positions will not form a lattice configuration, which is assumed to derive Equation 2.22.

It is also of interest to estimate the size of the limiting volume, ΔV_{mo} , which would be needed to have a stationary average. If 10,000 particles were needed to form a stationary average, then the volume would be

$$\Delta V_{mo} = 10^4 \left(\frac{\ell}{D}\right)^3 D^3 \quad (2.23)$$

where $\Delta V_{mo} = L^3$. The size of the cube representing the volume becomes

$$L \sim 20 \left(\frac{\ell}{D}\right) D \quad (2.24)$$

Thus if the average spacing was 10 diameters and the element size was 100 microns, the size of the limiting volume would be a 2-cm cube. If this dimension is comparable to the system dimensions, then the dispersed phase cannot be regarded as a continuum in this flow system.

The significance of the volume required to have acceptably small variations is addressed in Chapters 6 and 9.

2.4 Response times

The response time of a particle or droplet to changes in flow velocity or temperature are important in establishing non-dimensional parameters to characterize the flow. The momentum response time relates to the time required for a particle or droplet to respond to a change in velocity. The equation of motion for a spherical particle in a gas is given by

$$m \frac{dv}{dt} = \frac{1}{2} C_D \frac{\pi D^2}{4} \rho_c (u - v) |u - v| \quad (2.25)$$

where v is the particle velocity and u is the gas velocity. Defining the dispersed phase Reynolds number (relative Reynolds number) as

$$Re_r = \frac{\rho_c D |u - v|}{\mu_c} \quad (2.26)$$

and dividing through by the particle mass gives

$$\frac{dv}{dt} = \frac{18 \mu_c}{\rho_d D^2} \frac{C_D Re_r}{24} (u - v) \quad (2.27)$$

where μ_c is the viscosity of the continuous phase. For the limits of low Reynolds numbers (Stokes flow), the factor $C_D Re_r / 24$ approaches unity. The other factor has dimensions of reciprocal time and defines the *momentum (velocity) response time*

$$\tau_V = \frac{\rho_d D^2}{18 \mu_c} \quad (2.28)$$

so the equation can be rewritten as

$$\frac{dv}{dt} = \frac{1}{\tau_V} (u - v) \quad (2.29)$$

The solution to this equation for constant u and an initial particle velocity of zero is

$$v = u(1 - e^{-t/\tau_V}) \quad (2.30)$$

Thus the momentum response time is the time required for a particle released from rest to achieve 63% ($\frac{e-1}{e}$) of the free stream velocity. The response time for a 100-micron water droplet in air at standard conditions is 30 ms. As one can see, the momentum response time is most sensitive to the particle size.

The *thermal response time* relates to the responsiveness of a particle or droplet to changes in temperature in the carrier fluid. The equation for particle temperature, assuming the temperature is uniform throughout the particle and radiative effects are unimportant, is

$$mc_d \frac{dT_d}{dt} = Nu \pi k_c D (T_c - T_d) \quad (2.31)$$

where Nu is the Nusselt number, c_d is the specific heat of the particle material and k'_c is the thermal conductivity of the continuous phase. Dividing through by the particle mass and specific heat gives

$$\frac{dT_d}{dt} = \frac{Nu}{2} \frac{12k'_c}{\rho_p c_d D^2} (T_c - T_d) \quad (2.32)$$

For low Reynolds numbers the ratio $Nu/2$ approaches unity. The other factor is the thermal response time defined as

$$\tau_T = \frac{\rho_d c_d D^2}{12k'_c} \quad (2.33)$$

Thus the equation for particle temperature becomes

$$\frac{dT_d}{dt} = \frac{1}{\tau_T} (T_c - T_d) \quad (2.34)$$

Once again, this is the time required for a particle to achieve 63% of a step change in the temperature of the carrier phase. The thermal response time for a 100-micron water droplet in air at standard conditions is 145 ms which is longer than the velocity response time.

The momentum and thermal response times are related through the properties of the fluid and the particles. Dividing the momentum response time by the thermal response time gives

$$\frac{\tau_V}{\tau_T} = \frac{\rho_d D^2}{18\mu_c} \frac{12k'_c}{\rho_d c_d D^2} = \frac{2}{3} \frac{k'_c}{\mu_c c_d} = \frac{2}{3} \frac{k'_c}{\mu_c c_c} \frac{c_c}{c_d}$$

where c_c is the specific heat of the fluid (if a gas, specific heat at constant pressure). Thus the relationship between response times becomes

$$\frac{\tau_V}{\tau_T} = \frac{2}{3} \frac{c_c}{c_d} \frac{1}{Pr}$$

where Pr is the Prandtl number. For gases, the Prandtl number is on the order of unity so the response times are of the same order of magnitude. For a liquid, the Prandtl number can be the order of 10^2 which means that velocity equilibrium is achieved much more rapidly than thermal equilibrium in a liquid.

Even though the above relations for the ratio of response times have been derived for low Reynolds number (Stokes flow), the ratio changes little for higher Reynolds numbers.

2.5 Stokes number

The *Stokes number* is a very important parameter in fluid-particle flows. The Stokes number related to the particle velocity is defined as

$$St_V = \frac{\tau_V}{\tau_F} \quad (2.35)$$

where τ_F is some time characteristic of the flow field. For example, the characteristic time for the flow through a venturi may be D_T/U where D_T is the throat diameter and U is the flow velocity. The Stokes number then becomes

$$St_V = \frac{\tau_V U}{D_T} \quad (2.36)$$

If $St_V \ll 1$, the response time of the particles is much less than the characteristic time associated with the flow field. Thus the particles will have ample time to respond to changes in flow velocity. Thus the particle and fluid velocities will be nearly equal (velocity equilibrium). On the other hand, if $St_V \gg 1$, then the particle will have essentially no time to respond to the fluid velocity changes and the particle velocity will be little affected during its passage through the venturi.

An approximate relationship for the particle/fluid velocity ratio as a function of the Stokes number can be obtained from the “constant lag” solution. The velocity ratio is expressed as $\phi = v/u$ and is assumed to vary slowly with time. Substituting this variable into the particle motion equation, Equation 2.29, one has

$$\phi \frac{du}{dt} = \frac{u}{\tau_V} (1 - \phi) \quad (2.37)$$

The carrier phase acceleration can be approximated by

$$\frac{du}{dt} \sim \frac{u}{\tau_F} \quad (2.38)$$

which, when substituted into Equation 2.37 yields

$$\phi St_V \sim (1 - \phi). \quad (2.39)$$

Finally solving for ϕ gives

$$\phi = \frac{v}{u} \sim \frac{1}{1 + St_V} \quad (2.40)$$

One notes that as $St_V \rightarrow 0$, the particle velocity approaches the carrier phase velocity and as $St_V \rightarrow \infty$, the particle velocity approaches zero. In this case the particle velocity is unaffected by the fluid.

2.6 Dilute versus dense flows

A dilute dispersed phase flow is one in which the particle motion is controlled by the fluid forces (drag and lift). A dense flow, on the other hand, is one in which the particle motion is controlled by collisions or continuous contact.

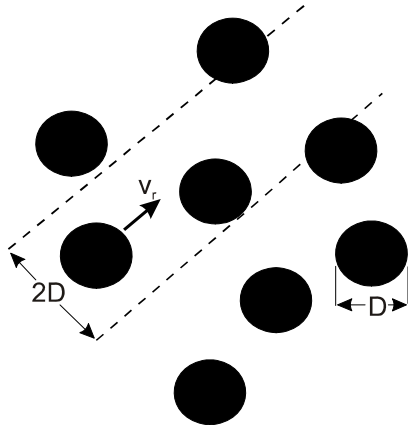


Figure 2.4: Particle-particle collisions.

A qualitative estimate of the dilute or dense nature of the flow can be made by comparing the ratio of momentum response time of a particle to the time between collisions. Thus the flow can be considered *dilute* if

$$\frac{\tau_V}{\tau_C} < 1 \quad (2.41)$$

where τ_C is the average time between particle-particle collisions because the particles have sufficient time to respond to the local fluid dynamic forces before the next collision. On the other hand, if

$$\frac{\tau_V}{\tau_C} > 1 \quad (2.42)$$

then the particle has no time to respond to the fluid dynamic forces before the next collision and the flow is *dense*.

There is no definitive scaling parameter that defines the boundary between dilute and dense flows. The time between collisions can be estimated from the classic equations for collision frequency. Consider a group of particles with uniform diameter D as shown in Figure 2.4 through which one particle is traveling with a relative velocity v_r with respect to the other particles. In a time δt , the one particle will intercept all the particles in tube with radius $2D$ and length $v_r \delta t$. The number of particles in this tube is

$$\delta N = n\pi D^2 v_r \delta t \quad (2.43)$$

where n is the number density of particles. Thus the collision frequency is

$$f_c = n\pi D^2 v_r \quad (2.44)$$

and the time between collisions is

$$\tau_C = \frac{1}{f_c} = \frac{1}{n\pi D^2 v_r} \quad (2.45)$$

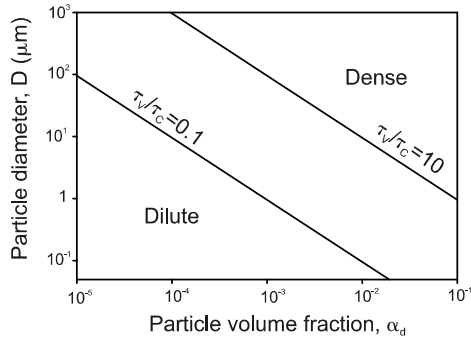


Figure 2.5: Ranges for dilute and dense flows for glass particles in air which with a fluctuating velocity magnitude of 1 m/s.

There are many mechanisms responsible for the relative velocity between particles such as local turbulence, carrier-flow velocity changes, particle-wall impact and so on. Abrahamson (1975) suggested that the particle collision frequency for particles with a mean fluctuation velocity of v' is

$$f_C = 4\sqrt{\pi}nD^2v' \quad (2.46)$$

With this collision frequency, the ratio of response times is

$$\frac{\tau_V}{\tau_C} = \frac{4n\sqrt{\pi}\rho_d D^4 v'}{18\mu_c} \quad (2.47)$$

Solving for the particle diameter gives

$$D = \frac{3\sqrt{\pi}\mu_c}{4\rho_d v' \alpha_d} \frac{\tau_V}{\tau_c} \quad (2.48)$$

The particle diameter as a function of particle volume fraction for τ_V/τ_C equal to 0.1 and 10 with glass particles in air and a fluctuation velocity of 1 m/s is shown in Figure 2.5. For this case it would appear that for a particle volume fraction of 10^{-4} the particle diameter would have to be less than 10 μm to ensure a dilute flow.

As stated above, there are many mechanisms that are responsible for particle-particle collisions so it is difficult to establish the limits of dilute and dense flows. However the magnitude of the particle volume fraction provides a general indicator for dilute or dense flows as suggested in Figure 2.6. The dense flow region is separated into collision-dominated and contact-dominated regimes. A *collision-dominated* flow is a flow in which the particles collide and rebound with a different trajectory. The time during contact is small compared with the time between collisions. A *contact-dominated* flow is one in which the particles are in continuous contact and the contact forces are responsible for particle motion. For particle volume fractions 0.001 or smaller, the

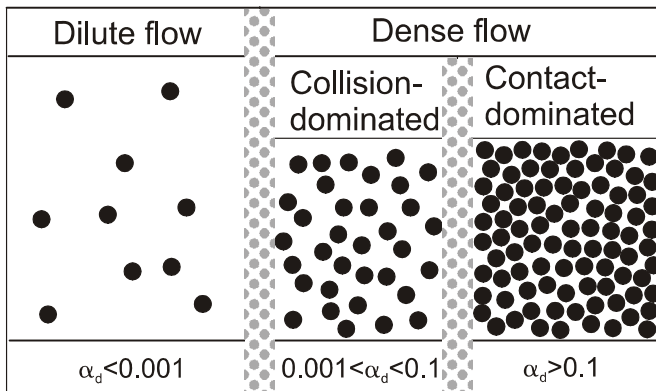


Figure 2.6: Flow regimes for dilute and dense flows.

flow can be regarded as dilute. An example of dilute flow would be gas-particle flows in an electrostatic precipitator or cyclone separator. The classic example of a collision-dominated flow is a fluidized bed in which the particles are suspended by the fluid and collide with each other and the walls of the vessel. The particle volume fraction for a collision-dominated flow may lie between particle volume fractions of 0.001 to 0.1. The limit for a contact-dominated flow would be a granular flow such as the flow of particles by gravity in a chute. However dense phase pneumatic transport is also a contact dominated flow. The particle volume fraction in this case may be 0.1 or greater. Of course, flow fields may include regions of all three flow types.

Each of these particle-flow regimes requires a different modeling approach for the dispersed phase.

2.7 Phase coupling

An important concept in the analysis of multiphase flows is coupling. If the flow of one phase affects the other while there is no reverse effect, the flow is said to be *one-way coupled*. If there is a mutual effect between the flows of both phases, then the flow is *two-way coupled*.

A schematic diagram of coupling is shown in Figure 2.7. The carrier phase is described by the density, temperature, pressure and velocity field. Of course, it may be important to include the concentrations of the gaseous species in a gas phase. The particle or droplet phase is described by concentration, size, temperature and velocity field. Coupling can take place through mass, momentum and energy transfer between phases. Mass coupling is the addition of mass through evaporation or the removal of mass from the carrier stream by condensation. Momentum coupling is the result of the drag force on the dispersed and continuous phase. Momentum coupling can also occur with

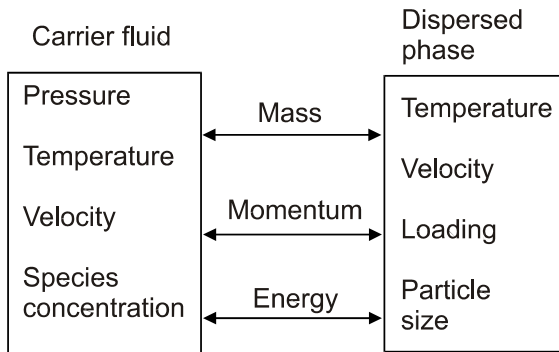


Figure 2.7: Schematic diagram of coupling effects.

momentum addition or depletion due to mass transfer. Energy coupling occurs through heat transfer between phases. Thermal and kinetic energy can also be transferred between phases owing to mass transfer. Obviously, analyses based on one-way coupling are straightforward. One must estimate through experience or parameter magnitude if two-way coupling is necessary.

The best way to illustrate coupling is through an example. Assume that hot particles were injected into a cool gas flowing in a pipe as shown in Figure 2.8. Also assume that the void fraction is near unity. One can calculate the trajectory and the corresponding thermal history of the particles by using the local velocity and temperature of the gas. Thus particle temperature will decrease toward the gas temperature while the particle velocity will increase toward the gas velocity. One-way coupling implies that the presence of the particles does not affect the gas flow field while the gas flow field is responsible for the change in particle temperature and velocity.

If the effect of the particles on the gas were included (two-way coupling), the temperature of the gas would increase and the gas density would decrease. This, in turn, would lead to an increased gas velocity to satisfy mass conservation. Thus the particle cooling rate would be reduced (smaller temperature difference) and the particles would be accelerated to a higher velocity. The acceleration of the particles together with the increased gas velocity would lead to a more negative pressure gradient. The coupling parameters provide a measure of the importance of coupling effects (Crowe, 1991).

2.7.1 Mass coupling

Suppose there are n droplets per unit volume in a box with side L as shown in Figure 2.9. Each droplet is evaporating at a rate \dot{m} . Thus the mass generated by the dispersed phase per unit time due to evaporation is

$$\dot{M}_d = nL^3\dot{m} \quad (2.49)$$

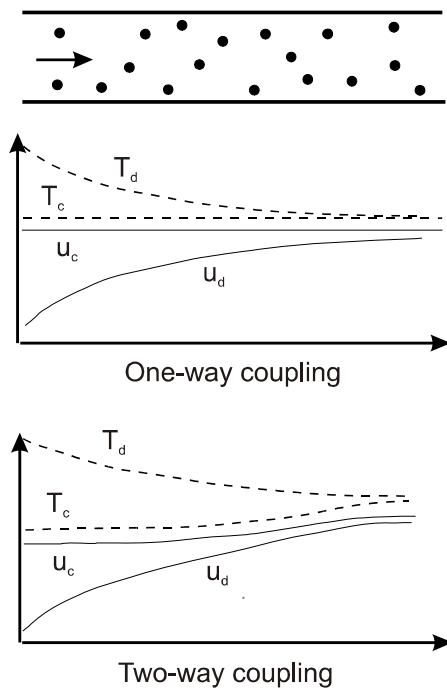


Figure 2.8: Illustration of one- and two-way coupling for droplets evaporating in a duct.

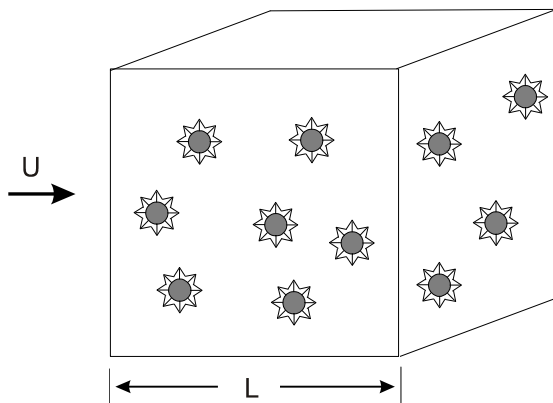


Figure 2.9: Droplets evaporating in a control volume.

The mass flux of the continuous phase through this volume is

$$\dot{M}_c \sim \bar{\rho}_c u L^2 \quad (2.50)$$

A *mass coupling parameter* is defined as²

$$\Pi_{\text{mass}} = \frac{\dot{M}_d}{\dot{M}_c} \quad (2.51)$$

If $\Pi_{\text{mass}} \ll 1$, then the effect of mass addition to the continuous phase would be insignificant and mass coupling could be neglected. This ratio can be expressed as

$$\frac{\dot{M}_d}{\dot{M}_c} \sim \frac{\bar{\rho}_d}{\bar{\rho}_c} \frac{L \dot{m}}{u m} \quad (2.52)$$

The ratio $\frac{\dot{m}}{m}$ scales as the reciprocal of a characteristic evaporation, burning or condensation time, τ_m , so the ratio in Equation 2.52 can be rewritten as

$$\Pi_{\text{mass}} \sim C \frac{L}{u \tau_m} \quad (2.53)$$

Taking L as some characteristic dimension of the system, this ratio can be used to assess the importance of mass coupling on the continuous phase flow. Notice that the ratio $\tau_m u / L$ can be regarded as the ratio of a time associated with mass transfer to a time characteristic of the flow. Thus the ratio can be thought of as the Stokes number associated with mass transfer

$$St_{\text{mass}} = \frac{\tau_m u}{L} \quad (2.54)$$

so the mass transfer parameter can be expressed as

$$\Pi_{\text{mass}} = \frac{C}{St_{\text{mass}}} \quad (2.55)$$

If the velocity of both phases is comparable, then the loading is a measure of the concentration and the mass coupling parameter can be evaluated as

$$\Pi_{\text{mass}} = \frac{Z}{St_{\text{mass}}}$$

Thus if the dispersed phase mass concentration (or loading) and the mass exchange rate of the dispersed phase are low (large τ_m and St_{mass}), then mass coupling can probably be neglected.

²Note that \dot{M}_d is the mass generated by the dispersed phase and not \dot{M}_d which is the mass flow of the dispersed phase.

2.7.2 Momentum coupling

The importance of momentum coupling can be assessed by comparing the drag force due to the dispersed phase with the momentum flux of the continuous phase. A *momentum coupling parameter* can be defined as

$$\Pi_{mom} = \frac{F_D}{Mom_c} \quad (2.56)$$

where F_D is the drag force due to the particles in the volume and Mom_c is the momentum flux through the volume. The drag associated with droplets in volume with side L is

$$F_D = nL^3 3\pi \mu_c D(u - v) \quad (2.57)$$

based on Stokes drag. The momentum flux of the continuous phase is given by

$$Mom_c = \bar{\rho}_c u^2 L^2 \quad (2.58)$$

The momentum coupling parameter can be expressed as

$$\Pi_{mom} = \frac{nmL}{\bar{\rho}_c u \tau_V} \left(1 - \frac{v}{u}\right) \quad (2.59)$$

where m is the mass of an individual element of the dispersed phase. However, the product nm is the bulk phase density of the dispersed phase, so the importance of momentum coupling can be assessed by the parameter

$$\Pi_{mom} \sim C \frac{L}{u \tau_V} \left(1 - \frac{v}{u}\right) \quad (2.60)$$

The velocity factor is not included since it depends on the dynamics of the flow field. As with mass transfer, the ratio $\tau_V u / L$ is the ratio of the time associated with momentum transfer to a time characteristic of the flow or the Stokes number for momentum transfer.

$$St_{mom} = \frac{\tau_V u}{L} \quad (2.61)$$

The momentum coupling parameter can be expressed as

$$\Pi_{mom} = \frac{C}{St_{mom}} \left(1 - \frac{v}{u}\right) \quad (2.62)$$

As the Stokes number approaches zero, the velocity of the dispersed phase approaches that of the continuous phase so the above equation develops an indeterminacy (0/0). However, using Equation 2.40 for the velocity ratio, the momentum coupling parameter becomes

$$\Pi_{mom} = \frac{C}{1 + St_{mom}} \quad (2.63)$$

which shows the correct limit as the Stokes number approaches zero. Momentum coupling effects become less important for small concentrations (loadings) and large Stokes numbers.

Example: Coal particles, 100 μm in diameter and with a material density of 1200 kg/m^3 , flow in an air stream into a venturi section with a 2-cm diameter throat. The throat velocity is 10 m/s, the loading is 1 and the air viscosity is $1.8 \times 10^{-5} \text{ Ns/m}^2$. Evaluate the magnitude of the momentum coupling parameter. Assume that the loading is a measure of the concentration.

Solution: The velocity response time of the coal particles is

$$\tau_V = \frac{\rho_d d^2}{18\mu_c} = 0.037 \text{ sec}$$

The Stokes number is

$$St_{mom} = \frac{\tau_V U}{L} = 18.5$$

The momentum coupling parameter is

$$\Pi_{mom} = \frac{Z}{St_{mom} + 1} = 0.051$$

One would estimate that the momentum coupling effects are unimportant.

2.7.3 Energy coupling

Energy coupling follows the same model as used for mass and momentum coupling. The significance of energy coupling can be assessed by comparing the heat transfer to (or from) the dispersed phase and the energy flux of the continuous phase. The *energy coupling parameter* is defined as

$$\Pi_{ener} = \frac{\dot{Q}_d}{\dot{E}_c} \quad (2.64)$$

Obviously if $\Pi_{ener} \ll 1$, then energy coupling is unimportant.

The heat transfer associated with the dispersed phase elements in volume L^3 is

$$\dot{Q}_d = nL^3\pi Nu k'_c D(T_d - T_c) \quad (2.65)$$

where Nu is the Nusselt number and k'_c is the thermal conductivity of the continuous phase. The energy flux of the continuous phase is

$$\dot{E}_c = \bar{\rho}_c u c_p T_c L^2 \quad (2.66)$$

where c_p is the specific heat at constant pressure of the continuous phase. The thermal coupling parameter can be expressed as

$$\Pi_{ener} \sim \frac{C}{St_T} \left(1 - \frac{T_c}{T_d}\right) \quad (2.67)$$

where St_T is the Stokes number based on the thermal response time ($St_T = u\tau_T/L$). As with the momentum coupling parameter, there is an indeterminacy as the Stokes number approaches zero. Using the same arguments as before, the energy coupling parameter can be expressed as³

$$\Pi_{ener} = \frac{C}{St_T + 1} \quad (2.68)$$

For gaseous flows, the momentum and thermal response times are of the same order so

$$\Pi_{mom} \sim \Pi_{ener}$$

and justification for one-way coupling for momentum usually justifies one-way coupling for energy transfer.

If most of the energy transfer in a system is associated with latent heat in the dispersed phase, there is another form of the energy coupling parameter which may be appropriate. The energy associated with change of phase in a volume L^3 is

$$\dot{E}_d = nL^3\dot{m}h_L \quad (2.69)$$

where h_L is the latent heat. Comparing this energy with the energy flux of the continuous phase results in the following energy coupling parameter

$$\Pi_L \sim C \frac{L}{u\tau_m} \frac{h_L}{c_p T_c} \quad (2.70)$$

which is the mass coupling parameter with an additional factor, $h_L/c_p T_c$. This factor can be large causing energy transfer due to phase change to be important even though mass transfer itself is unimportant. In many spray problems, the energy coupling due to phase change may be the only two-way coupling which must be included in developing an analysis for a gas-droplet flow.

2.8 Properties of an equilibrium mixture

A limiting case in the flow of a dispersed phase mixture is when the two phases are in dynamic and thermal equilibrium. This is the situation when the Stokes number approaches zero. In this situation, the mixture can be regarded as the flow of a single phase with modified properties.

When the flow is in dynamic equilibrium, the loading and mass ratio have the same value.

$$z = \frac{\bar{\rho}_d v}{\bar{\rho}_c u} = C \quad (2.71)$$

³Another factor should be included in the energy coupling parameter; namely, the ratio of the specific heat of the particle to the specific heat of the continuous phase, c_d/c_c . In general this ratio is of the order unity.

The mixture density can then be written as

$$\rho_m = \bar{\rho}_d + \bar{\rho}_c = \bar{\rho}_c(1+z) = \rho_c \alpha_c(1+z) \quad (2.72)$$

If the void fraction (α_c) were near unity, the mixture could be treated as a gas with a modified gas constant.

The enthalpy of the equilibrium mixture would be

$$h_m = (\bar{\rho}_c c_c + \bar{\rho}_d c_d)T = \bar{\rho}_c c_p(1 + z \frac{c_d}{c_p})T \quad (2.73)$$

where c_c is the specific heat of the carrier phase (specific heat at constant pressure for a gas) and c_d is the specific heat of the dispersed phase material. The specific heat of the mixture would be

$$c_m = c_c \left(\frac{1 + z \frac{c_d}{c_p}}{1 + z} \right) \quad (2.74)$$

These relationships are useful in establishing the limiting cases of dispersed phase flows as the Stokes number approaches zero.

2.9 Summary

The discrete nature of a dispersed phase flow requires the use of volume average properties such as bulk density. In addition to the parameters that characterize a single-phase flow, two additional non-dimensional parameters are important in fluid-particle flows: Stokes number and concentration (or loading). Dilute and dense refer to the importance of particle-particle interaction. Coupling refers to the property exchange between phases where a one-way coupled flow describes the condition where the carrier phase affects the dispersed phase but the dispersed phase has no influence on the continuous phase. The importance of coupling is quantified through the coupling parameters. A flow with a Stokes number approaching zero is characterized by velocity and thermal equilibrium and can be regarded as a single-phase flow with modified properties.

2.10 Exercises

2.1. A sand-water slurry has a solids volume fraction of 40%. Find the average ratio of the average interparticle spacing to the particle diameter.

2.2. The bulk density of water droplets in air at standard conditions (25°C and 1 atm) is 0.5 kg/m³. The droplets are monodisperse (uniform size) with a diameter of 100 μm. Find the number density, void fraction and the concentration.

2.3. Particles of uniform size are stacked in a packed bed such that each particle sits in the “pocket” of the four particles adjacent to it. This is a “body-centered” cubic configuration and represents the maximum void fraction. Find

the solids volume fraction. Evaluate the volume fraction for the “lattice” configuration.

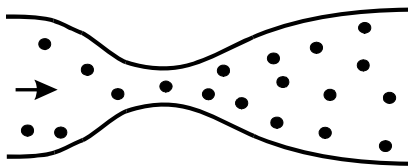
2.4. Droplets are released in a hot air stream and evaporate as they are convected with the flow as shown. The mass coupling parameter is small while the latent heat coupling parameter is large. Sketch the variation of the gas temperature, gas velocity, gas density and droplet velocity for both one-way and two-way coupling in the duct.



Problem 2.4

2.5. A pneumatic flow consists of particles conveyed by an air stream in a circular duct with diameter D_p . Ten percent of the particle mass impinges on the wall per diameter of length. The rebound velocity is $1/2$ the impingement velocity. The gas velocity is u and the average particle velocity is v . The loading is Z . The skin friction coefficient is C_f . Find an expression for the Darcy-Weisbach friction factor as a function of C_f , Z , v and u . Assume a void fraction of unity.

2.6. A gas-particle flow accelerates through a venturi as shown. Sketch the pressure distribution through the venturi for a small momentum and large momentum coupling parameter and explain the rationale for your choice.



Problem 2.6

2.7. Water droplets are evaporating in an air flow at standard pressure and temperature. The air flow rate is 1 kg/s and the water flow rate is 0.01 kg/s . The droplet velocity is 30 m/s and the droplet diameter is 100 microns . The pipe diameter is 5 cm . The evaporation time for a water droplet is given by

$$\tau_e = \frac{D^2}{\lambda}$$

where D is the droplet diameter and λ is the evaporation constant equal to $0.02 \text{ cm}^2/\text{s}$ for water droplets. Evaluate the mass coupling parameter and the energy coupling due to mass transfer (latent heat). Is mass coupling or energy coupling important?

2.8. Ice particles flow in a duct with air at 60°F . The ice particles are not completely melted at the end of the duct. The ice particles and air are in

dynamic equilibrium. Sketch how the air temperature, particle temperature, gas velocity and pressure would change along the duct assuming one-way and two-way coupling. Provide a physical argument explaining your results.

Chapter 3

Size Distribution

Droplet or particle size can be a very important parameter governing the flow of a dispersed two-phase mixture. For this reason, it is useful to have a basic knowledge of the statistical parameters relating to particle size distributions. For spherical particles or droplets, a measure of the size is the diameter. For nonspherical particles, an equivalent diameter must be selected to quantify the size (see Chapter 10).

The most general definition of the spread of the particle size distribution is monodisperse or polydisperse. A monodisperse distribution is one in which the particles are close to a single size, whereas polydisperse suggests a wide range of particle sizes. An approximate definition of a monodisperse distribution is one for which the standard deviation is less than 10% of the mean particle diameter.

3.1 Discrete size distributions

Let us begin by assuming that one has the task of determining the size distribution of a sample of particles. Assume that the sizes of many particles in the sample have been measured by some technique, such as photography. One would choose size intervals, ΔD , which would be large enough to contain many particles yet small enough to obtain sufficient detail. The representative size for the interval could be the diameter corresponding to the mid-point of the interval. The number of particles in each size interval would be counted, recorded, and divided by the total number of particles in the sample. The results would be plotted in the form of a histogram (bar chart) shown in Figure 3.1a. This is identified as the discrete number frequency distribution for the particle size¹. The ordinate corresponding to each size interval is known as the *number frequency*, $\tilde{f}_n(D_i)$. The sum of each bar is unity since the number

¹This frequency distribution is often referred to as the “probability density function” or “pdf.”

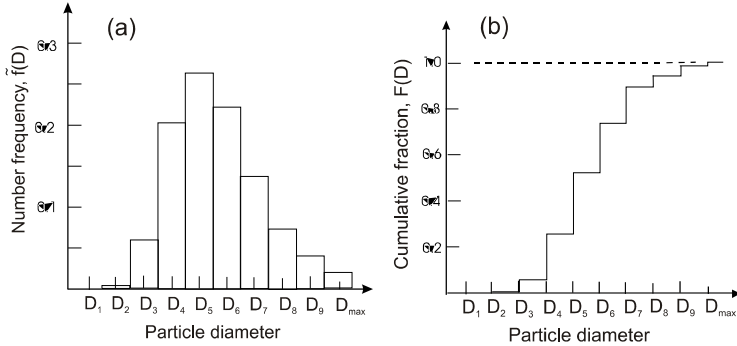


Figure 3.1: Particle size distribution: (a) Discrete number frequency distribution and (b) discrete cumulative number distribution.

in each size category has been divided by the total number in the sample. The distribution has been normalized; that is,

$$\sum_{i=1}^N \tilde{f}_n(D_i) = 1 \quad (3.1)$$

where N is the total number of intervals.

The *number-average* particle diameter in the distribution is obtained from

$$\overline{D}_n = \sum_{i=1}^N D_i \tilde{f}_n(D_i) \quad (3.2)$$

and the *number variance* is defined as²

$$\sigma_n^2 = \sum_{i=1}^N (D_i - \overline{D}_n)^2 \tilde{f}_n(D_i) \quad (3.3)$$

The variance is a measure of the spread of the distribution; a large variance implies a wide distribution of sizes. An alternate expression for the number variance is

$$\sigma_n^2 = \sum_{i=1}^N D_i^2 \tilde{f}_n(D_i) - \overline{D}_n^2 \quad (3.4)$$

which is sometimes more convenient for calculations. The *standard deviation* is the square root of the variance.

$$\sigma_n = \sqrt{\sigma_n^2}.$$

²The sum should be multiplied by the factor $N/(N-1)$ to account for the one degree of freedom removed by using the average diameter. However, for $N \gg 1$ we have $N/(N-1) \sim 1$.

Another approach to describing size distribution is to use the particle or droplet mass (or volume) in lieu of the number as the dependent variable. Thus the mass of each particle would be obtained, or inferred, from measurement and the fraction of mass associated with each size interval would be used to construct the distribution. This is known as the *discrete mass frequency distribution* and identified as $\tilde{f}_m(D_i)$. With this distribution, one can calculate the *mass-average* particle diameter and mass variance,

$$\overline{D}_m = \sum_{i=1}^N D_i \tilde{f}_m(D_i) \quad (3.5)$$

$$\sigma_m^2 = \sum_{i=1}^N (D_i - \overline{D})^2 \tilde{f}_m(D_i) = \sum_{i=1}^N D_i^2 \tilde{f}_m(D_i) - \overline{D}_m^2 \quad (3.6)$$

A very large number of particles or droplets have to be counted to achieve a reasonably smooth frequency distribution function. This is feasible with modern experimental techniques.

Another commonly used method to quantify particle size is the cumulative distribution, which is the sum of the frequency distribution. The *cumulative number distribution* associated with size D_k is

$$\tilde{F}_n(D_k) = \sum_{i=1}^{D_k} \tilde{f}_n(D_i) \quad (3.7)$$

The cumulative number distribution corresponding to the number frequency distribution shown in Figure 3.1a is illustrated in Figure 3.1b. The value of \tilde{F} is the fraction of particles with sizes less than or equal to D_k . Thus $\tilde{F}(100\mu) = 0.4$ means that 40% of the distribution has particles of 100 microns or less. Also, by definition, the value of cumulative distribution is unity for the largest particle size, provided the frequency distribution has been normalized. Both cumulative number and mass distributions can be generated from the corresponding frequency distributions.

3.2 Continuous size distributions

If the size intervals were made progressively smaller then, in the limit, as ΔD approaches zero, the continuous frequency function would be obtained.

$$f_n(D) = \lim_{\Delta D \rightarrow 0} \frac{\tilde{f}_n(D)}{\Delta D} \quad (3.8)$$

The number fraction of particles with diameters between D and $D + dD$ is given by the differential quantity $f_n(D)dD$. The variation of the frequency distribution with particle size is a continuous function as shown in Figure 3.2a. Similarly, the differential quantity $f_m(D)dD$ is the fraction of particle mass associated with sizes between D and $D + dD$.

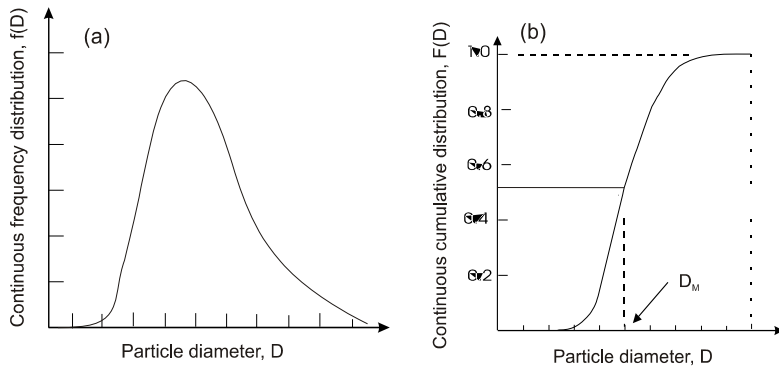


Figure 3.2: Continuous distributions: (a) Frequency size distribution and (b) cumulative size distribution.

If the distribution has been normalized, then the area under the frequency distribution curve is unity,

$$\int_0^{D_{max}} f(D)dD = 1 \quad (3.9)$$

where D_{max} is the maximum particle size.

The *continuous cumulative distribution* is obtained from the integral of the continuous frequency distribution,

$$F_n(D) = \int_0^D f_n(\lambda)d\lambda \quad (3.10)$$

and illustrated as the *S*-shaped curve in Figure 3.2b. By definition, the cumulative distribution approaches unity as the particle size approaches the maximum size.

The equivalent continuous frequency and cumulative distributions for mass (or volume) fraction are obvious.

In general, size data are not available as a continuous distribution. It is common practice to consider the data obtained for a discrete distribution as values on a curve for a continuous distribution and to proceed accordingly to evaluate the appropriate statistical parameters.

3.3 Statistical parameters

There are several parameters used to quantify distribution functions. Those used most commonly for dispersed phase flows are presented below.

3.3.1 Mode

The mode corresponds to the point where the frequency function is a maximum as shown in Figure 3.2a. The modes of the number and mass frequency distributions for a given sample will not be the same. A distribution which has two local maxima is referred to as a “bimodal” distribution.

3.3.2 Mean

The mean of a continuous distribution is analogous to the average of a discrete distribution. The mean is calculated from the frequency distribution by evaluating the integral,

$$\mu = \int_0^{D_{max}} D f(D) dD \quad (3.11)$$

Of course there is a number mean (μ_n) or mass mean (μ_m) size depending on the frequency function used.

3.3.3 Variance

The variance of the distribution is calculated from

$$\sigma^2 = \int_0^{D_{max}} (D - \mu)^2 f(D) dD \quad (3.12)$$

or by the equivalent expression,

$$\sigma^2 = \int_0^{D_{max}} D^2 f(D) dD - \mu^2 \quad (3.13)$$

Once again the variance can be based on the number or mass distribution for particle size. As previously mentioned, the variance is a measure of the spread of the distribution. The standard deviation is the square root of the variance and has dimensions of diameter.

A distribution can be classified as monodisperse if

$$\frac{\sigma}{\mu} < 0.1.$$

3.3.4 Median

The median diameter (D_M) corresponds to the diameter for which the cumulative distribution is 0.5. The median shown in Figure 3.2b (D_M) corresponds to the number median diameter (D_{nM}). The corresponding mass median diameter (D_{mM}) is determined from the cumulative mass distribution function.

3.3.5 Sauter mean diameter

The Sauter mean diameter (SMD) is encountered frequently in the spray and atomization literature. It is defined as

$$D_{32} = \frac{\int_0^{D_{max}} D^3 f_n(D) dD}{\int_0^{D_{max}} D^2 f_n(D) dD} \quad (3.14)$$

The Sauter mean diameter can be thought of as the ratio of the particle volume to surface area in a distribution which may have physical significance in some applications.

3.4 Frequently used size distributions

There are two size distribution functions that are frequently used to correlate particle or droplet size measurements. The characteristics of these distributions are discussed below.

3.4.1 Log-normal distribution

The log-normal distribution is frequently used to represent the size of solid particles. The log-normal distribution derives from the normal or Gaussian distribution which is defined as

$$f(x) = \frac{1}{\sqrt{2\pi}\sigma} \exp\left[-\frac{1}{2}\left(\frac{x-\mu}{\sigma}\right)^2\right] \quad (3.15)$$

where σ is the standard deviation and μ is the mean. This distribution is the well-known “bell-shaped” curve, shown in Figure 3.3a, which is symmetric about the mean and trails off to plus and minus infinity. The distribution has been normalized so the area under the curve is unity; that is,

$$\int_0^{\infty} f(x) dx = 1. \quad (3.16)$$

The log-normal distribution is obtained from the normal distribution by replacing the independent variable with the logarithm of the particle diameter. The number of particles with diameters between D and $D + dD$ is

$$f(D)dD = \frac{1}{\sqrt{2\pi}\sigma_o} \exp\left[-\frac{1}{2}\left(\frac{\ln D - \mu_o}{\sigma_o}\right)^2\right] \frac{dD}{D} \quad (3.17)$$

where, now, σ_o and μ_o are the standard deviation and the mean of the log normal distribution. The shape of the log-normal distribution is shown in Figure 3.3b. The limits of the log-normal distribution range from zero to infinity³.

³The independent variable $\ln D$ approaches $-\infty$ as D approaches zero.

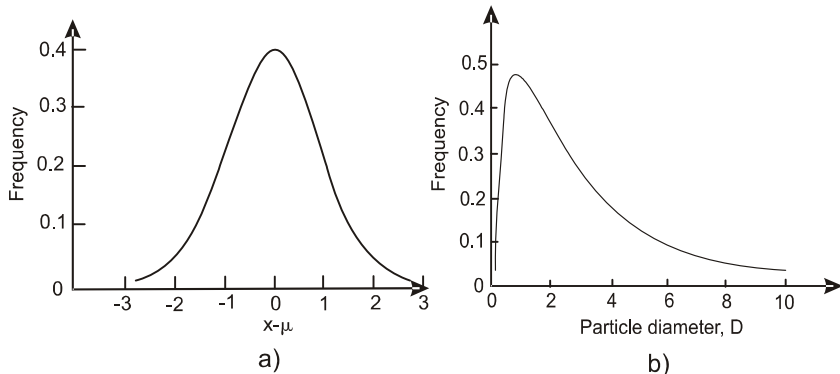


Figure 3.3: Frequency distributions: (a) normal (Gaussian) and (b) log-normal.

The corresponding cumulative number distribution is given by

$$F(D) = \frac{1}{\sqrt{2\pi}\sigma_o} \int_0^D \exp\left[-\frac{1}{2}\left(\frac{\ln D - \mu_o}{\sigma_o}\right)^2\right] \frac{dD}{D} \quad (3.18)$$

This integral can be expressed in terms of the error function

$$F(D) = \frac{1}{2} [1 + erf\left(\frac{\ln D - \mu_o}{\sqrt{2}\sigma_o}\right)] \quad (3.19)$$

where the error function is defined as

$$erf(t) = \frac{2}{\sqrt{\pi}} \int_0^t e^{-\lambda^2} d\lambda. \quad (3.20)$$

The number median diameter is defined as the particle diameter for which the cumulative distribution is 0.5, which corresponds to an error function of zero. The value of the error function is zero when its argument is zero. Thus, the mean of the log-normal distribution is the logarithm of the number median diameter, $\ln D_{nM}$, so the log-normal number frequency distribution can be conveniently expressed as

$$f_n(D) = \frac{1}{\sqrt{2\pi}\sigma_o} \exp\left[-\frac{1}{2}\left(\frac{\ln D - \ln D_{nM}}{\sigma_o}\right)^2\right] \frac{1}{D} \quad (3.21)$$

The corresponding mean for the log-normal mass frequency distribution is the logarithm of the mass median diameter, $\ln D_{mM}$, so

$$f_m(D) = \frac{1}{\sqrt{2\pi}\sigma_o} \exp\left[-\frac{1}{2}\left(\frac{\ln D - \ln D_{mM}}{\sigma_o}\right)^2\right] \frac{1}{D} \quad (3.22)$$

The variance of the log-normal distribution can be found by plotting the cumulative distribution on log-probability paper ($\ln D$ vs. probability) as

shown in Figure 3.4. The distribution plots as a straight line on these coordinates. One can also obtain σ_o from the relation

$$\sigma_o = \ln \frac{D_{84\%}}{D_M} \quad (3.23)$$

where $D_{84\%}$ is the diameter corresponding to the 84th percentile on the log-probability curve. This relation derives from the fact that the value of the cumulative distribution (Equation 3.19) is 0.84 when the argument of the error function is unity. The value for σ_o is the same for both the number and mass distributions.

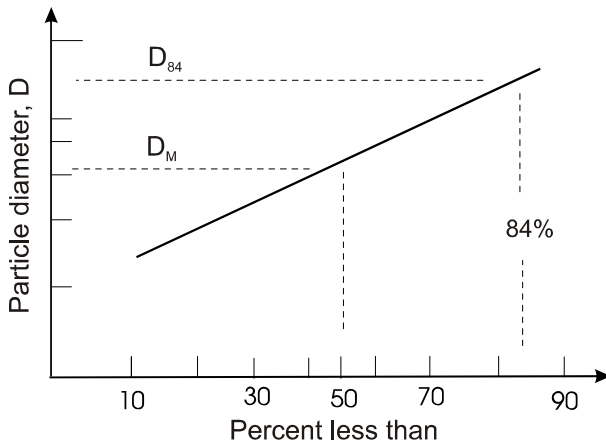


Figure 3.4: Log-normal distribution on log-probability coordinates.

A very useful relationship for manipulation of the log-normal distribution is

$$D_M^k e^{\sigma_o^2 k^2 / 2} = \frac{1}{\sqrt{2\pi}\sigma_o} \int_0^\infty D^k \exp\left[-\frac{1}{2}\left(\frac{\ln D - \ln D_M}{\sigma_o}\right)^2\right] \frac{dD}{D} \quad (3.24)$$

or

$$D_M^k e^{\sigma_o^2 k^2 / 2} = \int_0^\infty D^k f(D) dD \quad (3.25)$$

An example illustrating the use of this relationship is calculating the number mean of the distribution which is defined as

$$\mu_n = \int_0^\infty D f_n(D) dD \quad (3.26)$$

For this example, k in Equation 3.24 is unity so the number mean diameter is

$$\mu_n = D_{nM} e^{\sigma_o^2 / 2} \quad (3.27)$$

The number median diameter is related to the mass median diameter through the relation

$$D_{mM} = D_{nM} e^{3\sigma_o^2} \quad (3.28)$$

With information on the median diameter and σ_o , one can easily evaluate all the statistical parameters corresponding to the log-normal distribution by applying Equations 3.24 and 3.28.

Example: The mass median diameter of a log-normal distribution with $\sigma_o = 0.3$ is 200 microns. Find the standard deviation of the mass distribution.

Solution: From Equation 3.13, the variance is given by

$$\sigma^2 = \int D^2 f(D) dD - \mu^2$$

The value of the mass mean is

$$\mu_m = D_{mM} e^{\sigma_o^2/2}$$

The mass variance is

$$\sigma_m^2 = D_{mM}^2 (e^{2\sigma_o^2} - e^{\sigma_o^2})$$

so the standard deviation is

$$\sigma_m = 200 \sqrt{1.197 - 1.094} = 64.2 \mu m$$

An off-shoot of the log-normal distribution is the log-normal upper limit which is designed to set a maximum particle diameter as the upper limit of the distribution. This is accomplished by replacing $\ln D$ with the independent variable

$$\ln \left[\frac{aD}{D_{max} - D} \right]$$

where D_{max} is the maximum diameter and a is a constant to be selected which normalizes the distribution. Obviously, the modified independent variable approaches $-\infty$ as D approaches zero and $+\infty$ as D approaches D_{max} .

3.4.2 Rosin-Rammler distribution

The Rosin-Rammler distribution (Mugele & Evans, 1951) is frequently used for representing droplet size distributions in sprays. It is expressed in terms of the cumulative mass distribution in the form

$$F_m(D) = 1 - \exp \left[- \left(\frac{D}{\delta} \right)^n \right] \quad (3.29)$$

where δ and n are two empirical constants. One notes that $F_m(0) = 0$ and $F_m(\infty) = 1$.

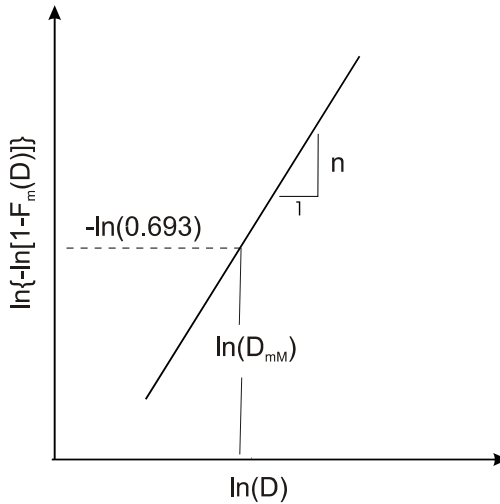


Figure 3.5: Rosin-Rammler distribution.

The empirical constants can be determined by plotting the cumulative distribution on log-log coordinates. Taking the logarithm of Equation 3.29 twice gives

$$\ln[-\ln(1 - F_m(D))] = n \ln D - n \ln \delta \quad (3.30)$$

Thus the slope of the line obtained by plotting $-\ln[1 - F_m(D)]$ versus diameter on log-log paper as shown in Figure 3.5 provides n . The parameter δ can be obtained using n and the mass median diameter with

$$\delta = \frac{D_{mM}}{0.693^{\frac{1}{n}}} \quad (3.31)$$

The mass frequency distribution is obtained by taking the derivative of the cumulative distribution,

$$f_m(D) = \frac{dF_m}{dD} = e^{-(\frac{D}{\delta})^n} \frac{n}{\delta} \left(\frac{D}{\delta}\right)^{n-1} \quad (3.32)$$

A very useful function for evaluating the statistical parameters for the Rosin-Rammler distribution is the gamma function which is defined as

$$\Gamma(t) = \int_0^\infty e^{-\lambda} \lambda^{t-1} d\lambda \quad (3.33)$$

It can be shown that

$$\int_0^\infty n D^\alpha \left(\frac{D}{\delta}\right)^{n-1} \exp\left[-\left(\frac{D}{\delta}\right)^n\right] d\left(\frac{D}{\delta}\right) = \delta^\alpha \Gamma\left(\frac{\alpha}{n} + 1\right) \quad (3.34)$$

so

$$\delta^\alpha \Gamma\left(\frac{\alpha}{n} + 1\right) = \int_0^\infty D^\alpha f_m(D) dD \quad (3.35)$$

An example application of this equation is evaluating the mass mean diameter which is given by

$$\mu_m = \int_0^\infty D f_m(D) dD = \int_0^\infty D e^{-(\frac{D}{\delta})^n} \frac{n}{\delta} \left(\frac{D}{\delta}\right)^{n-1} dD \quad (3.36)$$

Setting α equal to unity in Equation 3.34 gives

$$\mu_m = \delta \Gamma\left(\frac{1}{n} + 1\right) \quad (3.37)$$

Having n , one can obtain the value for the gamma function from a mathematics table.

Example: A Rosin-Rammler distribution has a mass median diameter of 120 microns with a n -value of 2.0. Find the mass mean of the distribution.

Solution: First we must evaluate δ from

$$\delta = \frac{D_{mM}}{0.693^{\frac{1}{n}}} = \frac{120}{0.693^{\frac{1}{2}}} = 144 \mu m$$

The mass mean is

$$\mu_m = \delta \Gamma\left(\frac{1}{n} + 1\right) = 144 \Gamma\left(\frac{3}{2}\right) = 128 \mu m$$

The Rosin-Rammler distribution is a special case of the more general Nukiyama-Tanasawa distributions, descriptions of which are available through other sources.

3.4.3 Log-hyperbolic distribution

In some studies with sprays, it has been shown that neither the log-normal nor the Rosin-Rammler distributions fit the data sufficiently well. Two droplet size distributions fitted with a Rosin-Rammler distribution may have the same parameters but the actual distribution may be quite different.

One of the shortcomings of both the log-normal and Rosin-Rammler distributions is the representation of the tails of the distribution (values of the frequency function for large and small values of the independent variable). Another distribution which is a better fit for the tails of the distributions is the log-hyperbolic distribution proposed by Barndorff-Nielsen (1977). The form of the frequency function is

$$f = A \exp \left[-\alpha \sqrt{\delta^2 + (x - \mu)^2} + \beta(x - \mu) \right] \quad (3.38)$$

where α, β, δ and μ are fitting parameters and x is the random variable which, in this case, is the logarithm of the particle diameter. The coefficient A is a normalization factor which is related to the parameters by

$$A = \frac{\sqrt{\alpha^2 - \beta^2}}{2\alpha\delta K_1(\delta\sqrt{\alpha^2 - \beta^2})}$$

where K_1 is the third-order Bessel function of the third kind.

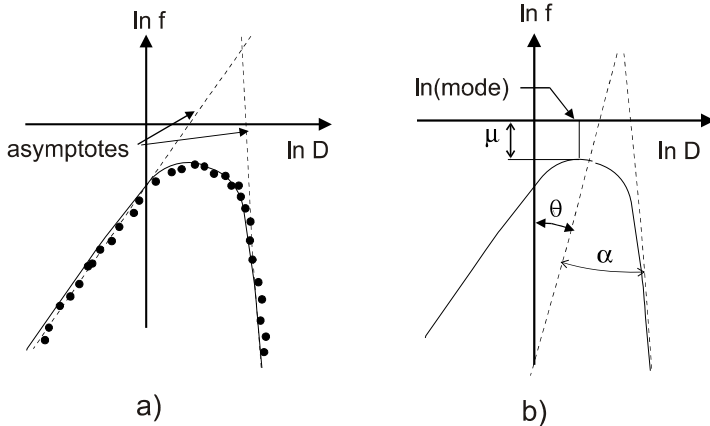


Figure 3.6: Log-probability distribution: (a) Frequency function, (b) fitted with rotated parabola.

The logarithm of the frequency function is

$$\ln f = \ln A - \alpha\sqrt{\delta^2 + (x - \mu)^2} + \beta(x - \mu) \quad (3.39)$$

which is the equation of a hyperbola. For $(x - \mu)/\delta < 0$ the slope of the asymptote is $\alpha + \beta$, while for $(x - \mu)/\delta > 0$ the slope of the asymptote is $-\alpha + \beta$. Thus the logarithm of the frequency data can be plotted versus $\ln D$ as shown in Figure 3.6a and the slopes of the asymptotes can be measured to find α and β . The parameter μ is the mode of the distribution. The value for δ must be obtained from some fitting procedure.

One of the problems with the log-hyperbolic distribution is the stability of the parameters. If the tails of the distribution are not long enough to yield accurate values of slopes of the asymptotes, there can be an instability in the parameters; that is, the parameters are not unique so the same distribution can be matched by various combinations of the parameters. A method to circumvent this problem has been proposed by Xu et al. (1993). The data are fitted with a hyperbola which is rotated at an angle θ with respect to the y-axis as shown in Figure 3.6b. The inclination angle θ , the slope of the asymptotes with respect to the inclination angle (which will now be the same)

and the mode are sufficient to define the distribution. This is referred to as the “three-parameter log-hyperbolic distribution.”

3.5 Summary

The distribution of particle or droplet sizes are usually formulated in terms of particle number or particle mass and the parameters used to describe the distribution are the mean, median, mode and variance. Example distribution functions are the traditional log-normal and Rosin-Rammler distributions and the more recently developed log-hyperbolic distribution. There are numerous other distributions which have been developed for specific purposes. The reader is referred to the abundant literature in this area.

3.6 Exercises

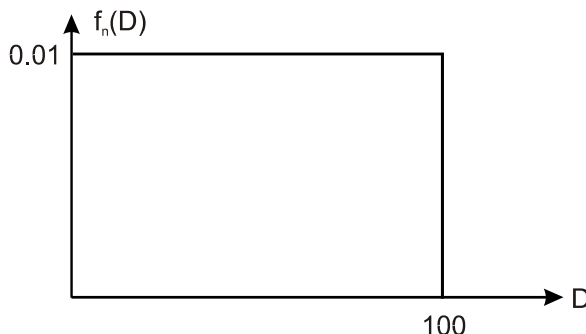
3.1. A measurement of a particle size distribution indicates that the distribution is log-normal with a mass median diameter of $60 \mu\text{m}$ and a slope (σ_0) of 0.3. Find the following parameters:

1. number median diameter
2. Sauter mean diameter
3. mass mean diameter
4. mode of mass distribution.

3.2. Data taken for a size distribution of droplets produced by an atomizer indicate that the data fit the Rosin-Rammler distribution with $n=1.8$ and a mass median diameter of $120 \mu\text{m}$. Evaluate the following statistics:

1. the parameter δ for the distribution
2. the mass mean diameter and the mass variance for the distribution
3. the Sauter mean diameter.

3.3. The continuous number frequency distribution is uniform as shown. The maximum diameter is $100 \mu\text{m}$.



Problem 3.3

1. Find the mean, standard deviation and the Sauter mean diameter.
 2. Derive an expression for the cumulative distribution and the number mean diameter.
 3. Derive an expression for the mass frequency distribution and find the mode, mean and standard deviation.
 4. Obtain an expression for the mass cumulative distribution and find the mass median diameter.
- 3.4. The following data were obtained for the cumulative mass distribution of a particle sample.

% less than	D (microns)
94	50
90	40
76	32
60	25.4
42	20
26	16
14	12.7
7	10
3	8

Carry out the following procedures:

1. Plot the data on log-probability paper and find D_{mM} and σ_0 .
2. Calculate D_{nM} and SMD (Sauter mean diameter).
3. Find the standard deviation for both the mass and number distribution. Is the distribution monodisperse?

3.5. The data for a Rosin-Rammler distribution show that $n = 2$ and the mass median diameter is 20 microns.

1. Show that

$$\int_0^\infty n D^\alpha \left(\frac{D}{\delta}\right)^{n-1} \exp\left(-\frac{D}{\delta}\right)^n d\left(\frac{D}{\delta}\right) = \delta^\alpha \Gamma\left(\frac{\alpha}{n} + 1\right)$$

2. Using the expression generated above, find an expression for the mass variance of the Rosin-Rammler distribution in the form $\sigma_m^2 = \delta^2 f[\Gamma(n)]$ and evaluate for the distribution parameters.
3. Given that

$$f_n(D) = \frac{\frac{f_m(D)}{D^3}}{\frac{\int_0^\infty f_m(D)dD}{D^3}}$$

show that

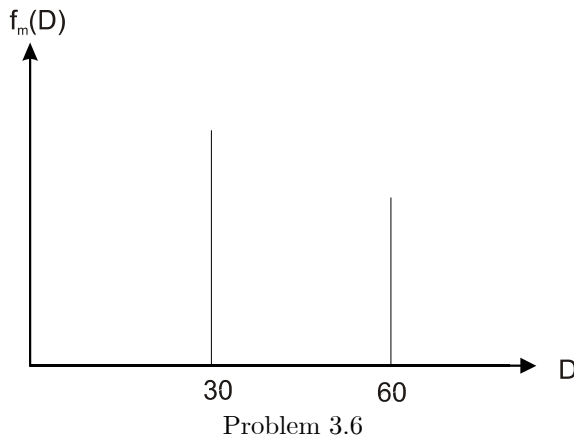
$$f_n(D) = \frac{n}{\delta} \left(\frac{D}{\delta}\right)^{-3} \frac{\exp[-(\frac{D}{\delta})^n]}{\Gamma(1 - \frac{3}{n})} \left(\frac{D}{\delta}\right)^{n-1}$$

for the Rosin-Rammler distribution.

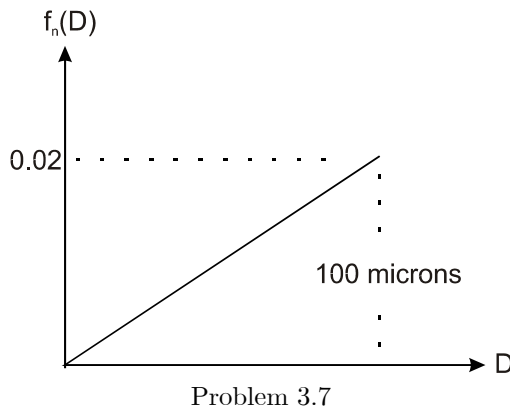
Also find an equation for the Sauter mean diameter in the form $SMD = \delta f[\Gamma(n)]$ and evaluate for the above parameters.

3.6. A bimodal distribution consists of two peaks as shown. Forty percent of the mass of the particles is associated with 60 microns and the remaining 60% of the mass is associated with 30 micron particles.

Find the number average and the mass average diameters and the corresponding standard deviations.



3.7. The continuous number frequency distribution for a particle sample is shown in the following figure.



Find:

1. the number mean diameter, Sauter mean diameter and the number variance,
2. the mass mean and standard deviation, and
3. the number median and mass median diameter.

3.8. Show that

$$D_m^k \exp\left(\frac{\sigma_0^2 k^2}{2}\right) = \frac{1}{\sqrt{2\pi}\sigma_0} \int_0^\infty D^k \exp\left[-\frac{1}{2}\left(\frac{\ln D - \ln D_m}{\sigma_0}\right)^2\right] \frac{dD}{D}$$

3.9. Using the definition

$$f_n(D) = \frac{D^3 f_n(D)}{\int_0^\infty D^3 f_n(D) dD}$$

find the relationship

$$\frac{D_{nm}}{D_{mm}} = f(\sigma_0)$$

3.10. The results of a digital image analysis of a particle sample yield the frequency distribution of the particle cross-sectional area. The following results for a sample were obtained

$f(D)$	A, m^2
0.2	0.286×10^{-8}
0.3	0.785×10^{-8}
0.5	1.13×10^{-8}

Assume each area is the projected area of a spherical particle. Find

1. the number averaged diameter
2. the mass averaged diameter
3. the Sauter mean diameter.

3.11. The following data were obtained with a Coulter Counter. The population refers to the number of particles of the given diameter.

Bin No.	Diameter (μm)	Population
1	1.75	0
2	2.21	3797
3	2.78	3119
4	3.51	2522
5	4.42	1878
6	5.75	1396
7	7.02	850
8	8.58	523
9	11.15	297
10	14.0	179
11	17.7	93
12	22.3	18
13	28.1	2

Form the cumulative number distribution and plot on log-probability paper. Find the

1. number median diameter,
2. mass median diameter, and
3. Sauter mean diameter.

3.12. The following data are obtained from the measurement of a particle size distribution. The particles are spherical.

D (microns)	Number
10	20
20	50
30	73
40	62
50	33
60	18
70	5

Find the mass and number averaged diameters. Estimate the number and mass median diameters. You may want to use a spread sheet or write a small computer program to address this problem.

3.13. Show for the log-hyperbolic distribution that the mode of the distribution is given by

$$x = \ln D = \mu + \frac{\beta\delta}{\sqrt{\alpha^2 - \beta^2}}$$

and the value of the frequency function at the mode is

$$f = A \exp(-\delta \sqrt{\alpha^2 - \beta^2})$$

Chapter 4

Particle-Fluid Interaction

Particle-fluid interaction refers to the exchange of properties between phases and is responsible for coupling in dispersed phase flows. The conservation equations for single particles or droplets are introduced. The phenomena responsible for mass, momentum and energy transfer between phases are then presented. The purpose of this chapter is not to provide an extensive review of fluid-particle interaction but to present some of the basic ideas and observations. Reference to books by Clift et al. (1978), Michaelides (2006) and the *Multiphase Flow Handbook* [Crowe (ed.), 2006] as well as review papers in the literature provide more details.

4.1 Single-particle equations

The equations for the mass, velocity and temperature of a given mass (system) are¹

$$M = \text{const} \quad (4.1\text{a})$$

$$F_i = \frac{d}{dt}(Mu_i) \quad (4.1\text{b})$$

$$T_i = \frac{d}{dt}[M\epsilon_{ijk}r_j u_k] \quad (4.1\text{c})$$

$$\frac{dE}{dt} = \dot{Q} - \dot{W} \quad (4.1\text{d})$$

where M is the system mass, u_i is the velocity with respect to an inertial reference frame, F_i is the force on the system, T_i is the torque acting on the system, E is the total energy (kinetic plus internal), \dot{Q} is the heat transfer rate to the system and \dot{W} is the work per unit time done by the system on the surroundings. Equation 4.1a is simply the definition of a system. Obviously, Equations 4.1b and 4.1c are Newton's second law and Equation 4.1d is the

¹Index notation is used for the vectors. The cross product $\mathbf{r} \times \mathbf{u}$ is expressed as $\epsilon_{ijk}r_j u_k$.

first law of thermodynamics for a closed system. These equations, referred to as the Lagrangian form of the equations, would suffice to calculate the properties of a system with a constant mass, however, they are not appropriate for a droplet which may be evaporating or condensing or a coal particle which is undergoing devolatilization. In this case, the Reynolds transport theorem is needed to account for the change in mass. A detailed derivation of the Reynolds transport equation applicable to particles with mass transfer (droplets) is provided in Appendix A.

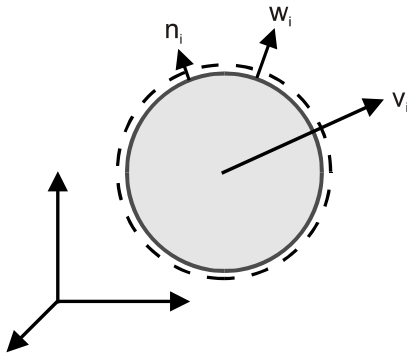


Figure 4.1: Droplet moving with respect to coordinate system.

Consider the droplet shown in Figure 4.1. The droplet has a mass m and the center of mass of the droplet is moving with a velocity v_i with respect to an inertial reference frame. A control surface surrounds the droplet and is adjacent to the surface of the droplet so it assumes the instantaneous surface area of the droplet. The vector n_i is the unit outward normal vector from the control surface. The velocity of the gases through the control surface with respect to the control surface is w_i .

4.1.1 Continuity equation

The droplet continuity equation simply states that the rate of change of droplet mass is the negative value of the mass efflux through the droplet surface,

$$\frac{dm}{dt} = -\rho_s w S \quad (4.2)$$

where S is the area of the control (droplet) surface and $\rho_s w$ is the average mass flux over the surface due to evaporation or condensation.

4.1.2 Translational momentum equation

The formal statement of the momentum equation is that the rate of change of momentum within the control volume plus the net efflux of momentum through the control surface is equal to the forces acting on the system (both surface and body forces). The final result (see Appendix A) is

$$F_i = m \frac{dv_i}{dt} + \int_{cs} \rho_s (\dot{r} n_i + w_i) w_i n_i dS \quad (4.3)$$

where \dot{r} is the regression rate of the surface and the integral is taken over the control surface. Index notation has been used for the vectors. The last term represents the thrust on the droplet due to a momentum mass flux from the droplet surface. If all the mass were to come off the droplet in one direction, the droplet would develop a thrust analogous to a rocket motor. However, if the momentum flux is uniform over the droplet surface, which is usually a good approximation, then

$$\dot{r} n_i + w_i = (\dot{r} + w) n_i = w' n_i \quad (4.4)$$

and the thrust term becomes zero

$$\int_{cs} (\dot{r} n_i + w_i) \rho_s w_i n_i dS = w' w \rho_s \int_{cs} n_i dS = 0 \quad (4.5)$$

so the droplet momentum equation simplifies to

$$F_i = m \frac{dv_i}{dt} \quad (4.6)$$

where m is the instantaneous mass of the droplet.

The forces acting on the droplet are subdivided into body forces and surface forces. The *body force* is a force acting on the mass of the droplet, such as gravity, and the *surface force* is due to drag and lift which represent a momentum coupling between the two phases.

4.1.3 Angular momentum equation

The conservation equation for the angular momentum states that the rate of change of angular momentum within the control volume plus the net efflux of angular momentum through the control surfaces is equal to the torque acting on the particle. If the particle is spherical, the mass efflux from the surface contributes no torque so the equation for rotation (see Appendix A) becomes

$$T_i = I \frac{d\omega_{d,i}}{dt} \quad (4.7)$$

where I is the instantaneous moment of inertia about an axis of symmetry and $\omega_{d,i}$ is the particle rotation vector.

4.1.4 Energy equation

The energy of a droplet consists of the external (kinetic energy) and the internal energy as well as the energy associated with surface tension. The heat transfer term includes both convective and radiative heat transfer. The work term includes the flow work due to the efflux of fluid through the control surface as well as the work associated with the forces on the droplet. The detailed derivation of the droplet energy equation is provided in Appendix A. The final result is

$$mc_d \frac{dT_d}{dt} = \dot{Q} + \dot{m}(h_{cs} - h_d + \frac{w'w'}{2}) \quad (4.8)$$

where \dot{m} is the rate of mass change of the droplet, h_{cs} is the enthalpy of the vapor at the control surface and w' is the efflux velocity through the droplet surface with respect to the droplet center. The enthalpy difference $h_{cs} - h_d$ is the enthalpy associated with the change of phase at the droplet temperature or, simply, the latent heat of vaporization. The kinetic energy associated with the efflux velocity is typically very small compared to the enthalpy change so it can be neglected. The final form of the energy equation reduces to

$$mc_d \frac{dT_d}{dt} = \dot{Q} + \dot{m}h_L \quad (4.9)$$

where h_L is the latent heat and c_d is the specific heat of the droplet material. During a change in phase, when the droplet temperature remains constant at the saturation temperature, the heat transfer is just sufficient to balance the energy required for the change of phase.

4.2 Mass coupling

Mass coupling can occur through a variety of mechanisms such as evaporation, condensation or chemical reaction.

4.2.1 Evaporation or condensation

Evaporation or condensation is the transport of the droplet vapor to or from the droplet surface and the change of phase at the surface. The driving force for evaporation is the difference in concentration of the droplet vapor between the droplet surface and the free stream. In general it is assumed that the mixture is a binary mixture consisting of the carrier gas and the vapor of the droplet liquid. For example, a water droplet evaporating in a nitrogen stream would be a binary mixture of water vapor and nitrogen. It is common practice to consider air as a single species and to regard water vapor in air as a binary mixture.

By *Fick's law* the mass flux at the surface of an evaporating or condensing droplet in a binary mixture is

$$\rho_s w = -D_v \frac{\partial \rho_A}{\partial n} \quad (4.10)$$

where n is the coordinate normal to and away from the surface, ρ_A is the mass density of species A (one species of the binary mixture) and D_v is the diffusion coefficient. This equation can be expressed as

$$\rho_s w = -\rho_s D_v \frac{\partial(\rho_A/\rho_s)}{\partial n} = -\rho_s D_v \frac{\partial \omega_A}{\partial n} \quad (4.11)$$

where ω_A is the mass fraction of species A in the mixture².

For a droplet of diameter D the gradient in mass fraction must be proportional to the mass fraction difference between the surface and the freestream and inversely proportional to the droplet diameter,

$$\rho_s w = -\rho_s D_v \frac{\partial \omega_A}{\partial n} \sim \rho_c D_v \frac{\omega_{A,s} - \omega_{A,\infty}}{D} \quad (4.12)$$

where $\omega_{A,s}$ is the mass fraction of species A (vapor corresponding to the droplet liquid) at the droplet surface and $\omega_{A,\infty}$ in the freestream. The density ρ_c is the representative density and may be the average density between the surface and the freestream. The average properties between the surface and the freestream are called the *film conditions*. Except for very high evaporation rates, the density change through the boundary layer is small so ρ_c could be considered the gas density in the freestream (continuous phase). The sign on the difference in mass fraction between the surface and freestream indicates evaporation or condensation. For evaporation $\omega_{A,s} > \omega_{A,\infty}$ so $\rho_s w > 0$.

From Equation 4.2 the mass rate of change of the droplet due to mass flux through the control surface is

$$\frac{dm}{dt} = -\rho_s w S$$

Thus the rate of change of droplet mass should be proportional to

$$\frac{dm}{dt} \sim \pi D^2 \rho_c D_v \frac{\omega_{A,\infty} - \omega_{A,s}}{D} \quad (4.13)$$

The constant of proportionality is the *Sherwood number* so the equation becomes

$$\frac{dm}{dt} = Sh \pi D \rho_c D_v (\omega_{A,\infty} - \omega_{A,s}) \quad (4.14)$$

The Sherwood number is 2 for a droplet which is evaporating with radial symmetry (no forced or free convection effects).

²The development here is based on the mass fraction of species A being much less than unity, which is the situation for typical evaporation problems. More general information of mass transfer can be found in standard textbooks (Bird et al., 1960).

The mass fraction of the vapor at the droplet surface can be evaluated if the droplet temperature is known. The partial pressure of the vapor at the surface is the saturation pressure corresponding to the droplet temperature. The mole fraction of the droplet vapor at the surface is the ratio of the partial pressure to the local pressure

$$\frac{n_A}{n_M} = \frac{p_A}{p} \quad (4.15)$$

The corresponding vapor mass fraction is

$$\omega_{A,s} = \frac{\mathcal{M}_A}{\mathcal{M}_M} \frac{p_A}{p} \quad (4.16)$$

where \mathcal{M}_A is the molecular weight of the species A and \mathcal{M}_M is the molecular weight of the mixture. If the mole fraction of species A is small, then the molecular weight of the mixture is essentially the molecular weight of the carrier phase. For water vapor in air

$$\frac{\mathcal{M}_A}{\mathcal{M}_M} \sim \frac{18}{29}$$

The effect of a relative velocity between the droplet and the conveying gas is to increase the evaporation or condensation rate. This effect is usually represented by the *Ranz-Marshall* correlation³

$$Sh = 2 + 0.6Re_r^{0.5} Sc^{0.33} \quad (4.17)$$

where Re_r is the *relative Reynolds number* based on the relative speed between the droplet and the carrier gas

$$Re_r = \frac{D|u_i - v_i|}{\nu_c}$$

where u_i and v_i are the velocity vectors of the continuous and dispersed phases, respectively, and Sc is the *Schmidt number* defined by

$$Sc = \frac{\nu_f}{D_v}$$

where ν_f is the kinematic viscosity of the mixture at the film conditions. One notes that the Sherwood number reduces to the stagnant flow case as the Reynolds number approaches zero.

The Ranz-Marshall correlation holds for Reynolds numbers from 2 to 200. Rowe et al. (1965) report that a better correlation for Sherwood number is provided if 0.69 is used in lieu of 0.6 in Equation 4.17 for Reynolds numbers from 30 to 2000. Other correlations for the Sherwood number are found in Michaelides (2006).

³This correlation was originally proposed by Frössling (1938) but commonly attributed to Ranz and Marshall (1952).

The evaporation of a droplet is sometimes represented by the D^2 - law which states that the square of the droplet diameter varies linearly with time. This can be shown by application of the evaporation equation which can be rewritten as

$$\frac{dm}{dt} = \frac{d}{dt}(\rho_d \frac{\pi D^3}{6}) = \frac{\pi}{2} \rho_d D^2 \frac{dD}{dt} \quad (4.18)$$

Thus

$$\frac{\pi}{2} \rho_d D^2 \frac{dD}{dt} = Sh\pi D \rho_c D_v (\omega_{A,\infty} - \omega_{A,s}) \quad (4.19)$$

or

$$D \frac{dD}{dt} = -\frac{2Sh\rho_c D_v}{\rho_d} (\omega_{A,s} - \omega_{A,\infty}) \quad (4.20)$$

Taking the right side as constant and integrating gives

$$D^2 = D_o^2 - \lambda t \quad (4.21)$$

where λ is the *evaporation constant* and is equal to

$$\lambda = \frac{4Sh\rho_c D_v}{\rho_d} (\omega_{A,s} - \omega_{A,\infty}) \quad (4.22)$$

This form of the evaporation equation has been used extensively in the past. Data for droplet evaporation and combustion have been frequently reported as a value for λ . Obviously λ will not be a constant in a flow with changing freestream conditions but for many situations the approximation may be adequate.

The lifetime or evaporation time of a droplet is obtained by setting $D = 0$ resulting in

$$\tau_m = \frac{D_o^2}{\lambda} \quad (4.23)$$

A model has been developed for droplets evaporating in clusters (Bellan and Harstad, 1987). They find that in dense clusters, evaporation occurs primarily due to diffusional effects ($Sh \sim 2$), while convection plays the dominant role in very dilute clusters.

4.2.2 Mass transfer from slurry droplets

The mass transfer from a slurry droplet represents an important technological problem. For example, food products to be dried (such as powdered milk) consist of water and solids. These slurries are atomized and sprayed into a hot gas stream where the water is driven off and the dried products are collected. The droplet material can be thought of as a porous medium formed by the solids. As the drying proceeds, the size of the droplet may not change appreciably (it may actually increase slightly in diameter), but the mass decreases as the moisture is removed.

The drying process is generally regarded as happening in two stages: the *constant rate* and the *falling rate periods* (Masters, 1972). As the droplet

dries, the liquid is brought to the surface through capillary forces. During the constant rate period, the drying rate proceeds as if the slurry droplet were a liquid droplet. In this case a liquid layer forms on the slurry droplet so the rate of mass decrease is

$$\frac{dm}{dt} = \pi Sh D_p \rho_c D_v (\omega_{A,\infty} - \omega_{A,s}) \quad (4.24)$$

Because the droplet diameter will not change significantly with time, the mass removal rate is nearly constant so this is called the *constant rate period*.

The amount of moisture in the droplet is quantified by the moisture ratio or *wetness* defined as

$$x = \frac{m_w}{m_s}$$

where m_w is the mass of moisture and m_s is the mass of the solids when “bone dry.”

When the wetness reaches the critical moisture ratio, the drying enters the falling rate period. In this period the primary resistance to mass transfer is the transfer of the liquid through the pores of the solid phase and the mass transfer rate may be considerably slower. The rate becomes progressively slower as the moisture content is reduced, hence it is called the *falling rate period*.

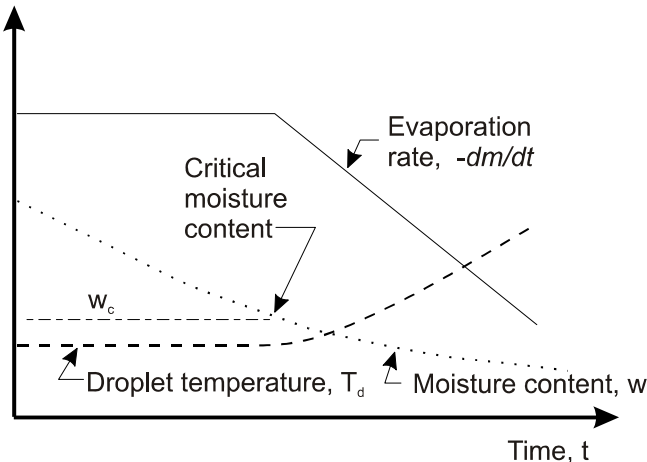


Figure 4.2: Property variation with time in a drying slurry droplet.

A typical variation of drying rate, moisture content and particle temperature with time is shown in Figure 4.2. During the initial period of the drying process, the drying rate and droplet temperature are constant while the moisture content is continuously reduced. After the critical moisture content is reached, the drying rate decreases and the temperature rises toward the temperature of the drying medium.

Few models or data are available in the open literature for the mass transfer rate during the falling rate period. A common approach is to assume that the rate of moisture removal is proportional to the moisture content

$$\frac{dm_w}{dt} = m_s \frac{dx}{dt} \sim m_s x \quad (4.25)$$

Thus the moisture content would vary with time as

$$x \sim \exp(-kt) \quad (4.26)$$

The proper drying model will depend on the nature of the porous material in the droplet as well as the bound and free moisture and the thermal conductivity of the droplet.

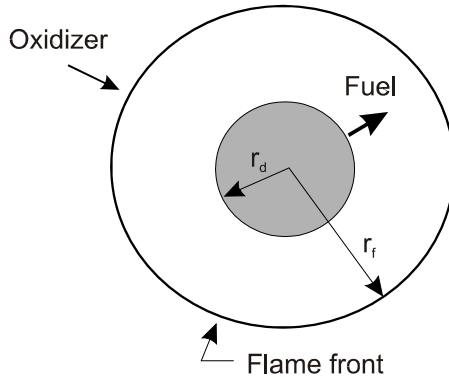


Figure 4.3: Burning fuel droplet.

4.2.3 Combustion

The combustion of a single droplet is modeled as a liquid fuel droplet surrounded by a flame as shown in Figure 4.3. The simplest model (Hedley et al., 1971) is based on a spherically symmetric flow of vapor from the droplet and oxidizer from the surroundings. A flame front occurs where the fuel vapor and oxidizer meet and react. The position of the flame front is established by the heat transfer necessary to evaporate the droplet and supply fuel to support the flame.

The basic model equates the convective and conductive heat transfer

$$-\dot{m}c_p \frac{dT}{dr} = -k_c \frac{d}{dr}(r^2 \frac{dT}{dr}) \quad (4.27)$$

where \dot{m} is the evaporation rate of the droplet, k is the thermal conductivity of the gas and c_p is the specific heat of the gas at constant pressure. Integration

of this equation between the flame radius r_f and the droplet radius r_d yields

$$\dot{m} = \frac{4\pi k_c \ln(1 - \frac{c_p \Delta T}{h_L})}{c_p (\frac{1}{r_d} - \frac{1}{r_f})} \quad (4.28)$$

Expressing the standoff distance between the flame and droplet surface as

$$r_f - r_d = \delta$$

allows one to write the above equation in the form

$$\dot{m} \cong \frac{2\pi k_c D \ln(1 - \frac{c_p \Delta T}{h_L})}{c_p \frac{\delta}{r_d}} \quad (4.29)$$

where D is the droplet diameter. The linear proportionality between burning rate and droplet diameter leads to a D^2 - law for burning rate where the *burning rate constant* is

$$\lambda = \frac{8k_c}{\delta c_p} \ln(1 - \frac{c_p \Delta T}{h_L}) \quad (4.30)$$

The value for the standoff distance δ depends on the heat released by the flame. Typical values (Strehlow, 1984) for the burning rate constant are provided in Table 4.1.

Example: Calculate the burning time of a 200 micron diesel oil droplet.

Answer: The total burning time is given by Equation 4.23. From Table 4.1 the burning rate constant is $7.9 \times 10^{-7} m^2/s$ so the burning time is

$$\tau_b = (2 \times 10^{-4})^2 / (7.9 \times 10^{-7}) = 0.051s$$

Fuel	$\lambda \times 10^7 m^2/s$
Benzene	9.9
Kerosene	9.6
Diesel oil	7.9
Isooctanes	11.4

Table 4.1. Burning rate constants for different fuels burning in air at 20°C and 100 kPa.

The effect of a relative velocity between the droplet and the oxidizer is to increase the burning rate. One way to estimate this effect is to assume that the Ranz-Marshall correlation is valid in the form (Williams, 1990)

$$\lambda = \lambda_o (1 + 0.24 Re_r^{\frac{1}{2}} Sc^{\frac{1}{3}}) \quad (4.31)$$

where λ_o is the burning rate with no convection effects.

Conceptual models for droplet combustion in sprays (Chigier, 1995) suggest that combustion does not occur as flames around individual droplets, but rather as flames around groups of droplets.

The combustion of a coal particle is an entirely different phenomenon (Smoot and Smith, 1985). A coal particle consists of four components: volatiles, moisture, char and ash. The volatiles are the combustible gases such as methane. The combustion takes place in two steps. First, the volatile and moisture are driven off. This occurs quickly and depends on the heating rate of the particle. The combustible volatiles then contribute to a gas-phase flame. There are no well-established models for the release rate of the volatiles but it appears to vary with temperature as

$$\dot{m} \sim \exp\left(-\frac{E}{RT}\right) \quad (4.32)$$

where E is an activation energy and T is the temperature.

After the combustibles are driven off, the char burns very slowly. Char burning is not well-quantified and depends strongly on the coal type and grade.

More detailed discussion of droplet combustion is available in Chapter 12 of the *Multiphase Flow Handbook* [Crowe (ed.), 2006].

4.3 Linear momentum coupling

Linear momentum coupling between phases occurs as the result of mass transfer and interphase drag and lift. Momentum transfer due to mass transfer was discussed in the derivation of the particle momentum equation. If the momentum efflux from the particle surface is uniform, then it does not contribute to the force on the particle.

4.3.1 Particle drag forces

The first analytic solution for the flow around a sphere at low Reynolds numbers (the order of unity or less) in a uniform, steady flow was provided by Stokes in 1851. Several authors after Stokes (Basset, 1888, Boussinesq, 1895 and Oseen, 1927) analyzed the motion of a sphere falling in a quiescent fluid. Traditionally, the equation of motion for a spherical particle in a fluid has been called the BBO (Basset-Boussinesq-Oseen) equations in their honor. Tchen (1949) attempted to extend the previous work to include nonuniform and unsteady flow. Inconsistencies in previous works were identified by Corrsin and Lumley (1956) and Beuvich (1966).

A rigorous derivation of the equation of motion for small particles in non-uniform, unsteady flows at low Reynolds numbers was performed by Maxey

and Riley in 1983 and the result was

$$m \frac{dv_i}{dt} = mg_i + \underbrace{V_d \left(-\frac{\partial p}{\partial x_i} + \frac{\partial \tau_{ij}}{\partial x_j} \right)}_{\text{undisturbed flow}} + \underbrace{3\pi\mu_c D \left[(u_i - v_i) + \frac{D^2}{24} \nabla^2 u_i \right]}_{\text{steady state drag}} + \underbrace{\frac{1}{2} \rho_c V_d \frac{d}{dt} \left[(u_i - v_i) + \frac{D^2}{40} \nabla^2 u_i \right]}_{\text{virtual or apparent mass term}} + \underbrace{\frac{3}{2} \pi \mu_c D^2 \int_o^t \left[\frac{d/d\tau (u_i - v_i + D^2/24 \times \nabla^2 u_i)}{\pi \nu_c (t - \tau)^{1/2}} \right] d\tau}_{\text{Basset or history term}} \quad (4.33)$$

where m is the particle mass. The first term on the right is the body force due to gravity. Any additional body forces would have to be included here. The terms contributing to the fluid dynamic force on the particle are (1) the pressure and shear stress due to the undisturbed flow, (2) the steady state drag, (3) the virtual or apparent mass term and finally (4) the Basset or history term. The last two terms are operative only in unsteady flows. Each of these terms will be addressed individually and rewritten for conditions outside the realm for which Maxey and Riley's equation is valid.

Undisturbed flow

The pressure and shear stress fields in the flow undisturbed by the presence of the particle contribute to the force on the particle.

The local pressure gradient gives rise to a force in the direction of the pressure gradient. The net pressure force acting on a particle is given by

$$F_{p,i} = \int_{cs} -pn_i dS \quad (4.34)$$

where $F_{p,i}$ is the force due to the pressure gradient and n_i is the unit outward normal vector at the particle surface. Applying the divergence theorem gives

$$F_{p,i} = - \int_{cv} \frac{\partial p}{\partial x_i} dV \quad (4.35)$$

By assuming the pressure gradient is constant over the volume of the particle one has

$$F_{p,i} = -V_d \frac{\partial p}{\partial x_i} \quad (4.36)$$

where V_d is the particle volume. This is valid for any particle shape.

The pressure gradient produced by a hydrostatic pressure is

$$\frac{\partial p}{\partial x_i} = -\rho_c g \delta_{iz} \quad (4.37)$$

where z is in the direction opposed to gravity (upward) and δ_{iz} is the Kronecker delta. The corresponding pressure force is the *buoyant force* given by

$$F_{p,z} = \rho_c g V_d$$

which states that the force is equal to the weight of the fluid displaced. This is known as *Archimedes principle*.

The force due to shear stress acting on the particle is evaluated by

$$F_{\tau,i} = \int_{cs} \tau_{i,k} n_k dS \quad (4.38)$$

where τ_{ij} is the shear stress tensor in the flow external to the particle. Applying the divergence theorem results in

$$F_{\tau,i} = \int_{cv} \frac{\partial \tau_{ik}}{\partial x_k} dV = V_d \frac{\partial \tau_{ik}}{\partial x_k} \quad (4.39)$$

Finally the force due to the undisturbed flow, F_{ud} , is

$$F_{ud} = F_{p,i} + F_{\tau,i} = V_d \left(-\frac{\partial p}{\partial x_i} + \frac{\partial \tau_{ik}}{\partial x_k} \right) \quad (4.40)$$

This term does not contribute significantly to the motion of a particle in gas-particle flows where the ratio of material densities is generally of the order of 10^{-3} . However it is important in liquid-solid flows where the material density ratio is the order of unity.

Steady-state drag forces

The *steady-state* drag is the drag force which acts on the particle or droplet in a velocity field when there is no acceleration of the relative velocity between the particle and the conveying fluid. The term in Maxey and Riley's equation can be re-expressed as

$$F_{ss,i} = 3\pi\mu_c D(u_i - v_i) + \mu_c \pi \frac{D^3}{8} \nabla^2 u_i \quad (4.41)$$

where $\nabla^2 u_i$ is evaluated at the position of the particle. The last term in the equation is the *Faxen force* which is the correction to Stokes drag for the curvature of the velocity profile in the conveying flow field. For a rectilinear flow field, the Faxen force reduces to zero. It has the same form as the force due to the shear stress, $F_{\tau,i}$, in the undisturbed flow but is not the same force. The Faxen force will be neglected here because other effects, such as Reynolds number effects, are more important in practical problems.

The steady-state force is quantified by the drag coefficient through the equation

$$F_{ss,i} = \frac{1}{2} \rho_c C_D A |u_i - v_i| (u_i - v_i) \quad (4.42)$$

where C_D is the drag coefficient, A is the representative area of the droplet and u_i and v_i are the velocities of the continuous phase and the droplet or particle phase, respectively. Typically the area is the projected area of the particle or droplet in the direction of the relative velocity.

Reynolds number effects In general, the drag coefficient will depend on the particle shape and orientation with respect to the flow as well as on the flow parameters such as Reynolds number, Mach number, turbulence level and so on. The most fundamental configuration is the sphere, which is addressed first.

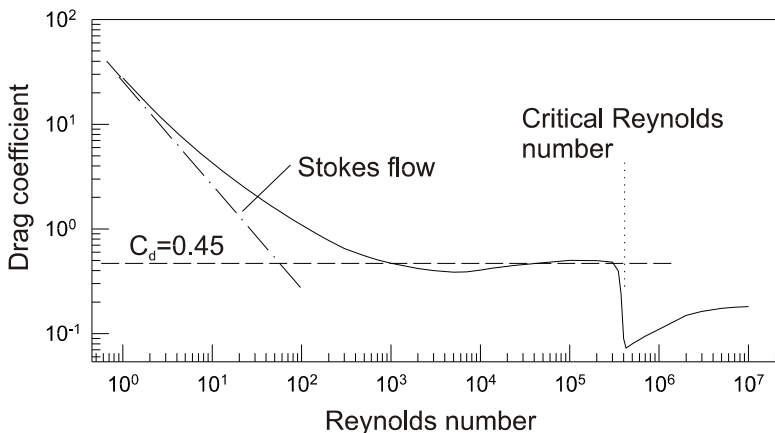


Figure 4.4: Variation of the drag coefficient of a sphere with Reynolds number.

The variation of the drag coefficient with Reynolds number for a non-rotating sphere is shown in Figure 4.4.⁴ At low Reynolds numbers the drag coefficient varies inversely with Reynolds number. This is referred to as the *Stokes flow* regime. With increasing Reynolds number the drag coefficient approaches a nearly constant value which is known as the *inertial range*⁵. For $750 < Re < 3.5 \times 10^5$ the drag coefficient varies by only 13% from $C_D = 0.445$. With increasing Reynolds number there is a sudden decrease in drag coefficient at the *critical Reynolds number*.

In the Stokes flow regime ($Re < 1$), the flow is regarded as a creeping flow in which the inertial terms in the Navier-Stokes equations are unimportant.

⁴This variation in drag coefficient with Reynolds number in steady flow is known as the *standard drag curve*.

⁵This regime is also known as “Newton’s law” (Clift et al., 1978).

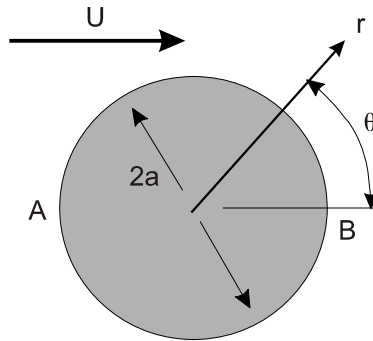


Figure 4.5: Coordinate system for Stokes flow over a sphere.

Thus the governing equation is

$$\frac{\partial p}{\partial x_i} = \mu_c \frac{\partial^2 u_i}{\partial x_j \partial x_j} \quad (4.43)$$

The application of this equation to the flow over a sphere was first addressed by C.G. Stokes in 1851. He expressed the equations in spherical coordinates and introduced a stream function (Stokes stream function for axisymmetric flows) which reduced the equations to an ordinary fourth-order differential equation for the stream function. The coordinate system used by Stokes is shown in Figure 4.5.

Solution of Equation 4.43 yields the following velocity components

$$u_\theta = -U \sin \theta \left[1 - \frac{3}{4} \frac{a}{r} - \frac{1}{4} \left(\frac{a}{r} \right)^3 \right] \quad (4.44)$$

$$u_r = U \cos \theta \left[1 - \frac{3}{2} \frac{a}{r} + \frac{1}{2} \left(\frac{a}{r} \right)^3 \right] \quad (4.45)$$

where U is the freestream velocity and a is the sphere radius. One notes that the velocity is zero at the surface ($r = a$) and equal to the uniform flow condition when $r \rightarrow \infty$.

Because of viscosity there is a pressure gradient along the surface of the sphere; that is, a pressure gradient is needed to move the fluid adjacent to the surface against the shear forces. This gives rise to a higher pressure at the forward stagnation point (A) than at the rearward point (B). Thus there is a form drag on the sphere which, when evaluated, is

$$F_p = \pi \mu_c D U \quad (4.46)$$

Similarly, the shear stress contribution to the drag force is

$$F_\tau = 2 \pi \mu_c U D \quad (4.47)$$

The sum of both contributions gives a total drag force of

$$F_D = 3\pi\mu_c D U \quad (4.48)$$

or, in terms of the velocity difference

$$F_{i,D} = 3\pi\mu_c D(u_i - v_i) \quad (4.49)$$

Using this force to solve for the drag coefficient in Equation 4.42 results in

$$C_D = \frac{24}{Re_r} \quad (4.50)$$

where Re_r is the Reynolds number based on the relative velocity. This is the classic *Stokes drag coefficient* which is valid for $Re_r < 1$.

An extension of Stokes analysis is the *Hadamard-Rybczynski drag law* for a spherical fluid particle in which the shear stress on the surface induces an internal motion (see Clift et al., 1978). In this case the drag coefficient becomes

$$C_D = \frac{24}{Re_r} \left(\frac{1 + \frac{2}{3}\bar{\mu}}{1 + \bar{\mu}} \right) \quad (4.51)$$

where $\bar{\mu}$ is the ratio of the viscosity of the carrier phase to that of the fluid sphere. For a droplet in air, $\bar{\mu} \rightarrow 0$ and Stokes law is recovered. For a bubble in a liquid, $\bar{\mu} \rightarrow \infty$ so the drag coefficient becomes $16/\text{Re}$.

For increasing Reynolds number, the inertial forces become more important and the drag coefficient is higher than Stokes drag. In 1910 Oseen extended Stokes analysis to include first-order inertial effects and concluded

$$C_D = \frac{24}{Re_r} \left(1 + \frac{3}{16} Re_r \right) \quad (4.52)$$

which is valid up to a Reynolds number of 5.

With increasing Reynolds number (~ 100), the flow begins to separate and form vortices behind the sphere. With the formation of vortices the pressure in the wake is further reduced, increasing the form drag. Finally, as the flat portion of the C_D versus Re_r curve is approached, the drag is almost entirely due to form drag with the shear drag contributing little. In this region the drag coefficient can be approximated by a constant value of 0.445 and is referred to as *Newton's drag law*.

At the critical Reynolds number ($Re_r \sim 3 \times 10^5$) the boundary layer becomes turbulent and the separation point is moved rearward, sharply reducing the form drag and decreasing the drag coefficient. This phenomenon is entirely due to boundary layer effects. If the particle is rough, transition to turbulence occurs at a lower Reynolds number and the critical Reynolds number is reduced. Also the critical Reynolds number is less well-defined as the drop in C_D is less severe. The same trend is observed with increased free stream

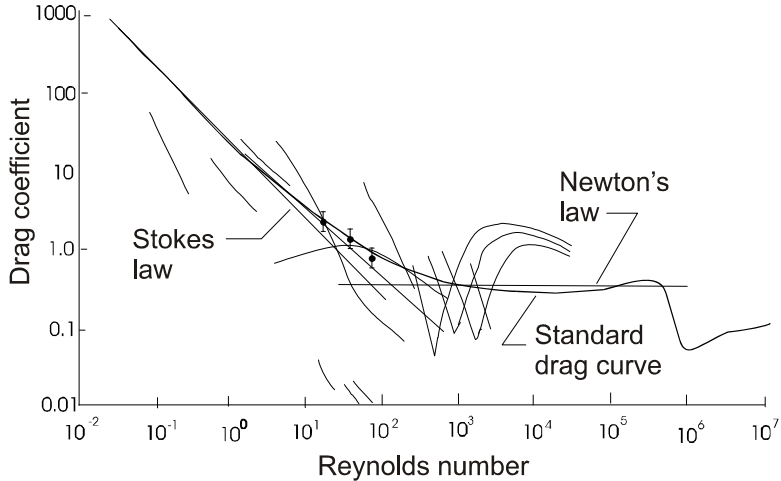


Figure 4.6: The spread of data obtained for the drag coefficient of a sphere.

turbulence. If the particle has sharp edges, the separation is controlled by geometry (separation at the sharp edges) and the critical Reynolds number effect is not observed.

There have been numerous experiments performed over the years to measure particle and droplet drag coefficients. Experiments have been performed in wind tunnels, ballistic ranges and fluidized beds. A summary of some of the data is shown in Figure 4.6. The many discrepancies between these data have never been resolved. A popular drag coefficient used for droplet motion in combustion studies is that of Ingebo (1956),

$$C_D = \frac{27}{Re^{0.84}}$$

This drag coefficient falls below the standard drag curve which Ingebo attributed to acceleration effects. Subsequent work suggested the observed trend was due to free stream turbulence effects (Crowe, 1961).

The drag force, Equation 4.42, can also be expressed as

$$\frac{1}{2} \rho_c C_D A |u_i - v_i| (u_i - v_i) = 3\pi \mu_c D f (u_i - v_i) \quad (4.53)$$

where f is the *drag factor* or the ratio of the drag coefficient to Stokes drag⁶.

$$f = \frac{C_d}{24} \frac{\rho_c |u_i - v_i| D}{\mu_c} = \frac{C_D Re_r}{24} \quad (4.54)$$

⁶The relative Reynolds number is based on the relative speed between the continuous and dispersed phase, $Re_r = D |u_i - v_i| / \nu$.

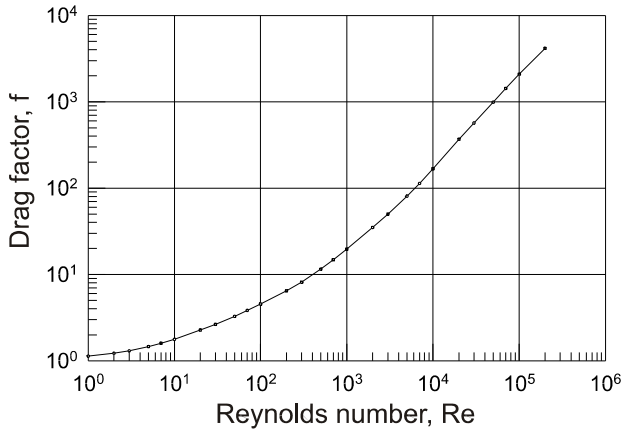


Figure 4.7: Variation of drag factor with Reynolds number.

Obviously $f \rightarrow 1$ for Stokes flow. The variation of the drag factor with Reynolds number is shown in Figure 4.7.

There are several correlations available in the literature for f as a function of Reynolds number. One correlation (Schiller and Naumann, 1933) that is reasonably good for Reynolds numbers up to 800 is

$$f = (1 + 0.15Re_r^{0.687}) \quad (4.55)$$

This correlation yields a drag coefficient with less than 5% deviation from the standard drag coefficient. A correlation suitable to higher Reynolds numbers has been proposed by Putnam (1961); namely,

$$\begin{aligned} f &= 1 + \frac{Re_r^{2/3}}{6} & Re_r < 1000 \\ f &= 0.0183Re_r & 1000 \leq Re_r < 3 \times 10^5 \end{aligned} \quad (4.56)$$

The advantage of this correlation is that the equation for particle motion can be integrated analytically. A shortcoming is the discontinuity in the value for f at $Re_r = 1000$. A more accurate correlation over the entire subcritical Reynolds number range is that of Clift and Gauvin (1970) which is an extension of Schiller and Naumann's equation.

$$f = 1 + 0.15Re_r^{0.687} + 0.0175(1 + 4.25 \times 10^4 Re_r^{-1.16})^{-1} \quad (4.57)$$

This correlation provides a fit for f within $\pm 6\%$ of the experimental value over the entire subcritical Reynolds number range.

Terminal velocity The *terminal velocity*, v_T , is the final velocity a particle attains falling in a quiescent fluid. The equation of motion for the particle is

$$m \frac{dv}{dt} = -3\pi\mu_c D \left(\frac{C_D \text{Re}_r}{24} \right) v + mg - \rho_c g V_d \quad (4.58)$$

where v is positive in the direction of gravity (downward). Once the particle has achieved terminal velocity, there is no more acceleration so the terminal velocity is

$$v_T 3\pi\mu_c D f = V_d g (\rho_d - \rho_c) = \frac{\pi D^3}{6} g (\rho_d - \rho_c) \quad (4.59)$$

$$v_T = \frac{g\tau_V}{f} \left(1 - \frac{\rho_c}{\rho_d} \right) \quad (4.60)$$

where τ_V is the particle velocity response time. For Stokes flow and $\rho_c/\rho_d \ll 1$, the terminal velocity simplifies to

$$v_T = g\tau_V \quad (4.61)$$

When $\rho_c = \rho_d$ the terminal velocity is zero and the particles are *neutrally buoyant*.

In order to calculate the terminal velocity at higher Reynolds numbers, the effect of Reynolds number on the drag factor has to be incorporated. This requires an iterative solution where the value of f is estimated, the terminal velocity is calculated from Equation 4.60, a new Reynolds number is calculated and the process is continued until the solution converges.

Another approach is to rewrite Equation 4.59 as

$$\frac{1}{2} C_D \rho_c v_T^2 \frac{\pi}{4} D^2 = \frac{\pi D^3}{6} g (\rho_d - \rho_c) \quad (4.62)$$

$$\left(\frac{v_T D}{\nu_c} \right)^2 = \frac{4}{3} \frac{1}{C_D} \frac{g D^3 (s-1)}{\nu_c^2} = \frac{4}{3} \frac{1}{C_D} G_a \quad (4.63)$$

where s is the density ratio, ρ_d/ρ_c and G_a is the Galileo number. Since C_D is a function of the terminal velocity Reynolds number, $v_T D / \nu$, one has

$$\frac{v_T D}{\nu_c} = f(G_a) \quad (4.64)$$

An empirical relationship⁷ that fits the data from Stokes flow up to the critical Reynolds number is

$$\begin{aligned} \frac{v_T D}{\nu_c} &= \left(\sqrt{22 + \sqrt{4.89 G_a}} - \sqrt{22} \right)^2 & G_a < 4 \times 10^5 \\ \frac{v_T D}{\nu_c} &= 1.74 \sqrt{G_a} & 4 \times 10^5 < G_a < 3 \times 10^{10} \end{aligned} \quad (4.65)$$

⁷The original form for this empirical relationship was proposed by Camenon (2007). It has been slightly modified here to fit the data for an extended range.

where $Ga = 3 \times 10^{10}$ corresponds to the critical Reynolds number, $v_T D / \nu = 3 \times 10^5$. The terminal velocity Reynolds number lies within $\pm 4\%$ of the value that would be obtained using drag coefficients from the standard drag curve. For $Ga \rightarrow 0$, the empirical relationship reduces to

$$\frac{v_T D}{\nu_c} = \frac{Ga}{18} \quad (4.66)$$

or

$$v_T = g \frac{\rho_d D^2}{18 \mu_c} \left(1 - \frac{\rho_c}{\rho_d}\right) \quad (4.67)$$

which corresponds to Equation 4.60 with $f = 1$.

Example: Calculate the terminal velocity of a 500-micron glass bead ($\rho_d = 2500 \text{ kg/m}^3$) in air at standard conditions ($\rho_c = 1.2 \text{ kg/m}^3$ and $\nu = 1.51 \times 10^{-5} \text{ m}^2/\text{s}$).

Solution: The Galileo number for this particle is

$$Ga = \frac{g D^3 (\rho_d / \rho_c - 1)}{\nu_c^2} = \frac{9.81 \times (5 \times 10^{-4})^3 (2500 / 1.2 - 1)}{(1.51 \times 10^{-5})^2} = 1.12 \times 10^4$$

Substituting this value into Equation 4.65 for the terminal velocity Reynolds number, one finds

$$\frac{v_T D}{\nu_c} = \left(\sqrt{22 + \sqrt{4.89 \times 1.12 \times 10^4}} - \sqrt{22} \right)^2 = 128$$

The terminal velocity is

$$v_T = 128 \times \frac{1.51 \times 10^{-5}}{5 \times 10^{-4}} = 3.86 \text{ m/s}$$

Compressibility and rarefaction effects The typical variation of drag coefficient with the relative Mach number at high and low Reynolds numbers is shown in Figure 4.8. At a high Reynolds number, the drag coefficient shows an increase with Mach number reaching a maximum value for slightly supersonic flow. This increase is due to the formation of shock waves on the particle and the attendant wave drag (essentially form drag). Mach number effects become significant for a Mach number of 0.6 which is the *critical Mach number*; that is, when sonic flow first occurs on the sphere.

At a low Reynolds number, the drag coefficient uniformly decreases with increasing Mach number and does not display a maximum value near unity. This is due to the prevalence of rarefied flow.

The importance of rarefaction effects are assessed by the magnitude of the *Knudsen number* which is the ratio of the mean free path of the molecules to the particle diameter,

$$Kn = \frac{\lambda}{D} \quad (4.68)$$

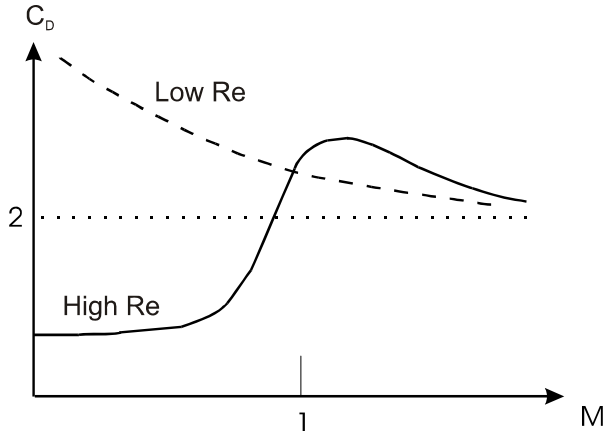


Figure 4.8: Dependence of drag coefficient on Mach number for low and high Reynolds numbers.

where λ is the mean free path of the molecules. If the Knudsen number is large, the flow cannot be regarded as a continuum. The wave drag due to a shock wave would no longer appear for particles with Knudsen numbers of the order of unity because the thickness of the shock wave would be comparable to the particle size so the particles would be engulfed by the wave.

The Knudsen number can be related directly to the Mach number and Reynolds number. The viscosity of a gas is proportional to

$$\mu \sim c \rho_c \lambda \quad (4.69)$$

where c is the speed of sound in the gas. Thus the Knudsen number can be written as

$$Kn = \frac{\lambda}{D} \sim \frac{\mu_c}{\rho_c c D} = \frac{M_r}{Re_r} \quad (4.70)$$

Four regimes have been identified (Schaaf and Chambré, 1958), as shown in Table 4.2, to describe rarefaction effects. *Free molecule flow* occurs for Knudsen numbers greater than 10. In this regime, the flow is treated as the motion of individual molecules which impact and rebound from a surface with the approaching molecules unaffected by the rebounding molecules. *Transitional flow* occurs when approaching-rebounding molecular collisions become significant to the flow field. In the *slip flow* regime one assumes that there is a slip velocity and temperature jump between the fluid adjacent to the surface and the surface. Finally *continuum flow* corresponds to a Knudsen number less than 10^{-3} . Studies (Crowe et al., 1969) show that a particle in a rocket nozzle passes through all these flow regimes.

Continuum	$Kn < 10^{-3}$	$M < 0.01\sqrt{Re_r}$
Slip flow	$10^{-3} < Kn < 0.25$	$0.01\sqrt{Re_r} < M < 0.1\sqrt{Re_r}$
Transitional flow	$0.25 < Kn < 10$	$0.1\sqrt{Re_r} < M < 3Re_r$
Free molecule flow	$Kn > 10$	$M > 3Re_r$

Table 4.2. Rarefied flow regimes.

There is no analytic nor numerical model available which provides the particle drag coefficient for particles over all the regimes of rarefied flows. The earlier methods to correct for rarefied flow effects were based on a correction to Stokes drag derived by Basset to account for velocity slip at the surface. In this case the drag coefficient can be expressed as

$$\frac{C_D}{C_{D,Stokes}} = \frac{1 + 4C_mKn}{1 + 6C_mKn} \quad (4.71)$$

where C_m is the *momentum exchange coefficient*⁸. This equation is valid only in the limit of $Kn \rightarrow 0$.

The classic experiment for free molecule flow effects was performed by Millikan (1923) as part of his oil drop experiment. He found that the drag of the oil drop varied as

$$\frac{C_D}{C_{D,Stokes}} = \frac{1}{1 + Kn[2.49 + 0.84\exp(-\frac{1.74}{Kn})]} \quad (4.72)$$

which can be regarded as an extension of the Basset correction. This equation has been used for many years as the correction for rarefied flow effects and is commonly referred to as the *Cunningham correction factor*. For large Mach numbers this equation reduces to

$$C_D \sim \frac{C_{D,Stokes}}{\frac{M}{Re_r}} \quad (4.73)$$

or

$$C_D \sim \frac{1}{M} \quad (4.74)$$

so as $M \rightarrow \infty$ the drag coefficient approaches zero. Analytic results available for free molecule flows (Schaaf and Chambré, 1958) show that the sphere drag coefficient approaches 2 as the Mach number approaches infinity. This is a shortcoming of the Cunningham correction factor but it is still useful for low Mach numbers.

Several authors (Crowe et al., 1973; Walsh, 1975; Bailey and Hiatt, 1972; Henderson, 1976) have proposed equations for the drag coefficient over the Mach number Reynolds number range for rarefied flows. An approximate surface contour of the drag coefficient of a sphere as a function of the Mach number and Reynolds number is shown in Figure 4.9. The steady-state drag

⁸From kinetic theory the best value for C_m appears to be 1.14 (Talbot, 1981).

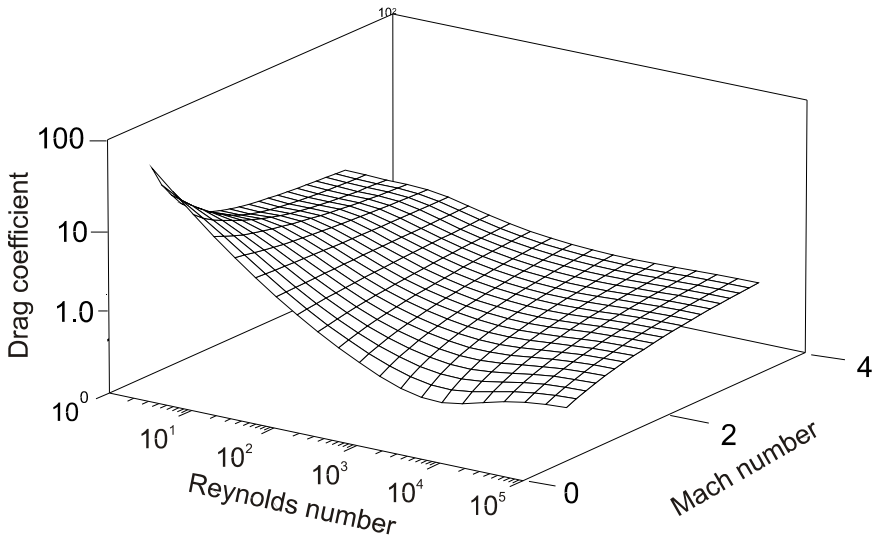


Figure 4.9: Variation of drag coefficient for a sphere with Mach number and Reynolds number.

curve corresponds to the plane for $M = 0$. For low Reynolds numbers, the drag coefficient decreases with an increasing Mach number as shown by Millikan's experiments. At high Reynolds numbers, the drag coefficient increases with an increasing Reynolds number. The contours for the drag coefficient beyond the critical Reynolds number are not included.

The following empirical equation for drag coefficient proposed by Crowe et al. (1973) and simplified by HermSEN (1979) has been used extensively in the numerical analysis of the flow in solid propellant rocket nozzles.

$$C_D = 2 + (C_{Do} - 2)e^{-3.07\sqrt{k}g(Re_r)M/\text{Re}} + \frac{h(M)}{\sqrt{k}M}e^{-\frac{Re_r}{2M}} \quad (4.75)$$

where g and h are the two functions;

$$g(Re) = \frac{1 + Re_r(12.278 + 0.548Re_r)}{1 + 11.278Re}$$

and

$$h(M) = \frac{5.6}{1 + M} + 1.7\sqrt{\frac{T_d}{T_c}}$$

and where T_d is the particle temperature and T_c is the temperature of the gas. C_{D_0} is the drag coefficient for a Mach number of zero, or the steady-state (standard) drag curve. Note that for large Knudsen numbers (large M/Re) the drag coefficient approaches two. For a Mach number approaching zero, the drag coefficient approaches the “standard” drag curve. The model is not valid beyond the Reynolds number where critical Reynolds number effects begin to appear (reduction in drag coefficient).

Turbulence effects Two parameters are used to quantify the effect of carrier phase turbulence on the particle drag: the relative turbulence intensity and the turbulence length scale-particle diameter ratio. The *relative turbulence intensity* is defined as

$$I_r = \frac{\sqrt{u'^2}}{|u_i - v_i|} \quad (4.76)$$

where $\sqrt{u'^2}$ is the root mean square of the carrier fluid turbulence fluctuations. Obviously the relative turbulence intensity is augmented as the relative velocity between the carrier and dispersed phases is reduced.

There is a spectrum of length scales in a turbulent flow. The smallest length scale is the Komolgorov length scale. For particles smaller than the Komolgorov length scale, the primary effects are probably those due to unsteady flow and flow field curvature. The length scale ratio which has been the subject of experimental investigation (Neve and Shansonga, 1989) is L_x/D where L_x is the macroscale of turbulence. Although the results do not always show a consistent trend, the general tendency is for the drag coefficient to increase with an increasing length scale ratio at a given relative turbulence intensity. Intuitively one would expect that the length scale of the turbulence should be less than the particle size to affect the boundary layer, while length scales larger than the particle size would produce effects attributable to unsteady flow and velocity profile nonuniformity. Obviously if the particle is much smaller than large-scale turbulent structures, such as produced in a wake flow, the primary effect of the turbulence is to transport the particle in the nonstationary flow field.

It is well known (Horner, 1965) that free stream turbulence reduces the critical Reynolds number for the drag coefficient of a sphere. This trend is the result of a premature transition to turbulence of the sphere boundary layer and the attendant decrease in form drag. Torobin and Gauvin (1961) report a series of experiments on the effect of relative turbulence intensity on the drag coefficient of a spherical particle. They found that increasing the relative turbulence intensity decreases the critical Reynolds number. In fact, the critical Reynolds number is reduced to the order of 500 with a relative turbulence intensity of 40%. Clamen and Gauvin (1969) found that, after the precipitous decrease in drag coefficient at the critical Reynolds number, the drag coefficient increases again with Reynolds number and passes through a

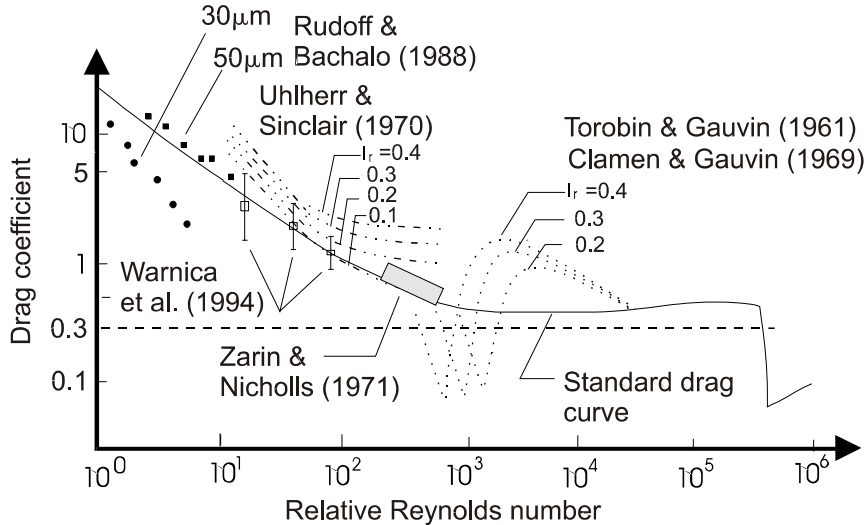


Figure 4.10: A summary of data for turbulence effects on particle drag coefficient.

maximum value.

The composite results from Torobin and Gauvin and Clamen and Gauvin, together with other data, are shown in Figure 4.10. Torobin and Gauvin's experiments were carried out in a ballistic wind tunnel using a radioactive tracer velocity measuring technique. The turbulence scale (integral scale) to particle diameter ratio ranged from 0.4 to 5 but was not used to correlate the data.

Torobin and Gauvin (1961) found that the relative turbulence intensity and critical Reynolds number correlated as

$$I_r Re_c = 45 \quad (4.77)$$

In order to provide a better correlation at the higher turbulence intensities, Clift and Gauvin (1970) suggested

$$\begin{aligned} \log_{10} Re_c &= 5.477 - 15.8I_r & (I_r \leq 0.15) \\ &= 3.371 - 1.75I_r & (I_r > 0.15) \end{aligned} \quad (4.78)$$

The data for the drag coefficient in the critical Reynolds number regime were found to vary as

$$C_D = 0.3 \left(\frac{Re}{Re_c} \right)^{-3} \quad \text{for } 0.9Re_c < Re_r < Re_m \quad (4.79)$$

where Re_m is the Reynolds number at which the drag coefficient is a minimum. Clamen and Gauvin (1969) chose to define the Reynolds number at which the drag coefficient in the supercritical regime increased through 0.3 as the *metacritical* Reynolds number. This Reynolds number was also found to correlate with the relative turbulence intensity as

$$\begin{aligned}\log_{10} Re_M &= 6.878 - 23.2.8I_r \quad (I_r \leq 0.15) \\ &= 3.633 - 1.8I_r \quad (I_r > 0.15)\end{aligned}\tag{4.80}$$

The particle drag coefficient in the supercritical Reynolds number regime was fitted with the following empirical equations.

$$\begin{aligned}C_D &= 0.3 \left(\frac{Re_r}{Re_M} \right)^{(0.45+20I_r)} \quad Re_m < Re_r < Re_M \\ C_D &= 3990Re_r^{-6.10} - 4.47 \times 10^5 I_r^{-0.97} Re_r^{-1.8} \quad Re_M < Re_r < 3 \times 10^4 \\ &\quad I_r > 0.7\end{aligned}\tag{4.81}$$

Neve and Jaafar (1982) conducted experiments on the drag coefficients of spheres in turbulent jets. Their data showed a connection between the supercritical data of Clamen and Gauvin (1969) and the limiting drag coefficient of 0.2 measured by Achenbach (1972) at a very high Reynolds number. Neve and Jaafar also propose a curve for the variation of drag coefficient of a sphere in turbulent flow over the entire Reynolds number range and suggest how the curve would change with a varying relative turbulence intensity. The need for more data was emphasized.

A very limited amount of data have been taken for the effect of turbulence on drag coefficient in subcritical turbulent flows. Uhlerr and Sinclair (1970) found that the drag coefficient was increased with turbulence intensity and suggested the following correlation

$$\begin{aligned}C_D &= 162I_r^{0.33} Re_r^{-1} \quad Re_r < 50, \quad 0.05 < I_r < 0.5 \\ C_D &= 0.133(1 + \frac{150}{Re_r})^{1.565} + 4I_r \quad 50 < Re_r < 700, \quad 0.07 < I_r < 0.5\end{aligned}\tag{4.82}$$

These equations have to be used with extreme caution and not be extrapolated to other conditions. There is reason to doubt their validity in that they predict a drag coefficient of 0.48 for a Reynolds number of 500 and relative turbulence intensity of 0.07. This is less than the standard drag coefficient for a sphere at this Reynolds number. Zarlin and Nicholls (1971) found, on the other hand, that the drag coefficient in this Reynolds number range increased uniformly with relative turbulence intensity from the standard value. They also found that the turbulence scale-particle size ratio had an effect on the results in that the drag coefficient increased with smaller particles which is opposite to the general trend observed by Neve and Shansonga (1989).

Rudoff and Bachalo (1988) report the results of an experimental study to measure droplet drag in a spray using a PDA system. The Reynolds number range was from 0.1 to 10. Both the droplet velocities and carrier phase velocities were measured. No attempt was made to correlate the data with relative turbulence intensity. In general the drag coefficients were below the standard values. The data also showed an increase in drag coefficient with droplet size which parallels Zarlin and Nicholls' findings.

Brucato et al. (1998) measured the drag coefficients of particles in turbulent flows with turbulence intensities up to 0.5% and Reynolds number from 0.2 to 40. They found that the drag coefficient was higher than the standard correlation and the deviation varied linearly with the ratio of the particle size to Kolmogorov length scale.

A numerical study on the effect of turbulence on the drag coefficient of a sphere between Reynolds numbers of 60 and 600 has been reported by Bagchi and Balachandar (2003). The particles were 1.5 to 10 times the Kolmogorov length scale and the turbulence intensity was between 10 and 25%. They found that the free-stream turbulence had little effect on the time-averaged drag coefficient and that the standard drag curve yields an adequate prediction of the drag force.

Studies on the drag coefficient of spherical liquid droplets in turbulent fields for Reynolds numbers from 20 to 100 have been reported by Warnica et al. (1994). In this study it was concluded that there is no experimental evidence to suggest that the drag of droplets is significantly different than standard drag coefficient.

Obviously there is considerable discrepancy in the data for drag coefficient dependence on turbulence. It seems most reasonable, at this point, to use the standard drag curve for particles in subcritical turbulent flow. The correlations developed by Torobin and Gauvin (1961) and Clamen and Gauvin (1969) seem most appropriate for critical and supercritical Reynolds numbers. More detailed experiments are needed to better understand the effect of turbulence on particle drag coefficients.

Drag on rotating particles in velocity gradients Very little information is available on the drag coefficient of spinning particles primarily because of the difficulties in measuring drag coefficients and quantifying spin rate. The nondimensional parameter used for *spin rate* is the ratio of the equatorial velocity to the particle-fluid relative velocity,

$$\Omega = \frac{\omega_d D}{2 |u_i - v_i|} \quad (4.83)$$

Davis (1949), who was interested in the dynamics of golf balls, measured drag and lift on smooth and roughened balls up to $\Omega = 0.6$ at a Reynolds number of 9×10^4 . He found that the drag coefficient for a spinning smooth ball did not change appreciably with the spin parameter, but a dimpled ball showed a continual increase in drag coefficient with spin. Barkla and Auchterlonie (1971)

measured drag coefficients at spin parameters from 1.5 to 12 at a Reynolds number of 2×10^3 . They also found no significant trend in drag coefficient with spin parameter. Their data did not reduce to the standard drag coefficient at zero spin which they attributed to their experimental approach. A similar insensitivity of drag coefficient to spin parameter was found in the early work of MacColl (1928).

The theoretical work of Rubinow and Keller (1961) also shows that spin has no effect on drag for Reynolds numbers on the order of unity.

The general finding is that particle spin does not affect the drag coefficient of smooth balls. The data, however, are limited to Reynolds numbers exceeding 2×10^3 , which is beyond the range of many fluid-particle flows.

Very little information is available on the drag coefficient of particles in velocity gradients. One study of note is that of Patnaik et al. (1992) who measured the drag coefficients of spheres suspended in a turbulent boundary layer. The Reynolds number range was 10^4 and the sphere diameter/boundary layer thickness varied from 0.29 to 1.0. They found that the drag coefficient based on the velocity of the undisturbed flow at the sphere center correlated well with the standard drag coefficient for a sphere.

A numerical study by Bagchi and Balachandar (2002) also indicates that the drag force is not significantly influenced by rotation.

Nonspherical particles The earliest work on the drag of irregular particles was reported by Waddell in 1933. Several reviews on the drag of irregular particles are available in the literature (Clift et al., 1978; Michaelides, 2006). A comprehensive experimental and analytic study was reported by Tran-Cong et al. (2004) and a more recent study has been published by Hölzer and Sommerfeld (2008).

The degree of nonsphericity of particles is quantified by the *shape factor*. In his early work on the drag of irregular particles, Waddell (1933) defined the *sphericity* which was defined as

$$\Psi = \frac{A_s}{A} \quad (4.84)$$

where A_s is the surface area of the sphere of the same volume (smallest possible area per unit volume) and A is the actual surface area. The diameter usually used to characterize an irregularly shaped particle is the *volume-equivalent-sphere diameter*

$$D_n = \left(\frac{6V_d}{\pi} \right)^{1/3} \quad (4.85)$$

where V_d is the particle volume. Following the work of Tran-Cong et al. (2004) this diameter will be referred to as the *nominal diameter*. Another shape parameter is the *surface-equivalent-sphere diameter*

$$D_A = \left(\frac{4A_p}{\pi} \right)^{1/2} \quad (4.86)$$

where A_p is the projected area of the particle in the direction of the relative velocity. An additional shape parameter is the *particle circularity* which is defined as

$$c = \pi D_A / P_p \quad (4.87)$$

where P_p is the projected perimeter of the particle in the direction of relative motion.

Tran-Cong et al. (2004) performed a series of terminal velocity measurements for a variety of shapes fabricated from glass spheres glued together and dropped in water-glycerine solutions. They correlated their data to fit the drag coefficient for a sphere given by Equation 4.57. The result for the drag factor was

$$f = \frac{D_A}{D_n} \left[1 + \frac{0.15}{\sqrt{c}} \left(\frac{D_A}{D_n} \text{Re}_r \right)^{0.687} \right] + \frac{0.0175 \text{Re} \left(\frac{D_A}{D_n} \right)^2}{\sqrt{c} \left[1 + 4.25 \times 10^4 \left(\frac{D_A}{D_n} \text{Re}_r \right)^{-1.16} \right]} \quad (4.88)$$

where the Reynolds number is based on the nominal diameter

$$\text{Re}_r = \frac{\rho_c D_n |u - v|}{\mu_c} \quad (4.89)$$

The drag force is given by

$$F_i = 3\pi\mu_c D_n f(u_i - v_i) \quad (4.90)$$

This correlation is valid in the ranges of $0.15 < \text{Re}_r < 1500$, $0.8 < D_A/D_n < 1.5$ and $0.4 < c < 1$ which covers the range of most engineering applications. The average absolute error between the data and correlation is less than 10%.

In the work of Hölzer and Sommerfeld (2008), the *crosswise sphericity*, ϕ is the ratio of the cross-sectional area of the volume-equivalent sphere to the projected area of the particle in the flow direction, or

$$\phi = \left(\frac{D_n}{D_A} \right)^2 \quad (4.91)$$

The drag factor they propose is⁹

$$f = \frac{1}{3\sqrt{\phi}} + \frac{2}{3\sqrt{\Psi}} + \frac{\text{Re}_r^{1/2}}{8\Psi^{3/4}} + 0.0175 \frac{\text{Re}_r}{\phi} 10^{0.4(-\log \phi)^{0.2}} \quad (4.92)$$

where Ψ is the sphericity defined by Equation 4.84. The relative deviation of f for all the data included is up to 14.4% and the equation is valid up to the critical Reynolds number.

⁹This equation differs slightly than the one recommended in the paper. The improved accuracy of the recommended equation does not merit the increased complexity.

Example: Find the drag force on a 1-mm cubical particle with the relative velocity normal to a face of the cube in an airstream at standard conditions with a relative velocity of 1 m/s.

Solution: The volume, projected surface area and perimeter are

$$\begin{aligned} V &= (1 \times 10^{-3})^3 \text{ m}^3 = 10^{-9} \text{ m}^3 \\ A_p &= (10^{-3})^2 = 10^{-6} \text{ m}^2 \\ P_p &= 4 \times 10^{-3} \text{ m} \end{aligned}$$

The volume and surface equivalent diameters are

$$\begin{aligned} D_n &= (6V/\pi)^{1/3} = (6 \times 10^{-9}/\pi)^{1/3} = 1.24 \times 10^{-3} \text{ m} \\ D_A &= (4A_p/\pi)^{1/2} = (4 \times 10^{-6}/\pi)^{1/2} = 1.13 \times 10^{-3} \text{ m} \end{aligned}$$

and the circularity is

$$c = \pi D_A / P_p = \pi \times 1.13 \times 10^{-3} / 4 \times 10^{-3} = 0.887$$

The Reynolds number of the equivalent sphere is

$$Re_r = UD_n/\nu_c = 1 \times 0.00124 / 1.51 \times 10^{-5} = 821$$

The ratio $D_A D_n$ is equal to 0.911. From Equation 4.88 the drag factor is

$$f = 15.1$$

so the drag force is

$$\begin{aligned} F_D &= 3\pi\mu_c D_n f (u - v) \\ &= 3\pi \times 1.81 \times 10^{-5} \times 1.24 \times 10^{-3} \times 15.1 \times 1 = 3.2 \times 10^{-6} \text{ N} \end{aligned}$$

Blowing effects The blowing from the surface of a burning or evaporating droplet tends to reduce the drag coefficient. The correlation generally used is (Eisenklam et al., 1967)

$$C_D = \frac{C_{D,0}}{1 + B} \quad (4.93)$$

where B is the transfer number and $C_{D,0}$ is the drag coefficient with no blowing. For evaporating droplets the transfer number is

$$B = \frac{c_p \Delta T}{h_L} \quad (4.94)$$

where h_L is the latent heat of vaporization and ΔT is the temperature difference between the droplet and the surroundings. For a burning droplet, the transfer number is expressed as

$$B = \frac{c_p \Delta T + x_{O_2} H / s}{h_L} \quad (4.95)$$

where x_{O_2} is the oxygen concentration in gas, H is the heat of combustion and s is the stoichiometric rate for oxygen.

Yuen and Chen (1976) suggest that blowing effects can be accounted for by adjusting the Reynolds number to account for the viscosity change in the film around the droplet. The standard drag coefficient based on this Reynolds number is then used for the droplet drag coefficient. They found that application of the 1/3 rule for the film properties provides a good fit with the data. In this case the film temperature is

$$T_f = T_d + \frac{1}{3} (T_c - T_d) \quad (4.96)$$

The same relationship is used for the vapor mass fraction. This temperature and mass fraction are then used to calculate a viscosity. The Reynolds number is based on this viscosity and the free stream gas density. Yuen and Chen's correlation showed a good fit of the data, including Eisenklam's data. Another correlation for the effect of blowing on the particle drag coefficient was developed by Chiang and Sirignano (1993) based on numerical studies.

It is generally found that the drag of burning or evaporating droplets is only slightly modified from the non-burning case unless the droplets are burning in a pure oxidizing environment. A comprehensive review of droplet dynamics and evaporation in sprays can be found in Sirignano (1999).

Particle clouds There is little information available on the drag of particles in particle clouds. Analytical models are difficult because an adequate model must account for the surface of every particle. Experimental studies are hindered by the difficulties of measuring the force and the local flow field on an individual particle in a cloud. Most of the data for particle drag have been inferred from sedimentation and fluidization studies.

The drag force on the continuous phase per unit volume of mixture is

$$\begin{aligned} \frac{F_D}{V} &= n f 3\pi \mu_c D (\tilde{v} - \langle u \rangle) \\ &= \frac{\alpha_d \rho_d}{\tau_V} f (\tilde{v} - \langle u \rangle) \\ &= \beta (\tilde{v} - \langle u \rangle) \end{aligned} \quad (4.97)$$

where \tilde{v} is the mass-averaged velocity of the particles and $\langle u \rangle$ is the interstitial, or phase-averaged, velocity of the fluid.

The classic study of pressure drop in a packed bed where the particles are motionless was performed by Ergun (1952). He found that the pressure drop

through the bed varied as

$$\frac{\Delta p}{\Delta L} = 150 \frac{\alpha_d^2 \mu_c U}{\alpha_c^3 D^2} + 1.75 \frac{\alpha_d \rho_c U^2}{\alpha_c^3 D} \quad (4.98)$$

where U is the superficial velocity (or local volume-averaged velocity). The interstitial velocity is related to the superficial velocity by $\alpha_c \langle u \rangle = U$ where α_c is the volume fraction of the continuous or fluid phase. The first term in this equation represents the pressure loss due to viscous drag on the particles, while the second term adds the contribution of inertial drag. This correlation is valid up to minimum fluidization velocity; that is, just before the bed becomes fluidized (particles supported by hydrodynamic forces). The fluid phase volume fraction at which this occurs is about 0.42 for a bed of spherical particles.

Ergun preformed his experiments in a fixed bed where the particle velocity was zero. In the general case, however, the particles are moving so the superficial velocity in Ergun's equation is replaced by $U = \alpha_c(\langle u \rangle - \tilde{v})$. Ergun's equation then becomes¹⁰

$$\frac{\Delta p}{\Delta L} = 150 \frac{\alpha_d^2 \mu_c (\langle u \rangle - \tilde{v})}{\alpha_c^2 D^2} + 1.75 \frac{\alpha_d \rho_c (\langle u \rangle - \tilde{v}) |\langle u \rangle - \tilde{v}|}{\alpha_c D} \quad (4.99)$$

The total force by the particles on the fluid in a volume $A\Delta L$ must equal the pressure drop times in the cross-sectional area of the flow; that is,

$$\Delta p A = nA\Delta L F_D \quad (4.100)$$

or

$$\Delta p A = nA\Delta L \left[V_d \frac{\Delta p}{\Delta L} + 3\pi \mu_c D f_E (\langle u \rangle - \tilde{v}) \right] \quad (4.101)$$

where the subscript stands for the Ergun equation. This equation can be reduced to

$$\alpha_c \frac{\Delta p}{\Delta L} = 3\pi n \mu_c D f_E (\langle u \rangle - \tilde{v}) \quad (4.102)$$

Solving for f_E gives

$$f_E = 8.33 \frac{\alpha_d}{\alpha_c} + 0.0972 \text{Re}_r \quad (4.103)$$

where $\text{Re}_r = \rho_c D |\langle u \rangle - \tilde{v}| / \mu_c$. Gidaspow (1994) suggests this equation is valid for $\alpha_c < 0.8$.

Richardson and Zaki (1954) carried out a series of experiments on sedimentation to determine how particle concentration affects the sedimentation

¹⁰The absolute value of the velocity difference is taken to ensure the correct sign for the pressure loss in the same way that it is used in the equation for particle motion.

velocity. They correlated the ratio of the settling velocity to the terminal velocity, Equation 4.60, with the volume fraction of the continuous phase. They also accounted for wall effects. For Reynolds numbers based on the terminal velocity between 200 and 500, the factor f works out to be

$$f = \alpha_c^{-k} \quad (4.104)$$

where $k = 4.45 \text{ Re}^{-0.1}$ and $\text{Re} = v_t D / \nu$ and v_t is the terminal velocity of the particle.

Wen and Yu (1966) also conducted a series of fluidization experiments to infer the drag force on particles in dense mixtures. They were looking for a correction to the equation for drag force in the form

$$F_D = g(\alpha_c) 3\pi \mu_c D f_o (\langle u \rangle - \tilde{v}) \quad (4.105)$$

where f_o is the drag factor for an isolated particle. Wen and Yu used the Schiller-Naumann correlation, Equation 4.55, in their analysis with the relative Reynolds number based on the superficial velocity. They were able to correlate their data and those of previous investigators (including Richardson and Zaki) by setting

$$g(\alpha_c) = \alpha_c^{-3.7} \quad (4.106)$$

The contribution of their analysis is that they included Reynolds number effects on the terminal velocity and, in so doing, were able to develop an empirical correlation over the entire Reynolds number regime. The drag factor for the Wen-Yu correlation now becomes

$$f_{\text{WY}} = \alpha_c^{-3.7} f_0 \quad (4.107)$$

As $\alpha_c \rightarrow 1$, $f \rightarrow f_0$.

Wen and Yu (1966) also claimed that their correlation provides the same results as Ergun's for volume fractions corresponding to minimum fluidization. This claim is somewhat dubious, however, since $g(\alpha_c)$ is so sensitive to α_c near minimum fluidization. This equation is only useful for particle volume fractions less than 0.7. If the particle volume fraction lies in the range between 0.7 and 0.8, the following linear interpolation is useful (Leboreiro, J. et al., 2008).

$$f = f_E \frac{\alpha_c - 0.7}{0.1} + f_{\text{WY}} \frac{0.8 - \alpha_c}{0.1} \quad (4.108)$$

A frequently used correlation for the drag factor is that of Di Felice (1994). He found through the analysis of various data sets available in the literature that

$$f = f_o \alpha_c^{-\beta} \quad (4.109)$$

where β is a function of the relative Reynolds number. In the low Reynolds number regime the value of β approaches 3.65 based on the data of Richardson

and Zaki (1954). At high Reynolds numbers β approaches 3.7 from the data of Wen and Yu (1966) and others. In the intermediate range of Reynolds numbers β goes through a minimum value of approximately 3 for Reynolds numbers in the range 20 to 80. Di Felice recommends the following empirical correlation for β ,¹¹

$$\beta = 3.7 - 0.65 \exp \left[-\frac{(1.5 - \log \text{Re}_r)^2}{2} \right] \quad (4.110)$$

for relative Reynolds numbers from 10^{-2} to 10^4 .

There have been studies (Hill et al., 2001a and b) with Lattice Boltzmann methods (LBM) on the drag of particles in clouds of particles. Benyahia et al. (2006) fit the numerical results with equations which span the entire range of volume fraction and Reynolds number. They express the general form as two sets of equations for specific ranges of volume fraction and Reynolds number. However the linear form¹²

$$f = F_0 + F_1 \text{Re}_r \quad (4.111)$$

appears to give identical results for two test cases when compared to the more complex two sets of equations. For $\alpha_d < 0.4$

$$F_0 = (1 - w)\alpha_c^2 \left[\frac{1 + 3\sqrt{\alpha_d/2} + 2.11\alpha_d \ln \alpha_d + 17.9\alpha_d}{1 + 0.681\alpha_d - 11.0\alpha_d^2 + 15.4\alpha_d^3} \right] + w \left(10 \frac{\alpha_d}{\alpha_c} \right)$$

and for $\alpha_d \geq 0.4$

$$F_0 = 10 \frac{\alpha_d}{\alpha_c}.$$

with

$$w = e^{[-10(0.4 - \alpha_d)/\alpha_d]}$$

For $\alpha_d < 0.095$

$$F_1 = 0.467\alpha_c^3\alpha_d + 0.0183\alpha_c^3$$

and for $\alpha_d \geq 0.095$

$$F_1 = 0.033\alpha_c^3 + 0.106\alpha_d\alpha_c^3 + 0.0116/\alpha_c^2$$

For $\alpha_d = 0.4$ ($\alpha_c = 0.6$) the above equations give

$$f = 6.67 + 0.0458 \text{Re}_r \quad (4.112)$$

compared with

$$f = 5.55 + 0.0972 \text{Re}_r \quad (4.113)$$

¹¹The log Re is the log-based 10 Reynolds number.

¹²The coefficients differ in these equations from the original source in that the superficial velocities are used in lieu of the interstitial velocities and the Reynolds number is based on the particle diameter and not radius.

from Equation 4.103. The results do not fit perfectly because the curve fits are designed to minimize the deviations over the entire $\text{Re} - \alpha_d$ range.

Additional studies using LBM have been done for the drag due to polydisperse mixtures of particles (Van der Hoef, M.A. et al., 2005). Correlations are developed for the ratio of the drag force to the drag force for a monodisperse mixture as a function of the disperse phase volume fraction and the ratio of the particle size to the average particle diameter.

Virtual or apparent mass effect

When a body is accelerated through a fluid, there is a corresponding acceleration of the fluid which is at the expense of work done by the body. This additional work relates to the virtual mass effect.

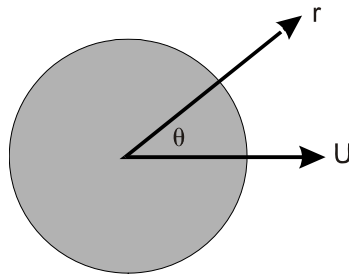


Figure 4.11: Coordinate system for a sphere accelerating in a fluid.

Consider a sphere in a fluid as shown in Figure 4.11. The total kinetic energy of the fluid surrounding the sphere is

$$KE = \frac{1}{2}\rho_c \int_V u^2 dV \quad (4.114)$$

where the integral is taken over all the fluid. It is assumed that the fluid is inviscid and incompressible (ideal fluid) so the velocity can be expressed as the derivative of a potential function

$$u_i = \frac{\partial \phi}{\partial x_i} \quad (4.115)$$

The continuity equation in terms of the potential function is

$$\frac{\partial u_i}{\partial x_i} = \frac{\partial^2 \phi}{\partial x_i \partial x_i} = 0 \quad (4.116)$$

The kinetic energy of the fluid can be expressed in terms of the potential function as

$$KE = \frac{1}{2}\rho_c \int_V \frac{\partial \phi}{\partial x_i} \frac{\partial \phi}{\partial x_i} dV \quad (4.117)$$

However, because of the continuity equation, this integral can be written as

$$KE = \frac{1}{2}\rho_c \int_V \left[\frac{\partial\phi}{\partial x_i} \frac{\partial\phi}{\partial x_i} + \phi \frac{\partial^2\phi}{\partial x_i \partial x_i} \right] dV = \frac{1}{2}\rho_c \int_V \frac{\partial}{\partial x_i} \left(\phi \frac{\partial\phi}{\partial x_i} \right) dV \quad (4.118)$$

Using the divergence theorem, this volume integral can be expressed as a surface integral over the sphere (the sphere surface is the boundary “enclosing” the fluid)

$$KE = \frac{1}{2}\rho_c \int_V \frac{\partial}{\partial x_i} \left(\phi \frac{\partial\phi}{\partial x_i} \right) dV = \frac{1}{2}\rho_c \int_{cs} \phi \frac{\partial\phi}{\partial x_i} n'_i dA \quad (4.119)$$

where n'_i is the unit outward normal vector from the fluid.

The potential function for a sphere moving with a relative velocity u through a fluid is

$$\phi = -\frac{ua^3}{2r^2} \cos\theta \quad (4.120)$$

where the angle θ is defined in the figure and a is the radius of the sphere. The radial component of velocity is

$$u_r = \frac{\partial\phi}{\partial r} = \frac{ua^3}{r^3} \cos\theta \quad (4.121)$$

which on the surface of the sphere reduces to

$$u_r = u \cos\theta \quad (4.122)$$

At $\theta = 0$ the velocity u_r is $-u$ which is the velocity at that point in the radial direction. The dot product in Equation 4.119 becomes

$$\frac{\partial\phi}{\partial x_i} n'_i = \frac{\partial\phi}{\partial r} \vec{e}_r \cdot (-\vec{e}_r) = -\frac{\partial\phi}{\partial r} = -u \cos\theta \quad (4.123)$$

where \vec{e}_r is the radial outward unit vector. Substituting the above expressions for ϕ and the gradient of ϕ into the equation for kinetic energy of the fluid gives

$$KE = \frac{1}{2}\rho_c \int_0^\pi \frac{ua}{2} \cos\theta U \cos\theta a^2 \sin\theta 2\pi d\theta \quad (4.124)$$

where $a^2 \sin\theta 2\pi d\theta$ is the element of surface area on the sphere. This equation evaluates to

$$KE = \frac{\pi\rho_c a^3 u^2}{2} \int_0^\pi \cos^2\theta \sin\theta d\theta = \frac{\pi\rho_c a^3 u^2}{3} \quad (4.125)$$

The work rate required to change the kinetic energy is

$$uF_{vm} = \frac{dKE}{dt} \quad (4.126)$$

where F_{vm} is the *virtual mass* force. Thus

$$uF_{vm} = \frac{2\pi\rho_c a^3}{3} u \frac{du}{dt} \quad (4.127)$$

so the force is equal to

$$F_{vm} = \frac{M_f}{2} \frac{du}{dt} \quad (4.128)$$

where M_f is the mass of fluid displaced by the sphere. This force is the force of the particle on the fluid so the drag force is the opposite sense of this force. The relative acceleration of the fluid with respect to the particle acceleration is $\dot{u}_i - \dot{v}_i$. Auton et al. (1988) has shown that the acceleration of the fluid should be represented by the substantial derivative. Thus the virtual mass force acting on the particle is given by

$$F_{vm,i} = \frac{\rho_c V_d}{2} \left(\frac{Du_i}{Dt} - \frac{dv_i}{dt} \right) \quad (4.129)$$

This force is sometimes called the *apparent mass* force because it is equivalent to adding a mass to the sphere. Analyses are available for shapes other than spheres for which the form of the equation is the same but the mass of fluid displaced is different.

Experiments for a sphere in simple harmonic motion (Odar & Hamilton, 1964) indicate that the virtual mass term also depends on the acceleration parameter which is defined as¹³

$$Ac = \frac{u_r^2}{D \frac{du_r}{dt}}$$

where u_r is the relative velocity. The acceleration parameter decreases as the relative velocity decreases or the relative acceleration increases. They proposed that Equation 4.129 be multiplied by a coefficient, C_{vm} , to correct to the virtual mass term. Odar (1966) suggested an empirical correlation for C_{vm} , as a function of the acceleration parameter. This correlation was developed from data using a sphere in simple harmonic motion. Subsequent work by Odar (1966) demonstrated the validity of the correlation for spheres dropping due to gravity in a tank of liquid. Further work by Schöneborn (1975) showed the utility of the correlation for predicting the fall velocity of particles in a tank of oscillating fluid.

More recently, however, Michaelides and Roig (2010) have reconstructed and reinterpreted Odar and Hamilton's data. They suggest, based on technical arguments and data reported in the literature, that C_{vm} is not a function of the acceleration parameter and should be taken as unity.

$$C_{vm} = 1 \quad (4.130)$$

Basset force

In that the virtual mass force accounts for the form drag due to acceleration, the *Basset term* accounts for the viscous effects. This term addresses the

¹³The acceleration parameter is the reciprocal of the “acceleration modulus” defined by Clift et al. (1978).

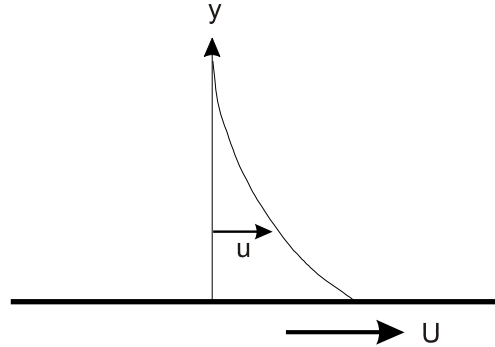


Figure 4.12: Impulsively accelerated flat plate.

temporal delay in boundary layer development as the relative velocity changes with time. This term is sometimes called the *history term*.

The most direct approach to understanding the Bassett force is to consider an impulsively accelerated infinite flat plate shown in Figure 4.12. The equation of motion for the fluid is

$$\frac{\partial u}{\partial t} = \nu_c \frac{\partial^2 u}{\partial y^2} \quad (4.131)$$

with the initial condition $u(0, y) = 0$ and the boundary conditions $u(t, 0) = u_0$ and $u(t, \infty) = 0$ where u_0 is the velocity of the plate. Thus the plate is started impulsively with a step change in velocity from 0 to u_0 .

The solution to this equation is

$$u = u_0 \operatorname{erf}(\eta) \quad (4.132)$$

where $\eta = \frac{y}{2\sqrt{\nu t}}$ or

$$u = \frac{2u_0}{\sqrt{\pi}} \int_0^\eta e^{-\lambda^2} d\lambda \quad (4.133)$$

The local shear stress is

$$\tau = \mu_c \frac{\partial u}{\partial y} \Big|_{y=0} = \mu_c \frac{2u_0}{\sqrt{\pi}} \frac{\partial \eta}{\partial y} = \frac{\mu u_0}{\sqrt{\pi \nu t}} \quad (4.134)$$

or

$$\tau = \frac{\sqrt{\rho_c \mu_c} u_0}{\sqrt{\pi t}} \quad (4.135)$$

Now assume that a general temporal variation in plate velocity can be broken up into a series of step changes as shown in the Figure 4.13. At time 0 there is a change Δu_0 , at time t_1 a change Δu_1 and so on. The cumulative effect on shear stress would be

$$\tau = \sqrt{\frac{\rho_c \mu_c}{\pi}} \left[\frac{\Delta u_0}{\sqrt{t}} + \frac{\Delta u_1}{\sqrt{t - t_1}} + \frac{\Delta u_2}{\sqrt{t - t_2}} \dots \right] \quad (4.136)$$

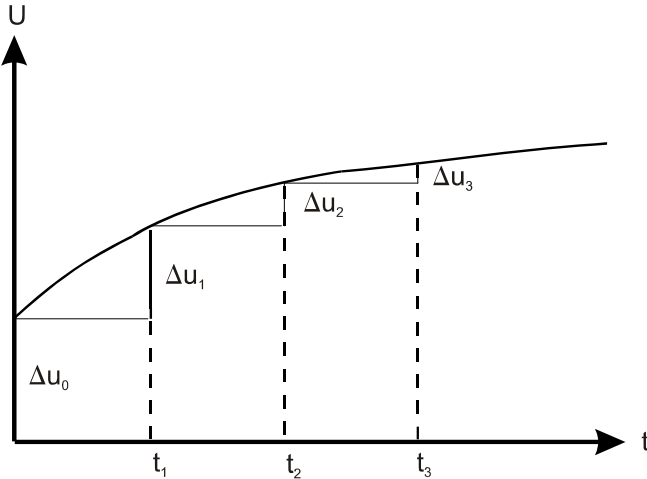


Figure 4.13: Stepwise impulsive acceleration of a flat plate.

For a time step $\Delta t'$ the change in velocity would be $\frac{du}{dt'} \Delta t'$ so the above sum can be expressed as

$$\tau = \sqrt{\frac{\rho_c \mu_c}{\pi}} \sum_{n=0}^N \frac{\frac{du}{dt'}}{\sqrt{t - n\Delta t'}} \Delta t' \quad (4.137)$$

where $N\Delta t'$ represents the time interval from the initiation of the acceleration to the present time; that is, from 0 to t . In the limit as $\Delta t'$ approaches zero and $N\Delta t' \rightarrow t'$ the equation becomes

$$\tau = \sqrt{\frac{\rho_c \mu_c}{\pi}} \int_0^t \frac{\frac{du}{dt'}}{\sqrt{t - t'}} dt' \quad (4.138)$$

Applying this same approach to the impulsive flow over a sphere at low Reynolds number, Basset found that the drag force was equal to

$$F_{Basset,i} = \frac{3}{2} D^2 \sqrt{\pi \rho_c \mu_c} \int_0^t \frac{\frac{d}{dt'}(u_i - v_i)}{\sqrt{t - t'}} dt' \quad (4.139)$$

The “historical” nature of this term is evident; the value of the Basset force depends on the acceleration history up to the present time. This term is often difficult to evaluate although important in many unsteady applications. According to the calculations of Hjemfelt and Mockros (1966), the Basset term and virtual mass term become insignificant for $\rho_c/\rho_d \sim 10^{-3}$ if $(\mu/\rho_c \omega D^2)^{1/2} > 6$. Thus the Basset term would not be important for a 10- μm particle in a stream oscillating at less than 700 Hz (Rudinger, 1980). Voir and Michaelides (1994) have also shown that the Basset term is negligible for oscillatory velocity fields if $\rho_c/\rho_d < 0.002$ and $\omega \tau_V < 0.5$.

As with the virtual mass term, an empirical coefficient C_B , which multiplies Equation 4.139, was proposed by Odar and Hamilton (1964) to account for the effect of acceleration on the Basset term. A reinterpretation of the Odar and Hamilton data by Michaelides and Roig (2010) suggests that the empirical coefficient, C_B , is not a function of the acceleration parameter but rather a function of the particle Reynolds number and Strouhal number. They recommend

$$C_B = 1.0 - 0.527 \left[1 - \exp(-0.14 \text{Re}_r Sl^{0.82})^{2.5} \right] \quad (4.140)$$

where the Strouhal number, Sl , is defined as

$$Sl = \frac{1}{2\pi f \tau_V}$$

with f being the oscillation frequency.

Reeks and McKee (1984) have shown that the Basset term has to be modified to include the case when there is an initial velocity. The term becomes

$$F_{Basset,i} = \frac{3}{2} D^2 \sqrt{\pi \rho_c \mu_c} \left[\int_0^t \frac{\frac{d}{dt'}(u_i - v_i)}{\sqrt{t - t'}} dt' + \frac{(u_i - v_i)_0}{\sqrt{t}} \right] \quad (4.141)$$

where $(u_i - v_i)_0$ is the initial velocity difference. Mei et al. (1991) developed a numerical model for stationary flow over a sphere with small free-stream velocity fluctuations. They found that the unsteady Stokes equation does not describe the character of unsteady drag at low frequencies and suggested that this effect may explain the observations of McKee and Reeks that the initial velocity difference has a finite contribution to the long-term particle diffusivity in a turbulent flow.

4.3.2 Particle lift forces

Lift forces on a particle are due to particle rotation. This rotation may be caused by a velocity gradient or may be imposed from some other source such as particle contact and rebound from a surface.

Saffman lift force

The *Saffman lift force* is due to the pressure distribution developed on a particle in a velocity gradient as shown in Figure 4.14. The higher velocity on the top of the particle gives rise to a low pressure, and the high pressure on the low velocity side gives rise to a lift force. Saffman (1965, 1968) analyzed this force for low Reynolds numbers and found the magnitude of the force to be

$$F_{Saff} = 1.61 \mu_c D |u_i - v_i| \sqrt{Re_G} \quad (4.142)$$

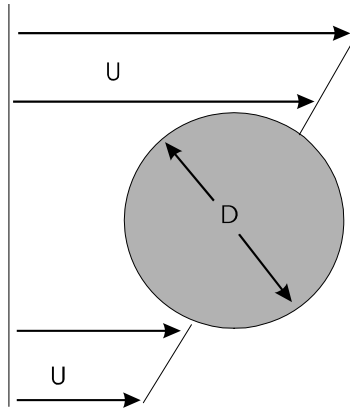


Figure 4.14: Particle in a shear flow.

where Re_G is the shear Reynolds number defined as

$$Re_G = \frac{D^2}{\nu_c} \frac{du}{dy} \quad (4.143)$$

This can be thought of as the Reynolds number based on the velocity difference between the bottom and top of the particle. The above equation can also be expressed as

$$F_{Saff,i} = 1.61 D^2 (\mu_c \rho_c)^{\frac{1}{2}} |\omega_{c,i}|^{-\frac{1}{2}} \left[\varepsilon_{ijk} (u_j - v_j) \boldsymbol{\omega}_{c,k} \right] \quad (4.144)$$

where

$$\boldsymbol{\omega}_{c,i} = \varepsilon_{ijk} \frac{\partial u_j}{\partial x_k}$$

One notes that if the relative velocity is positive, there is a lift force toward the higher velocity of the continuous phase. On the other hand, if the relative velocity is negative the lift force is toward the lower velocity of the continuous phase.

Saffman's analysis is based on the conditions that the Reynolds number based on the velocity difference is much less than the shear Reynolds number,

$$Re_r \ll \sqrt{Re_G}$$

and both Reynolds numbers are much less than unity. McLaughlin (1991) extended Saffman's analysis to allow the relative Reynolds number to exceed the shear Reynolds number and found that the lift force rapidly decreases. Mei (1992), using numerical results obtained by Dandy and Dwyer (1990), proposed an empirical fit based on Re_r and Re_G for a correction to the Saffman lift force in the form

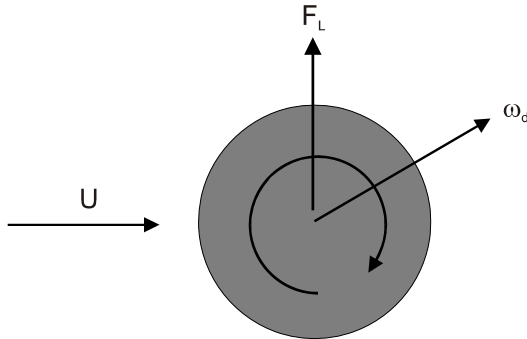


Figure 4.15: Magnus lift force on a particle rotating in a fluid.

$$\begin{aligned}
 F_L/F_{Saff} &= (1 - 0.3314\beta^{1/2}) \exp(-\frac{Re_r}{10}) + 0.3314\beta^{1/2} & Re_r \leq 40 \\
 &= 0.0524(\beta Re_r)^{1/2} & Re_r > 40
 \end{aligned} \tag{4.145}$$

where

$$\beta = \frac{D}{2|u_i - v_i|} |\omega_{c,i}|, \quad 0.005 < \beta < 0.4$$

Mei (1992) showed that the above empirical equation provided a reasonable fit for McLaughlin's results as well. The Saffman lift force then becomes

$$F_{s,i} = C_S 1.61 D^2 (\mu_c \rho_c)^{\frac{1}{2}} |\omega_{c,i}|^{-\frac{1}{2}} [\varepsilon_{ijk} (u_j - v_j) \omega_{c,k}] \tag{4.146}$$

where C_S is ratio F_L/F_{Saff} in Equation 4.145 which accounts for Reynolds number effects.

Magnus force

The *Magnus force* is the lift developed due to rotation of the particle as shown in Figure 4.15. The lift is caused by a pressure differential between both sides of the particle resulting from the velocity differential due to rotation. The rotation may be caused by sources other than the velocity gradient.

The Magnus lift force derived by Rubinow and Keller (1961) for Reynolds numbers the order of unity is

$$F_{Mag,i} = \frac{\pi}{8} D^3 \rho_c [\varepsilon_{ijk} \omega_{d,j} (v_k - u_k)] \tag{4.147}$$

where $\omega_{d,i}$ is the particle rotation vector. The force is in the direction normal to the plane formed by the rotation and relative velocity vector. If the rotation

vector is normal to the relative velocity vector then the Magnus lift force is

$$F_{Mag} = \frac{\pi}{8} D^3 \rho_c \omega_d (v - u) \quad (4.148)$$

The lift produced by the Magnus force can be quantified by a lift coefficient in the form

$$F_{Mag} = \frac{1}{2} \rho_c C_{LR} A |v - u| (v - u) \quad (4.149)$$

where A is the projected area of the particle and C_{LR} is the lift coefficient due to rotation. The lift coefficient based on Rubinow and Keller's lift force is

$$C_{LR} = \frac{D\omega_d}{|u-v|} = 2\Omega \quad (4.150)$$

where Ω is the spin parameter defined as

$$\Omega = \frac{D\omega_d}{2|u-v|} \quad (4.151)$$

This equation shows that the lift coefficient due to particle spin in Stokes flows should increase linearly with the spin parameter.

There have been numerous experiments to measure C_{LR} . These experiments (MacColl, 1928; Davis, 1949; Barkla & Auchterlonie, 1971; Tanaka et al., 1990) were conducted at Reynolds numbers exceeding 2×10^3 . At low spin ratios MacColl and Davis both found the lift coefficient to be actually negative and then to become positive with increasing spin ratio. The negative lift coefficient is attributed to a premature transition to turbulence of the boundary layer of the side of the sphere with the largest relative velocity. This, in turn, causes the wake to deflect in the direction opposite to that expected due to rotation and a negative lift ensues.

Tanaka et al. (1990), on the other hand, found that the lift coefficient increases linearly with spin ratio at low spin ratios and then rapidly decreases with increasing spin ratio, actually becoming negative at the lower Reynolds number. These results suggest that the increasing spin gives rise to transition which changes the character of the wake and the pressure distribution, thereby affecting the lift. The observed trends still lack a definitive explanation.

Tanaka et al. (1990) suggest the following relationship for lift coefficient due to rotation

$$C_{LR} = \min(0.5, 0.5\Omega) \quad (4.152)$$

which is a ramp function up to a lift coefficient of 0.5 and a constant value thereafter.

Experimental studies by Oesterlé and Dinh (1998) provide the following empirical correlation for lift coefficient

$$C_{LR} = 0.45 + (2\Omega - 0.45) \exp(-0.075\Omega^{0.4} \text{Re}_r^{0.7}) \quad (4.153)$$

for $1 < \Omega < 6$ and $10 < \text{Re}_r < 140$. This equation reduces to the correct limit for low Reynolds number. It is recommended that this equation be used for Magnus effects.

The Magnus force is then

$$F_{Mag,i} = \frac{1}{2} \rho_c A C_{LR} [\varepsilon_{ijk} \bar{\omega}_{d,j} (v_k - u_k)] |v_i - u_i| \quad (4.154)$$

where $\bar{\omega}_{d,j}$ is the normalized rotational vector, $\omega_{d,i} / |\omega_{d,i}|$.

4.3.3 Equation summary

Summing the various contributions presented above, the complete equation for the fluid dynamic force on a particle is

$$\begin{aligned} F_i &= V_d \left(-\frac{\partial p}{\partial x_i} + \frac{\partial \tau_{ik}}{\partial x_k} \right) && \text{undisturbed flow} \\ &+ 3\pi\mu_c D f(u_i - v_i) && \text{steady state drag} \\ &+ C_{vm} \frac{\rho_c V_d}{2} \left(\frac{D u_i}{D t} - \frac{d v_i}{d t} \right) && \text{virtual mass term} \\ &+ C_B \frac{3}{2} D^2 \sqrt{\pi \rho_c \mu_c} \left[\int_0^t \frac{\frac{d}{dt'}(u_i - v_i)}{\sqrt{t - t'}} dt' + \frac{(u_i - v_i)_0}{\sqrt{t}} \right] && \text{Basset term} \\ &+ C_S 1.61 D^2 (\mu_c \rho_c)^{\frac{1}{2}} |\omega_{c,i}|^{-\frac{1}{2}} \left[\varepsilon_{ijk} (u_j - v_j) \omega_{c,k} \right] && \text{Saffman lift} \\ &+ C_{LR} \frac{\pi}{8} D^3 \rho_c [\varepsilon_{ijk} \omega_{d,j} (v_k - u_k)] && \text{Magnus lift} \end{aligned} \quad (4.155)$$

There are no corrections for particle cloud effects in the last four terms of this equation..

4.3.4 Body forces

The most common body force is gravity which is simply the product of the particle mass and the vector representing the acceleration due to gravity. There are other body forces which may be important depending on the application. For example, Coulomb forces are responsible for the operation of an electrostatic precipitator. Thermophoretic forces may be important to the motion of small particles in flows with high temperature gradients such as plasmas.

Coulomb forces

The Coulomb force is the product of the charge on the particle or droplet and the local electric field intensity.

$$F_{c,i} = -q E_i \quad (4.156)$$

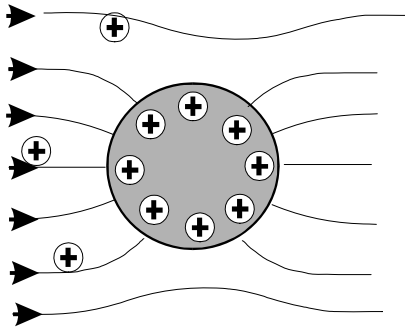


Figure 4.16: Field lines and charge accumulation on a sphere in an electric field.

In an electrostatic precipitator ions are created by a corona around the charging wire. The charge on a particle can result from one of two sources: field charging or diffusion charging.

If a particle is in a uniform electric field, as shown in Figure 4.16, ions will travel along the electric field lines and deposit on the particle (White, 1963). This is *field charging*. Ultimately a charge is accumulated sufficient to repel additional ions and the *saturation* charge is attained. For a spherical particle of diameter D the saturation charge is

$$q_s = 3\pi D^2 \epsilon_0 E_0 \quad (4.157)$$

where ϵ_0 is the permittivity of free space and E_0 is the electric field strength.

Diffusion charging occurs because of collisions between ions and particles due to the random thermal motion of the ions. *Diffusion charging* is a much slower process than field charging but becomes the dominant charging mechanism for submicron particles. The rate of charge increase due to diffusion charging is given by

$$q(t) = \frac{DkT}{2e} \ln\left(1 + \frac{\pi DcN_0 e^2 t}{2kT}\right) \quad (4.158)$$

where k is Boltzmann's constant, e is the electronic charge, N_0 is the number density of the molecules, c is the rms velocity of the ions, t is time and T is the gas temperature. Note that the charge continues to accumulate with time but the accumulation rate decreases with increasing time.

Thermophoretic forces

The thermophoretic force arises due to a temperature gradient in the continuous phase. The higher molecular velocities on one side of a particle due to a higher temperature gives rise to more momentum exchange and a resulting force in the direction of decreasing temperature. Epstein (1929) reports one

of the earliest efforts to develop an equation for the thermophoretic force. He proposed

$$F_{T,i} = -\frac{9}{2}\mu_c D^2 Kn \sqrt{\frac{2\pi R}{T}} \frac{k_c/k_d}{1 + 2k_c/k_d} \frac{\partial T}{\partial x_i} \quad (4.159)$$

where R is the gas constant for the carrier gas and k_c and k_d are the thermal conductivities of the carrier and dispersed phases, respectively. It was found that this equation is valid for Knudsen numbers and thermal conductivity ratios of the order of unity but greatly underpredicted the thermophoretic force on particles with high thermal conductivity.

An extensive review of thermophoresis by Talbot (1981) indicates that the equation developed by Brock (1962) provides the best fit with experimental data over a wide range of Knudsen numbers and thermal conductivity ratios. Brock's equation is

$$F_{T,i} = -6\pi\mu_c\nu_c DC_s \frac{1}{1 + 6C_mKn} \frac{k_c/k_d + 2C_tKn}{1 + 2k_c/k_d + 4C_tKn} \frac{1}{T} \frac{\partial T}{\partial x_i} \quad (4.160)$$

where C_s is the thermal slip coefficient and C_t is the thermal exchange coefficient¹⁴. The best values for the thermal slip and thermal exchange coefficients based on kinetic theory are $C_s = 1.17$ and $C_t = 2.18$.

4.3.5 Rotational momentum coupling

The equation for rotational motion of a spherical particle in the Stokes flow regime was derived by Feuillebois and Lasek (1978) in the form

$$\begin{aligned} & I \frac{d\omega_{d,i}}{dt} \\ &= T_i - \pi\mu_c D^3 \omega_{d,i} - \pi\mu_c D^3 \left(\frac{D}{6\sqrt{\pi\nu_c}} \int_0^t \frac{d\omega_{d,i}}{dt} \frac{d\tau}{\sqrt{t-\tau}} \right) + \\ & \quad \frac{\pi\mu_c D^3}{3} \left\{ \int_0^t \frac{d\omega_{d,i}}{dt} \exp \left[\frac{4\nu_c(t-\tau)}{D^2} \right] \operatorname{erfc} \left[\sqrt{\frac{4\nu_c(t-\tau)}{D^2}} \right] d\tau \right\} \end{aligned} \quad (4.161)$$

where I is the moment of inertia of the particle, $\omega_{d,i}$ is the rotation vector of the particle and T_i is the torque applied to the particle. The second term is the rotational resistance due to the fluid and the remaining terms are the history terms which are equivalent to the Basset term in rectilinear acceleration. Under steady-state conditions,

$$T_i = \pi\mu_c D^3 \omega_{d,i} \quad (4.162)$$

¹⁴The momentum exchange coefficient is introduced in Equation 4.71.

For a particle with no externally applied torque and moving in a flow at the same velocity, the torque on the particle is

$$T_i = \pi \mu_c D^3 \left(\frac{1}{2} \varepsilon_{ijk} \frac{\partial u_j}{\partial x_k} \right) \quad (4.163)$$

so the steady-state rotational rate would be

$$\omega_{d,i} = \frac{1}{2} \varepsilon_{ijk} \frac{\partial u_j}{\partial x_k} \quad (4.164)$$

which is simply the local rotational rate of the fluid.

Denis et al. (1980) performed an analytic study on the torque required to rotate a sphere in a viscous fluid which is at rest at large distances. A good representation of the results for Reynolds numbers from 20 to 1000 is

$$T = -2.01 \mu_c D^3 \omega_d (1 + 0.201 \text{Re}_r^{\frac{1}{2}}) \quad (4.165)$$

where the Reynolds number is based on the rotational velocity of the sphere and defined as

$$\text{Re}_r = \frac{\rho_c \omega_d D^2}{4 \mu_c}$$

There appears to be no data in the literature for the torque produced on particles at higher Reynolds numbers spinning in a moving fluid.

4.4 Energy coupling

In 1994, Feng and Michaelides developed the energy equation for a spherical particle through a rigorous analysis which paralleled the work of Maxey and Riley (1983) for the particle momentum equation. The final form of the equation assuming no mass transfer is

$$\begin{aligned} m_d c_d \frac{dT_d}{dt} &= m_c c_c \frac{DT_c}{Dt} - 2\pi D k_c \left(T_d - T_c - \frac{1}{24} D^2 \nabla^2 T_c \right) \\ &\quad - \pi D^2 k_c \int_0^t \frac{\frac{d}{d\tau} (T_d - T_c - \frac{1}{24} D^2 \nabla^2 T_c)}{[\pi \alpha_c (t - \tau)]^{1/2}} d\tau \end{aligned} \quad (4.166)$$

where c_d and c_c are the specific heats of the particle and continuous phase, respectively, and k_c is the thermal conductivity of the fluid. The factor α_c in the last term is the thermal diffusivity of the fluid defined as $k_c / \rho_c c_c$. The first term on the left is the rate of energy change of a mass of fluid with a volume equal to the volume of the particle. It is analogous to the “undisturbed flow” term in Equation 4.33. In gas-particle flows this term is unimportant but can become significant when the densities of the particles and conveying fluids are comparable. The second term is the convective heat transfer and the

last term is the history term equivalent to the Basset term in Equation 4.33. Unlike the momentum equation, there is no virtual mass term. The Laplacian terms in the convection and history terms are equivalent to the Faxen force in the momentum equation. These terms can be neglected if the particle size is much smaller than the characteristic dimension of the flow, which is usually the case.

The above equation does not include radiative heat transfer which can be added if applicable.

4.4.1 Convective heat transfer

The equation for convective heat transfer can be rewritten as

$$\dot{Q}_c \sim -\pi D^2 k'_c \frac{(T_c - T_d)}{D} \quad (4.167)$$

Using the definition of *Nusselt number* (Nu), the equation becomes

$$\dot{Q}_c = Nu \pi D k'_c (T_s - T_c) \quad (4.168)$$

The rate of heat transfer to a particle in a stagnant medium with no forced or free convection effects is

$$\dot{Q}_c = 2\pi D^2 k'_c \frac{(T_c - T_s)}{D} = 2\pi D k'_c (T_c - T_d) \quad (4.169)$$

in which case the Nusselt number is two.

Reynolds number effects

The rate of heat transfer increases with a relative flow with respect to the sphere in the same fashion as the Sherwood number increases. The *Ranz-Marshall correlation* (1952) for forced convection effects; namely,

$$Nu = 2 + 0.6 Re_r^{\frac{1}{2}} Pr^{\frac{1}{3}}, \quad (4.170)$$

where Re_r is the Reynolds number based on the relative velocity and Pr is the Prandtl number, $Pr = \frac{\mu c_p}{k'_c}$, provides a good fit with the data up to a relative Reynolds number of approximately 5×10^4 . One notes the similarity with the Sherwood number for mass transfer. Other correlations for the Nusselt number are discussed in Rowe et al. (1965) and Michaelides (2006).

The energy equation for a particle with no mass transfer assuming convective heat transfer as the primary heat transfer mechanism is

$$mc_d \frac{dT_d}{dt} = Nu \pi k'_c D (T_c - T_d) \quad (4.171)$$

or

$$\frac{dT_d}{dt} = \frac{Nu}{2} \frac{12k'_c}{c_d\rho_d D^2} (T_c - T_d) \quad (4.172)$$

The parameter $c_d\rho_d D^2/12k_c$ has the units of time and is thermal response time, τ_T . Thus the equation becomes

$$\frac{dT_d}{dt} = \frac{Nu}{2} \frac{1}{\tau_T} (T_c - T_d) \quad (4.173)$$

where $Nu/2$ is analogous to the drag factor f in Equation 4.54. $Nu/2 \rightarrow 1$ as $Re_r \rightarrow 0$.

The energy equation for a droplet with mass transfer (Equation 4.9) can be expressed as

$$\frac{dT_d}{dt} = \frac{Nu}{2} \frac{1}{\tau_T} (T_c - T_d) + \frac{Sh\rho_c\pi DD_v(w_{A,\infty} - w_{A,s})h_L}{c_d\rho_d\pi D^2/6} \quad (4.174)$$

or

$$\frac{dT_d}{dt} = \frac{Nu}{2} \frac{1}{\tau_T} (T_c - T_d) + \frac{Sh}{2} \frac{1}{\tau_T} \frac{\text{Pr}}{Sc} \frac{h_L}{c_p} (w_{A,\infty} - w_{A,s}) \quad (4.175)$$

where c_p is the specific heat at constant pressure of the carrier gas. Because of evaporation, the rate of increase in droplet temperature is reduced. When the droplet temperature reaches saturation conditions, the *wet-bulb* condition is achieved and the temperature remains constant until evaporation is complete.

Example: Find the wet-bulb temperature for a water droplet in air at $20^\circ C$, at a pressure of 1 bar and with a relative humidity of 40%. Assume $Nu = Sh$, a Prandtl of 0.76 and a Schmidt number of 0.65. The specific heat of the air is 1.005 kJ/kg and the latent heat is 2454 kJ/kg.

Solution: Setting $dT_d/dt = 0$ in Equation 4.175, one has

$$\frac{Nu}{2} (T_c - T_d) = \frac{Sh}{2} \frac{\text{Pr}}{Sc} \frac{h_L}{c_p} (w_{A,s} - w_{A,\infty})$$

The saturation pressure of water vapor at 293 K is 0.02339 bar so the partial pressure is 0.02239. The mass fraction of water vapor in the free stream is

$$w_{A,\infty} = 0.02239 \times \frac{18}{29} \times 0.4 = 0.00556$$

Substituting in the above values, one has

$$293 - T_d - 2855(w_{A,s} - 0.00556) = F$$

where the value for T_d at which $F = 0$ is the solution. The solution must be obtained iteratively from the following table.

T_d	p_{sat}	$w_{a,s}$	F
280	0.009912	0.00615	11.31
285	0.01388	0.00862	-0.74
290	0.01919	0.01191	-15.13

Interpolating to find temperature for $F = 0$ gives $T_d = 284.7$ K or 11.7°C .

Rarefied flows

For rarefied flows the Nusselt number is reduced and a good correlation is (Kavanau, 1955)

$$Nu = \frac{Nu_0}{1 + 3.42Nu_0 \frac{M}{Re_r Pr}} \quad (4.176)$$

where Nu_0 is the Nusselt number for incompressible flows. This is valid over all flow regimes and yields the correct limit for free molecule flow.

Blowing effects

Mass transfer at the surface tends to reduce the Nusselt number since it lowers the temperature gradient at the surface. Renksizbulut and Yuen (1983) proposed the following empirical correlation based on experimental data,

$$Nu_f = \frac{2 + 0.584 Re_r^{1/2} Pr^{1/3}}{(1 + B_f)^{0.7}} \quad (4.177)$$

where the Nusselt number, transfer number and Prandtl number are based on the film properties (average temperature) and the Reynolds number is defined as

$$Re_r = \frac{\rho_c D |u_i - v_i|}{\mu_f}$$

where μ_f is the viscosity of the mixture at the film temperature. This correlation provides a good fit with the available data. One notes that it essentially reduces to the Ranz-Marshall correlation as the transfer number approaches zero.

Turbulence effects

Experimental studies on the heat transfer to spheres in turbulent flows generated by grids have been reported by Raithby and Eckert (1968) for Reynolds numbers from 3×10^3 to 5×10^4 . These studies show that the Nusselt number at the lower Reynolds numbers increases rapidly with turbulence intensity for turbulence intensities up to 1% and then appears to vary linearly with turbulence intensity thereafter. At the higher Reynolds numbers the linear

variation of Nu with turbulence intensity extrapolates linearly back to the values for the flows with no grids. Clift et al. (1978) propose

$$\frac{Nu}{Nu_0} = 1 + 4.8 \times 10^{-4} \frac{I_r}{I_{rc}} Re_r^{0.57} \quad (4.178)$$

where I_r is the relative turbulence intensity and I_{rc} is the critical turbulence intensity; that is, the turbulence intensity required to have a critical Reynolds number at the relative Reynolds number of the particle (see Section 4.3.1).

Yearling and Gould (1995) conducted an experimental study on the effects of free stream turbulence on the Nusselt number of evaporating water, ethanol and methanol droplets. They found that the Nusselt correlated with

$$Nu_f = \frac{2 + 0.584 Re_r^{1/2} Pr_f^{1/3}}{(1 + B_f)^{0.7}} (1 + 3.4 I_r^{0.843}) \quad (4.179)$$

where the definitions for the Reynolds number, Prandtl number and the transfer number are the same as those for Equation 4.177. The data were obtained for $50 < Re_r < 1500$. The authors report that the same correlation is valid for nonevaporating particles ($B_f = 0$).

4.4.2 Transient term

As with the equation of motion, the transient, or history term, has to be extended to account for an initial temperature difference between the particle and the fluid.

$$\dot{Q}_{\text{transient}} = -\pi D^2 k'_c \int_0^t \frac{\frac{d}{d\tau}(T_d - T_c)}{\sqrt{\pi \alpha_c (t - \tau)}} d\tau - \pi D^2 k'_c \frac{T_d(0) - T_c(0)}{\sqrt{\pi \alpha_c t}} \quad (4.180)$$

where α_c is the thermal diffusivity of the continuous phase and the time rate of change of the temperature field is evaluated at the position of the particle. $T_d(0)$ and $T_c(0)$ are the initial temperatures of the particle and fluid, respectively. This equation for unsteady heat transfer is valid only for small Peclét numbers.

Gay and Michaelides (2003) have looked at the importance of the transient term. They defined a volumetric heat capacity ratio

$$\beta' = \frac{\rho_c c_c}{\rho_d c_d} \quad (4.181)$$

and determined that the transient term is important when β' lies between 0.002 and 0.5. Thus the term may not be significant in gas-solid flows where the density ratio is 10^{-3} but certainly must be included in liquid-solid flows. Neglecting the transient term could lead to as much as a 30% error in the predicted heat transfer rate.

4.4.3 Radiative heat transfer

The radiative heat transfer is the net heat transfer due to absorption and emission of radiant energy through

$$\dot{Q}_r = \pi D^2 (\alpha J - \epsilon \sigma T_d^4) \quad (4.182)$$

where α is the absorptivity of the particle material, J is the radiosity and σ is the Stephan-Boltzmann constant and ϵ is the emissivity. The radiosity depends on the surroundings including the presence of other particles. If the particle is considered a *grey body* then the absorptivity is equal to the emissivity. The simplest model is to assume that the particle is in a black body enclosure and then the equation for heat radiative heat transfer becomes

$$\dot{Q}_r = \epsilon \sigma \pi D^2 (T_s^4 - T_d^4) \quad (4.183)$$

where T_s is the temperature of the surrounding black body.

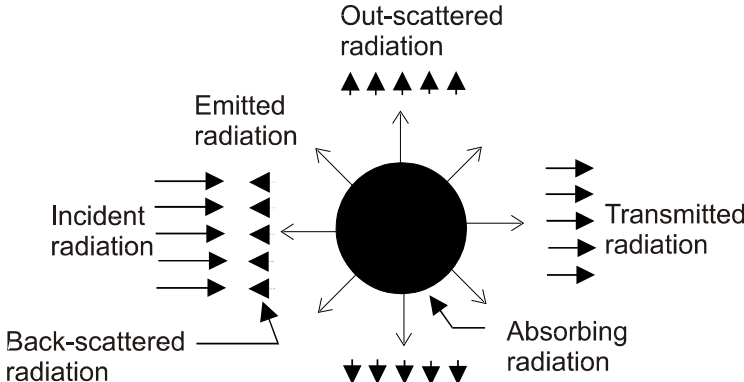


Figure 4.17: Absorption, scattering and emmision by a particle.

The model becomes much more complex for a cloud of particles and will not be discussed in detail here. A very simplified description of the effect of a particle on the radiation intensity is shown in Figure 4.17. The incident radiative energy is scattered by the particle in all directions. Part of the incident beam is transmitted in the forward direction, part is backscattered in the opposite direction of the incident beam and part is out-scattered. The distribution of the scattered intensity depends on the parameter $\pi D/\lambda$ where λ is wave length. For $\pi D/\lambda < 1$, the scattering is defined as Rayleigh scattering while for $\pi D/\lambda > 5$ the scattering is known as *Mie scattering*. Analytic results are available for the scattering distribution for Rayleigh and Mie scattering (Van de Hulst, 1981) as well as numerical programs. Special treatment is needed to evaluate scattering in the intermediate range. For Mie scattering one finds that the ratio of the transmitted radiation (forward scattering) to the

backscattering increases as $\pi D/\lambda$ increases. The particle affects the scattering distribution as well. Part of incident energy is also absorbed by the particle and energy is emitted by the particle as well.

Assuming the particle is a grey body the amount of energy emitted from the particle is

$$I_{emit} = \varepsilon \pi D^2 \sigma T_d^4 \quad (4.184)$$

The amount of scattering is quantified by an efficiency factor, Q_s , also known as the Mie coefficient, and is a function of $\pi D/\lambda$, particle shape refractive index. The fraction of the incident beam energy which is scattered by a single spherical particle is $\pi \frac{D^2}{4} Q_s$. Thus the total energy scattered by N particles in a control volume is

$$I_{scattered} = I \frac{\pi}{4} \sum_{n=1}^N D_n^2 Q_{s,n} = K_s I \quad (4.185)$$

where I is the intensity of the incident beam and K_s is the *scattering coefficient*. If all the particles have the same size and efficiency factor, the scattered intensity is

$$I_{scattered} = I \frac{\pi}{4} D^2 Q_s n V = K_s I \quad (4.186)$$

This is called *single particle scattering* in that the cumulative effect is the sum of the scattering of an isolated, individual particle. As the number density of the particles increases, the scattering becomes considerably more complex and is known as *multiple scattering*.

In the same fashion the fraction of energy absorbed by a single particle is $\pi \frac{D^2}{4} Q_a$, where Q_a is the efficiency factor for absorption. The energy absorbed by all the particles in a control volume, provided all the particles have the same size and efficiency factor, is

$$I_{abs} = I \frac{\pi}{4} D^2 Q_a n V = K_a I \quad (4.187)$$

where K_a is the *absorption coefficient*.

Modeling radiation in a particle cloud involves setting up an energy balance that accounts for the scattering, absorption and emission including the contributions of the particles and the surrounding walls (or flames). Many simplifications have to be made to make the problem tractable to obtain a solution. The main area of difficulty is accounting correctly for the scattering. Several models have been developed and applied to industrial systems. These include Hottel's classic zone method (Siegel and Howell, 1981) in which control volumes are set up which can exchange energy with all other control volumes. Chu and Churchill (1955) introduced the six-flux model in which the radiation is discretized into six directions. A model with improved accuracy over Chu and Churchill's, but more expensive, is the discrete ordinate model

proposed by Fiveland (1988) in which finite difference equations are derived for discrete directions of the radiative intensity.

4.4.4 Dielectric heating

Dielectric, or microwave, heating is used in many industrial processes such as plywood manufacturing, drying of textiles and food products and curing rubber. A dielectric is a nonconductor in which there are no free electrons. In an electric field, the positive and negative charges within an atom or molecule (dipoles) are displaced and aligned in a direction opposite to the field direction. If the direction of the voltage is changed, the dipoles will attempt to rotate. This rotation dissipates energy and heat is released to the medium.

The power dissipated or heat released per unit volume produced by the alternating electric field is given by

$$\frac{\dot{Q}}{V} = 0.556 \times 10^{-10} f \epsilon''_{eff} E_{rms}^2 \quad (4.188)$$

where E_{rms} is the electric field intensity, f is the frequency in Hz and ϵ''_{eff} is the effective dielectric constant. If a material experiences magnetic losses as well, this equation has to be extended to include magnetic wall domain and electron spin losses.

4.5 Summary

There have been a large number of experiments and analyses performed for the transfer of properties between particles and droplets and the carrier phase. Most of the studies have been done for isolated particles in uniform flow fields. The effect of turbulence on particle drag, especially at low Reynolds numbers, is still open to question. The drag on a particle in a cloud of particles has been inferred from experiments from fluidized beds because of the difficulty in making detailed local measurements. There also seems to be considerable confusion concerning the data on the Magnus lift force as a function of spin. The heat transfer relationships for isolated particles and droplets appear to be reasonably well-founded. Like particle drag, there is a need to better quantify the heat transfer between the carrier fluid and particles in a particle cloud.

4.6 Exercises

- 4.1. Measurements indicate that the mass transfer rate on the windward side of an evaporating droplet is 10% higher than that on the leeward side. Assume that the local mass efflux rate can be subdivided into a uniform flow over the windward hemisphere and a uniform flow over the leeward hemisphere.

Determine the non-dimensional thrust on the droplet in the form

$$\frac{T}{\rho_f \left(\frac{\dot{m}}{\rho_c S} \right)^2 A_d} = f \left(\frac{\rho_d}{\rho_c} \right)$$

where \dot{m} is the evaporation rate of the droplet, A_d is the projected area of the droplet, ρ_c is the density of the gas adjacent to the droplet surface, S is the surface area of the droplet and ρ_d is the density of the droplet material.

4.2. The second law of thermodynamics for a system is

$$\frac{dS}{dt} \geq \frac{\dot{Q}}{T}$$

Using Reynolds transport theorem, write out the second law for an evaporating droplet.

4.3. A spherical droplet is rotating with an angular velocity ω_i as it moves with a translational velocity of U_i at its center of mass. Assume that the droplet is evaporating uniformly. Is the expression

$$m \frac{dU_i}{dt} = F_i$$

where F_i is the force acting on the particle, still applicable? Determine by applying Reynolds transport theorem to the rotating, evaporating droplet.

4.4. A rigid spherical droplet is spinning with an angular velocity about its z-axis as shown. The magnitude of the velocity due to spin is

$$|v_i| = \omega r \sin \phi$$

The velocity with respect to an inertial reference frame is $U_i + v_i$ where U_i is the velocity of the droplet center with respect to an inertial reference frame. The specific kinetic energy is

$$e_k = \frac{|U_i + v_i|^2}{2}$$

1. Show that the kinetic energy of the droplet is

$$\int_{cv} \rho_d e_k dV = m \frac{U^2}{2} + AI\omega^2$$

where A is a constant and I is the moment of inertia of the droplet. Evaluate the constant A .

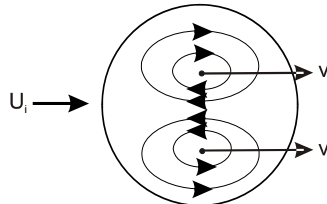
2. The velocity at the surface of a non-evaporating spherical particle is given by

$$v_{i,s} = v_i + v_t t_i$$

where v_t is the magnitude of the tangential velocity and t_i is the unit vector in the tangent plane of the particle surface. Show that the work term in the energy equation due to surface forces becomes

$$W = -v_i F_{i,s} - \int_{cs} v_t t_i \tau_{ij} n_j dA$$

4.5. Droplets can have an internal circulation as shown in the figure. This is called a “Hill Vortex.” For a droplet with internal circulation, the velocity field with respect to an inertial reference frame is $v_i + \delta v_i$, where v_i is the velocity of the droplet (at the center of the Hill vortex) and δv_i is the velocity of the internal motion with respect to the center of the vortex. Using Reynolds transport theorem, write down the continuity and momentum equation for the droplet. What effect do you think the internal motion will have on the momentum equation for the droplet? Also what effect might it have on the pressure and shear force distribution; that is, the aerodynamic forces acting on the droplet. Provide a qualitative assessment.

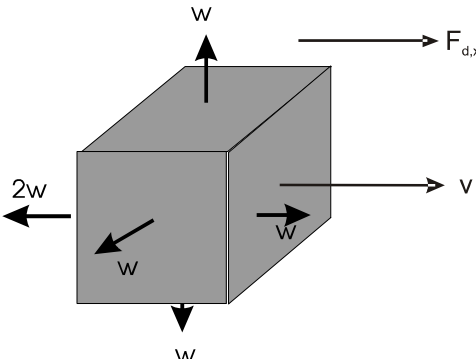


Problem 4.5

4.6. A coal particle is modeled as a cube as shown. Mass is ejected from the surface due to burning but the size does not change with time. The efflux is uniform and equal to w over the surface except for the leeward face where it is $2w$. Find the equation of motion for the particle in the x-direction in the form

$$m \frac{dv}{dt} + A \dot{m} w = F_{d,x}$$

where $F_{d,x}$ is the drag force in the x-direction, m is the mass of the particle and \dot{m} is the burning rate.



Problem 4.6

4.7. The following questions refer to the energy equation for a droplet (or particle).

1. How would the energy equation be altered if the dependence of surface tension on temperature was to be included?
2. What changes would occur to the energy equation if internal circulation of the fluid was included? Do not work the problem out, only indicate what changes you might expect and explain why.
3. How would the equation change if the particle was porous and the surface was a solid material with pores.

4.8. A droplet is injected with a velocity v_0 into a quiescent medium (no motion). The droplet evaporates according to the D^2 -law and Stokes drag is applicable. The drag force is the only force acting on the droplet (no gravity) and the mass flux is uniform over the surface.

1. Derive an equation for the droplet velocity and distance as a function of v_0 , t and τ_V/τ_m .
2. Setting $t = \tau_m$, evaluate the distance traveled for τ_V/τ_m much less than unity and much greater than unity.

4.9. A particle is in a harmonically oscillating gas flow field. The flow velocity is given by

$$u = u_0 e^{i\omega t}$$

Assume Stokes drag is applicable so the equation of motion is

$$\frac{dv}{dt} = \frac{u - v}{\tau_V}$$

1. Determine the amplitude and phase lag between the gas and the particle in terms of ω and τ_A . Provide a physical interpretation of the result.

2. Evaluate the amplitude ratio and phase lag of a 10-micron glass ($\rho_p = 2500 \text{ kg/m}^3$) in air at standard conditions oscillating with a frequency of 100 Hz.

4.10. The energy equation for an evaporating droplet is

$$mc\frac{dT_d}{dt} = Nu\pi D_d k (T_g - T_d) + Sh\pi\rho_c D_v D_d (\omega_\infty - \omega_s) h_{fg}$$

1. Discuss the relative interaction of the terms ensuing as a cold droplet is injected into a hot stream.
2. Determine the wet-bulb temperature for a water droplet in air at 20°C and 40% relative humidity. Assume that $Nu = Sh$ and $Sc=0.65$. You will need properties from a thermodynamics table for water to do this problem.
3. Write out an equation which represents a perturbation about the wet-bulb temperature; that is,

$$T_g = T_{g,0} + T'_g$$

and

$$T_d = T_{wb} + T'_d$$

yielding

$$\frac{dT'_p}{dt} = f(T'_p, T'_g)$$

- 4.11. During the falling rate period, the wetness of a spherical slurry droplet is assumed to vary as

$$\frac{dW}{dt} = -kW$$

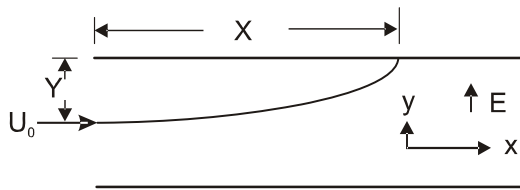
where k is a rate constant. The wetness is defined as the ratio of the moisture to the dry solids in the droplet. Derive an equation for the velocity variation with time during this time assuming Stokes law is valid, the gas is quiescent and the droplet size remains constant. The result should be in the form

$$v = v_0 f(W_0, D, \mu, k, m_s, t)$$

where v_0 is the initial velocity, W_0 is the initial wetness, D is the droplet diameter, μ is the gas viscosity and m_s is the mass of dry solids.

- 4.12. A charged particle is injected into a channel with quiescent fluid and a uniform electric field strength. The initial velocity of the particle is U_0 and the distance from the injection point to the wall (collecting surface) is L . Find the axial distance the particle will travel before it impacts the wall in terms of electric field strength, E , the aerodynamic response time of the particle,

the charge to mass ratio on the particle (q/m), the initial velocity and the distance to the wall. Neglect gravitational effects.



Problem 4.12

4.13. A cubical coal particle, with a side equal to 1 mm and a material density of 1400 kg/m^3 drops in air at standard conditions. Find the terminal velocity.

4.14. A spherical particle, 200 microns in diameter, drops in a duct with an upward moving flow of air at 10 m/s . The turbulence intensity is 20% and the particle density is 1500 kg/m^3 . Will the terminal velocity be higher or lower than one dropping through the same flow with zero turbulence intensity?

4.15. Assume a 100 micron glass bead (density = 2500 kg/m^3) is injected into stagnant water at 5 m/s at 20°C . Reduce and solve Equation 4.33 numerically to find the velocity and distance as a function of time. Use the modified Euler method and any ingenious method to integrate the Basset term! Compare your result with those obtained if the Basset and virtual mass terms were neglected.

4.16. An evaporating droplet is accelerated from rest in a uniform flow with a velocity of v_0 . The droplet evaporates according to the D^2 - law and Stokes drag is applicable. Derive an expression for the droplet velocity as a function of aerodynamic response time based on initial droplet diameter, the fluid velocity and droplet evaporation time. How far does the droplet travel before completely evaporating? Neglect gravity.

4.17. An evaporating droplet is released from rest in a quiescent medium and drops due to gravity. Buoyancy effects are negligible. The D^2 -law and Stokes law apply. Find an expression for the maximum velocity in terms of aerodynamic response time based on initial diameter, acceleration due to gravity and evaporation time.

4.18. An expression sometimes used for the drag coefficient of a particle is

$$C_D = \frac{1}{2} + \frac{24}{Re}$$

A 100-micron particle with a material density of 2000 kg/m^3 is fired into still air at a velocity of 10 m/s . The air is at standard conditions. Using the above drag law, calculate how far it will travel before stopping. What will the velocity be after one aerodynamic response time? How does this velocity compare with the velocity calculated using Stokes drag? Explain the difference. Neglect gravitational effects.

4.19. The rate of mass decrease of a porous particle is modeled as

$$\frac{dm_w}{dt} = -k \frac{m_w}{m_s}$$

where m_w is the mass of the water in the particle and m_s is the mass of the solids. As the particle dries, its diameter remains constant but the mass decreases. Assuming Stokes law is valid, derive an expression for the penetration distance of a wet particle in terms of the initial velocity, initial wetness, particle diameter, gas viscosity and mass of the solid component. Neglect gravity.

4.20. A 0.1-micron particle with a material density of 800 kg/m^3 falls in air at standard conditions ($p = 101 \text{ kPa}$, $T = 20^\circ\text{C}$). Find the terminal velocity assuming Cunningham correction is valid. What is the terminal velocity based on Stokes drag?

4.21 Neglecting the transient terms, the equation for the rotational motion of a spherical particle is

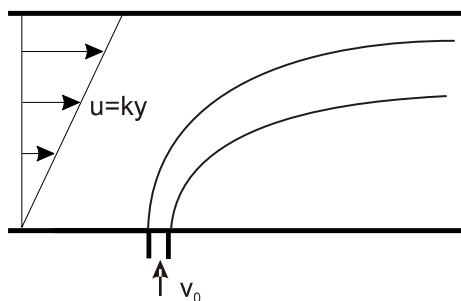
$$I \frac{d\omega_{d,i}}{dt} = T_i - \pi \mu_c D^3 \omega_{d,i}$$

Determine an expression for the rotational response time and compare with the velocity response time, τ_V .

4.22. How important do you think the Basset term is for a prismatic particle (with angular edges)? Explain.

4.23. Using the equation for the velocity field around a particle in Stokes flow and the Navier-Stokes equations in spherical coordinates, show that the form drag is $\pi \mu_c D U$.

4.24. Particles are injected into a cross-flow as shown. The initial particle velocity is v_0 and the gas velocity has a linear profile from the wall in the form $u = ky$. The particles have diameter D , density ρ_p and the fluid viscosity is μ_c . Find an expression for the particle trajectory. Assume Stokes drag is valid. Upon what parameters does the maximum penetration from the wall depend?



Problem 4.24

4.25. A glass particle with a material density of 2500 kg/m^3 is located in the laminar sublayer of a turbulent boundary layer in air flow in a smooth (no roughness) 5-cm duct. The mean air velocity is 10 m/s and the temperature is 20°C . Assuming the particle has zero velocity, for what particle diameter will the Saffman lift force just balance the particle weight?

4.26. The equation of motion for a particle in a gas flow field is

$$\frac{dv}{dt} = \frac{f}{\tau_V}(u - v) + g$$

It is difficult to solve this equation for small τ_V because $u - v$ also becomes small. By using $(v - u)/\tau_V$ as the dependent variable, show that

$$v = u + \frac{\tau_V g}{f} - \frac{\tau_V}{f} \frac{du}{dt} + \left(\frac{\tau_V}{f} \right)^2 \frac{d^2 u}{dt^2} + O(\tau_V^3)$$

This page intentionally left blank

Chapter 5

Particle-Particle Interaction

Particle-particle interaction controls the motion of particles in dense particle flows. Also particle-wall interaction is important in dense flows as well as wall-dominated dilute flows. This chapter first addresses particle-particle interaction and then particle-wall interaction. The application of this information in the development of numerical models is discussed in Chapter 9.

5.1 Particle-particle interaction

Particle-particle collision is unimportant in dilute gas-particle flows. As the particle concentration becomes higher, particles collide with each other and the loss of particle kinetic energy due to inter-particle collision cannot be neglected. With respect to particle-particle interactions in multiphase flow dynamics, two phenomena are identified: collision and contact. From the viewpoint of physics, collision and contact do not differ significantly. Collision is merely contact with short time duration, however, the modeling approach is different for each. For collision or contact, two models are normally used, the hard sphere model and the soft sphere model.

The *hard sphere model* is easy to use but applicable only to binary collisions. The relation between the pre- and post-collision velocities is given explicitly using the coefficient of restitution and friction coefficient. Fortunately, as long as the particulate phase is dispersed, it is sufficient to consider only simple binary collisions and not multiple collisions.

The *soft sphere model* is modeled by using mechanical elements such as a spring and a dash-pot. The soft sphere model is called as DEM (Discrete Element Method or Distinct Element Method). The technical term “DEM” is more popular than “soft sphere model.” In the soft sphere model, the whole process of collision or contact is solved by numerical integration of the equa-

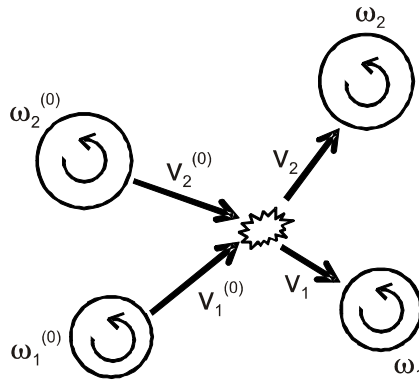


Figure 5.1: Particle-particle collision.

tions of motion. The computation time is much longer in the soft sphere model than in the hard sphere model, but the applicability for the soft sphere model is wider than the hard sphere model. The hard sphere model is described in Section 5.1.1 and the soft sphere model in Section ??

5.1.1 Hard sphere model

The collision of two particles is shown in Figure 5.1. The hard sphere model is based on the impulsive force which is defined by the integral of the force acting on a particle versus time. If the particles are assumed to be rigid spheres, the impulse equations are given as follows,

$$m_1(\mathbf{v}_1 - \mathbf{v}_1^{(0)}) = \mathbf{J} \quad (5.1a)$$

$$m_2(\mathbf{v}_2 - \mathbf{v}_2^{(0)}) = -\mathbf{J} \quad (5.1b)$$

$$I_1(\boldsymbol{\omega}_1 - \boldsymbol{\omega}_1^{(0)}) = r_1 \mathbf{n} \times \mathbf{J} \quad (5.1c)$$

$$I_2(\boldsymbol{\omega}_2 - \boldsymbol{\omega}_2^{(0)}) = r_2 \mathbf{n} \times \mathbf{J} \quad (5.1d)$$

where \mathbf{n} is the unit normal vector from particle 1 to particle 2 at the moment of contact and \mathbf{J} is the impulsive force exerted on particle 1 (which also acts on particle 2 as the reaction force). The subscripts 1 and 2 refer to the two particles. The superscript (0) means values before collision. I is moment of inertia given by $I = (2/5)m a^2$. In the above equations, the particle mass m , size (radius = r), velocities before collision, $\mathbf{v}^{(0)}$ and positions before collision are given. The unknown variables are the impulsive force \mathbf{J} and the post-collisional velocities \mathbf{v} . To solve the problem, the following assumptions apply:

1. particle deformation is neglected so, throughout the collision process,

the distance between the particle centers of mass is constant and equal to the sum of particle radii,

2. the friction on sliding particles obeys Coulomb's friction law, and
3. once a particle stops sliding no further sliding occurs.

In the problem of particle-wall collision, the analysis is made by dividing the collision process into the *compression* and *recovery* periods. The reason for dividing periods in this way is that the *coefficient of restitution* is defined as the ratio of impulsive forces in the compression and recovery periods. Through such a definition of the restitution coefficient, it is convenient to extend the analysis to non-spherical particles. In this section, the particle shape is limited to a sphere, and thus the ratio of the pre-collisional and post-collisional velocities, which is more familiar, is used as the definition of the restitution coefficient. Thus, the analytical procedure is somewhat simpler than that for a particle-wall collision.

The relative velocities between particle centers before and after collision, $\mathbf{G}^{(0)}$ and \mathbf{G} , are

$$\mathbf{G}^{(0)} = \mathbf{v}_1^{(0)} - \mathbf{v}_2^{(0)} \quad (5.2)$$

$$\mathbf{G} = \mathbf{v}_1 - \mathbf{v}_2 \quad (5.3)$$

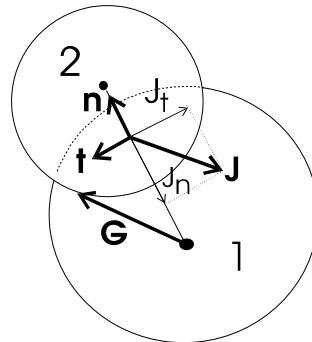


Figure 5.2: Relative motion of two spheres.

From this point, the analysis is made based on the relative particle motion shown in Figure 5.2. The relative velocity of the contact point before collision is

$$\mathbf{G}_c^{(0)} = \mathbf{G}^{(0)} + r_1 \omega_1^{(0)} \times \mathbf{n} + r_2 \omega_2^{(0)} \times \mathbf{n} \quad (5.4)$$

In the above equation, the second and third terms (vectors) of the right side lie in the tangential direction while the first term has normal and tangential

components. The tangential component of the relative velocity $\mathbf{G}_c^{(0)}$ is given by

$$\begin{aligned}\mathbf{G}_{ct}^{(0)} &= \mathbf{G}_c^{(0)} - (\mathbf{G}_c^{(0)} \cdot \mathbf{n})\mathbf{n} \\ &= \mathbf{G}^{(0)} - (\mathbf{G}_c^{(0)} \cdot \mathbf{n})\mathbf{n} + r_1\omega_1^{(0)} \times \mathbf{n} + r_2\omega_2^{(0)} \times \mathbf{n}\end{aligned}\quad (5.5)$$

The impulsive force \mathbf{J} is divided into the normal and tangential components,

$$\mathbf{J} = J_n \mathbf{n} + J_t \mathbf{t} \quad (5.6)$$

The unit vector \mathbf{t} in the tangential direction is given by

$$\mathbf{t} = \frac{\mathbf{G}_{ct}^{(0)}}{\left| \mathbf{G}_{ct}^{(0)} \right|} \quad (5.7)$$

The post-collisional relative velocity \mathbf{G} is related to the pre-collisional velocity through the restitution coefficient

$$\mathbf{n} \cdot \mathbf{G} = -e(\mathbf{n} \cdot \mathbf{G}^{(0)}) \quad (5.8)$$

This equation is regarded as the definition of the restitution coefficient e . The restitution coefficient is assumed to be a constant. From Equations 5.1a, 5.1b and the definition of the relative velocities, $\mathbf{G}^{(0)}$ and \mathbf{G} , one has

$$\mathbf{G} = \mathbf{G}^{(0)} + \frac{m_1 + m_2}{m_1 m_2} \mathbf{J} \quad (5.9)$$

Multiplying by the unit vector \mathbf{n} , one obtains

$$\mathbf{n} \cdot \mathbf{G} = \mathbf{n} \cdot \mathbf{G}^{(0)} + \frac{m_1 + m_2}{m_1 m_2} \mathbf{n} \cdot \mathbf{J} \quad (5.10)$$

Substituting Equation 5.8 into the left side of the above equation results in

$$-e(\mathbf{n} \cdot \mathbf{G}^{(0)}) = \mathbf{n} \cdot \mathbf{G}^{(0)} + \frac{m_1 + m_2}{m_1 m_2} J_n \quad (5.11)$$

From Equation 5.11, the normal component of the impulsive force, J_n , is given explicitly as

$$J_n = -\frac{m_1 m_2}{m_1 + m_2} (1 + e)(\mathbf{n} \cdot \mathbf{G}^{(0)}) < 0 \quad (5.12)$$

Assuming that the particles slide, the tangential component of the impulsive force, J_t , is

$$J_t = f J_n < 0 \quad (5.13)$$

from *Coulomb's law for friction*. The friction coefficient f and the coefficient of restitution are regarded as known parameters. By substituting the impulsive

force \mathbf{J} given by Equations 5.12 and 5.13 into Equations 5.1a to 5.1d, all the post-collisional velocities are obtained. The results are

$$\mathbf{v}_1 = \mathbf{v}_1^{(0)} - (\mathbf{n} + f\mathbf{t})(\mathbf{n} \cdot \mathbf{G}^{(0)})(1+e) \frac{m_2}{m_1 + m_2} \quad (5.14a)$$

$$\mathbf{v}_2 = \mathbf{v}_2^{(0)} + (\mathbf{n} + f\mathbf{t})(\mathbf{n} \cdot \mathbf{G}^{(0)})(1+e) \frac{m_1}{m_1 + m_2} \quad (5.14b)$$

$$\boldsymbol{\omega}_1 = \boldsymbol{\omega}_1^{(0)} - \left(\frac{5}{2r_1} \right) (\mathbf{n} \cdot \mathbf{G}^{(0)}) (\mathbf{n} \times \mathbf{t}) f (1+e) \frac{m_2}{m_1 + m_2} \quad (5.14c)$$

$$\boldsymbol{\omega}_2 = \boldsymbol{\omega}_2^{(0)} - \left(\frac{5}{2r_2} \right) (\mathbf{n} \cdot \mathbf{G}^{(0)}) (\mathbf{n} \times \mathbf{t}) f (1+e) \frac{m_1}{m_1 + m_2} \quad (5.14d)$$

Equations 5.14a to 5.14d show the solutions corresponding to the case where the two spheres slide during the collision process. If the two spheres stop sliding, the results are different.

From the value for the tangential component of the relative velocity of the contact point it is determined whether or not the particles continue to slide. Consider the component based on the case in which the particles slide. The post-collisional relative velocity is given by

$$\mathbf{G}_c = \mathbf{G} + r_1 \boldsymbol{\omega}_1 \times \mathbf{n} + r_2 \boldsymbol{\omega}_2 \times \mathbf{n} \quad (5.15)$$

By using Equations 5.1c, 5.1d and 5.9, Equation 5.16 can be rewritten as

$$\mathbf{G}_c = \mathbf{G}_c^{(0)} + \left\{ J_n \mathbf{n} + \left(\frac{7}{2} \right) J_t \mathbf{t} \right\} \frac{m_1 + m_2}{m_1 m_2} \quad (5.16)$$

Taking the scalar product of \mathbf{t} (given by Equation 5.7) the above equation yields the tangential component of \mathbf{G}_{ct} in the form

$$\mathbf{G}_{ct} = \frac{\mathbf{G}_{ct}^{(0)}}{\left| \mathbf{G}_{ct}^{(0)} \right|} \left\{ \left| \mathbf{G}_{ct}^{(0)} \right| + \left(\frac{7}{2} \right) J_t \frac{m_1 + m_2}{m_1 m_2} \right\}. \quad (5.17)$$

The case for which the particles continue to slide during the collision process is given by the condition that the sign of the above parenthesis is positive; that is,

$$J_t > - \left(\frac{2}{7} \right) \frac{m_1 m_2}{m_1 + m_2} \left| \mathbf{G}_{ct}^{(0)} \right|. \quad (5.18)$$

The impulse J_t in the above inequality can be expressed in terms of the pre-collisional conditions through Equations 5.12 and 5.13. Rewriting the above relation one has

$$\frac{\mathbf{n} \cdot \mathbf{G}^{(0)}}{\left| \mathbf{G}_{ct}^{(0)} \right|} < \left(\frac{2}{7} \right) \frac{1}{f(1+e)} \quad (5.19)$$

$\mathbf{G}^{(0)}$ is the pre-collisional relative velocity at the contact point which is given by Equation 5.2 and $\mathbf{G}_{ct}^{(0)}$ is given by Equation 5.5. If Equation 5.18 is not satisfied, the particle stops sliding. This case corresponds to the condition that the post-collisional relative velocity at the contact point is zero; i.e., the left side of Equation 5.17 is equal to zero. Therefore,

$$J_t = -\left(\frac{2}{7}\right) \frac{m_1 m_2}{m_1 + m_2} \left|\mathbf{G}_{ct}^{(0)}\right| \quad (5.20)$$

Substituting the impulsive force \mathbf{J} given by Equations 5.12 and 5.13 into Equations 5.1a to 5.1d, all the post-collisional velocities are obtained for the case where the particles stop sliding during the collision. The results are as follows,

$$\mathbf{v}_1 = \mathbf{v}_1^{(0)} - \left\{ (1+e)(\mathbf{n} \cdot \mathbf{G}^{(0)})\mathbf{n} + \frac{2}{7} \left|\mathbf{G}_{ct}^{(0)}\right| \mathbf{t} \right\} \frac{m_2}{m_1 + m_2} \quad (5.21a)$$

$$\mathbf{v}_2 = \mathbf{v}_2^{(0)} + \left\{ (1+e)(\mathbf{n} \cdot \mathbf{G}^{(0)})\mathbf{n} + \frac{2}{7} \left|\mathbf{G}_{ct}^{(0)}\right| \mathbf{t} \right\} \frac{m_1}{m_1 + m_2} \quad (5.21b)$$

$$\boldsymbol{\omega}_1 = \boldsymbol{\omega}_1^{(0)} - \frac{5}{7r_1} \left|\mathbf{G}_{ct}^{(0)}\right| (\mathbf{n} \times \mathbf{t}) \frac{m_2}{m_1 + m_2} \quad (5.21c)$$

$$\boldsymbol{\omega}_2 = \boldsymbol{\omega}_2^{(0)} - \frac{5}{7r_2} \left|\mathbf{G}_{ct}^{(0)}\right| (\mathbf{n} \times \mathbf{t}) \frac{m_1}{m_1 + m_2} \quad (5.21d)$$

5.1.2 Soft sphere model (DSEM)

Modelling

Consider a particle approaching and colliding with a group of contacting particles as shown in Figure 5.3. When solid bodies exert a force on each other, they deform. If this phenomenon is described rigorously, one should note a deformation of all particles, more or less. The deformation is transmitted and decayed, as shown in Figure 5.3b. When accounting for the computational load for a large number of particles, a certain simplification is inevitable in practical computation. The soft sphere model was developed for the purpose of simplification (Cundall & Strack, 1979). First, it is assumed that the influence of the particle of interest is limited to only neighboring particle(s) which is(are) in direct contact with that particle. For instance, Particle A is influenced by only Particle B in Figure 5.3. Particle B is influenced by Particle A and Particle C. Next, the deformation is replaced with the overlap of two particles. That is, instead of dealing with the deformation, the particles contacting each other under the influence of external forces are made to overlap as shown in Figure 5.3c. The more the overlap distance, the larger the repulsive force. This repulsive force can be expressed by equating the overlap distance with compression of a spring. In general, deformation of a body accompanies energy loss. This is the reason why the coefficient of restitution is less than one. The energy loss depends on the deformation speed. A dash pot or a viscous damper is a suitable mechanical element to model the energy loss.

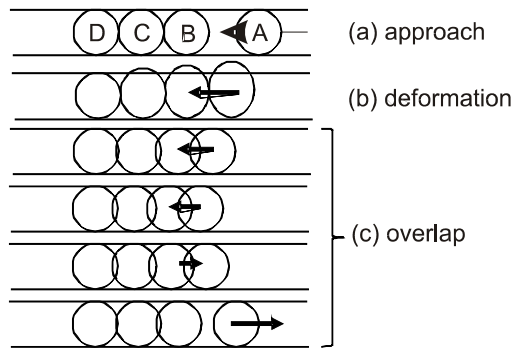


Figure 5.3: Assumptions for the soft sphere model.

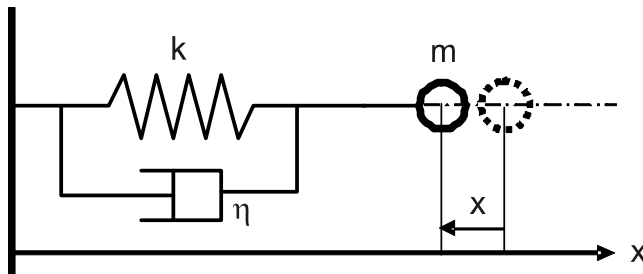


Figure 5.4: Spring-mass-damper system.

The mechanism described above is the same as the spring-damper system shown in Figure 5.4. The motion of the body with mass m is given by the following differential equation

$$m\ddot{x} + \eta\dot{x} + kx = 0 \quad (5.22)$$

where x is the distance from the equilibrium position of the mass, η , the damping coefficient of the dash-pot and k , the stiffness of the spring. In Equation 5.22, the relationship between the force and displacement is assumed to be linear. The kinetic energy is lost in the dash-pot. The work done by the dash-pot is proportional to the velocity of the mass. There are three modes of motion depending on the parameters; that is, *underdamped*, *overdamped* and *critically damped*. Usually the particle bounces after collision which corresponds to the underdamped mode.

The analogy between the spring-damper system shown in Figure 5.4 and particle-particle/wall interaction is as follows. The dotted circle in Figure 5.4 signifies the position of particle center before interaction and the spring is in equilibrium state. The particle center moves to the solid circle in Figure 5.4 under the effect of external force(s). When the center moves, the spring

compresses and a repulsive force ensues. This repulsive force is the reaction force acting on the particle. Due to the reaction force, the particle begins to return to the original position after reaching the maximum displacement. The velocity of the particle returning to the original position is less than the velocity before collision due to the energy loss in the dash-pot.

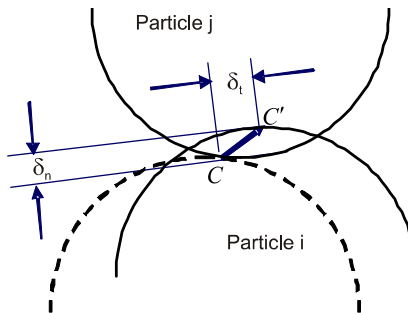


Figure 5.5: Two particles making contact.

The above explanation addresses the motion in the normal direction. In general, the motion of a particle has two components, normal and tangential, as shown in Figure 5.5 where particle i approaches particle j obliquely. Particle i at the moment of contact is shown by the dotted line and the two particles contact at the point C . In the soft sphere model, the two particles overlap without changing their shapes as, described above. The overlap distance δ has two components: δ_n , the normal component and δ_t , the tangential component.

The force model can be separated into separate components for the tangential and normal forces as shown in Figure 5.6 where a spring, dash-pot and other mechanical elements are positioned between particle i and particle j . The coupler shown in Figure 5.6a allows the particles to separate when the particles are released from the contact force. If the tangential force exceeds the yield stress, the two particles slide. Before such sliding occurs, the tangential force is modelled by the spring and dash-pot, but when the particles slide, the friction force is the tangential component of the force. To express this friction force, a friction slider is set in Figure 5.6b.

The difference between the hard sphere and soft sphere models depends on whether Newton's equations of motion are expressed in integral or differential form. The hard sphere model uses integral form. With this model the momentum difference between two points in time is equal to the impulsive force defined as the integral of the force versus time. The soft sphere model starts with the differential equations. If the motion of a particle is given by Equation 5.22, analytical solutions are available. Usually, however, in particle flows or multiphase flows the relation between the force and displacement is non-linear. Further the influence from more than one particle should be considered and thus the integration is carried out numerically by using an

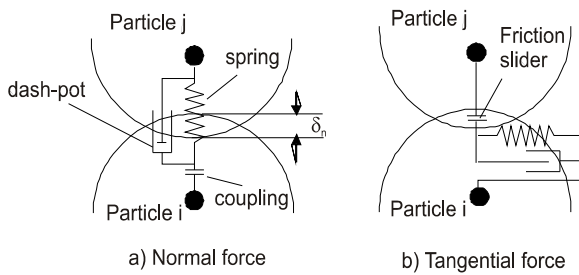


Figure 5.6: Soft-sphere model: (a) Normal force, (b) tangential force.

appropriate time step. Therefore, the variations in momentum and displacement are obtained for arbitrary times as solutions of the differential equations. This means that not only the relationship between pre- and post-collisional velocities are calculated but also the velocities during the whole process of contact are calculated as well. For this reason, the computation time is much longer for the soft sphere model than for the hard sphere model.

Formulation

The effects of spring, dash-pot and friction slider on particle motion appear through the following parameters:

stiffness, k

damping coefficient, η

friction coefficient, f

The normal component of the contact force, F_{nij} , acting on particle i is given by the sum of the forces due to the spring and the dash-pot. If the particles are assumed to be two-dimensional disks, the effect of the spring is linear against the overlap distance and the force is expressed by

$$\mathbf{F}_{nij} = (-k_n \delta_n - \eta_{nj} \mathbf{G} \cdot \mathbf{n}) \mathbf{n} \quad (5.23)$$

where δ_n is the displacement of particle caused by the normal force, \mathbf{G} is the velocity vector of particle i relative to particle j ($\mathbf{G} = \mathbf{v}_i - \mathbf{v}_j$), and \mathbf{n} is the unit vector in the direction of the line from the center of particle i to that of particle j . According to *Hertzian contact theory*, the normal force varies as the $3/2$ power of the displacement in the case of three-dimensional spheres and therefore the force \mathbf{F}_{nij} acting on spherical particle i can be expressed by

$$\mathbf{F}_{nij} = (-k_n \delta_n^{3/2} - \eta_{nj} \mathbf{G} \cdot \mathbf{n}) \mathbf{n} \quad (5.24)$$

The tangential component of the contact force, is given by

$$\mathbf{F}_{tij} = -k_t \boldsymbol{\delta}_t - \eta_{tj} \mathbf{G}_{ct} \quad (5.25)$$

where k_t and η_{tj} are, respectively, the stiffness and damping coefficient in the tangential direction. In the above equations, the suffixes n and t designate the components in the normal and tangential directions. G_{ct} is the slip velocity of the contact point, which is given by

$$\mathbf{G}_{ct} = \mathbf{G} - (\mathbf{G} \cdot \mathbf{n})\mathbf{n} + a_i \boldsymbol{\Omega}_i \times \mathbf{n} + a_j \boldsymbol{\Omega}_j \times \mathbf{n} \quad (5.26)$$

where a_i and a_j are the radii of particle i and particle j , respectively. Note that the tangential displacement δ_t is a vector and its direction, in general, is not equal to the slip velocity vector \mathbf{G}_{ct} in three-dimensional motion. If the following relation is satisfied

$$|\mathbf{F}_{tii}|_j > f |\mathbf{F}_{nij}| \quad (5.27)$$

particle i slides and the tangential force is given by

$$\mathbf{F}_{tij} = -f |\mathbf{F}_{nij}| \mathbf{t} \quad (5.28)$$

instead of Equation 5.25. Equation 5.28 is the Coulomb-type friction law. The friction coefficient f is measurable and regarded as a parameter which can be obtained empirically. The vector \mathbf{t} is the unit vector defined by

$$t = \frac{\mathbf{G}_{ct}}{|\mathbf{G}_{ct}|} \quad (5.29)$$

In general, several particles are in contact with particle i at the same time as shown in Figure 5.7. Therefore, the total force and torque acting on particle i is obtained by taking the sum of the above forces with respect to j .

$$\mathbf{F}_i = \sum_j (\mathbf{F}_{nij} + \mathbf{F}_{tij}) \quad (5.30a)$$

$$\mathbf{T}_i = \sum_j (a\mathbf{n} \times \mathbf{F}_{tij}) \quad (5.30b)$$

Determination of stiffness The stiffness k_n can be given using the Hertzian contact theory (Johnson, 1985) when the physical properties such as the Young's modulus and Poisson ratio are known. The stiffness of a sphere is expressed

$$k_n = \frac{4}{3} \left(\frac{1 - \sigma_i^2}{E_i} + \frac{1 - \sigma_j^2}{E_j} \right)^{-1} \left(\frac{r_i + r_j}{r_i r_j} \right)^{-1/2} \quad (5.31)$$

where E and σ are Young's modulus and Poisson ratio, respectively, and r is particle radius. Suffices i and j denote particle i and particle j , respectively. If particle i and j have the same radius r and the same physical properties, the stiffness simplifies to

$$k_n = \frac{\sqrt{2r} E}{3(1 - \sigma^2)} \quad (5.32)$$

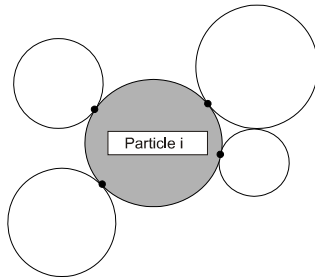


Figure 5.7: Particle i in contact with surrounding particles.

The stiffness k_t can be given using the Mindlin's theory (Mindlin, 1949)

$$k_t = 8 \left(\frac{1 - \sigma_i^2}{H_i} + \frac{1 - \sigma_j^2}{H_j} \right)^{-1} \left(\frac{r_i + r_j}{r_i r_j} \right)^{-1/2} \delta_n^{1/2} \quad (5.33)$$

where H_i and H_j are shear modulus of particle i and particle j , respectively. If both particles have the same properties, the stiffness also simplifies to

$$k_t = \frac{2\sqrt{2}H}{2 - \sigma^2} \delta_n^{1/2} \quad (5.34)$$

where H is related to the Young's modulus, E , and Poisson ratio, σ , as follows

$$H = \frac{E}{2(1 + \sigma)} \quad (5.35)$$

Example: Calculate the normal force due collision of two 100-micron aluminum particles due to a displacement of $2 \mu\text{m}$.

Solution: Poisson's ratio and modulus of elasticity for aluminum is 0.33 and 68 GPa, respectively. The spring constant for a Hertzian contact is

$$k_n = \frac{\sqrt{2r}E}{3(1 - \sigma^2)} = \frac{\sqrt{10^{-4}} \times 68 \times 10^9}{3(1 - 0.33^2)} = 0.234 \times 10^9 \text{ N/m}^{3/2}$$

The force due to a $2 \mu\text{m}$ displacement is

$$P_n = k_n \delta^{3/2} = 0.254 \times 10^9 \times (2 \times 10^{-6})^{3/2} = 0.719 \text{ N}$$

As shown above, the stiffness can be determined by material properties. This is the advantage of this model. Unfortunately, it is often difficult in practice to use the stiffness calculated by the Hertzian theory, because a time step Δt for numerical integration must be so small that an excessive amount of computational time is needed. It is empirically known that the time step

Δt should be less than one-tenth of the natural oscillation period $2\pi\sqrt{m/k}$ of a mass-spring system. Therefore, in many cases a small value of stiffness is assumed for the convenience of the calculation. In some cases, the results based on a stiffness much smaller than an actual value are not so different from those based on the precise stiffness value. Fortunately, this is the case for fluid-particle multiphase flows, where fluid forces acting on particles make the difference in stiffness a minor effect.

Determination of damping coefficient Cundall and Strack (1979) proposed two expressions for the damping coefficients; namely

$$\eta_n = 2\sqrt{mk_n} \quad (5.36a)$$

$$\eta_t = 2\sqrt{mk_t} \quad (5.36b)$$

which were derived for the critical damping condition of a single degree-of-freedom system consisting of a mass, spring and dash-pot. The reason for choosing the critical damping condition, as shown in Equations 5.36a and 5.36b comes from the requirement that bouncing motion after collision should be damped as soon as possible.

Another method for determining the damping coefficient is based on the idea that the damping coefficient should be related to the coefficient of restitution which is regarded as a physical property of the particle material. Fortunately the coefficient of restitution can be measured in a simple experiment.

If the relationship between spring force and displacement is linear, the solution of Equation 5.22 can be used to relate the damping coefficient to the coefficient of restitution (Tsuji et al., 1993). Assume that x denotes the distance of particle center from the wall and the particle collides with the wall at time $t = 0$ with the initial velocity $v = v_0$ and initial position of particle center $x = x_0$. The initial velocity is negative. The under-damped solutions are given

$$\text{Position } x = \frac{v_0}{q} \sin(qt) \exp(-\gamma\omega t) + x_0 \quad (5.37a)$$

$$\text{Velocity } \dot{x} = \frac{v_0}{q} \exp(-\gamma\omega t) q \cos(qt) - \gamma\omega \sin(qt) \quad (5.37b)$$

where $\omega = \sqrt{k/m}$, $\gamma = \eta / (2\sqrt{mk})$ and $q = \omega\sqrt{1 - \gamma^2}$.

The particle position becomes negative, reaches the minimum value and then recovers to the initial position $x = x_0$ at $t = \pi/q$ which is equal to half of the oscillation period. The particle velocity at $t = \pi/q$ is expressed as

$$v_1 = [\dot{x}]_{t=\pi/q} = -v_0 \exp\left(-\frac{\gamma\omega\pi}{q}\right) \quad (5.38)$$

The ratio of v_1 to v_0 corresponds to the coefficient of restitution e .

$$e = \exp\left(-\frac{\gamma\omega\pi}{q}\right) \quad (5.39)$$

From the above equations,

$$\eta = -\frac{2 \ln e}{\sqrt{\pi^2 + \ln e}} \sqrt{mk} \quad (5.40)$$

In the case of a non-linear spring, Tsuji et al. (1992) showed a method for relating the damping coefficient η_n to the restitution coefficient. According to Tsuji et al., the damping coefficient η_n is expressed by

$$\eta_n = \alpha \sqrt{mk} \delta_n^{1/4} \quad (5.41)$$

where α is a constant related to the coefficient of restitution. The relationship between α and coefficient of restitution is shown in Figure 5.8. The same value is used for the damping coefficient in the tangential direction with no firm justification.

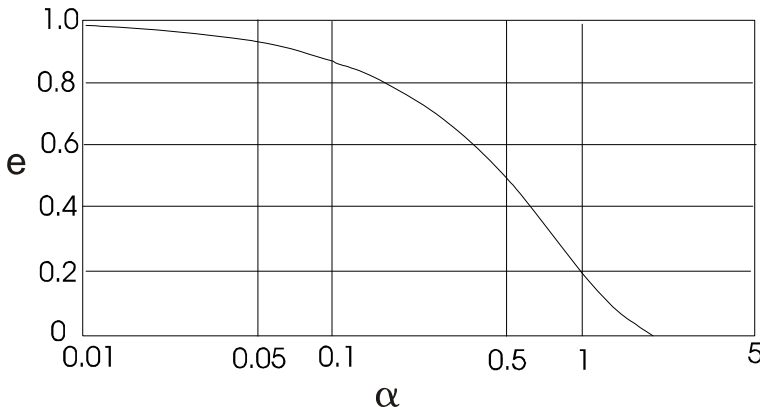


Figure 5.8: Relationship between a and the coefficient of restitution. (Reprinted from *Powder Technology*, 71, Tsuji, Y., Tanaka, T. and Ishida, T., Lagrangian numerical simulation of plug flow of collisionless particles in a horizontal pipe, 239, 1992, with kind permission from Elsevier.)

Originally the soft sphere model was used to model the flow of granular materials without considering the effects of the interstitial fluid. Many papers have been reported for flows in chutes and hoppers, as well as for vibrating beds, packing, attrition and pulverization.

Computer simulation using the soft sphere model is called a DEM simulation. Application of the soft sphere model has expanded dramatically by coupling it with CFD (Computational Fluid Dynamics). Zhu et al. (2008) made a comprehensive review of this field which shows that almost all the unit operations of powder technology are examples of the application of the soft sphere model. The soft sphere model is very useful for discrete particle simulation of dense phase flows such as fluidized beds and dense phase pneumatic conveying. In this section, a description has been provided mainly for

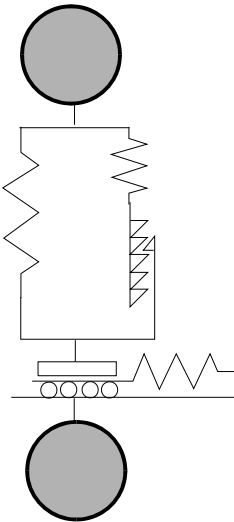


Figure 5.9: Partially latching spring model. (Reprinted with permission from Walton, O.R. and Braun, R.L. 1986, Viscosity, granular-temperature, and stress calculations for shearing assemblies of inelastic, frictional disks, *J. Rheology*, **30**, 949. Copyright [1986], The Society of Rheology.)

the model shown in Figure 5.6. However, other elements can be added, if necessary (Walton & Braun, 1986), as shown in Figure 5.9.

5.1.3 Hard sphere simulation of a soft sphere model

The primary problem with the implementation of the soft sphere model is the small time steps needed to calculate the motion during collision. Walton (1993) has proposed a hard sphere analogy of the soft sphere model which can be used if only two particles are in contact at one time. This model is based on a normal coefficient of restitution, e , and a rotational restitution coefficient, β . First of all, a calculation is done assuming that sliding occurs and a predetermined maximum value of β is calculated,

$$\beta^* = -1 + f(1 + e)(1 + \frac{1}{K}) \frac{|\mathbf{n} \cdot \mathbf{G}^{(0)}|}{|\mathbf{G}_{ct}^{(0)}|} \quad (5.42)$$

where $K = 4I/mD^2$. For a uniform density sphere, $K = 0.4$. If β^* exceeds the maximum value for β ; namely β_o , then $\beta = \beta_o$. This corresponds to the rolling solution. Otherwise, $\beta = \beta^*$ which corresponds to the sliding solution. For computational convenience and to obviate the need to take square roots, Walton rewrote Equation 5.42 as

$$(\beta^* + 1)^2 = f^2(1+e)^2\left(1 + \frac{1}{K}\right)^2 \frac{\left(\left|\mathbf{n} \cdot \mathbf{G}^{(0)}\right|\right)^2}{\mathbf{G}_{ct}^{(0)} \cdot \mathbf{G}_{ct}^{(0)}} \quad (5.43)$$

The condition for β then becomes

$$\text{If } (\beta^* + 1)^2 > (\beta_o + 1)^2 \quad \text{then } \beta = \beta_o$$

$$\text{Otherwise } \beta = \beta^*$$

Finally for two colliding particles of the same size, the post-collisional translational velocities are

$$\mathbf{v}_1 = \mathbf{v}_1^{(0)} - \frac{1}{2}(1+e)(\mathbf{n} \cdot \mathbf{G})\mathbf{n} - \frac{K}{2} \frac{1+\beta}{1+K}(\mathbf{G}_{ct}^{(0)}) \quad (5.44a)$$

$$\mathbf{v}_2 = \mathbf{v}_2^{(0)} + \frac{1}{2}(1+e)(\mathbf{n} \cdot \mathbf{G})\mathbf{n} + \frac{K}{2} \frac{1+\beta}{1+K}(\mathbf{G}_{ct}^{(0)}) \quad (5.44b)$$

and the rotational velocities are

$$\boldsymbol{\omega}_1 = \boldsymbol{\omega}_1^{(0)} - \frac{1+\beta}{a(1+K)} \mathbf{n} \times \mathbf{G}_{ct}^{(0)} \quad (5.45a)$$

$$\boldsymbol{\omega}_2 = \boldsymbol{\omega}_2^{(0)} - \frac{1+\beta}{a(1+K)} \mathbf{n} \times \mathbf{G}_{ct}^{(0)} \quad (5.45b)$$

The value for β_o has to be obtained from experiment. For plastic spheres, $\beta_o \approx 0.35$.

This hard sphere analogy of the soft sphere collision dynamics greatly reduces the computational time for a soft sphere model. The model has been developed for collisions of particles of unequal size as well.

5.1.4 Cohesive force

Inter-particle forces due to the wetness of particle surfaces, due to electrostatic charges and the van der Waals' forces are known to cause adhesion of particle to a wall or to another particle.

Force due to a liquid bridge As shown in Figure 5.10, a liquid bridge is formed between particles due to condensation under an environment of high humidity. The liquid surface is concave due to surface tension and the pressure is negative inside the bridge. The force acting on the particle is the sum of the force due to the negative pressure and the cohesive force due to capillarity.

The force due to the liquid bridge F_1 is given

$$F_1 = \pi a_2^2 \sigma \left(\frac{1}{a_1} + \frac{1}{a_2} \right) + 2\pi a_2 \sigma \cos \theta \quad (5.46)$$

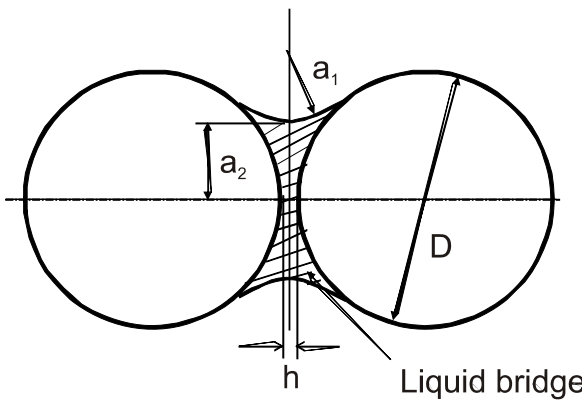


Figure 5.10: Liquid bridge between two spheres.

where a_1 is the curvature radius of the bridge, a_2 , the radius of the liquid bridge (see Figure 5.10) and σ is the *capillary force* (N/m) and θ is the contact angle between liquid and particle surface. The contact angle θ can be assumed to be zero in the case of water. This equation is called *Laplace-Young equation*. From the geometric conditions and some assumptions, Equation 5.46 can be reduced to a simpler form.

Electrostatic force Particles in a gas are usually charged and an electrostatic force acts on the particles. The electrostatic force between two charged particles is given by the Coulomb formula

$$F_c = \frac{1}{4\pi\varepsilon_0} \frac{q_1 q_2}{l^2} \quad (5.47)$$

where q_1 and q_2 are respective charges on the particles, ε_0 is dielectric constant (F/m) in a vacuum and l is the distance between particle centers. If the signs of q_1 and q_2 are different, an attractive force acts on the two particles and, if not, the force is repulsive.

The cohesive force acting on the spherical particles of the same size (diameter $=D$) in contact with each other is given by

$$F_E = \frac{\pi\sigma_1\sigma_2}{\varepsilon_0} D^2 \quad (5.48)$$

where σ_1 and σ_2 are charge densities (C/m^2) of the two particles. The above equation is derived under the assumption that the particles are charged uniformly and that the effective charge is concentrated at the particle centers. The effect of the particle size on the force is larger for the Coulomb cohesive force than for the van der Waals force.

5.1.5 van der Waals forces

Inter-particle forces due to particle wetness, electrostatic charges and van der Waals forces are known to cause adhesion of a particle to a wall or onto another particle. The *van der Waals forces* arise from molecular interaction between solid surfaces. This force becomes apparent when very smooth surfaces are brought into contact. To estimate the magnitude of van der Waals forces acting on solid bodies, the contribution of the many molecules constituting the surfaces must be considered. Hamaker (1937) carried out calculations for various geometries. The force F between two infinite flat plates with separation z is expressed by

$$F = \frac{A}{6\pi z^3} \quad (5.49)$$

where F is force per unit area and A is referred to as the *Hamaker constant*. The minimum separation distance for two plates in air at standard conditions is 0.4 nm which is the mean free path of the air molecules.

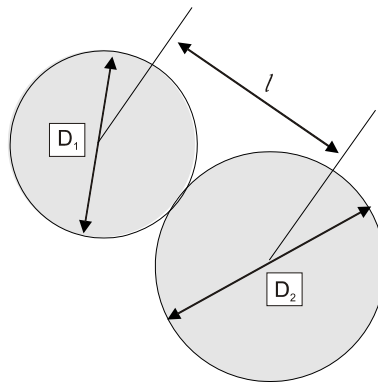


Figure 5.11: Two particles in contact.

The force between two spheres shown in Figure 5.11 is expressed by

$$F = \frac{Ad}{12z^2} \quad (5.50)$$

where

$$d = \frac{D_1 \cdot D_2}{D_1 + D_2} \quad (5.51)$$

and where z is the separation distance at the point of “contact.” Czarnecki and Dabros (1980) suggest that the effect of roughness of the sphere surfaces modifies the van der Waals force by

$$F = \frac{Ad}{12(z + b)^2} \quad (5.52)$$

where $b = (b_1 + b_2)/2$ and b_1 and b_2 are the roughness heights of the two spheres. The force between a sphere and a flat plate can be obtained by putting the diameter of one sphere equal to infinity; i.e., $d = D$ in Equation 5.51.

Examples of the Hamaker constant for various materials are shown in Table 5.5.

Material	Hamaker constant [$J \times 10^{20}$]
Water	4.38
Polystyrene	6.15-6.6
Al_2O_3	15.5
Cu	28.4
Au	45.5

Table 5.5. Hamaker constant.

Example: Determine the maximum roughness of a 10- μm copper particle that would be suspended by the van der Waals force on the bottom side of a perfectly smooth flat copper plate in air.

Solution: The Hamaker constant for copper is 28.4×10^{-20} J. Equating the van der Waals force to the weight gives

$$\frac{AD}{12(z + b)^2} = \frac{\pi}{6} \rho_d D^3 g$$

Solving for $z + b$ one has

$$z + b = \frac{1}{D} \sqrt{\frac{A}{2\pi\rho_d g}}$$

The density of copper is 8900 kg/m³. Using this value in the above equation, one finds $z + b = 7.2 \times 10^{-8}$ m. Taking z as 0.4×10^{-9} m, the value for the maximum roughness of the sphere is 1.43×10^{-7} m or 0.143 μm !

The Hamaker constant between different materials is given by

$$A_{12} = \sqrt{A_{11} \cdot A_{22}} \quad (5.53)$$

where A_{11} and A_{22} are the Hamaker constants for each material. The above relation is used for “dry” solids. If two solids are separated by a third material, the Hamaker constant is expressed by

$$A_{132} = \left(\sqrt{A_{11}} - \sqrt{A_{33}} \right) \left(\sqrt{A_{22}} - \sqrt{A_{33}} \right) \quad (5.54)$$

where A_{33} is the Hamaker constant of the third material. The Hamaker constant A_{33} for air is very small and thus Equation 5.53 is reduced to Equation 5.54. Comparing Equations 5.53 and 5.54, one finds that the attractive force between two solids becomes smaller in water than in air. In the above equation the sign of the van der Waals force between two solids can be negative, i.e., a repulsive force arises if A_{33} has a value between A_{11} and A_{22} .

5.1.6 Solid particle agglomeration

Agglomeration of solid particles occurs because of the van der Waals force, electrostatic effects and liquid bridges. When two particles collide and deform, energy is dissipated during collision. If the energy dissipated is greater than the impact kinetic energy, there is no energy available for particle rebound. Ho and Sommerfeld (2002) show that the critical impact velocity to establish the criterion for rebound or collision is

$$v_{\text{crit}} = \frac{1}{D} \frac{\sqrt{1-e^2}}{e^2} \frac{A}{\pi z_0^2 \sqrt{6P_{\text{pl}}\rho_d}} \quad (5.55)$$

where D is the particle diameter, e the restitution coefficient, A the Hamaker constant, z_0 the contact distance and P_{pl} is the yield pressure of the particle material. Depending on the process, particle properties and residence time agglomerates may consist from ten to several thousand primary particles. The geometry of the agglomerate may be spherical, chain-like or have a dendritic appearance. Different parameters can be used to characterize the agglomerates such as volume-specific surface area, fluid dynamic radius and so on. Fractal-like agglomerates are often characterized by a fractal dimension in which a dimension of unity would be a straight chain of particles and a dimension of three would be a sphere.

Because of different morphologies and shapes, it is virtually impossible to determine the fluid dynamic forces on the agglomerates. Well-known correlations for porous media or particle packings provide some reasonable estimates. The results clearly demonstrate that the drag coefficient decreases significantly as the fractal dimension is reduced. For a fractal dimension of 1.5, the drag is one half that of a rigid sphere.

5.1.7 Fluid forces on approaching particles

Consider two spheres in a fluid approaching one another. As the distance between the spheres becomes smaller, the fluid pressure between the spheres becomes larger to move the fluid outward and the resulting force acts to prevent contact. This force can be deduced theoretically from the equations of fluid motion using the lubrication approximations for creeping flow. Here, the two spheres are assumed to be the same size so the flow is symmetric about the center plane between the spheres and axisymmetric along the line connecting the centers of the spheres. Although not addressed here, there is

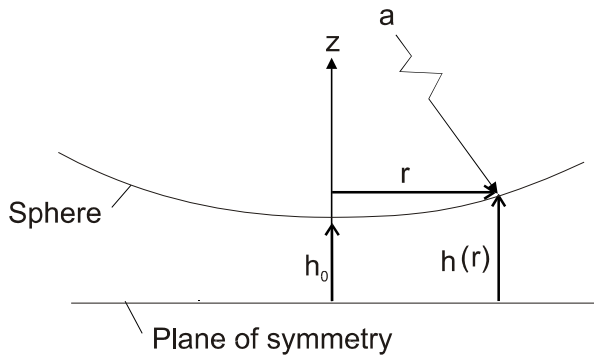


Figure 5.12: Coordinate system for two approaching particles.

a model for the case where a liquid bridge is formed but the bridge does not affect the final result so long as the separation distance is small.

As shown in Figure 5.12, fluid motion is described by the cylindrical coordinates (r, θ, z) . The basic equations to be used are the continuity equation and the Navier-Stokes equations with the lubrication approximation. In this case, the inertia terms and some of the viscous stress terms can be neglected and the pressure is assumed to be a function only of r so the Navier-Stokes equations reduce to

$$\frac{dp}{dr} = \mu_c \frac{\partial^2 u_r}{\partial z^2} \quad (5.56)$$

where u_r is the velocity component in the r -direction. Integrating Equation 5.56 in the region $z = 0 - h$ with the boundary conditions of zero shear rate in the center plane ($\partial u_r / \partial z = 0$ at $z = 0$) and no slip at the wall ($u_r = 0$ at $z = h$) yields,

$$u_r = \frac{1}{2\mu} \frac{dp}{dr} (z^2 - h^2) \quad (5.57)$$

Conservation of mass over the region bounded by the radius r and the space between the symmetry plane and the sphere requires

$$2\pi r \int_0^h u_r dz + \pi r^2 h = 0 \quad (5.58)$$

where \dot{h} is the rate at which the sphere is approaching the symmetry plane. Substituting u_r from Equation 5.57 and integrating yields

$$\frac{dp}{dr} = \mu \left(\frac{3}{2} \right) \frac{r \dot{h}}{h^3} \quad (5.59)$$

The pressure difference $\Delta p = p - p_0$ is obtained by integrating Equation 5.59 from $r = r$ to $r = a$;

$$\Delta p = \mu_c \frac{3\dot{h}}{2} \int_a^r \frac{r}{h^3} dr \quad (5.60)$$

The force due to the pressure is obtained by integrating Equation 5.60 over the regions, $\theta = 0 \rightarrow 2\pi$ and $r = 0 \rightarrow a$ which results in

$$F = \int_0^{2\pi} \int_o^a \left[\mu_c \frac{3\dot{h}}{2} \int_a^r \frac{r}{h^3} dr \right] r d\theta dr = -\pi \mu_c \frac{3\dot{h}}{2} \int_0^a \frac{r^3}{h^3} dr \quad (5.61)$$

The distance $h - h_0$ is approximated by

$$h - h_0 = \frac{r^2}{2a} \quad (5.62)$$

By substituting Equation 5.62 into Equation 5.61 with the assumption of small h_0 one obtains

$$F = -\frac{3\pi\mu_c a^2 \dot{h}}{2h_0} \quad (5.63)$$

This is the force acting on two approaching spheres. Note that the distance R corresponding to the liquid bridge disappears. The more general case in which the shear stress is expressed by a power law in the form

$$\tau = \mu_c \left(\frac{\partial u_r}{\partial z} \right)^n \quad (5.64)$$

can be found in Adams and Edmondson (1987).

5.2 Particle-wall interaction

The problem of particle-wall interaction is encountered when analyzing fluid-particle flows contained within walls such as pipe flows, channel flows and fluidized beds. The particle-wall interaction falls into two categories: hydrodynamic interaction due to the proximity of a wall and mechanical interaction caused by contact with the wall. The Saffman lift force due to velocity gradient near the wall is one example of the hydrodynamic interaction. Another example is the fluid force acting on a particle approaching the wall in the normal direction. This interaction is explained in Section 5.1 where the case of two approaching particles is addressed. Assuming the diameter of one particle to be infinitely large, particle-particle interaction is reduced to particle-wall interaction. Hydrodynamic interaction of this kind prevents a particle from making contact with the wall. This hydrodynamic interaction can be neglected if the particle inertia force is so large that collision takes place in a time much less than the hydrodynamic relaxation time of the particle.

The treatment of the mechanical behavior associated with particle-wall interaction depends on the inertia of the particle. When a massive particle collides with a wall, it rebounds but loses kinetic energy due to friction and inelasticity effects. For a very small particle approaching a wall, molecular forces become dominant compared with the inertial force. As a result, the particle is captured by the wall due to cohesive forces, and neither rebounds from nor slides along the wall. This cohesive force is identified as the van der Waals force.

Section 5.2.1 deals with formulation of the collision of a single spherical particle with a flat wall. Section 5.2.2 treats irregular bouncing. Irregularity bouncing is modeled by considering non-sphericity of a particle and roughness of the wall. Section 5.2.3 deals with problems of erosion.

5.2.1 Momentum and energy exchange at walls

The particle velocities change continuously from the value of the pre-collision to the value of the post-collision. There are two models used to deal with particle-wall and particle-particle collisions, the hard sphere model and the soft sphere model. The hard sphere model is based on the integrated forms of the equations of motion, namely the impulsive equations, and instantaneous deformation of the particle does not appear in the formulation explicitly. In the soft sphere model the instantaneous motion during the whole collision process is obtained. In this section, the hard sphere model is explained while the soft model is dealt with in Section 5.1.

The hard sphere model considers momentum difference between periods. The difference in momentum between two instants of time is equal to the impulsive force acting on the particle during that time period

$$m \left(\mathbf{v}^{(2)} - \mathbf{v}^{(1)} \right) = \mathbf{J} \quad (5.65)$$

where $\mathbf{v}^{(1)}$ and $\mathbf{v}^{(2)}$ are velocities at time 1 and time 2, respectively, and \mathbf{J} is the impulsive force acting on the particle during the period between the two times. The difference in angular momentum is expressed

$$I \left(\boldsymbol{\Omega}^{(2)} - \boldsymbol{\Omega}^{(1)} \right) = -\mathbf{r} \times \mathbf{J} \quad (5.66)$$

where $\boldsymbol{\Omega}^{(1)}$ and $\boldsymbol{\Omega}^{(2)}$ are angular velocities at time 1 and time 2, respectively, and I is the moment of inertia of the particle. The impulsive force is defined by integral of the force versus time when the force acts on the body. In general, Equations 5.65 and 5.66 are not sufficient to determine the relationship between the pre- and post-collisional velocities. Auxiliary equations are necessary to close a set of equations. The auxiliary equations come from the concept of the coefficient of restitution and friction coefficient.

Before proceeding to the analysis, it is necessary to define the coefficient of restitution e used in this section because definition of e is somewhat arbitrary

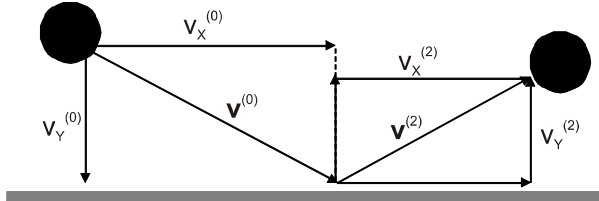


Figure 5.13: Particle colliding with a wall.

and there are a few definitions available in the literature. Consider a particle colliding with a wall as shown in Figure 5.13. The symbol \mathbf{v} signifies the translation velocity. The velocity vector has two components: longitudinal component (x -component) and the component normal to the wall (y -component). The suffixes (0) and (2) denote the pre-collisional velocity and post-collisional velocities, respectively. The following definitions have been used in general.

$$\text{Definition (1)} \quad e = \frac{|\mathbf{v}^{(2)}|}{|\mathbf{v}^{(0)}|} \quad (5.67\text{a})$$

$$\text{Definition (2)} \quad e = \frac{v_Y^{(2)}}{v_Y^{(0)}} \quad (5.67\text{b})$$

$$\text{Definition (3)} \quad e_x = \frac{v_X^{(2)}}{v_X^{(0)}} \quad e_y = \frac{v_Y^{(2)}}{v_Y^{(0)}} \quad (5.67\text{c})$$

$$\text{Definition (4)} \quad e = \frac{J_Y^{(2)}}{J_Y^{(1)}} \quad (5.67\text{d})$$

$J_Y^{(1)}$ and $J_Y^{(2)}$ are the impulses acting on the particle. To understand Definition (4), an explanation is necessary for $J_Y^{(1)}$ and $J_Y^{(2)}$. As shown in Figure 5.14, the process of collision is divided into two periods, one in which the material is compressed and the other in which the compression is released. $J_Y^{(1)}$ and $J_Y^{(2)}$ are the normal (y)-components of the impulsive force during the compression and recovery periods, respectively.

Among the above four definitions, the second definition is used most widely. However if this definition is adopted, the value of the coefficient for non-spherical particles depends on the location of the contact point between the particle and the wall. If the restitution coefficient is regarded as a property of the material, its value should not depend on the location of the contact point. With this point of view, a reasonable definition for the coefficient of restitution is Definition (4). If the particle is a sphere, it is found that the impulse ratio $J_Y^{(2)}/J_Y^{(1)}$ is equal to the velocity ratio $-v_Y^{(2)}/v_Y^{(0)}$.

Consider a three-dimensional collision of a spherical particle with a smooth flat wall, as shown in Figure 5.15. The velocities $\mathbf{v}^{(0)}$ and $\boldsymbol{\omega}^{(0)}$ are the pre-

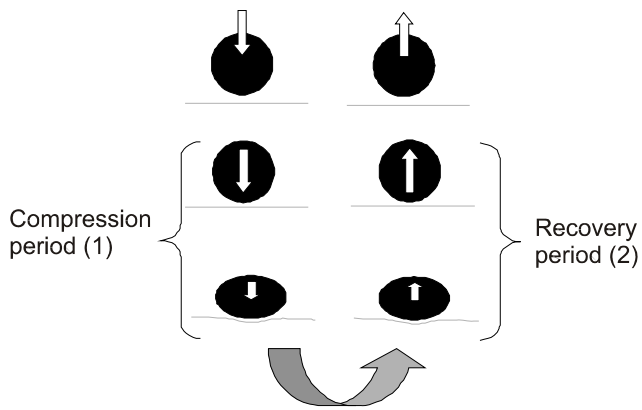


Figure 5.14: Compression and recovery periods in collision process.

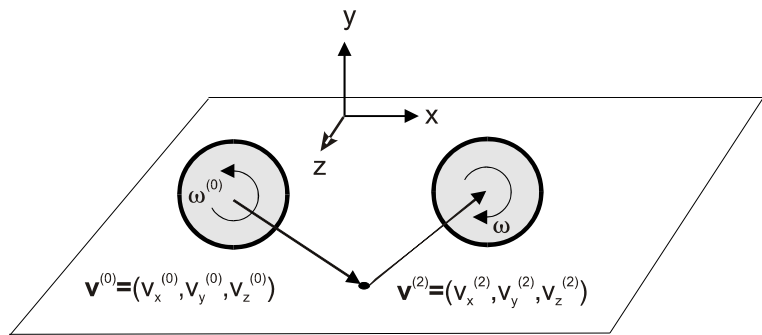


Figure 5.15: Three-dimensional particle-wall collision.

collisional translation and angular velocities, respectively. The corresponding post-collisional velocities are expressed by $\mathbf{v}^{(2)}$ and $\boldsymbol{\omega}^{(2)}$. The Y -axis is normal to the wall and the X and Z axes are in the plane of the wall. The subscripts X , Y and Z signify component directions. If the coefficient of restitution e and kinetic (sliding) friction f are known, the post-collisional translation and angular velocities can be obtained by solving the impulse equations. Readers unfamiliar with the impulse equations should refer to textbooks on classical dynamics (Hibbeler, 2007; Bedford and Fowler, 2005). To solve the problem, the following assumptions are made:

- 1) particle deformation is neglected so, throughout the collision process, the distance between the particle center of mass and the contact point is constant and equal to the particle radius;
- 2) Coulomb's friction law applies to particles sliding along a wall; and
- 3) once a particle stops sliding, there is no further sliding.

In general, the process of collision is divided into two periods: one in which the material is compressed and the other in which the compressive force is released. These are often referred to as the compression and recovery periods. Depending on the period during which the particle slides along the wall, the formulation is separated into the following three cases:

Case I: the particle stops sliding in the compression period.

Case II: the particle stops sliding in the recovery period.

Case III: the particle continues to slide throughout the compression and recovery periods.

A detailed explanation for each case is given below.

Case I

The symbols used for the translation velocities, angular velocities and impulses for each moment and period in Case I are shown in Table 5.1. The *compression period* in Case I is subdivided into sliding and non-sliding periods. The superscripts of (0), (s), (1) and (2) on velocities relate to the values at the end of the period. The superscripts (s), (r) and (2) on impulses signify the values which act on the particle during the corresponding periods. The particle velocities change continuously from the pre-collisional to the post-collisional values, but the method based on the impulse equations considers only the momentum difference between periods. The difference in momentum is equal to the impulsive force acting on the particle. The *impulsive force* is defined by the integral of the force versus time over the interval in which the force acts on the particle. The only known variables in Table 5.1 are the initial velocities, $\mathbf{v}^{(0)}$ and $\boldsymbol{\omega}^{(0)}$. The other variables are unknown. The objective is to evaluate the post-collisional velocities, $\mathbf{v}^{(2)}$ and $\boldsymbol{\omega}^{(2)}$. Each variable in the table has three components corresponding to the X , Y and Z -axes and thus there are a total of 27 unknown variables.

The coordinate system used for the impulse equations is shown in Figure 5.16. The origin is at the point of contact between the sphere and the wall.

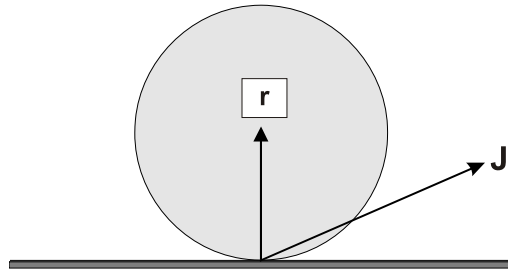


Figure 5.16: Coordinate system for analysis of particle-wall impact.

The vector \mathbf{r} is directed from the point of contact to the center of the particle. The cross product of the radius and impulse vector \mathbf{J} is normal to the plane of the paper and the right-hand rule is used for sign conventions. The impulse equations are written as

$$m(\mathbf{v}^{(s)} - \mathbf{v}^{(0)}) = \mathbf{J}^{(s)} \quad (5.68a)$$

$$m(\mathbf{v}^{(1)} - \mathbf{v}^{(s)}) = \mathbf{J}^{(r)} \quad (5.68b)$$

$$m(\mathbf{v}^{(2)} - \mathbf{v}^{(1)}) = \mathbf{J}^{(2)} \quad (5.68c)$$

$$I(\omega^{(s)} - \omega^{(0)}) = -\mathbf{r} \times \mathbf{J}^{(s)} \quad (5.68d)$$

$$I(\omega^{(1)} - \omega^{(s)}) = -\mathbf{r} \times \mathbf{J}^{(r)} \quad (5.68e)$$

$$I(\omega^{(2)} - \omega^{(1)}) = -\mathbf{r} \times \mathbf{J}^{(2)} \quad (5.68f)$$

Pre-collision	Compression period (1)		Recovery period (2)	Post-collision
Trans. velocity	sliding period			
	$\mathbf{v}^{(0)}$	$\mathbf{v}^{(s)}$	$\mathbf{v}^{(1)}$	$\mathbf{v}^{(2)}$
Angular velocity	$\omega^{(0)}$	$\omega^{(s)}$	$\omega^{(1)}$	$\omega^{(2)}$
Impulse	$\mathbf{J}^{(s)}$	$\mathbf{J}^{(r)}$	$\mathbf{J}^{(2)}$	
$\mathbf{J}^{(1)} = \mathbf{J}^{(s)} + \mathbf{J}^{(r)}$				

Table 5.1. Velocities and impulses for Case I.

The first three equations are for translational velocities and the last three are for angular velocities. The variables m and I are the mass and moment of inertia about the axis of the diameter, respectively; that is, $m = (3\pi/4)a^3\rho_p$ and $I = (2/5)ma^2$ where a is the sphere radius. Each impulse equation

also has three components corresponding to the three axes. To obtain the post-collisional velocities, several auxiliary relations are necessary to close the system of equations for the unknown variables. Such auxiliary relations are deduced from boundary conditions, the definition of the coefficient of restitution and Coulomb's friction law. The boundary conditions relate to the surface velocity of the particle. The surface velocity is given by

$$\mathbf{U} = \mathbf{v} + \mathbf{r} \times \boldsymbol{\omega} = (v_X + a\omega_Z)\mathbf{i} + v_Y\mathbf{j} + (v_Z - a\omega_X)\mathbf{k} \quad (5.69)$$

where \mathbf{i} , \mathbf{j} and \mathbf{k} are unit vectors corresponding to the X , Y and Z -axes, respectively. The Y -component of $\mathbf{r} \times \boldsymbol{\omega}$ is zero because the direction of vector \mathbf{r} coincides with the Y -axis. The condition that the particle stops sliding is obtained by setting the tangential component of the surface velocity equal to zero. Therefore, at the end of the sliding period, the following equation

$$(v_X^{(s)} + a\omega_Z^{(s)})\mathbf{i} + (v_Z^{(s)} - a\omega_X^{(s)})\mathbf{k} = 0 \quad (5.70)$$

must be satisfied. Since all the components of the surface velocity are zero at the end of the compression period, one has

$$(v_X^{(1)} + a\omega_Z^{(1)})\mathbf{i} + v_Y^{(1)}\mathbf{j} + (v_Z^{(1)} - a\omega_X^{(1)})\mathbf{k} = 0 \quad (5.71)$$

Also since there is no sliding in the *recovery period*, one has

$$(v_X^{(2)} + a\omega_Z^{(2)})\mathbf{i} + (v_Z^{(2)} - a\omega_X^{(2)})\mathbf{k} = 0 \quad (5.72)$$

The above three Equations 5.70, 5.71 and 5.72 express the boundary conditions.

Up to this point, only the relationships derived from the impulse equations and boundary conditions have been established. From here, the relationships related to the coefficient of restitution and Coulomb's friction law are developed.

As mentioned earlier, Equation 5.67d is adopted here as the reasonable definition of the coefficient of restitution. In Case I, $J_Y^{(1)}$ is the sum of $J_Y^{(s)}$ and $J_Y^{(r)}$ as shown in Table 5.1. When the value of e is given, the Y -component of $\mathbf{J}^{(2)}$ is expressed by

$$J_Y^{(2)} = e(J_Y^{(s)} + J_Y^{(r)}) \quad (5.73)$$

Coulomb's law states that the friction force is the product of the normal force and the coefficient of kinetic friction f . The friction force corresponds to the tangential component of impulse in the sliding period. Applying Coulomb's law to the sliding period in Case I, one has

$$J_X^{(s)}\mathbf{i} + J_Z^{(s)}\mathbf{k} = -\varepsilon_X f \cdot J_Y^{(s)}\mathbf{i} - \varepsilon_Z f \cdot J_Y^{(s)}\mathbf{k} \quad (5.74)$$

where ε_X and ε_Z are factors indicating the proportion of the velocity in each component direction; that is, the direction cosines of the approach velocity in the $X - Z$ plane. They satisfy the relation

$$\varepsilon_X^2 + \varepsilon_Z^2 = 1 \quad (5.75)$$

Since ε_X and ε_Z are new unknown variables, there are twenty-nine unknowns in total. There are also twenty-nine equations; eighteen from Equations 5.68a to 5.68f, seven from Equations 5.70 to 5.73, and two from Equations 5.74 and 5.75. Whether Case I occurs or not is determined by the condition

$$J_Y^{(s)} > 0 \quad \text{and} \quad J_Y^{(r)} > 0 \quad (5.76)$$

Case II

The procedure for Case II follows that for Case I except that the period of sliding falls in the recovery period. The appropriate variables are shown in Table 5.2.

Pre-collision	Compression period (1)	Recovery period (2)		Post-collision
	sliding period			
Trans. velocity	$\mathbf{v}^{(0)}$	$\mathbf{v}^{(1)}$	$\mathbf{v}^{(s)}$	$\mathbf{v}^{(2)}$
Angular velocity	$\boldsymbol{\omega}^{(0)}$	$\boldsymbol{\omega}^{(1)}$	$\boldsymbol{\omega}^{(s)}$	$\boldsymbol{\omega}^{(2)}$
Impulse	$\mathbf{J}^{(1)}$	$\mathbf{J}^{(s)}$	$\mathbf{J}^{(r)}$	
	$\mathbf{J}^{(2)} = \mathbf{J}^{(s)} + \mathbf{J}^{(r)}$			

Table 5.2. Velocities and impulses for Case II.

The impulse equations are

$$m(\mathbf{v}^{(1)} - \mathbf{v}^{(0)}) = \mathbf{J}^{(1)} \quad (5.77a)$$

$$m(\mathbf{v}^{(s)} - \mathbf{v}^{(1)}) = \mathbf{J}^{(s)} \quad (5.77b)$$

$$m(\mathbf{v}^{(2)} - \mathbf{v}^{(s)}) = \mathbf{J}^{(r)} \quad (5.77c)$$

$$I(\boldsymbol{\omega}^{(1)} - \boldsymbol{\omega}^{(0)}) = -\mathbf{r} \times \mathbf{J}^{(1)} \quad (5.77d)$$

$$I(\boldsymbol{\omega}^{(s)} - \boldsymbol{\omega}^{(1)}) = -\mathbf{r} \times \mathbf{J}^{(s)} \quad (5.77e)$$

$$I(\boldsymbol{\omega}^{(2)} - \boldsymbol{\omega}^{(s)}) = -\mathbf{r} \times \mathbf{J}^{(r)} \quad (5.77f)$$

The boundary conditions are

$$v_Y^{(1)} = 0 \quad (5.78)$$

$$(v_X^{(s)} + a\omega_Z^{(s)})\mathbf{i} + (v_Z^{(s)} - a\omega_X^{(s)})\mathbf{k} = 0 \quad (5.79)$$

$$(v_X^{(2)} + a\omega_Z^{(2)})\mathbf{i} + (v_Z^{(2)} - a\omega_X^{(2)})\mathbf{k} = 0 \quad (5.80)$$

From the definition of the coefficient of restitution,

$$J_Y^{(s)} + J_Y^{(r)} = eJ_Y^{(1)} \quad (5.81)$$

and from Coulomb's friction law,

$$J_X^{(1)}\mathbf{i} + J_Z^{(1)}\mathbf{k} = -\varepsilon_X f \cdot J_Y^{(1)}\mathbf{i} - \varepsilon_Z f \cdot J_Y^{(1)}\mathbf{k} \quad (5.82a)$$

$$J_X^{(s)}\mathbf{i} + J_Z^{(s)}\mathbf{k} = -\varepsilon_X^{(s)} f \cdot J_Y^{(s)}\mathbf{i} - \varepsilon_Z^{(s)} f \cdot J_Y^{(s)}\mathbf{k} \quad (5.82b)$$

The proportion factors for the compression period, ε_X and ε_Z , are the same values as used in Case I. The proportion factors, $\varepsilon_X^{(s)}$ and $\varepsilon_Z^{(s)}$, for Case II are also constrained in the same way as expressed by Equation 5.75; namely,

$$\varepsilon_X^{(s)2} + \varepsilon_Z^{(s)2} = 1 \quad (5.83)$$

The condition for the occurrence of Case II is given by

$$J_Y^{(s)} > 0 \text{ and } J_Y^{(r)} > 0 \quad (5.84)$$

Case III

Case III is the simplest because it is not necessary to distinguish between the period of sliding and non-sliding. The variables for Case III are shown in Table 5.3.

The impulse equations are

$$m(\mathbf{v}^{(1)} - \mathbf{v}^{(0)}) = \mathbf{J}^{(1)} \quad (5.85a)$$

$$m(\mathbf{v}^{(2)} - \mathbf{v}^{(1)}) = \mathbf{J}^{(2)} \quad (5.85b)$$

$$I(\boldsymbol{\omega}^{(1)} - \boldsymbol{\omega}^{(0)}) = -\mathbf{r} \times \mathbf{J}^{(1)} \quad (5.85c)$$

$$I(\boldsymbol{\omega}^{(2)} - \boldsymbol{\omega}^{(1)}) = -\mathbf{r} \times \mathbf{J}^{(2)} \quad (5.85d)$$

The boundary condition is

$$v_Y^{(1)} = 0 \quad (5.86)$$

From the definition of the coefficient of restitution,

$$J_Y^{(2)} = eJ_Y^{(1)} \quad (5.87)$$

and from Coulomb's friction law, one has

$$J_X^{(1)}\mathbf{i} + J_Z^{(1)}\mathbf{k} = -\varepsilon_X f \cdot J_Y^{(1)}\mathbf{i} - \varepsilon_Z f \cdot J_Y^{(1)}\mathbf{k} \quad (5.88a)$$

$$J_X^{(2)}\mathbf{i} + J_Z^{(2)}\mathbf{k} = -\varepsilon_X^{(2)} f \cdot J_Y^{(2)}\mathbf{i} - \varepsilon_Z^{(2)} f \cdot J_Y^{(2)}\mathbf{k} \quad (5.88b)$$

Pre-collision	Compression period (1)	Recovery period (2)	Post-collision
Trans. velocity	$\mathbf{v}^{(0)}$	$\mathbf{v}^{(1)}$	$\mathbf{v}^{(2)}$
Angular velocity	$\omega^{(0)}$	$\omega^{(1)}$	$\omega^{(2)}$
Impulse	$\mathbf{J}^{(1)}$	$\mathbf{J}^{(2)}$	

Table 5.3 Velocities and impulses in Case III.

In Case II, $\varepsilon_X^{(s)}$ and $\varepsilon_Z^{(s)}$ turn out to be equal to ε_X and ε_Z . The suffix (2) in Case III is practically the same as the suffix (s) in Case II. Therefore,

$$\varepsilon_X^{(2)} = \varepsilon_X \quad (5.89a)$$

$$\varepsilon_Z^{(2)} = \varepsilon_Z \quad (5.89b)$$

The solutions for Cases I, II and III obtained using the above procedure are summarized in Table 5.4. There are two sets of solutions for three cases because the solutions for $v = v^{(2)}$ and $\omega = \omega^{(2)}$ turn out to be the same for Cases I and II.

Example: A 100-micron nylon particle bounces off a flat, steel wall. The particle speed is 10 m/s and the angle of incidence is 30° . The particle has no initial rotation and moves in the $x - y$ plane. The coefficient of friction is 0.2 and the coefficient of restitution is 0.8. Find the rebound speed, the angle of rebound and the spin rate (with correct sign). In this problem, $\epsilon_X = 1.0$.

Solution: The incident velocities are $v_y = -5$ m/s, $v_x = 8.66$ m/s. Therefore $v_y/|v| = -0.5$. The value of $2/7f(e+1)$ is 0.79 so the second condition in Table 5.4 is satisfied. The rebound velocities are

$$v_x = 8.66 - 0.2 \times 1.8 \times 5 = 6.86 \text{ m/s}$$

$$v_y = -0.8 \times (-5) = 4 \text{ m/s}$$

The rebound angle is $\arctan(v_y/v_x) = 30.2^\circ$. The spin velocity on rebound will be

$$\omega_Z = 0 + \frac{5}{2(5 \times 10^{-5})} 0.2 \times 1.8 \times (-5) = -9 \times 10^4 \text{ rad/s}$$

Condition	$\frac{v_Y^{(0)}}{ v } < -\frac{2}{7f(e+1)}$	$-\frac{2}{7f(e+1)} < \frac{v_Y^{(0)}}{ v } < 0$
Translational velocity	$v_X = \left(\frac{5}{7}\right) (v_X^{(0)} - \frac{2a}{5} \omega_Z^{(0)})$ $v_Y = -ev_Y^{(0)}$ $v_Z = \left(\frac{5}{7}\right) (v_Z^{(0)} + \frac{2a}{5} \omega_X^{(0)})$	$v_X = v_X^{(0)} + \varepsilon_x f(e+1) v_Y^{(0)}$ $v_Y = -ev_Y^{(0)}$ $v_Z = v_Z^{(0)} + \varepsilon_z f(e+1) v_Y^{(0)}$
Angular velocity	$\omega_X = \frac{v_Z}{a}$ $\omega_Y = \omega_Y^{(0)}$ $\omega_Z = -\frac{v_x}{a}$	$\omega_X = \omega_X^{(0)} - \frac{5}{2a} \varepsilon_z f(e+1) v_Y^{(0)}$ $\omega_Y = \omega_Y^{(0)}$ $\omega_Z = \omega_Z^{(0)} + \frac{5}{2a} \varepsilon_x f(e+1) v_Y^{(0)}$

Table 5.4. Relation between pre- and post-collisional velocities.

5.2.2 Irregular bouncing

When the coefficients of restitution e and dynamic friction f are given as physical properties of the particles, the post-collisional velocities can be expressed in terms of the pre-collisional velocities. The relation between these velocities for the case of a spherical particle and smooth wall is shown in Table 5.4. This relationship is useful for calculating particle trajectories in a field enclosed by walls. However, in some cases, the trajectory calculation in multiphase flows is not as straightforward as it might appear. The coefficient of restitution e defined by Equation 5.67b or 5.67d must be less than unity. If trajectory calculations were made for a long horizontal pipe or duct, particles colliding repeatedly with the wall would ultimately lose their vertical velocity component and result in sliding along the wall as shown in Figure 5.17(a).

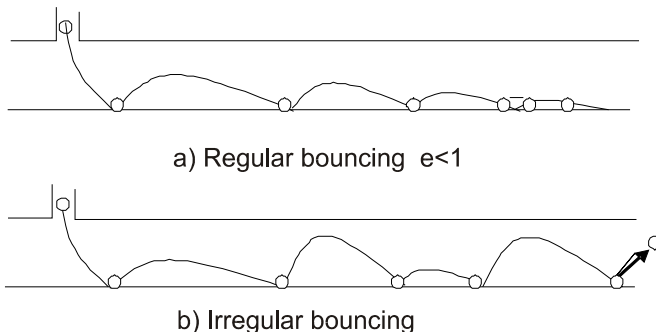


Figure 5.17: Bouncing of (a) regular and (b) irregular particles.

To avoid such an unrealistic result, the irregularity of collisions must be

considered. If this irregularity is neglected, large particles cannot be suspended in the carrier fluid. Fluid dynamic forces, such as Magnus or shear lift forces, and fluid turbulence acting on the particles are sufficient to suspend small particles. However, the mechanism responsible for suspending large particles in horizontal pipes is the irregular bouncing of the particles against the wall. In general, the irregularity is caused by particle shape (non-spherical particles) and/or roughness of the wall. In practice, both mechanisms are operative. Several models in regard to the irregular bouncing have been proposed to make particles repeat bouncing motion shown in Figure 5.17(b). Those models are classified into two types: one in which the irregularity is attributed to the non-sphericity of the particle (Matsumoto & Saito, 1970a; Tsuji et al., 1989; Tsuji et al., 1991) and the other to wall roughness (Matsumoto & Saito, 1970b; Tsuji et al., 1987; Sommerfeld and Zivkovic, 1992; Frank et al., 1993; Sommerfeld & Huber, 1999).

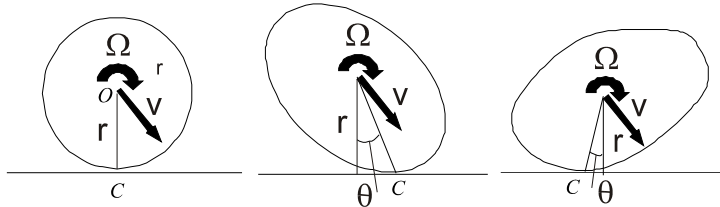


Figure 5.18: Contact point between particle and wall.

In the following paragraphs, the non-spherical model is described first and then the rough wall model. If the problem is two-dimensional, the treatment is relatively easy, because the shape of the particle is limited to the circle, ellipse or an arbitrary shape. As shown in Figure 5.18, the distance between the non-spherical particle center of gravity O and the contact point C depends on the incident attitude of the particle while that distance does not change in the case of a circular particle. A set of values for r and θ shown in Figure 5.14 (b) and (c) describes any particle shape. Impulsive equations are formed for a set of values for r and θ . In the numerical simulation, a pair of values for r and θ is chosen by random numbers. The post-collisional velocities are obtained from solutions of the impulsive equations.

It is difficult to deal, in a rigorous way, with the collision of an arbitrary three dimensional, non-spherical particle having three components of translational and angular velocity. The complexity of the problem is reduced by using some assumptions. Examples of such assumptions are explained in Tsuji et al. (1991).

The wall roughness model for irregular bouncing is shown in Figure 5.19. The choice of wall roughness is arbitrary. Several configurations could be considered; a wavy pattern, a combination of inclined plates and so on. The calculation for a spherical particle bouncing on the rough wall is simpler than

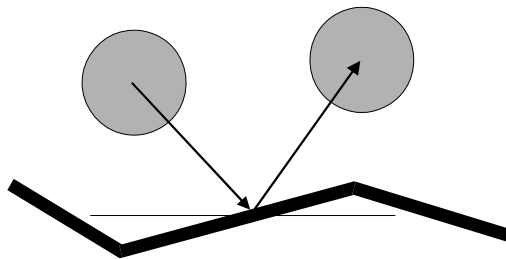


Figure 5.19: Particle collision with rough wall.

that for a non-spherical particle on a flat wall, if the pattern of roughness is specified. In the rough wall model, the point at which the particle collides with the wall is assumed to be on an inclined plane. Each inclined plane has its own coordinate system. The relationship between the coordinates, with and without an inclination angle, is easily described by using a matrix. Once particle velocities are transformed by the usual linear transformation technique into the coordinates corresponding to the inclined plane, the results shown in Table 5.4 can be used to obtain the post-collisional velocities. After that, the post-collisional velocities based on the coordinate on the inclined plane are re-transformed into the original coordinate system.

As with the non-spherical particle model, the rough wall models make it possible for the particles to move along with a bouncing motion in long, horizontal pipes or ducts.

Predicting the impact-rebound relations for particles with sharp edges, such as quartz particles, would be very difficult. Experiments (Tabakoff, 1982) with quartz particles impacting on an aluminum surface show that for a given impact angle, there is a distribution of rebound angles. In this case, it is more pragmatic to use a Monte Carlo method with the measured distribution of rebound angles to model particle-surface impact.

5.2.3 Erosion

Particle-wall impact leads to erosion which is an important consideration in the design and operation of fluid-particle systems. There have been many studies reported on the erosion of materials by impinging particles. An important early work was that by Finnie (1972) who developed a model for the mass of surface material removed by the impact of a single particle. The model is based on the cutting and displacement process common to metal cutting or grinding. For ductile materials, Finnie predicted that the maximum erosion for an impact angle of 13° would vary as the square of the impact velocity. Subsequent experiments with SiC particles impinging on pure aluminum showed good agreement with the model in that the maximum erosion occurred at approximately 15° . The data for normal (perpendicular) impact

deviated from the model and the erosion dependence on velocity varied as $v^{2.4}$.

Since Finnie's original work, there have been many studies reported on particle erosion. An example of data (Magnée, 1995) obtained on erosion of aluminum and high chromium cast iron by alumina particles is shown in Figure 5.20 which gives the mass of material removed normalized with respect to the mass of the impacting particle. One notes that maximum erosion occurs near 15° for ductile materials (aluminum) and at 90° for brittle materials. The basic premise is that the cutting action of the particles is more important for ductile materials and deformation (or displacement) is more significant for brittle materials. The data also show that the erosion varies as the square of the impact velocity. Similar tests have been done on coatings for protecting jet engine parts and steam turbine components (Shanov et al., 1996).

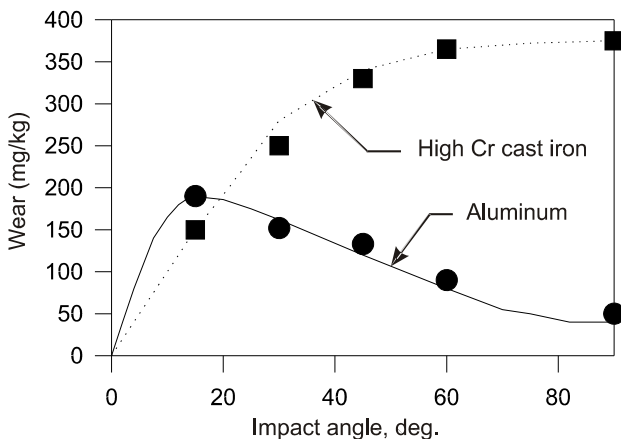


Figure 5.20: Erosion rate of aluminum and high chromium cast iron by alumina particles impinging at 50 m/s.

Data of this type have been used in numerical models for erosion in ducts (Shimizu, 1993) and turbine blades (Tabakoff, 1982). An extensive summary on erosion in pneumatic conveying can be found in Marcus et al. (1990). Erosion in liquid-solid flows (slurries) is addressed in Wilson et al. (1992).

More complete information on erosion due to particle flow can be found in Chapter 12 of the *Multiphase Flow Handbook* ([Crowe (ed.), 2006].

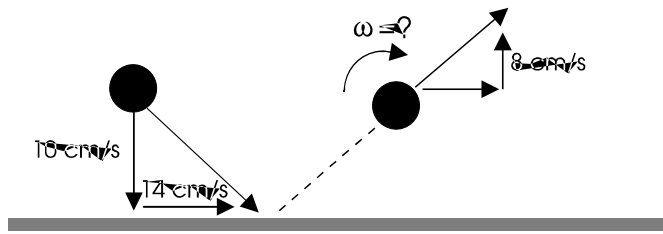
5.3 Summary

Particle-particle interaction is the key element in dense phase flows. The two models for particle-particle interaction are the hard sphere and the soft sphere models. With the hard sphere model the post-collisional velocities

and rotations are determined as a function of the pre-collisional conditions, coefficient of restitution and coefficient of friction. The soft sphere model describes the particle history during the collision process and can be modeled with spring-damper arrangements. Particle-wall collisions are treated with the hard sphere model. Wall roughness can be simulated with a local wall slope at the surface.

5.4 Exercises

- 5.1. A 100- μm spherical particle on a smooth surface. The velocity components are shown in the figure. The initial angular velocity is zero. The coefficient of friction is 0.2. Find the coefficient of restitution, the post-collisional angular velocity and velocity component in the x-direction. Assume $\epsilon_X = 1.0$.



Problem 5.1

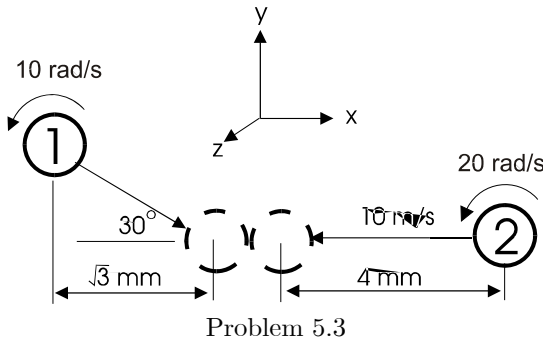
- 5.2. A spherical ball, 38 cm in diameter, impinges on a flat surface. The incident translational and angular velocities are

$$\mathbf{v} = (1.13\mathbf{i} - 1.62\mathbf{j} - 0.48\mathbf{k}) \text{ m/s}$$

$$\boldsymbol{\omega} = (0.1\mathbf{i} - 0.02\mathbf{j} + 0.05\mathbf{k}) \text{ rad/s}$$

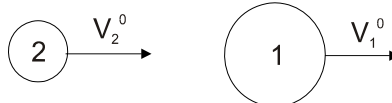
The coefficient of restitution is 0.65 and the coefficient of friction is 0.3. Find the post-collisional velocity and rotation vector.

- 5.3. Use the soft sphere model to analyze the collision of two 600- μm spherical aluminum particles shown in the figure. The particles deform such that the overlap displacement is 25 μm . The coefficient of restitution is 0.8 and the coefficient of friction is 0.35. Determine if sliding occurs.



5.4. Two particles, with coefficient of restitution e , collide while traveling in the same direction as shown in the figure. Both particles are not rotating.

1. Using the momentum conservation, find the velocities of each particle after collision.
2. Simplify Equations 5.21a and 5.21b in the text and compare the results with those obtained in first part of this problem.
3. Particle 1 is $10 \mu\text{m}$ in diameter and is moving at 5 m/s . Particle 2 is $5 \mu\text{m}$ in diameter and is moving at 10 m/s . Both particles have a density of 2500 kg/m^3 . The coefficient of restitution is 0.9. Find the velocities after collision.



Problem 5.4

5.5. Show that

$$F = -\pi\mu_c \frac{3\dot{h}}{2} \int_0^a \frac{r^3}{h^3} dr$$

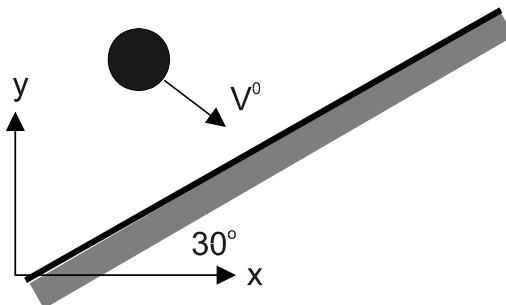
reduces to

$$F = -3\pi\mu_c \frac{a^2\dot{h}}{2h_0}$$

for $h_0/a \ll 1$ and $h = r^2/2a + h_0$.

5.6. Determine the post-collisional translation velocities resulting from collision of a 2-mm particle with a smooth inclined wall. The inclination angle of the wall is 30° . The pre-collision velocities are $v_x^0 = 5 \text{ m/s}$, $v_y^0 = -3 \text{ m/s}$.

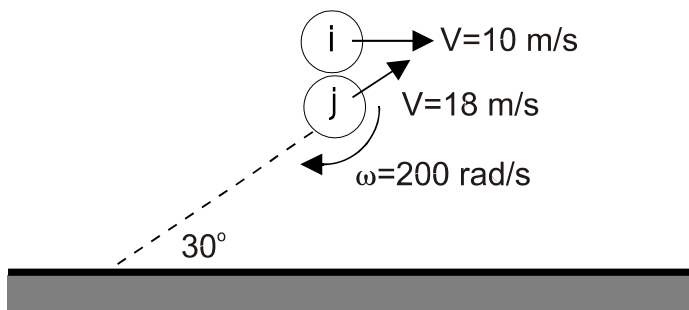
m/s and $v_z^0 = 1 \text{ m/s}$. Assume $f = 0.4$ and $e = 0.8$. The initial angular velocity is zero.



Problem 5.6

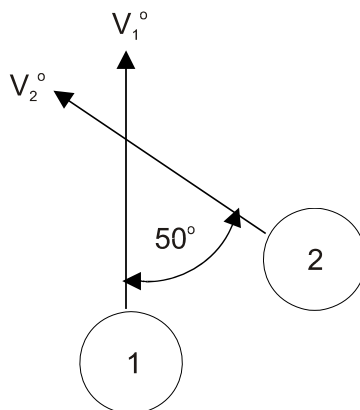
5.7. Assume two hard spheres collide with no initial rotation. Identify the condition (relations between \mathbf{G} , \mathbf{n} and \mathbf{t}) for which the collision occurs without sliding. What are the translation velocities (as a function of $\mathbf{v}_1^0, \mathbf{v}_2^0, \mathbf{G}^0, e, m_1$ and m_2) and angular velocities after collision?

5.8. Low density polyethylene (LDPE) particles are pneumatically transported through a duct. All the particles are spheres with a diameter of 1 mm. Two particles, i and j , move through the duct in the manner illustrated in the figure. Find the magnitude of the force of collision for a normal displacement (δ_n) and tangential displacement (δ_t) of $1 \mu\text{m}$. LDPE has the following properties: $E = 30 \text{ GPa}$, $\sigma = 0.5$, $\rho = 920 \text{ kg/m}^3$, $f = 0.1$ and $e = 0.2$. Assume aerodynamic forces are insignificant and that the two particles move in the same plane.



Problem 5.8

5.9. A particle drops vertically onto a flat plate. Just before collision with the wall, the ratio $a\omega_Z^{(0)}/v_Y^{(0)} = -0.5$. The coefficient of restitution is 0.8 and the friction factor is 0.2. Find the angle with respect to the vertical with which the particle bounces from the surface.



Problem 5.10

5.10. Two particles of equal mass, m , collide as shown in the figure. The particles are glass beads, $50 \mu\text{m}$ in diameter. The velocity of bead 1 is 10 m/s and the velocity of bead 2 is 5 m/s at the point of collision when bead 2 is directly above bead 1. Bead 1 has a rotational velocity of $10,000 \text{ rad/s}$ in the CW (clockwise) direction while bead 2 has a rotational velocity of $5,000 \text{ rad/s}$ in the CCW (counter-clockwise) direction. The coefficient of restitution is 0.9 and the material density is 2500 kg/m^3 . Assume the particles have stopped sliding during collision. Find the impulsive force vector, \mathbf{J} , and the post-collisional rotational and translational velocities of both particles.

5.11. Find the size of an alumina particle which would be suspended (van der Waals force = weight) by 3-cm copper sphere. The roughness of the copper sphere is $1 \mu\text{m}$ and the roughness of the alumina sphere is 1% of its diameter. The density of alumina is 4000 kg/m^3 .

5.12. As a particle approaches a plate, how far (in terms of h_o/a) from the plate is the force on the particle due to the plate being equal to Stokes drag?

Chapter 6

Continuous Phase Equations

Unlike the flow of a single phase liquid or gas, the carrier phase of a dispersed phase flow contains dispersed particles or droplets as shown in Figure 6.1. For purposes of analysis, the ideal situation would be to solve the governing conservation (continuity, momentum and energy) equations for the carrier phase by accounting for the boundary conditions imposed by each and every particle or droplet in the field together with the boundary condition at the wall. This would provide a complete description of the carrier phase throughout the mixture. For computation, this would require a grid dimension smaller than the smallest particle in the field. In addition, provision would have to be made for the continuous movement of the surfaces. Such a solution would be regarded as complete numerical simulation. An industrially relevant application may require the solution with trillions of particles or droplets. Such a solution is beyond current computer capability.

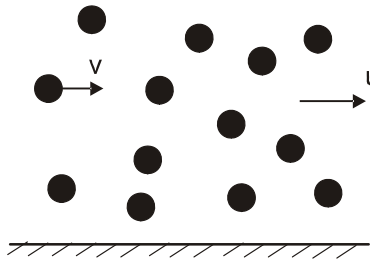


Figure 6.1: Fluid-particle flow field.

Solutions have been obtained in limited cases with a finite number of particles in a low Reynolds number accounting for the boundary conditions at the

particle surfaces. Also solutions have been obtained using the "point particle" method in which the particles occupy no volume but represent a force on the conveying fluid at the locations of the particles. These solutions have provided an improved level of understanding for particle-fluid interaction, especially for turbulent flows. In general, however, for practical applications one must resort to equations based on the average properties of a flow.

The purpose of this chapter is to first introduce the most commonly used averaging procedures; namely, time, space (volume) and ensemble averaging. The conservation equations are then presented for a quasi-one-dimensional flow in a duct to illustrate the essential features of the equations. In addition the volume-averaged form of the multidimensional equations, derived and developed in Appendix C, are presented and discussed. The formal volume averaging procedures are provided in Appendix B.

6.1 Averaging procedures

In essence, there are three approaches to averaging the continuous phase equations: time, volume and ensemble averaging.

6.1.1 Time averaging

The *time average* is the result of averaging the flow properties over time at a point in the flow field shown in Figure 6.2. The time average of some property B of the flow is defined as

$$\overline{\overline{B}} = \frac{1}{T} \int_0^T B dt \quad (6.1)$$

where T is the averaging time¹. Time averaging has been used extensively in single phase flows to treat turbulent fluctuations and develop time-averaged conservation equations with additional terms, such as Reynolds stress, to account for the effects of turbulence.

Assume that the phase can be identified as the particles and fluid pass by the point in the flow field. If B is the indicator function $\phi(x, t)$ defined such that

$$\begin{aligned} \phi(x, t) &= 1 && \text{point in carrier phase} \\ \phi(x, t) &= 0 && \text{point in particle phase} \end{aligned} \quad (6.2)$$

then the variation of ϕ with time will be as shown in Figure 6.3. The volume fraction of the continuous phase at location x is obtained from

$$\alpha_c(x) = \overline{\overline{\phi}} = \frac{1}{T} \int_T \phi(x, t) dt \quad (6.3)$$

¹The double overbar is used to denote time averaging. Usually the single bar is used for time averaging, but is utilized in this work for volume averaging.

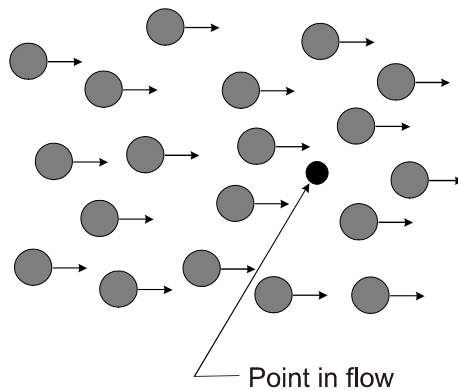
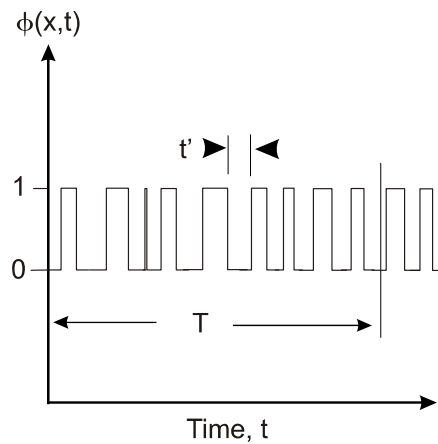


Figure 6.2: Point in multiphase flow field.

Figure 6.3: Variation of phase function ϕ with time.

By inverting the definition of ϕ and carrying out the same time averaging yields the volume fraction of the dispersed phase. Obviously the averaging time, T , must be large compared to the local fluctuation time, t' , in order to define a true average value; that is, an average value that is independent of the averaging time. Also, the averaging time must be smaller than a characteristic time associated with the flow system, T' .

$$t' \ll T \ll T' \quad (6.4)$$

In some transient flow systems, this condition may not be realizable.

Ishii (1975) has developed general equations that can be applied to obtain the time-averaged formulations of the conservation equations for multiphase flows. The primary application of the time-averaged equations appears to have been in gas-liquid flows common to the nuclear power industries.

6.1.2 Volume averaging

Volume averaging is carried out by averaging properties at an instant in time over a volume. For example, the *volume average* of property B would be defined as

$$\bar{B} = \frac{1}{V} \int_{V_c} BdV \quad (6.5)$$

where V is the averaging volume and V_c is the volume of the continuous phase. As an example, consider the volume average of the indicator function defined by Equation 6.2. By definition

$$\overline{\phi(x, t)} = \frac{1}{V} \int_{V_c} \phi(x, t)dV = \frac{V_c}{V} = \alpha_c(t) \quad (6.6)$$

where V_c is the volume of the continuous phase and the space dimension has been integrated out leaving only time.

Besides the volume average defined by Equation 6.5 there is also a *phase average* which is the average over the volume occupied by the phase.

$$\langle B \rangle = \frac{1}{V_c} \int_{V_c} BdV \quad (6.7)$$

where V_c is the volume associated with the continuous phase. If B is the density of the fluid, then $\langle \rho_c \rangle$ is the average material density of the fluid. If the density is constant, then $\langle \rho_c \rangle = \rho_c$. The relationship between the volume averaged property and the phase average is $\bar{B} = \alpha_c \langle B \rangle$. The bulk density defined in Chapter 2 is the same as the volume averaged density defined here.

Assume the distribution of the dispersed phase mixture appears as shown in Figure 6.4 where ℓ is the average interparticle spacing and L is a distance which characterizes the spatial change in mixture properties. Obviously, in order to obtain a near stationary average (an average which does not change

with a change in the size of the averaging volume), the averaging volume must be much larger than ℓ^3 . However, in order that \bar{B} vary smoothly in the field the averaging volume must be much less than L^3 . Thus the constraints on the averaging volume are

$$\ell^3 \ll V \ll L^3 \quad (6.8)$$

This constraint is essential to approximate the spatial derivatives of \bar{B} in the flow field.

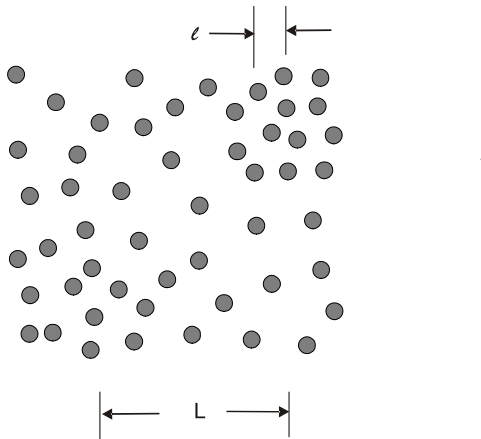


Figure 6.4: Spatial distribution of particles in averaging field.

As stated above, the averaging volume must be sufficiently large that the average value does not depend on the size of the volume. This is the same requirement in time averaging that the averaged values do not depend on the averaging time. An idea of the size required for an averaging volume can be determined by the number of particles needed to ensure a valid average. This is the same concept introduced in Chapter 2 and illustrated in Figure 2.1 in which the limiting volume has to contain sufficient molecules such that variations are maintained below a minimum value so the flow properties within the volume can be regarded as "point" values.

The probability $P(N)$ that a volume V contains N particles is the *Poisson distribution*

$$P(N) = (nV)^N \exp(-nV)/N! \quad (6.9)$$

where n is the particle number density (number of particles per unit volume) and nV is the mean value. The standard deviation of this distribution is $(nV)^{1/2}$. For large values of nV this distribution approaches the Gaussian distribution. The number of particles in a volume varies between $nV \pm \Delta N$ so $2\Delta N/nV$ is the limit of the fractional variation. Using the Poisson distribution for the probability, the fractional variation as a function of nV at the 90, 95

and 99% confidence levels is shown in Figure 6.5. As noted on the figure,

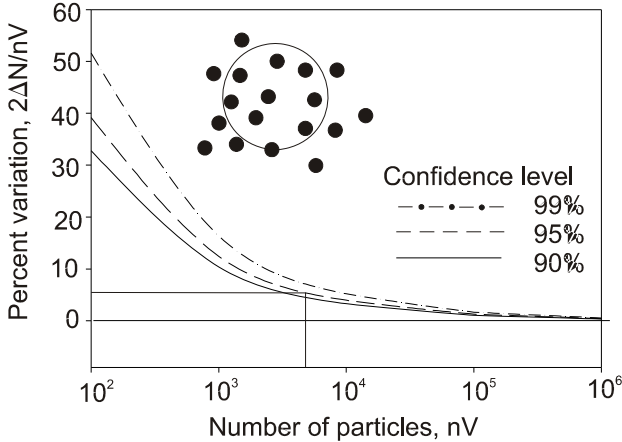


Figure 6.5: Percentage variation of the number of particles in an averaging volume as function of total number of particles at the 90, 95 and 99% confidence levels.

to limit the variations to less than 5% ($\pm 2.5\%$) at the 95% confidence level, the number of particles would have to be of the order of 6000. The volume associated with one particle is $1/n$ so the average interparticle spacing would be

$$\ell \sim 1/n^{1/3} \quad (6.10)$$

Thus the dimension of the volume needed to ensure variations less than 5% would have be $6000^{1/3}\ell$ or

$$V^{1/3} \sim 18\ell \quad (6.11)$$

A higher confidence level or a smaller variation would require a larger number of particles in the volume.

A formalism has been developed for obtaining volume averaged equations for a mixture by averaging the differential equations for a single phase over a volume. This approach is used in Appendix C to obtain the continuity, momentum and energy equations for the carrier phase in a dispersed phase flow.

6.1.3 Ensemble averaging

Ensemble averaging avoids the shortcomings of time and volume averaging but is much more difficult to implement. *Ensemble averaging* is based on the probability of the flow field being in a particular configuration at a given time (Zhang and Prosperetti, 1994). Consider a dispersed phase field with spherical, homogeneous particles; that is, one particle cannot be distinguished from

another. A specific configuration χ^N describes a set of position vectors and velocity vectors which describe a flow field. The probability that the configuration occurs at time t is $P(N, t)$. The total number of possible configurations is $N!$ so the appropriate normalization is

$$\frac{1}{N!} \int d\chi^N P(N, t) = 1 \quad (6.12)$$

Using the indicator function given by Equation 6.2, but defined for the configuration N

$$\begin{aligned}\phi(x, N) &= 1 && \text{point in carrier phase} \\ \phi(x, N) &= 0 && \text{point in particle phase}\end{aligned} \quad (6.13)$$

the volume fraction of the continuous phase is

$$\alpha_c(x, t) = \frac{1}{N!} \int d\chi^N \phi(x, N) P(N, t) \quad (6.14)$$

A formalism has been developed by Zhang and Prosperetti for spatial and time derivatives that are used to express the conservation equations with ensembled-averaged properties. Obviously, ensemble averaging is not limited by volume or time constraints.

6.2 Volume averaging

The most widely used averaging technique is volume averaging. This is a natural choice because many flow models are based on discretizing the flow field into computational cells that essentially are averaging volumes. One of the earliest papers on the development of multiphase flow equations was by Van Deemter and van der Laan (1961). They simply identified a volume V of which a volume V_c is occupied by the continuous phase and wrote the momentum equation for the fluid in volume V_c . The resulting equation was

$$(1 - \alpha_d)\rho_c \frac{Du_i}{Dt} = (1 - \alpha_d)\rho_c g_i - \frac{\partial}{\partial x_j}(p\delta_{ij} - \tau_{ij}) + f_i \quad (6.15)$$

where u_i is the velocity of the continuous phase, α_d is the particle volume fraction, ρ_c is the continuous phase material density, δ_{ij} is the Kronecker delta and τ_{ij} is the shear stress tensor. The force f_i is the force per unit volume of the particles on the continuous phase. This force would be the negative of the drag force on all the particles per unit volume of fluid.

The question here is how large the volume V would have to be to ensure that the value for f_i has minimal variations. For example, consider a flow with $20 \mu\text{m}$ particles with a volume fraction of α_d of 0.01. This condition corresponds to mass concentration of 10 for water droplets in air at standard

conditions. From Equation 2.17, the interparticle spacing is $\ell \simeq 4D$. From Equation 6.11, the dimension of the averaging volume would be about $72D$ which, for a $20\mu\text{m}$ particle is $1440\mu\text{m}$ or 1.4 mm . This is four orders of magnitude larger than “point” volume for the carrier phase.

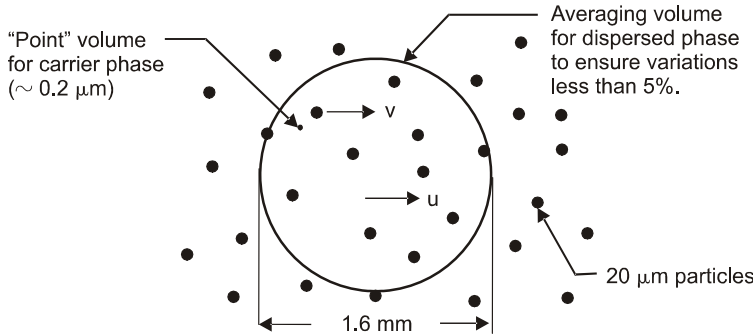


Figure 6.6: Comparison of magnitude of averaging volume for dispersed phase and “point” volume for carrier phase.

The difference in size for the averaging volume for the dispersed phase and “point” volume for the carrier phase is shown, but not to scale, in Figure 6.6. It is obvious that the velocity of the carrier phase can vary dramatically over the averaging volume and cannot be represented by a single value. For a turbulent flow, the smallest volume of fluid associated with a given velocity would be an eddy with the dimension of the Komolgorov length scale. This dimension would still be at least an order of magnitude smaller than the size of the averaging volume. Thus, the velocity in Equation 6.15 must be the average over the volume and replaced by a volume-averaged quantity, $u_i \rightarrow \langle u_i \rangle$.

Marble (1963), using essentially the same ideas as van Deemter and van der Laan, derived the following form of the Navier-Stokes equations by neglecting the volume occupied by the particles.

$$\rho_c \frac{\partial u_i}{\partial t} + \rho_c u_j \frac{\partial u_i}{\partial x_j} = - \frac{\partial p}{\partial x_i} + \frac{\partial}{\partial x_j} \tau_{ij} + f_i \quad (6.16)$$

where f_i has the same definition as in Equation 6.15. Marble stated that “it is appropriate to treat the particle cloud as a continuum whenever possible.” This equation is often referred to in the literature as the “dusty gas equation.” The same problem exists here as with van Deemter and van der Laan’s equation; that is, the averaging volume for the dispersed phase is so large that the continuous phase velocity cannot be represented by a single value at a point. It is an average value over the volume. The assumption that the force per unit volume due to the particles is a continuous function leads to incorrect physics. The fact that the particles occupy no volume does not change the outcome, the same magnitude of the averaging volume is still needed to ensure small

variations. Thus, the “point” value in Marble’s equation must be replaced by a volume averaged value, $u_i \rightarrow \langle u_i \rangle$.

Many researchers (Chen and Wood, 1985; Rogers and Eaton, 1991) have applied the dusty gas equation to develop models for turbulence kinetic energy and dissipation using the same time-averaging approach as used for single phase flows. The problem with using this equation is that the velocity fluctuations of the volume-averaged velocity are not representative of the fluctuations at a point in the averaging volume as shown in Figure 6.7. The resulting equations for turbulence properties are obviously invalid and fail to provide realistic solutions for basic flow fields (see Chapter 7).

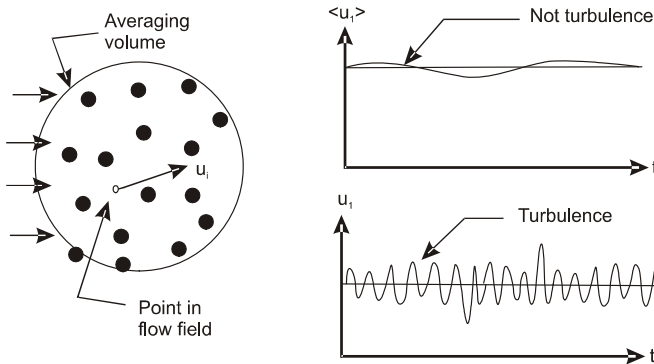


Figure 6.7: Comparison of temporal fluctuations of volume-averaged velocity and velocity at point in averaging volume.

Anderson and Jackson (1967) recognized the need to have an averaging procedure for the fluid properties in a multiphase flow parallel to the needs in gas kinetic theory. Starting with an arbitrary point in the flow field and defining r as the radial distance from the point, they chose to define a function $g(r)$ which was always positive, decreased monotonically with increasing r and was continuously differentiable. The function was normalized such that

$$\int_{V_\infty} g(r) dV = 1 \quad (6.17)$$

where V_∞ is the averaging volume. They stated that the dimension of the averaging volume has to be large compared to the interparticle spacing and small compared to the system dimensions, which repeats the arguments presented above. They made no attempt to quantify the size of the averaging volume. They then defined point properties with the primed notation. For example, the velocity at a point in the averaging volume is u'_i . Non-primed variables were used to define the averaged properties so

$$\alpha_c u_i = \int_{V_\infty} g(r) u'_i dV \quad (6.18)$$

The continuity and momentum equations were then developed using this averaging procedure. Anderson and Jackson did find a term equivalent to the Reynolds stress in time averaging the single-phase momentum equations and combined it with the averaged stress of the continuous phase. These equations have been used extensively in the literature for multiphase flow modeling.

Subsequent to Anderson and Jackson's work, the idea of the "two-fluid" model evolved to describe a fluid-particle flow. With the two-fluid model it is assumed that both phases constitute "interpenetrating continua." This description implies that the properties of each phase can be identified at any point in the field. The concept is convenient because it suggests that solution procedures used for single-phase flows can also be used for each phase of a multiphase flow; however, the idea is flawed because the magnitude of the averaging volume and point volume are so different as shown in Figure 6.6. The concept of interpenetrating continua may have relevance in a gaseous mixture containing two or more components with point volumes of comparable size; however, this is not the case for a dispersed phase flow. One can only say that the averaged properties, such as $\langle u_i \rangle$, vary continuously as the averaging volume is moved, not the point properties. It is interesting to postulate if the "two-fluid" concept would have evolved had Anderson and Jackson chosen not to use u_i as the notation for the volume-averaged velocity.

Other descriptions of volume, or spatial, averaging have appeared in the literature such as Nigmatulin (1979) and Drew (1983). Most recently, Prosperetti and Tryggvason (2007) have provided further discussions on volume-averaging.

The presumed validity of the two-fluid model continues to exist in the literature. It is common practice to write the equations for the continuous phase of a dispersed phase flow as the Navier-Stokes equations with source terms added to account for the dispersed phase. For example,

$$\frac{\partial \rho_c}{\partial t} + \frac{\partial}{\partial x_i} (\rho_c u_i) = s_{\text{mass}} \quad (6.19a)$$

$$\frac{\partial}{\partial t} (\rho_c u_i) + \frac{\partial}{\partial x_i} (\rho_c u_i u_j) = -\frac{\partial p}{\partial x_i} + \frac{\partial \tau_{ij}}{\partial x_j} + \rho g_i + s_{\text{mom},i} \quad (6.19b)$$

$$\begin{aligned} \frac{\partial}{\partial t} (\rho_c e) + \frac{\partial}{\partial x_i} (\rho_c u_i e) &= -\frac{\partial (p u_i)}{\partial x_i} + \frac{\partial (\tau_{ij} u_i)}{\partial x_j} \\ &\quad -\frac{\partial q_i}{\partial x_i} + \rho g_i u_i + s_{\text{energy}} \end{aligned} \quad (6.19c)$$

where it is assumed that the fluid properties represent values at a fluid point. Based on the arguments presented above, these forms of the equations are invalid.

The purpose of this chapter is to present the correct conservation equations based on volume averaging. The equations for a quasi-one-dimensional flow are presented first to introduce the basic concepts. Then the corresponding multidimensional equations are presented and discussed.

The word "particle" will be used to describe the dispersed phase but applies to both droplets and particles.

6.3 Property flux through a particle cloud

The conservation principles are applied to a finite size volume which is enclosed by an arbitrary boundary. The boundary may pass through several particles which are referred to as *boundary particles*. The presence of these particles reduces the cross-sectional area of the carrier flow and, thereby affect the flow rate of mass, momentum and energy in the flow.

Consider the portion of the boundary surface shown in Figure 6.8. The surface with area A cuts through several particles in the field. The area of the particles intersected by the surface, or severed by the surface, is A_s . The objective here is to quantify the ratio of the severed area to the total area (A_s/A) as a function of particle volume fraction.

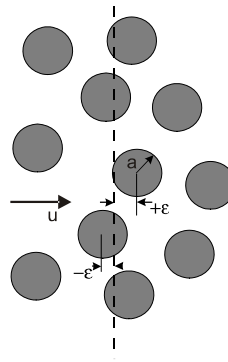


Figure 6.8: Boundary particles on surface of averaging volume.

Assume that all the particles are spherical and of the same size. The cross-sectional area of the cut where the surface passes through the particle is given by

$$A_c = \pi(a^2 - \epsilon^2) \quad (6.20)$$

where ϵ is the distance from the particle center to the surface. The centers of all the particles will lie in the volume defined by a distance $-a$ and $+a$ from the surface area.

There is a uniform probability that a particle will lie at a distance ϵ from the surface so the probability distribution function is

$$f(\epsilon) = \frac{1}{2a} \quad (6.21)$$

for $|\epsilon| \leq a$ and is equal to zero for $|\epsilon| > 0$. If there is a total of N particles

intersected by the surface, the severed area is given by

$$A_s = N \int_{-a}^{+a} \pi(a^2 - \epsilon^2) f(\epsilon) d\epsilon \quad (6.22)$$

Integrating this equation using the above distribution for $f(\epsilon)$ gives

$$A_s = N \frac{2\pi a^2}{3} \quad (6.23)$$

The number of particles intersected by the surface is related to the number density, n , by

$$N = 2aAn \quad (6.24)$$

Substituting this value for N into Equation 6.23 results in

$$\frac{A_s}{A} = n \frac{4}{3} \pi a^3 \quad (6.25)$$

and the product of the number density and the volume of a single particle is the dispersed phase volume fraction so

$$\frac{A_s}{A} = \alpha_d \quad (6.26)$$

This same approach can be carried out with a distribution of particle sizes and the result is unchanged. The cross-sectional area associated with the continuous phase is

$$\frac{A_c}{A} = \frac{A - A_s}{A} = 1 - \alpha_d = \alpha_c \quad (6.27)$$

where α_c is the volume fraction of the continuous phase.

The mass flow rate of the continuous phase through the particle field is

$$\dot{M}_c = \langle \rho_c u \rangle \alpha_c A \quad (6.28)$$

where $\langle \rho_c u \rangle$ is the volume average and ρ_c is the material density of the continuous phase. Defining \tilde{u} as the *mass-averaged velocity*; that is,

$$\tilde{u} = \frac{\langle \rho_c u \rangle}{\langle \rho_c \rangle} \quad (6.29)$$

the equation for mass flow rate can be expressed as

$$\dot{M}_c = \langle \rho_c \rangle \tilde{u} \alpha_c A \quad (6.30)$$

Of course, if the density is constant over the volume then $\tilde{u} = \langle u \rangle$ and the mass flow rate equation reduces to

$$\dot{M}_c = \rho_c \langle u \rangle \alpha_c A \quad (6.31)$$

The flux of other properties is obtained by multiplying the mass flux by the intensive value (value per unit mass) by the mass flow rate.

The mass flux of particles through a surface is

$$\dot{M}_p = \rho_p \tilde{v} \alpha_d A \quad (6.32)$$

where ρ_p is the particle material density and \tilde{v} is the mass-averaged velocity defined as

$$\tilde{v} = \frac{\sum_k m_k v_k}{\sum_k m_k} \quad (6.33)$$

The conservation equations are presented below.

6.4 Volume-averaged conservation equations

The mass, momentum and energy equations for the continuous phase of a dispersed phase flow are presented here. The equations are first derived for a quasi-one dimensional flow and then the corresponding equations for a multi-dimensional flow, developed in Appendix C, are presented and discussed.

6.4.1 Quasi-one-dimensional flow

A *quasi-one-dimensional flow* is a flow in which the flow variations in one direction are considered but the variations in the cross-stream direction are neglected. This model can be applied to a flow with gently sloping walls. The control volume used for the quasi-one-dimensional flow is shown in Figure 6.9. The control surface can be broken into two parts: the surface through the continuous phase at stations 1 and 2 and along the wall and the surface adjacent to the particles inside the control volume. In keeping with the definition of a quasi-one-dimensional flow, the continuous phase density is uniform across each station but can vary from station to station. The mass flux of the continuous phase at each station is then $\alpha_c \rho_c \langle u \rangle$. A shear stress of τ_w acts on the fluid at the wall. The average pressure acting on the continuous phase along the sloping wall is \bar{p} which is the average pressure between stations 1 and 2; $\bar{p} = (\langle p \rangle_1 + \langle p \rangle_2)/2$. The mass rate of change and velocity of each particle is k is m_k and v_k , respectively. There are boundary particles on the control surface at stations 1 and 2. The number of particles in the control volume is N . The volume of the control volume is V and is equal to the product of the average area, \bar{A} , between stations 1 and 2 and the length Δx .

6.4.2 Continuity equation

The *continuity equation* states that the rate of change of mass in the control volume plus the net efflux of mass through the control surfaces is equal to zero.

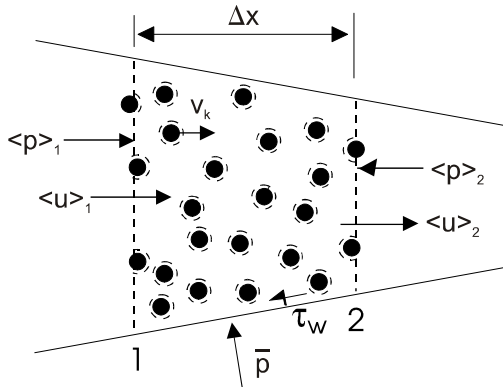


Figure 6.9: Quasi-one dimensional control volume with dispersed phase elements.

$$\boxed{\text{Rate of mass accumulation}} + \boxed{\text{Net efflux of mass}} = 0$$

Referring to Figure 6.9 the control surfaces are the stations 1 and 2 and the surfaces surrounding every particle. The continuous phase crosses the control surfaces at stations 1 and 2 and also passes through the surfaces surrounding every particle, including the boundary particles. The continuity equation for the continuous phase is

$$V\Delta_t(\rho_c\alpha_c) + \alpha_c\rho_c \langle u \rangle A|_2 - \alpha_c\rho_c \langle u \rangle A|_1 + \sum_k \dot{m}_k = 0 \quad (6.34)$$

where \dot{m}_k is the rate of mass change of particle k . The summation is carried out over all the elements inside the volume. If the center of a boundary particle is inside the volume it is included in the summation. The difference operator Δ_t is defined as

$$\Delta_t(\rho_c\alpha_c) = \frac{\Delta(\rho_c\alpha_c)}{\Delta t}$$

or, simply, the rate of change bulk density in the volume with time.

If all the particles are evaporating at the same rate, the dispersed phase flux term becomes

$$\sum_k \dot{m}_k = N\dot{m} \quad (6.35)$$

where N is the total number of particles inside the volume. The continuity equation can then be rewritten as

$$V\Delta_t(\rho_c \alpha_c) + \alpha_c \rho_c \langle u \rangle A |_2 - \alpha_c \rho_c \langle u \rangle A |_1 = -N\dot{m} = S_{\text{mass}} \quad (6.36)$$

where S_{mass} is the mass source term. Obviously, the mass source term is positive for evaporating particles.

If the continuous phase is composed of several gaseous components such as nitrogen, oxygen or other chemical species, a continuity equation can be written for each species. The flux terms through the continuous phase and from the particle surfaces would have a factor expressing the mass fraction of the species in question. Also a diffusional velocity would have to be included. These details will not be addressed here.

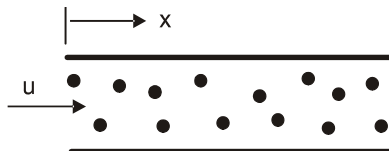
For convenience later, the difference in quantities between stations 1 and 2 will be expressed as

$$\Delta B = B_2 - B_1$$

so the shorthand form for the continuity equation is

$$V\Delta_t(\rho_c \alpha_c) + \Delta(\alpha_c \rho_c \langle u \rangle A) = S_{\text{mass}} \quad (6.37)$$

Example: Evaporating particles flow in a constant area duct as shown. The flow is steady. The particles have the same size and evaporate at the same rate. The particle volume fraction is negligible and the fluid density is constant. The mass concentration of particles is 1.0 and the evaporation rate, \dot{m}/m is $-1/20$ ms. Find the fluid velocity gradient, $\Delta \langle u \rangle / \Delta x$ in the duct.



For steady flow in a constant area duct, the continuity equation, Equation 6.37, reduces to

$$A\Delta(\alpha_c \rho_c \langle u \rangle) = S_{\text{mass}}$$

Since the fluid density is constant and the volume fraction of the particles is negligible ($\alpha_c \rightarrow 1$), the equation further reduces to

$$\frac{\Delta \langle u \rangle}{\Delta x} = -\frac{1}{\rho_c} \frac{Nm}{V} \frac{\dot{m}}{m} = -C \frac{\dot{m}}{m}$$

where C is the mass concentration. Substituting in the values for concentration and evaporation rate yields

$$\frac{\Delta \langle u \rangle}{\Delta x} = \frac{1}{0.02 \text{ s}} = 50 \text{ s}^{-1}$$

The change in velocity with distance represents a convective acceleration of the flow in the duct.

The volume-averaged continuity equation, developed in Appendix C, is

$$\frac{\partial}{\partial t} (\alpha_c \langle \rho_c \rangle) + \frac{\partial}{\partial x_i} (\alpha_c \langle \rho_c \rangle \bar{u}_i) = s_{\text{mass}} \quad (6.38)$$

where the source term, s_{mass} , is

$$s_{\text{mass}} = -\frac{1}{V} \sum_k \dot{m}_k \quad (6.39)$$

If the density of the continuous phase is constant, the continuity equation reduces to

$$\frac{\partial}{\partial t} (\alpha_c \rho_c) + \frac{\partial}{\partial x_i} (\alpha_c \rho_c \langle u_i \rangle) = s_{\text{mass}} \quad (6.40)$$

If, in addition, volume fraction of the particles is negligible (point particles), the continuity equation simplifies to

$$\frac{\partial \rho_c}{\partial t} + \frac{\partial}{\partial x_i} (\rho_c \langle u_i \rangle) = s_{\text{mass}} \quad (6.41)$$

This equation is to be used in lieu of Equation 6.19a. The velocity $\langle u_i \rangle$ cannot be replaced by u_i because of the magnitude of the volume required to minimize variations in the properties of the dispersed phase.

If all the particles are the same size and exchange mass at the same rate, then

$$s_{\text{mass}} = -n\dot{m} \quad (6.42)$$

For an evaporating particle, $\dot{m} < 0$ so the mass coupling term would be positive. If the mass coupling parameter, Π_{mass} defined in Chapter 2 is small, then s_{mass} can be neglected.

With no mass coupling and constant continuous phase material density, the continuity equation reduces to

$$\frac{\partial}{\partial t} (\alpha_c \rho_c) + \frac{\partial}{\partial x_i} (\alpha_c \rho_c \langle u_i \rangle) = 0 \quad (6.43)$$

or

$$\frac{\partial}{\partial t} (\alpha_c) + \frac{\partial}{\partial x_i} (\alpha_c \langle u_i \rangle) = 0 \quad (6.44)$$

which is a statement of conservation of volume². If the particles occupy insignificant volume, then Equation 6.43 further reduces to

$$\frac{\partial}{\partial t} (\rho_c) + \frac{\partial}{\partial x_i} (\rho_c \langle u_i \rangle) = 0 \quad (6.45)$$

²This is the volume associated with the mass of the system which is also constant.

The continuity equation for the dispersed phase can be expressed as

$$\frac{\partial}{\partial t} (\alpha_d \rho_d) + \frac{\partial}{\partial x_i} (\alpha_d \rho_d \tilde{v}_i) = -s_{\text{mass}} \quad (6.46)$$

where \tilde{v}_i is the mass averaged velocity of the dispersed phase defined as

$$\tilde{v}_i = \frac{\sum_k m_k v_{i,k}}{\sum_k m_k} \quad (6.47)$$

where m_k and $v_{i,k}$ are the mass and velocity of particle k , respectively, and the summation is carried out over every particle in the volume. The source term is simply the negative of the source term for the continuous phase.

Adding the continuity equations for both phases, Equation 6.38 and Equation 6.46, yields

$$\frac{\partial}{\partial t} (\alpha_c \langle \rho_c \rangle + \alpha_d \rho_d) + \frac{\partial}{\partial x_i} (\alpha_c \langle \rho_c \rangle \tilde{u}_i + \alpha_d \rho_d \tilde{v}_i) = 0 \quad (6.48)$$

The combination $\alpha_c \rho_c + \alpha_d \rho_d$ is the mixture density ρ_m . If the velocities of both phases are the same, $\langle u_i \rangle = \tilde{v}_i$ (equilibrium flow), the continuity equation for the mixture is

$$\frac{\partial}{\partial t} (\rho_m) + \frac{\partial}{\partial x_i} (\rho_m \tilde{u}_i) = 0 \quad (6.49)$$

If there is no mass coupling and the two phases have constant material densities, then

$$\frac{\partial}{\partial t} (\alpha_c + \alpha_d) + \frac{\partial}{\partial x_i} (\alpha_c \langle u_i \rangle + \alpha_d \tilde{v}_i) = 0 \quad (6.50)$$

or

$$\frac{\partial}{\partial x_i} (\alpha_c \langle u_i \rangle + \alpha_d \tilde{v}_i) = 0 \quad (6.51)$$

because $\alpha_c + \alpha_d = 1$.

6.4.3 Momentum equation

The *momentum equation* for the continuous phase can be expressed as the rate of change of momentum in the control volume plus the net efflux of momentum from the control volume is equal to the net forces acting on the continuous phase in the control volume.

Rate of momentum accumulation in control volume	+	Net efflux of momentum from control volume	=	Force on fluid in control volume
---	---	--	---	----------------------------------

The momentum per unit mass is simply the velocity. Thus, the momentum flux of the continuous phase through an element of area ΔA is $\rho_c u^2 \Delta A$. Integrating across a given station in the flow, the momentum flux is

$$Mom = \alpha_c A \rho_c \langle u \rangle^2 + \alpha_c A \rho_c \langle \delta u \delta u \rangle \quad (6.52)$$

where $\delta u = u - \langle u \rangle$. The second term, sometimes called “streaming stress,” (Prosperetti & Tryggvason, 2007) is the one-dimensional form of the Reynolds stress. Because $\delta u \ll \langle u \rangle$ the Reynolds stress is small compared to $\alpha_c A \rho_c \langle u \rangle^2$ and can be neglected. Combining the momentum flux across stations 1 and 2 and through the surfaces surrounding the dispersed phase, the momentum equation becomes

$$V \Delta t (\alpha_c \rho_c \langle u \rangle) + \alpha_c \rho_c \langle u \rangle^2 A |_2 - \alpha_c \rho_c \langle u \rangle^2 A |_1 + \sum_k \dot{m}_k v_k = F \quad (6.53)$$

where F is the force acting on the continuous phase. The assumption has been made that the mass flux is uniform over the particle surface.

The forces acting on the fluid are the pressure forces on the boundary, the shear stress at the wall, the drag forces due to the dispersed phase, and the body forces on the fluid (such as the gravitational force).

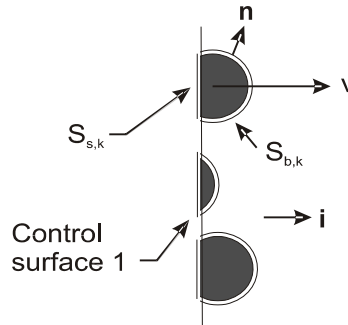


Figure 6.10: Boundary particles severed by control surface 1.

Boundary particles require special consideration. Consider the boundary particle k on control surface 1 shown in Figure 6.10. The surface is comprised of the surface $S_{b,k}$ inside the control volume and the surface $S_{s,k}$ severed by the control surface. The particle velocity is v_k . The average pressure at station 1 is $\langle p \rangle_1$. The force on the continuous phase due to pressure on the portion of the particle inside the control volume is

$$\Delta \mathbf{F}_p = \int_{S_{b,k}} p_s \mathbf{n} dS \quad (6.54)$$

where p_s is the pressure on the particle surface. The unit normal vector \mathbf{n} is directed outward from the particle surface. The pressure on the particle surface is expressed as the sum of the average pressure and a deviation

$$p_s = \langle p \rangle_1 + \delta p \quad (6.55)$$

so the force becomes

$$\Delta \mathbf{F}_p = \langle p \rangle_1 \int_{S_{b,k}} \mathbf{n} dS + \int_{S_{b,k}} \delta p \mathbf{n} dS \quad (6.56)$$

The first integral reduces to

$$\langle p \rangle_1 \int_{S_{b,k}} \mathbf{n} dS = \langle p \rangle_1 S_{s,k} \mathbf{i} \quad (6.57)$$

where \mathbf{i} is the unit vector in the flow direction. The sum of the severed areas of the boundary particles, $\sum_k S_{s,k}$ is $\alpha_d A$. The pressure force on the continuous phase is $\alpha_c \langle p \rangle_1 A$. Thus the total force due to pressure at station 1 is

$$\alpha_c A_1 \langle p \rangle_1 + \alpha_d A_1 \langle p \rangle_1 = \langle p \rangle_1 A_1 \quad (6.58)$$

The corresponding force due to pressure at station 2 is $-\langle p \rangle_2 A_2$.

The integral of δp over S_b yields the negative of the force due to pressure (or "form" force) on a particle. The sum of all the "form forces" on the boundary particles contributes to the drag force on all the particles in the volume.

The force in the flow direction due to the pressure on the sloping surface is $\bar{p}(A_2 - A_1)$ or $\bar{p}\Delta A$. Thus, the net force due to pressure is

$$F_p = \langle p \rangle_1 A_1 - \langle p \rangle_2 A_2 + \bar{p}\Delta A \quad (6.59)$$

or

$$F_p = \langle p \rangle_1 A_1 - \langle p \rangle_2 A_2 + \frac{\langle p \rangle_2 + \langle p \rangle_1}{2} (A_2 - A_1) \quad (6.60)$$

Rearranging the terms,

$$F_p = (\langle p \rangle_1 - \langle p_2 \rangle) \frac{A_1 + A_2}{2}$$

the pressure force can be expressed as

$$F_p = -\bar{A}\Delta \langle p \rangle \quad (6.61)$$

The force due to wall friction is³

$$F_f = -\tau_w P \Delta x \quad (6.62)$$

³The slope of the wall is small so the cosine of the wall angle is taken as unity.

where P is the perimeter (average) of the duct.

The force due to gravity is

$$F_g = \rho_c \alpha_c g \bar{A} \Delta x \quad (6.63)$$

where the gravity vector is in the flow direction.

Finally the force on the fluid due to dispersed phase drag is the negative sum of the drag force on every particle, $F_{D,k}$, in the volume

$$F_d = - \sum_k F_{D,k} \quad (6.64)$$

Combining all the terms, the quasi-one dimensional momentum equation becomes

$$\begin{aligned} & V \Delta_t (\alpha_c \rho_c \langle u \rangle) + \Delta \left(\alpha_c \rho_c \langle u \rangle^2 A \right) \\ &= - \sum_k \dot{m}_k v_k - \bar{A} \Delta \langle p \rangle - \tau_w P \Delta x + \rho_c \alpha_c g \bar{A} \Delta x - F_d \end{aligned} \quad (6.65)$$

This is the general form of the momentum equation. Various other forms arise depending on how the drag force term is treated.

There are several ways to treat the force term. One way is to apply the equation of motion for every particle, k ,

$$m_k \frac{dv_k}{dt} = F_{D,k} + m_k g \quad (6.66)$$

solve for $F_{D,k}$ and express the force term as

$$F_d = - \sum_k m_k \frac{dv_k}{dt} + \alpha_d \rho_d \bar{A} \Delta x g \quad (6.67)$$

This approach is especially useful if the Lagrangian approach is implemented for the dispersed phase and the trajectory of every particle is calculated⁴. For this case the quasi-one-dimensional momentum equation becomes

$$\begin{aligned} & V \Delta_t (\alpha_c \rho_c \langle u \rangle) + \Delta (\alpha_c \rho_c \langle u \rangle^2 A) \\ &= - \sum_k \dot{m}_k v_k - \bar{A} \Delta \langle p \rangle - \tau_w P \Delta x - \sum_k m_k \frac{dv_k}{dt} + \rho_m \bar{A} \Delta x g \end{aligned} \quad (6.68)$$

Another way to include the drag force due to the particles is to sum the forces on all the particles in the volume.

$$F_d = - \sum_k \left[3\pi \mu_c D_k f_k (\langle u \rangle - v_k) - V_{d,k} \frac{d \langle p \rangle}{dx} \right] \quad (6.69)$$

⁴This approach has to be modified if body forces other than gravity are responsible for particle motion. It does not apply to contact-dominated flows.

where the virtual mass effect, the Basset force as well as the Faxen force have been neglected (see Chapter 4). Using this equation to represent the forces, the momentum equation becomes

$$V\Delta_t(\alpha_c\rho_c \langle u \rangle) + \Delta(\alpha_c\rho_c \langle u \rangle^2 A)$$

$$\begin{aligned} = & -\sum_k \dot{m}_k v_k - \alpha_c \bar{A} \Delta \langle p \rangle - \tau_w P \Delta x \\ & - \sum_k [3\pi\mu_c D_k f_k (\langle u \rangle - v_k)] + \alpha_c \rho_c \bar{A} \Delta x g \end{aligned} \quad (6.70)$$

If all the particles have the same mass m and move with the same velocity v , Equation 6.70 simplifies to

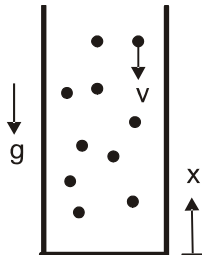
$$\begin{aligned} & V\Delta_t(\alpha_c\rho_c \langle u \rangle) + \Delta(\alpha_c\rho_c \langle u \rangle^2 A) \\ = & S_{\text{mass}} v - \alpha_c \bar{A} \Delta \langle p \rangle - \tau_w P \Delta x - Nm \frac{f}{\tau_V} f (\langle u \rangle - v) + \alpha_c \rho_c \bar{A} \Delta x g \end{aligned} \quad (6.71)$$

where τ_V is the velocity response time. This equation is referred to in the discussion numerical model development in Chapter 9.

For dense flows, the particle force term is obtained from empirical equations. For example, for contact-dominated flows, the Ergun equation, Equation 4.99 applies so the particle force term in Equation 6.65 becomes

$$F_d = \left\{ 150 \frac{\alpha_d^2 \mu_c (\tilde{v} - \langle u \rangle)}{\alpha_c^2 D^2} + 1.75 \frac{\alpha_d \rho_c (\tilde{v} - \langle u \rangle) |\tilde{v} - \langle u \rangle|}{\alpha_c D} \right\} V \quad (6.72)$$

Example: Uniform size particles are falling at constant velocity in a closed, constant area duct as shown. The velocity of the continuous phase is zero. There is no mass coupling. Find the pressure gradient in the duct using both Equations 6.68 and 6.71. Interpret your results.



Solution: With no fluid motion, no mass exchange and constant particle velocity, Equation 6.68 reduces to

$$-A\Delta \langle p \rangle - \rho_m A \Delta x g = 0$$

where the sign has been changed on the gravity term because the gravity acts in the opposite direction of x . The pressure gradient is

$$\frac{\Delta \langle p \rangle}{\Delta x} = -\rho_m g$$

Under the same conditions, Equation 6.71 reduces to

$$-\alpha_c A \Delta p - Nm \frac{f}{\tau_V} fv - \alpha_c \rho_c A \Delta x g = 0$$

since g and v are in the negative x direction. Because the particles are falling at constant speed (not accelerating), the drag force on a particle must equal its weight so

$$3\pi\mu_c D f v - V_d \frac{d \langle p \rangle}{dx} = mg$$

or

$$\begin{aligned} m \frac{f}{\tau_V} v - V_d \frac{\Delta \langle p \rangle}{\Delta x} &= mg \\ Nm \frac{f}{\tau_V} v - \alpha_d A \Delta x \frac{\Delta \langle p \rangle}{\Delta x} &= \alpha_d \rho_d A \Delta x g \end{aligned}$$

Substituting the equation for $Nmfv/\tau_V$ into the reduced form of Equation 6.71 and dividing by $A\Delta x$ gives

$$\frac{\Delta \langle p \rangle}{\Delta x} = -\rho_m g$$

which agrees with the result starting with Equation 6.68.

The negative sign on the pressure gradient shows that the pressure force has to be in the positive x -direction to support the weight of the particles. This is basically the hydrostatic equation with the density being the mixture density.

The volume-averaged carrier phase momentum equation for a multidimensional flow is derived in Appendix C. The equation is

$$\begin{aligned} \frac{\partial}{\partial t} (\alpha_c \langle \rho_c \rangle \tilde{u}_i) + \frac{\partial}{\partial x_j} (\alpha_c \langle \rho_c \rangle \tilde{u}_i \tilde{u}_j) &= -\frac{\partial}{\partial x_j} \alpha_c \overbrace{\langle \rho_c \delta u_i \delta u_j \rangle}^{\text{Reynolds stress}} \\ &\quad \underbrace{- \frac{\partial}{\partial x_i} \langle p \rangle + \frac{\partial}{\partial x_j} \langle \tau_{ij} \rangle}_{\text{Momentum coupling}} - \frac{1}{V} \sum_k v_{k,i} \dot{m}_k - \frac{1}{V} \sum_k F_{k,i} + \alpha_c \langle \rho_c \rangle g_i \end{aligned} \tag{6.73}$$

and the additional terms that appear due to volume-averaging and multiphase flow effects are the volume-averaged Reynolds stress and the momentum coupling. It will be assumed that the density of the continuous phase is constant so the momentum equation reduces to

$$\begin{aligned} \frac{\partial}{\partial t} (\alpha_c \rho_c \langle u_i \rangle) + \frac{\partial}{\partial x_j} (\alpha_c \rho_c \langle u_i \rangle \langle u_j \rangle) &= -\frac{\partial}{\partial x_j} (\alpha_c \rho_c \langle \delta u_i \delta u_j \rangle) \\ -\frac{\partial}{\partial x_i} \langle p \rangle + \frac{\partial}{\partial x_j} \langle \tau_{ij} \rangle - \frac{1}{V} \sum_k v_{k,i} \dot{m}_k - \frac{1}{V} \sum_k F_{k,i} + \alpha_c \rho_c g_i \end{aligned} \quad (6.74)$$

The *volume-averaged Reynolds stress*

$$R_{ij} = \langle \delta u_i \delta u_j \rangle \quad (6.75)$$

arises because of velocity deviations from the mass-averaged velocity in the averaging volume. It is directly analogous to the Reynolds stress, $\overline{u'_i u'_j}$, obtained by temporal averaging the Navier-Stokes equations with velocity fluctuations in single-phase flow. The volume-averaged Reynolds stress is dependent on the turbulence in the averaging volume as well as the velocity deviations owing to the flow around the particles. Neglecting the volume-averaged Reynolds stress is equivalent to neglecting the Reynolds stress in a single-phase turbulent flow. One way to model the volume-averaged Reynolds stress is to use the *Boussinesq model* which relates the Reynolds stress to the turbulent kinematic viscosity, ν_T , the turbulence kinetic energy, k_c , and the rate of strain of the flow field based on the volume-averaged velocities,

$$-R_{ij} = \nu_T \left(\frac{\partial \langle u_i \rangle}{\partial x_j} + \frac{\partial \langle u_j \rangle}{\partial x_i} \right) - \frac{2}{3} k_c \delta_{ij} \quad (6.76)$$

where turbulence kinetic energy is defined by

$$k_c = \frac{1}{2} \langle \delta u_i \delta u_i \rangle \quad (6.77)$$

In single-phase flow the additional term is required to ensure that when i equals j and the continuity equation is applied that $R_{ii} = 2k_c^5$. Using the same scaling arguments as used for the $k - \varepsilon$ model the effective viscosity can be expressed as

$$\nu_T = C_\mu k_c^2 / \varepsilon_c \quad (6.78)$$

where C_μ is a constant of proportionality and ε is the rate of dissipation defined as

$$\varepsilon_c = \nu_c \left\langle \frac{\partial \delta u_i}{\partial x_j} \frac{\partial \delta u_i}{\partial x_j} \right\rangle \quad (6.79)$$

These concepts are referred to as *turbulence modeling* and are further discussed in Chapter 7. The equations for the volume averaged turbulence kinetic energy and dissipation are developed in Appendix D.

⁵This is not the case for volume-averaged multiphase flow where the continuity equation reduces to

$$\frac{\partial \alpha_c}{\partial t} + \frac{\partial}{\partial x_i} (\alpha_c \langle u_i \rangle) = 0$$

In addition to the Boussinesq approximation, another approach is to develop equations for the Reynolds stress directly. This approach is also discussed in Chapter 7 and the equations for volume averaged Reynolds stress are developed in Appendix D.

The first term of the momentum coupling is

$$-\frac{1}{V} \sum_k v_{k,i} \dot{m}_k$$

which is the momentum coupling due to mass transfer. Some derivations reported in the literature suggest that the velocity used in this coupling term depends on the direction of mass transfer; that is, evaporation or condensation. However, it must always be the velocity of the surface at which the mass exchange takes place, namely, the particle velocity. If all particles in the averaging volume have the same velocity, v_i , and mass exchange rate, \dot{m} , then

$$-\frac{1}{V} \sum_k v_{k,i} \dot{m}_k = -n v_i \dot{m} = s_{\text{mass}} v_i \quad (6.80)$$

For evaporating particles, this term would be positive so the mass evaporated from the surface contributes to the carrier phase momentum in the direction of the moving particle. If the mass coupling parameter is small, this coupling term can be neglected.

The force coupling term

$$-\frac{1}{V} \sum_k F_{k,i}$$

is the sum of all the fluid-dynamic forces acting on the particles in the averaging volume. The fluid dynamic forces acting on a single particle is given by Equation 4.155. The continuous phase velocity, pressure and shear stress have to be replaced by the local phase averaged (interstitial) values. The force on particle k becomes

$$F_{k,i} = V_k \left(-\frac{\partial \langle p \rangle}{\partial x_i} + \frac{\partial \langle \tau_{ij} \rangle}{\partial x_j} \right) + F'_{k,i}$$

where V_k is the volume of particle k and $F'_{k,i}$ is the sum of the remaining forces. For example if the forces due to unsteady effects (Basset and virtual mass) and the lift force (Magnus and Saffman) are insignificant then

$$F'_{k,i} = 3\pi\mu_c D_k f_k (\langle u_i \rangle - v_{k,i})$$

The force coupling term can be rewritten as

$$-\frac{1}{V} \sum_k F_{k,i} = \alpha_d \left(\frac{\partial \langle p \rangle}{\partial x_i} - \frac{\partial \langle \tau_{ij} \rangle}{\partial x_j} \right) - \frac{1}{V} \sum_k F'_{k,i}$$

Substituting this term into Equation 6.74 yields

$$\begin{aligned} \frac{\partial}{\partial t} (\alpha_c \rho_c \langle u_i \rangle) + \frac{\partial}{\partial x_j} (\alpha_c \rho_c \langle u_i \rangle \langle u_j \rangle) &= -\frac{\partial}{\partial x_j} (\alpha_c \rho_c R_{ij}) \\ -\alpha_c \frac{\partial}{\partial x_i} \langle p \rangle + \alpha_c \frac{\partial}{\partial x_j} \langle \tau_{ij} \rangle - \frac{1}{V} \sum_k v_{k,i} \dot{m}_k - \frac{1}{V} \sum_k F'_{k,i} + \alpha_c \rho_c g_i \end{aligned} \quad (6.81)$$

Thus there are two forms for the momentum equation. One form is given by Equation 6.74 where the fluid dynamic force on the particles includes all the forces acting on a particle and the other form is Equation 6.81 where the forces due to the undisturbed flow in the particle force equation are incorporated into the pressure and shear stress gradients. The choice depends on the application.

If the steady state drag is the only significant fluid dynamic force acting on the particles and all the particles have the same size and move with the same velocity, Equation 6.81 simplifies to

$$\begin{aligned} \frac{\partial}{\partial t} (\alpha_c \rho_c \langle u_i \rangle) + \frac{\partial}{\partial x_j} (\alpha_c \rho_c \langle u_i \rangle \langle u_j \rangle) &= -\frac{\partial}{\partial x_j} (\alpha_c \rho_c R_{ij}) \\ -\alpha_c \frac{\partial}{\partial x_i} \langle p \rangle + \alpha_c \frac{\partial}{\partial x_j} \langle \tau_{ij} \rangle + s_{mass} v_i + \beta_V (v_i - \langle u_i \rangle) + \alpha_c \rho_c g_i \end{aligned} \quad (6.82)$$

where β_V is $\alpha_d \rho_d f / \tau_V$.

This equation can be further simplified by assuming "point particles" and setting $\alpha_c = 1$. This does not imply that the volume-averaged quantities can be replaced by point values or that the Reynolds stress is negligible. As stated above, there still has to be an averaging volume sufficiently large to ensure small variations of the terms associated with the particle phase. This is the correct form of the momentum equation and must be used in lieu of Equation 6.19b.

6.4.4 Energy equation

The *first law of thermodynamics* states that the rate of change of energy in the control volume plus the net efflux of energy through the control surface is equal to the net heat transfer to the system minus the rate at which work is done by the system.

Rate of energy accumulation	+	Net efflux of energy	=	Heat transfer rate to system	-	Work rate done by system
-----------------------------------	---	----------------------------	---	------------------------------------	---	--------------------------------

The control volume used to develop the energy equation is shown in Figure 6.11. Energy is convected through the control surfaces at stations 1 and 2 as well as through the control surfaces surrounding the particles. The energies consist of both the internal and external (kinetic) energy⁶. Work is done by

⁶The potential energy is not included here because the work against gravitational forces will be included in the work term.

flow work associated with motion across the control surfaces and the surfaces enclosing the particles. Work is also done by the drag force on the particles and by the body forces (gravity). There is no work associated with the wall shear stress since the velocity at the wall is zero. Heat is transferred through the control surfaces, through the wall and from the particles to the continuous phase.

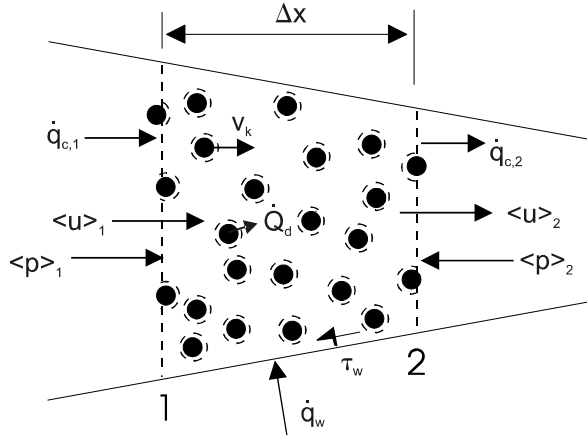


Figure 6.11: Quasi-one dimensional volume for energy equation.

Relating the change in energy in the control volume plus the net efflux through the control surfaces to the rate of work and heat transfer gives

$$V\Delta t \left[\alpha_c \rho_c (\langle i_c \rangle + \frac{\langle u \rangle^2}{2}) \right] + \Delta \left[\alpha_c \rho_c \langle u \rangle (\langle i_c \rangle + \frac{\langle u \rangle^2}{2}) A \right] + \sum_k \dot{m}_k (i_s + \frac{v^2}{2})_k = \dot{Q} - \dot{W} \quad (6.83)$$

where i_c is the specific internal energy of the continuous phase and $i_{s,k}$ is the internal energy of the fluid at the surface enclosing particle k . The velocity v_k is the particle velocity. The kinetic energy at the particle surface should also include the efflux velocity from the particle surface. This is usually negligible and not included here. The summation is carried out over all the particles in the volume.

Work rate

There are three sources of work done by the continuous phase. The first is the *flow work* due to the fluid and particle motion at stations 1 and 2. The second is the flow work associated with the mass efflux from the particle surface. The third is the flow work associated with the change in particle volume which is generally very small compared to other terms and will be neglected here.

First, consider the flow work associated with fluid and particle motion across the control surfaces. The flow work due to the continuous phase is

$$\dot{W}_{f,c} = \alpha_c \langle p \rangle A \langle u \rangle |_1^2 = \Delta(\alpha_c \langle p \rangle A \langle u \rangle) \quad (6.84)$$

To evaluate the flow work owing to the particle motion, refer to the boundary particle k shown in Figure 6.10. The pressure around the particle is the sum of the pressure at station 1 plus the deviation from that pressure as used previously in the development of the momentum equation, Equation 6.53. The flow work associated with a boundary particle k shown in Figure 6.10 is

$$\dot{W}_{f,k} = - \int_{S_{b,k}} (\langle p \rangle_1 + \delta p) v_k \mathbf{n} \cdot \mathbf{i} dS \quad (6.85)$$

where \mathbf{n} is the unit normal vector from the surface and \mathbf{i} is the unit vector in the flow direction.

$$\dot{W}_{f,k} = - \langle p \rangle_1 S_{s,k} v_k - v_k \int_{S_{b,k}} \delta p \mathbf{n} \cdot \mathbf{i} dS \quad (6.86)$$

where $S_{s,k}$ is the area severed by the control surface. Summing over all the boundary particles on control surface 1 gives

$$\dot{W}_{f,d} = \sum_k \dot{W}_{f,k} = - \langle p \rangle \alpha_d A \tilde{v} |_1 - \sum_k v_k \int_{S_{b,k}} \delta p \mathbf{n} \cdot \mathbf{i} dS \quad (6.87)$$

The sum of the integrals is the work done by the form force (force due to pressure distribution) on the boundary particles and will be included with that of the interior particles to yield the work due to all the particles in the control volume. The flow work associated with the flow across the 1 and 2 surfaces is

$$\dot{W}_f = \alpha_c \langle p \rangle A \langle u \rangle |_1^2 + \alpha_d \langle p \rangle A \tilde{v} |_1^2 = \Delta(\alpha_c \langle p \rangle A \langle u \rangle) + \Delta(\alpha_d \langle p \rangle A \tilde{v}) \quad (6.88)$$

The flow work associated with the mass flux from the particle surface is

$$\dot{W}_f = \sum_k \dot{m}_k \left(\frac{p_s}{\rho_{c,s}} \right)_k \quad (6.89)$$

where \dot{m}_k is the evaporation rate of particle k and $(p_s/\rho_{c,s})_k$ is the pressure/fluid density ratio at the particle surface. The summation is carried out over every particle in the volume. If the particle is evaporating, work is being done on the continuous phase so the sign on the work term is negative which is represented correctly here since \dot{m} is negative. Because of the change in momentum for the fluid coming off the particle surface, the pressure at the surface may be slightly different than the local average pressure. This difference is not considered here.

Also there is a flow work associated with the rate of volume change of the particles. The contribution of this work is generally very small and will not be included in the quasi-one dimensional equations.

The work rate associated with the drag force on the particles is

$$\dot{W}_d = \sum_k v_k F_{D,k} \quad (6.90)$$

where $F_{D,k}$ is the drag force on the particle k . The summation is carried out over all the interior particles and those on the boundary corresponding to the second term in Equation 6.87. The drag force on the particle can be replaced by (from Equation 6.66 above)

$$F_{D,k} = m_k \frac{dv_k}{dt} - m_k g \quad (6.91)$$

so the work rate due to particle drag is

$$\dot{W}_d = \sum_k \left[m_k \frac{d}{dt} \left(\frac{v_k^2}{2} \right) - m_k v_k g \right] \quad (6.92)$$

If the unsteady terms (Basset and virtual mass) can be neglected, the work due to particle drag is

$$\dot{W}_d = \sum_k \left[3\pi\mu_c D_k f(\langle u \rangle - v_k) v_k - V_{d,k} v_k \frac{\Delta \langle p \rangle}{\Delta x} \right] \quad (6.93)$$

which can be expressed as

$$\dot{W}_d = \sum_k \left[m_k \frac{f_k}{\tau_{V,k}} (\langle u \rangle - v_k) v_k \right] - \alpha_d \tilde{v} \bar{A} \Delta \langle p \rangle \quad (6.94)$$

where f_k and $\tau_{V,k}$ are the drag factor and velocity response time for particle k .

Finally the work done against body (gravitational) forces is

$$\dot{W}_g = -\alpha_c \rho_c g V \langle u \rangle \quad (6.95)$$

where g acts in the direction of 1 to 2 (positive x direction).

Heat transfer

Heat is transferred to the continuous phase through several means. There is heat transfer through the 1 and 2 surfaces of the control volume, heat transfer from the particles to the fluid and heat transfer through the walls.

The heat transfer across surfaces 1 and 2 can be broken down into two components: heat transfer through the fluid and heat transfer through the particles. The heat transfer across surface 1 with boundary particle k is depicted in Figure 6.12. The heat transfer by conduction through the continuous

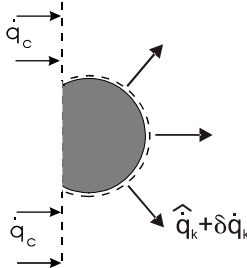


Figure 6.12: Heat transfer at boundary particle, k .

phase is $\dot{q}_c \alpha_c A_1$ where \dot{q}_c is the heat transfer rate per unit area through the carrier fluid.

It is convenient to express the heat transfer on the surface of the boundary particles as the sum of the average heat transfer rate over the surface of the particle and the deviation therefrom.

$$\dot{q}_k = \hat{\dot{q}}_k + \delta\dot{q}_k \quad (6.96)$$

The heat transfer rate to the fluid from the boundary particle becomes

$$\dot{Q}_{b,k} = \int_{S_b} \hat{\dot{q}}_k dS + \int_{S_b} \delta\dot{q}_k dS \quad (6.97)$$

The first integral is the heat transfer to the fluid from the surface of the boundary particle inside the boundary. This term will be combined with the heat transfer to the fluid by all the particles completely inside the control volume. The second integral represents the heat transfer rate *through* the particle. This term, combined with the heat transfer through the carrier phase, gives the composite conductive heat transfer to the fluid in the volume through the surface 1. Thus

$$\dot{Q}_{c,1} = (\dot{q}_c \alpha_c + \dot{q}_d \alpha_d) A_1 = \dot{q}_{c,\text{eff}} A_1 \quad (6.98)$$

where $\dot{q}_{c,\text{eff}}$ is the *effective heat transfer* through both phases across surface 1. The effective heat transfer may be represented by Fourier's law

$$\dot{q}_{c,\text{eff}} |_1 = -k'_{\text{eff}} \left\langle \frac{dT_c}{dx} \right\rangle |_1 \quad (6.99)$$

where k_{eff} is the effective thermal conductivity which will be a function of the thermal conductivity of each phase and the local volume fraction. For low particle volume fractions, the effective thermal conductivity is approximated as

$$k'_{\text{eff}} = \alpha_d k'_d + \alpha_c k'_c \quad (6.100)$$

where k'_d and k'_c are the thermal conductivity of the dispersed and continuous phase, respectively. The net heat transfer to the continuous phase across stations 1 and 2 is

$$\dot{Q}_c = -A\dot{q}_{c,\text{eff}} |_1^2 = -\Delta (Aq_{c,\text{eff}}) \quad (6.101)$$

The heat transfer to the wall is expressed as

$$\dot{Q}_w = -\dot{q}_w P \Delta x \quad (6.102)$$

where \dot{q}_w is the heat transfer to the wall per unit area. The minus sign reflects heat transfer from the fluid in the control volume. If the wall is insulated, \dot{q}_w is zero. If the wall temperature is fixed, the heat transfer will depend on the temperature difference between the fluid and the wall and the *Stanton number*.

The heat transfer rate from the particles to the fluid is

$$\dot{Q}_d = - \sum_k \dot{Q}_{d,k} \quad (6.103)$$

where $\dot{Q}_{d,k}$ is the conductive heat transfer rate from the fluid to particle k and the summation is carried out over every particle in the volume. This term includes the contribution due to the boundary particles, the first term in Equation 6.97. This heat transfer can be related to the rate of change of particle temperature by

$$m_k c_d \frac{dT_{d,k}}{dt} = \dot{Q}_{d,k} \quad (6.104)$$

where $T_{d,k}$ is the temperature of particle k so \dot{Q}_d can be expressed as

$$\dot{Q}_d = - \sum_k m_k c_d \frac{dT_{d,k}}{dt} \quad (6.105)$$

This form is not valid if radiative heat transfer is important and/or phase change of the particle occurs.

The heat transfer rate can also be expressed as

$$\dot{Q}_d = \sum_k N u_k \pi k'_c D_k (T_{d,k} - \langle T_c \rangle) \quad (6.106)$$

where $N u_k$ is the Nusselt number. An alternate form is

$$\dot{Q}_d = \sum_k m_k \frac{N u_k}{2} \frac{c_d}{\tau_{T,k}} (T_{d,k} - \langle T_c \rangle) \quad (6.107)$$

where c_d is the specific heat and $\tau_{T,k}$ is the thermal response time of particle k .

Substituting the equations for flow work, Equations 6.88 and 6.89, the work done by the continuous phase on particle motion, Equation 6.90, the work done

by gravity on the fluid, Equation 6.95, the conductive heat transfer in the flow direction, Equation 6.101, the heat transfer from the wall, Equation 6.102 and finally the heat transfer from the particle, Equation 6.103 into Equation 6.83 yields the basic form for the energy equation,

$$\begin{aligned} & V\Delta_t[\alpha_c\rho_c(\langle i_c \rangle + \frac{\langle u \rangle^2}{2})] + \Delta[\alpha_c\rho_c A \langle u \rangle (\langle h_c \rangle + \frac{\langle u \rangle^2}{2})] \\ = & -\Delta(\alpha_d \langle p \rangle A \tilde{v}) - \sum_k \dot{m}_k \left[(h_s + \frac{v^2}{2})_k \right] \\ & + \alpha_c \rho_c g V \langle u \rangle - \sum_k v_k F_{D,k} - \sum_k \dot{Q}_{d,k} - \dot{q}_w P \Delta x - \Delta(A q_{c,\text{eff}}) \end{aligned} \quad (6.108)$$

where h_c and h_s are the specific enthalpies of the continuous phase and fluid leaving the particle surface, respectively. Alternate forms are obtained by using the different equations for particle-fluid force interaction and heat transfer.

Substituting into Equation 6.83 all the above expressions for flow work and heat transfer rate and using Equations 6.92 and 6.105 for work and heat transfer rate from particle-fluid interaction, the total energy equation becomes

$$\begin{aligned} & V\Delta_t[\alpha_c\rho_c(\langle i_c \rangle + \frac{\langle u \rangle^2}{2})] + \Delta[\alpha_c\rho_c A \langle u \rangle (\langle h_c \rangle + \frac{\langle u \rangle^2}{2})] = -\Delta(\alpha_d \langle p \rangle A \tilde{v}) \\ & - \sum_k \dot{m}_k \left[(h_s + \frac{v^2}{2})_k \right] \\ & - \sum_k m_k \left[\frac{d}{dt} \left(\frac{v_k^2}{2} \right) + c_d \frac{dT_{d,k}}{dt} \right] + Vg(\rho_d \alpha_d \tilde{v} + \alpha_c \rho_c \langle u \rangle) \\ & - \Delta(A q_{c,\text{eff}}) - \dot{q}_w P \Delta x \end{aligned} \quad (6.109)$$

An alternate form of the total energy equation is obtained by using Equations 6.94 and 6.107 for work and heat transfer rate for particle fluid interaction

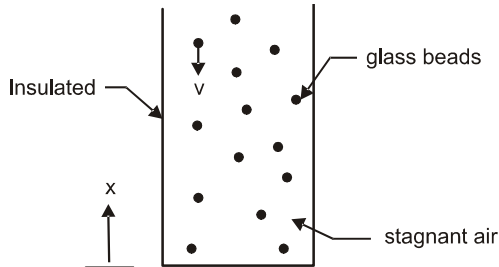
$$\begin{aligned} & V\Delta_t[\alpha_c\rho_c(\langle i_c \rangle + \frac{\langle u \rangle^2}{2})] + \Delta[\alpha_c\rho_c A \langle u \rangle (\langle h_c \rangle + \frac{\langle u \rangle^2}{2})] = -\langle p \rangle \Delta(\alpha_d A \tilde{v}) \\ & - \sum_k \dot{m}_k \left[(h_s + \frac{v^2}{2})_k \right] \\ & - \sum_k m_k \left[\frac{f_k}{\tau_{V,k}} v_k (\langle u \rangle - v_k) + \frac{N u_k c_d}{2 \tau_{T,k}} (\langle T_c \rangle - T_{d,k}) \right] \\ & + Vg \alpha_c \rho_c \langle u \rangle - \Delta(A q_{c,\text{eff}}) - \dot{q}_w P \Delta x \end{aligned} \quad (6.110)$$

If all the particles have the same mass (and diameter), the same velocity and

temperature and exchange mass at the same rate, this equation simplifies to

$$\begin{aligned}
 V\Delta_t[\alpha_c\rho_c(\langle i_c \rangle + \frac{\langle u \rangle^2}{2})] + \Delta[\alpha_c\rho_c A \langle u \rangle (\langle h_c \rangle + \frac{\langle u \rangle^2}{2})] &= -\langle p \rangle \Delta(\alpha_d A v) \\
 + S_{\text{mass}} \left[(h_s + \frac{v^2}{2}) \right] \\
 - Nm \left[\frac{f}{\tau_V} v (\langle u \rangle - v) + \frac{Nuc_d}{2\tau_T} (\langle T_c \rangle - T_d) \right] \\
 + Vg\alpha_c\rho_c \langle u \rangle - \Delta(Aq_{c,\text{eff}}) - \dot{q}_w P \Delta x
 \end{aligned} \tag{6.111}$$

Example: Heated 200 μm glass beads with a density of 2500 kg/m^3 and a temperature of 100°C fall through an insulated tube of stagnant air with a material density of 1.2 kg/m^3 and a temperature of 20°C as shown in the figure. The specific heat at constant volume, c_v , for the air is 0.17 kcal/kg·°C. The velocity of the beads is 1.5 m/s, the drag factor is 1.2 and the velocity response time is 0.31 s. The thermal response time of the particles is 0.51 s and the Nusselt number is 4.4. The specific heat of the beads is 0.19 kcal/kg·°C. The bulk density of the particles is 1 kg/m^3 . Find the rate at which the air in the tube is heating up. Neglect the effect of the particles accumulating at the bottom of the tube.



Glass beads falling in a tube of stagnant air.

Solution: The form of the energy equation most appropriate to solve this problem is Equation 6.111. The flow is stagnant so $\langle u \rangle = 0$. There is no mass transfer so $S_{\text{mass}} = 0$. Assume there is no temperature gradient along the tube so $\Delta(Aq_{c,\text{eff}}) = 0$. The particle velocity does not change in the tube so $\Delta(\alpha_d A v) = 0$. Also the tube is insulated so $\dot{q}_w = 0$. With these conditions the energy equation reduces to

$$V\Delta_t[\alpha_c\rho_c \langle i_c \rangle] = Nm \left[\frac{f}{\tau_V} v^2 + \frac{Nuc_d}{2\tau_T} (T_d - \langle T_c \rangle) \right]$$

Thus the sources of heating are the conversion of mechanical energy to heat and conductive heat transfer. The product $\alpha_c\rho_c$ is constant so the equation

may be further reduced to

$$\frac{\Delta \langle i_c \rangle}{\Delta t} = \frac{\bar{\rho}_d}{\alpha_c \rho_c} \left[\frac{f}{\tau_V} v^2 + \frac{Nuc_d}{2\tau_T} (T_d - \langle T_c \rangle) \right]$$

The specific internal energy is the product of the specific heat at constant volume and the continuous phase temperature so

$$\frac{\Delta \langle T_c \rangle}{\Delta t} = \frac{\bar{\rho}_d}{\alpha_c \rho_c} \left[\frac{f}{\tau_V c_v} v^2 + \frac{Nuc_d}{2\tau_T c_v} (T_d - \langle T_c \rangle) \right]$$

and the equation is now in the form to yield the air heating rate. The volume fraction of the particles is $\bar{\rho}_d/\rho_d = \alpha_d = 0.0004$ so $\alpha_c \simeq 1$. Substituting in the values for the variables gives

$$\begin{aligned} \frac{\Delta \langle T_c \rangle}{\Delta t} &= \frac{1.0 \text{ kg/m}^3}{1.2 \text{ kg/m}^3} \left[\frac{1.2}{0.31 \text{ s} \times 0.17 \text{ kcal/kg-}^\circ\text{C}} \left(1.5 \frac{\text{m}}{\text{s}} \right)^2 \right] \\ &\quad + \frac{1.0 \text{ kg/m}^3}{1.2 \text{ kg/m}^3} \left[\frac{4.4 \times 0.19 \text{ kcal/kg-}^\circ\text{C}}{2 \times 0.17 \text{ kcal/kg-}^\circ\text{C} \times 0.51 \text{ s}} (80^\circ\text{C}) \right] \\ &= 0.833 \times (0.0102 \text{ }^\circ\text{C/s} + 386 \text{ }^\circ\text{C/s}) = 322 \text{ }^\circ\text{C/s} \end{aligned}$$

Note that the contribution due to the mechanical energy conversion is negligible. This is usually the case unless the velocities are near sonic or greater.

The energy equation for the continuous phase is derived in Appendix C. Both the thermal and total energy equations are developed. Only the thermal energy equation will be addressed here. The thermal energy equation is

$$\begin{aligned} &\frac{\partial}{\partial t} (\alpha_c \rho_c \langle i_c \rangle) + \frac{\partial}{\partial x_i} (\alpha_c \rho_c \langle u_i i_c \rangle) \\ &= -\frac{1}{V} \sum_k \dot{m}_k i_{s,k} + \alpha_c \langle \Phi \rangle + \frac{\partial}{\partial x_i} \left(k'_{\text{eff}} \frac{\partial \langle T_c \rangle}{\partial x_i} \right) - \frac{1}{V} \sum_k \dot{Q}_k \end{aligned} \tag{6.112}$$

where $\langle i_c \rangle$ is the specific internal energy of the continuous phase, $\langle \Phi \rangle$ is the *thermal dissipation* and \dot{Q}_k is the heat transfer rate from the fluid to the particle. The coefficient of thermal conductivity, k'_{eff} , includes the heat transfer through the conveying fluid and the particle. The specific internal energy can be represented by $c_c T_c$ where T_c is the temperature of the carrier phase, and c_c is the specific heat of the continuous phase which, for an ideal gas, would be the specific heat at constant volume, c_v . The volume average of the product $\langle u_i T_c \rangle$ can be modeled as

$$\langle u_i T_c \rangle = \langle u_i \rangle \langle T_c \rangle + \langle \delta u_i \delta T_c \rangle \simeq \langle u_i \rangle \langle T_c \rangle - \rho_c c_c \frac{\nu_T}{\sigma_T} \frac{\partial \langle T_c \rangle}{\partial x_i} \tag{6.113}$$

where σ_T is the effective Prandtl number and ν_T is the turbulence kinematic viscosity⁷. Substituting $c_c \langle T_c \rangle$ for $\langle i_c \rangle$ in Equation 6.112, using Equation 6.113 for $\langle u_i T_c \rangle$ and dividing by c_c yields the equation for carrier-phase temperature,

$$\begin{aligned} & \frac{\partial}{\partial t} (\alpha_c \rho_c \langle T_c \rangle) + \frac{\partial}{\partial x_i} (\alpha_c \rho_c \langle u_i \rangle \langle T_c \rangle) \\ = & -\frac{1}{V} \sum_k \dot{m}_k T_{d,k} + \frac{\alpha_c}{c_c} \langle \Phi \rangle + \frac{\partial}{\partial x_i} \left[\left(\rho_c \alpha_c \frac{\nu_T}{\sigma_T} + \frac{k'_{\text{eff}}}{c_c} \right) \frac{\partial \langle T_c \rangle}{\partial x_i} \right] \\ & -\frac{1}{V} \sum_k \frac{\dot{Q}_k}{c_c} \end{aligned} \quad (6.114)$$

where $T_{d,k}$ is the temperature of particle k ⁸. The diffusion term now contains the heat transfer through the particles and through the turbulent fluid. The thermal conductivity of the mixture, k'_m , now becomes

$$\frac{k'_m}{c_c} = \rho_c \alpha_c \frac{\nu_T}{\sigma_T} + \frac{k'_{\text{eff}}}{c_c} \simeq \alpha_c \left(\rho_c \frac{\nu_T}{\sigma_T} + \frac{k'_c}{c_c} \right) + \alpha_d \frac{k'_d}{c_c} \quad (6.115)$$

where k'_c and k'_d are the thermal conductivity of the carrier phase and the particle phase materials, respectively. For a turbulent carrier phase, it is appropriate to take σ_T as unity.

The heat transfer from the carrier phase to particle k is

$$\dot{Q}_k / c_c = m \frac{c_d}{c_c} \frac{Nu_k}{2\tau_{T,k}} (\langle T_c \rangle - T_{d,k}) \quad (6.116)$$

where Nu_k is the Nusselt number and $\tau_{T,k}$ is the thermal response time of particle k . This equation is valid assuming the unsteady contributions to heat transfer are insignificant. These effects can be included if necessary. The thermal energy equation can be rewritten as

$$\begin{aligned} & \frac{\partial}{\partial t} (\alpha_c \rho_c \langle T_c \rangle) + \frac{\partial}{\partial x_i} (\alpha_c \rho_c \langle u_i \rangle \langle T_c \rangle) \\ = & -\frac{1}{V} \sum_k \dot{m}_k T_{d,k} + \frac{\alpha_c}{c_c} \langle \Phi \rangle + \frac{\partial}{\partial x_i} \left[\frac{k'_m}{c_c} \frac{\partial \langle T_c \rangle}{\partial x_i} \right] \\ & -\frac{1}{V} \sum_k m \frac{c_d}{c_c} \frac{Nu_k}{2\tau_{T,k}} (\langle T_c \rangle - T_{d,k}) \end{aligned} \quad (6.117)$$

If all the particles are the same size and have the same temperature, the thermal energy equation reduces to

⁷If the carrier phase is a gas, the specific heat should be the specific heat at constant pressure.

⁸This procedure assumes that the vapor that comes from the particle surface is the same gas mixture constituting the carrier phase. In general, this will not be the case.

$$\begin{aligned}
& \frac{\partial}{\partial t} (\alpha_c \rho_c \langle T_c \rangle) + \frac{\partial}{\partial x_i} (\alpha_c \rho_c \langle u_i \rangle \langle T_c \rangle) \\
&= s_{mass} T_d + \frac{\alpha_c}{c_c} \langle \Phi \rangle + \frac{\partial}{\partial x_i} \left[\frac{k'_m}{c_c} \frac{\partial \langle T_c \rangle}{\partial x_i} \right] - \alpha_d \rho_d \frac{c_d}{c_c} \frac{Nu}{2\tau_T} (\langle T_c \rangle - T_d)
\end{aligned} \tag{6.118}$$

The total energy equation derived in Appendix C can be written in terms of temperature in the same way as the thermal energy equation.

6.5 Equation summary

The continuity, momentum and energy equations developed in this section are summarized below.

$$\frac{\partial}{\partial t} (\alpha_c \rho_c) + \frac{\partial}{\partial x_i} (\alpha_c \rho_c \langle u_i \rangle) = -\frac{1}{V} \sum_k \dot{m}_k \tag{6.119a}$$

$$\begin{aligned}
& \frac{\partial}{\partial t} (\alpha_c \rho_c \langle u_i \rangle) + \frac{\partial}{\partial x_j} (\alpha_c \rho_c \langle u_i \rangle \langle u_j \rangle) \\
&= -\frac{\partial}{\partial x_j} (\alpha_c \rho_c R_{ij}) - \frac{\partial}{\partial x_i} \langle p \rangle + \frac{\partial}{\partial x_j} \langle \tau_{ij} \rangle + \alpha_c \rho_c g_i \\
&- \frac{1}{V} \sum_k v_{k,i} \dot{m}_k - \frac{1}{V} \sum_k F_{k,i}
\end{aligned} \tag{6.119b}$$

$$\begin{aligned}
& \frac{\partial}{\partial t} (\alpha_c \rho_c \langle T_c \rangle) + \frac{\partial}{\partial x_i} (\alpha_c \rho_c \langle u_i \rangle \langle T_c \rangle) \\
&= \frac{\alpha_c}{c_c} \langle \Phi \rangle + \frac{\partial}{\partial x_i} \left[\frac{k'_m}{c_c} \frac{\partial \langle T_c \rangle}{\partial x_i} \right] \\
&- \frac{1}{V} \sum_k \dot{m}_k T_{d,k} - \frac{1}{V} \sum_k m \frac{c_d}{c_c} \frac{Nu_k}{2\tau_{T,k}} (\langle T_c \rangle - T_{d,k})
\end{aligned} \tag{6.119c}$$

These equations can be simplified if the assumption is made that the all the particles have the same size, move with the same velocity and exchange mass at the same rate. Also the momentum equation, Equation 6.119b, can be written in a different form if the force due to undisturbed flow in the particle force equation is incorporated into the pressure and shear stress gradients.

The formulation for the volume-averaged Reynolds stress is discussed in Chapter 7.

6.6 Summary

The inability to model the local details of the continuous phase in a dispersed phase flow necessitates the use of averaging. The three general categories of

averaging are time, volume and ensemble. The conservation equations for a multiphase flow cannot be regarded as the single phase flow equations with coupling terms added to account for the particles. The mass, momentum and energy equations are derived for a quasi-one dimensional flow to illustrate the various features of the equations. The multidimensional equations resulting from formal volume-averaging procedures are also presented and discussed. A volume-averaged Reynolds stress based on velocity deviations in the averaging volume appears in the momentum equations. Also the heat transfer through the mixture involves the heat transfer through both the continuous and dispersed phases.

6.7 Exercises

6.1. A multiphase mixture consists of $20 \mu\text{m}$ particles with a particle volume fraction of 0.001. What would the size of the averaging volume have to be to ensure that the variation were less than 5% at the 99% confidence level?

6.2. Consider a flow of evaporating particles in a one-dimensional duct. The particles evaporate according to the D^2 -law and are always in kinetic equilibrium with the gas. The number flow rate \dot{n} of the particles is constant so

$$\dot{n} = n\tilde{v}A = n\langle u \rangle A = \text{const}$$

where n is the particle number density. The particle volume fraction is sufficiently small that the continuous phase volume fraction can be taken as unity, $\alpha_c \simeq 1$.

a) Find an expression for the mass source term in the form

$$S_m = -n\dot{m} = f(Z_0, \langle u \rangle_0 / \langle u \rangle, \rho_c, \tau_m, D/D_0)$$

where Z_0 , $\langle u \rangle_0$ and D_0 are the loading, velocity and particle diameter at the beginning station in the tube. The evaporation time constant is τ_m and ρ_c is the gas density. Make use of the conservation of particle number; namely, $n_0 \langle u \rangle_0 = n \langle u \rangle$.

b) Using the continuous phase continuity equation,

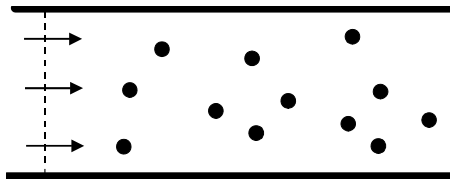
$$\frac{\Delta}{\Delta x}(\rho_c \langle u \rangle) = S_m$$

find how the velocity varies with time in the form

$$\frac{\langle u \rangle}{\langle u \rangle_0} = f(Z_0, t/\tau_m)$$

and find the velocity ratio when evaporation is complete. When you complete the expression for S_m you will find a velocity $\langle u \rangle$ in the denominator which when combined with the continuity equation allows you to express

$$\langle u \rangle \frac{\Delta}{\Delta x} (\rho_c \langle u \rangle) = \rho_c \frac{\Delta \langle u \rangle}{\Delta t}$$



Problem 6.2

6.3. Find an expression for the mass source term per unit volume for particles which evaporate according to the D²-law as a function of $\bar{\rho}_d, \tau_m, t$.

6.4. The volume-averaged continuity equation with no mass coupling and constant material density is

$$\frac{\partial}{\partial t} (\alpha_c) + \frac{\partial}{\partial x_i} (\alpha_c \langle u_i \rangle) = 0$$

The continuity equation for incompressible flow is

$$\frac{\partial u_i}{\partial x_i} = 0$$

Use Equation 20 in Appendix B to perform the volume averaging of this equation to arrive at the above equation. (Hint: Use the following integral over the boundary particles

$$\frac{1}{V} \int_{S_b} v_i n_i dS = -\frac{\partial}{\partial x_i} (\alpha_d \tilde{v}_i)$$

and then use Equation 6.46 together with $\alpha_d + \alpha_c = 1$).

6.5. The volume-averaged continuity equation for a constant density flow with mass coupling is

$$\frac{\partial}{\partial t} (\alpha_c \rho_c) + \frac{\partial}{\partial x_i} (\alpha_c \rho_c \langle u_i \rangle) = -\frac{1}{V} \sum_k \dot{m}_k = s_{\text{mass}}$$

Starting with the continuity equation for an incompressible fluid,

$$\frac{\partial u_i}{\partial x_i} = 0$$

and taking the volume average using Equation 20 in Appendix B, develop the volume-averaged continuity equation using the hint provided in Problem 6.4.

6.6. The rate of particle evaporation can be expressed in terms of the Sherwood number as (see Chapter 4)

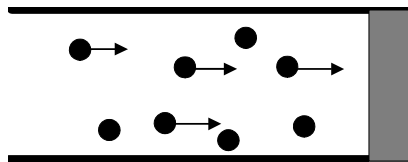
$$\dot{m} = Sh\pi\rho_c D_v D(\omega_\infty - \omega_s)$$

Assume that the Sherwood number, ω_s , is the same for all particles in a volume and that the particles have a Rosin-Rammler size distribution. Find the mass source term in the form

$$S_{mass} = NSh\pi\rho_c D_v (\omega_\infty - \omega_s) f(D_{mM}, \sigma)$$

6.7. Evaluate β_V defined in Equation 6.82 for a mixture of 100 μm coal particles in air at standard conditions ($\mu_c = 1.8 \times 10^{-5}$ Ns/m², $\rho_c = 1.2$ kg/m³). The particle volume fraction is 0.01, the material density of the coal is 1300 kg/m³ and the velocity difference is 1 m/s. Assume the coal particles can be treated as spherical. Use the Benyahia correlation (Equation 4.114) for the drag factor.

6.8. Two hundred-micron glass particles (sp. gr. = 2.5) are moving at 30 m/s through stagnant air at standard conditions and impinging on a plate as shown. The bulk density of the particles is 2 kg/m³. What is the pressure gradient in the gas?



Problem 6.8

6.9. The force coupling term in the momentum equation, Equation 6.74 is

$$-\frac{1}{V} \sum_k F_{k,i}$$

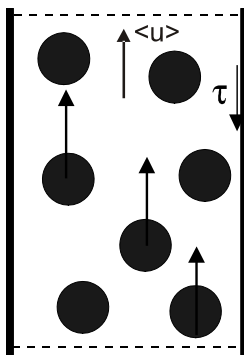
where $F_{k,i}$ is the hydrodynamic force acting on particle k . Some authors have expressed the equation of motion for a particle as

$$m_k \frac{dv_{k,i}}{dt} = 3\mu_c \pi D_k \left(\frac{C_D \text{Re}}{24} \right) (\langle u_i \rangle - v_i) + m_k g_i (1 - \frac{\rho_c}{\rho_d})$$

and then expressed the coupling term as

$$-\frac{1}{V} \sum_k F_{k,i} = \frac{1}{V} \sum_k \left[m_k \frac{dv_{k,i}}{dt} - m_k g_i (1 - \frac{\rho_c}{\rho_d}) \right]$$

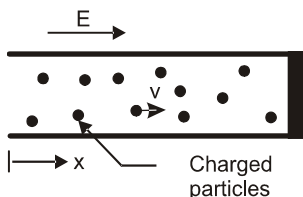
Is this a correct formulation for the coupling term? Justify your answer.



Problem 6.10

6.10. A fluid-particle flow is moving vertically in a tube as shown. The diameter of the tube is D_T . The flow is steady and uniform. The particles are not accelerating. Find how the pressure gradient in the tube varies with the mixture density, $\rho_m = \alpha_c \rho_c + \alpha_d \rho_d$, the shear stress τ and the tube diameter.

6.11. Charged particles are moving at constant speed in a horizontal tube of quiescent gas due to a Coulomb force. There is an electric field intensity, E , which produces a force $F = qE$ on the particle where q is the particle charge. Find the pressure gradient in the gas in terms of the particle bulk density, E , and the particle charge to mass ratio, q/m . Assume all particles are the same size and have the same charge to mass ratio.



Problem 6.11

6.12. There are many terms in the energy equation which, in general, can be neglected. One example is the kinetic energy compared to the enthalpy. The enthalpy of an ideal gas is $h_c = c_p T_c$ where c_p is the specific heat at constant temperature. Also $c_p T_c$ can be related to the speed of sound by $c_p T_c = c^2/(k - 1)$ where k is the ratio of specific heats. Express the ratio $U^2/2h_c$ in terms of Mach number and define those conditions under which the kinetic energy can be neglected compared to the enthalpy.

6.13. A technique to determine the relative magnitude of terms is to do a dimensional analysis. For example, if U_o , L , ρ_o , and T_o are a characteristic velocity, length scale, density and temperature of a flow, the convection term

of thermal energy can be written as

$$\frac{\partial}{\partial x_i} [\alpha_c \rho_c \langle u_i h_c \rangle] = \frac{\rho_o U_o c_p T_o}{L} \frac{\partial}{\partial \bar{x}_i} [\alpha_c \bar{\rho}_c \langle \bar{u}_i \bar{h}_c \rangle]$$

where the bar indicates a nondimensional value. Then one can say that the magnitude of the term is on the order of $\rho_o U_o c_p T_o / L$.

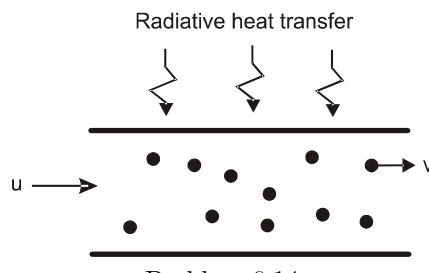
Perform the same nondimensionalization for the convective heat transfer term, $\partial(k_{\text{eff}} \partial T_c / \partial x_i) \partial x_i$ and find the ratio of this term to the convection term in terms of Reynolds number and Prandtl number.

6.14. The equation for thermal dissipation is

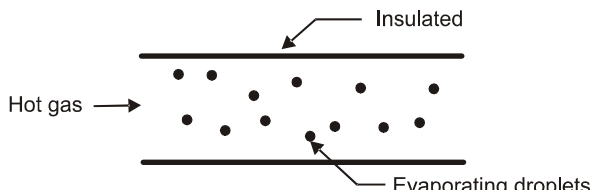
$$\Phi = \mu \left[\left(\frac{\partial u_i}{\partial x_j} \right) \left(\frac{\partial u_i}{\partial x_j} + \frac{\partial u_j}{\partial x_i} \right) \right] = \frac{\mu}{2} \left(\frac{\partial u_i}{\partial x_j} + \frac{\partial u_j}{\partial x_i} \right) \left(\frac{\partial u_i}{\partial x_j} + \frac{\partial u_j}{\partial x_i} \right) \quad (6.120)$$

Perform a dimensional analysis (as outlined in Problem 6.13) and compare magnitude with the thermal convection term, $\partial(\alpha_c \rho_c c_c \langle u_i \rangle \langle T_c \rangle) / \partial x_i$. Comment on your result.

6.15. Solid particles with no mass transfer, flowing in a constant area, horizontal channel, are being heated by an external source of radiant energy and simultaneously transfer this energy to the carrier gas such that the particle temperature remains constant. The flow is steady and the channel walls are insulated. The flow velocity is much less than sonic. The particle volume fraction is on the order of 0.01 and $Re >> 1$. The rate of heat absorption by radiation for particle k is $\dot{Q}_{R,k}$. Write out the energy equation, Equation 6.109 for this problem eliminating the terms that do not apply and neglecting those which may not be important.



6.16. A horizontal, constant area flow of hot air is convecting evaporating droplets. The channel is insulated and the flow is steady. The particle volume fraction is about 0.01 and the Reynolds number is much greater than unity. Write out the energy equation, Equation 6.109, for this application and eliminate the terms which don't apply and neglect those which may not be important.



Problem 6.15

6.17. The entropy equation for a fluid is

$$\frac{\partial}{\partial t}(\rho s) + \frac{\partial}{\partial x_i}(\rho u_i s) = -\frac{\partial}{\partial x_i} \left(\frac{\dot{q}_i}{T} \right) + \frac{\phi}{T} + \frac{k'_c}{T} \frac{\partial T}{\partial x_i} \frac{\partial T}{\partial x_i}$$

where ϕ is the dissipation. The dissipation and the last term are the entropy sources due to velocity and temperature gradients and are always positive. Using the relationships developed in Appendix B, show how you would carry out the volume averaging. Assume there is no mass coupling.

This page intentionally left blank

Chapter 7

Turbulence

Turbulence is inherently three-dimensional and consists of randomly varying motions in space and time. A formal definition of turbulence is given by Hinze (1975) as "...an irregular condition of flow in which the various quantities show a random variation with time and space coordinates, so that statistically distinct average values can be discerned." The Reynolds number has been traditionally used to characterize the transition from deterministic flow to stochastic or chaotic flow. The mechanisms that produce random variation have been the subject of much research and although science has come a long way in single phase turbulent flows, there is still much more to research in the area of multiphase and multicomponent turbulence. This chapter is intended to provide a short review of the general features of turbulence and single phase turbulence modeling. In addition, it will highlight current methods for modeling turbulence in dispersed phase flows.

7.1 Review of turbulence in single-phase flow

7.1.1 General features of turbulence

The quantities showing random variation in time and space can be decomposed into fluctuation (in a temporal sense) or deviation (in a spatial sense) quantities that occur about a mean (defined in Chapter 6). The velocity of a single-phase turbulence flow, shown in Figure 7.1, is simulated at a single point and over a duration of time. The chaotic nature is evident from the signal. This variation in time can be attributed to the non-linear effects of the Navier-Stokes equations, where rotations and irregular flow play a role in developing stochastic quantities.

Turbulence can be described by large-scale structures that generate turbulent energy which is then cascaded or transferred to small-scale structures where the energy is converted to heat. The transfer of energy from the large

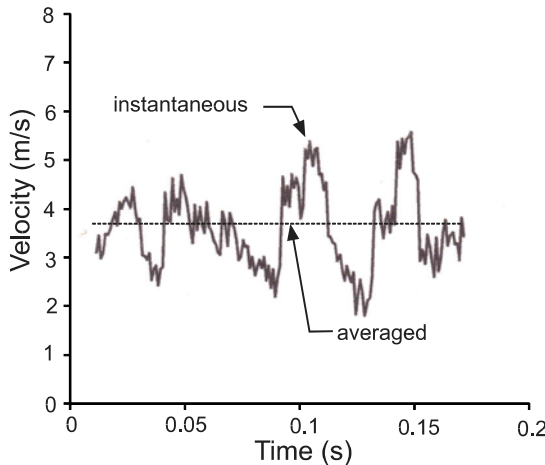


Figure 7.1: Variation of velocity over time at a point in space.

scales to the small scales is referred to as the *energy cascade*. This concept by which turbulence is viewed as a conglomeration of different sized eddies, through which energy is transferred, was introduced by Richardson (1922). The generation mechanisms are usually associated with gradients of the mean properties that occur at large scales in the flow, while the destruction mechanisms are associated with small scales and viscous properties of the flow.

Kolmogorov's hypotheses (Kolmogorov, 1941) are fundamental to understanding turbulence. His first hypothesis claims that the small scale turbulent quantities are statistically *isotropic* for high Reynolds number flows, meaning that they are independent of direction. In addition, small scale motions are universal, implying that such scales can be determined by the fluid viscosity and the flow dissipation. The smallest scales in a single phase turbulent flow are the *Kolmogorov scales*, defined as

$$\begin{aligned} \text{Length} &: \eta \equiv (\nu^3 / \varepsilon)^{1/4} \\ \text{Time} &: \tau_\eta \equiv (\nu / \varepsilon)^{1/2} \end{aligned}$$

The above mentioned theories are essential to the development of turbulence models or simulation packages. For instance, if the flow properties of the incompressible Navier-Stokes equations are decomposed and averaged, the advection term produces an apparent stress ($\overline{\rho u'_i u'_j}$)¹ due to averaging the coupled fluctuating velocities. The Reynolds stress has been historically defined as (Pope, 2000)

$$R_{ij} = \overline{\overline{u'_i u'_j}} \quad (7.1)$$

¹Henceforth, the double overbars will signify Reynolds (or temporal) averaging.

The resultant equations of a Reynolds decomposition are identified as the *Reynolds Averaged Navier-Stokes* (RANS) equations. When this approach is taken, additional transport equations for the turbulence quantities are needed to close the system of equations. This approach to modeling turbulence introduces additional terms such as pressure-strain, turbulence transport and dissipation terms which are difficult to compute. However, using the theories mentioned above, simple models can be developed to capture the essence of the basic physics in turbulent flows.

7.1.2 Modeling single-phase turbulence

In the area of turbulence research, *Direct Numerical Simulation* (DNS) is favored over turbulence modeling because the Navier-Stokes equations are used to directly solve for the instantaneous flow properties. The key to capturing the full spectrum of turbulence length scales is that the mesh must be sized to be smaller than the *Kolmogorov length scale* of the flow, which is the smallest length scale of the flow associated with the viscous dissipation. In addition, higher order discretization techniques are used to minimize numerical errors. Although DNS captures all the scales and statistics within a turbulent flow, it requires enormous computational power for high Reynolds number flows and is not practical for most engineering applications. Since DNS is limited to low Reynolds number flows, it is mainly used to discover new physics associated with turbulent flows and/or validate current hypotheses or models used to represent certain phenomena within turbulent flow.

Practical methods for modeling turbulence in engineering applications involve averaging techniques. While the averaged terms can be easily solved for, this avenue presents a second-moment term within the momentum equation referred to as the Reynolds stress. The objective of turbulence modeling is to accurately predict the Reynolds stress for a variety of flows. There are several methods of modeling this term; these include zero equation models², one-equation models, the two-equation model and a full closure model.

Most models assume that the Reynolds stress behaves as a shear stress. With this assumption, a simple model can be developed where the Reynolds stress is approximated as a turbulent viscosity multiplied by a mean rate of strain, referred to as the *Boussinesq approximation* or the *turbulent-viscosity hypothesis*. Using this approximation, a simple formulation for the diagonal and off-diagonal components of the incompressible Reynolds stress tensor is (Pope, 2000)

$$\overline{\overline{u'_i u'_j}} = \frac{2}{3} k \delta_{ij} - \nu_T \left(\frac{\partial \bar{u}_i}{\partial x_j} + \frac{\partial \bar{u}_j}{\partial x_i} \right) \quad (7.2)$$

where k is the turbulent kinetic energy and ν_T is the turbulence kinematic

²Zero equation models will not be discussed in this context; the reader is referred to Wilcox (2004) for information on zero equation models.

viscosity defined as

$$\nu_T = C_\mu \frac{k^2}{\varepsilon} \quad (7.3)$$

and C_μ is an empirical constant (0.09). An equation for k can be obtained by taking the dot product of the RANS equations with the fluctuating velocity and averaging the result, producing an equation for kinetic energy of the fluctuating velocity field. After numerous assumptions and insightful physical reasoning, an equation is developed which relates the rate of change in turbulence energy to terms representing the diffusion, generation and dissipation of turbulence energy. The *one equation model* involves solving a turbulent kinetic energy transport equation and assumes that the dissipation is proportional to some length scale in the flow such as

$$\varepsilon = C_l \frac{k^{3/2}}{l} \quad (7.4)$$

where C_l is a constant. For simple flows where l can be related to the grid or geometry, this type of modeling works well.

Traditionally, turbulence in a single-phase flow is characterized by the turbulence energy k and the dissipation ε . This is the popular and well-known *two-equation model*. Although an evolution equation for the dissipation of turbulent energy can be obtained by manipulating the Navier-Stokes equations (Bernard and Wallace, 2002), this equation is difficult to solve and a simple model is usually developed by scaling the turbulence energy equation (Pope, 2000). Once again the rate of change of dissipation is related to diffusion, generation and dissipation. There have been many modifications suggested to improve the $k - \varepsilon$ model but the essential features remain the same.

A *full closure model* refers to solving a transport equation for the Reynolds stress and dissipation. A Reynolds stress transport equation can be obtained from the following expression: $\overline{\overline{u_i N S_j + u_j N S_i}} - (\overline{\overline{u_i}} \overline{\overline{N S_j}} + \overline{\overline{u_j}} \overline{\overline{N S_i}})$. The main differences between adopting the above modeling approaches and this approach are related to complexity and stability. Over the last two decades, the Reynolds stress model has shown to better predict complex flows than the two-equation model (Pope, 2000).

Large Eddy Simulation (LES) has become a suitable alternative to modeling turbulence in engineering applications. LES is a hybrid between DNS and Reynolds averaging. The large scales of motion are solved for directly, while the small scale effects are modeled. A filter separates the scales. In the recent years, more attention has been devoted to improving the sub-grid turbulence models. Overall, LES is considered an improvement over the $k - \varepsilon$ model and is used to solve many engineering problems.

7.2 Turbulence modulation by particles

Turbulence modulation is the effect of inertial particles or droplets on the turbulence of the carrier phase relative to the single phase. The presence of the

disperse phase can either augment or attenuate turbulence relative to single phase turbulence. Prior to the 1970s, some practitioners were already aware of the fact that the presence of particles can significantly change the rates of heat transfer and chemical reaction, which could not be explained except through the effect of the particles on the fluid turbulence. Turbulence modulation can have a significant impact on industrial flows, energy conversion, efficiency, etc., and while the study of particle dispersion in turbulent flows has a long history, research on the physics of how particles affect the fluid turbulence has gained some traction over the last few decades.

The primary obstacle in obtaining fluid turbulence data in particulate flows has been the difficulty in making fluid property measurements in the presence of solid particles. It was not until the 1970s that direct measurements of turbulence in the presence of particles were possible with *laser Doppler velocimetry* (LDV). Before the invention of LDV, hot-wire or hot-film anemometry were the only means to acquire a direct measurement of fluid turbulence. Hot-wire probes cannot be used in flows with solid particles but a conical probe coated with a hot-film is durable, to some degree, in solid-liquid flows. For this reason, the early data on fluid turbulence in the presence of solid particles were obtained in liquid-solid flows in connection with sediment transport. Some researchers (Hetsroni & Sokolov, 1971) attempted to use a hot-wire probe in gas-droplet free jets in the study of a two-fluid atomizer and obtained results showing that particles (liquid droplets) suppress the turbulence intensity of gas.

The invention of LDV has had a large impact on turbulence research in multi-phase flows. Because of the availability of LDV systems, the number of studies on fluid turbulence in fluid-solid flows increased dramatically. Various configurations of particle-laden flows including pipe flows, channel flows, free jets, confined jets, impinging jets and boundary layers have been investigated using LDV. The radial distributions of turbulence intensities based on centerline velocities in a gas-solid flow in a vertical pipe (Tsuji et al., 1984) are shown in Figure 7.2. The turbulence profiles with no turbulence are designated by the $Z = 0$ lines (where Z is the loading). From this data, it is evident that both attenuation and augmentation of turbulence occur, depending on particle size and loading. Additional data in pipe flows are provided by Sheen et al. (1993); Sato and Hishida (1996), Hosokawa et al. (1998); Savolainen and Karvinen (1998) and Varaksin et al. (1998). The data of Sheen et al. (1993), shown in Figure 7.3, illustrates the anisotropy within a pipe flow. Relative to the unladen case, small particles are shown to decrease R_{11} and R_{22} ³. However, larger particles show an increase in R_{11} near the centerline and decrease it near the wall, yet R_{22} is shown to decrease across the pipe radius. The R_{12} component is shown to attenuate turbulence across the pipe radius, with the most attenuation being associated with the smaller particle diameter. At the centerline of the flow, the particles do not affect the R_{12} component.

³In the context of describing the data of Sheen et al. (1993), the Reynolds stress subscripts 1 and 2 refer to the axial and radial directions, respectively.

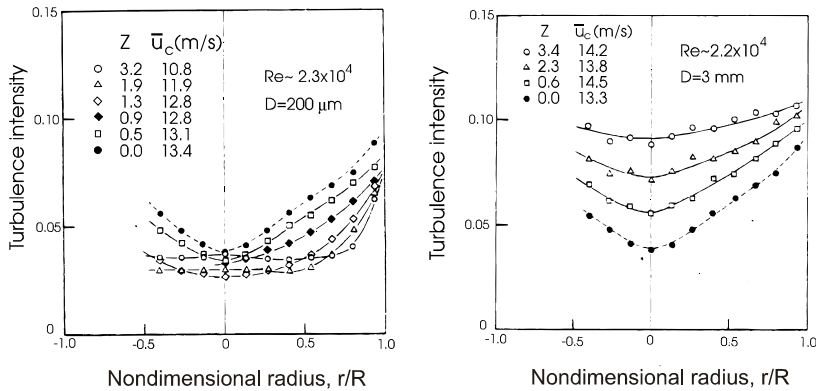


Figure 7.2: Radial variation of turbulence intensity for gas-particle flow in a vertical pipe with different particle sizes. (Reprinted from the *J. Fluid Mech.*, **139**, Tsuji, Y., Morikawa, Y. and Shiomi, H., LDV measurements of an air-solid two-phase flow in a vertical pipe, 417, 1984, with kind permission from Cambridge University Press.)

Varaksin et al. (1998) showed a reduction in R_{11} and R_{22} relative to single phase near the centerline of turbulent pipe flow for increased loading with small particles ($50 - 100 \mu\text{m}$). Kulick et al. (1993, 1994) and Paris and Eaton (2001) both measured attenuation of turbulence energy for small particles ($50 - 150 \mu\text{m}$) with increased loading in vertical channel flows. In horizontal channel flows, Kussin and Sommerfeld (2002) showed augmentation for large particles ($625 - 1000 \mu\text{m}$) with increased loading and attenuation for small particles ($60 - 190 \mu\text{m}$) with increased loading.

In order to isolate the effect of turbulence generated by particles from turbulence generated by velocity gradients, Mizukami et al. (1992) and Parthasarathy and Faeth (1990) performed experiments with particles falling in a bath of initially quiescent fluid. They were able to measure turbulent energy within the fluid that was generated by the particles.

Two papers (Gore & Crowe, 1989; Hetsroni, 1989) summarize the available data on turbulence modulation (until 1989). These papers suggest criteria for the suppression and enhancement of turbulence. One criterion is based on the length scale ratio D/L_e , where D is the particle diameter and L_e is the length scale characteristic of the most energetic turbulent eddies. A summary of the data until 1989 is shown in Figure 7.4. It is qualitatively observed that turbulence intensity is attenuated for D/L_e less than ~ 0.1 while the turbulence level is increased for larger length scale ratios. The effects of particles on fluid turbulence are thought to be similar to those of a grid or screen in a turbulent flow; that is, turbulence is generated or attenuated depending on the size of grid and turbulence intensity. Another criterion (Hetsroni, 1989) is based on the relative particle Reynolds number. This

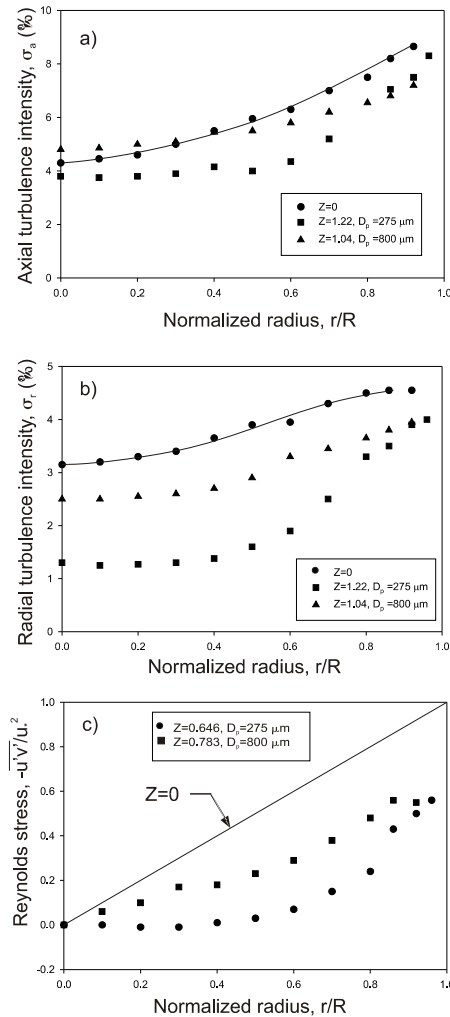


Figure 7.3: Data for longitudinal and radial turbulence intensities and Reynolds stress (abstracted from data in Sheen et al., 1993).

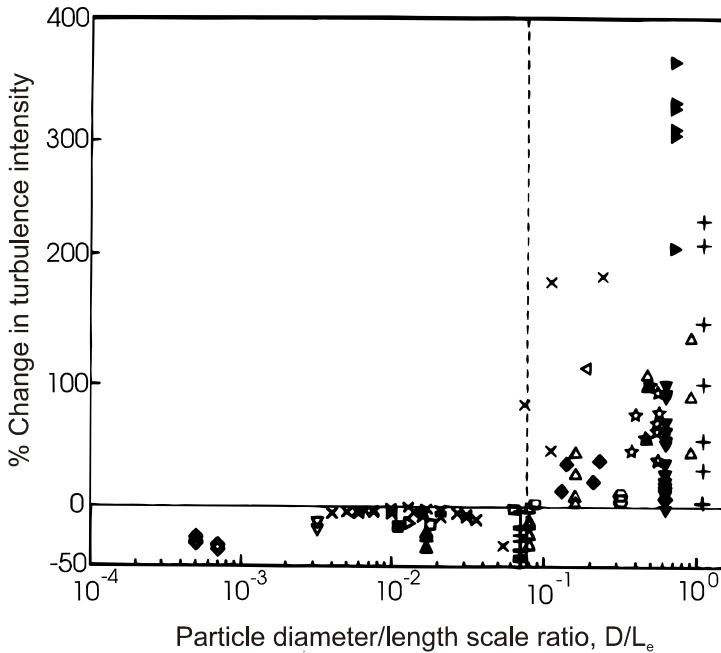


Figure 7.4: A summary of the data for the change in turbulent intensity due to the presence of the dispersed phase. (Reprinted from *Intl. J. Multiphase Flow*, 15, Gore, R.A and Crowe, C.T., The effect of particle size on the modulating turbulence intensity, 280, 1989, with kind permission from Elsevier.)

work suggests that particles with a low Reynolds number tend to suppress the fluid turbulence and particles with high particle Reynolds number tend to increase turbulence.

Since the work of Gore and Crowe (1989) and Hetsroni (1989), additional experimental studies of particles in fully developed channel flows were published by Kulick et al. (1994), Paris and Eaton (2001), and Kussin and Sommerfeld (2002). The experiments of Kulick et al. (1994) and Paris and Eaton (2001) suggested that mass loading ratio also contributes to turbulence attenuation at low particle Reynolds number. The data of Kussin and Sommerfeld (2002) showed that augmentation occurred at the center of the channel when the particle Reynolds number was high, a phenomenon also observed by Tsuji et al. (1984) and Sheen et al. (1993) and also suggested by Hetsroni (1989). Varaksin et al. (1998) showed attenuation in turbulence kinetic energy (TKE) in pipe flow for a low particle Reynolds number and varying concentration. The work of Ferrante and Elghobashi (2003) showed a decrease in TKE with certain particle properties, but they also showed an increase in TKE and no change in TKE all relative to the unladen flow. The particles that produced

no net change in TKE relative to an unladen flow were referred to as *ghost particles*. One of the parameters used by Ferrante and Elghobashi to distinguish between these regimes is the ratio of the particle response time to the Kolmogorov time scale (τ_p/τ_K). Yamamoto et al. (2001) modeled the particle-particle and particle-wall interactions for the experiment of Kulick et al. (1993). They showed that these interactions were a key player in attenuating turbulence.

From the above studies, five key factors arise that appear contribute to turbulence modulation due to particles:

- Surface effects: particle size normalized by a length scale
- Loading effects: particle concentration or mass loading, which includes fluid displacement
- Inertial effects: particle Reynolds number
- Response effects: particle response time, or Stokes number
- Interaction effects: particle-particle, particle-wall

The above mentioned observations are in agreement with Crowe's (1993) summary on ways that the presence of particles can affect the carrier phase turbulence. Balachandar and Eaton (2010) also note that turbulence modulation in dilute flows may be caused by (1) particles enhancing the dissipation, (2) particles transferring kinetic energy to the fluid, and (3) formation of particle wakes. Although some qualitative trends have been observed for the effects of particles on the turbulence energy of the carrier phase, there is currently no general model that can be used reliably to predict carrier phase turbulence in particle-laden flows.

7.3 Review of modulation models

In a short review of the modeling status on particle laden turbulence, Eaton (2006) states that many models have been developed to understand turbulence modulation associated with dilute particle laden flows, yet there still remains a need for a general model that can account for factors such as particle size, relative Reynolds number, volume fraction, number density, mass density, surface roughness, etc. The mechanisms responsible for turbulence modulation, or the effect of particles on carrier phase turbulence, are not well understood. As shown in the experimental data, when particles are introduced, the statistics of the continuous phase turbulence are altered. Depending on particle characteristics, the level of turbulent kinetic energy and dissipation changes relative to the corresponding unladen flow. Because of these complex fluid-particle interactions, no general model exists and numerical models for turbulence modulation are still in development. In this section, a general overview of the modeling progress is presented.

7.3.1 Empirical Models

There are several empirical models in the literature. Although the research trend in the last decade has focused on the development of two equation models, full closure models, LES, and DNS, for completeness, a few empirical models are presented and discussed.

Yuan and Michaelides (1992) developed an equation to represent the total turbulence modification by particles. It can be expressed in the form

$$\Delta k = -\frac{\pi}{12} D^3 \rho_a (u - v)^2 \left[1 - \exp \left(-2f \frac{\tau}{\tau_V} \right) \right] + \frac{\pi}{12} D^2 \rho_c f (l_w) (u^2 - v^2) \quad (7.5)$$

where f is the drag coefficient and $f(l_w)$ is a measure of the region (length scale) behind the particle where the particle and fluid velocity are similar. For the simple case of large particles falling into a bath of stationary fluid, where $\tau \ll \tau_V$ and $v \gg u$, the above equation would show a decrease in turbulent energy relative to the single phase turbulent energy. The last term seems to suggest that the modulation depends on the direction and magnitude of the particle velocity relative to the fluid velocity, which is not a physically reasonable outcome. However, their model does show good agreement with the data of Tsuji et al. (1984).

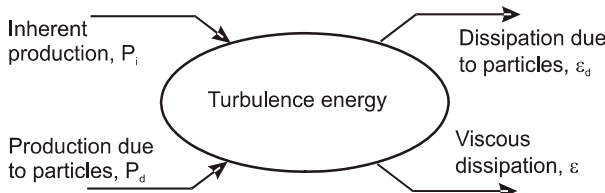


Figure 7.5: Schematic model for turbulence modulation. (Reprinted from the *Intl. J. Multiphase Flow*, **23**, Kenning, V.M. and Crowe, C.T., Effect of particles on the carrier phase turbulence in gas-particle flows, 406, 1997, with kind permission from Elsevier.)

Another simple model has been proposed by Kenning and Crowe (1997). The model they proposed is illustrated in Figure 7.5. The dissipation of energy due to the fluid can be modeled as

$$\epsilon = \frac{k^{3/2}}{l_\epsilon} \quad (7.6)$$

where l_ϵ is the dissipation length scale. However, in a dispersed phase flow, several new length scales are introduced: the particle size and the interparticle spacing. If the interparticle spacing is less than the intrinsic length scale for the flow, then the interparticle spacing should influence the dissipation. Kenning and Crowe defined a “hybrid” length scale, l_h , which approached the

correct limits and used this for the dissipation length scale. They showed that the change in turbulence intensity for particles transported by air in a vertical duct should vary as,

$$\frac{\sigma - \sigma_o}{\sigma_o} = P = \left[\frac{l_h}{l_\varepsilon^{sp}} + \frac{l_h}{(k^{sp})^{3/2}} \frac{f}{\tau_V} \frac{\bar{\rho}_d}{\bar{\rho}_c} (u - v)^2 \right]^{1/3} - 1 \quad (7.7)$$

where l_ε^{sp} and k^{sp} are the dissipation length scale and turbulence energy in the flow without particles⁴. As shown in Figure 7.6 the predictions with this model compare reasonably well with the data of Levy and Lockwood (1981), Tsuji et al. (1984), and Lee and Durst (1982). Still, the model is not particularly useful because the dissipation length scale is not generally available.

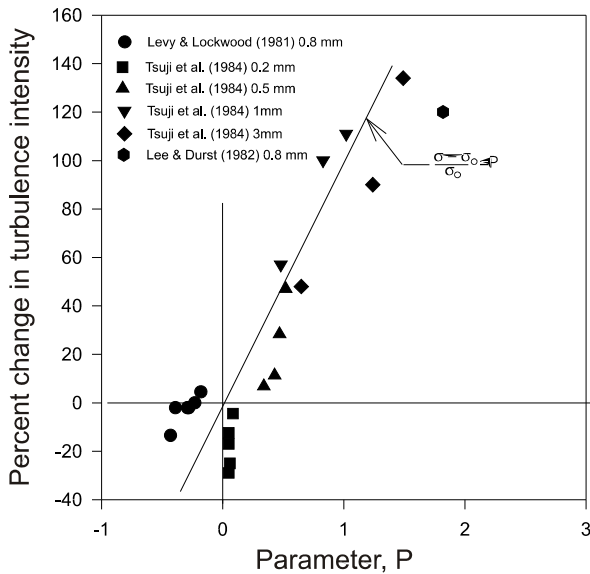


Figure 7.6: Comparison of Kenning and Crowe model for turbulence modulation with experimental data. (Reprinted from the *Intl. J. Multiphase Flow*, **23**, Kenning, V.M. and Crowe, C.T., Effect of particles on the carrier phase turbulence in gas-particle flows, 407, 1997, with kind permission from Elsevier.)

7.3.2 Turbulence models with dusty-gas equations

There are several turbulent energy and dissipation equations for multi-phase flows presented in literature. Most of them are based on Reynolds (temporal)

⁴sp refers to single phase.

averaging and stem from the work of Chen and Wood (1985) who started with the *dusty-gas* momentum equation, originally developed by Marble (1963)⁵, namely

$$\rho_c \frac{Du_i}{Dt} = -\frac{\partial p}{\partial x_i} + \frac{\partial \tau_{ij}}{\partial x_j} + \rho g_i + f_i \quad (7.8)$$

where f_i is the force due to the particles. This idea stems from the *two-fluid* modeling approach in which the two phases are treated as separate interpenetrating continua. The $k - \varepsilon$ equations for the continuous phase are then developed for dilute flows ($\alpha_c \approx 1$). The turbulence energy model presented by Chen and Wood is

$$\begin{aligned} \frac{Dk}{Dt} = & -\overline{u'_i u'_j} \frac{\partial \bar{u}_i}{\partial x_j} - \frac{k}{3} \frac{\partial \bar{u}_i}{\partial x_i} \\ & + \frac{\partial}{\partial x_i} \left(\frac{\nu_t}{\sigma_k} \frac{\partial k}{\partial x_i} \right) - \varepsilon \\ & + \frac{\bar{\rho}_d}{\rho_c \tau_V} \left(\overline{u'_i v'_i} - \overline{u'_i u'_i} \right) \\ & + \frac{1}{\rho_c \tau_V} \left(\overline{\bar{\rho}'_d u'_i v'_i} - \overline{\bar{\rho}'_d u'_i u'_i} + (\bar{v}_i - \bar{u}_i) \overline{\bar{\rho}'_d u'_i} \right) \end{aligned} \quad (7.9)$$

where $\bar{\rho}_d$ is the bulk particle density, τ_V is the particle response time and v_i is particle velocity. Using the same method, Chen and Wood also derived an equation for turbulence dissipation in the form

$$\begin{aligned} \frac{D\varepsilon}{Dt} = & -C_{\varepsilon 1} \overline{u'_i u'_j} \frac{\partial \bar{u}_i}{\partial x_j} \frac{\varepsilon}{k} - C_{\varepsilon 2} \frac{\varepsilon^2}{k} \\ & - C_{\varepsilon 3} \frac{\varepsilon}{3} \frac{\partial \bar{u}_i}{\partial x_i} + \frac{\partial}{\partial x_i} \left(\frac{\nu_t}{\sigma_\varepsilon} \frac{\partial \varepsilon}{\partial x_i} \right) \\ & + \frac{2\bar{\rho}_d}{\rho_c \tau_V} \left(\nu_c \overline{\frac{\partial u'_i}{\partial x_j} \left(\frac{\partial v'_i}{\partial x_j} - \frac{\partial u'_i}{\partial x_j} \right)} \right) \end{aligned} \quad (7.10)$$

Reynolds averaging was also applied to dispersed phase flows by Zhou and Chen (2001) to obtain a Reynolds stress model. The modeled form of the Reynolds stress equation for the carrier phase is

$$\frac{\partial \rho_c R_{ij}}{\partial t} + \frac{\partial}{\partial x_k} (\rho_c \bar{u}_k R_{ij}) = P_{ij} + \Pi_{ij} + D_{ij} - \varepsilon_{ij} + G_{ij}^p \quad (7.11)$$

where P_{ij} are the unmodeled production terms, Π_{ij} , D_{ij} , and ε_{ij} are the traditional modeled forms of the pressure-strain, transport and dissipation tensors. The tensor G_{ij}^p is the effect of the particles, shown as

$$G_{ij}^p = \sum_k \left(\frac{\rho_p}{\tau_V} \right)_k \left(\overline{(v'_i)_k u'_j} + \overline{u'_i (v'_j)_k} - 2 \overline{u'_i u'_j} \right) \quad (7.12)$$

⁵See Chapter 6 for an in-depth discussion on Marble's approach.

where k is the particle number. They also formulated a transport equation for the dissipation

$$\begin{aligned} & \frac{\partial \rho_c \varepsilon}{\partial t} + \frac{\partial}{\partial x_k} \rho_c \bar{u}_k \varepsilon \\ = & C_{\varepsilon 1} \frac{\varepsilon}{k} \left(\rho_c R_{ik} \frac{\partial \bar{u}_i}{\partial x_k} + \sum_k \left(\frac{\rho_d}{\tau_V} \right)_k \left(\overline{(v'_i)_k u'_i} - \overline{u'_i u'_i} \right) \right) \\ & + C_\varepsilon \frac{\partial}{\partial x_k} \left(\rho_c \frac{k}{\varepsilon} R_{kl} \frac{\partial \varepsilon}{\partial x_l} \right) - C_{\varepsilon 2} \rho_c \frac{\varepsilon^2}{k} \end{aligned} \quad (7.13)$$

The above models have been applied to several types of flows and appear to predict the data reasonably well. However, Zhang and Reese (2001) showed that Reynolds averaged $k-\varepsilon$ models cannot properly predict the effect of mass loading on turbulence intensity. In addition, Crowe and Gillilandt (1998) argue that this type of averaging does not properly account for the coupling of the drag force because the drag force per unit volume cannot be regarded as a “point value.” Or, in other words, it cannot be evaluated at an arbitrary point in the flow. This issue is discussed in more detail below.

7.3.3 Point particle models

In the recent decade, direct numerical solution (DNS) has been used to study the effects of particles on the modulation of the turbulence within the carrier phase; a review on this topic is presented by Balachandar and Eaton (2010). This approach is advantageous because it requires no Reynolds stress modeling. The downside is that the effects of particles are traditionally treated as point forces that do not displace any fluid volume. Liljegren (1996) has questioned the adequacy of modeling the effect of the particles as point forces in that the no slip condition at the particle surfaces is not correctly accounted for. Additional information on DNS point particle simulations are discussed in Chapter 9.

7.3.4 Models based on volume averaging

Crowe and Gillilandt (1998) derived a transport equation for the volume averaged turbulent kinetic energy. They found additional terms which represent production and redistribution mechanisms that were due to the effect of particle surfaces; however, they did not apply it to any experimental data. After the work of Crowe and Gillilandt, a few researchers adopted these additional modulation terms and proposed dissipation equations with a similar effect. Lain et al. (1999) proposed that an additional term be included in the dissipation transport equation to represent the effects of particles. This term is merely the modulation terms proposed by Crowe and Gillilandt multiplied by the inverse turbulence time scale and a constant.

Zhang and Reese (2001) applied Crowe and Gilliland's turbulent kinetic energy model to the pipe flow data of Tsuji et al. (1984) and compared it with the model of Chen and Wood (1985). They concluded that the volume averaged model of Crowe and Gilliland was an overall improvement over the Reynolds averaged model of Chen and Wood. Similar to Lain et al. (1999), Zhang and Reese (2003) used the additional terms proposed by Crowe and Gilliland to form a modulation term within the dissipation equation of the form

$$\alpha_c \rho_c \frac{D\epsilon}{Dt} = P_\epsilon + D_\epsilon - C_{\epsilon 2} \alpha_c \rho_c \frac{\epsilon^2}{k} + C_{\epsilon 3} \frac{\epsilon}{k} \Delta k \quad (7.14)$$

where Δk represents the production and redistribution terms proposed by Crowe and Gilliland. They applied the model to experimental data of Maeda et al. (1980), Lee and Durst (1982) and Tsuji et al. (1984). Overall, they showed that the model reasonably matches the experimental data.

7.4 Basic test case for turbulence models

For all turbulence models, it is good practice to identify flow configurations that are simple and in essence minimize some of the contributing mechanisms. For instance, near the wall in steady, fully developed turbulent pipe flow, the diffusion of turbulent energy can be neglected, and therefore production mechanisms must balance with destruction mechanisms. Likewise in homogeneous turbulent decay flows, production and diffusion are neglected and the time rate of change of turbulent energy is balanced by dissipation. These simple flow conditions allow the model developer to test new models and determine if the model demonstrates the correct trends.

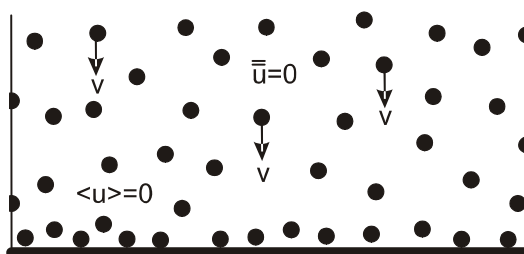


Figure 7.7: Basic test case for evaluation of turbulence models.

A simple, ideal flow configuration to evaluate turbulence modulation by particles is particles falling at constant speed through a quiescent (mean velocity everywhere zero) fluid with no walls, as shown in Figure 7.7. The distribution of particle mass flux is uniform. As the particles accumulate on the bottom plate, the plate is moved downward to maintain a zero average velocity in the flow. In this case there would be no convection of turbulence, no

turbulence generation by averaged-velocity gradients and no diffusion within the carrier-phase. After an initial transient period, the turbulence kinetic energy would become steady and uniform and the turbulence generation would equal the dissipation. There would be a pressure gradient in the vertical direction to balance the weight of the fluid and the drag force due to the falling particles (see Problems 6.2 and 6.3). Of course it is not possible to design an experiment in which the particles fall at constant speed in an unbounded field but this ideal basic case is a configuration to assess the validity of a turbulence model. Experiments to measure turbulence generated by particles dropping in an initially quiescent bath of fluid in a vertical duct have been reported by Parthasarathy and Faeth (1990) and Mizukami et al. (1992).

Example: Apply Chen and Wood's equations (Equations 7.9 and 7.10) to the basic test case to assess their validity.

Solution: For the basic test case

$$\bar{v} = \text{constant}, \quad v' = 0, \quad \bar{u} = 0$$

Since the particle phase is assumed to behave as a continuous medium, the continuity equation for particle mass is

$$\frac{\partial}{\partial t}(\alpha_d \rho_d) + \frac{\partial}{\partial x_i}(\alpha_d \rho_d v_i) = 0$$

For steady flow and constant material density, the above equation reduces to

$$\frac{\partial}{\partial x_i}(\alpha_d v_i) = v \frac{\partial \alpha_d}{\partial z} = 0$$

showing $\alpha_d = \text{constant}$ and therefore $\bar{\rho}'_d = \alpha'_d \rho_d = 0$. Also since the kinetic energy distribution is uniform, $\partial k / \partial x_i = 0$. Applying these conditions to Equation 7.9 gives

$$\varepsilon = -\frac{\bar{\rho}_d}{\rho_c t_V} \overline{\overline{u'_i u'_i}}$$

In the above equation, the bulk particle density $\bar{\rho}_d$, the continuous phase density ρ_c , the particle response time t_V , and the turbulence energy $\overline{\overline{u'_i u'_i}} = 2k$ are all positive so this condition cannot be satisfied.

Applying the basic test to Chen and Wood's dissipation equation, Equation 7.10, shows

$$C_{\varepsilon 2} \frac{\varepsilon^2}{k} = -\frac{2\bar{\rho}_d}{\rho_c t_V} \left(\nu_c \frac{\overline{\overline{\partial u'_i / \partial x_j \partial u'_i}}}{\partial x_j} \right)$$

However

$$\frac{\overline{\overline{\partial u'_i / \partial x_j \partial u'_i}}}{\partial x_j} > 0$$

and $C_{\varepsilon 2} > 0$, so this equation also cannot be satisfied. These results indicate there is a problem with the model.

In the above example, a question arises as to why does the approach by Chen and Wood (1985) fail? The answer to this question lies in the equation they used to develop the turbulence model. The dusty gas momentum equation, 7.8, implies that the drag force due to particles is continuous and can be applied to any arbitrary point within the flow field. As shown in Chapter 6, even though the volume needed to ensure that the variation of the number of particles in the averaging volume is sufficiently small, it is many orders of magnitude larger than the volume needed to define point (or measured) values of the conveying fluid. In other words, the value of the instantaneous carrier phase velocity can vary significantly over the volume needed to define the particle force per unit volume. Thus the velocity in the dusty gas equation should not be the value at a point in the fluid, but rather an average over the volume needed to define the properties for the particulate phase. The velocity in the dusty gas equation should be replaced by the volume average velocity, $u_i \rightarrow \langle u_i \rangle$. The fallacy lies in the fact that the fluctuation of the velocity, u'_i in the dusty gas equations is actually the fluctuation of the volume averaged velocity, $\langle u_i \rangle'$ which is not the local velocity fluctuation (as shown in Chapter 6). For this reason, the results obtained by using the dusty gas equation for turbulence analyses lead to non-physical outcomes.

7.5 Volume-averaged turbulence models

Modeling turbulence in particle laden flows is a non-trivial task. The ideal approach to capturing the effects of the particles is to treat the particles as moving boundaries within fluid. This approach is applicable to flows with very few particles, where the particles are large compared to the dissipation length scale, thus providing enough cells for a proper discretization around the particle. In contrast, a large number of particles, or very small particles would require enormous computational power to track each particle and their effects on the continuous phase turbulence. This may be impractical for industrial applications and an interim solution is to use a set of volume-averaged turbulence equations to compliment the volume-averaged momentum and energy equations introduced in Chapter 6. The development of these equations is based on the following assumptions:

1. The continuous phase density is constant.
2. No mass transfer across the particle surface.
3. Particles are spherical and non-rotating.

The purpose of these assumptions is to simplify the analysis. All these assumptions could be relaxed and the derivation would be carried out in a similar fashion but the inclusion of more details would be required.

7.5.1 Defining volume-averaged turbulence

In a single phase flow regime, the instantaneous momentum equation can be decomposed into temporal averaged and fluctuating terms. The fluctuating components or statistics in the flow are used to characterize the turbulence. This tactic introduces an additional term in the momentum equation known as the apparent stress, and turbulence models are developed to predict the trends and magnitudes associated with the averages of coupled fluctuating components.

When using volume-averaged methods, a similar practice can be used. At a single instance in time, each point in the continuous phase, a fluid or flow property can be decomposed into a volume-averaged and deviation term, such as

$$u_i = \langle u_i \rangle + \delta u_i \quad (7.15)$$

This idea is depicted in Figure 7.8. The deviation terms, when volume averaged, form quantities that are related to the continuous phase turbulence of dispersed phase flows.

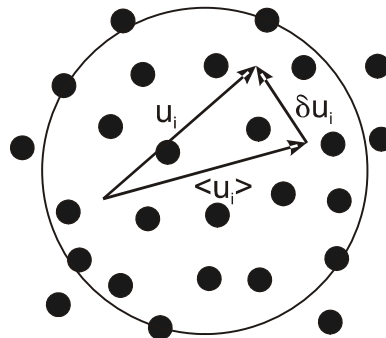


Figure 7.8: Relationship between local, volume-averaged and deviation velocities at a point in conveying fluid and at an instance in time.

For incompressible flows⁶, the continuous phase volume-averaged turbulence energy and dissipation were defined by Crowe and Gillilandt (1998) as

$$k_c = \frac{1}{V_c} \int_{V_c} \frac{\delta u_i \delta u_i}{2} dV = \left\langle \frac{\delta u_i \delta u_i}{2} \right\rangle \quad (7.16)$$

$$\varepsilon_c = \frac{1}{V_c} \int_{V_c} \nu_c \frac{\partial \delta u_i}{\partial x_j} \frac{\partial \delta u_i}{\partial x_j} dV = \left\langle \nu_c \frac{\partial \delta u_i}{\partial x_j} \frac{\partial \delta u_i}{\partial x_j} \right\rangle \quad (7.17)$$

The definition of the incompressible, continuous phase volume-averaged Reynolds

⁶Compressible flow requires a different definition.

stress⁷ follows the pattern set by Crowe and Gillilandt (1998)

$$R_{ij} = \frac{1}{V_c} \int_{V_c} \delta u_i \delta u_j dV = \langle \delta u_i \delta u_j \rangle \quad (7.18)$$

The Reynolds stress can be solved for directly by using a Reynolds stress model, or it can be estimated using the *Boussinesq approximation*.

7.5.2 Turbulence kinetic energy equation

The volume-averaged turbulent kinetic energy transport equation is derived following the same procedure outlined for single phase flows. The procedure begins by dotting the fluid velocity with the Navier-Stokes equations to form the mechanical energy equation. The flow properties are then decomposed into phase average and deviation components. The resultant equation is volume averaged using the relationships developed in Appendix B. The mean kinetic energy is then subtracted leaving a transport equation for the turbulent kinetic energy (see Appendix D). For the case where the steady-state drag is the only significant force acting on the particles, the resulting equation is

$$\begin{aligned} & \frac{\partial}{\partial t} (\alpha_c \rho_c k_c) + \frac{\partial}{\partial x_j} (\rho_c \alpha_c \langle u_j \rangle k_c) \\ = & \frac{\partial}{\partial x_j} \left(\alpha_c \rho_c \xi_k \frac{\partial k_c}{\partial x_j} \right) && \text{diffusion of turbulence} \\ & - \rho_c \alpha_c R_{ij} \frac{\partial \langle u_i \rangle}{\partial x_j} && \text{generation by gradients} \\ & + n 3 \pi \mu_c D f |\langle u_i \rangle - \hat{v}_i|^2 && \text{generation by particle drag} \\ & + n 3 \pi \mu_c D f \left(\widehat{\delta v_i \delta v_i} - \widehat{\delta u_i \delta v_i} \right) && \text{redistribution} \\ & - \alpha_c \rho_c \varepsilon_c && \text{dissipation} \end{aligned} \quad (7.19)$$

where R_{ij} is the Reynolds stress, ξ_k is the diffusion coefficient which is related to the turbulence viscosity by ν_T / σ_k , where σ_k is an empirical constant usually taken as unity. The terms in the redistribution contribution are defined as

$$\widehat{\delta v_i \delta v_i} = \frac{1}{N} \sum_k (\delta v_i \delta v_i)_k \quad (7.20)$$

where the summation is carried out over every particle location, k , in the averaging volume.

There are two generation terms, one of which is the standard single phase production term and the other is the production due to the presence of particles. The production term due to particles is always positive. In wall flows

⁷The volume-averaged apparent stress should be referred to as a sub-volume stress. However, it is analogous to a Reynolds stress and therefore the nomenclature of the Reynolds stress is adopted here.

with small particles, the production due to velocity gradients near the walls can outweigh the production due to particles. However, towards the center of the confined flow, the production due to large dense particles can dominate.

The redistribution terms account for the net change in carrier phase turbulence energy due to particles interacting with each other, the walls or the turbulent eddies in the carrier phase. Methods for modeling these redistribution terms were used by Zhang and Reese (2001, 2003).

If the particle volume fraction approaches zero, $\alpha_d \rightarrow 0$ ($\alpha_c \rightarrow 1$), the kinetic energy equation for single phase flow is recovered.

Example: Evaluate the validity of the volume averaged turbulence equation (Equation 7.19) by applying it to the basic configuration of particles falling in a quiescent fluid.

Solution: The conditions for the basic configuration are

$$\frac{\partial k_c}{\partial t} = 0 \quad \frac{\partial k_c}{\partial x_i} = 0 \quad \langle v_i \rangle \rightarrow v = \text{constant} \quad \delta v_i = 0$$

These conditions reduce Equation 7.19 to

$$n3\pi\mu_c D f v^2 = \alpha_c \rho_c \varepsilon_c$$

showing that the production of turbulence energy due to particles is balanced by dissipation. Thus, the equation yields the expected result.

7.5.3 Turbulence dissipation equation

A transport equation for dissipation of turbulent energy can be found by taking the gradient of the Navier-Stokes equations and dotting the result with the gradient of the volume deviation velocity and volume averaging the result, which can be expressed as

$$\overline{2\nu_c \frac{\partial \delta u_i}{\partial x_j} \frac{\partial}{\partial x_j} N S_i} \quad (7.21)$$

With the assumptions given above, the following general equation for dissipation is obtained (details are shown in Appendix D)

$$\begin{aligned}
 & \frac{\partial}{\partial t} (\alpha_c \varepsilon_c) + \frac{\partial}{\partial x_k} (\alpha_c \langle u_k \rangle \varepsilon_c) \\
 = & -\alpha_c \varepsilon_{ik} \frac{\partial \langle u_i \rangle}{\partial x_k} \quad \text{Production} \\
 & -2\nu_c \alpha_c \left\langle \frac{\partial \delta u_i}{\partial x_j} \frac{\partial \delta u_i}{\partial x_k} \right\rangle \frac{\partial \langle u_k \rangle}{\partial x_j} \\
 & -2\nu_c \alpha_c \left\langle \delta u_k \frac{\partial \delta u_i}{\partial x_j} \right\rangle \frac{\partial^2 \langle u_i \rangle}{\partial x_j \partial x_k} \\
 & -2\nu_c \alpha_c \left\langle \frac{\partial \delta u_i}{\partial x_j} \frac{\partial \delta u_k}{\partial x_j} \frac{\partial \delta u_i}{\partial x_k} \right\rangle \\
 & -\nu_c \frac{\partial}{\partial x_k} \left(\alpha_c \left\langle \delta u_k \frac{\partial \delta u_i}{\partial x_j} \frac{\partial \delta u_i}{\partial x_j} \right\rangle \right) \quad \text{Transport} \\
 & -2\frac{\nu_c}{\rho_c} \frac{\partial}{\partial x_i} \left(\alpha_c \left\langle \frac{\partial \delta u_i}{\partial x_j} \frac{\partial \delta p}{\partial x_j} \right\rangle \right) \quad \text{Pressure Diffusion} \\
 & +\nu_c \frac{\partial^2}{\partial x_k^2} (\alpha_c \varepsilon_c) \quad \text{Molecular Diffusion} \\
 & -2\nu_c^2 \left\langle \frac{\partial^2 \delta u_i}{\partial x_k \partial x_j} \frac{\partial^2 \delta u_i}{\partial x_k \partial x_j} \right\rangle \quad \text{Dissipation of Dissipation} \\
 & -\nu_c^2 \frac{1}{V} \frac{\partial}{\partial x_k} \int_{S_d} \frac{\partial \delta u_i}{\partial x_j} \frac{\partial \delta u_i}{\partial x_j} n_k dS \quad \text{Effect of Particles} \\
 & +2\frac{\nu_c}{\rho_c} \frac{1}{V} \int_{S_d} \frac{\partial \delta u_i}{\partial x_j} \frac{\partial \delta p}{\partial x_j} n_i dS \\
 & -\nu_c^2 \frac{1}{V} \int_{S_d} \frac{\partial}{\partial x_k} \left(\frac{\partial \delta u_i}{\partial x_j} \frac{\partial \delta u_i}{\partial x_j} \right) n_k dS \tag{7.22}
 \end{aligned}$$

where $\varepsilon_{ik} = 2\nu \left\langle \frac{\partial \delta u_i}{\partial x_j} \frac{\partial \delta u_k}{\partial x_j} \right\rangle$ is the volume averaged dissipation tensor and ν_c is the continuous phase kinematic viscosity. The nomenclature for the terms in the above equation was adopted from Bernard and Wallace (2002). Applying the above equation to single phase flow (i.e. $\alpha_c = 1$, and eliminating all the integrals over the particle surfaces), the result is analogous to the single phase dissipation transport equation found from Reynolds averaging by Bernard and Wallace (2002). The effects of the displaced fluid volume are accounted for with the void fraction and the effect of particles on turbulence dissipation are represented by the surface integrals in Equation 7.22.

Understanding the effects of particles on the turbulence dissipation is not straightforward. As a first attempt, the integrals were evaluated assuming Stokes drag with a drag factor f to account for non-Stokesian effects (Schwarzkopf et al. 2009a). The purpose of this exercise was to find the basic

form of the terms and then extend them to turbulent flows. Based on this rudimentary approach (see Appendix D) and following the traditional modeling practices for the single phase turbulence dissipation, a simple model for spherical particles was introduced of the form

$$\begin{aligned} \alpha_c \frac{D\varepsilon_c}{Dt} = & -\alpha_c C'_{\varepsilon 1} \frac{\varepsilon_c}{k_c} R_{ij} \frac{\partial \langle u_i \rangle}{\partial x_j} + \frac{\partial}{\partial x_j} \left(\alpha_c \left(\nu_c + \frac{\nu_T}{\sigma_\varepsilon} \right) \frac{\partial \varepsilon_c}{\partial x_j} \right) \\ & - C'_{\varepsilon 2} \alpha_c \frac{\varepsilon_c^2}{k_c} + C_{\varepsilon 3} \frac{\nu_c^2}{V} \sum_k f_k \frac{|u_i - v_i|_k^2}{D_k} \end{aligned} \quad (7.23)$$

where σ_ε is an empirical constant usually taken as 1.3, and the primed coefficients are not necessarily the single phase coefficients. The last term in this equation is the source term due to the particles. Some models (see Equation 7.14) reported in the literature suggest that the particle source term should be

$$S_{\varepsilon p} = C_{\varepsilon 3} \frac{\varepsilon_c}{k_c} S_{kp} \quad (7.24)$$

where S_{kp} is the source for turbulence energy due to particles and $C_{\varepsilon 3}$ is an empirical constant. This equation is not developed from fundamentals, but rather is based on time scale arguments.

If no particles are present within the control volume of interest, the last term in Equation 7.23 reduces to zero, and the equation for single phase flow is recovered ($\alpha_c = 1$).

Evaluating the coefficients

In an effort to evaluate the coefficients, Equation 7.23 was applied to the data reported by Parthasarathy and Faeth (1990) and Mizukami et al. (1992) for the generation of continuous phase turbulence by particles falling through a quiescent bath of fluid. In this experiment, the production of turbulence energy by the particles is balanced by the dissipation. Applying Equations 7.19 and 7.23 to these conditions and assuming that all the particles are spherical, the following expression is obtained

$$\frac{C_{\varepsilon 3}}{C'_{\varepsilon 2}} = \frac{18^2 \pi}{6} \frac{\alpha_d}{\alpha_c} f \frac{v^2}{k_c} \quad (7.25)$$

Crowe and Wang (2000) observed that under certain conditions the production of turbulence by particles must equal the dissipation⁸. Based on this idea they developed an equation for the ratio of the Taylor length scale to the particle diameter, namely

$$\frac{\lambda}{D} \propto \left(\frac{\alpha_c}{\alpha_d} \frac{1}{18f} \frac{k_c}{\Delta u^2} \right)^{1/2} \quad (7.26)$$

⁸Such cases include the centerline of fully developed pipe flows and particles dropping in a quiescent environment.

where λ is the Taylor length scale, D is the particle diameter and Δu is the velocity difference between the particle and fluid. The data were reduced from data sets which spanned a wide range of relative Reynolds numbers ($1 - 1000$), volume fractions ($10^{-6} - 10^{-2}$), particle density ($900 - 3600 \text{ kg/m}^3$), and carrier phase density ($1 - 1000 \text{ kg/m}^3$). Overall, Crowe and Wang (2000) showed that the above equation strongly depended on the relative Reynolds number.

Combining Equations 7.25 and 7.26, one finds

$$\frac{C_{\varepsilon 3}}{C'_{\varepsilon 2}} \propto \left(\frac{D}{\lambda} \right)^2 \quad (7.27)$$

which implies that the ratio of the coefficients for particle production and dissipation of turbulence is dependent on the relative Reynolds number. The results for $C_{\varepsilon 3}/C'_{\varepsilon 2}$ as a function of relative Reynolds number are shown in Figure 7.9. The data do appear to correlate remarkably well at high relative Reynolds numbers. However, at low relative Reynolds numbers, the data of Varaksin et al. (1998) show that the particle mass loading may affect the coefficient, although additional data are needed to substantiate this claim. Schwarzkopf et al. (2009a) found an expression for the ratio of coefficients, namely

$$\frac{C_{\varepsilon 3}}{C'_{\varepsilon 2}} = C_{\varepsilon p} \text{Re}_r^{1.416} \quad (7.28)$$

where $C_{\varepsilon p} = 0.058$. The correlation is shown on the figure.

To estimate the effect of particles on the dissipation of dissipation coefficient, Schwarzkopf et al. (2009b) conducted a numerical study using DNS to simulate the decay of homogeneous, isotropic turbulence in a field of stationary particles⁹. For this special case, the DNS studies showed that as the point force was increased, the turbulence decayed much more rapidly than if there were no particles at all. This effect cannot be captured with the production term and shows an effect of particle loading at low Stokes numbers. A further investigation showed that the fluid viscosity, particle loading, and the interparticle spacing ratio (discussed in Chapter 2) have an effect on the dissipation rate; however, more data are needed before a correlation can be developed. Although there is an effect on the dissipation of dissipation, for the present time it is best to take $C'_{\varepsilon 2} \approx C_{\varepsilon 2}^{sp}$.

The production coefficient $C'_{\varepsilon 1}$ is difficult to evaluate, mainly due to the lack of information near the wall. Schwarzkopf et al. (2009c) assumed that this coefficient was equal to the single phase value (1.44) and then varied it slightly to determine its effect on predicting the data in particle-laden turbulent channel flow. The results showed that increasing the value of this

⁹ “Stationary particles” takes on the interpretation that the mean particle velocity was equal to the mean fluid velocity, yet the particle was not allowed to follow the fluctuating velocity field.

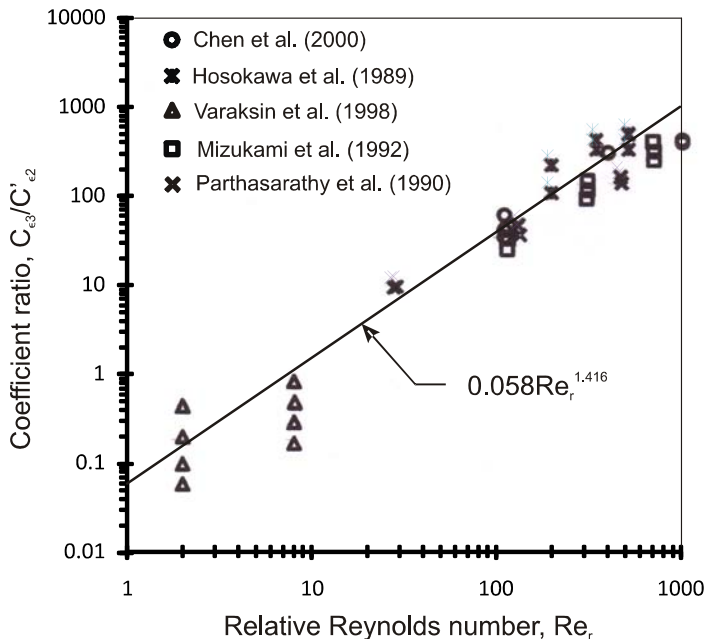


Figure 7.9: Variation of the ratio of the production of dissipation coefficient ($C_{\varepsilon 3}$) to the dissipation of dissipation coefficient ($C'_{\varepsilon 2}$) over a wide range of Reynolds numbers for various types of particle-laden flows. (Reprinted from the *AICHE J.*, **55**, Schwarzkopf, J.D., Crowe, C.T. and Dutta, P., A turbulence dissipation model for particle laden flow, 1416, 2009a, with kind permission from John Wiley and Sons.)

coefficient decreased the turbulent kinetic energy near the wall and decreasing the value increased the turbulent kinetic energy near the wall¹⁰. Further studies and experimental data are needed over a wide range of flow conditions to determine how near-wall effects can be accommodated in $C'_{\varepsilon 1}$.

Overall, reasonable approximations for the coefficients within the dissipation equation are $C'_{\varepsilon 1} = 1.44$, $C'_{\varepsilon 2} = 1.92$, and $C_{\varepsilon 3}/C'_{\varepsilon 2} = 0.06 \text{Re}_r^{1.42}$. Still, further studies are needed to extend these coefficients to a wider range of flows. Additional studies related to the application of these coefficients will be presented later in this chapter.

Example: Apply the dissipation transport Equation 7.23 to the basic test case and assess if the results are reasonable. Also apply Equation 7.24 for the dissipation source term and evaluate the results.

¹⁰Caution should be used when assuming these trends and when assuming that the single phase values apply to flows where the turbulence is augmented and the law of the wall may not apply.

Solution: For the basic test case, $\langle u_i \rangle = 0$, $v_i \rightarrow v = \text{constant}$, $\delta v_i = 0$, $\partial \varepsilon_c / \partial t = 0$, $\partial \varepsilon_c / \partial x_i = 0$.

These assumptions reduce the dissipation equation to

$$C_{\varepsilon 3} \frac{\nu_c^2}{V} \sum_k \frac{f_k}{D_k} (\delta u_i \delta u_i - 2\delta u_i v_i + v_i v_i)_k = C'_{\varepsilon 2} \alpha_c \frac{\varepsilon_c^2}{k_c}$$

For uniform particle size the terms in the above equation can be further reduced to

$$C_{\varepsilon 3} \nu_c^2 n \frac{f}{D} (v^2 + 2k_c) = C'_{\varepsilon 2} \alpha_c \frac{\varepsilon_c^2}{k_c}$$

showing that the production of turbulence dissipation due to particles is balanced by dissipation of dissipation. This is the expected result.

Using the source term defined by Equation 7.24, the dissipation equation reduces to

$$\begin{aligned} C_{\varepsilon 3} \frac{\varepsilon_c}{k_c} S_{kp} &= C_{\varepsilon 2} \alpha_c \frac{\varepsilon_c^2}{k_c} \\ C_{\varepsilon 3} S_{kp} &= C_{\varepsilon 2} \alpha_c \varepsilon_c \end{aligned}$$

The source term for turbulence energy for the basic case (see example above) is

$$S_{kp} = n 3 \pi \mu D f v^2$$

Thus the dissipation equation reduces to

$$C_{\varepsilon 3} n 3 \pi \mu D f v^2 = C_{\varepsilon 2} \alpha_c \varepsilon_c$$

This is the turbulence energy equation with two new coefficients. Thus $C_{\varepsilon 3}$ would have to equal $C_{\varepsilon 2}$. If this is done, then the above equation reduces to the turbulence energy equation and no new information is added. This conclusion challenges the validity of Equation 7.24.

7.5.4 Turbulence Reynolds stress equation

A transport equation for the volume average Reynolds stress can be obtained by $(\overline{u_i N S_j + u_j N S_i}) - (\overline{\langle u_i \rangle N S_j + \langle u_j \rangle N S_i})$. With the assumptions outlined above, the general equation for the volume averaged Reynolds stress where the steady-state drag is the only significant force acting on the parti-

cles is (details provided in Appendix D)

$$\begin{aligned}
& \frac{\partial}{\partial t} (\alpha_c \rho_c R_{ij}) + \frac{\partial}{\partial x_k} (\alpha_c \rho_c \langle u_k \rangle R_{ij}) \\
= & -\alpha_c \rho_c R_{jk} \frac{\partial \langle u_i \rangle}{\partial x_k} - \alpha_c \rho_c R_{ik} \frac{\partial \langle u_j \rangle}{\partial x_k} \quad \text{Production} \\
& - C'_{r1} \alpha_c \rho_c \frac{\varepsilon_c}{k_c} \left(R_{ij} - \frac{1}{3} R_{kk} \delta_{ij} \right) \quad \text{Return to Isotropy} \\
& + C'_{r2} \left(\begin{array}{c} \alpha_c \rho_c R_{jk} \frac{\partial \langle u_i \rangle}{\partial x_k} + \alpha_c \rho_c R_{ik} \frac{\partial \langle u_j \rangle}{\partial x_k} \\ - \frac{2}{3} \alpha_c \rho_c R_{km} \frac{\partial \langle u_k \rangle}{\partial x_m} \delta_{ij} \end{array} \right) \quad \text{Rapid Distortion} \\
& + C'_r \frac{\partial}{\partial x_k} \left(\alpha_c \rho_c R_{km} \frac{k_c}{\varepsilon_c} \frac{\partial R_{ij}}{\partial x_m} \right) \quad \text{Diffusion} \\
& - \frac{2}{3} \alpha_c \rho_c \varepsilon_c \delta_{ij} \quad \text{Dissipation} \\
& + \frac{3\pi\mu_c}{V} \sum_k D_k f_k \left[\begin{array}{c} (\langle u_j \rangle - v_{k,j}) (u_{k,i} - v_{k,i}) \\ + (\langle u_i \rangle - v_{k,i}) (u_{k,j} - v_{k,j}) \end{array} \right] \quad (7.29) \\
& \qquad \qquad \qquad \text{Effect of Particle Drag}
\end{aligned}$$

The first two terms on the right-hand side of the above equation are production terms. The third and fourth terms are a modeled form of the pressure-strain term. These models follow the lead of Rotta (1951) and Launder et al. (1975); however, they do not account for the effect of particles. The coefficients have been designated with a prime which includes the single- and multi-phase effects, such as

$$C'_{() \circ} = C^{sp}_{() \circ} + C_{() p} \quad (7.30)$$

where $C^{sp}_{() \circ}$ is the single-phase coefficient and $C_{() p}$ is the contribution by the dispersed phase. The fifth term is the diffusion model proposed by Daly and Harlow (1970). Based on the work of Schwarzkopf et al. (2009c), the diffusion coefficients in the volume averaged $k - \varepsilon$ equation appear to be similar to the single phase coefficients, and therefore it is assumed that $C'_r \approx C_r^{sp} = 0.22$ (given by Launder, 1989). The sixth term is an isotropic model of the dissipation tensor, which is valid for high Reynolds number flows. The last term is the production due to particles and can be modeled in an averaged form

$$\begin{aligned}
& \frac{3\pi\mu_c}{V} \sum_k D_k f_k \left[\begin{array}{c} (\langle u_j \rangle - v_{k,j}) (u_{k,i} - v_{k,i}) \\ + (\langle u_i \rangle - v_{k,i}) (u_{k,j} - v_{k,j}) \end{array} \right] \\
= & 2\alpha_d \rho_d \frac{f}{\tau_V} [(\langle u_i \rangle - \tilde{v}_i)(\langle u_j \rangle - \tilde{v}_j)] \\
& + 2\alpha_d \rho_d \frac{f}{\tau_V} \left(\widehat{\delta v_i \delta v_j} - \widehat{\delta v_j \delta v_i} \right) \quad (7.31)
\end{aligned}$$

which represents the production and redistribution of turbulent energy by the dispersed phase.

The turbulent kinetic energy k is one-half the trace of R_{ij} and the dissipation is modeled by Equation 7.23 which includes the effects of the dispersed phase. It is important to note that if the particle volume fraction approaches zero, $\alpha_d \rightarrow 0$ ($\alpha_c \rightarrow 1$), the Reynolds stress equation for single phase flow is recovered.

Evaluating the coefficients

The pressure strain terms are modeled by assuming that

$$\alpha_c \left\langle \delta p \left(\frac{\partial \delta u_i}{\partial x_j} + \frac{\partial \delta u_j}{\partial x_i} \right) \right\rangle \approx \alpha_c (\Phi_{ij,1} + \Phi_{ij,2}) \quad (7.32)$$

where $\Phi_{ij,1}$ represents the return to isotropy (Rotta, 1951) and $\Phi_{ij,2}$ is the isotropization of production (IP) model proposed by Naot et al. (1970). The first term serves to bring the Reynolds stress components to an isotropic state, whereas the second term is intended to increase the anisotropy. The presence of particles should contribute to both roles and therefore it is hypothesized that these terms may contain effects of the particles. The purpose of this section is to identify if there is an effect of particles on these models.

Slow-Return Model Rotta's (1951) model was chosen to model the slow return to isotropy. However, the interest here is in identifying if there might be an effect of particles on the slow return term within the Reynolds stress equation. The coefficient is proposed as $C'_{r1} = C_{r1}^{sp} + C_{r1p}$, where C_{r1p} represents the effect of particles and should be zero when applied to single phase turbulence. This requires that C_{r1p} be a function of particle properties, i.e., $C_{r1p} = f(\alpha_d, Re_p, C, St)$. Applying Equation 7.29 to particles falling in a quiescent bath of fluid gives a simple equation of the form

$$0 = -\alpha_c \rho_c (C_{r1}^{sp} + C_{r1p}) \frac{\varepsilon_c}{k_c} \left(R_{ij} - \frac{1}{3} R_{nn} \delta_{ij} \right) - \frac{2}{3} \alpha_c \rho_c \varepsilon_c \delta_{ij} + 2 \alpha_d \rho_d \frac{f}{\tau_V} \left[\tilde{v}_i \tilde{v}_j + \widehat{\delta v_i \delta v_j} - \widehat{\delta v_j \delta u_i} \right] \quad (7.33)$$

In the direction of the falling particles, $\widehat{\delta v \delta v} - \widehat{\delta v \delta u}$ can be neglected when compared to \tilde{v}^2 . However, in the transverse directions, $\tilde{v}^2 = 0$, and $\widehat{\delta v \delta v} - \widehat{\delta v \delta u}$ becomes an important term. The redistribution terms basically reflect the effect of the particle size distribution and their interactions with other particles, the wall and the turbulent eddies. Zhang and Reese (2001, 2003) used the granular temperature concept to model the redistribution terms. Still, more research is needed to understand the effect of the redistribution terms on the return to isotropy. For the present time, it is best to assume $C_{r1p} \approx 0$.

Rapid Distortion Model There are additional challenges associated with determining the effect of particles on the coefficient C'_{r2} . A simpler approach is to assume that the rapid distortion terms in Equation 7.29 apply to the continuous phase and $C'_{r2} = C'^{sp}_{r2}$. A model can then be developed for the particulate effects on the increase in anisotropy.

Following the lead of Naot et al. (1970), Launder et al. (1975), and Launder (1989), an additional term should be applied to Equation 7.29. This term represents the increase in Reynolds stress anisotropy (the IP model), which is due to the rapid pressure partially counteracting the effect of production (Pope, 2000). The IP model is extended to particle laden turbulent flows by

$$\Phi_{ij,3} = -C_{r3} \left(P_{ij}^p - \frac{1}{3} P_{mm}^p \delta_{ij} \right) \quad (7.34)$$

where P_{ij}^p is the production tensor due to particles, given as

$$P_{ij}^p = 2\alpha_d \rho_d \frac{f}{\tau_V} [(\langle u_i \rangle - \tilde{v}_i)(\langle u_j \rangle - \tilde{v}_j)] \quad (7.35)$$

The IP model for particle laden turbulent flows takes the form

$$\Phi_{ij,3} = -C_{r3} \alpha_d \rho_d \frac{f}{\tau_V} \left([(\langle u_i \rangle - \tilde{v}_i)(\langle u_j \rangle - \tilde{v}_j)] - \frac{1}{3} \delta_{ij} [|\langle u_m \rangle - \tilde{v}_m|^2] \right) \quad (7.36)$$

where it is expected that the range of the coefficient should be $0 < C_{r3} < 2$. This term should be included in Equation 7.29.

Recommended equation

There appears to be no research conducted in the area of applying this form of a volume averaged Reynolds stress to dispersed phase flows. In order to understand the anisotropic effects, several experiments need to be developed to distinguish the particle effects from the continuous phase effects. From such experiments, altered forms of the pressure strain model could be developed to properly account for the effect of particles. The recommended form for the modeled Reynolds stress transport equation applied to dispersed phase flows

is

$$\begin{aligned}
 & \frac{\partial}{\partial t} (\alpha_c \rho_c R_{ij}) + \frac{\partial}{\partial x_k} (\alpha_c \rho_c \langle u_k \rangle R_{ij}) \\
 = & -\alpha_c \rho_c R_{jk} \frac{\partial \langle u_i \rangle}{\partial x_k} - \alpha_c \rho_c R_{ik} \frac{\partial \langle u_j \rangle}{\partial x_k} && \text{Production} \\
 & - (C_{r1}^{sp} + C_{r1p}) \alpha_c \rho_c \frac{\varepsilon_c}{k_c} \left(R_{ij} - \frac{1}{3} R_{kk} \delta_{ij} \right) && \text{Return to isotropy} \\
 & + C_{r2}^{sp} \left(\begin{array}{c} \alpha_c \rho_c R_{jk} \frac{\partial \langle u_i \rangle}{\partial x_k} + \alpha_c \rho_c R_{ik} \frac{\partial \langle u_j \rangle}{\partial x_k} \\ - \frac{2}{3} \alpha_c \rho_c R_{km} \frac{\partial \langle u_k \rangle}{\partial x_m} \delta_{ij} \end{array} \right) && \text{Rapid Distortion} \\
 & + C_r^{sp} \frac{\partial}{\partial x_k} \left(\alpha_c \rho_c R_{km} \frac{k_c}{\varepsilon_c} \frac{\partial R_{ij}}{\partial x_m} \right) && \text{Diffusion} \\
 & - \frac{2}{3} \alpha_c \rho_c \varepsilon_c \delta_{ij} && \text{Dissipation} \\
 & + \frac{3\pi\mu_c}{V} \sum_k D_k f_k \left[\begin{array}{c} (\langle u_j \rangle - v_{k,j}) (u_{k,i} - v_{k,i}) \\ + (\langle u_i \rangle - v_{k,i}) (u_{k,j} - v_{k,j}) \end{array} \right] && \text{Effect of particle drag} \\
 & - C_{r3} \alpha_d \rho_d \frac{f}{\tau_V} \left(\begin{array}{c} [(\langle u_i \rangle - \tilde{v}_i) (\langle u_j \rangle - \tilde{v}_j)] \\ - \frac{1}{3} \delta_{ij} [\langle u_m \rangle - \tilde{v}_m]^2 \end{array} \right) && \text{Rapid Distortion due to particles} \tag{7.37}
 \end{aligned}$$

The above Reynolds stress model has not been applied to any particle laden turbulent flows and compared with experimental data. Therefore, it is recommended that the single phase coefficients be applied to establish if there is a need to include additional particle effects. The single phase values given by Launder (1989) are: $C_{r1}^{sp} = 1.8$, $C_{r2}^{sp} = 0.6$, $C_r^{sp} = 0.22$ and C_{r1p} is assumed to be zero. An estimated range for the rapid distortion coefficient is $0.6 \leq C_{r3} \leq 1.2$; an uncalibrated value of unity could be used as a starting place.

7.6 Application to experimental results

The above-mentioned volume averaged two equation $k - \varepsilon$ model is applied to particles falling in a high aspect ratio downward channel flow. The experimental setup of Kulick et al. (1993, 1994) consists of a long channel that has a cross-section of 4.0×45.7 cm. The carrier phase was air, and the experiments were run with various dispersed phase materials, such as glass and copper. The length of the channel was long enough so that the particles could reach terminal velocity. Kulick et al. (1993) used LDV while Paris and Eaton (2001) used PIV to obtain air and particle velocity measurements for various particle sizes and loadings. The data of Kulick et al. (1993) demonstrated

that 50 μm and 90 μm glass particles produce little attenuation, while 70 μm copper particles at mass loadings greater than 0.1 produce significant turbulence attenuation. Paris and Eaton (2001) demonstrated that 150 μm glass particles with 20% mass loading also produce significant attenuation.

The volume-averaged two-equation $k - \varepsilon$ model (Equations 7.19 and 7.23) were reduced to represent steady, fully developed conditions. The representative 1-D equations were then discretized using finite volume techniques (discussed in Chapter 9). Boundary conditions (discussed in Chapter 9) were applied to the center of the cell adjacent to the wall. The pressure gradient was iterated until the centerline velocity matched that of the data.

A comparison of the velocity profile normalized by the centerline velocity for the laden case of 150 μm glass particles with 20% mass loading and 70 μm copper particles at mass loadings of 10% and 20% is shown in Figure 7.10. For all three cases the magnitude of the velocity profile is lower than the measured values near the wall, but the predicted trend agrees well with the PIV data of Paris and Eaton (2001).

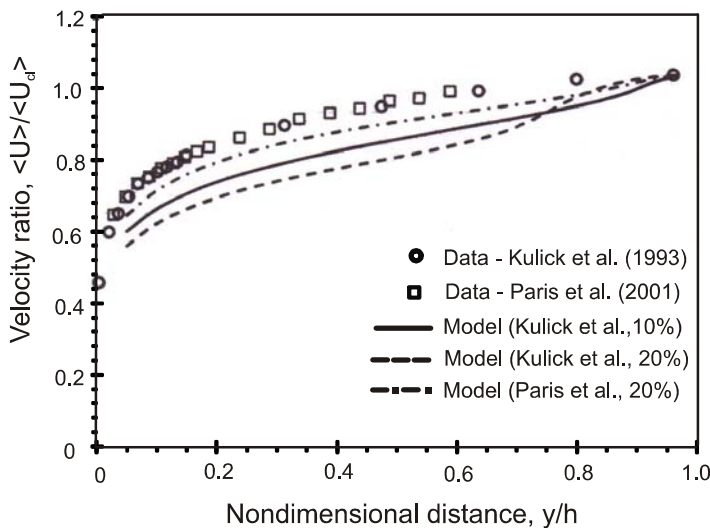


Figure 7.10: Predicted and measured velocity distribution in the channel. (Reprinted from the Proceedings of the ASME, FEDSM2009-78385, Schwarzkopf, J.D., Crowe, C.T. and Dutta, P., A $k - \varepsilon$ model for particle laden turbulent flows, 2009, with kind permission from ASME.)

The turbulent kinetic energy from the experiment was computed based on

$$k = \frac{1}{2} \overline{u_1' u_1'} + \overline{u_2' u_2'} \quad (7.38)$$

where the transverse components were assumed to be similar in magnitude. The turbulent kinetic energy (TKE) predicted by the model was compared to the $70 \mu\text{m}$ copper measurements of Kulick et al. (1993) and $150 \mu\text{m}$ glass measurements of Paris and Eaton (2001), shown in Figure 7.11. Comparing the model predictions with the data of Kulick et al. (1993) show good agreement near the wall but the predictions deviate from the data near the center of the channel. In this region, the model produces constant TKE. This same profile near the centerline of pipe flow is found in the data of Tsuji et al. (1984) and Sheen et al. (1993) for similar sized particles. The model does show a decrease in TKE with increased mass loading. The model was also compared to the PIV measurements of TKE by Paris and Eaton (2001), although this data does not extend to the center of the channel. Comparing the model shows a pronounced deviation near the wall.

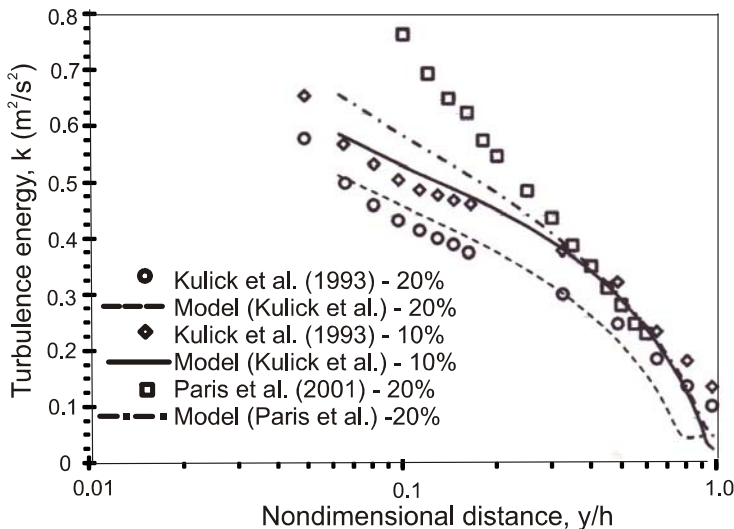


Figure 7.11: Measured and predicted profiles of turbulence energy across the channel. (Reprinted from the Proceedings of the ASME, FEDSM2009-78385, Schwarzkopf, J.D., Crowe, C.T. and Dutta, P., A $k - \varepsilon$ model for particle laden turbulent flows, 2009, with kind permission from ASME.)

In the above data, the particle Reynolds numbers were low (~ 10). A deeper look at Figure 7.9 shows that at low Reynolds numbers, there is an effect of mass loading. A reason for the deviation of turbulent kinetic energy near the center of the channel may be partly due to the fact that the coefficient $C_{\varepsilon 3}$ was calibrated with minimal data at low particle Reynolds numbers, where the data suggest that particle loading affects the coefficient.

To evaluate the effectiveness of the additional production term in the dissipation model, the production coefficient ($C_{\varepsilon p}$) is varied. Within this coefficient, $C_{\varepsilon p}$ is varied from 0 – 0.06, while the exponent m remained at 1.42. When $C_{\varepsilon p}$ is set to zero, the additional production of dissipation due to particulate surfaces is suppressed; in other words, the dissipation is essentially modeled as the single phase dissipation with the standard coefficients, yet the effects of the particles are still included in the turbulent kinetic energy equation. This case (see Figure 7.12) shows that the turbulent kinetic energy is nearly constant across the channel, significantly over predicting the data with a comparatively different trend. Increasing $C_{\varepsilon p}$ to 0.015 shows a drastic reduction in the turbulent kinetic energy with a well-matched trend. As $C_{\varepsilon p}$ is increased to 0.06 the turbulent kinetic energy near the wall matches well; however, the model tends to under-predict the measurements near the centerline of the channel, producing constant turbulent kinetic energy.

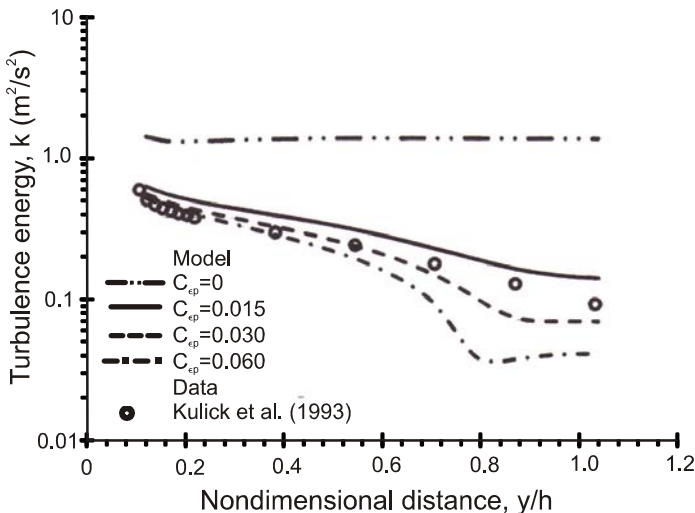


Figure 7.12: Effect of the coefficient $C_{\varepsilon p}$ on the turbulence energy distribution in particle laden channel flow. (Reprinted from the *J. of Fluids Eng.*, **131**, Schwarzkopf, J.D., Crowe, C.T. and Dutta, P., Application of a volume averaged $k - \varepsilon$ model to particle-laden turbulent channel flow, 101301, 2009, with kind permission from ASME.)

The production of dissipation coefficient ($C'_{\varepsilon 1}$) due to mean velocity gradients also has an unknown effect due to particles. To grasp an understanding of this coefficient for this type of flow, the coefficient $C_{\varepsilon p}$ was set to 0.025 to match the magnitude of turbulent kinetic energy at the center of the channel and $C'_{\varepsilon 1}$ was varied from 1.30 to 1.60 as shown in Figure 7.13. The results may indicate a slight dependence on the presence of particles; however, this is

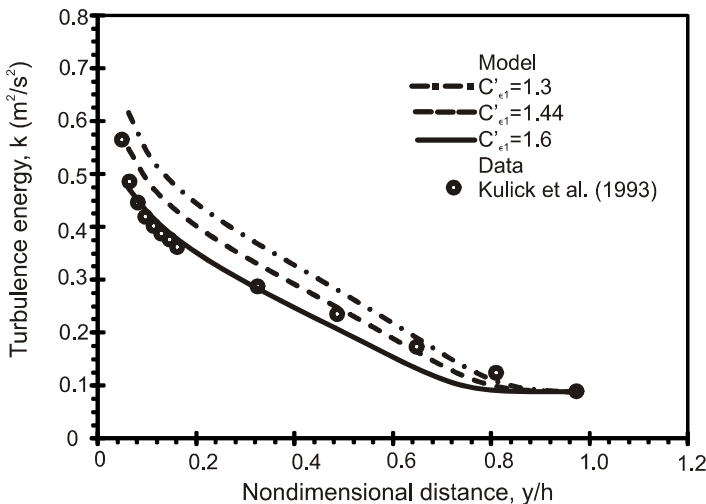


Figure 7.13: Effect of the coefficient $C'_{\varepsilon 1}$ on the turbulence energy distribution near the wall in a channel. (Reprinted from the *J. of Fluids Eng.*, **131**, Schwarzkopf, J.D., Crowe, C.T. and Dutta, P., Application of a volume averaged $k - \varepsilon$ model to particle-laden turbulent channel flow, 101301, 2009, with kind permission from ASME.)

a single data set and more data are needed to make an accurate assessment.

The purpose of the above exercises was to show the sensitivity of the coefficients within the volume averaged dissipation, Equation 7.23, and to highlight the necessity of the additional production of dissipation term, which is due to the presence of particles. However, the above exercises do show that more data are needed to further calibrate and/or validate the dissipation coefficients. Overall, the results produced by volume averaged momentum and turbulence models are encouraging.

The recommended coefficients are shown in Table 7.1. The coefficient 0.06 in the correlation for $C_{\varepsilon 3}$ may have to be re-evaluated for low relative Reynolds numbers.

7.7 Summary

The subject of multiphase and multicomponent turbulent flows ratchets up the complexity when compared to the already complex topic of single phase, single component turbulence. These additional complexities arise due to jump conditions (usually characterized by a surface) in properties throughout the flow. These immiscible effects can attenuate or augment turbulent energy relative to single fluid turbulence. Over the last few decades, experimental and numerical research have shown that mechanisms such as surfaces, loading,

Coefficient	Recommended value	Description
$C'_{\varepsilon 1}$	1.44	Production of dissipation due to mean velocity gradients
$C'_{\varepsilon 2}$	1.92	Dissipation of dissipation
$C'_{\varepsilon 3}$	$0.06C'_{\varepsilon 2} \text{Re}_r^{1.42}$	Production of dissipation
C'_r	0.22	Reynolds stress diffusion
C'_{r1}	1.8	Slow return to isotropy
C'_{r2}	0.6	Rapid distortion due to production
C_{r3}	1.0	Rapid distortion due to particle production, $0 < C_{r3} < 2$
C_μ	0.09	Turbulent viscosity
σ_k	1.0	Empirical constant for diffusion of turbulence kinetic energy
σ_ε	1.3	Empirical constant for diffusion of dissipation

Table 7.1: Recommended coefficients.

inertial, response and interaction contribute to the altered turbulence level. However, there is still more research needed in areas that combine these effects over a wide range of flows before a universal model can be identified that can be applied to a wide range of engineering applications.

In the last few decades, several attempts at modeling particle laden turbulence using Reynolds averaging have been pursued. Although these models seem to predict selected experimental data rather well, when applied to a simple flow, they fail to capture the balance between turbulence production and dissipation. In this chapter, a basic test is introduced that is based on a balance between turbulence production due to particles and dissipation in the fluid. This test is then applied to a Reynolds averaged $k - \varepsilon$ model. Under the conditions of the basic test, both models fail to show that the production of turbulent energy due to particle motion balances the dissipation in the fluid.

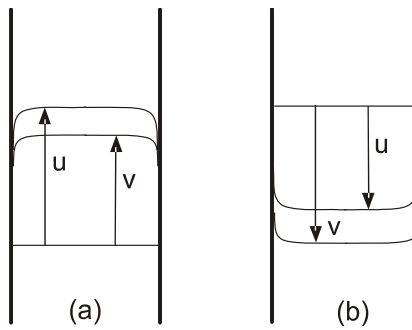
Recently, volume average techniques have shown to produce encouraging results in the area of particle laden turbulent flows when compared to experimental data. For this reason, a portion of this chapter highlights the development and features of volume averaged $k - \varepsilon$ and Reynolds stress models. The volume averaged $k - \varepsilon$ model is applied to particles in a channel flow showing good agreement with experimental data.

In addition, this chapter also highlights DNS techniques that capture the effects of particles on the carrier phase turbulence. Historically, point particle methods have been used with DNS, which requires that the particle size be much less than the smallest length scale in the flow. The ideal method uses an overset grid to capture the local turbulence near the surfaces of particles. These methods are useful for research purposes, providing a “set of eyes” in areas that may be difficult to measure experimentally.

Overall, research in modeling particle laden turbulent flows has significantly advanced in the last decade. This chapter is intended to present a glimpse of some of these advances.

7.8 Exercises

- 7.1. Consider a dilute, particle laden, wall-bounded flow in a vertical channel as shown in the figure. The flow is fully developed and steady. The void fraction and continuous phase density are constant. In case (a), the fluid velocity is greater than the particle velocity. In case (b), the particles are falling faster than the flow velocity. In both cases, how would the turbulent energy and dissipation vary relative to the case where there were no particles? Explain.



Problem 7.1

- 7.2. For the simple case of particles steadily falling in a bath of fluid with velocity v , show that the turbulent kinetic energy and dissipation equations reduce to

$$\text{Turbulent Kinetic Energy: } 18\alpha_d\nu_c f v^2 \frac{1}{\alpha_c D^2} = \varepsilon_c$$

$$\text{Dissipation: } C_{\varepsilon 3} \frac{6}{\pi} \frac{\nu_c^2}{D^4} \alpha_d f v^2 = C'_{\varepsilon 2} \alpha_c \frac{\varepsilon_c^2}{k_c}$$

Determine the turbulence intensity ($\sqrt{k_c}/v$) if the particle Reynolds number is 300, the particle volume fraction is 5×10^{-4} . Use Equation 7.28 for the ratio of the coefficients.

- 7.3. Consider a simple dilute particle-laden channel flow where the particles do not interact with the walls. Derive an expression that shows how the pressure gradient is altered (relative to single phase) by the presence of particles. Comment on how the Reynolds stress and particle drag affect the continuous phase pressure gradient. What condition(s) would be required to have (a) “ghost particles” (i.e., the addition of particles does not affect the

pressure gradient), and (b) a reduced pressure gradient? Assume that there is no mass transfer between the particles and the continuous phase fluid, and that the wall shear is the same for both the single phase and particle laden flow.

7.4. Contract the Reynolds stress transport Equation 7.37 and show that the volume averaged TKE Equation 7.19 is obtained (use the condition $C_r^{sp} = \frac{3}{2} \frac{C_\mu}{\sigma_k}$).

7.5. A turbulence model for particle-laden flows has appeared in the literature. In this model the turbulence kinetic energy and dissipation transport equations are

$$\begin{aligned} \frac{Dk}{Dt} &= \nu_t \left(\frac{\partial \bar{u}_i}{\partial x_j} + \frac{\partial \bar{u}_j}{\partial x_i} \right) \frac{\partial \bar{u}_i}{\partial x_j} + \frac{\partial}{\partial x_i} \left(\frac{\nu_t}{\sigma_k} \frac{\partial k_c}{\partial x_i} \right) - \varepsilon \\ &\quad + \frac{\alpha_d \rho_d}{\rho_c \tau_V} \left(\overline{u'_i v'_i} - \overline{\bar{u}'_i \bar{v}'_i} \right) + \left| \frac{\alpha_d \rho_d}{\rho_c \tau_V} \bar{u}_i (\bar{u}_i - \bar{v}_i) (f - 1) \right| \\ \frac{D\varepsilon}{Dt} &= C_{\varepsilon 1} \nu_t \left(\frac{\partial \bar{u}_i}{\partial x_j} + \frac{\partial \bar{u}_j}{\partial x_i} \right) \frac{\partial \bar{u}_i}{\partial x_j} \frac{\varepsilon}{k} + \frac{\partial}{\partial x_i} \left(\frac{\nu_t}{\sigma_\varepsilon} \frac{\partial \varepsilon}{\partial x_i} \right) - C_{\varepsilon 2} \frac{\varepsilon^2}{k} \\ &\quad + \frac{2\alpha_d \rho_d}{\rho_c \tau_V} \left(\nu \frac{\partial u'_i}{\partial x_j} \left(\frac{\partial v'_i}{\partial x_j} - \frac{\partial u'_i}{\partial x_j} \right) \right) \\ &\quad + C_{\varepsilon 3} \frac{\varepsilon}{k} \left| \frac{\alpha_d \rho_d}{\rho_c \tau_V} \bar{u}_i (\bar{u}_i - \bar{v}_i) (f - 1) \right| \end{aligned}$$

where f is the drag factor. Apply the above equations to

(a) the basic test case, but assume that the mean velocity is non-zero and very small. What conditions are needed to ensure that the turbulent energy and dissipation are positive?

(b) the basic test case where the mean fluid velocity and the particle fluctuation velocity are zero. Comment on the result.

7.6. Derive equations for the boundary conditions for k_c and ε_c with particle effects near the wall. Begin with Equations 7.19 and 7.23 and assume that the log law applies and that diffusion and the redistribution terms near the wall are negligible. (Note: near the wall, $\frac{\partial \langle u \rangle}{\partial y} = \frac{u_\tau}{\kappa y}$, where u_τ is the friction velocity and κ is the von-Kármán constant, and the shear at the wall can be related to the friction velocity by $u_\tau^2 = C_\mu \frac{k_c^2}{\varepsilon_c} \frac{d \langle u \rangle}{dy}$.)

7.7. Apply Equation 7.9 to a free stream of fluid passing through a cloud of stationary particles. Assume the particles are spherical, with constant density and the flow is homogeneous and steady, such that the drag due to the particles is balanced by the pressure gradient. Determine an expression for the turbulence dissipation.

7.8. Apply Equation 7.37 to single phase channel flows and show that $R_{12} = -\nu_T \frac{\partial \langle u_1 \rangle}{\partial x_2}$ and determine an expression for C_μ . Assume diffusion can be neglected.

7.9. Apply Equation 7.37 to particles falling in an initially quiescent bath of fluid, where it is assumed that the mean velocity of the continuous phase is everywhere zero.

- (a) In the direction of the falling particles, show that the Reynolds stress is a function of the square of the particle velocity.
- (b) Show that the remaining components of the diagonal differ only by the redistribution terms.
- (c) Show that the off-diagonal components are dependent on the redistribution terms.
- (d) Using the equations found from (a) – (c), find an expression for the turbulent dissipation. Compare with Equation 7.19. Comment on the symmetry of the Reynolds stress tensor.

Chapter 8

Droplet-Particle Cloud Equations

The ideal numerical model for the particle phase would resolve the dynamics and thermal properties of each particle in the system. However, the many millions of particles in a typical industrial application makes such an approach currently intractable. Instead of tracking each individual particle, the *particle cloud approach* is used in which “bulk” properties are identified and interpreted in terms of mixing, chemical reactions and other processes.

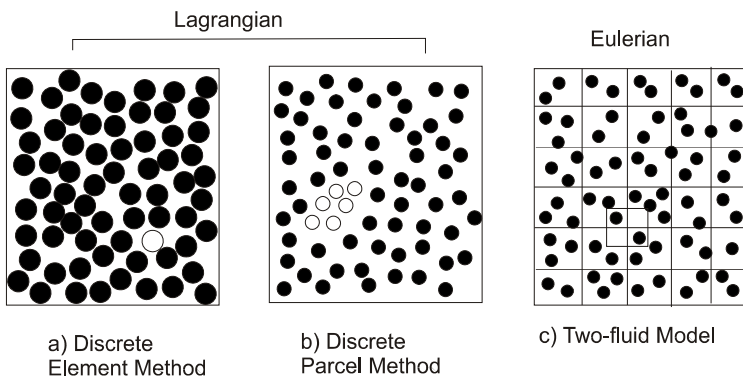


Figure 8.1: Different approaches for modelling particle and droplet clouds.

There are basically three approaches for the numerical simulation of a cloud of particles or droplets as shown in Figure 8.1. In *Discrete Element Method* (DEM), Figure 8.1a, the motion of each particle is analyzed incorporating the fluid dynamic forces, the contact forces and the moments due to the neighboring particles. The open circle in the figure represents one discrete element in the cloud. Solving the equations of motion for all the elements in

the field yields the properties of the particle cloud. Obviously a large number of discrete particles would be needed to represent a typical particle cloud. Another method, shown in Figure 8.1b, is to identify a parcel of particles (open circles) which move through the field. The dynamic properties (size, velocity, rotational rate, etc.) for each particle in the parcel are the same so the parcel is represented by one *computational particle*. Solving for the properties of the computational particles as they move through the field gives the local properties of the cloud. This method will be called the *Discrete Parcel Method* (DPM). The third approach is the *Two-Fluid* (TF) model, shown in Figure 8.1c. In this case, the properties of the particles are assumed to be continuous like those of a fluid. Differential conservation equations are written for every node in the field, discretized and the solution of the resulting a set of algebraic equations gives the properties of the cloud.

The above-mentioned methods can be categorized into *Lagrangian tracking* or *Eulerian modeling* approaches. With the discrete element and discrete parcel methods, individual particles or parcels of particles are tracked through the field and the local properties of the cloud are determined by the properties of the particle or parcel as they pass the point in the field. This is the Lagrangian approach. The two-fluid approach, in which set of algebraic conservation equations are solved simultaneously for each node in the field, is the Eulerian approach.

The dense or dilute character of the disperse phase, introduced in Chapter 2, is fundamental to determining the approach to be used for modeling the dispersed phase. A dilute flow is one in which the time between collisions is much larger than the velocity response time which means that the particle-fluid interaction is responsible for the particle motion, not the particle-particle collisions. In other words, information, such as particle velocity, size and temperature, travels along particle trajectories. This condition is unlike the flow of a continuous substance in which information travels in all directions (subsonic flows). The cloud of particles in a dilute flow cannot be treated as a continuous fluid so the Lagrangian approach is the only approach suitable for a dilute flow.

In a dense flow, on the other hand, particle collisions allow information to travel in all directions and the particle clouds can be modeled as a continuous fluid. In this case, the Eulerian approach is applicable.

In order to calculate the motion and thermal properties of particles in a cloud, information is needed for the continuous phase velocity and temperature. The continuous, or conveying, phase is always modeled using the Eulerian approach. In a “complete” numerical simulation, as shown in Figure 8.2a, the velocity of the continuous phase is obtained by solving the Navier-Stokes equations with the appropriate boundary conditions corresponding to the particle surfaces and the walls. The complexity and cost of such simulations limit the application to a few particles at low Reynolds numbers. Another approach is *Direct Numerical Simulation* (DNS) for which the primary focus is modeling carrier-phase turbulence. The Navier-Stokes equations are

written in spectral form to capture the higher frequencies and smallest scales of turbulence. Thus the flow velocity is available, through appropriate interpolation, at every point in the flow. The particles are “point” particles which occupy no volume as shown in Figure 8.2b. This calculation is also limited to low flow Reynolds numbers. *Large Eddy Simulation* (LES) can also be used to model a turbulent flow field. With this method the Navier-Stokes equations are “filtered” so the numerical calculations yield the large scale turbulent motion and the small scale contribution is modeled with a residual stress tensor. This approach enables calculations at higher Reynolds numbers than achievable with DNS.

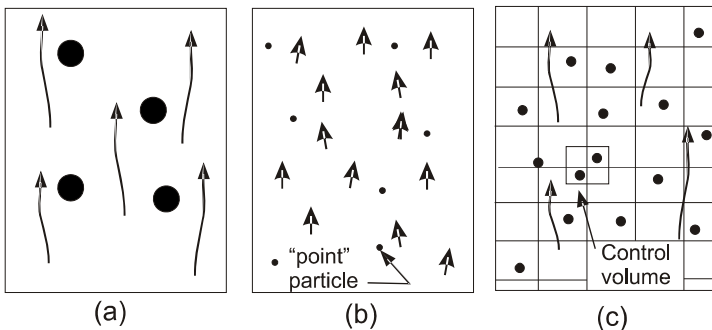


Figure 8.2: Carrier flow field descriptions.

The majority of practical applications use a computational grid as shown in Figure 8.2c. The equations are discretized to apply over a control volume and the set of algebraic equations are solved for the flow field. In a multiphase flow, the control volume becomes the averaging volume where the particles within the averaging volume are responsible for mass, momentum and energy coupling. Solution of the governing carrier-phase equations yields values for phase-averaged properties, $\langle u_i \rangle$, $\langle p \rangle$, etc. associated with every control volume in the field. The phase-averaged velocity is defined as

$$\langle u_i \rangle = \frac{1}{V_c} \int_{V_c} u_i dV \quad (8.1)$$

where u_i is the local velocity (which varies throughout the averaging volume) and V_c is the volume of the continuous phase in the averaging volume. The phase-averaged velocity is equivalent to the interstitial velocity.

The finest level of detail available for the continuous phase properties is the phase-averaged value. This is the velocity that must be used for the continuous phase in the equations of particle motion. Similarly, the phase-averaged temperature is used for continuous phase temperature in solving for the thermal properties of the cloud.

The size of the averaging volume is discussed in Chapter 9.

8.1 Discrete Element Method (DEM)

The Discrete Element Method (DEM) has found numerous applications in granular flows and fluidized beds. It is particularly applicable to contact-dominated flows. With this model the particle flow is resolved down to the particle level. The equation of motion of for each particle is

$$m \frac{dv_i}{dt} = \sum_k (F_{n,k,i} + F_{t,k,i}) + mg_i + F_i \quad (8.2)$$

where m is the particle mass, $F_{n,k,i}$ is normal contact force and $F_{t,k,i}$ is the tangential contact force due to neighboring particle k and F_i is the force on the particle due to the conveying fluid. The summation is carried out over all particles in contact with the particle of interest. The equation for rotational motion of a single particle is¹

$$I \frac{d\omega_i}{dt} = \sum_k a \varepsilon_{ijl} n_j F_{t,k,l} \quad (8.3)$$

where I is the particle moment of inertia, a is the particle radius and n_i is the unit normal vector at the particle surface. The force equations for the soft sphere model, developed in Chapter 5, are used for the normal and tangential forces. The equations for particle-wall contact, also developed in Chapter 5, are used to implement the boundary conditions.

The fluid force on a single particle is²

$$F_i = -V_d \frac{\partial \langle p \rangle}{\partial x_i} + 3\pi\mu D f(\langle u_i \rangle - v_i) \quad (8.4)$$

where f is the drag factor discussed in Chapter 4 for dense flows and V_d is the volume of the particle.

The above equations are integrated over time from a known starting condition. The position, velocity and rotational rate of every particle is updated at each time step using

$$x_i = x_{i,0} + v_i \Delta t \quad (8.5a)$$

$$v_i = v_{i,0} + \frac{dv_i}{dt} \Delta t \quad (8.5b)$$

$$\omega_i = \omega_{i,0} + \frac{d\omega_i}{dt} \Delta t \quad (8.5c)$$

where the subscript 0 indicates the initial values and Δt is the time step. The values for the velocities and rotational rates at the position of every particle in the field yields the properties of the cloud.

¹The torque due to the conveying fluid is usually not included. Index notation is used for the cross derivatives.

$$\varepsilon_{ijl} n_j F_{t,k,l} = \mathbf{n} \times \mathbf{F}_{t,k}$$

²The force due to the gradient in phase-averaged shear stress is usually not included.

DEM has also been used for studies of particle-fluid interaction in turbulent flow using DNS formulation for the carrier flows. The particles are *point particles* (have zero volume); that is, the assumption is made that the volume of the particles has no effect on the carrier flow field ($\alpha_c \rightarrow 1$). The equations of motion for the point particles is simply

$$\frac{dv_i}{dt} = \frac{u_i - v_i}{\tau_V} + g_i \quad (8.6)$$

where v_i is the particle velocity and τ_V is the particle response time. This equation is based on a Stokes drag coefficient. Corrections can be made for non-Stokesian effects by including a drag factor based on the assumed particle size and Reynolds number.

DEM has the advantage that a detailed description of the cloud is provided by the numerical model. The problem is that a very large number of discrete elements are needed to model practical systems. For example, approximately 10^9 particles would be needed to model a one liter volume of $200 \mu\text{m}$ particles. This is out of the range of conventional computational capabilities and the cost would be prohibitive.

8.2 Discrete Parcel Method (DPM)

The Discrete Parcel Method (DPM) involves identifying a group (parcel) of particles and tracking the parcel through the flow field. A parcel of particles is illustrated by the open circles in Figure 8.1b. All the particles in the parcel are assumed to have the same properties (size, velocity, rotational rate) so the group is represented by one computational particle. The calculated velocities and other properties of the computational particles, as they travel through the field, provide the properties of the cloud.

There are several different names for the Lagrangian descriptions of the particle field. DEM seems to be most commonly used for models based on individual particles but DPM (discrete particle method) is also found. There appear to be several descriptors in the literature for models based on tracking the motion of particle parcels. These include Lagrangian-Eulerian, particle-in-cell and so on. It is recommended here that DPM be used as the generic label for such methods.

There are basically two approaches to the DPM. One approach applies to dilute and near-dilute flows in which the fluid dynamic forces (drag and lift) acting on the particle are responsible for the particle motion. This model was initially introduced as the Particle Source In Cell (PSI-Cell) (Crowe et al., 1977). In this approach, models for turbulence dispersion, particle collision and agglomeration and other detailed phenomena can be implemented. This approach has also been used for collision-dominated flows. The other approach is called the Multiphase Particle In Cell method (MP-PIC) (Andrews and O'Rourke, 1996) in which the equation for particle motion includes the effect

of particle-particle interaction by incorporating the gradient of the solids stress tensor as a force on the computational particle.

In the discussion that follows, the DPM methods are divided into two classes: non-dense flows and dense flows. A non-dense flow is one in which the fluid dynamic forces play the major role on particle motion. The word non-dense is used in lieu of dilute because dilute implies that the fluid dynamic forces totally control the particle motion. However, there are cases where particle-particle collisions can be a contributing factor. In dense flows, on the other hand, particle-particle interaction plays the major role in particle motion.

8.2.1 Non-dense flows

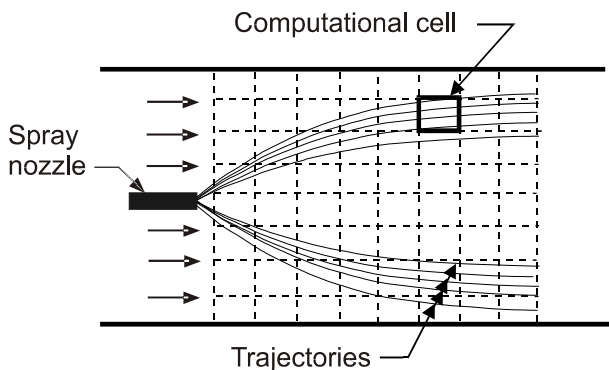


Figure 8.3: Particle trajectories for a spray issuing into a pipe flow.

The precursor to the DPM was the “trajectory method” in which particle trajectories were used to quantify the properties of a cloud. The droplet trajectories associated with a spray issuing into a duct flow is illustrated in Figure 8.3. The flow field is discretized into an assembly of computational cells, as shown, which are also the averaging volumes used to formulate the set of algebraic expressions for the carrier-phase continuity, momentum and energy equations. The inlet flow for the droplets is discretized into a series of initial conditions for the trajectories. The number flow associated with a trajectory j is

$$\dot{N}_p(j) = \frac{\dot{M}_p(j)}{m_p(j)} \quad (8.7)$$

where $\dot{M}_p(j)$ is the mass flow rate assigned to trajectory j and $m_p(j)$ is the initial mass of the droplet. Further refinement is possible by breaking the mass flow down into a sum of values according to a discrete mass frequency distribution discussed in Chapter 3. Also the mass flow rate could be further subdivided to accommodate a distribution of starting angles and velocities.

If there are no collisions with droplet agglomeration or droplet break-up, the number flow rate along a given trajectory is constant.

Once all the trajectories have been calculated, the properties of the cloud in each computational volume can be determined. The local particle number density is

$$n = \frac{\sum_{\text{traj}} \dot{N}_p \Delta t_j}{V_c}$$

where Δt_j is the time required for the droplet to traverse the cell along trajectory j , and V_c is the cell volume. The summation is carried out over all the trajectories which traverse the cell. The corresponding droplet volume fraction, average droplet velocity and other cloud properties are obtained in the same way.

Although conceptually simple the “trajectory method” is not convenient for analysis of unsteady flows with two-way coupling. The DPM is more suitable and versatile.

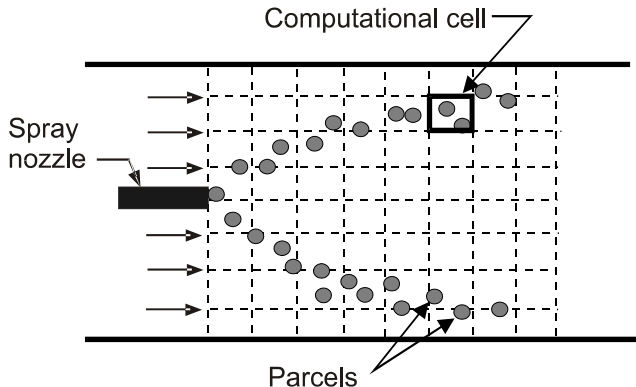


Figure 8.4: Parcels of droplets injected into a duct flow.

The application of DPM for droplets sprayed into a duct flow is shown in Figure 8.4. The parcels, introduced at the location of the spray nozzle, consist of many physical droplets that are convected through the flow field as a unit. The initial conditions for the droplet field can be represented by a number of starting trajectories with different angles, initial velocities and droplet sizes using the same procedure outlined for the trajectory method. Thus the number of droplets in each parcel is $N_p = \dot{N}_p \Delta t$ where \dot{N}_p is the number flow rate for the specific starting trajectory and Δt is the time step used to the computations. Of course, the time step must be small enough such that the parcel travels a distance much less than the cell dimension in one time step.

The motion of each parcel over one time interval is obtained by integrating the equation of motion for the computational particle representing the parcel.

For the same time interval the droplet temperature and other properties can be calculated. Also, there may deviations in the path due to carrier-phase turbulence and droplet collisions.

At every time step, the properties of the droplet cloud can be determined by summing over all the parcels in a computational volume. For example, the number density would be

$$n = \frac{\sum_p N_p}{V_c} \quad (8.8)$$

where the summation is carried out over all the parcels in the computational cell. Also the droplet volume fraction would be

$$\alpha_d = \frac{\sum_p N_p V_p}{V_c} \quad (8.9)$$

where V_p is the volume associated with an individual droplet in the parcel. The calculation of other properties such as bulk density and droplet velocity distribution is obvious.

Particle tracking

The discrete parcel of identical particles is represented by a computational particle. The fluid dynamic forces acting on a computational particle, p , were developed and presented in Chapter 4 (Equation 4.155). The general form is³

$$\begin{aligned} & F_{p,i} \\ = & -V_p \frac{\partial \langle p \rangle}{\partial x_i} + V_p \frac{\partial \langle \tau_{ij} \rangle}{\partial x_j} && \text{undisturbed flow} \\ & + 3\pi\mu_c D f (\langle u_i \rangle - v_{p,i}) && \text{steady state} \\ & + C_{vm} \frac{\rho_c V_p}{2} \left(\frac{D \langle u_i \rangle}{Dt} - \frac{dv_{p,i}}{dt} \right) && \text{virtual mass} \\ & + C_B \frac{3}{2} D^2 \sqrt{\pi\rho_c\mu_c} \left[\int_0^t \frac{\frac{d}{dt'} (\langle u_i \rangle - v_{p,i})}{\sqrt{t-t'}} dt' + \frac{(\langle u_i \rangle - v_{p,i})_0}{\sqrt{t}} \right] && \text{Basset} \\ & + C_S 1.61 D^2 (\mu_c \rho_c)^{\frac{1}{2}} |\omega_{c,i}|^{-\frac{1}{2}} \left[\varepsilon_{ijk} (\langle u_j \rangle - v_{p,j}) \boldsymbol{\omega}_{c,k} \right] && \text{Saffman} \\ & + \frac{1}{2} \rho_c A C_{LR} [\varepsilon_{ijk} \omega_{p,j} (v_{p,k} - \langle u_k \rangle)] |v_{p,i} - \langle u_i \rangle| && \text{Magnus lift} \end{aligned} \quad (8.11)$$

where the virtual mass and Basset terms can be significant for unsteady flows and the Saffman and Magnus lift forces come into play if lift forces due to

³Index notation is used here. The vector cross products are represented by

$$(\langle \mathbf{u} \rangle - \mathbf{v}) \times \boldsymbol{\omega}_c = \varepsilon_{ijk} (\langle u_j \rangle - v_j) \boldsymbol{\omega}_{c,k} \quad (8.10)$$

particle and fluid rotation are considered important. The pressure in this equation includes the hydrostatic pressure. If the pressure does not include the hydrostatic pressure, a buoyancy term has to be added, namely

$$F_{\text{buoy},i} = -\rho_c V_p g_i \quad (8.12)$$

It is convenient to write Equation 8.11 as

$$F_{p,i} = -V_p \frac{\partial \langle p \rangle}{\partial x_i} + V_p \frac{\partial \langle \tau_{ij} \rangle}{\partial x_j} + F'_{p,i} \quad (8.13)$$

where $F'_{p,i}$ includes all the fluid dynamic forces other than the forces due to the undisturbed flow. If there are no forces due to particle-particle contact or body forces other than gravity, the equation for particle motion is

$$m_p \frac{dv_{p,i}}{dt} = -V_p \frac{\partial \langle p \rangle}{\partial x_i} + V_p \frac{\partial \langle \tau_{ij} \rangle}{\partial x_j} + F'_{p,i} + m_p g_i \quad (8.14)$$

If the flow is steady and the lift forces are unimportant, the equation of motion simplifies to

$$\frac{dv_{p,i}}{dt} = \frac{1}{\rho_d} \left(-\frac{\partial \langle p \rangle}{\partial x_i} + \frac{\partial \langle \tau_{ij} \rangle}{\partial x_j} \right) + \frac{f}{\tau_V} (\langle u_i \rangle - v_{p,i}) + g_i \quad (8.15)$$

The magnitude of the second term on the right, the force due to the gradient of the averaged shear stress, compared to the first term is

$$\frac{\left| \frac{\partial \langle \tau_{ij} \rangle}{\partial x_j} \right|}{\left| \frac{\partial \langle p \rangle}{\partial x} \right|} \sim \frac{\mu}{\rho_c U L} = \frac{1}{Re} \quad (8.16)$$

where U and L are the characteristic velocity and dimension of the flow. For most flows, the Reynolds number is much larger than unity so the second term can generally be neglected. The terms to be included in calculating the motion of the particles depends on the problem. The new position of the particle is obtained using Equation 8.5a.

The rotational rate of the computational particle as it moves along its path is obtained by integrating the Equation 4.161 from Chapter 4, namely

$$I \frac{d\omega_{p,i}}{dt} = T_i - \pi \mu D^3 \omega_{p,i} \quad (8.17)$$

where the transient terms have not been included. Impact with a wall or collision with another particle is modeled as a step change in particle rotation.

Also the temperature history of the computational particle along the trajectory is obtained by integrating the energy equation introduced in Chapter 4, namely

$$m_p c_d \frac{dT_p}{dt} = Nu \pi k'_c D (\langle T_c \rangle - T_p) + \dot{m}_p h_L \quad (8.18)$$

where the transient terms and temperature change associated with the “undisturbed flow” term have been neglected. Also, radiative heat transfer has not been included.

Other factors which affect the particle motion are carrier phase turbulence, boundary conditions at walls and collisions and coalescence.

Turbulent dispersion

Calculation of particle motion is feasible, for the most part, in laminar flows using established formulas for forces acting on the particle. Very small particles (less than a micron) will be in velocity equilibrium with the carrier flow and will follow the fluid motion. However, there can still be diffusion due to *Brownian motion* which is diffusion associated with molecular impact on the particles. Diffusion due to Brownian motion is presented in Appendix E. The fundamental assumption in Brownian motion is that the time between molecular impacts is long compared to the particle response time, so molecular impacts can be regarded as random impulses, that is, there is no history of the previous impact. In this case the variance of the displacement varies linearly with time and gas temperature

$$\langle x^2 \rangle = 2kBTt \quad (8.19)$$

where k is Boltzmann's constant and B is the mobility and depends on the particle size, fluid viscosity and the Cunningham correction factor (see Chapter 4).

The prediction of particle motion in turbulent flow fields is not straightforward because there are few detailed models for turbulence in single-phase flows, let alone multiphase flows. Moreover, the effects of turbulence on particle motion are significant except for massive particles which are unresponsive to turbulent velocity fluctuations. Therefore, the problem of particle-fluid interaction in turbulent flows has been the subject of extensive research.

Particles disperse in a turbulent flow field due to fluctuating fluid forces. This phenomenon is similar to the Brownian motion where dispersion is caused by a random force but now the forces are continuous and vary in magnitude throughout the field. If particles are small enough to follow the instantaneous fluid motion, particle dispersion is equal to that of a fluid element. In general, however, particles do not follow the fluid motion due to their inertia. Moreover, the velocity non-equilibrium characteristic of large particles enables these particles to interact with several turbulent eddies, which reduces the particle's residence time in each eddy and mitigates the influence of the eddy on the particle trajectory⁴. This effect is called the *crossing trajectory effect* (Csandy, 1963). Because of particle inertia, velocity non-equilibrium and the complexity of turbulent flows, the analysis of particle dispersion in turbulence is much more complicated than Brownian motion. The subject dates back to the pioneering work by G. I. Taylor (1921). Since that time,

⁴A source of particle-fluid velocity difference is the terminal velocity due to gravity.

many studies of particle dispersion in homogeneous turbulence have been reported in the literature (Synder & Lumley, 1971; Reeks, 1977; Wells & Stock, 1983; Wang & Stock, 1992; Pascal & Oesterlé 2000, Oesterlé 2009).

If the turbulent flow field is known, the local flow velocity can be incorporated directly into Equation 8.6 to evaluate the effects of turbulence on particle dispersion. Direct numerical simulation (DNS) provides a direct solution to the Navier-Stokes equations for turbulent flow with no empirical closure models. This scheme resolves the smallest length scale in turbulence (Komolgorov length scale). Through suitable interpolation, the velocity at any point in the flow field can be calculated. Because of the large number of grid points and computational time needed to achieve a statistically steady state, the scheme has been limited to small Reynolds numbers. Many (Squires & Eaton, 1991; Elghobashi & Truesdell, 1992, Ferrante & Elghobashi, 2003) have used DNS, assuming one-way coupling and point particles, to predict the effect of turbulence on particle dispersion. More recently, large eddy simulation (LES) has been used to provide the turbulent flow field for particle dispersion studies with one-way coupling (Sommerfeld, 2001, Berrouk et al., 2007, Jin et al., 2010).

In general, a detailed description of the turbulence is not available and other approaches are necessary. A very common approach is to regard the turbulent flow as a collection of turbulent eddies with discrete velocities and life times (or scales). In the eddy life time model, originally proposed by Yiu et al. (1978), the fluid velocity encountered by a particle is constant during the time that the particle spends in the eddy. The velocity is taken as the sum of the local time-averaged fluid velocity, \bar{u}_i , and a fluctuation velocity, u'_i selected from a Gaussian distribution⁵ with a variance proportional to the turbulence energy.

$$u_i = \bar{u}_i + u'_i \quad (8.20)$$

The same idea can be used with volume averaging so the local velocity is

$$u_i = \langle u_i \rangle + \delta u_i \quad (8.21)$$

where δu_i is the deviation of the velocity from the phase-averaged value. Using this velocity in the particle motion equation leads to the zigzag motion shown in Figure 8.5. Each arrow in the figure corresponds to an eddy encountered by the particle. The *eddy life time* is assumed equal to the Lagrangian integral time scale. Unfortunately, the Lagrangian time scale T_L is not known *a priori* so it is usually deduced from the Eulerian properties through the following relationship

$$T_L = \frac{\ell}{\sqrt{k}} \quad (8.22)$$

⁵The selection of a velocity through a random number generator is called the “Monte Carlo” method.

where ℓ is the Eulerian length scale and k is the local turbulence energy. The *Eulerian length scale* is defined by

$$\ell = \int_0^\infty R_E dr \quad (8.23)$$

where R_E is the *Eulerian correlation function* of the fluctuating velocities. Measurement of the Eulerian correlation function is much easier to carry out than measurement of the Lagrangian correlation function so Eulerian length scales, as well as velocity profiles and RMS velocity fluctuation data, are available for a wide variety of flow fields.

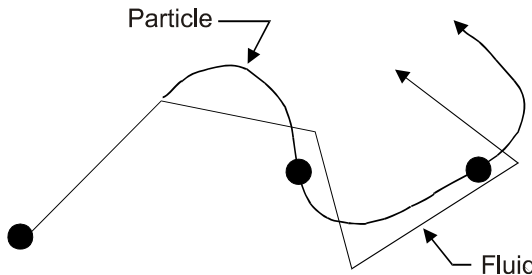


Figure 8.5: Particle motion in a turbulent velocity field.

A variety of other schemes to simulate particle dispersion due to turbulence have been proposed in the literature. Dukowicz (1980) suggested displacing the particle after every time step in the trajectory calculation by a distance selected randomly from a Gaussian distribution corresponding to a given particle dispersion coefficient. Lockwood et al. (1980) proposed augmenting at every time step the local fluid velocity by a value related to the local gas velocity gradient and turbulence energy. Jurewicz and Stock (1976) and later, Smith et al. (1981) added a *diffusional velocity* proportional to the gradient of the calculated particle bulk density to the calculated particle velocity. All these schemes fail to account for crossing trajectory effects.

Gosman and Ioannides (1981) introduced a scheme which was an improvement over Yuu et al.'s model because it accounted for the relative velocity between the turbulent eddy and the particle. This model was developed in concert with the two-equation ($k - \varepsilon$) model for the turbulence of the carrier phase. They estimated the length scale of the turbulent eddy to be

$$\ell = C_\mu \frac{k^{\frac{3}{2}}}{\epsilon} \quad (8.24)$$

and the eddy lifetime as

$$T_E = \frac{\ell}{\sqrt{\frac{2k}{3}}} \quad (8.25)$$

where ϵ is the dissipation rate and C_μ is an empirical constant. The residence time of a particle in an eddy due to a relative velocity between the particle and the eddy is

$$T_R = \frac{\ell}{|\mathbf{u} - \mathbf{v}|} \quad (8.26)$$

Thus, the interaction time between the fluid and the turbulent eddy is the minimum of the eddy lifetime and residence time,

$$T_I = \min(T_R, T_E) \quad (8.27)$$

The fluctuation velocity associated with the turbulent eddy is selected randomly from a Gaussian distribution with a variance equal to $2k/3$. The particle is assumed to be in the eddy for the duration of the interaction time and then a new eddy with lifetime and scale corresponding to the local turbulence field is established and a new fluctuation velocity is selected with a random number generator. This scheme has been used extensively in Lagrangian models because of its simplicity and robustness.

Several improvements of the Gosman and Ioannides scheme have appeared in the literature. Berlemont et al. (1990) proposed a technique to avoid the step change in velocity when the particle passes from one eddy to another. The relative displacement between the eddy and the particle is tracked with time and the velocity in the eddy is assumed to change according to the velocity correlation for the Eulerian field. Zhou and Leschziner (1991) propose a similar approach, but use a simpler technique for selection of the fluctuation velocity in the eddy. Lu et al. (1993) present a scheme whereby the relative displacement between the eddy and particle need only be recorded over one time step. A review of turbulent dispersion models is provided by Berlemont in Chapter 14 of the *Multiphase Flow Handbook* [Crowe (ed.), 2006].

A robust and reliable model for fluid velocity fluctuations has been proposed by Lain and Sommerfeld (2008). It will be reformulated here using the velocity deviations from volume averaging in lieu of the velocity fluctuations corresponding to time averaging. The velocity variation at the new particle position is given by

$$\delta u_{i,n+1} = \delta u_{i,n} R_{p,i}(\Delta t, \Delta r) + \sigma \sqrt{1 - R_{p,i}^2(\Delta t, \Delta r)} \xi_i \quad (8.28)$$

where $R_{p,i}(\Delta t, \Delta r)$ is the correlation function, σ is the mean fluctuation velocity given by

$$\sigma = \sqrt{2k_c/3} \quad (8.29)$$

and ξ_i is a Gaussian random number with mean zero and standard deviation of unity. The correlation function is expressed as the product of a Lagrangian and Eulerian part

$$R_{p,i}(\Delta t, \Delta r) = R_L(\Delta t) \times R_{E,ii}(\Delta r) \quad (8.30)$$

The Lagrangian part is determined from

$$R_L(\Delta t) = \exp(-\Delta t/T_L) \quad (8.31)$$

where T_L , the Lagrangian integral time scale is modeled as

$$T_L = 0.24 \frac{\sigma^2}{\epsilon_c} \quad (8.32)$$

where ϵ is the turbulence energy dissipation rate. The Eulerian part is obtained from the two-point auto-correlation function for homogeneous isotropic turbulence (Pope, 2000)

$$R_{ij} = \langle u'_i(x_i + r_i, t) u'_j(x_i, t) \rangle \quad (8.33)$$

and is expressed by

$$R_{E,ij} = [f(\Delta r) - g(\Delta r)] \frac{r_i r_j}{r^2} + g(\Delta r) \delta_{ij} \quad (8.34)$$

Only the main components are used so

$$R_{E,ii} = [f(\Delta r) - g(\Delta r)] \frac{r_i r_i}{r^2} + g(\Delta r) \quad (8.35)$$

The longitudinal and transverse correlation coefficients are

$$f(\Delta r) = \exp\left(-\frac{\Delta r}{L_E}\right) \quad g(\Delta r) = \left(1 - \frac{\Delta r}{2L_E}\right) \exp\left(-\frac{\Delta r}{L_E}\right) \quad (8.36)$$

and the integral length scales for the streamwise and lateral direction become (Lain and Sommerfeld, 2008)

$$L_E = 3T_L \sigma \quad (8.37)$$

This scheme was initially tested in isotropic turbulence (Sommerfeld, 2001). The continued use and refinement of the scheme has led to small changes in the empirical parameters.

Collisions and agglomeration

Collisions between droplets can result in bouncing, coalescence and fragmentation. A commonly used model for collisions of water droplets is that of O'Rourke (1981). An empirical expression is provided for critical collision angle between two colliding drops to establish if the collision is a grazing collision or results in the coalescence. The critical angle is given by

$$\sin^2 \phi_{\text{crit}} = \min \left[2.4 \frac{\gamma^3 - 2.4\gamma^2 + 2.7\gamma}{We}; 1 \right] \quad (8.38)$$

where $\gamma = D_1/D_2$ and We is the Weber number. If the collision angle is less than ϕ_{crit} , coalescence occurs. A detailed discussion is provided by Fritsching

in Chapter 8 and by Tropea and Roisman in Chapter 12 of the *Multiphase Flow Handbook* [Crowe (ed.), 2006].

In the Discrete Parcel Method, the details of individual particle positions and velocities are unavailable. The approach, described by Sommerfeld (2001), is to use a stochastic scheme in which a fictitious particle is generated with each time step and the likelihood of collision with this fictitious particle and the computational particle is assessed. The *collision frequency* between the two particles with diameters D_c and D_f is given by

$$f_c = \frac{\pi}{4} n(D_c + D_f)^2 |v_i(D_c) - v_i(D_f)| \quad (8.39)$$

where n is the number density, $v_i(D_c)$ and $v_i(D_f)$ are the velocities of the computational particle and the fictitious particle, respectively.

The velocity of the computational particle is composed of a local mean and RMS value. This information is obtained by an initial Lagrangian calculation with computational particles assuming no collisions to calculate the particle velocities, particle velocity RMS values and number density in each computational cell. These calculations may be done with discrete sizes of computational particles representing a size distribution.

As the Lagrangian calculation proceeds along a particle path, the local velocity of the computational particle is available. At each time step, the size of the fictitious particle is chosen randomly from the particle sizes present in the computational cell. The mean velocity of the fictitious particle is obtained from the information stored in the initial calculation. The fluctuation velocity of the fictional particle is obtained from

$$v'_{i,\text{fict}} = R(St)v'_{i,\text{real}} + \sigma_{i,p}\sqrt{1 - R^2(St)}\xi \quad (8.40)$$

where $v'_{i,\text{real}}$ is the fluctuation velocity of the real particle, $\sigma_{i,p}$ is the RMS value of the particle velocity, ξ is a Gaussian random number with zero mean and standard deviation of unity. The function $R(St)$ comes from a correlation developed from numerical simulations and is given by

$$R(St) = \exp(-0.55 \times St^{0.4}) \quad (8.41)$$

where St is the Stokes number based on the integral turbulent length scale.

Substituting the values for velocity difference into Equation 8.39 gives the frequency of collision with the fictitious particle. If the information for the fictitious particle size comes from a random selection of the discrete sizes, then n is the number density for that size. If the size is selected randomly from a number distribution of all the particle sizes, then n is the number density of all the particles in the cell. The collision probability is the product of the collision frequency and the time step, Δt , and it is assumed that a collision takes place if

$$RN < f_c \Delta t \quad (8.42)$$

where RN is a random number uniformly distributed between zero and unity. If a collision does take place, all the particles in the packet undergo collision.

The dynamic properties after collision are also calculated using a stochastic process. The collision takes place within a collision cylinder shown in Figure 8.6. The point of contact between the two colliding particles is selected randomly assuming that all possible contact configurations within the collision cross-section can occur with equal probability. Once the point of contact is established, the equations for post-collision velocities and rotational rates are determined from the hard sphere relationships developed in Chapter 5. The computational particle then proceeds on with the new conditions. Calculations with all the computational particles (parcels) yields new information for the size and velocity distributions in each cell and the calculations, including collisions, are repeated until the results show no further change.

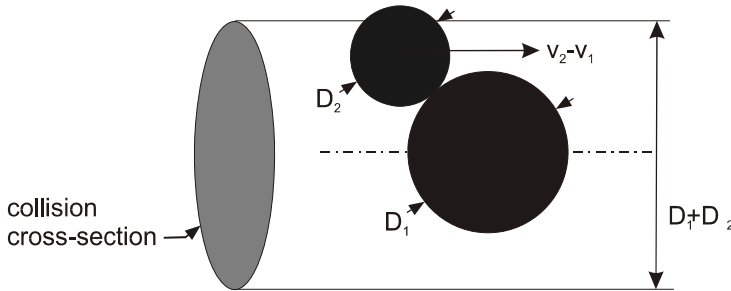


Figure 8.6: Collision cross-section for two colliding particles.

The above collision model assumes that particles travel in rectilinear trajectories until collision; that is, there is no effect of the flow field on the particle trajectory. However as a small particle approaches a large particle as shown in Figure 8.7, the flow field around the large particle (anchor particle) will tend to divert the trajectory of the small particle to avoid impact. There is a limiting particle trajectory which defines whether contact between the two particles will occur or not. Particles outside the limiting trajectory will miss the larger particle. The upstream displacement of this limiting trajectory from the stagnation streamline for the flow around the large particle is Y_i and the *impact efficiency* (also known as *collision efficiency*) is defined by

$$\eta_i = \left(\frac{2Y_i}{D_L} \right)^2 \quad (8.43)$$

The magnitude of the impact efficiency depends on the Stokes number associated with the characteristic time corresponding to the magnitude of the relative velocity between the small and large particle, namely

$$St_i = \frac{\rho_d D_S^2}{18\mu} \frac{|v_{i,S} - v_{i,L}|}{D_L} \quad (8.44)$$

where $v_{i,S}$ and $v_{i,L}$ are the velocity of the small and large particle, respectively. If the Stokes number is very large, the impact efficiency must approach

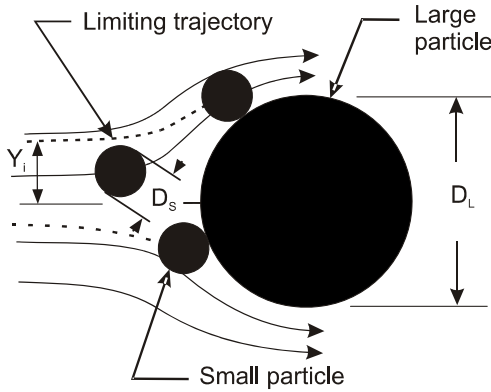


Figure 8.7: Small particle impact with large particle.

Re_L	a	b
>80	0.25	2.0
60-80	0.506	1.84
40	1.03	2.07
10-20	1.24	1.95
<1	0.65	3.7

Table 8.1: Values for the empirical constants a and b .

unity and for Stokes numbers approaching zero, the impact efficiency should approach zero. An empirical correlation for impact efficiency (Schuch and Löffler, 1978) as a function of Stokes number is

$$\eta_i = \left(\frac{St_i}{St_i + a} \right)^b \quad (8.45)$$

where a and b are empirical constants which depend on Reynolds number of the flow over the large particle; that is

$$Re_L = \frac{|v_{i,L}| D_L}{\nu} \quad (8.46)$$

The constants are given in Table 8.1.

The impact efficiency given by Equation 8.45 is valid for small particles with diameters less than 10% of the anchor particle. For larger impacting particles, the effective radius of the anchor particle is the sum of the radii of the small particle and anchor particle. For small particles, the collection efficiency does not approach zero because the random motion owing to Brownian motion enhances collection efficiency.

The criteria for the agglomeration of two dry particles depends on whether the energy before collision can be dissipated by the energy associated with

particle deformation and the van der Waal's attractive force (Ho and Sommerfeld, 2002) as presented in Chapter 5. The modes of collisions of several types of particles are discussed by Blei and Sommerfeld (2007) and Sommerfeld (2010). These models are important to many industrial processes, such as spray drying.

Boundary conditions

The boundary conditions are the result of particle contact with the wall.

In the case of droplets, there may be splattering or deposition. A detailed review of droplet breakup, coalescence and wall impact are provided by Tropea and Roisman in Chapter 12 of the *Multiphase Flow Handbook* [Crowe (ed.), 2006].

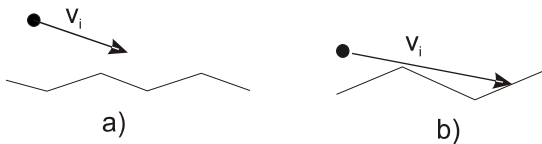


Figure 8.8: Particle impact with a rough wall. (a) Particle approaching rough wall, (b) shadow effect.

The particle collision with a rough wall is modeled as shown in Figure 8.8a. The roughness is simulated as a saw-tooth type configuration and the slope encountered by the computational particle is determined stochastically (Sommerfeld and Huber, 1999). The angle at which the particle impacts the wall, α_i , is given by

$$\alpha_i = \alpha + RN \quad (8.47)$$

where α is the approach angle with respect to a wall with no roughness and RN is a normally distributed random number with variance $\Delta\gamma$ which depends on the wall roughness and the particle size. One method to determine the value for $\Delta\gamma$ is by comparing numerical predictions for pressure drop in a channel with experiment. Particles approaching the rough wall at a low angle can miss the leeward side of the roughness as shown in Figure 8.8b. This is known as the “shadow effect.” This skews the probability toward the particle hitting the windward sides of the roughness elements.

The particle velocity and rotation after collision with the wall are given by the hard sphere equations in Chapter 5. Correlation of data with numerical simulations show that the particle-wall restitution and friction coefficients depend on the impact angle and the suggested relationships are (Lain and Sommerfeld, 2008)

$$e_w = \max(0.7, 1 - 0.0136\alpha_i) \quad (8.48)$$

$$\mu_w = \max(0.15, 0.5 - 0.0175\alpha_i) \quad (8.49)$$

The equations for particle-wall collisions were developed for spherical particles, so caution is advised for applications with non-spherical particles.

Small particles may remain deposited on the wall due to van der Waals forces.

8.2.2 Dense flows

The use of Lagrangian modeling in dense flows was introduced by Andrews and O'Rourke (1996) and identified as the multiphase particle-in-cell (MP-PIC) method. Particles with identical properties are grouped into parcels so the motion of a computational particle represents the dynamics of the parcel. The difference in the equation of motion compared to the non-dense equation, Equation 8.15, is that the effect of interparticle collisions is modeled by adding a force equal to the gradient of the *solids stress*. The equation of motion is

$$\frac{dv_{p,i}}{dt} = \frac{f}{\tau_V}(\langle u_i \rangle - v_{p,i}) - \frac{1}{\rho_d} \frac{\partial \langle p \rangle}{\partial x_i} + g_i - \frac{1}{\rho_d \alpha_d} \frac{\partial \tau}{\partial x_i} \quad (8.50)$$

where τ is the solids stress and f is the drag factor discussed in Chapter 4. An empirical equation often used for the solids stress is from Harris and Crighton (1994) and expressed as

$$\tau = \frac{P_s \alpha_d^\beta}{\alpha_{d,cp} - \alpha_d} \quad (8.51)$$

where P_s is an empirical constant with units of pressure, $\alpha_{d,cp}$ is the particle volume fraction at close packing and β is an empirical constant. Snider (2007) recommends modifying this expression by

$$\tau = \frac{P_s \alpha_d^\beta}{\max[(\alpha_{d,cp} - \alpha_d), \epsilon(1 - \alpha_d)]} \quad (8.52)$$

where ϵ is a small number of the order of 10^{-7} . This modification avoids the singularity produced as $\alpha_d \rightarrow \alpha_{d,cp}$.

When a parcel encounters a wall and rebounds, the following equations are used (Leboreiro et al., 2008)

$$v_{2,n} = -e_n v_{1,n} \quad (8.53)$$

$$v_{2,t} = -e_t v_{1,t} \quad (8.54)$$

where $v_{1,n}$, $v_{2,n}$, $v_{1,t}$ and $v_{2,t}$ are the impact (1) and rebound (2) velocities for the normal (n) and tangential (t) components. The normal and tangential restitution coefficients, e_n and e_t , are selected empirically.

The MP-PIC method proceeds by identifying parcels of particles, establishing starting conditions and then integrating Equation 8.50 for the parcel velocities and updating parcel position using Equation 8.5a. The properties of the cloud are resolved by mapping the particle volume fractions, particle velocity fractions, etc., on to an Eulerian grid. A commercial chemical reactor

may have 10^{13} particles and the properties of the cloud can be adequately represented by 10^6 parcels.

The MP-PIC method can be extended to dilute flows as the contribution of the gradient of the solids stress term becomes small. The details on particle dispersion due to turbulence and other effects would have to be added.

8.3 Two-fluid model

In the Two-Fluid Model, the particle cloud is treated as a continuous fluid. Equations are developed for the conservation of mass, momentum and energy at a point in the cloud. These equations are discretized into algebraic equations at the computational nodes in the field and solved using the same procedures as used for the conveying fluid. This is the Eulerian approach.

The constitutive equations for the particle cloud have been developed using the kinetic theory approach; that is, the kinetic theory developed at the molecular level for gases is applied to particles. The origin of the kinetic theory approach is generally accredited to Bagnold (1954) who derived an equation for particle pressure in uniform shear flow based on the square of the velocity gradient. Ogawa et al. (1980) recognized the importance of particle motion and formulated an equation for the kinetic energy produced by shear. Savage and Jeffrey (1981) noted the correspondence of random particle motion to the classical treatment for molecular motion and initiated the kinetic theory approach. Others (Jenkins and Savage, 1983; Lun et al., 1984; Johnson and Jackson, 1987) continued to develop the kinetic theory approach. Gidaspow (1994) summarizes the underlying ideas in his book. Van Wachem et al. (2001) summarizes the various forms of the equations

The subject of granular flows in which the interstitial fluid plays no role will not be addressed here. The recent book by Rao and Nott (2008) is an excellent source on this subject.

The kinetic theory approach is structured around the *granular temperature* defined as

$$\Theta = \frac{1}{3} \langle C^2 \rangle \quad (8.55)$$

where C is the deviation of the particle velocity from the mean velocity. The operator $\langle \rangle$ signifies the mean value based on the Gaussian distribution. The transport properties of the particulate cloud depend on the granular temperature, so an additional equation for the granular temperature is needed.

The continuity and momentum equations for the particle cloud as derived

by Jackson (1997 and 1998) and reported by van Wachem et al. (2001) are

$$\frac{\partial}{\partial t}(\alpha_d) + \frac{\partial}{\partial x_i}(\alpha_d \hat{v}_i) = 0 \quad (8.56a)$$

$$\begin{aligned} \alpha_d \rho_d \frac{\partial \hat{v}_i}{\partial t} + \alpha_d \rho_d \hat{v}_k \frac{\partial \hat{v}_i}{\partial x_k} &= \alpha_d \frac{\partial \langle \tau_{ij} \rangle}{\partial x_j} - \alpha_d \frac{\partial \langle p \rangle}{\partial x_i} \\ &+ \frac{\partial \tau_{s,ij}}{\partial x_j} - \frac{\partial p_s}{\partial x_i} + \beta(\langle u_i \rangle - \hat{v}_i) + \alpha_d \rho_d g_i \end{aligned} \quad (8.56b)$$

where p_s and $\tau_{s,ij}$ are the *solids pressure* and shear stress, respectively. The averaging procedure for the dispersed phase follows from the original work of Anderson and Jackson (1967) in which a weighting function, g , is used in the integral of properties over space. The solids volume fraction is defined as

$$\alpha_d = \sum_p V_p g(|x_i - x_{i,p}|) \quad (8.57)$$

where V_p is the volume of the particle p at location $x_{i,p}$ and the summation is carried out over all the particles in a unit volume. Similarly the product of the solids phase volume fraction and the average velocity of the solid phase, \hat{v}_i , is

$$\alpha_d \hat{v}_i = \sum_p V_p v_{i,p} g(|x_i - x_{i,p}|) \quad (8.58)$$

where $v_{i,p}$ is the velocity of particle p . The volume-average of the continuous phase is designated by $\langle \cdot \rangle$. These equations are the same as those in Gidaspow (1994) except for the pressure and shear stress forces due to the conveying fluid (the first and second terms on the RHS of Equation 8.56b).

There is no mention of the magnitude of the averaging volume required for definition of the volume averages. As discussed in Section 6.2, the volume has to contain sufficient particles such that the averaged properties do not depend on the size of the averaging volume. For example, an averaging volume would have to contain 10^4 particles to ensure that the number density would vary by less than 5% ($\pm 2.5\%$) at the 99% confidence level. For this case, a flow with $200 \mu\text{m}$ particles at a volume fraction of 0.1 would require an averaging volume with a diameter of 1 cm. This length would have to be much less than the system dimensions to assume the continuous variation of properties from point to point (averaging volume to averaging volume) through the system.

The equation for granular temperature (Gidaspow, 1994) is

$$\begin{aligned} \frac{3}{2} \left[\frac{\partial}{\partial t}(\rho_d \alpha_d \Theta) + \frac{\partial}{\partial x_i}(\alpha_d \rho_d \hat{v}_i \Theta) \right] \\ = [-p_s \delta_{ij} + \tau_{s,ij}] \frac{\partial \hat{v}_i}{\partial x_j} - \frac{\partial}{\partial x_i} \left(\kappa \frac{\partial \Theta}{\partial x_i} \right) - \gamma \end{aligned} \quad (8.59)$$

where the first term on the right is the conversion of energy due to pressure and shear in the particle phase, second is the conductivity of granular temperature

and the last is the dissipation due to inelastic collisions. One more term is added to the equations presented by van Wachem et al. (2001) to account for the transfer of fluctuating energy of the conveying fluid to the particles.

The solids pressure is related to the granular temperature by (Lun et al., 1984)

$$p_s = \rho_d \alpha_d \Theta [1 + 2(1+e)g_0\alpha_d] \quad (8.60)$$

where e is the coefficient of restitution and g_0 , identified as the radial distribution function, is given by

$$g_0 = \frac{3}{5} \left[1 - \left(\frac{\alpha_d}{\alpha_{d,\max}} \right)^{1/3} \right]^{-1} \quad (8.61)$$

and is related to the dimensionless distance between particles. Several other formulations have been used for the radial distribution function (van Wachem et al., 2001).

The solids shear stress tensor is given by

$$\tau_{s,ij} = \mu_s \left(\frac{\partial \hat{v}_i}{\partial x_j} + \frac{\partial \hat{v}_j}{\partial x_i} \right) + (\xi_s - \frac{2}{3}\mu_s) \frac{\partial \hat{v}_k}{\partial x_k} \delta_{ij} \quad (8.62)$$

where μ_s and ξ_s are the solids shear and bulk viscosity. The *solids phase bulk viscosity* is related to the granular temperature by (Lun et al., 1984)

$$\xi_s = \frac{4}{3} \alpha_d^2 \rho_d D g_0 (1+e) \sqrt{\frac{\Theta}{\pi}} \quad (8.63)$$

where D is the solids particle diameter.

The equation for the *solids phase shear viscosity* suggested by Gidaspow (1994) is

$$\mu_s = \frac{4}{3} \alpha_d^2 \rho_d D g_0 (1+e) \sqrt{\frac{\Theta}{\pi}} \quad (8.64)$$

$$+ \frac{2}{(1+e)g_0} \frac{5\sqrt{\pi}}{96} \rho_d D \Theta^{1/2} \left[1 + \frac{4}{5} (1+e) g_0 \alpha_d \right]^2 \quad (8.65)$$

Several other expressions for the solids shear viscosity have been proposed to account for various effects such as particle inelasticity, particle streaming and mean-free path constraints (Van Wachem et al., 2001).

Further formulations are needed for the *conductivity coefficient* and dissipation of granular temperature. For the coefficient of conductivity of granular temperature Gidaspow (1994) recommends

$$\kappa = 2 \alpha_d^2 \rho_d D g_0 (1+e) \sqrt{\frac{\Theta}{\pi}} \quad (8.66)$$

$$+ \frac{2}{(1+e)g_0} \frac{75\sqrt{\pi}}{384} \rho_d D \Theta^{1/2} \left[1 + \frac{6}{5} (1+e) g_0 \alpha_d \right]^2 \quad (8.67)$$

Once again, several other formulations have been suggested to account for various effects. The dissipation of granular temperature due to collisions is (Jenkins and Savage, 1983)

$$\gamma = 3(1 - e^2) \alpha_d^2 \rho_d g_0 \Theta \left[\frac{4}{D} \left(\frac{\Theta}{\pi} \right)^{1/2} - \frac{\partial \hat{v}_i}{\partial x_i} \right] \quad (8.68)$$

which is generally accepted without further corrections. Because the observation that the generation and dissipation are the largest contributors to granular temperature it is often more computationally efficient and expedient to set dissipation equal to the generation and have an algebraic equation for the granular temperature (van Wachem et al., 1999; McKeen and Pugsley, 2003).

The two-fluid equations are solved by expressing the differential equations as finite difference algebraic equations and using computational techniques to solve the systems of equations. Each phase is treated as a fluid and the interaction of the two phases has to be resolved at each time step.

The two-fluid model has often been described as two "interpenetrating continua" implying that properties of either phase can be quantified at any point in the mixture. This is obviously not the case because the cloud properties can only be defined over an averaging volume, not at a point. Perhaps the more appropriate description of the two-fluid model is that both phases share the same averaging volume.

The two fluid model has found extensive applications to modeling the dynamics of fluidized beds.

8.4 PDF models

PDF refers to the particle distribution function. In the PDF approach equations are developed for the phase space density, $W(v_i, x_i, t)$, which when integrated over all velocities would give the local number density at position x_i and time t .

$$n(x_i, t) = \int_{v_i} W dv_i \quad (8.69)$$

The phase space density can be extended to include particle mass and temperature. Equations can then be developed for probability density that a particle has a given position at a given time using concepts from kinetic theory or by using the Langevin equations. These models have been particularly useful for particle-turbulence interaction in which equations for carrier-particle velocity correlations have been developed with no empiricism. A review of PDF models up to 2005 is provided by Reeks and Simonin in Chapter 13 of the Multiphase Flow Handbook [Crowe (ed.), 2005].

Drobyshevsky, N.I.(2009) reports on a model for the PDF of particle motion in turbulent flow. The equation is

$$\frac{\partial P}{\partial t} + v_i \frac{\partial P}{\partial x_i} + \frac{\partial}{\partial v_i} \left[\left(\frac{U_i - v_i}{\tau_V} + F_i \right) P \right] = -\frac{1}{\tau_V} \frac{\partial}{\partial v_i} \overline{\overline{u'_i p}} + \frac{D_B}{\tau_V^2} \frac{\partial^2 P}{\partial v_i \partial v_i} \quad (8.70)$$

where F_i is a body force, such as gravity, acting on the particles, U_i is the averaged carrier-phase velocity and D_B is the Brownian diffusion coefficient. Correlations then developed for $\overline{\overline{u_i^p}}$ based on derivatives of the probability density function with space and particle velocity. Using this equation, additional equations for the particle average velocity and particle Reynolds stress are developed.

8.5 Summary

There are essentially three methods to model particle clouds in a fluid-particle flow: the Discrete Element Method (DEM), the Discrete Parcel Method (DPM) and the two-fluid (TF) model.

In the DEM equations are developed for each and every particle in the field accounting for the contact, fluid dynamic and body forces. The simultaneous solution for the motion and position of each element describes the properties of the cloud. This method has the advantage of including the details of particle interaction. The disadvantage is that the number of particles needed to model a practical problem is not within current computational capabilities. Also, the particle shapes are limited to spheres.

With the DPM, the particle field is broken down into identifiable parcels of particles which have the same properties and move together as a group. The motion of the parcel is quantified by the motion of a single particle in the parcel called the “computational” particle. In the non-dense application of the DPM, the equation of motion for the computational particle is extended to include turbulent fluctuations of the carrier phase, particle-particle collision and agglomeration and particle-wall contact. In the dense flow application, the equation of motion of the computational particle is extended to account for particle-particle interaction by including the gradient of the solids stress. By breaking down the particle cloud into parcels makes modeling gas-particle flow in practical applications computationally feasible. The effect of particle size distribution can easily be included by using parcels with different sized particles. The disadvantage of the method is the loss of details for particle-particle interaction.

The TF equations for the particle cloud are developed by treating the cloud as a fluid with a solids pressure, shear and normal bulk viscosity. Another parameter needed is the granular temperature, the energy associated with the particle fluctuation velocities. Relationships are developed from kinetic theory for the solids pressure and viscosities as function of granular temperature. The resulting differential equations are recast in finite difference form. The resulting set of algebraic equations are then solved for the properties of the particle cloud. The advantage of the two-fluid model is the similarity between the solution schemes for the conveying and particle phases. The disadvantage is the empiricism needed to formulate the constitutive equations for the transport coefficients and the assumption of uniform particle size.

Chapter 9

Numerical Modeling

The current literature abounds with the improvement of current and new numerical models for multiphase flows with droplets and particles. The state-of-the-art has advanced to the level that these computational models are not only fundamental components of multiphase-flow research but also find application to support engineering design. To adequately address the subject of numerical models for dispersed phase flows would require an extensive monograph. The purpose of this chapter is to present the basic ideas of the various modeling approaches and to show some examples of each.

The ideal numerical model would apply the Navier-Stokes equations to a field of particles in which the boundary conditions corresponding to each and every particle surface would be included. The fluid dynamic forces and body forces on the particles would be used to calculate the motion, rotation and the new position of every particle with each time step. The equations would be capable of handling the details of turbulent flow. Applying a numerical model with this capability to a large number of particles is not within current computational feasibility.

There have been several numerical models developed that directly apply the Navier-Stokes equations to a small number of moving and rotating particles in a laminar flow. Often these models are referred to as Direct Numerical Simulation or DNS. This is somewhat confusing because this category of simulations has more often been associated with detailed turbulence modeling of the carrier phase with point particle approximations for the dispersed phase. In this monograph, the term DNS will be reserved for the detailed turbulence modeling. The models which apply the Navier-Stokes equation to finite-size particles will be classified as Complete Numerical Simulations (CNS).

In this chapter the models developed for CNS will be briefly reviewed. Next the fundamental ideas underlying DNS and Large Eddy Simulation (LES) will be presented with their application to dispersed phase flows. Finally, the volume-averaged equations will be addressed with some numerical examples.

9.1 Complete Numerical Simulation

A simulation which solves the Navier-Stokes equations for the carrier fluid in a field of particles including the boundary conditions on each and every particle in the field would be the ideal. Such a simulation has been applied to flows with a small number of particles. The information gained from these studies have led to a better understanding of particle-fluid interaction. A good review of the various models can be found in Prosperetti and Tryggvason (2007).

One of the basic problems in the numerical simulation of fluid-particle flows is the generation of the grid. A body-fitted grid would have grid lines on the surface of the particle and boundary conditions could be easily applied at the nodal points. There are many packages available for grid generation, but they are computationally expensive. The expense is prohibitive for many particles that are moving and rotating. Another technique is to use a structured grid, like a Cartesian grid, and consider the details of the surfaces that cut through the computational cells. The properties at the nodes in the cells adjacent to the surface are adjusted to reflect the boundary conditions at the surface. Alternatively a forcing function can be added to the Navier-Stokes equations in the domain adjacent to the surfaces to enforce the correct boundary condition at the surface.

Another approach is the use of unstructured grids, that usually consist of triangular elements in two dimensions and tetrahedral shapes in three dimensions. With unstructured grids it is possible to align the grid with the local surface and also to use coarser grids in regions where the gradients are small. Still, the cost to model many particles is excessive.

The *Lattice Boltzmann method* (LBM) has become very popular in simulating fluid-particle flows. The LBM is derived from the lattice gas automata concept in which particles hop between nodes on a regular lattice configuration. Particle collision takes place at the nodes under specific rules for conservation of number and momentum. The LBM describes the change in particle populations instead of individual populations. A discrete velocity Boltzmann equation is written for the velocity distribution function. The numerical solution of these equations takes advantage of fast and massively parallel computers.

The treatment of solid boundaries by Ladd (1994a, 1994b) has made LBM a popular tool for fluid-particle flows. In the “bounce-back” method proposed by Ladd, there is a node in the fluid and a node in the solid and it is assumed that the fluid matter does not reach the node in the solid, but is bounced back to the fluid node. The bounce back occurs midway between the two nodes, which defines the wall. This leads to a step-wise boundary. There have been several schemes proposed to address this problem (Feng and Michaelides, 2009). The LBM will continue to develop and be an ever-more useful tool in particle-fluid simulation.

9.2 DNS models

Direct Numerical Simulation (DNS) is a high fidelity numerical solution to the unsteady, 3-D Navier-Stokes equations. The goal of this tool is to capture all the length and time scales associated with a turbulent flow. The effectiveness of DNS is based on maintaining minimal numerical error in estimating derivatives.

DNS is an effective tool to gain insight to understanding the coupling mechanisms in and the physics of complex fluid flows. However, because the Navier-Stokes are three-dimensional and inherently unsteady, the Reynolds number or domain size of DNS is limited by computational speed. In the 1990s, it appeared that most DNS studies were performed on a 64^3 - 512^3 domain with Reynolds numbers less than 100. Recently, Cabot and Cook (2006) used DNS to study a Rayleigh-Taylor instability on a $3,072^3$ domain with a reported Reynolds number of 32,000. To carry out a DNS computation for a Reynolds number of 10^4 (based on the Taylor microscale) may take the order of weeks (Davidson, 2004). Although DNS is very useful in the area of research, its extension to engineering applications is constrained by computational cost.

9.2.1 Model formulation and solution procedure

The equation formulation and solution procedures differ depending on the flow. There are two general categories of flows to which DNS is applied: homogeneous and heterogeneous flows.

In homogeneous flows, the turbulent velocity field and boundary conditions are periodic enabling analysis in cubic domains. These features allow one to transform the equations from physical space into Fourier space where the derivatives can be easily and accurately computed. The physical velocity at a single point in space is related to the spectral velocity by

$$u_i(\mathbf{x}, t) \equiv \sum_{\boldsymbol{\kappa}} e^{i\boldsymbol{\kappa}_n \cdot \mathbf{x}_n} \hat{u}_i(\boldsymbol{\kappa}, t) \quad (9.1)$$

where $\boldsymbol{\kappa}$ is the wave number vector, $\boldsymbol{\kappa} = \kappa_o(\mathbf{e}_1 n_1 + \mathbf{e}_2 n_2 + \mathbf{e}_3 n_3)$, and $\kappa_o = 2\pi/\mathcal{L}$ is the lowest wave number (Pope, 2000), where \mathcal{L} is the length of the domain. For constant density fluid with no body force, the Navier-Stokes equations are non-dimensionalized by a characteristic length (L) and velocity (U). The dimensionless Navier-Stokes equations are then

$$\frac{D\tilde{u}_i}{D\tilde{t}} = \frac{\partial \tilde{P}}{\partial \tilde{x}_i} + \frac{1}{\text{Re}_L} \frac{\partial^2 \tilde{u}_i}{\partial \tilde{x}_j^2} \quad (9.2)$$

where $\text{Re}_L = UL/\nu$. The above equation can now be transformed into Fourier space with 2π periodic boundary conditions yielding

$$\frac{\partial \hat{u}_i}{\partial \tilde{t}} = - \left(\delta_{ij} - \frac{\kappa_i \kappa_j}{\kappa^2} \right) \hat{C}_j - \frac{\kappa^2}{\text{Re}_L} \hat{u}_i \quad (9.3)$$

where \widehat{C}_j is the Fourier transform of the non-linear convection term (Pope, 2000).

Examples and procedures for simulating heterogeneous turbulent flows are discussed further in Pope (2000), Kim et al. (1987), and Le et al. (1997). These applications usually consist of complex geometries and non-periodic velocity fields and boundary conditions. For these reasons, unstructured mesh and physical boundary conditions are being incorporated into DNS. An alternative method is to combine homogeneous and heterogeneous techniques. For instance, turbulent flow between two parallel plates could be simulated with periodic boundary conditions in the streamwise and spanwise directions while the cross-stream direction incorporates a no-slip boundary condition at the wall.

Solution methods depend on the application. For isotropic homogeneous turbulence decay, pseudo-spectral methods are typically used. With pseudo-spectral methods, the non-linear term is evaluated in physical space then transformed into spectral space. This method introduces an aliasing error, which is known to produce wave numbers higher than κ_{\max} and is usually eliminated by truncation.

To obtain statistically steady solutions, energy is added at low wave numbers through a process called forcing described in further detail by Eswaran and Pope (1988).

The following is a solution procedure for homogeneous turbulence decay:

- Initialize the energy spectrum and the velocity field in spectral space
- Apply the Fast Fourier Transform (FFT) to transform the velocity field into physical space
- Compute the non-linear convection in physical space (C_j)
- Apply FFT to transform these terms to spectral space (\widehat{C}_j)
- Compute the remaining spectral terms
- Advance the velocity field according to the new time step

The solution of the DNS equations is considered valid when it is independent of the grid spacing and the energy spectrum shows the “rolloff” seen near the Kolmogorov length scale (Wilcox, 2004). In addition, the product of the Kolmogorov length scale and the highest wave number must be greater than one ($\eta\kappa_{\max} > 1$) and the aliasing effects must be resolved.

9.2.2 Application to particle-laden flows

Applying DNS to particle-laden flows is not a trivial task. The correct method is to treat each particle surface as a boundary condition, but this is costly when trying to understand the effects of many particles. Two techniques for

modeling particle-laden flows, the fully resolved approach and the *point force method*, are discussed below.

The fully resolved approach accounts for the smallest length and time scales around a particle surface. Burton and Eaton (2005) performed a high resolution DNS of turbulence around the surface of a single particle. For their conditions, they found that there was a strong effect within 1.5 particle diameters from the particle surface and a weaker effect between 1.5 and 5 particle diameters, after which there was no effect. Eaton (2009) pointed out that the presence of the particle effected a volume of fluid that was nearly 1000 times bigger than the volume of the particle and that when the particles are on the size of the smallest scales of turbulence they act as local dissipation mechanisms. For additional information on fully resolved approaches, the reader is referred to Bagchi and Balachandar (2003), Burton and Eaton (2005), Eaton (2009) and Balachandar and Eaton (2010).

The benefit of using DNS to resolve all the scales near the surface is unique in that it provides a detailed view of the flow that cannot be seen by experimental visualization. The drawback is the high computational cost. Another technique, referred to as the immersed boundary technique, is designed to capture some of the local effects of particle surfaces. Ulmann (2008) applied immersed boundary techniques to channel flow with $O(1000)$ particles. This technique was also used by Feng and Michaelides (2009) to investigate heat transfer in a field of multiple particles.

Point force methods treat particles as point forces within the turbulent flow. Although this method can be advantageous in studying the effects of many particles on the flow, it can be misinterpreted if not properly implemented.

Many researchers have added a particle drag force to the momentum equations to formulate the dusty-gas equations discussed in Chapter 6. This method assumes that the effect of a particle can be represented by applying a force on the fluid at the particle location. This implies that in order to add a point force, the particle size must be much smaller than the smallest turbulent length scale in the flow ($D \ll \eta$). Also representing the particle by an added force does not replicate the no slip condition at the particle surface and the ensuing velocity gradients. If $D \ll \eta$, then the point particle approach has some merit; otherwise, fully resolved simulations should be considered.

Non-dimensionalizing the momentum equations by a characteristic length (L) and velocity (U) gives

$$\frac{D\tilde{u}_i}{Dt} = \frac{\partial \tilde{P}}{\partial \tilde{x}_i} + \frac{1}{Re_L} \frac{\partial^2 \tilde{u}_i}{\partial \tilde{x}_j \partial \tilde{x}_j} + \tilde{g}_i - \tilde{F}_i \quad (9.4)$$

where $1/Re_L$ is the dimensionless kinematic viscosity and \tilde{F}_i is the dimensionless particle drag force described as

$$\tilde{F}_i = \frac{3\pi}{Re_L} \sum_p \frac{\tilde{D}^p}{V_{cell}} f^p (\tilde{u}_i - \tilde{v}_i^p) \quad (9.5)$$

For incompressible flows, the continuity equation is $\partial u_i / \partial x_i = 0$, and the dimensionless equation for the motion of particle p is

$$\frac{d\tilde{v}_i^p}{dt} = \frac{f^p}{St} (\tilde{u}_i - \tilde{v}_i^p) + \left(1 - \frac{\rho_c}{\rho_d}\right) \tilde{g}_i \quad (9.6)$$

Several researchers, Squires and Eaton (1990), Ferrante and Elghobashi (2003), and Schwarzkopf et al. (2009b), to name a few, applied variations of the above equations to different applications of particle laden turbulent flows. Overall, insights into preferential concentration, stokes number effects, and decay mechanisms have resulted from these studies.

9.2.3 Current status

Approximating particles as points within the carrier phase flow is a reasonable first step to modeling particle-laden turbulent flows. However, computational resources have advanced significantly since the point particle method was first proposed and fully resolved simulations have become feasible. Still, it will be a long time before computational capability will have advanced to the point that modeling industrial scale Reynolds numbers will be achievable.

Eaton (2009) points out that high-resolution simulations show that point-particle methods are inadequate outside of a certain particle size range. Furthermore, he also indicates that more research is needed to delineate the range of validity of the particle parameters for these techniques. Therefore, caution is advised when adopting point particle methods.

9.3 LES models

Large Eddy Simulation (LES) removes the Reynolds number limitation of DNS. Basically in LES the large, energy-containing eddies are computed exactly (within the accuracy of the computational scheme) and the small-scale structures are modeled. This idea is supported by the concept of the *energy cascade* in which the energy is generated by the large-scale structures and cascades to smaller scales where it is dissipated. LES is formulated by applying a filter function to the Navier-Stokes equations and generating a residual stress which is analogous to the Reynolds stress evolving from time averaging. Typically, the residual stress is accounted for by an eddy-viscosity model.

9.3.1 Model formulation

The Navier-Stokes equations are filtered by applying a filter function such as

$$\tilde{u}(x_i, t) = \int G(x_i - x'_i) u_i(x'_i, t) d^3 x'_i \quad (9.7)$$

By definition, the filter function G integrates to unity and decays to zero outside a certain spatial distance which is referred to as the filter range. It

is common to use a filter which is unity inside the filter range (usually the numerical grid dimension) and zero beyond¹. This is known as a “box” filter and is, essentially, volume averaging. Applying the filter to the Navier-Stokes equations gives

$$\frac{\partial \tilde{u}_i}{\partial x_i} = 0 \quad (9.8a)$$

$$\frac{\partial \tilde{u}_i}{\partial t} + \frac{\partial (\tilde{u}_i \tilde{u}_j)}{\partial x_j} = -\frac{1}{\rho} \frac{\partial \tilde{p}}{\partial x_i} + \frac{1}{\rho} \frac{\partial \tau_{ij}^R}{\partial x_j} + \nu \frac{\partial^2 \tilde{u}_i}{\partial x_j \partial x_j} \quad (9.8b)$$

where

$$\tau_{ij}^R = \rho (\tilde{u}_i \tilde{u}_j - \tilde{u}_i \tilde{u}_j)$$

is referred to as the *residual stress* and is similar to the Reynolds stress from Reynolds (time) averaging.

The most common formulation for the residual stress is

$$\tau_{ij}^R = \frac{1}{3} \delta_{ij} \tau_{kk}^R + \nu_s \left(\frac{\partial \tilde{u}_i}{\partial x_j} + \frac{\partial \tilde{u}_j}{\partial x_i} \right) \quad (9.9)$$

where ν_s is the *subgrid viscosity* for which a model has to be chosen. The most simple and popular choice for the subgrid viscosity is the Smagorinsky model (Smagorinsky, 1963) which is

$$\nu_s = (C_S L)^2 \left[\left(\frac{\partial \tilde{u}_i}{\partial x_j} + \frac{\partial \tilde{u}_j}{\partial x_i} \right) \left(\frac{\partial \tilde{u}_i}{\partial x_j} + \frac{\partial \tilde{u}_j}{\partial x_i} \right) \right]^{1/2} \quad (9.10)$$

where C_S is the Smagorinsky coefficient (usually taken as 0.1) and L is the order of the mesh size for the numerical model. The value of L is chosen to lie in the inertial subrange such that most of the energy-containing eddies are larger than L . Important refinements to the Smagorinsky model have been suggested by Germano et al. (1991).

9.3.2 Application to particle-laden flows

There have been several papers in the literature applying large eddy simulation to particle-laden flow. Many papers have been based on one-way coupling, meaning that the dispersed phase has no effect on the carrier flow. Like DNS, the fluid velocity at the position of the particle has to be obtained by interpolation. Wang and Squires (1996) applied LES to particle-laden channel flows and compared their results with DNS simulations. Berrouk et al. (2007) applied LES to high Reynolds number pipe flow and applied stochastic

¹ It is interesting to note that in the early derivation of the carrier-phase flow equations, Anderson and Jackson (1967) used a filtering function to carry out volume averaging. Thus the velocity resulting from their derivation was a “filtered” velocity. Unfortunately, they chose not to use a symbol or sign to indicate a filtered velocity so it has been incorrectly regarded by many model developers as the fluid velocity at a point and amenable to the same manipulations as the velocity in the Navier-Stokes equations.

modeling to inertial particle dispersion. Jin et al. (2010) investigated subgrid scale fluid velocity time scales as encountered by inertial particles in particle-laden turbulence.

There have been some applications of LES to include two-way coupling. Yuu (2001) reported the results of a numerical simulation of a gas-particle jet using LES with subgrid coupling. They used an equation for the turbulence energy of the carrier phase based on Reynolds averaging of the averaged equations. This is the same approach originally used by Chen and Wood (1985) which leads to nonphysical results as shown in Chapter 7. Other applications included Yamamoto et al. (2001) who modeled the downward gas-particle flow in a turbulent channel starting with the filtered LES equations. Also Bini and Jones (2008) basically use the same approach and applied it to a mixing layer.

These models start with fluid-phase conservation equations that are essentially the single-phase Navier-Stokes equations with terms added to account for the presence of the dispersed phase. These equations are invalid. In a single-phase flow, the flow properties can be defined at a point. In a multiphase flow, the properties of the carrier phase are averaged over a volume containing an adequate number of particles to define dispersed-phase properties, as discussed in Chapter 6. The continuity equation and momentum equation for an incompressible conveying phase assuming $\alpha_c \rightarrow 1$ are

$$\frac{\partial \langle u_i \rangle}{\partial x_i} = 0 \quad (9.11a)$$

$$\begin{aligned} \frac{\partial \langle u_i \rangle}{\partial t} + \frac{\partial}{\partial x_j} \langle u_i u_j \rangle &= -\frac{1}{\rho} \frac{\partial \langle p \rangle}{\partial x_i} + \frac{1}{\rho} \frac{\partial \langle \tau_{ij} \rangle}{\partial x_j} \\ &\quad + \alpha_d \frac{f}{\tau_V} (v_i - \langle u_i \rangle) + g_i \end{aligned} \quad (9.11b)$$

where $\langle \cdot \rangle$ signifies the volume (phase) average which is the same as the box filter. The averaging volume has to be large enough to ensure an acceptably small variation of α_d . In other words, it has to be large enough to ensure that the value to α_d is independent of the size of the averaging volume.

The question arises as to the suitability of using Equations 9.11a and 9.11b directly. Applying the same approach to obtain the residual stress as used for Equation 9.8b yields

$$\begin{aligned} \frac{\partial \langle u_i \rangle}{\partial t} + \frac{\partial}{\partial x_j} (\langle u_i \rangle \langle u_j \rangle) &= -\frac{1}{\rho} \frac{\partial \langle p \rangle}{\partial x_i} + \frac{1}{\rho} \frac{\partial \tau_{ij}^R}{\partial x_j} + \frac{1}{\rho} \frac{\partial \langle \tau_{ij} \rangle}{\partial x_j} \\ &\quad + \alpha_d \frac{f}{\tau_V} (v_i - \langle u_i \rangle) + g_i \end{aligned} \quad (9.12)$$

where now $\langle u_i \rangle$ is the filtered velocity and the residual stress is modeled as

$$\tau_{ij}^R = \frac{1}{3} \delta_{ij} \tau_{kk}^R + \nu_s \left(\frac{\partial \langle u_i \rangle}{\partial x_j} + \frac{\partial \langle u_j \rangle}{\partial x_i} \right) \quad (9.13)$$

There are two problems with this approach:

- The filter range cannot be chosen to separate the energy-containing eddies and dissipation scales, but rather must be large enough to define dispersed-phase properties with acceptable accuracy.
- The subgrid viscosity model would have to be extended to include the effect of the particles.

9.4 VANS numerical models

Typical engineering applications involve a very large number of particles or droplets. The time and resources to account for the forces and moments on every particle or droplet in the flow field is well beyond current computational capability. However, most engineers are not concerned about the detailed particle-fluid interaction, but are more interested in the gross effects as they relate to system design. The averaging techniques introduced in Chapter 6 enable the development of numerical models which can capture the effects of very large numbers of particles without excessive computational needs.

In single phase flows, the Navier-Stokes equations are averaged with time yielding a Reynolds stress which has to be approximated through $k-\epsilon$ models or Reynolds stress equations. These equations are referred to as Reynolds-averaged Navier-Stokes (RANS) equations. However, in a multiphase flow, properties per unit volume are needed so volume averaging is a common approach. Thus to distinguish the volume averaging from time averaging, the models described here are designated Volume-Averaged Navier-Stokes (VANS) equations.

One of the most important parameters in VANS is the force coupling term; that is, the force per unit volume that the particles apply to the conveying fluid. If all the particles are the same size and move with the same velocity, the force coupling term is

$$\alpha_d \frac{\rho_d f}{\tau_V} (v_i - \langle u_i \rangle) \quad (9.14)$$

where f is the drag factor. The volume fraction, α_d , is defined as

$$\alpha_d = \frac{NV_d}{V_c} \quad (9.15)$$

where V_d is the volume of one particle, N is the number of particles in the volume and V_c is the volume of the computational cell or averaging volume. The question is how many particles are needed in the volume to ensure an acceptably small variation in α_d ; that is, to assure that the value for α_d does not depend on the size of the averaging volume.

The same question was addressed for the conveying phase in Chapter 2. As the number of molecules included in a sampling volume is increased, the variation in number per unit volume becomes smaller. The volume for which an acceptably small variation occurs is identified as the point volume. For a

gas at standard conditions, a cube of $0.15 \mu\text{m}$ on side contains adequate molecules to define local properties, such as density and velocity, with a variation of less than 1%. Because this dimension is much smaller than typical system dimensions, the gas can be regarded as a continuum and the $0.15 \mu\text{m}$ cube as a point in the continuous field. For purposes of discussion here, a point value will mean the value of a continuous-phase property at a location in the flow.

As discussed in Chapter 6, the probability that a volume V contains N particles is given by the Poisson distribution

$$P(N) = (nV)^N \exp(-nV)/N! \quad (9.16)$$

where n is the number per unit volume and nV is the mean value. The dimension of the volume required to contain N particles is

$$\frac{\Delta x}{D} \simeq \left(\frac{N}{\alpha_d} \right)^{1/3} \quad (9.17)$$

where D is the particle diameter.

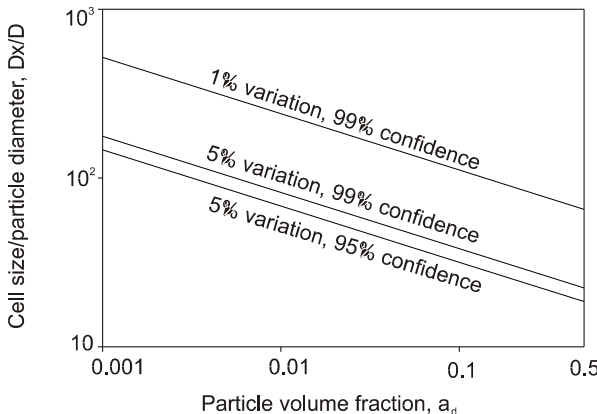


Figure 9.1: The cell size/particle diameter ratio required to control variation in particle cloud properties as a function of particle volume fraction.

The cell size/particle diameter ratio as a function of particle volume fraction for combinations of variation and confidence levels is shown in Figure 9.1. For example, for a particle volume fraction of 0.01 the ratio of cell size to particle diameter to yield a variation of less than 5% with a 95% confidence level is 68. A mixture with $100 \mu\text{m}$ particles would require an averaging volume with a cell size of 6.8 mm to maintain the variability within 5%. Thus to treat the averaged properties as continuously varying variables and to be able to define spatial derivatives of these properties, the system dimensions must be many magnitudes larger than a centimeter.

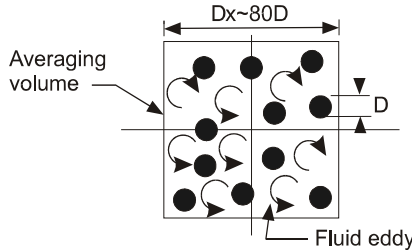


Figure 9.2: The presence of fluid eddies in an averaging volume to illustrate variation of continuous phase velocity throughout volume.

The instantaneous velocity of the continuous phase within the averaging volume cannot be taken as a uniform value. This idea is portrayed in Figure 9.2. For the 5% variation at the 99% confidence level and a particle volume fraction of 0.01, the dimension of the volume must be approximately 80 times larger than the particle diameter. The smallest scale for a fluid eddy in the volume would be the order of the Kolmogorov length scale which may be two orders of magnitude smaller than the side of the averaging volume. This means that the continuous phase velocity can vary significantly over the volume (especially if the flow is turbulent) and cannot be represented by a single value. With this observation, the conservation equations must be written with the phase-averaged properties. For example, the continuous phase continuity equation must be written as

$$\frac{\partial}{\partial t}(\rho_c \alpha_c) + \frac{\partial}{\partial x_i} (\rho_c \alpha_c \langle u_i \rangle) = 0 \quad (9.18)$$

where $\langle u_i \rangle$ is the phase-average (or interstitial average) over the volume and not be written as

$$\frac{\partial}{\partial t}(\rho_c \alpha_c) + \frac{\partial}{\partial x_i} (\rho_c \alpha_c u_i) = 0 \quad (9.19)$$

because using u_i implies that the velocity is uniform over the volume which is not the case. Thus it is important to recognize that the volume fraction and other carrier phase properties can only be defined for the averaging volume and not at a point; that is, the averaged property cannot be quantified at a point. However, the value of an averaged property can be associated with a point.

Another consequence related to the size of the averaging volume is the importance of the Reynolds stress in the momentum equation. The Reynolds stress is defined as

$$R_{ij} = \langle \delta u_i \delta u_j \rangle \quad (9.20)$$

where δu_i is the deviation of the local velocity from the volume-averaged value in the averaging volume. It is equivalent to the Reynolds stress evolving

from time averaging of the Navier-Stokes equations. Because the velocity of the carrier phase can vary significantly throughout the averaging volume, the Reynolds stress cannot be neglected nor discarded. It is common practice, as originally done by Anderson and Jackson (1967), to combine the Reynolds stress with the averaged shear stress and treat the combination as a Newtonian fluid. This approach does not take into account the significant influence of turbulence on the effective viscosity of the conveying phase.

A common misconception in developing turbulent models for fluid-particle flows is to start with the momentum equation for single-phase flow and add a term to account for coupling effects. For a mixture with a negligible particle volume fraction the momentum equation has often been written as

$$\rho_c \frac{\partial u_i}{\partial t} + \rho_c u_j \frac{\partial u_i}{\partial x_j} = - \frac{\partial p}{\partial x_i} + \frac{\partial}{\partial x_j} \left(\mu \frac{\partial u_i}{\partial x_j} \right) + \rho_d \frac{\alpha_d}{\tau_v} (v_i - u_i) \quad (9.21)$$

where the last term is the momentum coupling term. It is basically assumed that the velocities are point properties. Reynolds averaging procedures are then carried out to develop turbulence energy equations and so on. However, the velocities in this equation are volume-averaged; that is, $u_i \rightarrow \langle u_i \rangle$, and the fluctuation of a volume-averaged velocity is not turbulence,

$$\langle u_i \rangle' \neq u_i' \quad (9.22)$$

As shown in Chapter 7, turbulence models developed using Equation 9.21 yield non-physical results. For this reason, it is extremely important in writing out the conservation equations for the conveying phase to note the properties are volume-averaged values. This procedure avoids many misconceptions.

The solution of the conservation equations for the conveying phase requires setting up a grid system and expressing the equations in finite difference form. This is usually done by integrating the conservation equations over a computational cell and identifying the mass, momentum, and energy fluxes and source terms for property changes. The flow field is subdivided into a series of contiguous computational cells which exchange mass across cell boundaries. This corresponds to the “tank and tube” concept introduced by Gosman et al. in 1969. In the case of multiphase flow the computational cell also becomes the averaging volume. The resulting set of algebraic equations are solved simultaneously for each time step. The source terms are evaluated using the models for the particle clouds.

The general volume-averaged equation can be expressed as

$$\frac{\partial}{\partial t} (\alpha_c \rho_c \phi) + \frac{\partial}{\partial x_j} (\alpha_c \rho_c \langle u_j \rangle \phi) = \Gamma_\phi + S_\phi \quad (9.23)$$

where ϕ is a volume averaged property of the conveying phase, Γ_ϕ is the contribution to change due to the flow and S_ϕ is the source terms due to the dispersed phase.

The terms for Γ_ϕ for the conservation equations along with the turbulence energy, dissipation and Reynolds stress equations are provided in Table 9.1.

ϕ	Γ_ϕ
1	0
$\langle u_i \rangle$	$-\frac{\partial}{\partial x_j} (\alpha_c \rho_c R_{ij}) - \frac{\partial}{\partial x_i} \langle p \rangle + \frac{\partial}{\partial x_j} \langle \tau_{ij} \rangle + \alpha_c \rho_c g_i$
$\langle T_c \rangle$	$\alpha_c \langle \Phi \rangle + \frac{\partial}{\partial x_i} \left(\frac{k'_m}{c_c} \frac{\partial \langle T_c \rangle}{\partial x_i} \right)$
k_c	$\frac{\partial}{\partial x_j} \left(\rho_c \alpha_c \frac{\nu_T}{\sigma_k} \frac{\partial k_c}{\partial x_j} \right) - \rho_c \alpha_c R_{ij} \frac{\partial \langle u_i \rangle}{\partial x_j} - \alpha_c \rho_c \varepsilon_c$
ε_c	$-\alpha_c C'_{\varepsilon 1} \frac{\varepsilon_c}{k_c} R_{ij} \frac{\partial u_i}{\partial x_j} + \frac{\partial}{\partial x_i} \left(\alpha_c \left(\nu_c + \frac{\nu_T}{\sigma_\varepsilon} \right) \frac{\partial \varepsilon_c}{\partial x_i} \right) - C'_{\varepsilon 2} \alpha_c \frac{\varepsilon_c^2}{k_c}$
R_{ij}	$-\alpha_c \rho_c R_{jk} \frac{\partial \langle u_i \rangle}{\partial x_k} - \alpha_c \rho_c R_{ik} \frac{\partial \langle u_j \rangle}{\partial x_k} - C'_{r1} \alpha_c \rho_c \frac{\varepsilon_c}{k_c} \left(R_{ij} - \frac{1}{3} R_{kk} \delta_{ij} \right)$ $+ C'_{r2} \alpha_c \rho_c \left(R_{jk} \frac{\partial \langle u_i \rangle}{\partial x_k} + R_{ik} \frac{\partial \langle u_j \rangle}{\partial x_k} - \frac{2}{3} R_{km} \frac{\partial \langle u_k \rangle}{\partial x_m} \delta_{ij} \right)$ $+ C'_r \frac{\partial}{\partial x_k} \left(\alpha_c \rho_c R_{km} \frac{k_c}{\varepsilon_c} \frac{\partial R_{ij}}{\partial x_m} \right) - \frac{2}{3} \alpha_c \rho_c \varepsilon_c \delta_{ij}$
$R_{ij} = \frac{2}{3} k_c \delta_{ij} - \nu_T \left(\frac{\partial \langle u_i \rangle}{\partial x_j} + \frac{\partial \langle u_j \rangle}{\partial x_i} \right) \quad \langle \tau_{ij} \rangle = \mu \left(\frac{\partial \langle u_i \rangle}{\partial x_j} + \frac{\partial \langle u_j \rangle}{\partial x_i} \right)$	
$\nu_T = C_\mu k_c^2 / \varepsilon_c \quad \frac{k'_m}{c_c} = \alpha_c \left(\rho_c \frac{\nu_T}{\sigma_T} + k'_c \right) + \alpha_d k'_d \quad \sigma_T = 1.0$	
$\sigma_k = 1.0 \quad \sigma_\varepsilon = 1.3 \quad C_\mu = 0.09 \quad C'_{\varepsilon 1} = 1.44 \quad C'_{\varepsilon 2} = 1.92$	
$C'_r = 0.22 \quad C'_{r1} = 1.8 \quad C'_{r2} = 0.6$	

Table 9.1: The fluid-phase terms in the conservation equations.

The thermal energy dissipation term $\langle \Phi \rangle$ in the equation for $\langle T_c \rangle$ has no specific form and must be estimated based on the particular problem. In general, for low Mach number flows, it is negligible compared with the flux of thermal energy.

There are two options to evaluate the Reynolds stress. One is to use the $k - \varepsilon$ equations and the Boussinesq approximation and the other is to use the equation for Reynolds stress directly. The coefficients for the dissipation equation and Reynolds stress equation are based on single-phase flow and have not been adjusted for multiphase flow effects.

With Lagrangian methods the volume fraction of the conveying phase, α_c , is obtained by integrating the equations for the motion of a computational particle with time to find the position of each parcel at a given time. The equation of motion for the computational particle or a discrete particle in the DEM is

$$m_p \frac{dv_{p,i}}{dt} = F_{c,i} + F_{p,i} + m_p g_i \quad (9.24)$$

where $F_{c,i}$ is the force on the particle due to contact with neighboring particles, $F_{p,i}$ is the hydrodynamic force acting on the particle and $m_p g_i$ is the gravitational or body force. In the DPM, the particle contact force is not continuous and only acts instantaneously to change particle velocity and spin. With the MF-PIC method, the contact force is determined from the gradient of the solids-phase stress tensor. The pathlines and location of various particle parcels in a flow field is shown in Figure 9.3 at a given time. Several parcels will be located in the cell as shown. The volume fraction of the conveying phase is obtained from

$$\alpha_c = 1 - \frac{1}{V_c} \sum_p N_p V_p \quad (9.25)$$

where N_p is the number of real particles in parcel p and V_p is volume of an individual particle in the parcel and V_c is the cell volume. For DEM methods, the value for N_p is unity. The summation is carried out over all parcels in the cell.

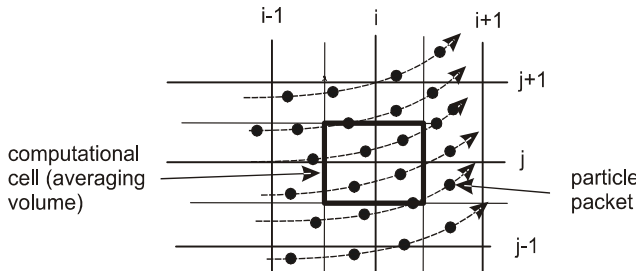


Figure 9.3: Averaging volume with particle packets (computational particles) passing through the volume.

ϕ	S_ϕ
1	$-(1/V_c) \sum_p N_p \dot{m}_p$
$\langle u_i \rangle$	$-(1/V_c) \sum_p N_p (\dot{m}_p v_{p,i} + F_{p,i})$
$\langle T_c \rangle$	$-(1/V_c) \sum_p N_p (\dot{m}_p T_{d,p} + m_p \frac{c_d}{c_c} \frac{N u_p}{2\tau_{T,p}} (\langle T_c \rangle - T_{d,p}))$
k_c	$(1/V_c) \sum_p N_p (\langle u_i \rangle - v_{p,i}) F'_{p,i}$
ε_c	$C_{\varepsilon 3} (\nu_c^2 / V_c) \sum_p N_p f_p \frac{ u_i - v_i _p^2}{D_p}$
R_{ij}	$(1/V_c) \sum_p N_p [(\langle u_i \rangle - v_{p,i}) F'_{p,j} + (\langle u_j \rangle - v_{p,j}) F'_{p,i}] - C_{r3} \alpha_d \rho_d (f/\tau_V) \begin{bmatrix} (\langle u_i \rangle - \tilde{v}_j)(\langle u_j \rangle - \tilde{v}_i) \\ (-\delta_{ij}/3) \langle u_m \rangle - \tilde{v}_m ^2 \end{bmatrix}$
$C_{3\varepsilon} = 0.058 C'_{\varepsilon 2} \text{Re}_r^{1.416}, \quad C_{r3} = 1.0$	

Table 9.2: Source terms for the conservation equations.

Following the same scheme, the mass source term is

$$s_{\text{mass}} = -\frac{1}{V_c} \sum_p N_p \dot{m}_p \quad (9.26)$$

where \dot{m}_p is the rate of change of mass of each particle in parcel p . For an evaporating or burning particle, $\dot{m}_p < 0$.

A summary of the equations for the particle source terms, S_ϕ , is shown in Table 9.2. The source terms for the turbulence energy, dissipation and Reynolds stress come from Appendix D; namely Equations D.49, D.109 and D.145. An additional source term for dissipation in dense flows is suggested in Appendix D but is not included in the table. The velocity vector, $u_{p,i}$, which appears in the source term for the dissipation is the carrier phase velocity at the position of the packet in the averaging volume. This presupposes that a model is available to estimate $u_{p,i}$, such as presented in Chapter 8. If however, no model is available or the choice is made not to include this refinement the phase-averaged velocity $\langle u_i \rangle$ is used for $u_{p,i}$ throughout the averaging volume.

The fluid dynamic force acting on the computational particle was presented in Chapter 4 (Equation 4.155) and is expressed as

$$F_{p,i} = -V_p \frac{\partial \langle p \rangle}{\partial x_i} + V_p \frac{\partial \langle \tau_{ij} \rangle}{\partial x_i} + F'_{p,i} \quad (9.27)$$

where

$$\begin{aligned}
& F'_{p,i} \\
= & m_p \left(\frac{f}{\tau_V} \right)_p (u_i - v_i) + C_{vm} \frac{\rho_c V_p}{2} \left(\frac{Du_{p,i}}{Dt} - \frac{dv_{p,i}}{dt} \right) \\
& + C_B \frac{3}{2} D^2 \sqrt{\pi \rho_c \mu_c} \left[\int_0^t \frac{\frac{d}{dt'} (u_{p,i} - v_{p,i})}{\sqrt{t-t'}} dt' + \frac{(u_{p,i} - v_{p,i})_0}{\sqrt{t}} \right] \\
& + C_S 1.61 D^2 (\mu_c \rho_c)^{\frac{1}{2}} |\omega_{c,i}|^{-\frac{1}{2}} \left[\varepsilon_{ijk} (u_{p,j} - v_{p,j}) \boldsymbol{\omega}_{c,k} \right] \\
& + \frac{1}{2} \rho_c A C_{LR} [\varepsilon_{ijk} \omega_{p,j} (v_{p,k} - u_{p,k})] |v_{p,i} - u_{p,i}|
\end{aligned}$$

and where, once again, the carrier-phase velocity, $u_{p,i}$ is the velocity at the position of the packet in the averaging volume. If the steady-state drag is the only significant force then

$$F'_{p,i} = m_p \left(\frac{f}{\tau_V} \right)_p (u_{p,i} - v_{p,i}) \quad (9.28)$$

where $v_{p,i}$ is the local velocity of computational particle p . As discussed above, if the choice is made not to include the variation of the carrier-phase velocity at the packet position, then the phase averaged velocity $\langle u_i \rangle$ is substituted for $u_{p,i}$ throughout the averaging volume². In this case, Equation 9.27 becomes identical to Equation 8.11 in Chapter 8.

There are two basic formulations to the carrier-phase momentum equation depending on the equations used for the force of the particles on the fluid per unit volume of mixture. One form is that shown in Table 9.1 for $\Gamma_{\langle u_i \rangle}$ with the fluid force, $F_{p,i}$, given by Equation 9.27. However, if $F'_{p,i}$ is taken as the fluid force on the particle, then $\Gamma_{\langle u_i \rangle}$ becomes

$$\Gamma_{\langle u_i \rangle} = - \frac{\partial}{\partial x_j} (\alpha_c \rho_c R_{ij}) - \alpha_c \frac{\partial}{\partial x_i} \langle p \rangle + \alpha_c \frac{\partial}{\partial x_j} \langle \tau_{ij} \rangle + \alpha_c \rho_c g_i \quad (9.29)$$

and the source term is expressed as

$$S_{\langle u \rangle} = - (1/V_c) \sum_p N_p (\dot{m}_p v_{p,i} + F'_{p,i}) \quad (9.30)$$

Another issue of importance is the force due to buoyancy. If the carrier phase momentum equation does not have the body force due to gravity; that is, if $\alpha_c \rho_c g_i$ is not included in $\Gamma_{\langle u_i \rangle}$, then a buoyancy term has to be added to particle motion equation, Equation 9.24, in the form

$$m_p \frac{dv_i}{dt} = F_{c,i} + F_{f,i} + m_p g_i - \rho_c V_p g_i \quad (9.31)$$

²The use of $\langle u_i \rangle$ in lieu of $u_{p,i}$ is the particle source terms introduces insignificant errors provided that $k_c \ll |\langle u_i \rangle|^2, |v_i|^2$. If $k_c \sim |\langle u_i \rangle|^2, |v_i|^2$ then the source terms must be re-evaluated to include the contribution of k_c .

The source term due to mass transfer in the thermal energy equation, $S_{(T_c)}$, is based on the assumption that fluid leaving the particle surface is the same as the conveying fluid. This is probably not true in the majority of situations so it has to be modified. The particle Nusselt number is obtained from relationships in Chapter 4.

For the case of dense flows, the Eulerian equations for the cloud are solved at each time step and the source terms are evaluated from the predicted cloud properties for each computational cell.

Many models that have appeared in the literature have used the RANS formulation and treated the carrier-phase velocities as point values which, as shown above, is incorrect. The main problem has been the modeling of turbulence in which Reynolds averaging has been used to develop models for turbulence energy and dissipation. The fact that the RANS equations have been used for many years for modeling the continuous phase and that reasonably good agreement with experimental data has been achieved does not justify their validity. It could very well be that the RANS equations will yield reasonable predictions of turbulence generation due to the effects of two-way coupling on flow gradients, but they will fail for particle-generated turbulence. The validity of any turbulence model should be tested with the data generated by Parthasarathy and Faeth (1990) and Mizukami et al. (1992) for particles falling in a quiescent medium. In this case, the particles are solely responsible for turbulence generation. Also the “ideal case” for testing turbulence models introduced in Chapter 7 can be used to assess a model’s validity.

The volume-averaged equations have been used extensively for modeling dense phase flows such a fluidized beds. In dense flows where the flow field is characteristically unsteady and non-homogeneous, the averaging volume has to be large enough to define the disperse phase properties as discussed above. There are problems with obtaining well-defined properties where there are rapid changes in dispersed phase properties such as at the boundary of a bubble in a fluidized bed. Also the particle volume fraction is small in the vicinity of the bubbles implying that a large averaging volume is needed to have small variations in dispersed phase properties. The problem, however, is mitigated somewhat by the fact that the coupling effects are small in those regions where the particle volume fractions are small. Thus the lack of accuracy in the phase-averaged property values in these regions do not compromise the solution as a whole.

There is no experimental technique readily available which can be used to compare local flow properties in dense flows with predictions using the volume-averaged equations. If the flow is steady, then measurements at different locations at different times can be used to quantify local average properties. However, most correlations with numerical modeling are based on visual observations such as bubble formation and bubble rise velocities or comparison with measured pressure fluctuations.

The large averaging volumes required for dilute flows question the use of the volume-averaged equations for subscale applications where system dimen-

sions are small. There are special situations, such as a fully developed flow, which permit the use of computational or averaging volumes with an adequate number of particles for acceptably small property variations. The use of computational particles, where a large number of particles are represented by a single particle, tends to mask the potential variations of properties in a computational cell.

9.4.1 Boundary conditions

The boundary conditions for the $k - \varepsilon$ model have to be modified to accommodate the turbulence production due to the particles. In single phase flow, the dissipation is equated to the production and the gradients are evaluated using the law of the wall. The dissipation at point x_p away from the wall is

$$\varepsilon = \frac{u_*^3}{\kappa x_p} \quad (9.32)$$

where u_* is the shear velocity. Assuming that the carrier phase velocity behaves according to the law of the wall incorporating the production of turbulence due to the particles, the dissipation equation becomes (Schwarzkopf, 2008)

$$\varepsilon_c = \frac{u_*^3}{\kappa x_p} + \frac{\beta}{\alpha_c \rho_c} |\langle u_i \rangle - \tilde{v}_i|^2 \quad (9.33)$$

where $\beta = \alpha_d \rho_d f / \tau_V$ and the velocities are evaluated at the node adjacent to the surface.

In single phase flow the turbulence kinetic energy at the point adjacent to the wall is

$$k = \frac{u_*^2}{\sqrt{C_\mu}} \quad (9.34)$$

The corresponding equation for particle-laden flow is

$$k_c = \frac{u_*^2}{\sqrt{C_\mu}} \left[1 + \frac{\beta \kappa x_p}{\alpha_c \rho_c u_*^3} |\langle u_i \rangle - \tilde{v}_i|^2 \right]^{1/2} \quad (9.35)$$

The above expressions are based on the law of the wall which may not be accurate for a two-phase boundary layer. However, they should provide a reasonable approximation until more accurate expressions are available.

9.4.2 Numerical solution procedures

The conventional numerical approach is to express the equations for the conveying fluid in finite difference form for values at the nodes of the computational grid. Solving the resulting system of algebraic equations yields a solution for the flow properties at the nodal points. Using the Lagrangian approach for the particle clouds, the particle motion is calculated to provide

source terms for the carrier phase equations. With the Eulerian approach the particle cloud equations are also expressed in finite difference form and solved using the same, or similar procedures, as used for the conveying phase. Iterative procedures are necessary to complete the solution; that is, to account for the interaction of the conveying and dispersed phases.

The majority of numerical schemes use staggered grids to separate the velocity and pressure nodes since the pressure gradient is responsible for fluid motion. Also, upwind differencing is used to achieve numerical stability.

Many of the basic concepts can be illustrated by applying the equations to the flow of a fluid-particle mixture in a quasi-one-dimensional duct.

Quasi-one-dimensional model

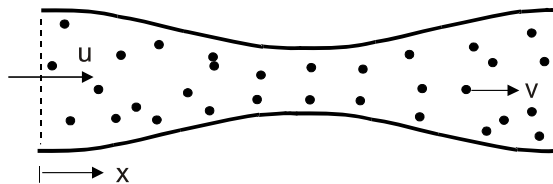


Figure 9.4: Particles flowing in a quasi-one-dimensional duct.

Consider the fluid-particle flow in the nozzle shown in Figure 9.4. In order to minimize the algebra, the continuous phase volume fraction, α_c , is taken to be unity and the fluid to be incompressible. There is no mass coupling and the particles are of uniform size. The pressure is known at the entrance and exit of the duct. The flow is steady and gravitational effects are negligible.

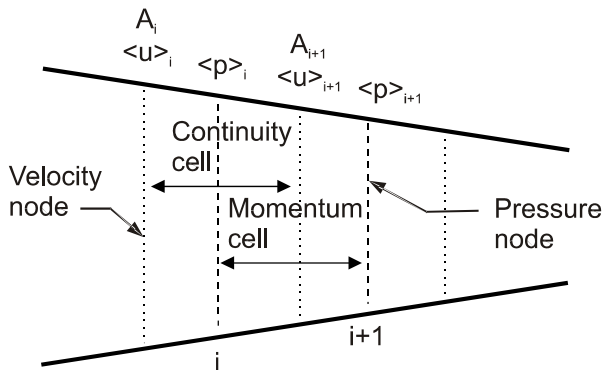


Figure 9.5: Continuity and momentum cells in a quasi-one-dimensional duct.

A computational cell in the duct is shown in Figure 9.5. The pressures are defined on the grid lines and the velocities are defined at points midway

between the grid lines as shown in the figure. The velocity node i is displaced half a grid spacing upstream from the pressure node i . This represents the staggered grid arrangement. The cell enclosed by the pressure nodes, or grid lines, is the *momentum cell*. The cell enclosed by the velocity nodes i and $i + 1$ is the *continuity cell*. Note also that the duct areas are defined at the velocity nodes and correspond to the average areas in the momentum cells.

The continuity equation for a steady flow is obtained from Equation 6.37 by setting $S_{\text{mass}} = 0$, $\alpha_c = 1$ and discarding the unsteady term³. The resulting equation is

$$\Delta(\rho_c A \langle u \rangle) = 0 \quad (9.36)$$

Applying the continuity equation to the continuity cell yields

$$\rho_c \langle u \rangle_i A_i - \rho_c \langle u \rangle_{i+1} A_{i+1} = 0 \quad (9.37)$$

The momentum equation for the steady quasi-one-dimensional flow of the carrier phase is given by Equation 6.71 with the unsteady term discarded, $S_{\text{mass}} = 0$, $\alpha_c = 1$ and the gravity term neglected. Applying the momentum equation to the momentum cell gives

$$\dot{M}_c \langle u \rangle_{i+1} - \dot{M}_c \langle u \rangle_i = A_{i+1}(p_i - \langle p \rangle_{i+1}) - \tau_w P \Delta x + S_{\langle u \rangle, i+1}$$

where

$$\dot{M}_c = \rho_c \langle u \rangle_i A_i \quad (9.38)$$

and $S_{\langle u \rangle, i+1}$ is the momentum coupling term at the $i + 1$ station due to the drag force of the particles on the fluid. The term $\tau_w P \Delta x$, where P is the local duct perimeter, represents the force due to shear stress at the wall. Notice that the specific momentum, namely the velocity, is not evaluated at the face of the momentum cell but at the velocity node upstream from the face. This corresponds to upwind differencing.

The source term can be expressed as (from Table 9.2)

$$S_{\langle u \rangle, i+1} = \sum_p N_p m_p \frac{f}{\tau_V} (v_{i+1} - \langle u \rangle_{i+1}) \quad (9.39)$$

For convenience, the particle parcel occupies the entire cell and the number of particles in the parcel is

$$N_p = \dot{N} \Delta t \quad (9.40)$$

where Δt is the time for the parcel to traverse the cell. Then the source term becomes

$$S_{\langle u \rangle, i+1} = \dot{M}_d \frac{f}{\tau_V} \Delta t (v_{i+1} - \langle u \rangle_{i+1}) \quad (9.41)$$

³In the case of constant fluid density and setting $\alpha_c = 1$, the product $\alpha_c \rho_c$ is constant and the unsteady term would be zero even in an unsteady flow.

where \dot{M}_d is the mass flow rate of the dispersed phase.

The wall friction term can also be expressed in terms of the mass flux by

$$\tau_w P \Delta x = \frac{1}{8} (f_c \rho \langle u \rangle A \Delta x)_{i+1} = \dot{M}_c \left(\frac{f_c \langle u \rangle \Delta x}{2D_H} \right)_{i+1} \quad (9.42)$$

where D_H is the hydraulic diameter and f_c is the Darcy-Weisbach friction factor. Substituting the momentum source term and friction term into the momentum equation gives

$$\begin{aligned} & \langle u_{i+1} \rangle \left[\dot{M}_c + \dot{M}_d \frac{f}{\tau_V} \Delta t + \dot{M}_c \left(\frac{f_c \Delta x}{2D_H} \right) \right] \\ &= \langle u \rangle_i \dot{M}_c + A_{i+1} (\langle p \rangle_i - \langle p \rangle_{i+1}) + \dot{M}_d \frac{f}{\tau_V} \Delta t v_{i+1} \end{aligned} \quad (9.43)$$

Dividing through by \dot{M}_c yields

$$\begin{aligned} & \langle u \rangle_{i+1} \left[1 + Z \frac{f}{\tau_V} \Delta t + \left(\frac{f_c \Delta x}{2D_H} \right) \right] \\ &= \langle u \rangle_i + \frac{A_{i+1}}{\dot{M}_c} (\langle p \rangle_i - \langle p \rangle_{i+1}) + Z \frac{f}{\tau_V} \Delta t v_{i+1} \end{aligned} \quad (9.44)$$

where Z is the loading and equal to \dot{M}_d / \dot{M}_c . Finally the momentum equation can be written as

$$\langle u \rangle_{i+1} = \frac{1}{E_{i+1}} \left[\langle u \rangle_i + \frac{A_{i+1}}{\dot{M}_c} (\langle p \rangle_i - \langle p \rangle_{i+1}) + Z \frac{f}{\tau_V} \Delta t v_{i+1} \right] \quad (9.45)$$

where

$$E_{i+1} = 1 + Z \frac{f}{\tau_V} \Delta t + \left(\frac{f_c \Delta x}{2D_H} \right) \quad (9.46)$$

Equation 9.45 represents a recursion relationship; that is, $\langle u \rangle_{i+1}$ is function of $\langle u \rangle_i$ so if $\langle u \rangle_1$ is known at the entrance, all the other $\langle u \rangle_i$ can be calculated to the end of the duct provided the values of all the other variables are available through the duct.

The continuity equation has not yet been applied and is needed to find the pressure distribution. The continuity equation is formulated in terms of a pressure correction. One begins by assuming that the velocity is a function of the pressure gradient only or, in other words, a function of the two pressures on each side of the velocity node. Applying a Taylor series expansion to estimate the effect of pressure change on velocity, one has

$$\langle u \rangle_{i+1} = \langle u^* \rangle_{i+1} + \frac{\partial \langle u \rangle_{i+1}}{\partial \langle p \rangle_i} (\langle p \rangle_i - \langle p \rangle_i^*) + \frac{\partial \langle u \rangle_{i+1}}{\partial \langle p \rangle_{i+1}} (\langle p \rangle_{i+1} - \langle p^* \rangle_{i+1}) \quad (9.47)$$

where the superscript * represents the values from the previous iteration. Taking the indicated derivatives of the momentum equation, Equation 9.45, results in

$$\frac{\partial \langle u \rangle_{i+1}}{\partial \langle p \rangle_i} = \frac{A_{i+1}}{\dot{M}_c E_{i+1}} \quad (9.48)$$

and

$$\frac{\partial \langle u \rangle_{i+1}}{\partial \langle p \rangle_{i+1}} = -\frac{A_{i+1}}{\dot{M}_c E_{i+1}} \quad (9.49)$$

Thus, the new velocity can be expressed as a function of the previously calculated velocity and the pressure change by

$$\langle u \rangle_{i+1} = \langle u^* \rangle_{i+1} + \frac{A_{i+1}}{\dot{M}_c E_{i+1}} (\Delta \langle p \rangle_i - \Delta \langle p \rangle_{i+1}) \quad (9.50)$$

where $\Delta \langle p \rangle_i = \langle p \rangle_i - \langle p^* \rangle_i$. The corresponding equation for $\langle u \rangle_i$ is

$$\langle u \rangle_i = \langle u^* \rangle_i + \frac{A_i}{\dot{M}_c E_i} (\langle \Delta p \rangle_{i-1} - \langle \Delta p \rangle_i) \quad (9.51)$$

Substituting the expressions for velocity back into the continuity equation yields the following equation for pressure change

$$\begin{aligned} (\rho_c \langle u \rangle A)_{i+1}^* - (\rho_c \langle u \rangle A)_i^* &= -\frac{\alpha_{c,i}^2 \rho_c A_i^2}{\dot{M}_c E_i} \Delta \langle p \rangle_{i-1} \\ &+ \left[\frac{\rho_c A_{i+1}^2}{\dot{M}_c E_{i+1}} + \frac{\alpha_{c,i}^2 \rho_c A_i^2}{\dot{M}_c E_i} \right] \Delta \langle p \rangle_i - \frac{\rho_c A_{i+1}^2}{\dot{M}_c E_{i+1}} \Delta \langle p \rangle_{i+1} \end{aligned} \quad (9.52)$$

In this problem the pressure at the beginning and end of the duct are fixed so Δp_1 and Δp_N are zero. This equation can be solved using the tri-diagonal matrix algorithm (TDMA)⁴. Notice that the left side of the equation is the form of the continuity equation based on the velocities from the previous iteration. When continuity is satisfied this term is zero. Thus the pressure changes calculated from Equation 9.52 correct the pressure field in a direction to satisfy the continuity equation. The reformulation of the continuity equation in terms of pressure is called the *SIMPLE* method (Patankar, 1980) which stands for “Semi-Implicit Method for Pressure-Linked Equations.”

A solution of the particle motion equation to evaluate v_i is needed to quantify the momentum source term in Equation 9.45. Writing the momentum equation for the particle cloud in a duct one obtains

$$\frac{dv_i}{dt} = v_i \frac{dv_i}{dx} = \frac{f}{\tau_V} (\langle u \rangle_i - v_i) - \frac{f_s |v_i| v_i}{2 D_H} \quad (9.53)$$

where the last term in the equation represents the resisting force on the particle cloud due to friction at the duct wall. The effect of the pressure gradient and the unsteady terms on the particle drag force have been neglected as well as the gravitational force. The factor f_s is the friction coefficient and D_H is the local hydraulic diameter.

Many schemes are available to integrate this equation such as the fourth-order Runge-Kutta methods, Adams-Basforth methods and so on. These

⁴TDMA is the tridiagonal matrix algorithm which is a procedure for solving a system of equations with a tridiagonal matrix (main diagonal and its two adjacent diagonals). A description of this algorithm can be found in Anderson et al. (1984).

will not be discussed here, but can be found in any textbook on numerical methods. A useful formulation for this problem where one wishes to find the velocity at specific distances, not times, is obtained by expressing the particle motion equation in implicit finite difference form as

$$v_{i+1} \frac{v_{i+1} - v_i}{\Delta x} = \frac{f}{\tau_V} (\langle u \rangle_{i+1} - v_{i+1}) - \frac{f_s |v_i| v_{i+1}}{2 D_H} \quad (9.54)$$

Expressing this equation as a quadratic equation for v_i one has

$$v_{i+1}^2 - v_{i+1} \left(v_i - \frac{f}{\tau_V} \Delta x - \frac{f_d |v_i|}{2 D_H} \Delta x \right) - \left(\frac{f}{\tau_V} \langle u \rangle_{i+1} \Delta x \right) = 0 \quad (9.55)$$

and solving for v_{i+1} yields

$$v_{i+1} = B + \sqrt{B^2 + C} \quad (9.56)$$

where

$$B = \frac{1}{2} \left(v_i - \frac{f}{\tau_V} \Delta x - \frac{f_d |v_i|}{2 D_H} \Delta x \right)$$

$$C = \frac{f}{\tau_V} \langle u \rangle_{i+1} \Delta x$$

This equation provides v_i at every station in the duct which is used to evaluate the momentum source term and the residence time in the cell ($\Delta t = \Delta x / v_{i+1}$).

The solution procedure is outlined in the flow diagram shown in Figure 9.6. First, a velocity $\langle u_i^* \rangle$ and pressure field $\langle p_i^* \rangle$ are assumed throughout the nozzle. Although it is not necessary, it is advantageous to have the initial flow assumptions satisfy the continuity equation. The particle velocity equations are then integrated to provide the parameters in the momentum source term. The continuous phase velocity distribution is calculated using the recursion formula for the carrier phase, Equation 9.45, with a relaxation factor, ω , in the form

$$\begin{aligned} \langle u \rangle_{i+1} &= (1 - \omega) \langle u^* \rangle_{i+1} + \frac{\omega}{E_{i+1}} [\langle u^* \rangle_i + \frac{A_{i+1}}{\dot{M}_c} (\langle p^* \rangle_i - \langle p^* \rangle_{i+1}) \\ &\quad + \frac{A_{i+1}}{\dot{M}_c} \rho_c g \Delta x + Z \frac{f}{\tau_V} \Delta t v_{i+1}] \end{aligned} \quad (9.57)$$

where ω is usually 0.5. The new velocity field calculated using this equation becomes the $\langle u_i^* \rangle$ field which is substituted into the equation for pressure change, Equation 9.52. If the continuity equation is satisfied, the solution has converged. If not, the TDMA is used to obtain new pressure changes and the velocities are corrected by applying Equations 9.50 and 9.51, while the pressure is updated by adding Δp to the previous pressure. Using the new fluid velocities, the particle velocity equations are implemented again and the source terms are updated. In this way, two-way coupling is included. For

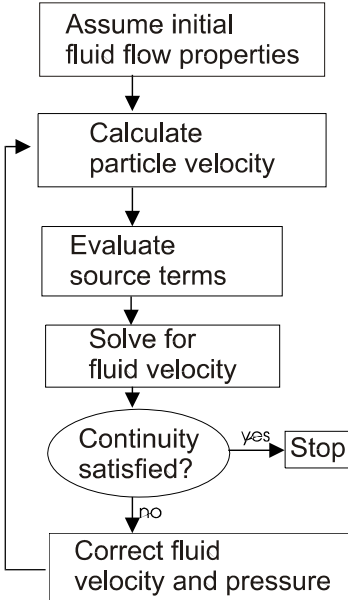


Figure 9.6: Flow diagram for solution scheme including two-phase coupling effects.

high levels of loadings, convergence is accelerated if the coupling terms are not updated on every iteration. The momentum equation is then solved again for the velocity distribution and the process is continued until convergence is achieved. Convergence is usually established by

$$\sum_{i=1}^{N-1} |\rho_c A_{i+1} \langle u^* \rangle_{i+1} - \rho_c A_i \langle u^* \rangle_i| \leq \epsilon \quad (9.58)$$

where ϵ is a preselected convergence criterion.

The main features of the above equations are the use of the staggered grid and the pressure-change equation to satisfy continuity. This algorithm carries over to two- and three-dimensional flows.

The same scheme can be used to obtain a numerical solution for unsteady flows. For an incompressible fluid, the continuity equation remains unchanged, but the momentum equation requires an additional term to account for the momentum change with time in a computational cell; namely, the unsteady term in Equation 6.71. The unsteady contribution appears as an additional source term in the momentum equation. The solution procedures are the same with convergence achieved at each time step when the continuity equation is satisfied.

The use of the staggered grid becomes unwieldy in multidimensional flows where separate continuity and momentum cells have to be identified in all

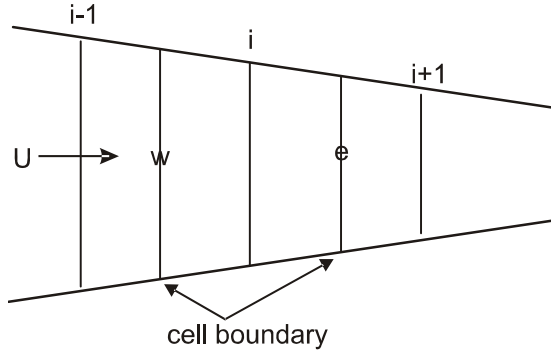


Figure 9.7: Non-staggered grid system in a quasi-one-dimensional duct.

coordinate directions. Rhie and Chow (1983) introduced a method to circumvent the need for a staggered grid. Consider the nonstaggered grid system shown in Figure 9.7. The steady flow continuity equation for cell i is

$$\rho_c \langle u \rangle A |_e - \rho_c \langle u \rangle A |_w = 0 \quad (9.59)$$

The momentum equation now uses a central difference formulation for the pressure gradient,

$$\dot{M}_c (\langle u \rangle_i - \langle u \rangle_{i-1}) = \frac{1}{2} (\langle p \rangle_{i-1} - \langle p \rangle_{i+1}) A_i - \frac{1}{8} (f_c \rho_c \langle u \rangle A \Delta x)_i + S_{\langle u \rangle, i} \quad (9.60)$$

which is a 2Δ center difference. For convenience, the momentum equation is written as

$$\langle u \rangle_i = -\frac{A_i}{\dot{M}_c} \frac{d \langle p \rangle}{dx} |_i \Delta x + B_i \quad (9.61)$$

where B_i is the remaining term. The velocity on the east face is the average of the velocity at the i and $i+1$ nodes,

$$\langle u \rangle_e = \frac{\langle u \rangle_i + \langle u \rangle_{i+1}}{2} = -\frac{A_e}{\dot{M}_c} \frac{1}{2} \left(\frac{d \langle p \rangle}{dx} |_i + \frac{d \langle p \rangle}{dx} |_{i+1} \right) \Delta x + \bar{B} \quad (9.62)$$

where \bar{B} is the average between the two nodes. When this equation is used in the continuity equation, an oscillation develops in the equation for pressure change. Rhie and Chow suggested that

$$\langle u_e \rangle + \frac{A_e}{\dot{M}_c} (\langle p \rangle_{i+1} - \langle p \rangle_i) = \frac{\langle u \rangle_i + \langle u \rangle_{i+1}}{2} + \frac{A_e}{\dot{M}_c} \frac{1}{2} \left(\frac{d \langle p \rangle}{dx} |_i + \frac{d \langle p \rangle}{dx} |_{i+1} \right) \Delta x \quad (9.63)$$

which yields the mass flux through the east face in the form

$$\rho A \langle u \rangle |_e = \rho A_e \frac{\langle u \rangle_i + \langle u \rangle_{i+1}}{2} - \rho \frac{A_e^2}{4\dot{M}_c} (-\langle p \rangle_{i-1} + 3\langle p \rangle_i - 3\langle p \rangle_{i+1} + \langle p \rangle_{i+2}) \quad (9.64)$$

A similar equation can be developed for the west face. The same equation, Equation 9.52, is used for the pressure change with the right side replaced by the mass flux given by the above equation. This approach essentially removes the pressure oscillations attributed to the 2Δ difference in the pressure gradient.

Multidimensional flows

The same approach used for numerical models of quasi-one-dimensional flows carries over directly to multidimensional flows. Consider the steady flow in a sudden expansion section shown in Figure 9.8.

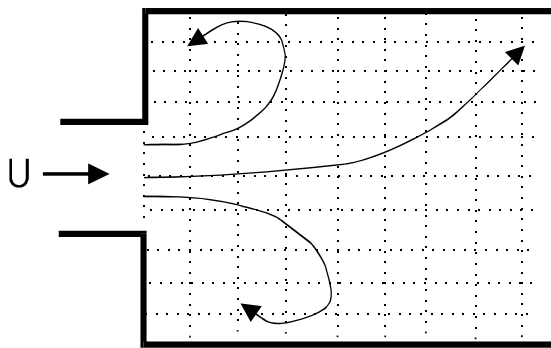


Figure 9.8: Sudden expansion section.

In this case the flow field is subdivided into a series of computational cells. The configuration of the cells around a grid point is shown in Figure 9.9. This is the staggered cell arrangement in two dimensions. A third momentum cell in the third direction would have to be added for three-dimensional flow. Many models have employed the Rhie-Chow scheme to avoid staggered grids and markedly reduce the number of computational cells. The finite difference forms of the conservation equations are written for each node yielding a set of algebraic equations for the flow properties. Higher order upwind difference schemes are used to reduce numerical diffusion. The solution of the equations applies the SIMPLE algorithm of Patankar (1980). Various schemes are used for time-stepping such as the second order backward difference scheme, fractional time steps or total variation diminishing (TVD) schemes. Various schemes to accelerate solutions and maintain accuracy are available in the literature.

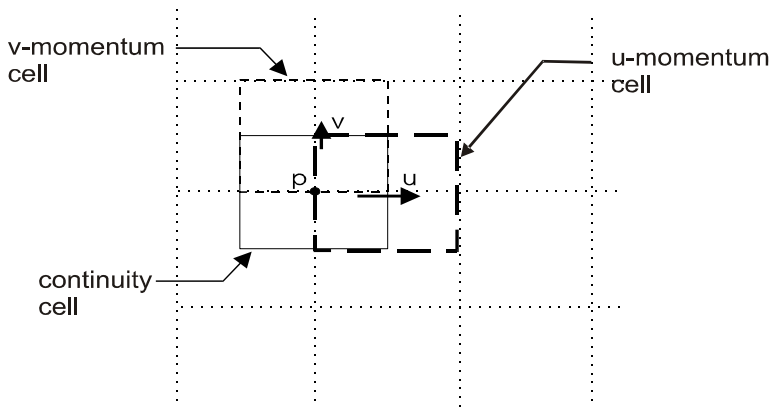


Figure 9.9: Staggered cell arrangement for two-dimensional flow.

There are some important issues that must be considered from the fact that the conservation equations for fully coupling flows do not provide the properties at a point but rather an averaged value. This feature has already been discussed with respect to turbulence modeling in that the usual $k - \varepsilon$ model based on time averaging of volume-averaged velocities is incorrect and leads to nonphysical results for simple flow fields as illustrated in Chapter 7.

9.4.3 Application examples

There are many examples of applications of the various numerical schemes reported in the literature. The purpose here is to present the results of a few and illustrate their capability. Many other examples are available in the technical literature.

Discrete element method (DEM)

Takeuchi et al. (2008) applied the DEM method to a three-dimensional, conical-based fluidized bed. The overall height and maximum diameter of the bed was 0.5 and 0.15 meters. Up to 3×10^5 particles were used in the simulation. The particles were 2.4 mm in diameter with a density of 1650 kg/m^3 . A soft sphere model was applied for particle collisions with the spring-dash pot model used to calculate contact forces as described in Chapter 5. The combination of Ergun and Wen-Yu model described in Chapter 4 was used to calculate the drag forces. Special boundary conditions were developed to handle the inclined wall. The continuous-phase momentum equations do not include a shear stress gradient of the continuous phase. This contribution is probably much less than the drag-force term but the authors do not acknowledge this assumption.

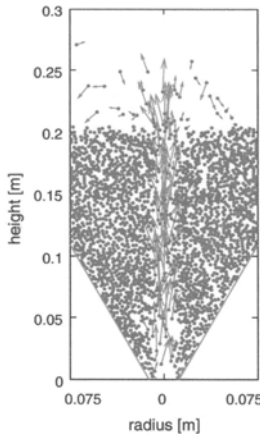


Figure 9.10: Results of DEM simulation applied to a spouted fluidized bed. (Reprinted from *Powder Technology*, **184**, Takeuchi, S., Wang, S. and Rhodes, M., Discrete element simulation of three-dimensional conical-base spouted beds, 141, 2008, with kind permission from Elsevier.)

The predicted particle distribution in a cross-section is shown in Figure 9.10. The results show a stream of particles moving up the central core, spouting out at the top of the bed and falling back to the surface of the bed. The authors claim good comparison with experimental measurements. The calculated motion of every particle provides a detailed description of the particle field. However, the bed is much smaller than a typical industrial scale.

Numerous modeling studies using DEM have continued to appear in the literature. Tsuji et al. (2008) have studied the formation of bubbles in a rectangular fluidized bed and compared the predictions with experiment. They tracked over 4×10^6 particles. Müller et al. (2008) simulated a two-dimensional bed with about 10^4 particles and compared the predictions for granular temperature with experiment. Shuyan et al. (2009) modeled a bubbling fluidized bed with two particle sizes using 800 large particles and 2200 small particles. Many other papers appear in the literature on the application of DEM. The number of particles needed to model industrial scale beds would require a prohibitively large number of particles which is beyond current computational capability. Still, the results of DEM simulations provide insight that is important to improved understanding of the basic processes.

Discrete parcel methods (DPM)

The predicted droplet trajectories in a pilot plant spray dryer using DPM are shown in Figure 9.11 (Verdurmen et al., 2004). The droplets enter through a swirl atomizer at the top and proceed downward. The fine droplets leave the

air outlet on the side of the dryer and the larger particles exit the bottom. The recirculation pattern of the particles in the dryer is evident. This simulation is used to predict moisture and temperature profiles in the dryer and the agreement with measurement is reasonable.

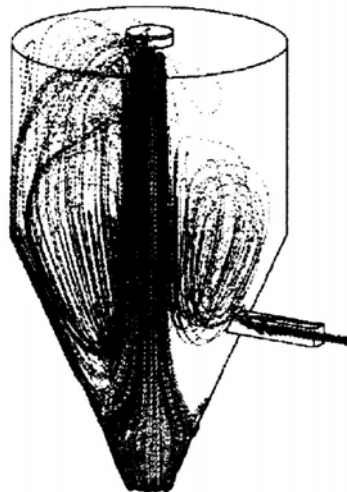


Figure 9.11: Predicted droplet trajectories in a spray dryer. (Reprinted from *Drying Technology*, **22**, Verdurnen, R.E.M., Menn, P., Ritzert, J., Blei, S., Nhumaio, G.C.S., Sonne Sørensen, T., Gunsing, M., Straatsma, J., Verschueren, M., Sibeijn, M., Schulte, G., Fritsching, U., Bauckhage, K., Tropea, C., Sommerfeld, M., Watkins, A.P., Yule, A.J., Schønfeldt, H., Simulation of agglomeration in spray drying installations: The EDECAD project, 1403, 2004, with kind permission from Taylor and Francis Group.)

DPM has been used in a wide diversity of applications. A few of the applications have been coal fired furnaces (Hill and Smoot, 1993), spray dryers (Dilber and Mereu, 1996), air pollution control (Griffiths and Boyson, 1996), fire suppression (Nam, 1995), materials processing (Muonio et al. 1996), aircraft icing (Valentine and Decker 1994) and gas-solids jets (Fairweather and Hurn, 2008). More recently Sommerfeld (2010) has applied DPM to particle agglomeration in gas-particle flows to better simulate processes in spray dryers.

The application of DPM to liquid sprays is discussed in Sirignano (1999) and Fritsching (2001).

Multiphase Particle-in-cell method (MP-PIC)

Snider (2007) applied the MP-PIC method to predict particle sedimentation in a three-dimensional vertical column. The computation was based on a bimodal distribution of glass beads. The smaller beads were between 125 and 150 μm with a material density of 992 kg/m^3 and the larger glass beads ranged from 177 to 219 μm with a material density of 2990 kg/m^3 . The calculation used a uniform random distribution within each size range. The initial volume fraction for the small beads was 3% and the large beads 1%.

The predicted particle sedimentation from the beginning to 500 seconds is shown in Figure 9.12. The clear liquid gradually appears at the top while the regions associated with the two particle sizes appear lower in the tube. The layer below the clear fluid contains the smaller particles, while the lower layer has both particle sizes. The predicted sedimentation rates compared well with experimental data.

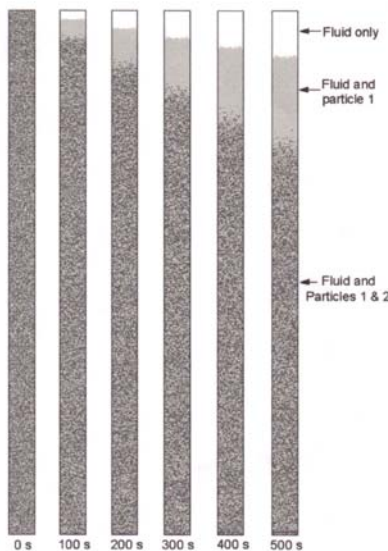


Figure 9.12: Sedimentation evaluation of two particle sizes in a vertical channel as predicted by MP-PIC method. (Reprinted from *Powder Technology*, **176**, Snider, D.M., Three fundamental granular flow experiments and CFD predictions, 36, 2007, with kind permission from Elsevier.)

The MP-PIC method has been applied to other problems. Snider (2001) applied the model to the impact of a particle jet on a flat plate. Using MP-PIC Snider (2007) also modeled sedimentation in a U-tube and from a hopper and showed good agreement with experiment. Snider and Banerjee (2010) also applied the model for ozone decomposition in a bubbling bed reactor.

Two-fluid model (TF)

McKeen and Pugsley (2003) applied the two-fluid model to a freely bubbling bed of fluid catalytic cracking (FCC) catalyst. Their goal was to compare the numerical simulation with an experimental study of a cylindrical bubbling bed which utilized an electrical capacitance tomography (ECT) imaging system. The bed was 1-m high. The Sauter mean diameter particle size was $79\text{ }\mu\text{m}$ with a material density of 1400 kg/m^3 . The test was run at different flow rates and parameters such as bed expansion, bubble diameters and rise velocities were measured.

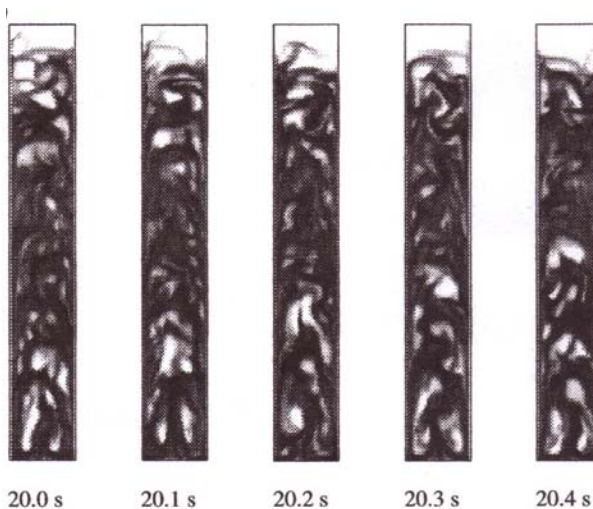


Figure 9.13: Bubbling in a fluidized bed as predicted using the two-fluid model. (Reprinted from *Powder Technology*, **129**, McKeen, T. and Pugsley, T., Simulation and experimental validation of a freely bubbling bed of FCC catalyst, 139, 2003, with kind permission from Elsevier.)

The model developed by McKeen and Pugsley was two-dimensional in order to avoid long computation times. They argue that the two-dimensional model captures the essence of the flow dynamics and is useful for comparison with experiment. They assumed uniform-sized particles with a diameter of $75\text{ }\mu\text{m}$ and a material density of 1500 kg/m^3 . The predicted bubbling motion of the bed is shown in Figure 9.13. They used a drag law suggested by Gibilaro et al. (1985) but had to modify the scale factor which corresponded to an agglomerate particle about twice the size of the actual particles in order to yield results for bed expansion comparable to the experimental findings.

Many other papers appear in the literature on the application of the two-fluid model. Taghipour et al. (2005) modeled a two-dimensional gas-solid

fluidized bed and report reasonable comparison with experiment. Benyahia et al. (2005) used the two-fluid model for turbulent gas-solids flow in a pipe. More recently Li et al. (2010) studied the effect of boundary conditions on the results for numerical simulation in fluidized beds.

PDF models

Kartushinsky et al. (2009) applied the PDF model to the flow of particles in a vertical pipe and compared the predictions with a RANS model. The results were somewhat similar but the solids concentration across the pipe were significantly different. The authors argue that the absence of lift forces in the PDF model is responsible for the discrepancy. Considerable more work needs to be done with PDF models to promote confidence in the model predictions for engineering applications.

9.5 Summary

A wide diversity of numerical models have been developed for fluid-particle flows. Detailed numerical simulations which solve the Navier-Stokes equations with the boundary conditions for each particle or droplet remain prohibitively expensive for practical applications. The DNS and LES provide viable models for the carrier phase turbulence and have yielded valuable insight for one-way coupling applications. The “point particle” model to represent the particles also has been useful, but lacks the detail for the flow gradients produced locally by the particles. The volume-averaged Navier-Stokes equations have been used to provide the continuous phase properties for the discrete element, discrete parcel methods as well as the two-fluid models. These models have specific applications in dilute and dense flows and are used routinely in industrial applications.

Chapter 10

Experimental Methods

Detailed measurements in two-phase flow processes and equipment are necessary for process and quality control, to characterize the global flow behavior and flow regimes, and to obtain local information about the characteristic properties in such flows. Moreover, experimental techniques are required to analyze the behavior and motion of individual particles in order to assess microprocesses occurring on the scale of the particles. Also, there is the need to determine typical particle dimensions and other characteristics including size distribution, shape and surface area.

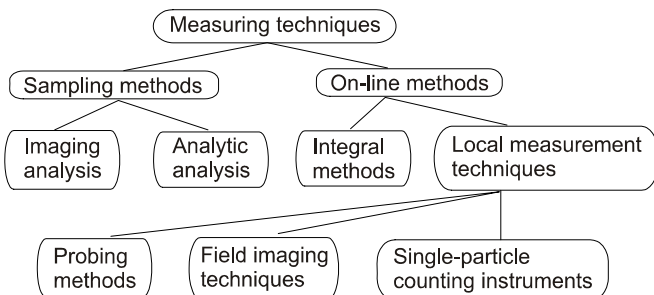


Figure 10.1: Categorization of measurement techniques for analysis of two-phase systems.

Numerous measuring techniques are available for such experimental studies on two-phase flows. These measuring techniques are categorized in certain groups according to their capabilities as shown in Figure 10.1. The first classification is based on the way the information is extracted from the two-phase system. Sampling methods are still quite frequently applied in the process industry and powder technology industries to provide a detailed characterization of bulk solids at the different stages of the process for quality and process

control (e.g., during milling or classification processes). Using mechanical sampling equipment, a number of characteristic samples of the bulk solids are collected and analyzed. The analysis of the samples may be performed using a microscope, mechanical methods such as sieving, fluid classification or sedimentation. Optical methods such as light scattering or light attenuation may also be applied. The result of these analyses could be, for example, characteristic dimensions of the particles, particle shape factors, equivalent particle diameters or particle surface area.

On-line measuring techniques are those methods which can be directly applied within the process or in a bypass line to analyze the properties of both the dispersed and continuous phases. Generally, these methods can be only applied in dispersed two-phase systems with relatively low concentrations of the particle phase. Moreover, on-line measuring techniques are widely used in research programs to characterize the development and the properties of a two-phase flow system. A further classification of on-line measurement techniques may be based on the spatial resolution of the measurement. Integral methods provide time-resolved, spatially averaged properties of two-phase systems over an entire cross-section of the flow or along a light beam passing through the flow, depending on the method applied.

On the other hand, local measurement techniques allow the determination of local properties in a two-phase system with a spatial resolution which depends on the measurement technique applied. Those techniques which allow the determination of the properties of a two-phase system with a high spatial resolution (i.e., probe volume dimensions of the order of $100\ \mu\text{m}$) are mainly based on optical principles. Such optical methods provide information either about the particle properties at a given instant of time or during a time sequence within a finite but relatively large probe volume (e.g., field imaging techniques, such as particle image velocimetry or holography), or are based on measuring the properties of the particles moving through a small finite probe volume within a certain measurement time interval (e.g., light scattering or laser-Doppler and phase-Doppler anemometry). Methods of the first kind are based on visualizing the particles by illuminating the probe volume and recording the images of the particles at a given instant of time or during a relatively short time sequence or at multiple times. Distribution functions of particle phase properties are therefore obtained for all particles that happen to be in the probe volume at a given instant of time. Hence, the result is weighted by the particle number concentration.

Instruments based on the second method are also called single particle counting techniques since they require that only one particle be in the probe volume at a given time. Therefore, the size of the probe volume quite often needs to be very small in order to fulfill this requirement, depending on the particle concentration. Since the particle phase properties and the respective distribution functions are obtained for all particles that pass through the probe volume during the measurement time, the result obtained by such methods is weighted by the particle number flux.

For the characterization of a two-phase flow system, the following properties of the dispersed phase are of primary interest:

- particle size (i.e., diameter of spherical particles, equivalent diameters of non-spherical particles),
- particle shape and surface area,
- particle concentration or mass flux,
- particle translational and rotational velocities,
- correlation between particle size and velocity.

In many cases, the velocity of the continuous phase (i.e., fluid) in the presence of the dispersed phase is also of interest in order to assess the influence of the particles on the fluid flow. All these properties are generally not obtained as single values, but as a distribution function which is characterized by a mean value, a standard deviation and higher moments of the distribution function.

Particle phase property	Sampling methods	On-line methods	
		Integral methods	Local measurement techniques
Size	Sieving Coulter principle Sedimentation	Laser diffraction	Light scattering Phase-Doppler anemometry
Concentration	Isokinetic sampling	Laser diffraction Light absorption	Isokinetic sampling Fiber optic probes Light scattering Phase-Doppler anemometry
Velocity	Direct velocity measurements are not possible with sampling methods	Correlation technique	Fiber optic probes Laser-Doppler anemometry Phase-Doppler anemometry Particle tracking velocimetry Particle image velocimetry

Table 10.1. Categorization of measurement techniques with respect to the measurable properties of a two-phase system.

A summary of the various measurement techniques and the dispersed phase properties which can be obtained by the above-described measurement techniques is given in Table 10.1. In the following sections, several of the most

common measurement techniques and their capabilities are introduced and the limitations of their applications are summarized.

10.1 Sampling methods

Sampling methods are mainly applied to characterize the shape, equivalent diameter, and surface areas of the solid particles. This implies that a number of representative samples of particles have to be collected from the flowing two-phase system or from the bulk solids conveyed on belts or stored in bins or containers. For this purpose, a number of sampling devices and methods are available which enable sampling from stationary or moving powders (Allen, 1990).

The sampling should be performed in such a way that the collected samples closely represent the properties of the two-phase system under consideration. Usually a number of samples have to be taken since the characteristics of the sample will vary and it is important to be sure that the samples represent the “real” powder. A further important aspect in sampling is the reduction of the sample size to obtain a sample for analysis which typically is on the order of a few grams, depending on the method of analysis. The reduction of the sample size is illustrated in Figure 10.2.

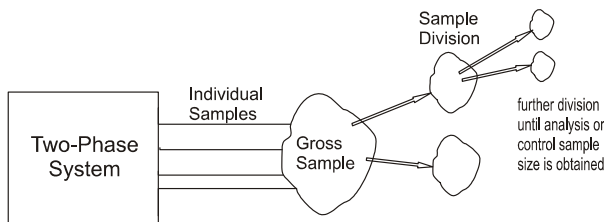


Figure 10.2: Process of sampling dividing.

First, a number of individual representative samples have to be taken from the two-phase system under consideration. This process can be continuous, such as sampling from a moving belt or a pneumatic conveying system, or periodic, such as sampling from bins or containers. These gross samples usually are too large for laboratory analysis and are therefore collected, mixed and then reduced to smaller size samples using a sample divider. This dividing process needs to be performed one or more times in order to obtain a sample size which can be analyzed. The required sample size depends on the method of analysis and usually is on the order of a few grams. The entire sampling process must be done very carefully in order to ensure that the sample for analysis is representative of the two-phase system under consideration. More details about sampling equipment and sampling procedures can be found in Allen (1990).

Various methods such as imaging methods, sieving, sedimentation, fluid classification or electrical sensing methods are available for the analysis of the particle samples with regard to shape, linear dimension and particle size. Some of the most common methods are summarized here. Others are described in detail by Allen (1990).

10.1.1 Imaging methods, microscopy

Microscopy is a direct imaging method to determine particle diameters, characteristic dimensions and shape factors of individual particles. This method can be used for the range of particle sizes between 1 and 200 μm . The lower limit is determined by diffraction (see Section 10.3.3 for more details) which may result in erroneous images of small particles. In order to determine number distributions of linear dimensions, a relatively large number of individual particles have to be analyzed, which is time consuming. In combination with digital image processing, however, such a direct imaging method becomes a powerful technique for particle characterization. The principle of this method is illustrated in Figure 10.3.

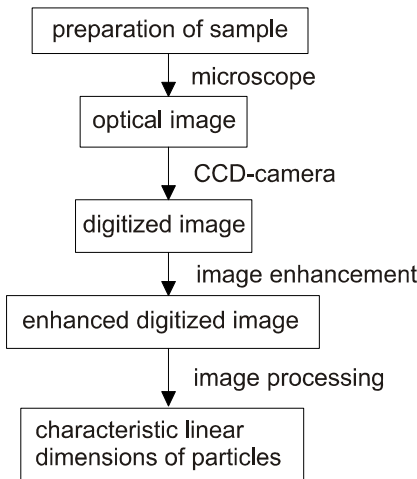


Figure 10.3: Principle of direct imaging technique using digital imaging processing.

First, the sample has to be prepared in such a way that individual particles can be observed under a microscope, which implies a uniform dispersion of the particles on the sample slide. Then, images of a number of particles are taken using a CCD camera (CCD stands for charged coupled device) which transforms the optical image into a digital image with a certain resolution of gray values for each pixel. Typically, 256 grey values are assigned to one pixel which is one of the photo-sensitive elements of the CCD array. The

number of pixels determines the spatial resolution of the CCD camera and is, for example, 512×1012 for a standard CCD camera. After enhancement of the image, i.e., thresholding and removing noise objects, the image can be processed to determine the characteristic linear dimensions of the particle. Such linear dimensions may be the diameter of spherical particles or certain dimensions of non-spherical particles, which are determined from the particle's projection since the image seen by a microscope is two-dimensional. Therefore, the analysis of non-spherical particles by an imaging method is biased by the fact that these particles will have a preferential orientation on the sample slide, i.e., plate-like particles will lay flat on the slide.

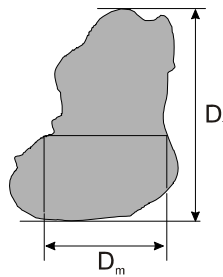


Figure 10.4: Typical linear dimensions of nonspherical particle or of images of nonspherical particle.

Typical statistical linear dimensions of non-spherical particles are shown in Figure 10.4. The so-called *Feret-diameter*, D_f , is the distance between two tangents on opposite sides of the particle image, parallel to some fixed direction. The *Martin-diameter*, D_m , is the length of the line which bisects the particle image and should be obtained in a fixed direction for one analysis. Other linear dimensions of the particle image are the *maximum chord* $D_{c,max}$, the largest dimension and the perimeter diameter, which is the diameter of a circle having the same circumference as the perimeter of the image. Moreover, a *projected area diameter* may be determined which is the diameter of a circle having the same area as the projected image of the particle.

10.1.2 Sieving analysis

Sieving is one of the oldest, simplest and most widely used methods for particle size classification. It yields the mass fractions of particles in specific size intervals from which the resulting particle size distribution can be obtained. Sieving analysis can be performed with a wide range of mesh sizes, from approximately $5 \mu\text{m}$ to about 125 mm . In order to cover this size range, different sieves and sieving methods have to be used. Also, the properties of the bulk solids determine the method of sieving to be used. Woven sieves are

quite often characterized on the basis of mesh size, which is the number of wires per linear measure (dimension). For example, the opening for a 400-mesh sieve is $37 \mu\text{m}$ and the wire thickness is $26.5 \mu\text{m}$ (see, for example, American ASTM). This corresponds to an open sieve area of 34%.

Sieving method	Particle size range	Particle properties
Hand or machine sieving	63-125 μm	Dry powder
Air-jet sieving	10-500 μm	Cohesive and wet powder
Wet sieving with micro-mesh sieves	5-50 μm	Wet powder

Table 10.2. Sieving methods with respect to particle size range and particle properties.

A classification of the sieving methods to be applied based on the size of the particles and the particle properties is given in Table 10.2. The sieves used for hand and machine sieving are usually woven from metal wires which are soldered together and clamped to the bottom of a cylindrical container. For sieving analysis, a series of sieves are mounted on top of one another with decreasing mesh size from top to bottom as shown in Figure 10.5.

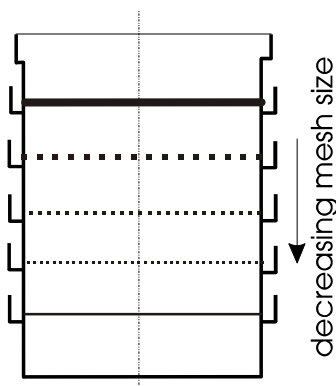


Figure 10.5: Arrangement of sieves for particle size analysis.

The powder to be analyzed is put into the upper sieve bin. By shaking the apparatus for a certain period of time, the particles which are smaller than the mesh size fall through the sieves and accumulate in the sieve bins according to the particle size. This suggests that for a series of sieves with mesh sizes of 1.6, 0.8, 0.4, 0.2 and 0.1 mm, particles in the size intervals $>1.6 \text{ mm}$, $0.8 - 1.6 \text{ mm}$, $0.4 - 0.8 \text{ mm}$, $0.2 - 0.4 \text{ mm}$, $0.1 - 0.2 \text{ mm}$ and $<0.1 \text{ mm}$ are collected in the different sieve bins. Then the content in the different sieve bins is weighed and a histogram of the particle size versus the mass fraction or probability

density in each size interval is obtained. This corresponds to the discrete mass distribution discussed in Chapter 3. The mass fraction in each size interval is determined from $\Delta m_i/m$ where Δm_i is the mass of particles collected in the different sieve bins and m is the total mass of the analysis sample. The mass probability density (frequency) distribution $f_m(D_i)$ is obtained from¹

$$f_m(D_i) \simeq \frac{\Delta m_i}{m\Delta D_i} \quad (10.1)$$

where ΔD_i is the size interval $D_{i+1} - D_i$. A typical histogram of such an analysis is shown in Figure 10.6. The sample size for sieve analysis with sieves which have a 200-mm bin diameter usually range between 100 and 200 grams. The sieving time for dry powder is dependent on the mesh size and generally lies in the range specified in Table 10.3.

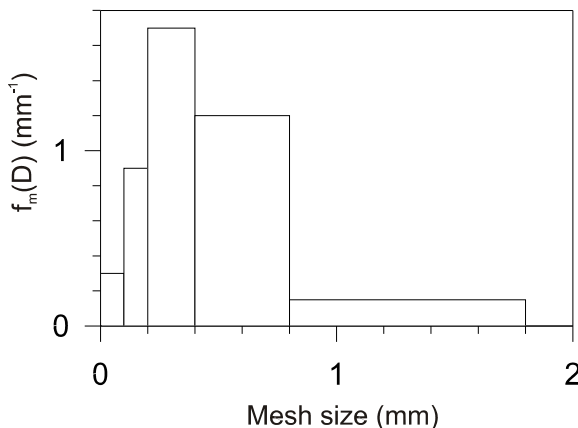


Figure 10.6: Histogram of particle size distribution.

Mesh size	Sieving times
$> 160 \mu\text{m}$	5–10 min
71–60 μm	10–20 min
40–71 μm	20–30 min

Table 10.3. Approximate sieving times for different mesh sizes.

Machine sieving is usually performed by placing the set of sieves on a vibrating support. Hand or machine sieving of powders which are cohesive or humid may be enhanced by putting additional large granular materials

¹The continuous mass frequency distribution is defined as the limit

$$f_m(D) = \lim_{\Delta D \rightarrow 0} \frac{\Delta m_i}{m\Delta D}.$$

on the sieves. This leads to de-agglomeration of the powder and avoids the blockage of the apertures; however, the sieving time is increased. Other sieving methods, such as air-jet sieving (see Table 10.2), should be used for powders which are difficult to sieve. For very fine and wet powders, wet sieving is recommended. Electroformed micromesh sieves are generally used for this method.

10.1.3 Sedimentation methods

The principle of the *sedimentation method* is based on recording the sedimentation of powders dispersed in a liquid and deriving the particle size distribution from the measured temporal change of the particle concentration. Since the sedimentation process is governed by the free-fall velocity of the particles, a free-fall or Stokes diameter will be determined. Usually small sedimentation columns are used to perform the measurement. Two methods may be applied to introduce the powder into the liquid. In the two-layer method, a thin layer of powder is introduced at the top of the liquid column; while in the second method, the powder is uniformly dispersed in the liquid by shaking the sedimentation column or by ultrasonic agitation before measurement. In order to maintain a stabilized dispersion, wetting agents are quite often introduced into the liquid to reduce the attractive forces and to increase the repulsive forces between the particles in the suspension.

Two approaches may be used to determine the particle size distribution using the sedimentation method. The first approach is the incremental method in which the rate of change of particle density or concentration is measured at a given location in the sedimentation column. In the second approach, the rate at which the particles accumulate at the bottom of the sedimentation column is measured. This method is called the cumulative method.

Incremental method

As stated above, the incremental method is based on the measurement of the temporal change of the particle concentration close to the bottom of the sedimentation column. The powder has to be homogeneously dispersed throughout the column at the beginning of the experiment so that the initial concentration at the measurement location corresponds to the overall particle concentration, i.e., the mass of particles introduced into the column divided by the volume of the mixture. Various methods such as light attenuation or X-ray attenuation can be applied for the measurement of the density or the concentration of the particles at the measurement location. The *light attenuation method* is based on transmitting a narrow horizontal beam of parallel light through the sedimentation cell at a known depth H and recording the attenuated light on the opposite side using a photodetector. Such instruments are called *photo-sedimentometers*. According to the *Lambert-Beer law*, the attenuation of light is proportional to the cross-sectional area of all particles in the light beam. Since the sedimentation analysis may take a very long time

for small particles, the sedimentation cell is often moved relative to the optical detection system so that the depth H of the measurement section is reduced with time.

The light attenuation method will be described in more detail in Section 10.2.1.

X-rays can also be used as a light source. In this case, the X-ray attenuation is directly proportional to the mass concentration (c) of the particles in the X-ray beam and according to the Lambert-Beer law, one obtains

$$\frac{I}{I_0} = \exp(-kc) \quad (10.2)$$

where I and I_0 are the intensities of the attenuated and incident X-rays and k is a constant of proportionality. Instruments based on this principle are called *X-ray sedimentometers*.

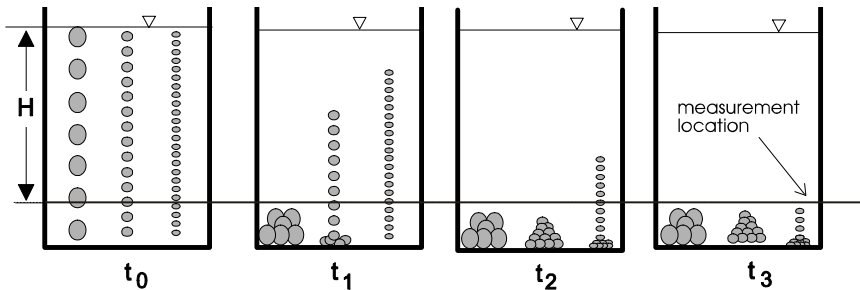


Figure 10.7: Sedimentation model to illustrate incremental method.

The principle of the incremental method is illustrated in Figure 10.7 for a powder with three distinct size classes. At the beginning of the sedimentation process, i.e., at $t_0 = 0$, the particle mass concentration at the measurement location, which is located at a distance H below the surface, corresponds to the concentration c_0 and is given by

$$c_0 = c_{t=0} = \frac{m_s}{V_s + V_l} \quad (10.3)$$

where m_s is the mass of solid particles and V_s and V_l are the respective volumes of the particles and the liquid in the sedimentation cell. After time $t_1 = H/v_{t1}$, all the largest particles with the highest settling (terminal) velocity v_{t1} will have passed the measurement location. Hence, the concentration has reduced to that of the other two remaining particle size classes as shown in Figure 10.8. Particles of these two size classes have sedimented a shorter distance from the surface due to their smaller free-fall velocity. At time $t_2 = H/v_{t2}$ the second largest particle size class will also have passed the measurement location and the concentration is again reduced. Finally, the smallest size class will have passed the measurement location and the particle concentration drops to zero.

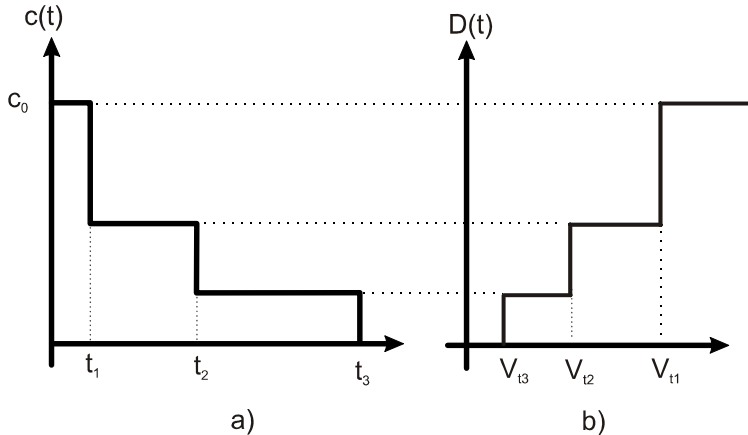


Figure 10.8: Sedimentation model for incremental method; (a) time-dependent concentration at measurement location, (b) cumulative mass distribution versus sedimentation (terminal) velocity.

Hence one obtains at the measurement location the concentration of the particles for which the sedimentation velocity is smaller than H/t . The cumulative mass fraction is determined by normalizing the measured concentration value by the initial concentration c_0 .

$$F_m(t) = 1 - \frac{c(t)}{c_0} \quad (10.4)$$

In order to determine the cumulative mass fraction as a function of particle size, it is necessary to correlate the sedimentation velocity with the particle size (i.e., Stokes diameter). By considering only the drag, the buoyancy and gravity forces, the equation of motion for the particle in a quiescent fluid becomes (see Chapter 4)

$$\frac{dv}{dt} = -\frac{18\mu}{\rho_d D^2} v + \left(1 - \frac{\rho_c}{\rho_d}\right) g \quad (10.5)$$

At steady state

$$\frac{dv}{dt} = 0 \quad (10.6)$$

Solving for D yields the Stokes diameter D_{St} :

$$D_{St} = \sqrt{\frac{18\mu v_t}{(\rho_d - \rho_c)g}} \quad (10.7)$$

This equation is valid for the Stokes regime, i.e., $Re_p < 1$, which is generally applicable for sedimentation analysis since small particles usually are considered.

In actuality, the measurement of particle concentration will be a continuous process so the cumulative percentage of undersize distribution becomes a continuous curve. The continuous curve can be represented by a series of steps and the same process for data reduction can be applied.

Cumulative method

In the cumulative method, the rate at which the powder is settling on the bottom of the sedimentation column is measured. One of the most commonly used instruments is the sedimentation balance where the particles collect on a balance pan and the weight of the particles accumulated is continuously measured. Again, the description of this method is based on three distinct particle size classes which are initially homogeneously dispersed in the sedimentation column. During the initial period, the weight of the particles increases at a constant rate until all particles of the large diameter fraction have accumulated on the balance pan as shown in Figure 10.9. Within the time interval $t_1 < t < t_2$ the rate of particle weight accumulation is reduced since all the large particles have already settled out. In the case of the simple three-size-class sedimentation model the accumulated particle mass increases, again at a constant rate. Similarly, a linear increase of the particle mass is observed for $t_2 < t < t_3$. Since only a portion of the smallest particles is in suspension, the rate of weight increase is again reduced.

The mass accumulated on the balance pan at a given time t can be expressed as

$$m = m_o[1 - F_m(D)] + m_o \int_0^D \frac{h}{H} f_m(\lambda) d\lambda \quad (10.8)$$

where D is the particle diameter just settled out in time t , m_o is the total mass of the sample and h is the distance that particle size λ has settled during time t . Obviously, the first term represents the mass of all particles with diameters larger than D and the second term represents the mass accumulated on the balance for all particles with diameters smaller than D . The distance h is related to the settling (terminal) velocity, $v_t(\lambda)$ by

$$h = v_t(\lambda)t. \quad (10.9)$$

Substituting Equation 10.9 into Equation 10.8 and dividing by m_o results in

$$\frac{m}{m_o} = 1 - F_m(D) + \frac{t}{H} \int_0^D v_t(\lambda) f_m(\lambda) d\lambda \quad (10.10)$$

Taking the derivative with respect to time yields

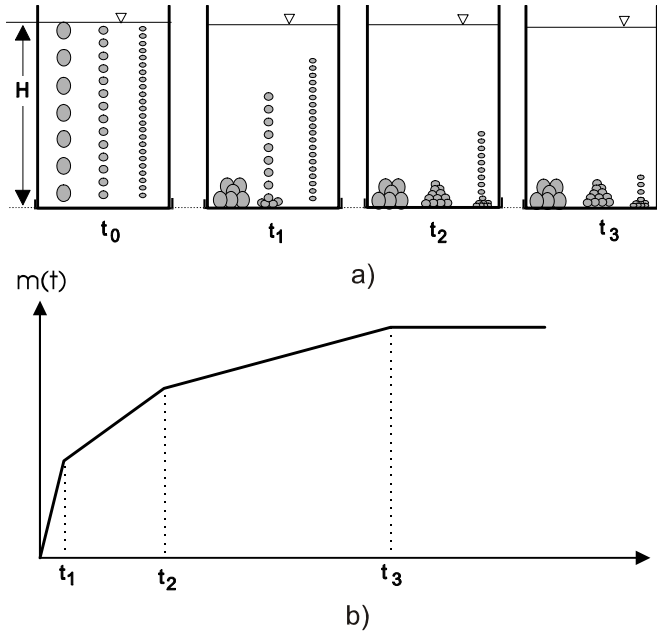


Figure 10.9: Sedimentation model to illustrate the incremental model, (a) sedimentation model, (b) temporal change of accumulated mass.

$$\frac{d}{dt}\left(\frac{m}{m_o}\right) = -\frac{d}{dt}F_m(D) + \frac{1}{H} \int_0^D v_t(\lambda) f_m(\lambda) d\lambda + \frac{t}{H} v_t(D) f_m(D) \frac{dD}{dt} \quad (10.11)$$

However, at time t , $H = v_t(D)t$ and, by definition, $F_m(D) = f_m(D)dD$, so the above equation reduces to

$$\frac{d}{dt}\left(\frac{m}{m_o}\right) = \frac{1}{H} \int_0^D v_t(\lambda) f_m(\lambda) d\lambda \quad (10.12)$$

Using Equation 10.10 to relate the integral to the mass accumulation and cumulative mass fraction, one can write the cumulative mass fraction as

$$F_m(D) = t \frac{d}{dt}\left(\frac{m}{m_o}\right) - \frac{m}{m_o} + 1 \quad (10.13)$$

This equation can be used to determine the cumulative mass fraction from the slope of the mass accumulation curve as illustrated in Figure 10.10. This is known as Oden's equation.

Example: A particle size analysis using a sedimentation balance is to be performed. At the beginning of the measurement, 100 grams of particles with

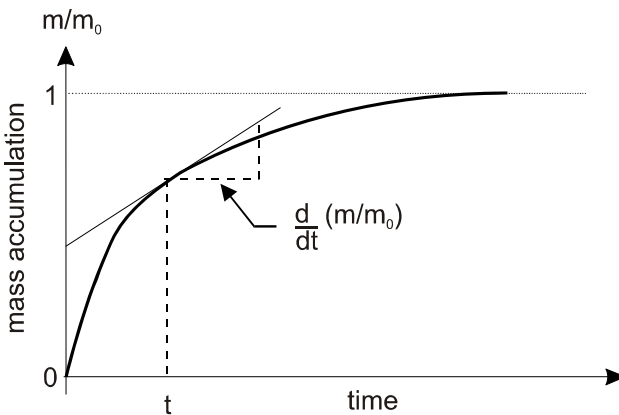


Figure 10.10: Graphical determination of mass fraction and slope from data using a sedimentation balance.

a density of 2500 kg/m^3 are homogeneously dispersed in a liquid with a density of 1000 kg/m^3 and a dynamic viscosity of 0.001 Ns/m^2 . The balance pan is located 0.3 m below the liquid surface. The measured mass accumulated on the balance pan and the rate of mass increase are provided in the following table:

Sedimentation time (s)	9	20	45	100	200	450	900
Accumulated mass (g)	32.0	55.0	76.0	89.4	95.3	98.7	99.9
Rate of mass increase (g/s)	3.11	1.55	0.49	0.11	0.026	6.0×10^{-3}	2.11×10^{-3}

- 1) Determine the cumulative mass distribution from the sedimented mass and rate of mass change using the Oden equation, Equation 10.13. Use the Stokes diameter to transform time to particle size.
- 2) Correct the Stokes diameter for Reynolds number effects.
- 3) Approximate the measured particle size distribution by a Rosin-Rammler distribution function and determine the empirical constant n (see Section 3.4.2). Comment on the quality of the approximation.
- 4) Determine the integral parameters of the size distribution such as the mass, median and Sauter mean diameter.
- 5) Determine the required measurement time for a particle of $10 \mu\text{m}$. Comment on the result.

Solution:

- 1) From the Oden equation

$$F_m(D) = t \frac{d}{dt} \left(\frac{m}{m_o} \right) - \frac{m(t)}{m_o} + 1$$

$$D_{St} = \sqrt{\frac{18\mu H}{(\rho_d - \rho_c)gt}}$$

with $v_t = H/t$. Substituting the values into the equation for Stokes diameter gives

$$D_{St} = 605/\sqrt{t} \text{ (microns)}$$

The results are shown in the table.

t (sec)	m/m_o	$d/dt(m/m_o)$ (1/sec)	$F_m(D)$	D_{St} microns	D microns
9	0.32	3.11×10^{-2}	0.96	202	255
20	0.55	1.55×10^{-2}	0.76	135	150
45	0.76	4.89×10^{-3}	0.46	90.2	95
100	0.894	1.14×10^{-3}	0.22	60.5	65
200	0.953	2.65×10^{-4}	0.11	42.8	45
450	0.987	6.0×10^{-5}	0.04	28.5	30
900	0.999	2.11×10^{-5}	0.02	20.2	21

2) The effect for non-Stokesian flow is obtained by solving, iteratively, the following equation for diameter, D .

$$fv_t = g\tau_V \left(1 - \frac{\rho_c}{\rho_d} \right)$$

$$\frac{H}{t} \left[1 + 0.15 \left(\frac{H}{t\nu_c} \right)^{0.67} D^{0.67} \right] = \frac{g\rho_d D^2}{18\mu_c} \left(1 - \frac{\rho_c}{\rho_d} \right)$$

The results are given in the table. One notes that the corrected diameter is larger than the Stokes diameter, but approaches the Stokes diameter for long sedimentation time (low velocity).

3) The Rosin-Rammler distribution is given by

$$F_m(D) = 1 - \exp \left[- \left(\frac{D}{\delta} \right)^n \right]$$

as discussed in Chapter 3. Plotting $\ln\{-\ln[1 - F_m(D)]\}$ versus $\ln D$ yields $n = 2.1$ and $\delta = 159.5$ microns.

4) From the Rosin-Rammler distribution

$$D_{32} = \frac{\delta}{\Gamma(1 - \frac{1}{n})} = 94.2 \text{ } \mu\text{m}$$

$$\mu_m = \delta \Gamma(1 + \frac{1}{n}) = 141.3 \text{ } \mu\text{m}$$

$$D_{mM} = \delta \left[\Gamma\left(1 - \frac{1}{n}\right) \right]^{1/2} = 207 \text{ } \mu\text{m}$$

5) For Stokes flow

$$v_t = \frac{(\rho_d - \rho_c) D^2}{18\mu_c} g = 0.082 \text{ mm/s}$$

However, $t = H/v_t = 3658\text{s}$. This measurement time is too long, so the use of a sedimentation balance is limited to larger particles.

Pipette method

In the pipette method according to Andreasen (see Allen, 1990), the concentration change near the bottom of the sedimentation cell is determined by drawing off known volumes (typically 10 ml) of the suspension at fixed time intervals by means of a pipette. The content of solids in the samples is generally determined by drying and weighing the remaining solids. This method provides the mass concentration of particles directly.

10.1.4 Electrical sensing zone method (Coulter principle)

The principle of electric sensing zone methods is based on the disturbance of an electrical field by a particle passing a probe volume. The disturbance can be related to the particle size by calibrating with mono-dispersed particles. A well-known instrument based on this principle is the Coulter counter, illustrated in Figure 10.11, which originally was used in medicine to count blood cells and subsequently modified to allow measurements of particle size and number.

The particles are suspended in an electrolyte and forced to pass through the small orifice. Electrodes are immersed in the fluid on both sides of the orifice which produces an electrical field. A particle passing the orifice will change the electrical impedance and generate a voltage pulse. The amplitude of the pulse is proportional to the volume of the particle as shown in Figure 10.12. The Coulter counter principle also belongs to the class of single particle counting techniques along with other optical methods described in Section 10.3. Therefore, the pulse amplitude can be uniquely related to the particle size when only one particle is in the probe volume at one time. To avoid plugging the orifice, the diameter of the orifice needs to be larger than the largest particle in the sample.

The probe volume is the volume of the orifice and a region outside the orifice where the signal amplitude is above the noise level as shown in Figure 10.12. The measurable particle size range is between 0.02 and 0.6 of the orifice diameter. This results in a dynamic range of 1:30. By using multiple

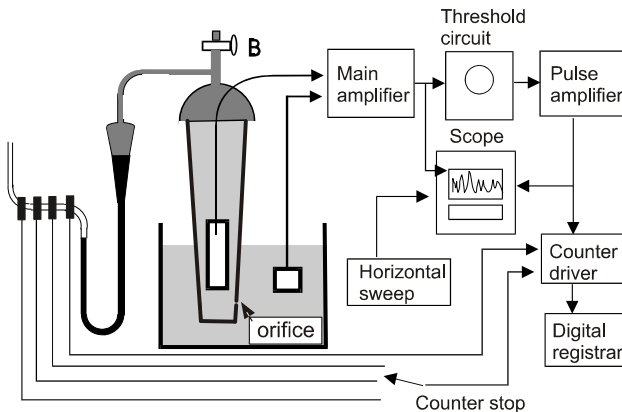


Figure 10.11: Principle of electrical sensing zone method (i.e., Coulter Counter). (*Particle Size Measurement, Vol. 1*, Allen, T., Chapter 9, p.329, Figure 9.2, Springer and Chapman and Hall, 1997, with kind permission of Springer Science-Business Media B.V.)

measurement cells with different orifice diameters, a particle size range of 0.5 to 1200 μm can be resolved. The upper limit of measurable particle size corresponds to the problem of keeping the particles in suspension. Large particles with density larger than the density of the electrolyte will tend to settle out. A solution to this problem is to increase the viscosity of the electrolyte or to apply stirrers in the reservoirs. The lower limit of detectable particle size is determined by the electronic noise of the system.

The operating principle of a Coulter counter is illustrated in Figure 10.11. Before measurement a vacuum is applied to the glass tube to produce an imbalance in the mercury siphon. After closing the valve (B), the flow through the orifice (A) is created as the mercury siphon is returned to equilibrium. The measurement is initiated and terminated by means of start and stop switches on the siphon. The resistance across the orifice is recorded by means of the electrodes mounted in the glass tube and in the reservoir where the glass tube is immersed. The voltage pulses generated by the modification of the resistance across the orifice as particles pass through are amplified, sized and counted. By setting an appropriate threshold level, only pulses above the noise level are detected and counted. This threshold level also determines the lower limit of the effective probe volume (see Figure 10.12).

The counts are collected in a number of pre-defined amplitude classes. By using a calibration curve which is determined, for example, with monosized Latex particles, the measured amplitude can be related to a particle size. Hence the measurement yields an equivalent diameter of a particle which gives the same voltage pulse as the calibration particle. The final output is a number weighted size distribution.

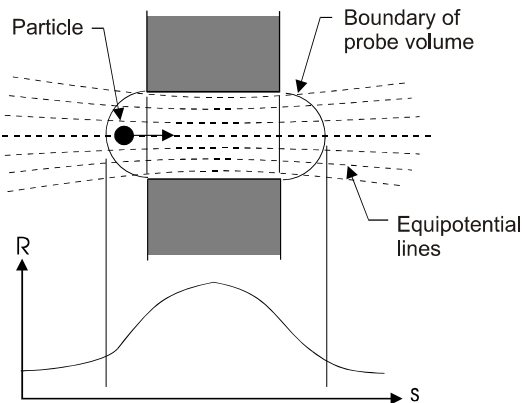


Figure 10.12: Probe volume and modification of resistance by particle in volume for Coulter principle.

More details about the theory of the Coulter principle and signal processing can be found in Allen (1990).

10.1.5 Optical analysis

Different methods are available for the optical analysis of particle samples based on the following physical principles:

- light attenuation
- scattering intensity
- light diffraction.

All these methods require careful preparation of the sample by dispersing the particles either in air or liquid. The dispersion must ensure that the agglomerates break up into the primary particles in order to allow the measurement of their properties. Some of the most common particle characterization methods based on optical analysis are described in more detail by Allen (1990). The physical principles of these techniques are identical with instrumentation used for on-line measurements and will be described in the following sections.

10.2 Integral methods

Integral methods are characterized as those measurement techniques which provide time-resolved but spatially integrated properties of a flowing two-phase system. Such methods are based on the distortion or attenuation of

some energy source such as light, sound, or atomic radiation passing through a two-phase flow system. Hence, these methods are nonintrusive, but provide only information integrated along the beam of the energy source. This is frequently an advantage for process control in industry. In the following sections, the most common integral methods for applications to dispersed two-phase flows are summarized.

10.2.1 Light attenuation

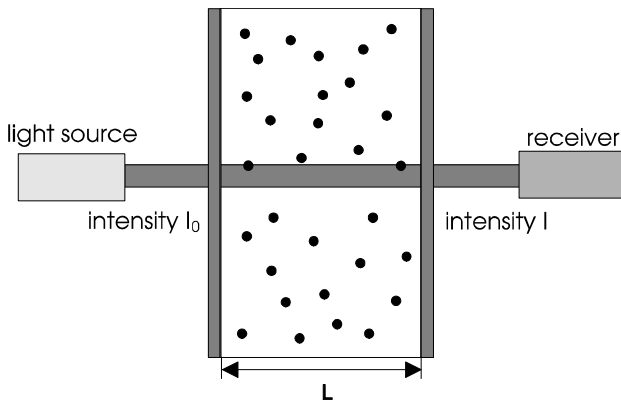


Figure 10.13: Principle of light attenuation method.

The intensity of a light beam passing through a fluid-particle mixture will be attenuated due to scattering and absorption by the particles. The intensity of the transmitted light is sensed by a photodetector and the change of the photodetector resistance can be monitored by appropriate electronic circuitry. According to the Lambert-Beer law, the light attenuation by a suspension of monodisperse particles is given by:

$$\frac{I}{I_0} = \exp\left(-k \frac{\pi}{4} D^2 n L\right) \quad (10.14)$$

where k is a constant of proportionality known as the extinction coefficient, D is the particle diameter, n is the particle number density and L is the optical path through the suspension as shown in Figure 10.13. Equation 10.14 shows that the light extinction depends on two properties of the particle phase: the particle concentration and the particle diameter. Hence, one of these properties has to be known to enable the measurement of the other property. Introducing $\bar{\rho}_d = nm$ into Equation 10.14 gives:

$$\ln\left(\frac{I}{I_0}\right) = -k' \left(\frac{L}{D}\right) \left(\frac{\bar{\rho}_d}{\rho_d}\right) \quad (10.15)$$

The change in light intensity I for a change in particle bulk density $\bar{\rho}_d$ is given for constant values of L and D by

$$\frac{dI}{I} = -k' \left(\frac{L}{D} \right) \frac{1}{\rho_d} d\bar{\rho}_d \quad (10.16)$$

Hence, for a given geometry, particle composition and particle diameter (i.e., particle diameter distribution) the change in light intensity is proportional to the change in particle cloud density so one has:

$$\frac{dI}{I} = -K d\bar{\rho}_d \quad (10.17)$$

The constant of proportionality, K , depends on the geometry of the flow system and properties of the particle material, such as refractive index, material density and diameter distribution. Therefore, the application of the light attenuation method requires the determination of the calibration constant K for each particle composition considered. For polydispersed particles, the dependence of the extinction coefficient on the particle size may result in larger measurement errors for the determination of the particle bulk density. Moreover, since the method requires optical access to the flow system, the build-up of particles at the windows must be either negligible or nonvarying during the measurement. As mentioned before, the particle concentration obtained by the light attenuation method provides an integral value along the optical path through the flow system. In many situations, this concentration is not representative for the entire cross-section, since there will always be a concentration distribution. Consider, for example, a particle-laden jet. In this case, the particle concentration distribution along the optical path of a light beam through the centerline of the jet follows a normal distribution function. Hence, the value for concentration obtained by light attenuation is some average value of this distribution.

For the determination of the local particle concentration based on the principle of light attenuation, fiber optical probes may be used as will be described in Section 10.3.2.

10.2.2 Laser-diffraction method

As described in Section 10.3.3, the scattering of particles considerably larger than the wavelength may be described by *geometrical optics* and *Fraunhofer diffraction theory*. It has been demonstrated for this regime that most of the light is scattered in the forward direction as a result of diffraction. The resulting forward scattering intensity pattern depends on particle size (see Figure 10.28), so the analysis of the scattering pattern may be used to infer information about particle size distribution. This principle, i.e., laser diffraction, has been used for many years to analyze particle samples and two-phase flows (Swithenbank et al., 1977; Hirleman et al., 1984) and a number of commercial instruments based on this principle are available.

Fraunhofer diffraction is one limit of the basic *Fresnel-Kirchhoff theory* of diffraction which describes the interaction of a monochromatic light beam with an aperture. In the *Fraunhofer limit*, the diffraction pattern of an aperture is the same for an opaque object with identical cross-section area and shape except for the shadow produced by the object. In the far-field, however, the diffraction pattern is much larger than the geometrical image. Two requirements have to be met in order to obtain the Fraunhofer limit (Weiner, 1984): (1) the area of the object must be smaller than the product of the wavelength of light and the distance from the point source of the light to the diffracting object and (2) the area of the object must be smaller than the product of the wavelength and the distance between the object and the observation plane. The first requirement is easily met for a parallel light beam since the point source can be considered to be at infinity. In order to fulfill the second requirement, the detection plane must be positioned far away from the object. Therefore, Fraunhofer diffraction is also known as far-field diffraction. Alternatively, a lens may be used to focus the diffracted light onto a photo-detector positioned in the focal plane of the lens. For such an optical configuration, the undeflected light is brought to a point focus on the axis (i.e., center of the detector) and the diffracted light is focused around this central spot as shown in Figure 10.14. Therefore, the diffraction pattern will also be stationary for a moving object and hence, the size measurement is not biased by the particle velocity, which is an important fact for in-process two-phase flow analysis.

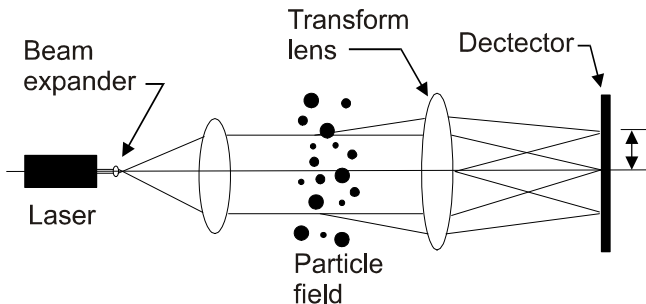


Figure 10.14: Optical arrangement of instruments for particle sizing by laser diffraction.

The intensity distribution of the diffraction pattern in the detector plane for a particle with diameter D may be obtained from

$$I(x) = I_o \left[\frac{2J_1(x)}{x} \right]^2 \quad (10.18)$$

where I_o is the intensity at the center of the pattern and J_1 is the first-order spherical Bessel function. The parameter x is a function of the particle diameter and the optical configuration

$$x = \frac{\pi D r}{\lambda \hat{f}} \quad (10.19)$$

where r is the radial distance from the center of the detection plane, \hat{f} is the focal length of the transform lens and λ is the wavelength of the incident light. By introducing

$$\sin \theta = \frac{r}{\hat{f}} \quad (10.20)$$

and using the fact that θ is usually very small, i.e., $\sin \theta = \theta$, one obtains

$$x = \frac{\pi D \theta}{\lambda}. \quad (10.21)$$

The intensity at the center of the diffraction pattern is given by

$$I_o = c I_{inc} \frac{\pi^2 D^4}{16 \lambda^2} \quad (10.22)$$

where c is a constant of proportionality and I_{inc} is the intensity of the incident light. This results in the following equation for the intensity pattern

$$I(D_p, \theta) = c I_{inc} \frac{\pi^2 D^4}{16 \lambda^2} \left[\frac{2 J_1 \left(\frac{\pi D \theta}{\lambda} \right)}{\frac{\pi D \theta}{\lambda}} \right]^2 \quad (10.23)$$

This functional relation is known as the *Airy function* and is plotted in Figure 10.15. The result shows that the diffraction pattern consists of a series of bright and dark concentric rings surrounding the central spot of undiffracted light with a radius which depends only on the dimensionless parameter x .

However, for on-line measurements of particle size distributions, the measurement of the radial intensity distribution is very cumbersome. Therefore, the photodetector consists of a number of concentric ring elements as shown in Figure 10.16 and the light energy over only a finite area between r_i and r_{i+1} needs to be measured and analyzed. By integrating Equation 10.23 from r_i and r_{i+1} , one obtains the light energy received by the detector element

$$E_{i,i+1} = c \pi D^2 \left\{ [J_o^2(x) + J_1^2(x)]_i - [J_o^2(x) + J_1^2(x)]_{i+1} \right\} \quad (10.24)$$

The constant c depends on the power of the light source and the sensitivity of the photodetector.

Since the diffraction analysis is done not only for one particle being in the laser beam, but for a suspension (i.e., particles dispersed in air or liquid) with a certain particle size distribution, the light energy falling on one ring element has to be multiplied by the number of particles. For a particle size distribution with M size classes, each with N_j particles, one obtains by neglecting multiple scattering

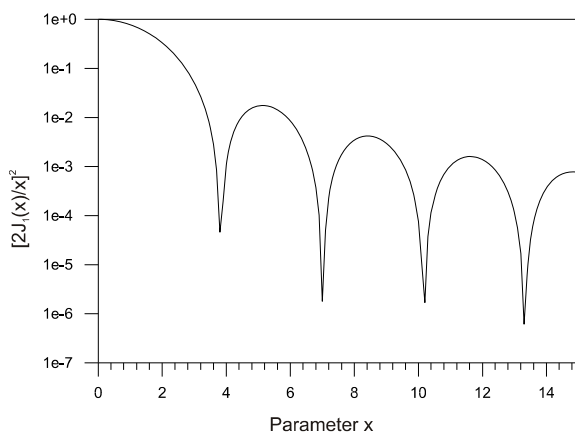


Figure 10.15: Fraunhofer diffraction pattern for a circular aperture or an opaque disk according to Equation 10.23

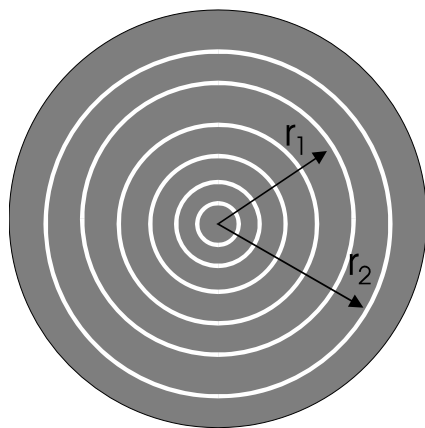


Figure 10.16: Illustration of ring detector element for measurement of diffraction pattern.

$$E_{i,i+1} = c\pi \sum_{j=1}^M N_j D_j^2 \left\{ [J_o^2(x_j) + J_1^2(x_j)]_i - [J_o^2(x_j) - J_1^2(x_j)]_{i+1} \right\} \quad (10.25)$$

where x_j corresponds to the value of x for the particle size D_j . This equation allows one to convert the measured light energy to the particle number distribution represented by M size classes each with N_j particles. The number of resolved particle size classes, M , is equal to the number of ring elements, L . Therefore, Equation 10.25 has to be solved L -times, for each ring element. The lower and upper limits of the size classes depend on the magnitude of the smallest and largest ring radii.

The set of L equations is usually solved using the least-squares criteria. Initial values of N_i are either estimated from the raw data or calculated from an assumed functional form of the particle size distribution, e.g., Rosin-Rammler distribution function. Using Equation 10.25 L light energy values are calculated and compared with the measured light energy values. The assumed N_j -values are then corrected and the final result is obtained iteratively by minimizing the least-square error.

10.2.3 Cross-correlation techniques

The cross-correlation technique allows one to determine the mean transit time of a flowing medium passing two sensors located a given distance apart. Hence, an average velocity can be obtained as the ratio of the sensor separation L to the transit time T_t

$$V_o = \frac{L}{T_t} \quad (10.26)$$

This principle has been used for the design of flow meters (Beck and Plaskowski, 1987). The cross-correlation technique may also be used to measure an average velocity in a flowing two-phase mixture, such as in pneumatic conveying (Kipphan, 1977; Williams et al., 1991) as illustrated in Figure 10.17a. The technique requires monitoring the fluctuations of any property of the dispersed phase with two sensors mounted a given distance apart. The type of sensor may be based on a variety of properties, such as ultrasound attenuation, light attenuation or scattering, electrostatic charge variation and conductance or capacitance variations. In most of these situations the resulting signals are proportional to the temporal variation of particle concentration. If the sensors are not positioned too far apart, the two signals generated by the fluctuation of particle concentration are, to some extent, identical but time-shifted as shown in Figure 10.17b. The time delay between the two signals $x(t)$ and $y(t)$ can be determined efficiently by computing the *cross-correlation function* of both signals over a certain measurement time period T_m . The cross-correlation function for the time delay τ is obtained from

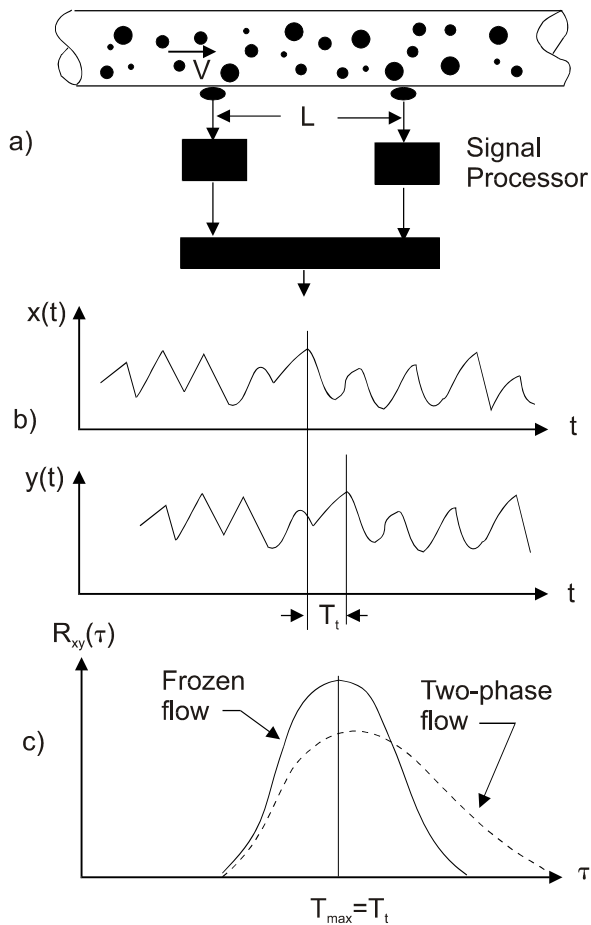


Figure 10.17: Cross-correlation method for particle velocity measurements: (a) pneumatic conveying line and sensor locations, (b) signals from both sensors and (c) cross-correlations functions.

$$R_{xy}(\tau) = \frac{1}{T_m} \int_0^{T_m} x(t - \tau)y(t)dt \quad (10.27)$$

For an ideal situation, i.e., a frozen concentration pattern, the signal $y(t)$ is exactly shifted by the transit time T_t , i.e., $y(t) = x(t - T_t)$. In this case the shape of the cross-correlation function is identical to the auto-correlation function (Kipphan, 1977)

$$R_{xx}(\tau) = \frac{1}{T_m} \int_0^{T_m} x(t - \tau)x(t)dt \quad (10.28)$$

and shifted by the transit time T_t as illustrated in Figure 10.17c. In real situations, and especially in turbulent two-phase flows, the concentration signals are stochastic in nature which results in a broadening of the cross-correlation function as shown in Figure 10.17c. For such a condition the transit time is obtained from the location of the maximum in the cross-correlation function T_{\max} . This was demonstrated by Kipphan (1977) using different models for the transport process. Moreover, Kipphan demonstrated that the broadening of the cross-correlation function in comparison with the *auto-correlation function* may be used to estimate the average particle velocity fluctuations. It is also obvious that the degree of correlation of the signals depends on the separation of the sensors and the intensity of the concentration fluctuation or particle fluctuating motion.

In order to achieve a maximum degree of correlation with a minimum scatter of the data, Kipphan (1977) suggests the following optimum sensor separation

$$L_{opt} \approx 0.35 \frac{b}{\sigma_v/V_0} \quad (10.29)$$

where b is the linear dimension of the sensor in the mainstream direction and σ_v is the mean intensity of the particle velocity fluctuation.

Since most of the sensor principles mentioned above enable the estimation of the average particle concentration, it is also possible to determine the particle mass flow rate from

$$\dot{m}_p = \bar{\rho}_d V_o A \quad (10.30)$$

where A is the cross-section of the sensing region perpendicular to the mainstream flow direction. To what extent the measured integral properties represent the real mean values in the flow system strongly depends on the type of sensor and the homogeneity of the dispersed phase. Considering, for example, horizontal pneumatic or hydraulic conveying, segregation effects due to gravitational settling may yield false measurements. This is illustrated in Figure 10.18. A horizontal arrangement of the two opposed sensors (e.g., based on the light attenuation method) will completely underestimate the particle mass flow rate, while a vertical arrangement results in an overestimation.

Hence, accurate measurements are only possible when the condition of the dispersed phase in the instrument probe volume is representative of the entire cross-section of the pipe. Such a condition can be only realized in vertical conveying and when the sensors are placed far enough away from pipe bends or feeding systems to ensure a homogeneous mixture.

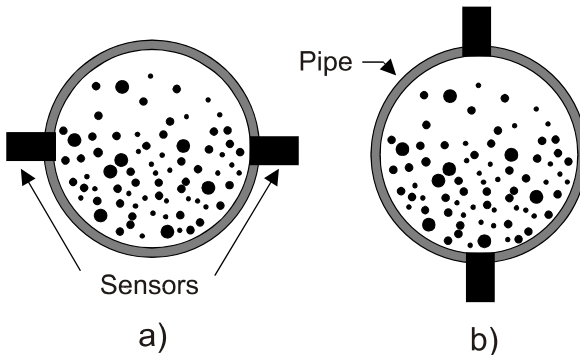


Figure 10.18: Possible sensor arrangements in horizontal pneumatic conveying: (a) horizontal arrangement, (b) vertical arrangement.

10.3 Local measurement techniques

Local measurement techniques enable the determination of properties in a two-phase flow with a relatively high spatial resolution, depending on the method applied. According to Table 10.1, local measurement techniques may be divided into three groups: probing methods (e.g., isokinetic sampling), field imaging techniques (e.g., particle image velocimetry) and single particle counting methods (e.g., light scattering, laser-Doppler and phase-Doppler anemometry). Probing methods are intrusive and may disturb the flow considerably depending on the application. They are, however, quite robust and hence widely used in industry for process control. The other methods described in this chapter are nonintrusive optical methods. These optical methods may be also divided according to the following two measurement principles:

- Single particle counting methods: The particle phase properties and the respective distribution functions are obtained for those particles passing through a small finite probe volume within a given measurement time. The result is therefore weighted by the particle number flux.
- Field imaging techniques: The distribution functions of the particle phase properties are obtained for those particles which happen to be in the probe volume at a give instant of time. Hence, the result is weighted by the particle number concentration.

Therefore, these two measurement principles yield different results which can be related, as demonstrated by Umhauer et al. (1990).

10.3.1 Isokinetic sampling

Isokinetic sampling can be used to measure particle mass flux, concentration, and density in a flowing suspension. Moreover, the collected particles may be further analyzed off-line to obtain the particle size distribution or other properties such as surface area and shape factor using methods described in Section 10.1.1.

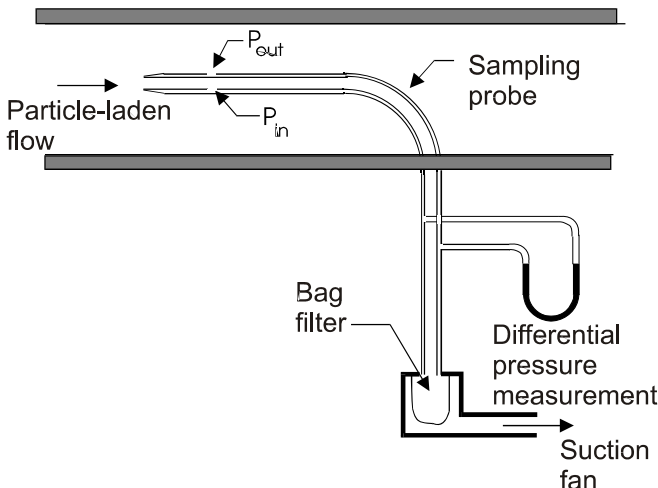


Figure 10.19: Operational principle of isokinetic sampling method.

The basic requirement for measuring local particle flux is that the sample extracted must be totally representative of the suspension at the sample point in the two-phase stream, which is not an easy task when using isokinetic sampling. The principle of this method is based on inserting a sampling probe into the flowing two-phase system and gathering a representative sample of particles by a suction fan as shown in Figure 10.19. The sampled particles are collected in a bag filter for a certain time interval and then the particle mass is obtained by weighing the bag filter with and without particles. Hence, a particle mass flux is obtained which, under certain conditions, may be related to the local particle flux, concentration or density of the flowing suspension. The first problem which has to be considered is that the suction velocity u_s established in the sampling probe should be identical with the local gas velocity (i.e., isokinetic sampling condition). This may be achieved by adjusting the suction velocity in such a way that the static pressures outside and inside the sampling probe become identical as shown in Figure 10.19.

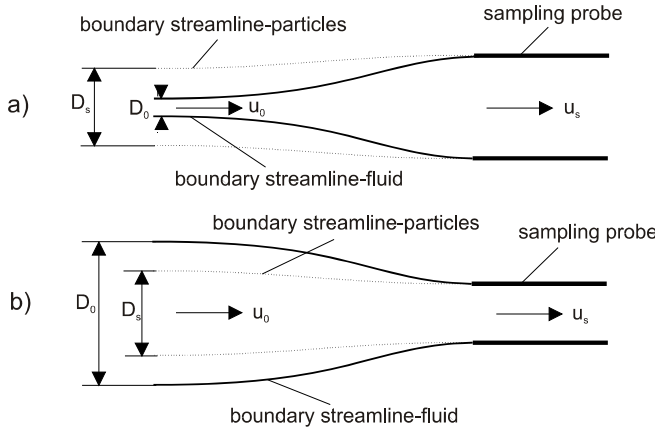


Figure 10.20: Streamline and particle trajectories for different sampling conditions: (a) $u_s < u_0$, (b) $u_s > u_0$.

In the event isokinetic conditions are not properly achieved the region from which particles are sampled is not identical with the cross-section of the sampling probe as illustrated in Figure 10.20 (Soo et al., 1969). When the suction velocity is smaller than the local fluid velocity, the region from which the particles are collected is smaller than the cross-section of the probe, as seen in Figure 10.20a, and when the suction velocity is larger the particles are collected from a larger area as illustrated in Figure 10.20b. Moreover, the boundary streamline of the flow and the boundary trajectory of the particle are not the same when the suction velocity does not match the local fluid velocity because of particle inertia. Hence, in this case, it is not possible to accurately determine the particle mass flux or concentration as will be shown below.

Determination of particle mass flux and bulk density

All the definitions used for this analysis are defined in Figure 10.21. The area A_d is the capture area for the particles and the area A_0 is the area of the continuous phase in the free stream that enters the probe. The mass flow rate of particles through the capture area in the free stream is equal to the mass flow rate in the probe.

$$\dot{M}_d = \bar{\rho}_{d,0} v_0 A_d = \bar{\rho}_d v A \quad (10.31)$$

Under isokinetic sampling conditions, $A_d = A$ and $v_0 = v$ so

$$\frac{\bar{\rho}_{d,0}}{\bar{\rho}_d} = 1 \quad (10.32)$$

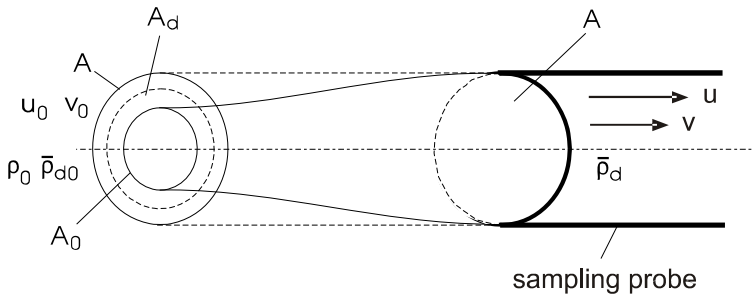


Figure 10.21: Definitions for analysis of sampling method.

If ΔM_d is the mass of material collected on the bag filter in time Δt , then the particle mass flux is

$$\bar{\rho}_{d,0}v_0 = \frac{\dot{M}_d}{A} = \frac{\Delta M_d}{A\Delta t} \quad (10.33)$$

The free stream bulk density is

$$\bar{\rho}_{d,0} = \frac{\Delta M_d}{v_0 A \Delta t} \quad (10.34)$$

Thus an additional measurement is needed for the particle velocity in the free stream.

Under nonisokinetic conditions the ratio of the particle mass flux in the free stream to the mass flux in the sampling probe is

$$\frac{\bar{\rho}_{d,0}v_0}{\bar{\rho}_d v} = \frac{A}{A_d} \quad (10.35)$$

and the area ratio A/A_d is not necessarily known. However, if the particles have high inertia and travel in rectilinear trajectories, then $A_d = A$ and

$$\frac{\bar{\rho}_{d,0}v_0}{\bar{\rho}_d v} = 1 \quad (10.36)$$

The mass flux in the probe is measured directly from the accumulation on the filter from Equation 10.33 which is equal to the mass flux in the free stream. The determination of the bulk density requires data on the free stream particle velocity.

If it is assumed that the particles are in velocity equilibrium with the conveying fluid ($u = v$) and that the conveying fluid is incompressible, then the continuity equation between the free stream and the probe can be written as

$$v_0 A_0 = v A \quad (10.37)$$

and the equation for ratio bulk densities becomes

$$\frac{\bar{\rho}_{d,0}}{\bar{\rho}_d} = \frac{A_0}{A_d} \quad (10.38)$$

Bohnert (1973) performed an analysis based on the above assumptions and developed correlations for the area ratio A_0/A_d . Since the particle trajectories around the sampling probe depend on particle inertia, Bohnert correlated his results with a non-dimensional Stokes number defined by

$$St_{Pr} = B = \frac{u_0 \tau_v}{D_{Pr}} = \frac{\rho_d D^2 u_0}{18 \mu D_{Pr}} \quad (10.39)$$

where D_{Pr} is the probe diameter. A diagram of the relative dust concentration plotted versus the ratio of sampling velocity to flow velocity is shown in Figure 10.22 with B as a parameter. It is obvious that the relative dust concentration increases with larger deviations from the isokinetic condition and larger values of the parameter B .

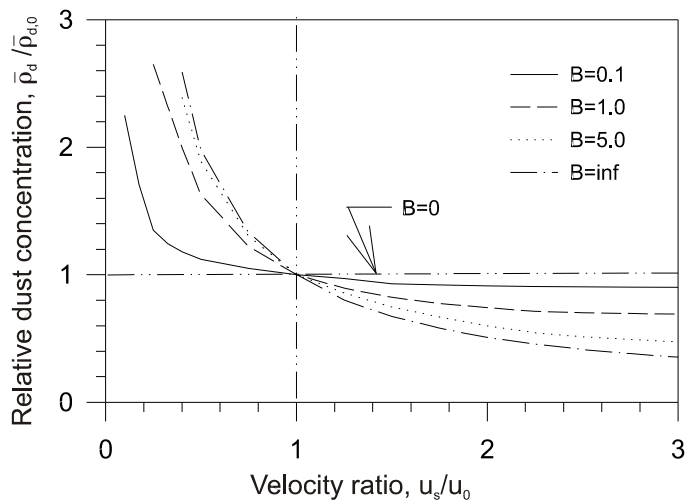


Figure 10.22: Relative error in particle concentration in the sampling probe under isokinetic conditions for different values of B . (Bohnert, M., 1973, Staubgehaltsbestimmung in strömenden Gasen, *Chemie.-Ing.-Tech.*, 1973, **45**, 22. Copyright Wiley-VCH Verlag GmbH & Co. KGaA. Reproduced with permission.)

Moreover, isokinetic sampling cannot give accurate values for the particle cloud density in a carrier phase with a velocity gradient, i.e., shear flow or wall boundary layer, since the flow around the sampling probe becomes asymmetric and isokinetic conditions can hardly be established.

10.3.2 Optical fiber probes

Measurement systems based on optical fiber probes have been used in various configurations to perform local measurements of particle velocity, size, and concentration in two-phase flows. An optical fiber probe system consists of the probe head, which is inserted into the flow, a light source, a photodetector and the signal processing unit. The probe construction may differ principally in the arrangement of the light emitting fiber, which is connected to the light source, and the light receiving fiber, which transmits the light to the photodetector. Two different measurement principles may be identified:

- light attenuation method
- light reflection method.

The principle of operation also establishes the arrangement of the emitting and receiving fibers. In the light attenuation method, the optical fibers are arranged opposite to each other and the light propagates a given distance through the two-phase mixture before reaching the receiving fiber as shown in Figure 10.23a. Particle concentration measurements using this optical fiber arrangement may be based on the Lambert-Beer law for light attenuation (see also Section 10.2.1), or on counting individual particles passing through the probe volume between the two fibers. The method which is most applicable depends on the ratio of fiber diameter to particle diameter. The particle counting technique may be applied when the particle diameter is of the same order as the fiber diameter so that the instrument operates as a single particle counter.

Fiber probes based on the reflection from particles are constructed in such a way that the transmitting and receiving fibers are mounted parallel in the probe head as shown in Figure 10.23b. Particles moving in front of the probe head are illuminated by the transmitting fiber and scatter light in the backward direction. This light is received by a second fiber which is usually mounted in line with the emitting fiber.

Instead of separate transmitting and receiving fibers, a single fiber may also be used. In this case, the light from the light source is coupled into the sensor fiber by a fiber optical beam splitter and the light scattered by the particles is received by the same sensor fiber, diverted by the beam splitter and transmitted to the photodetector. Such single fiber reflection probes have been used by Lischer and Louge (1991) and Rensner and Werther (1992) for measurements in dense two-phase flows, e.g., fluidized beds. The advantages of the single fiber reflection probe are its small size (typically smaller than 1 mm in diameter) and the ability to withstand erosion. On the other hand, it is only possible to measure particle concentration. This requires an estimate of the effective probe volume, i.e., the area from which the scattered light is received by the probe. A detailed analysis of the effective measuring volume of single fiber reflection probes was performed by Rensner and Werther (1992).

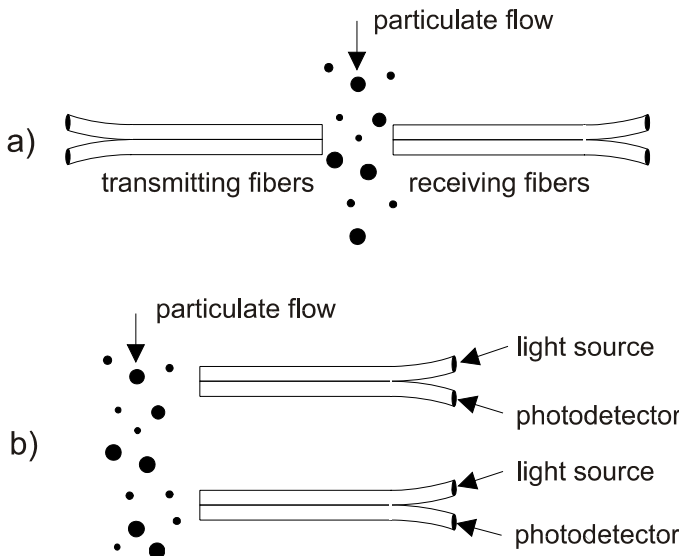


Figure 10.23: Primary arrangement of fiber optical probes: (a) light attenuation, (b) light scattering (reflection) method.

Particle velocity measurements by fiber optical probes are possible, without calibration, based on the passage time of the particles between two successive sensors or the frequency method which requires a special arrangement of a number of emitting and receiving fibers in the probe head. The *passage-time method* is based on the cross-correlation of the signals received by two sets of emitting and receiving fibers and can be realized for both the light attenuation and the light scattering method, except for the single fiber reflection probe which only allows for concentration measurements. The cross-correlation method requires that the two sensor pairs are aligned with the main flow direction in order to achieve a high degree of correlation. Furthermore, the required separation of the sensor pairs has to fulfill certain requirements in order to give a high degree of correlation, as recommended by Klipphan (1977). A more detailed description of the cross-correlation method has been given in Section 10.2.3.

The frequency method for measuring particle velocities (Petrak & Hoffmann, 1985) is based on using a number of illuminating fibers combined with a regular arrangement of receiving fibers at a given separation as illustrated in Figure 10.24. All the receiving fibers are connected to one photodetector; therefore, the line array of receiving fibers acts as a spatial grid whereby the scattered light is modulated so the signal from the photodetector shows a sinusoidal shape with a dominant frequency f_0 . This frequency can be related to the particle velocity by:

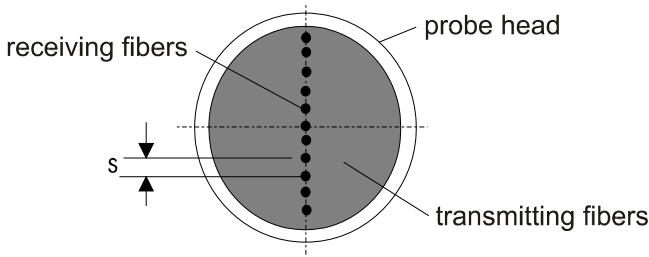


Figure 10.24: Cross-section of fiber optic probe used for the frequency method.

$$v = f_0 s \quad (10.40)$$

where s is the spacing between the receiving fibers. From the arrangement of the receiving fibers, it is obvious that the frequency method requires a particle motion parallel to the line of fibers; otherwise, the signal will have only a few zero-crossings which makes an evaluation of the signal frequency difficult.

A comprehensive review on measurement techniques applicable to fluidized bed analysis and process control was provided by Werther (1999). This article summarizes heat flux meters, sampling probes, optical probes for particle size, concentration and velocity measurements, as well as tomographic methods which are capable of imaging an entire cross-section of the two-phase flow field.

10.3.3 Scattering intensity measurements

In this section the basic theory of light scattering will be briefly summarized and results for the dependence of scattering intensity on particle size will be introduced. The principles of light scattering are also important for laser-Doppler and phase-Doppler anemometry and imaging techniques which will be introduced later.

The interaction of light with particles results in absorption and scattering of the light. The light scattered can be calculated using the theory of Mie (1908) which requires the solution of Maxwell's wave equations for the case of scattering of a plane electromagnetic wave by a homogeneous sphere. For more details about *Mie scattering theory*, the reader is referred to the relevant literature, e.g., van de Hulst (1981).

The absolute intensity of the light scattered by one particle, q , depends on the intensity of the incident light I_0 , the wavelength of the light λ , the polarization angle of the light γ , the particle diameter D , the complex index of refraction \bar{n} and the scattering angle φ

$$q = I_0 \frac{\lambda^2}{8\pi^2} i(\lambda, \gamma, \varphi, D, n, \kappa) \quad (10.41)$$

where I_0 represents the so-called *Mie intensity*. The complex refractive index is given by

$$\bar{n} = n(1 - i\kappa) \quad (10.42)$$

Optical arrangements for scattering intensity measurements usually also involve the integration of the scattered light over the receiving aperture for a selected mean scattering angle. Such a typical optical arrangement is illustrated in Figure 10.25 where $\Delta\delta$ indicates the receiving solid aperture angle. For parallel and monochromatic light as the illuminating source, the resulting scattering intensity is obtained by integration.

$$Q(\lambda, D, n, \kappa, \Delta\delta) = I_0 \frac{\lambda^2}{8\pi^2} \int_0^{2\pi} \int_{\Delta\delta} I(\lambda, \gamma, \varphi, D, n, \kappa) \sin \varphi d\varphi d\gamma \quad (10.43)$$

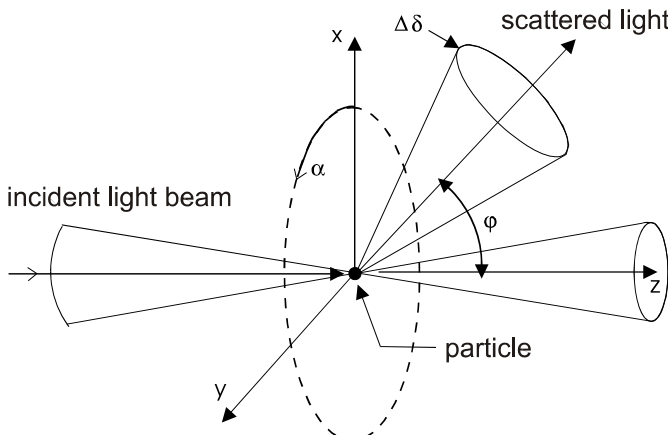


Figure 10.25: Optical arrangements for light scattering measurements.

In the event white light is used instead of monochromatic light, the scattering intensity is obtained by additionally integrating over the wavelength range, which has some advantages with regard to a smooth correlation between scattering intensity and particle size. In the following section, the principles of scattering intensity measurements will be introduced by using Mie calculations (DANTEC/Invent 1994), whereby one can get an idea of the range of applicability and design of the instrument.

Typical examples of the scattering intensity around a particle for various particle diameters are shown in Figure 10.26 for parallel polarization. For the smallest particle (i.e., $0.1 \mu\text{m}$) the angular intensity distribution has only two lobes for parallel polarization, which is characteristic of the Rayleigh scattering range. It is obvious that the absolute intensity of the scattered

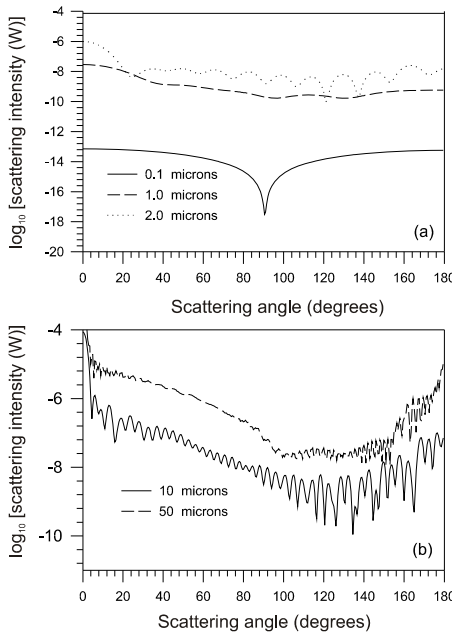


Figure 10.26: Angular distribution of scattering intensity around a particle ($I_0 = 10^7 \text{ W/m}^2$, $\lambda = 632.8 \text{ nm}$, $n = 1.5$, parallel polarization with respect to the polarization of the incident light), (a) particle diameters $0.1, 1$ and $2 \mu\text{m}$, (b) particle diameters 10 and $50 \mu\text{m}$.

light increases with particle size. Moreover, the number of lobes increases for larger particles. The highest scattering intensity is concentrated in the forward scattering direction and is mainly a result of diffraction. The influence of polarization on the scattering intensity around a $2.8 \mu\text{m}$ particle is illustrated in Figure 10.27. It is obvious that the intensity distribution for a polarization parallel to the incident light is much smoother compared to a perpendicular polarization.

In the following, the scattering intensity as a function of the particle diameter is analyzed in more detail for various properties of the particles and configurations of the optical system with the parameters specified in Figure 10.28. The results presented are again based on the Mie theory and the calculations were performed with the software package "STREU" (DANTEC/Invert, 1994). In Figure 10.28, a typical dependence of the scattering intensity on the particle diameter is shown. From this correlation, three scattering regimes may be identified which are often characterized by the *Mie parameter*, $\alpha = \pi D/\lambda$.

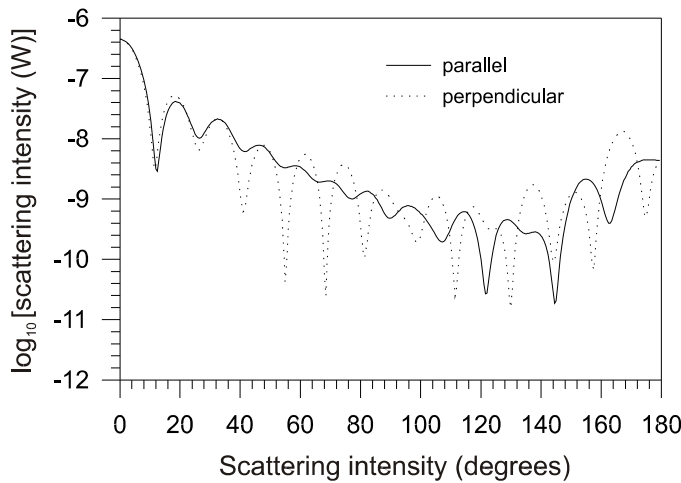


Figure 10.27: Angular distribution of scattering intensity around a particle; comparison and parallel and perpendicular polarization with respect to the polarization of the incident light ($I_o = 10^7 \text{ W/m}^2$, $\lambda = 632.8 \text{ nm}$, $D = 2.8 \mu\text{m}$, $n = 1.5$).

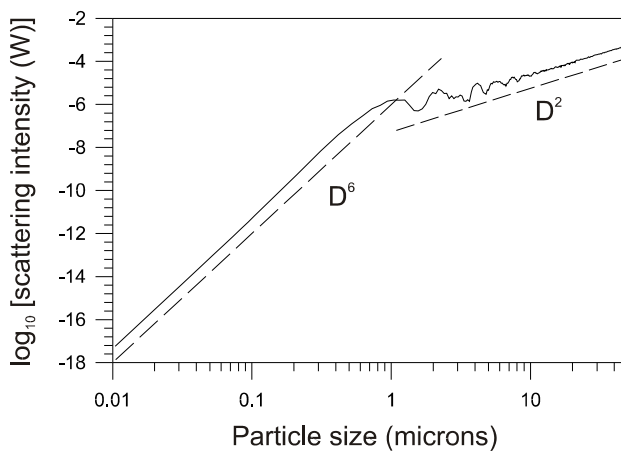


Figure 10.28: Dependence of scattering intensity on particle size ($I_o = 10^7 \text{ W/m}^2$, $\varphi = 15^\circ$, $\Delta\delta = 10^\circ$, $n = 1.5$).

- The so-called *Rayleigh-scattering* applies to particles that are small compared with the wavelength of the incident light, i.e., $\alpha \ll 1$ or $D < \lambda/10$. This regime is named after Lord Rayleigh, who first derived the basic scattering theory for such small particles (Strutt, 1871). Characteristic of this regime is a dependence of the scattering intensity on the fourth to sixth power of the particle diameter.
- For very large particles, i.e., $\alpha \gg 1$ or $D > 4\lambda$ the laws of *geometrical optics* are applicable under certain conditions (van de Hulst, 1981). The light scattering intensity varies approximately with the square of the particle diameter.
- The intermediate regime (i.e., $D \approx \lambda$) is called the Mie region, which is characterized by large oscillations in the scattering intensity, depending on the observation angle and the particle properties. Hence, the scattering intensity cannot be uniquely related to the particle size.

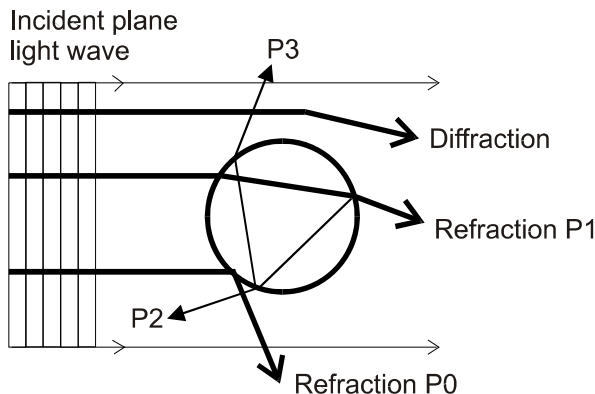


Figure 10.29: Different scattering modes for a spherical particle in the geometric optics regime.

For large particles, i.e., $D \gg \lambda$, the scattered light is composed of three components: namely, diffracted, externally reflected and internally refracted light as indicated in Figure 10.29. The refracted light may be separated in several modes depending on the number of internal reflections, i.e., $P_1, P_2, P_3, \dots, P_n$. Light diffraction is concentrated in the forward-scattering direction, i.e., the so-called forward lobe, and is the dominant scattering phenomenon. This regime of geometrical optics is called the *Fraunhofer diffraction regime*. The diffraction pattern and the angular range of this forward lobe are dependent on the wavelength of the light and the particle diameter. As already demonstrated in Figure 10.26, the angular range of diffracted light decreases with increasing particle diameter and is given by $\varphi < \pm \varphi_{\text{diff}}$ with

$$\sin \varphi_{\text{diff}} = \frac{5}{4} \frac{\lambda}{D} \quad (10.44)$$

Moreover, it is important to note that the intensity of the diffracted light is independent of the optical constants of the particle material, which might have some advantages in sizing particles of different or unknown refractive indices.

Externally reflected light is scattered over the entire angular range, i.e. $0^\circ < \varphi < 180^\circ$, whereas refracted light (i.e., $P1$) does not exceed an upper angular limit, $\varphi_{\text{refr.}}$, which is given by

$$\cos \left(\frac{\varphi_{\text{refr.}}}{2} \right) = \frac{n_m}{n_p} \quad (10.45)$$

for $n_p/n_m > 1.0$. Hence, this upper angular limit is determined by the relative refractive index. For a given fluid and $n_p/n_m > 1.0$, $\varphi_{\text{refr.}}$ decreases and more refracted light is concentrated in the forward direction with a decreasing refractive index of the particles. The properties of reflected and refracted light will be addressed in Section 10.3.5. The Mie response functions for three scattering angles, i.e., $\varphi = 0, 15$, and 90° , are shown in Figure 10.30 for different refractive indices in the size range between 0.1 and $20 \mu\text{m}$. The calculations were performed for a receiving aperture of $\Delta\delta = 10^\circ$. The results may be summarized as follows:

- In the narrow forward-scattering range, the scattering intensity is almost independent of the refractive index of the particle. This is a result of the dominance of diffraction in this angular region. As described above, diffraction is independent of the optical properties of the particles. Moreover, the scattering intensity varies approximately with the fourth power of the particle diameter.
- For off-axis locations, the scattering intensity shows large-scale fluctuations in the Mie range, i.e., the scattering intensity cannot be uniquely related to the particle size. In the Rayleigh range, the scattering intensity varies with the 6th power of the particle diameter and in the range of geometrical optics, the square law may be applied.
- At a 90° scattering angle, the largest differences in the scattering intensity are observed for the different refractive indices and the absolute value of the scattering intensity is considerably lower than for the other scattering angles.

To reduce the intensity fluctuations, especially in the Mie range, and to establish a smoother size-intensity correlation, the aperture of the receiving optics may be increased so the scattered light is received from a larger angular region and the oscillations in the angular distribution of the scattering intensity are smoothed out over a larger region as shown in Figure 10.31. Also, the use of white light can improve the smoothness of the response curve, since

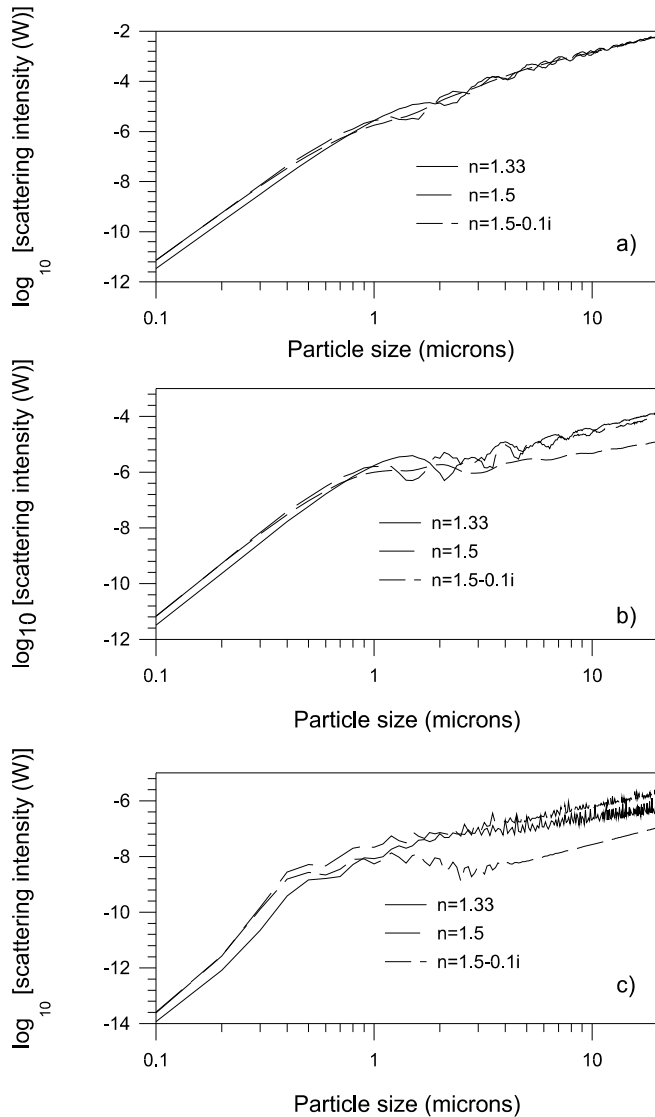


Figure 10.30: Mie response for three scattering angles: (a) $\varphi = 0^\circ$, (b) $\varphi = 15^\circ$, (c) $\varphi = 90^\circ$, for spherical particles with different refractive indices ($I_o = 10^7 \text{ W/m}^2$, $\lambda = 632.8 \text{ nm}$, $\Delta\delta = 10^\circ$).

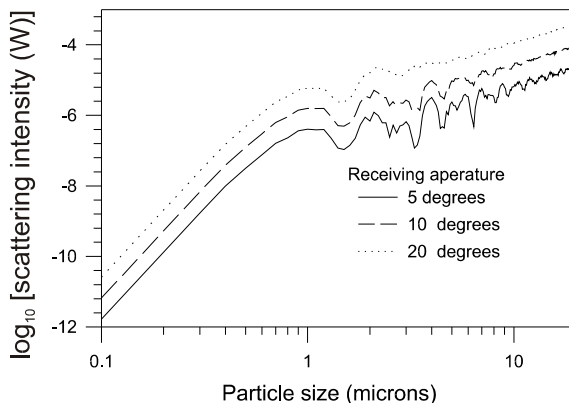


Figure 10.31: Influence of the receiving aperture opening on the Mie response function ($I_0 = 10^7 \text{ W/m}^2$, $\lambda = 632.8 \text{ nm}$, $\varphi = 15^\circ$).

this is associated with an additional integration over the wavelength spectrum (Broßmann, 1966).

Particle size measurements by the light intensity method require that only one particle be in the measurement volume at a time in order to enable the determination of the particle size from the measured signal amplitude. The simultaneous presence of more than one particle would result in an erroneous measurement called *coincidence error*. Therefore, sizing methods based on scattering intensity measurements are also called single particle counting techniques as described above. In order to fulfill this requirement, it is necessary to limit the measurement volume size.

In principle, the measuring volume can be defined in two ways. The first method is based on directing a narrow particle laden gas or liquid stream through the center portion of the measurement volume as shown in Figure 10.32a. In this case, the diameter of the stream determines the measurement volume size, not the optical arrangement. This method is also called *aerodynamic* or *hydrodynamic focusing* and can be only applied by sampling the particles from the two-phase system under consideration, i.e., by isokinetic sampling.

The second method for defining the measurement volume is based on an appropriate optical design of the transmitting and receiving optics using imaging masks in order to allow a demarcation of the probe volume as shown in Figure 10.32b. In so doing, it is also possible to apply the light scattering instrument for an on-line determination of particle size and concentration.

The size of the measurement volume has to be selected in such a way that, for a given maximum particle number concentration, the coincidence error is reduced to a large extent. The probability P_k for the presence of k -particles in the measurement volume follows a Poisson distribution

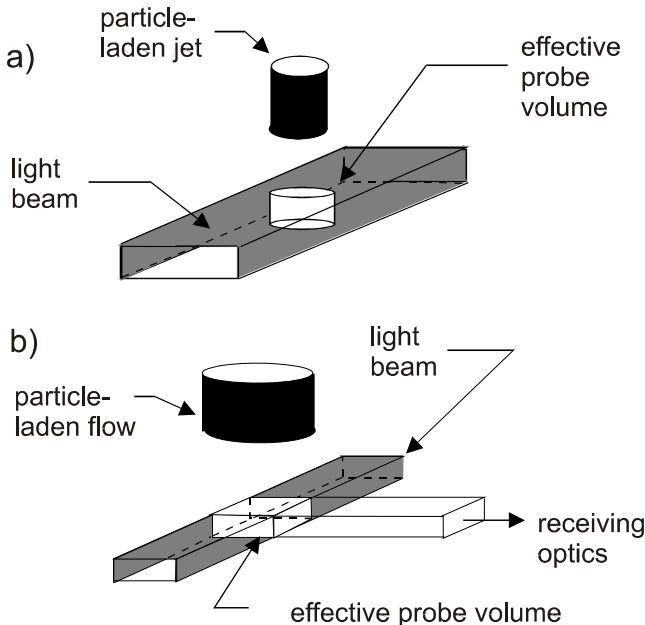


Figure 10.32: Methods to define the size of the measurement volume: (a) aerodynamic or hydrodynamic focusing, (b) optical demarcation of the probe volume.

$$P_k = \frac{N^k}{k!} e^{-N} \quad (10.46)$$

where, $N = nV_m$, is the number of particles in the probe volume V_m . The relative probability for the presence of two particles is

$$P'_2 = \frac{P_2}{P_1} = \frac{N}{2} \quad (10.47)$$

For a maximum allowable coincidence error of 5% (i.e., $P'_2 = 0.05$), the limiting averaged particle number in the measurement volume must be $N = 0.1$. This results in a maximum particle number concentration of

$$n_{\max} = \frac{0.1}{V_m} \quad (10.48)$$

This equation allows one to estimate the required size of the measurement volume for a given particle concentration. Especially for on-line measurements this criterion is quite often a limiting factor, so rather small measurement volumes have to be realized which are only possible by an appropriate optical configuration. Therefore, quite often, off-axis orientations of the receiving

optics have to be selected in order to allow a better demarcation of the measurement volume. This results in lower scattering intensities compared to a forward scattering arrangement (see Figure 10.30) and may limit the lower detectable particle size.

Moreover, the measurement volume must be illuminated uniformly, which can be achieved by properly shaping the light beam using masks in the transmitting optics. A more sophisticated approach is the elimination of the boundary zone error as illustrated in Figure 10.33. Particles passing through the edge of the illuminating light beam (i.e., particle 2) will be only partly illuminated and hence their scattered light intensity is too low and not proportional to their size. If the scattering intensity is still above the detection level (i.e., trigger level), such particles will be detected as smaller particles. For particles passing the edge of the beam which is imaged into the photodetector (i.e., particle 3 in Figure 10.33) only a portion of the scattered light will be received and again their size will be underestimated. The boundary zone error can be eliminated, for example, by extended optical systems with two collocated measurement volumes as introduced by Umhauer (1983).

A typical optical setup for a particle size analyzer operating with a 90° scattering angle together with the signal processing system (Umhauer, 1983) is shown in Figure 10.34. The transmitting optics consists of a white light source, a condenser, an imaging mask and an imaging lens. The scattered light is focused into the photomultiplier using a lens system and an imaging mask which limits the area from which scattered light is collected.

The photomultiplier provides an analog signal which is first filtered to remove signal noise and then digitized to obtain the pulse height of the signal. A counter is used to determine the number of signals detected. The data are then acquired by a computer and further processed to determine the particle size distribution. The number frequency distribution is obtained by grouping the pulse height U into a number of classes of width ΔU_i

$$f_n(U_i) = \frac{1}{N} \frac{\Delta N(U_i)}{\Delta U_i} \quad (10.49)$$

where $\Delta N(U_i)$ is the number of samples acquired in the amplitude interval i and N is the total number of samples acquired during the measuring time. In general, a calibration curve for U as a function of D has to be used to transform the distribution with respect to pulse height into a number frequency size distribution.

Moreover, it is possible to determine the particle number flux in the direction perpendicular to the probe volume cross-section from

$$\dot{n}_{tot} = \sum_{i=1}^I \dot{n}_i = \sum_{i=1}^I \frac{\Delta N(D_i)}{t_m A_m} = \frac{N}{t_m A_m} \quad (10.50)$$

where I is the number of size classes, t_m is the measuring time and A_m is the cross-section of the measurement volume. By multiplying the number flux \dot{n}_i by the particle mass $m_{d,i}$ the particle mass flux can also be obtained.

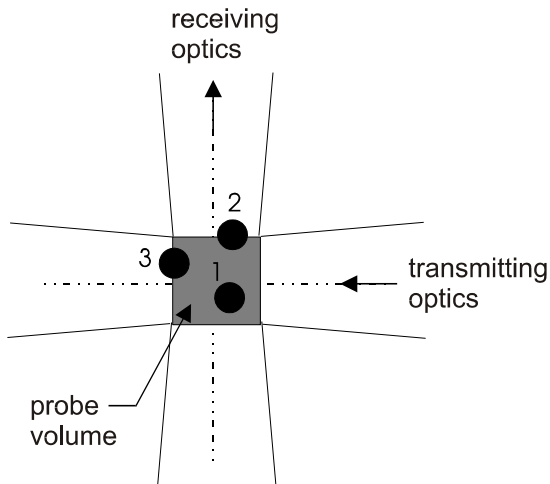


Figure 10.33: Illustration of the boundary zone error.

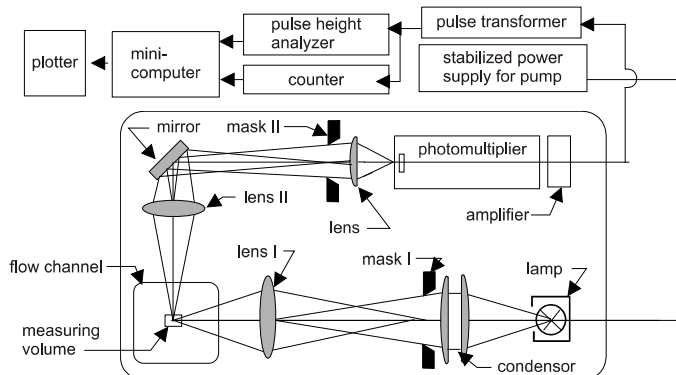


Figure 10.34: Optical configuration of a particle size analyzer operating at 90° scattering angle and signal processing. (Reprinted from *J. Aerosol Sci.*, 14, Umhauer, H., Particle size distribution analysis by scattered light measurements using an optically defined measuring volume, 765, 1983, with kind permission from Elsevier.)

Generally a calibration curve has to be used to relate pulse height (i.e., scattering amplitude) to some characteristic particle size, such as the diameter of a spherical particle or an equivalent diameter. A determination of the calibration curve using calculations based on the Mie theory is only possible for the rather limited case of homogeneous spherical particles.

10.3.4 Laser-Doppler anemometry

Laser-Doppler and Phase-Doppler anemometry, LDA and PDA, respectively, are the most advanced and accurate nonintrusive measuring techniques to obtain velocities of the fluid and particles in a two-phase flow. These measuring techniques enable one to obtain instantaneous (i.e., time series) and time-averaged measurements of the velocities with a high spatial resolution. Using PDA, the size of spherical particles, the refractive index of the particle and the particle concentration can be determined accurately as well.

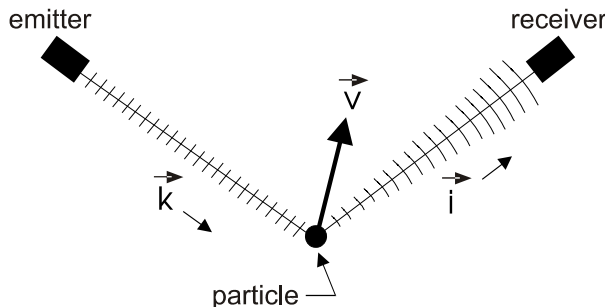


Figure 10.35: Doppler shift of scattered light from a moving particle.

The physical principle underlying LDA and PDA for velocity measurements is the *Doppler effect*, which relates the interaction of sound or light waves with a moving observer or the modulation of sound or light waves received by a stationary observer from a moving emitter. In LDA, this principle is used in such a way that a laser emits plane light waves which are received and transmitted from a moving emitter, the particle. Hence, the frequency or wavelength of the light received by the particle is already modulated. Since the moving particle scatters the light into space, an additional Doppler shift occurs when the scattered light is received from a stationary observer as shown in Figure 10.35. Hence, the frequency of light received at the photodetector can be determined from

$$f_r = f_e \frac{1 - \frac{\vec{v} \cdot \vec{l}}{c}}{1 - \frac{\vec{v} \cdot \vec{k}}{c}} \quad (10.51)$$

where f_e is the frequency of the laser source (emitter), \vec{v} is the velocity of the moving particle, c is the velocity of the light, and \vec{k}, \vec{l} are unit vectors in the

direction as defined in Figure 10.35. The frequency of the scattered light f_r is, however, too high to allow direct detection by a photodetector. Therefore, two different methods are used in LDA such that the frequency of light to be detected is considerably reduced: the *reference beam method* and the *Doppler frequency difference method*.

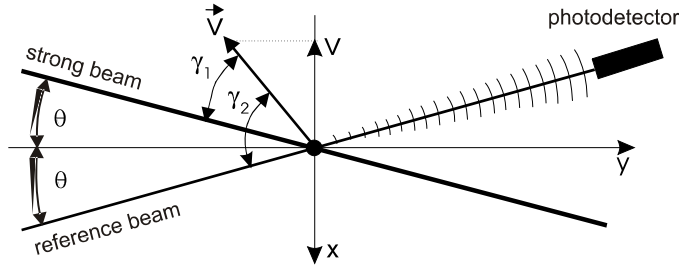


Figure 10.36: Configuration of reference beam LDA system.

This is achieved in the reference beam method by illuminating the particle with a strong light beam and interfering the resulting scattered light with a weak reference beam from the laser light source at the photodetector, as shown in Figure 10.36. Subtracting the frequency of the reference beam gives the Doppler frequency:

$$f_D = f_r - f_e \quad (10.52)$$

Using Equation 10.51 and introducing $\vec{v} \cdot \vec{k} = -|\vec{v}| \cos \gamma_1$ and $\vec{v} \cdot \vec{l} = -|\vec{v}| \cos \gamma_2$ gives

$$f_D = f_e \frac{1 + \frac{|\vec{v}|}{c} \cos \gamma_1}{1 + \frac{|\vec{v}|}{c} \cos \gamma_2} - f_e \quad (10.53)$$

$$f_D = \frac{1}{\lambda_e} \left(\frac{|\vec{v}| (\cos \gamma_1 - \cos \gamma_2)}{1 + \frac{|\vec{v}|}{c} \cos \gamma_2} \right) \quad (10.54)$$

The velocity component perpendicular to the bisector of the two incident beams is

$$v = -|\vec{v}| \sin \frac{\gamma_1 + \gamma_2}{2}$$

Using the trigonometric relationship

$$\cos \gamma_1 - \cos \gamma_2 = -2 \sin \frac{\gamma_1 + \gamma_2}{2} \sin \frac{\gamma_1 - \gamma_2}{2}$$

one obtains

$$f_D = \frac{1}{\lambda_e} \left[\frac{2v \sin \theta}{1 + \frac{|\vec{v}|}{c} \cos \gamma_2} \right] \quad (10.55)$$

where $\theta = \frac{1}{2}(\gamma_1 - \gamma_2)$. Since, in general, $|\vec{v}| \ll c$, Equation 10.55 finally becomes

$$f_D = \frac{2v \sin \theta}{\lambda_e} \quad (10.56)$$

It should be noted that the reference beam mode can be only operated at a fixed observation angle which coincides with the reference beam angle θ . Furthermore, the solid angle for light collection is limited to satisfy coherence requirements, i.e., the amount of scattered light which is collected is restricted.

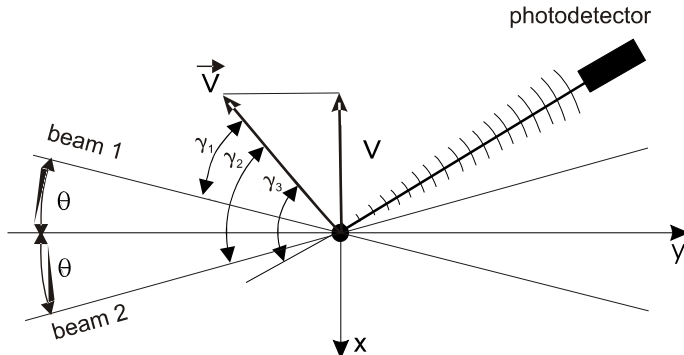


Figure 10.37: Configuration of Doppler difference frequency method (dual-beam LDA system).

More frequently, the Doppler frequency difference method is used for LDA measurements. Here the moving particle is illuminated by two laser beams from different directions as shown in Figure 10.37. In this case, the frequency of the scattered light is obtained from the difference of the contributions from two incident beams:

$$f_D = f_{r1} - f_{r2} \quad (10.57)$$

Using, once again, Equation 10.51 and the velocity components in the directions of the two beams, one obtains

$$\begin{aligned} f_D &= f_e \left(\frac{1 + (|\vec{v}|/c) \cos \gamma_1}{1 + (|\vec{v}|/c) \cos \gamma_3} - \frac{1 + (|\vec{v}|/c) \cos \gamma_2}{1 + (|\vec{v}|/c) \cos \gamma_3} \right) \\ &= \frac{|\vec{v}|}{\lambda_e} \frac{(\cos \gamma_1 - \cos \gamma_2)}{1 + (|\vec{v}|/c) \cos \gamma_3} \end{aligned} \quad (10.58)$$

For the velocity component perpendicular to the bisector of the two incident beams and with $|\vec{v}| \ll c$, Equation 10.58 becomes

$$f_D = \frac{2v \sin \theta}{\lambda_e} \quad (10.59)$$

This expression is identical to the one obtained for the reference beam method. However, the observation angle can be arbitrarily selected in the Doppler difference method. This implies that the observation angle and solid angle of scattered light collection may be selected for convenience according to the desired application.

The principle of the LDA may be explained using the *fringe model* in the following way. If two coherent light beams cross, the interference of the light waves results in a fringe pattern parallel to the bisector plane, (i.e., the $y - z$ plane in Figure 10.39) which can be visualized on a screen when a lens of small focal length is placed at the interaction of the beams. As the particle passes through the LDA probe volume, the scattering intensity detected by a photodetector is modulated in such a way that the Gaussian-shaped absolute scattering intensity (which results from the Gaussian intensity distribution in the probe volume) is superimposed with an alternating pattern produced by the particles passing through the bright and dark fringe pattern. As pointed out by Durst (1982), it should be noted, however, that the fringe pattern does not exist for the particle and is the result of integration by the human eye and the photodetector, both of which have a response time much larger than the inverse of the frequency of the light waves. The fringe spacing d_f is basically the conversion factor to determine the particle velocity from the measured Doppler difference frequency.

$$v = f_D \frac{\lambda_e}{2 \sin \theta} = f_D d_f \quad (10.60)$$

For particles smaller than the fringe spacing, a completely modulated Doppler signal will be generated as shown in Figure 10.42 as high visibility. As the particle becomes larger than the fringe spacing, the signal modulation is reduced and the scattering intensity received by the photodetector does not reduce to zero in the Doppler signal (low visibility in Figure 10.42)

A typical optical setup of an LDA system operated in the forward-scattering mode is shown in Figure 10.38. The transmitting optics consists of the laser, a beam splitter, one or two Bragg cells and a transmitting lens. The Bragg cells introduce a frequency difference between the two incident beams whereby it is possible to detect the direction of particle motion in the measurement volume (see, for example, Durst et al., 1981). The receiving optics consists of an imaging lens with a mask in front of it and a photodetector with a pinhole.

The spatial resolution of the velocity measurement depends on the dimensions of the LDA probe volume, which is determined by the initial laser beam diameter, the beam crossing angle (determined by the initial beam spacing and focal length of the transmitting lens), the focal length of the receiving lens

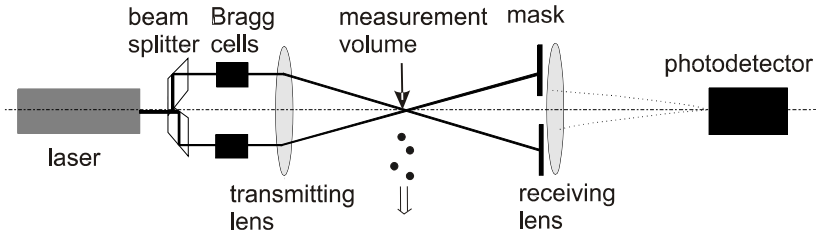


Figure 10.38: Typical optical setup of the dual beam laser Doppler Anemometer.

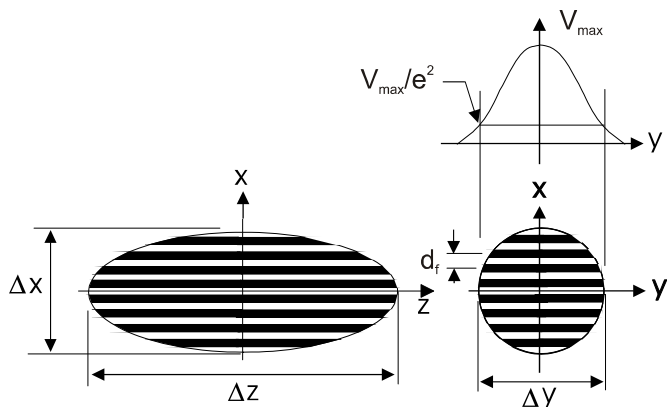


Figure 10.39: Dimensions of LDA probe volume.

and the observation angle of the receiving optics. Since the incident, focused laser beams have a Gaussian intensity distribution as shown in Figure 10.39, their waist diameter at the focal plane is taken to be that value at which the light intensity has diminished to $1/e^2$ of the maximum value at the beam axis. The waist diameter is given by

$$d_m = \frac{4\hat{f}_e \lambda_e}{\pi d_0} \quad (10.61)$$

where d_0 is the $1/e^2$ unfocused laser beam diameter and \hat{f}_e is the transmitting lens focal length. The probe volume established by the two crossing beams has an ellipsoidal shape as shown in Figure 10.39. The dimensions of the $1/e^2$ ellipsoid, corresponding to Figure 10.39, are given by

$$\Delta x = \frac{d_m}{\cos \theta} \quad (10.62a)$$

$$\Delta y = d_m \quad (10.62b)$$

$$\Delta z = \frac{d_m}{\sin \theta} \quad (10.62c)$$

The number of fringes in the $1/e^2$ measurement volume can be determined from

$$N_f = \frac{\Delta x}{d_f} = \frac{d_m}{\cos \theta} \frac{2 \sin \theta}{\lambda_e} = \frac{8 \hat{f}_e}{\pi d_o} \tan \theta = \frac{4 \Delta b}{\pi d_o} \quad (10.63)$$

where Δb is the initial spacing of the transmitting beams.

By using an off-axis orientation of the receiving optics, the length of the portion of the measurement volume imaged into the photodetector can be further reduced and the spatial resolution improved. However, due to the angular dependence of the light scattering intensity, any off-axis orientation of the receiving optics results in reduced scattering intensities as shown in Section 10.3.3.

For more details about the principle of the LDA, frequency shifting, properties of photodetectors and signal processing methods, the reader is referred to the relevant literature, such as Durst et al. (1981, 1987) and Tropea (2011). A review of signal processing is found in Tropea (1995). Applications of LDA for two-phase flow measurements are described below.

The basic ideas for LDA applications for two-phase flows were introduced by Farmer (1972, 1974), Durst and Zaré (1975) and Roberts (1977). They showed that LDA may also be used for velocity measurements of large reflecting and refracting particles. The light waves produced by the two incident laser beams either reflect or refract with large particles, as indicated in Figure 10.40, and produce fringes in space. The rate at which the fringes cross any point in space, i.e., at the photodetector, is the same at all points in the surrounding space and is linearly related to the velocity component of large non-deformable particles perpendicular to the symmetry line between the two incident beams. The theoretical derivations of Durst and Zaré (1975) revealed that the relations for the Doppler difference frequency for large reflecting or refracting particles are identical to the universal equation for laser-Doppler anemometry (Equation 10.59) when the intersection angle of the two incident beams is small and the photo-detector is placed at a distance much larger than the particle diameter from the measurement volume.

These findings are the basis for the application of LDA for particle velocity measurements in two-phase flows. Because LDA is a nonintrusive optical technique, it may be used for measurements in two-phase flow systems as long as optical access is possible and the two-phase system is dilute enough to allow the transmission of the laser beam and the scattered light. Numerous studies

have been published in the past where LDA has been applied to various types of gas-solid two-phase flows, liquid sprays, and bubbly flows.

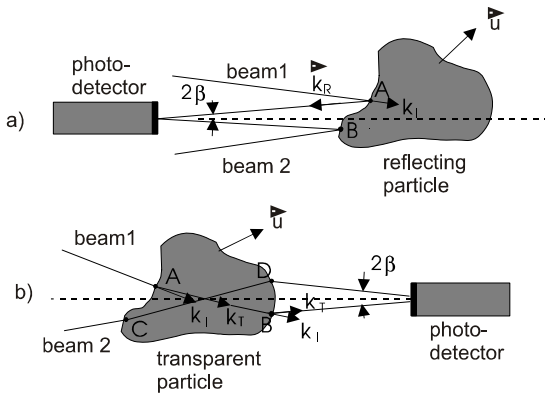


Figure 10.40: Interference of two laser beams for large reflecting (a) and refracting (b) particles. (The intersection points of the incident and refracting beams with the surface are indicated by A, B, C and D.)

There also have been several attempts to apply laser-Doppler anemometry for the simultaneous measurement of particle velocity, size and concentration (Farmer, 1972; Chigier et al., 1979; Durst, 1982; Hess, 1984; Hess and Espinosa, 1984; Allano et al., 1984; Negus and Drain, 1982). The sizing of particles by LDA is based on:

- the absolute value of the scattering intensity (i.e., pedestal of the Doppler signal, Figure 10.41), or
- the signal visibility (Figure 10.42)

The *pedestal* of the Doppler signal is the low frequency component of the signal obtained by using a low pass filter. As shown in Section 10.3.3, the intensity of the scattered light depends on the particle size. However, the size-amplitude relation shows strong fluctuations in the Mie region when the particle size is comparable to the laser wavelength. Moreover, particle sizing based on intensity measurements generally requires calibration. An additional problem with sizing particles by a standard LDA system is the effect of the non-uniform distribution of intensity within the measurement volume. Laser beams normally have a Gaussian intensity distribution. Particles passing through the edge of the measurement volume have a lower scattering intensity and are detected as smaller particles. This effect, which is also called *trajectory ambiguity*, or Gaussian beam effect, results in the effective dimensions of the probe volume being dependent on particle size. A small particle passing the edge of the measurement volume might not be detected by the

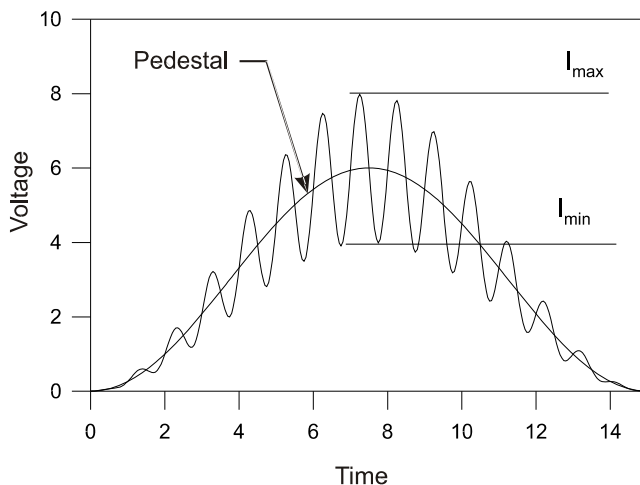


Figure 10.41: Doppler signal and definition of pedestal.

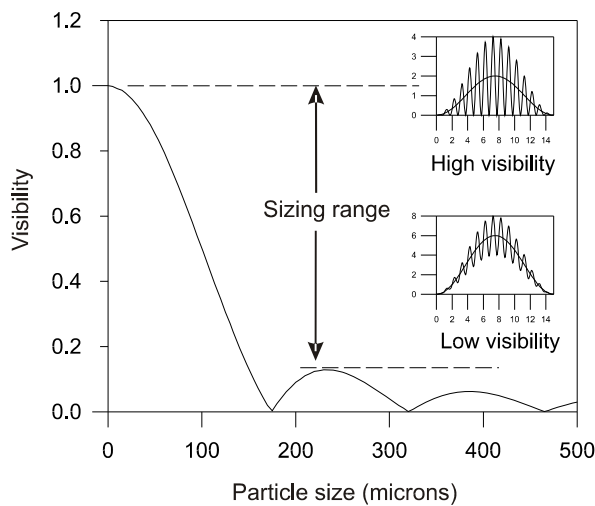


Figure 10.42: Variation of signal visibility with particle size (off-axis collection).

data acquisition system due to its low scattering intensity, while a large particle at the same location still produces a signal which lies above the detection level as shown in Figure 10.43. This effect also has consequences for the determination of particle concentration, which will be described later. Therefore, measurements of particle size and concentration by LDA require extensions of the optical system or data acquisition procedures in order to reduce errors due to the Gaussian beam effect.

The following methods have been mainly used for particle sizing by LDA:

- Limitation of the probe volume size by additional optical systems (i.e., gate photodetector or two-color systems),
- Modification of the laser beam to produce a “top-hat” intensity distribution,
- Combined measurements of visibility and pedestal amplitude.

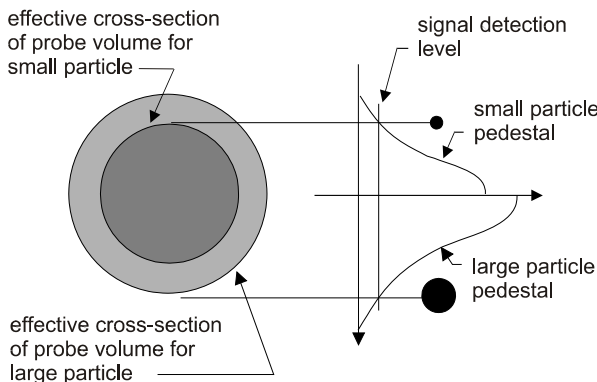


Figure 10.43: Illustration of the Gaussian beam effect on intensity measurements by LDA and its influence on the effective cross-section of the measurement volume.

There are several examples of particle size measurements using LDA which were developed before the introduction of PDA. Most of the techniques, based on intensity and visibility measurements described below, were shown not to be very reliable even though, in a few cases, they were used to develop commercial instrumentation. It should be emphasized, however, that there is still a need for reliable instruments for local, single point size and velocity measurements in two-phase flows with nonspherical particles common to industrial processes.

In order to limit the region of the probe volume from where signals are received, Chigier et al. (1979) used additional receiving optics placed at 90° off-axis to trigger an LDA receiving system mounted in forward-scattering. For

further reduction of the trajectory ambiguity, a sophisticated signal processing system was developed. A comparison of particle size distribution measurements by LDA with results obtained by the slide impaction method gave only fair agreement.

By superimposing two probe volumes of different diameter and color it is possible to trigger the data acquisition system only when the particles pass through the central part of the larger probe volume where the intensity is more uniform. Such a co-axial arrangement of two probe volumes may be realized by using a two-component LDA system with a different waist diameter for each color (Yeoman et al., 1982; Modarress and Tan, 1983) or by overlapping a large diameter single beam with the LDA probe volume (Hess, 1984; Morikita et al., 1994). When a particle passes through the LDA probe volume, the light-scattering intensity from the larger single beam is measured to determine the particle size as shown in Figure 10.44.

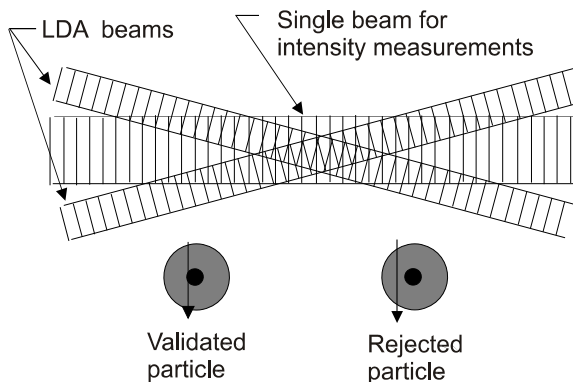


Figure 10.44: Co-axial arrangement of two probe volumes of different color.

For producing laser light beams with uniform intensity distribution, the “top-hat” technique may be applied. To produce such a top-hat profile, Allano et al. (1984) used a holographic filter and related the scattering intensity with the particle diameter by using the Lorenz-Mie theory. Grèhan and Gouesbet (1986) studied this system for simultaneous measurements of particle size and velocity. Also, a combination of LDA with light scattering instruments has been applied for simultaneous particle size and velocity measurements (Durst, 1982).

In addition, signal modulation may be used for particle sizing by LDA (Farmer, 1972). Compared to the scattering intensity measurements the method has a number of advantages since the visibility is independent of scattering intensity and, hence, is neither biased by laser power nor detector sensitivity. The visibility is determined from the maximum and minimum amplitudes of the low-pass filtered Doppler signal as indicated in Figure 10.42.

$$V = \frac{I_{\max} - I_{\min}}{I_{\max} + I_{\min}} \quad (10.64)$$

The visibility of the Doppler signal decreases with increasing particle size as illustrated in Figure 10.42. The first lobe in the visibility curve covers the measurable particle size range. With a further increase in particle size, secondary maxima appear in the visibility curve.

However, the visibility curve strongly depends on the optical configuration of the receiving optics, i.e., the off-axis angle and the size and shape of the imaging mask in the receiving optics. The latter effect was evaluated in detail by Negus and Drain (1982). Example Mie calculations for the visibility curves for different optical configurations are shown in Figure 10.45. It is obvious that the shape of the imaging mask influences the measurable size range. However, the measurable particle size range is significantly increased by using an off-axis arrangement of the receiving optics (see also Chigier, 1983).

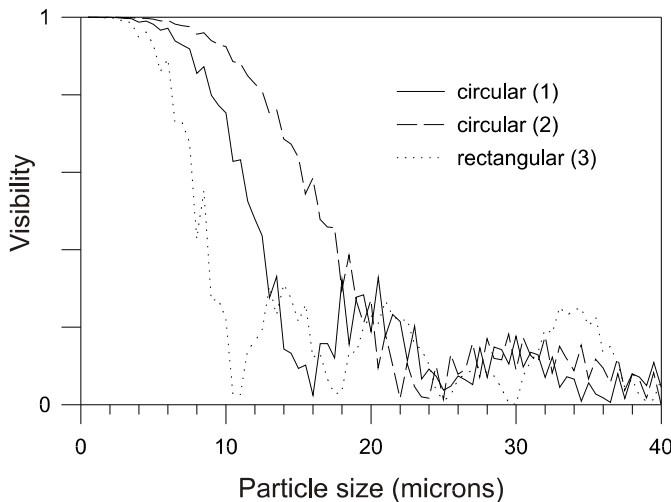


Figure 10.45: Visibility curves for different optical configurations of the receiving optics ($\lambda = 632.8$ nm, $\varphi = 0^\circ$; [1] $d_f = 10.2$ μm circular mask, $\Delta\delta = 4^\circ$; [2] $d_f = 18$ μm circular mask, $\Delta\delta = 4^\circ$; [3] $d_f = 6.55$ μm rectangular mask, receiving aperture angle in horizontal and vertical direction, $\Delta\delta_h = 11^\circ$, $\Delta\delta_v = 4^\circ$).

Extensive research has been performed on the suitability of the visibility method for particle sizing. It was found that this method appears to be very sensitive to the positioning of the aperture mask, the accuracy of the mask dimensions and the particle trajectory through the LDA probe volume. Therefore, additional optical systems are needed to enable a combination of visibility and signal amplitude for particle size evaluation. A detailed review

on the visibility method has been published by Tayali and Bates (1990) in which a number of other LDA-based methods are also described.

Because of the particle size-dependent dimensions of the probe volume and the difficulties associated with particle size measurements using LDA, the measurement of particle concentration is generally based on a calibration procedure using the information from a global mass balance. In practice, accurate particle concentration measurements by laser-Doppler anemometry are only possible for simple one-dimensional flows with mono-sized particles. In this case, the probe volume size may be determined by calibration. This, however, does not remove the problem related to a spatial distribution of particle concentration in the flow which affects the scattering intensity received by the photodetector from the measurement location due to different optical path lengths through the particle-laden flow and the associated different rates of light absorption (Kliafas et al., 1990).

For a simultaneous determination of fluid and particle velocity by LDA, the fluid flow has to be additionally seeded by small tracer particles which are able to follow the turbulent fluctuations. The remaining task is the separation of the Doppler signals resulting from tracer particles and the dispersed phase particles. In most cases, this discrimination is based on the scattering intensity combined with some other method to reduce the error due to the Gaussian beam effect. The discrimination procedure introduced by Durst (1982), for example, was based on the use of two receiving optical systems and two photodiodes which detect the blockage of the incident beams by large particles. Together with sophisticated signal processing, it was possible to successfully separate signals from large and tracer particles.

An improved amplitude discrimination procedure using two superimposed measurement volumes of a different size and color was developed by Modarress and Tan (1983). The smaller or pointer probe volume was used only to trigger the measurements from the larger control volume. By this scheme, it was ensured that the sampled signals were received only from the center part of the larger probe volume where the spatial intensity distribution is relatively constant.

A combined amplitude-visibility discrimination method, which did not rely on additional optical components, was proposed by Börner et al. (1986). After first separating the signals based on the signal amplitude, the visibility of all signals was determined to ensure that no samples from large particles passing the edge of the measurement volume were collected as tracer particles. This method required additional electronic equipment and sophisticated software for signal processing.

A much simpler amplitude discrimination method was introduced by Hishida and Maeda (1990). To ensure that only particles traversing the center of the measurement volume were sampled, a minimum number of zero crossings in the Doppler signal were required for validation.

The discrimination procedures described here can be successfully applied only when the size distribution of the dispersed phase particles is well sepa-

rated from the size distribution of the tracer particles.

An LDA combined with a direct imaging technique, referred to as the *shadow-Doppler technique*, has been developed for combined size and velocity measurements in two-phase flows with arbitrary shaped particles as found, for example, in coal combustion systems (Hardalupas et al., 1994).

A particle moving through the LDA probe volume produces a planar shadow of the non-spherical particle which is recovered by a line array of photodiodes. The temporal signals due to the particle velocity are converted to a planar image of the particle. With this information, the particle shape and orientation can be inferred. When using a typical shape indicator, such as sphericity or eccentricity, one should however keep in mind that these values are not necessarily a property of the particles, but are biased by the particle orientation which is affected by the flow structure and turbulence. Since the image produced is not influenced by the optical properties of the particle, shadow imaging can be also applied to optically inhomogeneous particles (e.g., droplet suspensions) in order to measure their size (Morikita and Taylor, 1998). The shadow Doppler technique has emerged in a commercial instrument.

10.3.5 Phase-Doppler anemometry

The principle of phase-Doppler anemometry (PDA) is based on the Doppler difference method used for conventional laser-Doppler anemometry and was first introduced by Durst and Zaré (1975). By using an extended receiving optical system with two or more photodetectors it is possible to measure particle size and velocity simultaneously. The phase shift of the light scattered by a spherical particle through either refraction or reflection from the two intersecting laser beams is used to obtain the particle size.

The operational principle of PDA can be explained using the simple fringe-type model assuming that the interference fringes in the intersection region of the two incident light beams of the LDA are parallel light rays (Saffman, 1987). A spherical transparent particle placed into this fringe pattern will act as a kind of lens with focal length \hat{f} which will project the light rays into space as indicated in Figure 10.46. The separation of the projected fringes at a distance ℓ from the particle is given approximately by

$$\Delta s \approx (\ell - \hat{f}) \frac{d_f}{\hat{f}} \quad (10.65)$$

where d_f is the fringe spacing in the measurement volume. The focal length of the particle is given by

$$\hat{f} = \frac{m}{m-1} \frac{D}{4} \quad (10.66)$$

where $m = n_d/n_m$ is the ratio of the refractive index of the particle to that of the surrounding medium. Since small particles are considered and ℓ is usually

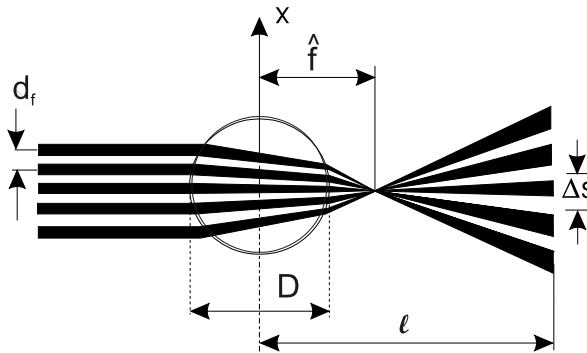


Figure 10.46: Fringe model for phase Doppler principle for case of refraction.

much larger than the particle diameter, one obtains

$$\Delta s \approx \ell \frac{d_f}{f} \quad (10.67)$$

The separation of the projected fringes is obtained from

$$\Delta s \approx \frac{4\ell d_f}{D} \frac{m-1}{m} \quad (10.68)$$

so the separation varies inversely as the particle diameter. A measurement of Δs can be used to determine particle size.

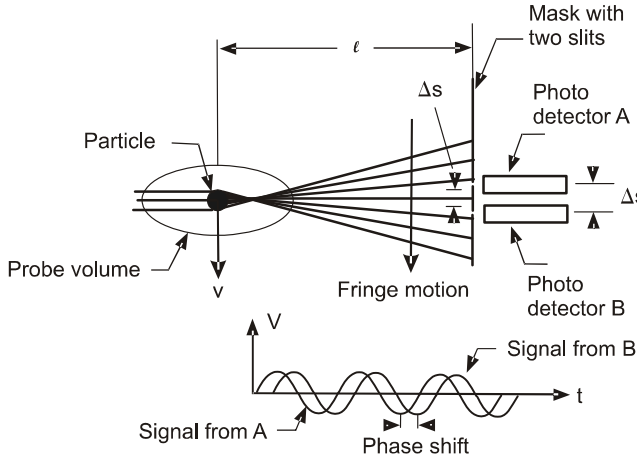


Figure 10.47: Sketch showing the basic concept of the PDA system.

A simple schematic diagram illustrating the operation of the PDA is shown in Figure 10.47. A mask with two slits is placed at the distance ℓ from the

particle. The two slits, separated by a distance $\Delta s'$, allow light to reach two photodetectors, A and B . As the particle passes through the probe volume, the fringe pattern sweeps across the mask and generates signals from the photodetectors as shown in the figure. If Δs were equal to $\Delta s'$, the two signals would be in phase. However, because Δs does not equal $\Delta s'$ a phase shift occurs between the two signals, as shown. This phase shift can be related directly to Δs and used in Equation 10.68 to determine particle size. Of course, the signal assumes the form of a Doppler burst but a sine wave is used in the figure for illustrative purposes. The frequency of the signal is Doppler difference frequency corresponding to the particle velocity, v .

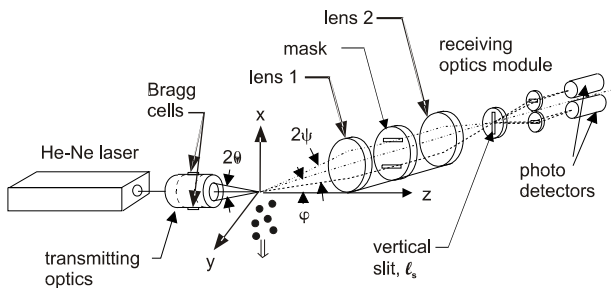


Figure 10.48: Optical configuration of a two-detector phase-Doppler anemometer.

A typical optical set-up of a two-detector PDA-system is shown in Figure 10.48. The transmitting optics is the conventional dual beam LDA optics which, in this case, uses two Bragg cells for frequency shifting. The PDA receiver is positioned at the off-axis angle φ (scattering angle) and a collection (or receiving) lens, lens 1, produces a parallel beam of scattered light. This parallel light beam passes through a mask which defines the elevation angles of the two photo-detectors. In this case, the mask has two rectangular slits in order to allow the light to pass through to the photo-detectors. The slits are located parallel to the $y - z$ plane at the elevation angle $\pm\psi$. The light is then focused by lens 2 on a spatial filter, i.e., a vertical slit which defines the effective length of the probe volume from where the scattered light can be received. The effective length of the probe volume is determined by the width of the spatial filter l_s (typically $100 \mu m$) and the magnification of the receiving optics; that is, the focal length of the collecting lens to the second lens, $L_s = l_s \hat{f}_1 / \hat{f}_2$. Finally, the scattered light passing the two rectangular slits is focused onto the photo-detectors using two additional lenses.

The signals seen by the two detectors will have a relative phase difference given by

$$\Delta\phi = 2\pi \frac{\Delta s'}{\Delta s} = 2\pi \frac{2\ell}{\Delta s} \sin \psi \quad (10.69)$$

where ψ is the elevation angle of one photodetector measured from the centerline in Figure 10.48, which is also the bisector plane of the two incident laser beams producing the measurement volume. The length ℓ now becomes the focal length of lens 1, f_1 . By using Equation 10.68 for the fringe separation distance, the phase shift becomes

$$\Delta\phi = \pi \frac{D}{d_f} \frac{m}{m-1} \sin \psi \quad (10.70)$$

Finally, using the equation relating laser wave length and fringe spacing

$$d_f = \frac{\lambda}{2 \sin \theta}$$

gives

$$\Delta\phi = \frac{2\pi D}{\lambda} \frac{m}{m-1} \sin \theta \sin \psi \quad (10.71)$$

It should be emphasized that Equation 10.71 is an approximation valid only for small scattering angles, φ , which represents the off-axis angle measured from the forward-scattering direction, to the optical axis of the receiver. The equation is very useful, however, to provide a rough estimate of the measurable particle size range for a given system or to perform a preliminary design of the optical configuration for small scattering angles.

To determine the particle size from the measured phase difference, the required correlations are derived from geometrical optics which is valid for particles that are large compared to the wavelength of light (van de Hulst, 1981). The phase due to the length of optical path is given by

$$\delta = \frac{2\pi D m}{\lambda} (\sin \tau - p m \sin \tau') \quad (10.72)$$

The parameter p indicates the type of scattering, i.e., $p = 0, 1, 2, \dots$ for reflection, first-order refraction, second-order refraction, and so on. Moreover, τ and τ' are the angles between the incident ray and the surface tangent and the refracted ray and the surface tangent, respectively, as shown in Figure 10.49. The relationship between τ and τ' is given by Snell's law.

$$\cos \tau' = \frac{1}{m} \cos \tau \quad (10.73)$$

For a dual-beam LDA system, the phase difference of the light scattered from each of the two beams is given in a similar way

$$\Delta\phi = \frac{2\pi D m}{\lambda} [(\sin \tau_1 - \sin \tau_2) - p m (\sin \tau'_1 - \sin \tau'_2)] \quad (10.74)$$

where the subscripts 1 and 2 are used to indicate the contributions from both incident beams. For two photodetectors placed at a certain off-axis angle φ and placed symmetrically with respect to the bisector plane at the elevation

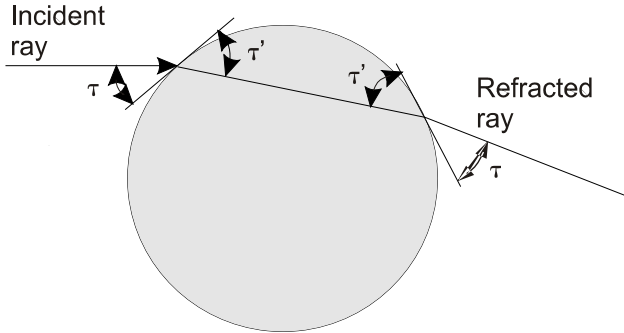


Figure 10.49: Phase difference of a light refracted at a spherical particle.

angles $\pm\psi$, one obtains the phase difference (see, for example, Bauckhage, 1988)

$$\Delta\phi = (2\pi Dm/\lambda) \Phi \quad (10.75)$$

The parameter Φ depends on the scattering mode. For reflection ($p = 0$)

$$\Phi = \sqrt{2}[(1 + \sin\theta \sin\psi - \cos\theta \cos\psi \cos\varphi)^{1/2} - (1 - \sin\theta \sin\psi - \cos\theta \cos\psi \cos\varphi)^{1/2}] \quad (10.76)$$

and for refraction ($p = 1$)

$$\Phi = 2 \left\{ \begin{array}{l} [1 + m^2 - \sqrt{2}m(1 - \sin\theta \sin\psi + \cos\theta \cos\psi \cos\varphi)^{1/2}]^{1/2} \\ -[1 + m^2 - \sqrt{2}m(1 + \sin\theta \sin\psi + \cos\theta \cos\psi \cos\varphi)^{1/2}]^{1/2} \end{array} \right\} \quad (10.77)$$

where 2θ represents the angle between the two incident beams. Since the phase difference is a function of p , one expects a linear relation for the correlation between particle size and phase for only those scattering angles where one scattering mode is dominant (i.e., reflection or refraction). Therefore, the values for Φ have been given for these two scattering modes only (i.e., Equations 10.76 and 10.77). Other scattering modes, i.e., $p = 2$, may be also used for phase measurements, especially in the region of backscattering as will be shown later. Such a backscatter arrangement may be used for opaque particles and also might have advantages with regard to optical access since both the incident beams and the scattered light may be transmitted through one window.

By recording the band-pass filtered Doppler signals from the two photodetectors the phase $\Delta\phi$ is determined from the time lag between the two signals as indicated in Figure 10.50.

$$\Delta\phi = 2\pi \frac{\Delta t}{T} \quad (10.78)$$

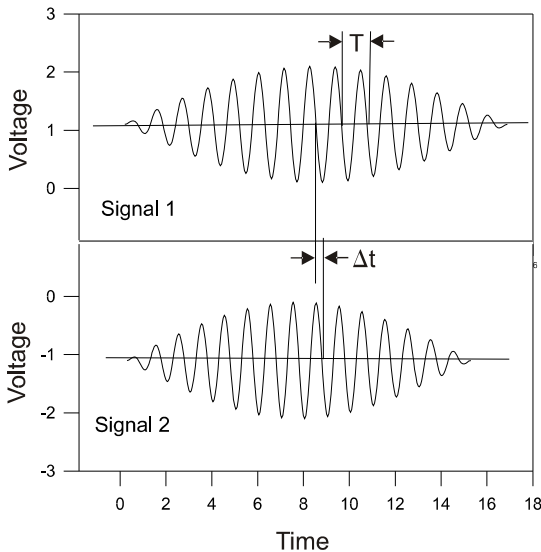


Figure 10.50: Determination of phase shift from two band-pass filtered Doppler signals.

where T is the time of one cycle of the signal. With Equation 10.78 it is now possible to determine the particle diameter for a given refractive index n_m and wavelength λ .

$$D = \frac{\lambda}{2\pi m} \frac{1}{\Phi} \Delta\phi \quad (10.79)$$

Obviously a PDA system with only two detectors can only distinguish a phase shift between 0 and 2π which limits the measurable particle size range for a given optical configuration. Therefore, three-detector systems are mainly used in which two phase differences are obtained from detector pairs having different spacing as shown in Figure 10.51. As shown in the figure, the measurement of a $\Delta\phi_{1-2}$ phase shift with a two-detector system would yield three possible particle diameters. However, the phase shift $\Delta\phi_{1-3}$ measured with the 1-3 detector removes the ambiguity. This method enables one to extend the measurable particle size range while maintaining the resolution of the measurement. With the detector pair 1-3 a high resolution of the measurement is achieved. However, the upper measurable particle size is limited by the 2π ambiguity. The upper size limit is eventually given by the phase size correlation ϕ_{1-3} . Moreover, the ratio of the two phase measurements may be used for additional validation, such as checking the sphericity of deformable

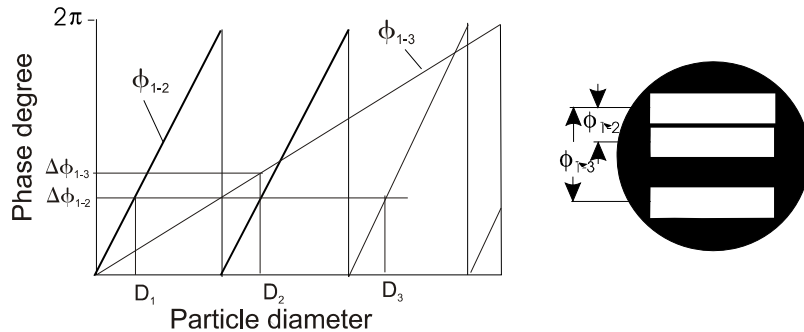


Figure 10.51: Phase size relations for a three-detector phase-Doppler system.

particles (liquid droplets or bubbles).

Example: The optical configuration of a two-detector PDA system for measurements in a particle-laden channel flow (air with $\rho_c = 1.18 \text{ kg/m}^3$) with a mass concentration of two is to be designed. The particles (spherical glass beads with $\rho_d = 2500 \text{ kg/m}^3$, $n_p = 1.52$) have a size range from 40 to 150 μm with a number averaged diameter of 60 μm . The relative refractive index is 1.52. Transmitting optics with a focal length of 500 mm and a beam spacing Δb of 30 mm together with a He-Ne laser ($\lambda = 632.8 \text{ nm}$) with a beam diameter d_o of 1 mm are available. The receiving optics should be positioned at an off-axis angle of 30° where refraction is the dominant scattering mode. The spatial filter in the receiving optics should have a width of 100 μm and a magnification of about 2 so that a length of 200 μm of the probe volume is imaged onto the receiver.

- Determine a suitable elevation angle for the rectangular slits to ensure that particles up to 200 μm can be measured.
- Estimate the coincidence error for the presence of two particles in the probe volume. Assume that the gas and particles have the same mean velocity and carry out the estimate assuming that the particles are monodisperse with a size corresponding to the most probable diameter in the size distribution, i.e., 60 μm .
- Redesign your optical system to reduce the coincidence error to 5% by considering changing the focal length transmitting lens.

Solution:

The half angle of the incident beam, θ , is

$$\tan \theta = \frac{\Delta b}{2f_e}, \quad \theta = 1.72^\circ$$

Using Equation 10.71, one can solve for ψ in the form

$$\sin \psi = \Delta\phi \frac{\lambda_e}{2\pi D} \frac{m-1}{m} \frac{1}{\sin \theta}$$

With $\Delta\phi = 2\pi$, $D = 200 \mu\text{m}$, the value for ψ is 2.06° . From Equation 10.75 with $\Delta\phi = 2\pi$ the maximum diameter is

$$D_{\max} = \frac{\lambda}{m\Phi} \quad (10.80)$$

Using Equation 10.77 with $\Psi = 2^\circ$ gives $\Phi = 0.0027$

$$D_{\max} = 154 \mu\text{m} \quad (10.81)$$

which is within the size range. However, extending the range to a $200\text{-}\mu\text{m}$ particle requires a smaller angle. For $\Psi = 1.5^\circ$, $\Phi = 0.00202$ which would allow measurement of a $206\text{-}\mu\text{m}$ particle. With a 500-mm lens, this would require a 2.6-cm spacing. The final choice will depend on the slit separation and receiver focal lengths that are available.

From Equation 10.61, the waist diameter is

$$d_m = \frac{4\hat{f}_e \lambda_e}{\pi d_o} = 402 \mu\text{m}$$

and the probe volume is

$$V_m = \frac{\pi}{4} d_m^2 L_s = 0.0254 \text{ mm}^3$$

The relative probability of having two particles in the probe volume is given by Equation 10.47 as

$$P'_2 = \frac{N_m}{2} = \frac{n V_m}{2}$$

For a mass concentration of 2

$$C = \frac{\alpha_d \rho_d}{\alpha_c \rho_c} = 2 \quad (10.82)$$

Taking $\alpha_c \simeq 1$

$$\alpha_d = 2 \frac{1.18}{2500} = 9.4 \times 10^{-4} \quad (10.83)$$

The volume fraction and number density are related by

$$\alpha_d = n \frac{\pi}{6} D^3 \quad (10.84)$$

For $60\text{-}\mu\text{m}$ particles

$$n = 8.3 / \text{mm}^3 \quad (10.85)$$

Thus

$$\frac{n V_m}{2} = \frac{8.3 \times 0.254}{2} = 0.1 \quad (10.86)$$

so the coincidence error is 0.1 or 10%.

For a coincidence error of 5%, the measuring volume has to be halved which can be done by decreasing the probe diameter by a factor $\sqrt{2}$. This requires the focal length to be 350 mm. A transmitting lens with a focal length of 350 mm or less would be adequate.

The principle of geometrical optics introduced previously to calculate light scattering from particles is limited to particle sizes larger than the wavelength of light and takes into account reflection and refraction. This implies that no interference of the scattering modes is considered (van de Hulst, 1981). In most cases, this theory is sufficient to support the optical layout of PDA systems. Also this theory can be easily extended to account for the Gaussian light intensity distribution in the probe volume (Sankar and Bachalo, 1991).

For small particles, diffraction represents a special contribution to the light scattering which may affect and disturb the phase measurement. Therefore, the more general Mie theory has to also be applied to determine the scattering characteristics for a particle of any given size. The Mie theory relies on the direct solution of Maxwell's equations for the case of the scattering of a plane light wave by a homogeneous spherical particle for arbitrary size and refractive index. In order to calculate the scattered field of a PDA system, it is necessary to add the contributions of the two incident beams and to average over the aperture of the receiving optics by taking into account the polarization and phase of each beam. Hence, it is possible to determine the intensity, visibility and phase for arbitrary optical configurations. To allow for the influence of the Gaussian beam, the generalized Lorenz-Mie theory (GLMT) has also been applied to optimize PDA systems (Grèhan et al., 1992).

There are several issues with regard to the optimum selection of the optical systems which can be exploited for different types of particles (i.e., reflecting and transparent particles) based on calculations by geometrical optics and Mie theory (DANTEC/Invent, 1994). The calculations using geometrical optics are performed for a point-like aperture, while the Mie calculations account for the integration over a rectangular aperture with given half-angles in the horizontal (δ_h) and vertical (δ_v) directions with respect to the $y - z$ plane. The half-angles are defined as

$$\delta_h = \Delta W / 2\hat{f}_1 \quad \delta_v = \Delta H / 2\hat{f}_1 \quad (10.87)$$

where ΔW and ΔH are the width and height of the aperture, respectively. It should be noted that the integration of the scattered light over the receiving aperture is important for obtaining a linear phase-size relation.

Flow	$m = n_p/n_m$	φ_B	φ_C	φ_R
air bubbles in water	1.0/1.33	106.12	82.49	-
water droplets in oil	1.33/1.50	96.88	55.09	-
oil droplets in water	1.5/1.33	283.1	55.09	94.10
water droplets in air	1.33/1.0	83.12	82.49	137.48
diesel droplets in air	1.46/1.0	68.82	93.54	153.34
glass particles in air	1.52/1.0	66.68	97.72	158.92

Table 10.4. Characteristic scattering angles for different combinations of the dispersed and continuous phase, i.e., different relative refractive indices.

Transparent particles may be distinguished between those having a refractive index larger or smaller than the surrounding medium. Liquid droplets or glass beads in air have a relative refractive index (i.e. n_p/n_m) which is larger than unity typically in the range 1.3 to 1.5, and bubbles in liquid have a relative refractive index less than unity (see Table 10.4).

The selection of the optimum optical configuration should be based mainly on the relative importance of the scattering mode considered (i.e., reflection, refraction or second-order refraction) with respect to the other modes and the resulting linearity of the phase-size relation. The intensity of the particular scattering mode considered should be at least 10 times larger than the sum of all the other scattering modes. The intensities of the different scattering modes are determined by using calculations based on geometrical optics where both parallel (p) and perpendicular (s) polarization are considered as shown in Figure 10.52. Diffracted light (not shown in Figure 10.52) is concentrated in the forward-scattering direction and independent of polarization. This region should be avoided, since this scattering mode is not suitable for PDA particle sizing. Reflected light covers the entire angular range for refractive index ratios below and above unity. However, a distinct minimum is found for parallel polarization at the so-called *Brewster's angle* which is given by

$$\varphi_B = 2 \tan^{-1}(1/m) \quad (10.88)$$

The Brewster angle decreases with an increasing refractive index ratio (see Table 10.4). First-order refraction is concentrated in the forward-scattering range and extends up to the critical angle which, for different relative refractive indices $m = n_p/n_m$, is given as:

$$\varphi_c = 2 \cos^{-1}(m) \quad m < 1 \quad (10.89)$$

$$\varphi_c = 2 \cos^{-1}(1/m) \quad m > 1 \quad (10.90)$$

The critical angle increases with an increasing relative refractive index (for $m > 1$) and first-order refraction becomes dominant over reflection for a wider angular range. For $m < 1$ the critical angle increases with decreasing refractive index ratio. Second-order refraction again covers the entire angular range for a relative refractive index less than unity. For m larger than unity, second-order

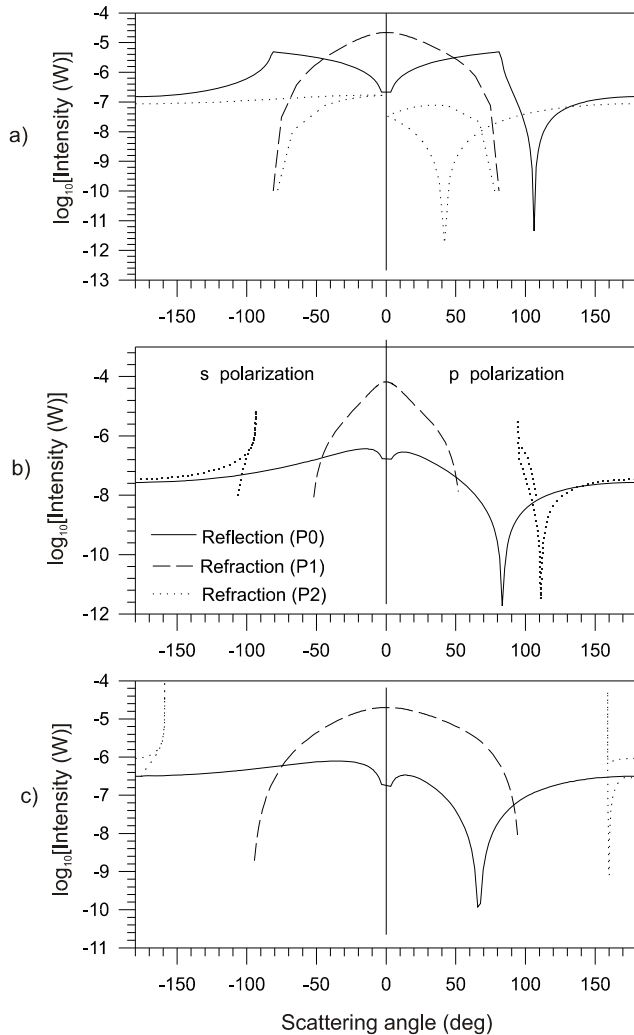


Figure 10.52: Angular intensity distribution of different scattering modes obtained by geometrical optics for a point receiving aperture and parallel (p) as well as perpendicular (s) polarization [$\lambda = 632.8$ nm, $D = 30 \mu\text{m}$; (a) $m = 0.75$, (b) $m = 1.128$, (c) $m = 1.52$].

refraction is concentrated in the backward-scattering range and is limited by the *rainbow angle*.

$$\varphi_R = \cos^{-1} \left[\frac{2}{m^4} \left(\frac{4 - m^2}{3} \right)^3 - 1 \right] \quad (10.91)$$

The angular range of second-order refraction is reduced with an increasing relative refractive index and the rainbow angle increases. The characteristic scattering angles given above are summarized in Table 10.4 for different typical refractive indices. A map of the presence of the different scattering modes as a function of scattering angles and relative refractive indices was introduced by Naqwi and Durst (1991) for supporting the layout of the optical configuration of PDA systems. In the book by Albrecht et al. (2003) detailed calculations of the intensity of different scattering modes based on the Lotentz-Mie theory and Debye series decomposition are presented for parallel and perpendicular polarization.

In the following, Mie calculations are presented for a range of the optimum scattering angles suggested by the relative intensity distributions. For bubbles in water, the optimum scattering angle seems to be rather limited, i.e., between 70° and about 85° where reflection is dominant for either polarization as shown in Figure 10.52a. The phase-size relations show reasonable linearity in this range, but a scattering angle of 55° also gives a linear response function as shown in Figure 10.53. Strong interference with refracted light exists in forward-scattering and the phase-size relation becomes nonlinear (i.e., at a scattering angle of 30°). Similar observations are made for water droplets in oil.

For two-phase systems with relative refractive indices larger than unity, refraction is dominant for both polarization directions in the forward-scattering range up to about 70° to 80° depending on the value of the refractive index ratio (see Figure 10.52c). Since below approximately 30° diffraction interferes with the refracted light, especially for small particles, the lower limit of the optimum scattering angle is bounded by this value. This is also obvious from the angular distribution of the phase for different particle diameters shown in Figure 10.54. Here it is obvious that the forward-scattering direction (i.e., between 30 and 80°) is dominated by first-order refraction (negative phase). Between 100 and 125° reflection (positive phase) seems to be dominant and between 140 and 160° second-order refraction makes the main contribution. This, however, does not imply that the phase-size relations are linear. The phase-size relations for water droplets in air, illustrated in Figure 10.55, show that a reasonable linearity is obtained in the range between 30 and 80° .

The intensity distributions shown in Figure 10.52c also suggest that for $m > 1$ reflected light is dominant between the critical angle and the rainbow angle. However, interference with third-order refraction exists here (not shown in Figure 10.52) and this angular range can be only recommended for perpendicular polarization where a reasonable linearity of the phase response curve is obtained for water droplets in air only around 100° as shown in Figure 10.56.

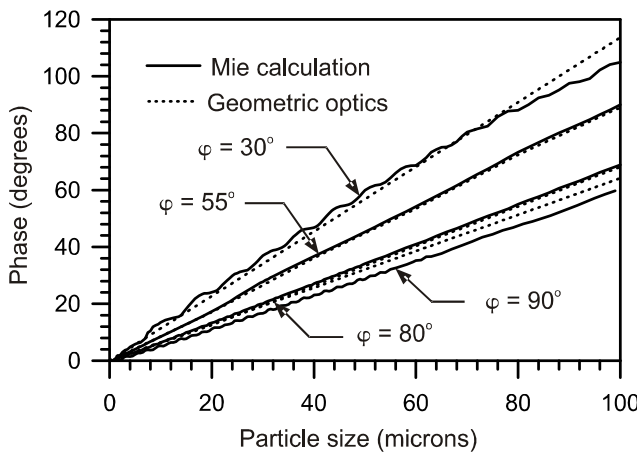


Figure 10.53: Mie calculation of the phase-size relations for different scattering angles between 30° and 80° and comparison with geometrical optics. ($\lambda = 632.8$ nm, p-polarization, $m = 0.75$ (i.e., air-bubble in water), $\theta = 2.77^\circ$, $\Psi = 1.85^\circ$, $\delta_h = 5.53^\circ$, $\delta_v = 1.85^\circ$.)

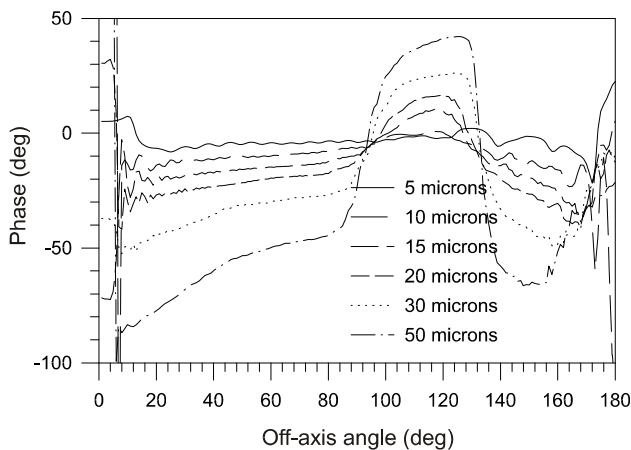


Figure 10.54: Angular distribution of phase for different particle diameters. ($\lambda = 632.8$ nm, p-polarization, $m = 1.33$ (i.e., water droplets in air), $\theta = 2.77^\circ$, $\Psi = 1.85^\circ$, $\delta_h = 5.53^\circ$, $\delta_v = 1.85^\circ$.)

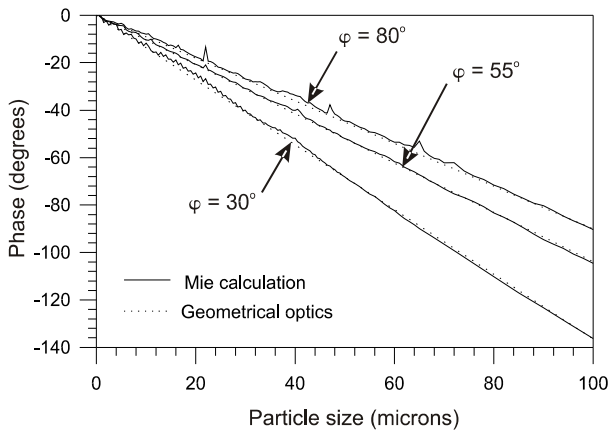


Figure 10.55: Mie calculation of phase-size relations for different scattering angles between 30° and 80° and comparison with geometrical optics. ($\lambda = 632.8$ nm, p-polarization, $m = 1.33$ (i.e., water droplets in air), $\theta = 2.77^\circ$, $\Psi = 1.85^\circ$, $\delta_h = 5.53^\circ$, $\delta_v = 1.85^\circ$.)

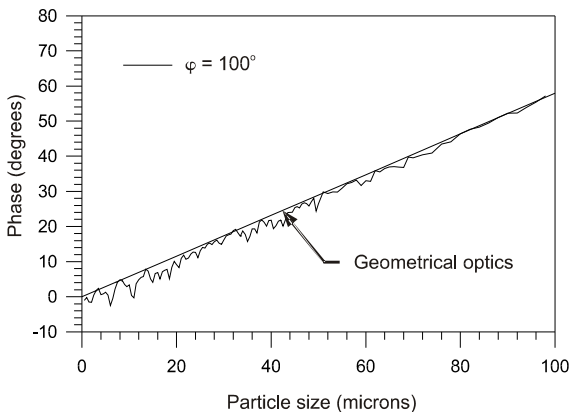


Figure 10.56: Mie calculation of phase-size relations for scattering angles of 100° and 120° . ($\lambda = 632.8$ nm, s-polarization, $m = 1.33$ (i.e., water droplets in air), $\theta = 2.77^\circ$, $\Psi = 1.85^\circ$, $\delta_h = 5.53^\circ$, $\delta_v = 1.85^\circ$.)

Up to droplet sizes of $60 \mu\text{m}$, however, some oscillations of the phase-size relation are observed which will result in some errors in size measurement.

In the region of backscatter, the intensity of secondary refraction is dominant only in a narrow range above the rainbow angle for perpendicular polarization. The optimum location of the receiving optics, however, strongly depends on the value of the relative refractive index, as shown in Figure 10.57, which is critical in fuel spray applications where the refractive index varies with droplet temperature and, hence, the location of the rainbow angle is not constant. From Figure 10.57 it becomes obvious that just above the rainbow angle, i.e., for $\varphi = 140^\circ$, a linear phase-size relation is also obtained. At an angle of 160° strong fluctuations and deviations from linearity are observed and hence this scattering angle is not recommended.

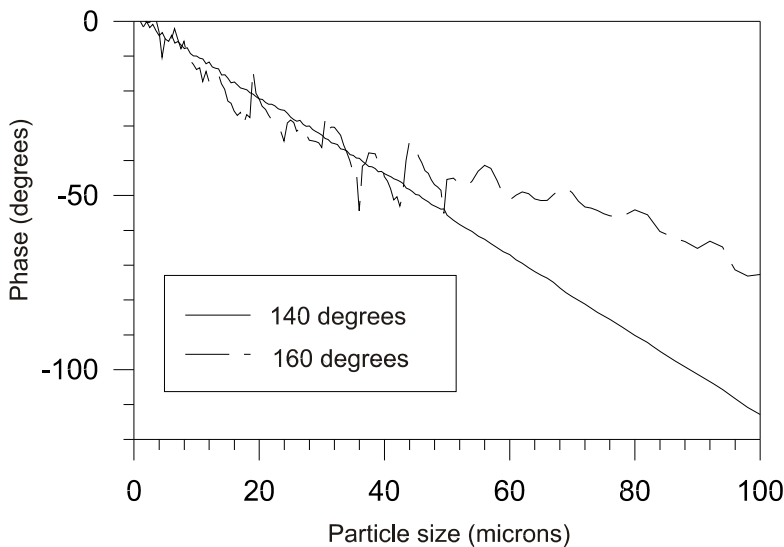


Figure 10.57: Mie calculations of phase-size relations for scattering angles of 140 and 160° . ($\lambda = 632.8 \text{ nm}$, s-polarization, $m = 1.33$ (i.e., water droplets in air), $\theta = 2.77^\circ$, $\Psi = 1.85^\circ$, $\delta_h = 5.53^\circ$, $\delta_v = 1.85^\circ$.)

As described above, the proper application of PDA requires that one scattering mode is dominant and the appropriate correlation (i.e., Equation 10.76 or Equation 10.77) has to be used to determine the size of the particle from the measured phase. However, on certain trajectories of the particle through the focused Gaussian beam, the wrong scattering mechanism might become dominant and lead to erroneous size measurements (Sankar and Bachalo, 1991; Gréhan et al., 1992). This error is called *trajectory ambiguity* and is illustrated in Figure 10.58 where a transparent particle moving in air is considered and the desired scattering mode is refraction, which is dominant for collection angles between 30 and 80° . When the particle passes through the part of the

measurement volume located away from the detector (i.e., negative y -axis), it is illuminated inhomogeneously. The refracted light is coming from the outer portion of the measurement volume where the light intensity is relatively low, while reflected light comes from a region close to the center of the probe volume where the illuminating light intensity is considerably higher due to the Gaussian profile. In this situation, the reflected light might become dominant resulting in an incorrect size measurement since the particle diameter is determined from the correlation to refraction. It is obvious from Figure 10.58 that the trajectory ambiguity is potentially very important for large particles whose size is comparable to the dimensions of the probe volume. A similar ambiguity occurs due to the so-called slit effect since a vertical slit (spatial filter) is used to demarcate the length of the probe volume (Xu and Tropea, 1994).

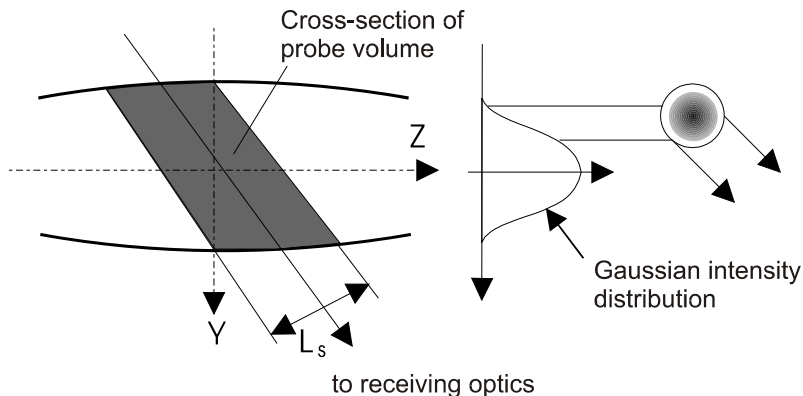


Figure 10.58: Illustration of Gaussian beam effect resulting in a trajectory ambiguity.

The phase error and scattering amplitude along the y axis for different particle sizes as they pass through a probe volume with a $100\text{-}\mu\text{m}$ diameter is illustrated in Figure 10.59. The phase and amplitudes are calculated using GLMT (Grèhan et al., 1992). The phase error might become negative or positive depending on the particle diameter. The smallest errors are observed, however, for small particles which lead to the recommendation that the probe volume diameter should be about 5 times larger than the largest particles in the size spectrum considered. This requirement has restrictions for applications in dense particle-laden flows where the probe volume must be small enough to ensure that the probability of two particles being in the probe volume at the same time is small (see Section 10.3.3).

In order to eliminate or reduce the errors due to the Gaussian beam and slit effects (Xu and Tropea, 1994) a dual-mode PDA system was developed (Tropea et al., 1996). Both errors can be grouped into the general category of

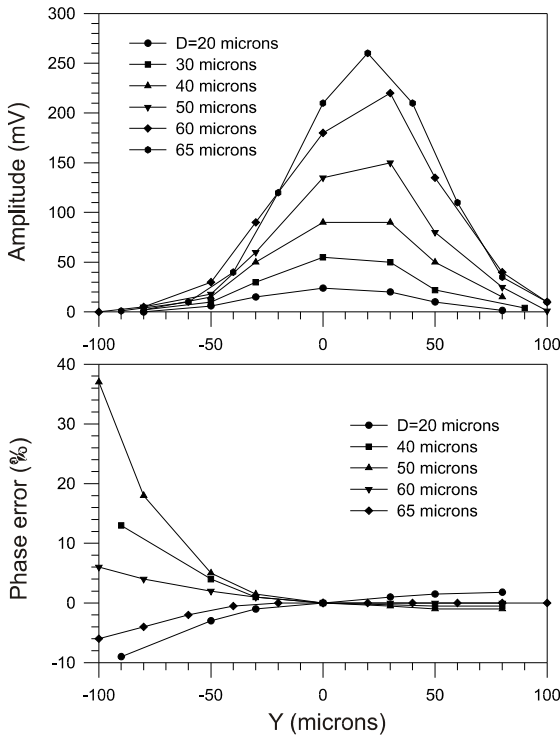


Figure 10.59: Phase error and scattering amplitude along the y-axis for different particle diameters and for probe volume diameter of 100 μm .

trajectory ambiguity and can lead, as the result of detecting the wrong scattering mode, to significant sizing errors as illustrated in Figure 10.60. The dual-mode PDA is a combination of the standard PDA (SPDA) and the planar PDA (PPDA) which supposedly has no Gaussian beam effect (Aizu et al., 1993) but suffers from strong oscillations in the phase-size relation. The optical system for the dual-mode PDA is based on standard two-component transmitting optics and a receiver with four detectors where two of them are aligned vertically (SPDA) and then other two horizontally (PPDA), as illustrated in Figure 10.60. Typically the four detectors are mounted in single fiber-based probe with an exchangeable mask having four rectangular openings (see, for example, Sommerfeld and Tropea, 1999). With such a dual-mode PDA the SPDA is basically used for the size measurement and the PPDA, with lower sensitivity, is used to resolve the 2π ambiguity. The correlation of the SPDA and PPDA phase differences are used to validate the measurement (Tropea et al., 1996). Hence this method essentially eliminates the errors due to trajectory effects (Gaussian beam and slit effects) and is also sensitive to droplet sphericity. Finally, the higher accuracy of the dual-mode PDA enables

more reliable particle flux measurements.

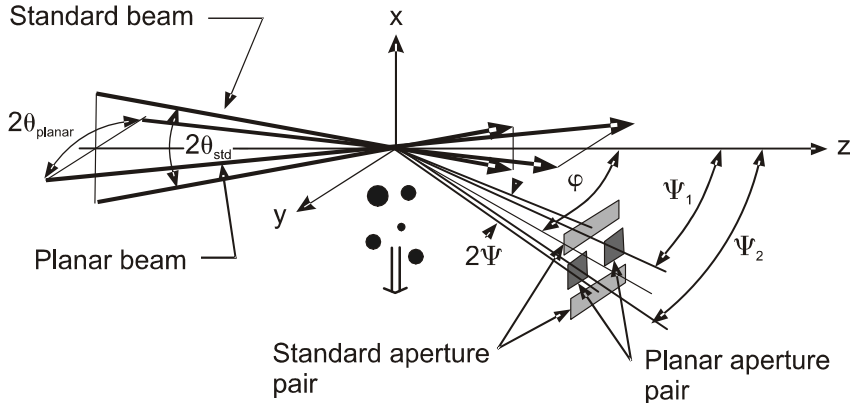


Figure 10.60: Optical configuration of a dual-mode PDA system with four receiving apertures. (Tropea, C., Xu, T.-H., Onofri, F., Grèhan, G., Haugen, P. and Stieglmeier, D., Dual mode phase-Doppler anemometer, *Particle and Particle System Characterization*, 1996, **13**, 165. Copyright Wiley-VCH Verlag GmbH & Co., KGaA. Reproduced with permission.)

Since PDA allows the measurement of particle size and velocity, it is also possible to estimate the particle number or mass concentration and the particle mass flux. The particle number concentration is defined as the number of particles per unit volume. This quantity, however, cannot be measured directly since the PDA is a single particle counting instrument which requires that, at most, only one particle at a time be in the probe volume. The particle concentration has to be obtained from the number of particles moving through the probe volume during a given measurement period. For each particle one has to determine the volume of fluid which passes through the probe volume cross-section with the particle during the measurement time Δt_s . The volume depends on the instantaneous particle velocity \mathbf{v} and the probe volume cross-section perpendicular to the velocity vector, i.e., $Vol = A' |\mathbf{v}| \Delta t_s$ as shown in Figure 10.61. Additionally, the effective cross-section of the probe volume is a function of the particle size and, therefore, $A = A(\alpha_k, D_i)$ where α_k is the particle trajectory angle for each individual sample k and D_i is the particle diameter of size class i . Hence, the concentration associated with one particle is

$$n = \frac{1}{Vol} = \frac{1}{|\mathbf{v}| A'(\alpha_k, D_i) \Delta t_s} \quad (10.92)$$

This implies that for accurate particle concentration measurements one has to know the instantaneous particle velocity and the effective probe volume cross-section. The dependence of the probe volume cross-section on particle

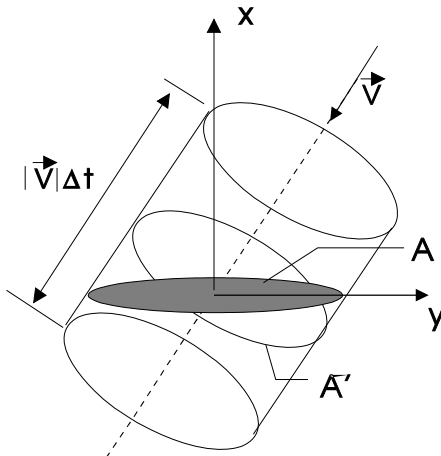


Figure 10.61: Probe volume associated with one particle moving across the detection region during the measurement of time Δt .

size is a result of the Gaussian intensity distribution in the probe volume and the finite signal noise. As illustrated in Figure 10.43, a large particle passing the edge of the probe volume will scatter enough light to produce a signal above the detection level. A small particle will produce a detectable signal for only a small displacement from the probe volume center. Therefore, the probe volume cross-section decreases with particle size and approaches zero for $D_p \rightarrow 0$.

Additionally, the effective probe volume cross-section is determined by the off-axis position of the receiving optics and the width of the spatial filter used to limit the length of the probe volume imaged onto the photodetectors. For a one-dimensional flow along the x-axis, as shown in Figure 10.62, the effective size-dependent cross-section of the measuring volume is determined from

$$A(D_i)_x = 2r(D_i)L_s / \sin \varphi \quad (10.93)$$

where L_s is the width of the image of the spatial filter in the receiving optics (see Figure 10.48) which depends on the slit width and the magnification of the optics, D_i is the diameter of size class i and $r(D_i)$ is the particle size-dependent radius of the probe volume as illustrated in Figure 10.62. For any other particle trajectory through the probe volume, the effective cross-section obtained with the particle trajectory angle α_k is

$$A'(\alpha_k, D_i) = \frac{2r(D_i)L_s}{\sin \varphi} \cos \alpha_k \quad (10.94)$$

The particle trajectory angle can be determined from the different instantaneous particle velocity components,

$$\cos \alpha_k = \frac{1}{\sqrt{1 + (\frac{w}{u})^2 + (\frac{v}{u})^2}} \quad (10.95)$$

The particle size-dependent radius of the probe volume $r(D_i)$ may be determined in situ by using the burst length method (Saffman, 1987) or the so-called logarithmic mean amplitude method (Qiu and Sommerfeld, 1992). The latter is more reliable for noisy signals, i.e., low signal-to-noise ratio as demonstrated by Qiu and Sommerfeld (1992). The reader is referred to the above publications for more details.

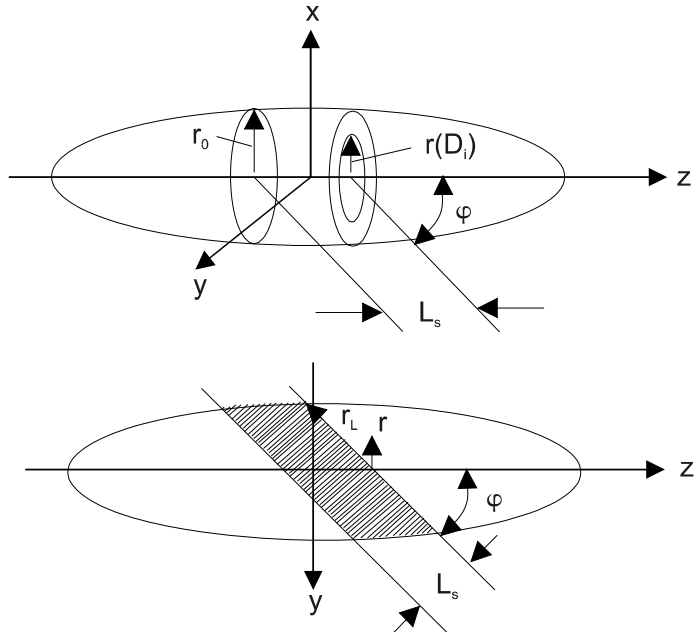


Figure 10.62: Geometry of a PDA measurement volume.

These findings suggest that in complex two-phase flows with random particle trajectories through the probe volume, a three-component PDA system is required for accurate concentration measurements. For a spectrum of particle sizes, the local particle number density is evaluated using

$$n = \frac{1}{\Delta t_s} \sum_{k=1}^M \left[\sum_{i=1}^{N_k} \frac{1}{A'(\alpha_k, D_i)} \sum_{j=1}^{N_j} \frac{1}{|\mathbf{v}_{k,j}|} \right] \quad (10.96)$$

The sums in Equation 10.96 involve the summation over individual realizations of particle velocities (index j), in predefined directional class (index k) and size class (index i). The summation over particle size classes includes

the appropriate particle-size dependent cross-section of the measurement volume for each size class, Equation 10.94, and finally the summation over all directional classes.

The particle bulk density can be obtained by multiplying Equation 10.96 with the mass of the particles. Quite often the particle mass flux, which is a vector quantity, becomes a useful quantity to characterize a two-phase flow. The mass flux in direction n is obtained from

$$\dot{M}_d = \frac{1}{\Delta t_s} \sum_{k=1}^M \left[\sum_{i=1}^{N_k} \frac{m_p}{A'(\alpha_k, D_i)} \sum_{j=1}^{N_j} \frac{v_n}{|\mathbf{v}_{k,j}|} \right] \quad (10.97)$$

where v_n is the particle velocity component in the direction in which the flux is to be determined and m_p is the mass of one particle. For a directed two-phase flow, i.e., when the temporal variation of the particle trajectory through the probe volume is relatively small (such as in a spray), the particle trajectory angle may be determined from independent measurements of the individual velocity components (Equation 10.95) as shown by Qiu and Sommerfeld (1992).

Accurate particle concentration or mass flux measurements, even in complex flows using a one-component PDA system, were also possible using the integral value method (Sommerfeld and Qiu, 1995). This integral value was determined under the envelope of the band-pass filtered Doppler signal in order to estimate the instantaneous particle velocity and its trajectory through the probe volume.

Finally it should be mentioned that a dual-mode PDA allows for very accurate measurements of particle mass flux because it provides more information on the effective size of the measurement volume (Tropea et al., 1996).

10.3.6 Imaging techniques

Imaging techniques may be used to determine the instantaneous spatial distribution of particles over a finite region of interest in the flow, but also properties of individual particles such as particle velocity, particle size and shape. Such instantaneous images can be obtained by either using pulsed light sources which can deliver a high light energy during a very short time period combined with a slow image recording system or by using a continuous light source in combination with high-speed photography or other high-speed recording systems, e.g., high-speed CCD cameras. Moreover, a continuous illumination combined with long-exposure photography can yield information about the time-averaged distribution of the dispersed phase within a flow field.

Light sources used for imaging techniques may deliver diffuse illumination or parallel light beams. Some of the most common light sources are:

- continuous white light sources, such as halogen lamps,
- spark discharges or flash lights (e.g., Xenon flash lamp), and

- continuous or pulsed laser light sources (e.g., Argon-Ion and Nd-Yag laser) and high-power LEDs or LED arrays.

The required power of the light source is determined by the particle size under consideration and the scattering properties of the particle (i.e., reflecting, transparent or absorbing particles). In the range of geometrical optics, i.e., for particles larger than the wavelength of the light, the scattering intensity is approximately proportional to the square of the particle diameter. Moreover, the sensitivity of the image recording system affects the required laser power.

The image recording system also determines the possible spatial resolution of the images. The highest spatial resolution is obtained by conventional film photography or high-speed motion picture cameras which also use photographic film. Such recording systems, however, have the disadvantage that the image evaluation is rather cumbersome and cannot be automated. The evaluation of the photographs requires postprocessing by scanning and digitizing which generally results in a reduction of the spatial resolution. More convenient for image analysis are methods using direct electronic imaging such as CCD (Charged Coupled Device) cameras which, however, have a limited spatial resolution. Typically, CCD cameras have 1024 x 768, 1280 x 1024 or 1048 x 2048 photo diodes which are called pixels. High-resolution CCD cameras have up to 4096 x 4096 pixels. On the other hand, digitized images can be more easily enhanced by various software-based algorithms and filter operations. Also statistical information on the properties of the dispersed phase can be evaluated more easily.

Imaging techniques for two-phase flows may be categorized according to the applied illuminating and recording systems and the information can be extracted from the images in the following way².

- direct imaging techniques,
- whole field visualization to determine the particle phase distribution,
- particle tracking velocimetry (PTV) or streak line technique,
- particle image velocimetry (PIV)

Direct imaging techniques are mostly based on continuous illumination with high-speed recording and are used to visualize the time-dependent motion and behavior of individual bubbles or droplets. Such a technique allows one to study the shape of bubbles or droplets under different flow conditions. Since there are numerous examples for applications of such techniques in two-phase flows, the reader is referred to the book by Van Dyke (1982) to appreciate the potential of this technique.

²Laser-speckle velocimetry and holographic methods will not be considered here. More information about laser-speckle velocimetry can be found in Adrian (1986, 1991). Applications of holographic methods to sprays can be found in the papers of Chigier (1991) and Chavez and Mayinger (1990).

Some recent work on the application of imaging techniques or shadow imaging for the analysis of various types of dispersed two-phase flows is summarized by Sommerfeld (2007). In addition Bröder and Sommerfeld (2007) give a brief summary of the edge-detection approach and image processing. Application examples include bubbly flows, spray evaporation, droplet collisions and particle-wall collisions.

Moreover, during the last 10 years multidimensional particle sizing techniques have been developed, which are based on interferometric particle imaging (IPI) and the phase Doppler principle (GPD). The combination of both methods yields further information. A detailed description of these methods and the underlying principles is provided by Damaschke et al. (2005). In both techniques, a light sheet illumination is used. In the IPI, a single light sheet illuminates a particle cloud such as a spray. A defocused image (far-field image) of the droplets is recorded, for example, by a CCD-camera. Due to the interference of the glare points from different scattering modes (e.g. reflection and refraction) on the droplet surface the droplet interference pattern appears as a circular object with fringes. The spatial separation of the fringes is proportional to droplet size. Similar to the PDA, the GPD uses two illuminating light sheets, which are adjusted to intersect within the measurement region. Again the far-field interference pattern resulting from glare points from the same scattering mode is recorded. In this case the droplets appear as circles with a fringe pattern which can be related to droplet size. Both techniques now provide field images with size information for all droplets captured in the light sheet. However, the application is limited to dilute systems due to the rather large images of the interference pattern.

The visualization of the instantaneous distribution of the dispersed phase particles in a two-phase flow is generally performed by producing a thin laser light sheet which illuminates a specific cross-section of the flow. Images are taken by a recording system oriented perpendicular to the light sheet as shown in Figure 10.63. To obtain an instantaneous image of the dispersed phase distribution, either the light source has to be operated in a single pulse mode or the recording systems must allow for short time exposure. The exposure time or the pulse duration of the laser determines the temporal resolution and has to be adjusted according to the flow velocity in order to yield sharp images. Moreover, the image recording system must be well-focused.

Such a visualization technique has been applied by Longmire and Eaton (1992) to evaluate the particle concentration distribution and, in turn, the particle response characteristics in a forced particle-laden free jet. A pulsed copper vapor laser was used as a light source and a light sheet was produced by a cylindrical-spherical lens combination. The light sheet was transmitted through the center region of the jet and aligned parallel to the flow direction. Images of the particles were taken with a 35-mm camera activated by an electronic trigger. The single-pulse photographs were printed on a 8 in. x 10 in. photographic paper so that the individual particle images could be identified. A scanner was used to produce a binary image matrix which was

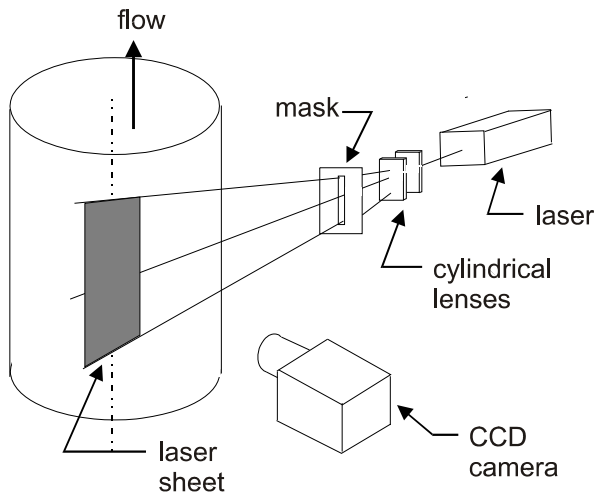


Figure 10.63: Light sheet flow visualization technique.

transferred to a PC for further processing. The images were enhanced and all individual particle images were identified. The particle concentration field was evaluated by dividing the image into a number of small cells and then counting the individual particles in each of the cells. In order to correlate the particle concentration distribution with the flow structure, independent images were recorded when the jet was only seeded with smoke particles.

A similar visualization technique was applied by Wen et al. (1992) for studies of the particle response to the vortical structures evolving in a plane shear layer. Either a diffuse flash light unit or a continuous Argon-Ion laser light sheet were used as light sources. The images were recorded by a large format camera (6×4 cm) using exposure times between $1/250$ and $1/10,000$ seconds. The photographs were processed by a commercial image processing system. The air flow and the vortical structures in the shear layer were visualized using the smoke wire technique. From the instantaneous images of the particle distribution in the shear layer, the response characteristics of different sized particles were analyzed.

In a study by Huber and Sommerfeld (1994), a continuous Argon-Ion laser light sheet was used together with a CCD camera for recording images of the cross-sectional particle concentration distribution in pneumatic conveying systems. Using digital image processing, the images were enhanced and the instantaneous particle concentration distribution in the pipe cross-section was evaluated. The mean particle concentration field was determined by averaging a number of individual images.

Particle tracking and particle image velocimetry (PTV and PIV) enable the determination of the instantaneous particle velocity distribution over a finite domain of the flow field. Both techniques have been used in single-phase

flows for more than 10 years, especially for the analysis of unsteady and turbulent flows. However, only recently have these methods become increasingly popular due to the enhanced computational capability of personal computers used in laboratories for data processing. In single-phase flows, small tracer particles are added as light scattering centers in order to trace the fluid elements. By observing the locations of the images of these marker particles two or more times, the velocity can be determined from the displacement $\Delta\vec{x}(\vec{x}, t)$ and the time period Δt between two successive light pulses or recordings from

$$\vec{u}(\vec{x}, t) = \frac{\Delta\vec{x}(\vec{x}, t)}{\Delta t} \quad (10.98)$$

The response time of the marker particles must be sufficiently small that the particles follow the turbulent fluctuations in the flow. In two-phase flows the velocity distribution of the dispersed phase can easily be determined by PTV or PIV since the particles are usually rather large and, therefore, ideal scatterers.

Methods for simultaneous velocity measurements of both phases in a two-phase flow are more sophisticated and have only recently been developed. In the following section, the basic principles of PTV and PIV are explained and some examples of applications to two-phase flow studies are provided.

According to the classification of Adrian (1991) both methods, i.e., PIV and PTV, may be grouped under the topic, pulse-light velocimetry (PLV), which indicates that pulsed light sources are used for illumination of the flow region of interest. For PLV, powerful laser light sources are used most of the time where the emitted light beam is expanded by a system of lenses to form a narrow light sheet typically up to a few millimeters in thickness. Moreover, it is possible to sweep a laser beam through the flow field using a rotating mirror (e.g., polygon mirror) whereby the effective intensity in the light sheet is increased. The time separation Δt between subsequent laser pulses determines the measurable particle velocity range and the pulse duration establishes the degree to which the image of the particle is frozen on the recording system.

Lasers typically used for PLV are:

- continuous lasers (e.g., Argon-Ion laser) which are continuously chopped using acousto-optical modulators,
- continuously pulsed metal-vapor lasers (e.g., copper-vapor laser),
- Q-switched ruby lasers,
- frequency double-pulsed Nd:Yag lasers which can produce trains of double pulses.

Several combinations of laser pulse coding (i.e., single, double or multiple pulse) and image recording (e.g., single frame recording and multiframing) may be used to determine the velocity of particles (see, for example, Adrian 1991).

The differences between PTV and PIV are the way the images are processed and the displacement is evaluated. With PTV, the tracks of individual particles are reconstructed from one or multiple images so this technique is only applicable for relatively dilute two-phase flows where the length of the recorded particle tracks should be smaller than the mean inter-particle spacing. Moreover, a sophisticated point-by-point analysis of the images is generally required. PIV requires higher particle concentrations since the displacement of a group of particles located in an interrogation area (a small subregion of one image) is determined by special processing techniques such as auto- and cross-correlation methods. Hence, with this method, an average displacement and an average velocity of all particles located in the interrogation area is determined. The number of particles in each interrogation area should typically be from 5 to 10 in order to yield reasonable averages of the particle velocity.

The resolution of velocity measurements by PIV and PTV depends on the accuracy of the displacement measurement Δx and the uncertainty in the time difference between the light pulses Δt . Normalized by the maximum velocity in the flow field, u_{\max} , the root mean square (rms) uncertainty of the velocity is determined from (Adrian, 1986)

$$\frac{\sigma_u}{u_{\max}} = \frac{\sigma_{\Delta x}}{\Delta x} + \frac{\sigma_{\Delta t}}{\Delta t} = \frac{\sigma_{\Delta x}}{u_{\max}\Delta t} + \frac{\sigma_{\Delta t}}{\Delta t} \quad (10.99)$$

where $\sigma_{\Delta x}$ is the root mean square uncertainty in the displacement between two images and $\sigma_{\Delta t}$ is the uncertainty in the time between two successive light pulses or recordings. In the determination of the displacement, the major source of error is related to establishing the centers of the images which is determined by the applied processing algorithm and the image size. With the assumption that this uncertainty is related to the image diameter through a number c which is established by the accuracy of the processing method used for particle location, one has

$$\sigma_{\Delta x} = cd_I \quad (10.100)$$

The image size depends on the resolution of the recording system, d_r (i.e., photographic film or electronic recording) and the magnification of the imaging system, M . It can be estimated from the following relation (Adrian, 1986)

$$d_I = (M^2 D^2 + d_s^2 + d_r^2)^{1/2} \quad (10.101)$$

where D is the particle diameter and d_s is the diffraction-limited spot diameter of the optical system given by (Adrian, 1986)

$$d_s = 2.44(M + 1)f^\# \lambda \quad (10.102)$$

where $f^\#$ is the f -number of the lens and λ is the wavelength of light. The relative importance of the first two terms in Equation 10.101 depends on particle size. For an optical system with $M = 1$, $f^\# = 8$ and $\lambda = 514.5$ nm, the image diameter becomes independent of particle size for diameters much

less than $20 \mu\text{m}$. On the other hand, for large particles (i.e., much larger than $20 \mu\text{m}$ which is mostly the case in two-phase flows) the image diameter is given by

$$d_I = (M^2 D^2 + d_r^2)^{1/2} \quad (10.103)$$

In addition the image size may be increased by particle motion during the exposure time or pulse duration Δt_{exp} . Hence the maximum velocity in the flow field times the pulse duration should be smaller than the image diameter to avoid this blur effect.

$$u_{\max} \Delta t_{\text{exp}} \leq d_I \quad (10.104)$$

If one also can assume that the pulse frequency of the light source can be adjusted with a high accuracy, i.e., the time jitter may be neglected, the uncertainty of velocity measurement is given by

$$\sigma_u = c \frac{d_I}{\Delta t} \quad (10.105)$$

This equation reveals that high accuracy for velocity determination is achieved with small image diameters.

Two different methodologies may be used for PTV, the single-frame/multipulse technique and the multiframe/single-pulse method where the particle trajectories are reconstructed by overlapping several single exposure images. The latter method actually corresponds to conventional cinematography and has the advantage that the particles may be tracked for a long time (i.e., to evaluate Lagrangian trajectories) and that the direction of particle motion is fully determined from the sequence of the recordings. The disadvantage is that the frequency of the image recording system must be equal to the laser pulse frequency or a known integer multiple lower. This limits the measurable velocity range when, for example, CCD cameras with a standard framing rate of 50 Hz are used. Otherwise, high speed videos or motion picture cameras are required. Such a method was used by Perkins and Hunt (1989) to experimentally study particle motion in the wake of a cylinder. In order to reconstruct the particle trajectories, a cross-correlation method was used to avoid a time-consuming search algorithm to identify images belonging to one particle track.

In the other mode of PTV, i.e., the single-frame/multipulse method, the time sequence of the particle images are recorded on one frame for a certain time interval. This method has the advantage that slow image recording systems such as standard CCD cameras may be used. However, the direction of particle motion cannot be resolved by this method so its applicability is limited to simple flows with a known direction of particle motion. This limitation can be overcome with pulse coding or image shifting which is described later. In combination with low-frequency laser light sources, this method produces a sequence of particle streak lines where the particle velocity is determined

from the displacement of the centers of individual streak lines. For this mode of operation the pulse duration needs to be longer than the image diameter divided by the particle velocity, i.e., $\Delta t > d_I / |\vec{u}|$ and the time between pulses needs to be longer than the pulse duration.

The analysis of PTV images usually consists of the following steps (see Hassan et al., 1992):

- thresholding of the image, i.e., removal of noise objects with intensity below a certain gray level scale,
- analysis of the image to determine the location of the particle images,
- point-by-point matching of the particle images from one frame to the next (if the multiframe technique is used),
- determination of the displacement and particle velocity for each individual particle,
- postprocessing in order to erase unreasonable velocity vectors resulting from errors in the previous analysis steps.

Some examples of the application of PTV techniques to two-phase flows are presented here. The particle streak line technique was used by Ciccone et al. (1990) to study the saltating motion of particles over a deposited particle layer. A section of the flow field was illuminated with a laser light sheet which was chopped by a rotating grid with an equal number of open and closed sections. The images were recorded by conventional film photography. Subsequently the photographs were digitized and enhanced using Fast Fourier Transforms to enable reconstruction of the trajectories of individual particles from a number of imaged streak lines.

A similar technique was used by Sommerfeld et al. (1993) to obtain statistical information on the collision of individual particles with rough walls. The laser light sheet was produced in such a way that it propagated along a horizontal channel and illuminated a thin sheet perpendicular to the wall of the channel. The light beam from a continuous Argon-Ion laser was chopped using a Bragg-cell. The images of particle trajectories in the near-wall region were recorded by a CCD camera. The CCD camera which was mounted perpendicular to the light sheet was equipped with a macro zoom lens and extension bellows. To enable the processing of a large number of individual wall collision events, the images were recorded on a videotape and processed off-line later using a frame grabber card and a personal computer. A special processing software package was developed to determine the streak lines belonging to one particle which collided with the wall. The processing routines involved the enhancement of the images, the identification of streak lines with a minimum of 50 pixels and the grouping of two streak lines before and after wall impact for each wall collision event. The particle velocity components and the trajectory angles before and after impact were determined from the separation of the geometric centers of the two respective streak lines.

A visualization scheme for solid particle motion in a turbulent pipe flow was reported by Govan et al. (1989) using an axial viewing technique. In these studies, an expanded laser light beam was transmitted axially through a vertical pipe. A high-speed motion picture camera was mounted at the opposite end of the pipe. The particle trajectories in the pipe cross-section were reconstructed from a sequence of 30 frames for the smallest to 200 frames for the largest particles. The axial viewing technique for visualizing particle motion in a pipe flow was further improved in subsequent studies (Lee et al., 1989). The particle motion in several cross-sections of the pipe was observed using a number of adjacent pulsed laser light sheets. The pulse frequency was adjusted in such a way that the images of the particles appeared as dots as opposed to streaks. The use of a number of adjacent light sheets pulsed in sequence allowed one to follow the particle trajectories in the cross-section of the pipe and to determine two components of particle velocity.

In PIV two methodologies are most common, the single-frame/double-pulse (or less common multipulse) technique and the multiframe (i.e., mostly two-frame)/single-pulse method. The first technique is usually combined with a spatial autocorrelation algorithm in order to evaluate the average displacement of image pairs in each interrogation area. This technique has the advantage of not requiring sophisticated recording systems with high-speed shutters. When used with a double-pulse laser, it cannot resolve the particle direction. Hence, additional means are required to determine the particle direction in complex or turbulent flows. Two methods, among others, are most common:

- The recording system (e.g., CCD or photographic camera) is placed on a linear rail and moves at a constant and defined speed during the exposure.
- A rotational mirror is mounted between the flow field and the recording system.

Both methods result in an additional known shift of the second image with respect to the first one. By subtracting this shift from the recorded image displacement, the effective displacement is determined which may be either positive or negative, depending on the sense of particles velocity vector.

The second methodology of PIV is the multiframe/single-pulse method. In this case subsequent images are recorded on separate frames and hence, similar to the corresponding PTV method, a high-speed recording system is required with a speed identical to the laser pulse frequency or a frequency which is an integer multiple smaller than the laser pulse frequency. Moreover, the shutter of the camera has to be synchronized with the laser pulses. Since the displacement is evaluated from at least two subsequent images, the direction of particle motion is fully determined and no additional equipment is needed. Cross-correlation methods are most favorable for the determination of the average displacement of the particles in the interrogation area.

Examples of the application of PIV in two-phase flows are numerous. In most cases, however, the velocity fields of both phases were not recorded

simultaneously in order to assess the effect of the dispersed phase on the fluid flow. A few examples of measuring the dispersed phase velocity field by PIV are described below.

The effect of vortices on the particle motion in a forced jet impinging onto a circular plate was investigated by Longmire and Anderson (1995). The velocity fields of both phases in the vicinity of the wall were evaluated independently using the single-frame/double-pulse PIV method. In order to resolve directional ambiguity, the image shift technique based on a rotating mirror placed between the flow field and the camera was used. For analyzing the vortex structure in the single-phase jet, both the jet and the outer flow were seeded with smoke. For the determination of the particle phase velocity field, it was required that a sufficient number of particles be present in each interrogation area in order to ensure a good autocorrelation. Since the particle loading was very low (i.e., dilute system), a complete velocity vector field could not be obtained for the dispersed phase, although ensemble averages of 10 realizations were evaluated. Moreover, problems in resolving the velocity of particles moving towards the wall and those rebounding from the wall using PIV became obvious. In those interrogation areas where both classes of particles were present, some average velocity depending on the number of particles in each class was determined. This special case represents a disadvantage of the PIV method.

For the simultaneous determination of the velocity fields of both phases using PTV or PIV, the fluid flow has to be seeded with appropriate tracer particles which are able to follow velocity fluctuations of the flow. In order to discriminate the images from tracer and dispersed phase particles, two approaches are most common:

- discrimination based on the size of the images which requires a considerable difference in the particle size of the dispersed phase particles and the tracer particles as, for example, in a bubbly flow.
- introduction of fluorescent tracer particles which are excited by the incident laser light and emit light with a different wavelength. This method requires two recording systems, each equipped with an appropriate color filter.

Simultaneous measurements of both velocity components in a bubbly two-phase flow were conducted by Hassan et al. (1992) using PTV and size discrimination. Bubbles about 1 mm in size were periodically released at the bottom of a test tank filled with transparent mineral oil which was seeded with 70 μm plastic particles. Particle and bubble trajectories and velocities were reconstructed from a sequence of 10 single-pulse images and a sophisticated point-by-point analysis.

The second discrimination approach is based on laser-induced fluorescence. In this case either the seed particles or the dispersed phase particles (i.e., solid particles or droplets) are treated with a fluorescent dye solution. Solid

particles have to be impregnated with the dye solution, while in the case of liquid droplets, the dye solution may be mixed with the liquid prior to atomization. When the dyed particles are illuminated by laser light with the appropriate wavelength, they emit light at a different wavelength. For example, rhodamine 6G may be excited by green light (i.e., 514.5 nm) and the emitted fluorescent light has a wavelength around 580.5 nm. By using two CCD cameras (or any other cameras) with appropriate color filters, one camera may receive only the scattered light around the laser wavelength and the other camera responds to the fluorescent light. Hence separate images of the seed particles and the dispersed phase particles are produced.

Such a method was for example applied by Philip et al. (1994) using red fluorescent seeds in order to visualize the flow near a collapsing steam bubble. By using a color filter in front of the CCD-camera, most of the green light reflected by the bubble was blocked and the red light emitted by the seeds was recorded. A similar technique was used by Tokuhiro et al. (1996) to measure the fluid velocity distribution around a stationary bubble. In this case a second CCD camera was used in order to image the bubble shape using a shadow technique.

The few examples presented on imaging techniques show the wide variety of applications and the potential of imaging techniques for analyzing two-phase flows. Further examples may be found in relevant journals or conference proceedings.

10.4 Summary

In this chapter some of the most common measurement techniques for particle characterization (i.e., sampling methods) and on-line analysis of two-phase systems have been introduced. Most of the techniques for the analysis of particle samples with regard to size, shape and surface area are well established. However, on-line methods such as light scattering, laser-Doppler and phase-Doppler anemometry for particle characterization and for the reliable and accurate measurement of flow properties in industrial processes or in research laboratories are still under development. The main emphases in these developments are related to improved measurement accuracies, more reliable mass flux and concentration measurements and extensions of the optical system to enable determination of additional properties, such as the refractive index and droplet temperature.

Industrial applications of single particle counting instruments for process control are, at present, minimal. More robust and easy-to-use instruments need to be developed for such applications. Miniaturized optical systems based on semiconductor lasers which have been developed over several years may give rise to compact robust systems in the future.

However, one should keep in mind that optical techniques are limited to applications in dilute two-phase systems only. For on-line measurements and control in dense systems, radiation sources, such as X-rays and gamma rays

which are highly penetrative due to their extremely short wavelengths, have to be used. Tomographic methods based on these radiation sources have received considerable attention for imaging the phase distribution in dense multiphase systems.

10.5 Exercises

10.1. The particle concentration in a particle-laden pipe flow is to be measured using a simple sampling probe. A homogeneous particle concentration in the pipe cross-section may be assumed. The suction velocity is adjusted to the average gas velocity in the pipe, i.e., 20 m/s. An accumulation of 60 grams of particles is measured on the filter over a one minute interval. Assume that the gas is incompressible and the gas velocity profile is given by:

$$\frac{u}{U_o} = \left(\frac{y}{R} \right)^{1/n} \quad (\text{with } n = 7)$$

$$\frac{\bar{u}}{U_o} = \frac{2n^2}{(n+1)(2n+1)}$$

where U_o is the centerline gas velocity, \bar{u} is the average velocity and y is the distance from the wall and R is the pipe radius.

Determine the particle concentration measurement on the pipe centerline and 50 mm away from the wall using the result given in Figure 10.22.

The following properties are given:

pipe diameter	200 mm
sampling probe diameter	10 mm
sampling time	20 s
particle size	200 μm
particle material density	2500 kg/m ³
density of gas	1.18 kg/m ³
kinematic viscosity	18.4×10^{-6} Ns/m ²

10.2. Determine the required dimensions of the probe volume for a light scattering instrument allowing a coincidence error of 5 percent. The measurements will be carried out in a gas-solid flow with a mass loading ratio of 2. Consider two particle sizes, 15 and 60 μm . The particle material density is 2500 kg/m³. Assume the gas density is 1.2 kg/m³.

10.3. Design an LDA system for measurements in a high-speed, gas-particle flow (initial velocity 500 m/s) through a normal shock wave. You have available a signal processor which is able to resolve a signal frequency of 50 MHz. No frequency shifting is to be used. The laser has a beam diameter of 2 mm. Determine the beam-crossing angle and select a suitable combination of initial beam spacing (typically: 10, 20, 30, 40, 50 mm) and focal length (typical focal lengths of lenses are: 160, 300, 500, 700 and 1000 mm). Also calculate the diameter of the probe volume and the number of fringes.

Ensure that the number of fringes is larger than 10 to allow for reliable signal processing. Assume the laser wave length is 514.5 nm.

10.4. Select an appropriate configuration of a PDA system for measurements in a spray of water droplets ($n_p = 1.33$) with a size spectrum from 50 to 200 μm . The spray is issuing into an air flow. A three-detector system with the following configuration is available:

laser wavelength	514.5 nm
laser beam diameter	1.35 mm
focal length of transmitting lens	500 and 1000 mm
initial beam spacing	variable between 20 and 40 mm
receiving lens focal length	variable between 160 and 400 mm

The receiving optics have interchangeable masks with the smallest detector spacing (i.e., detectors 1–2 in Figure 10.51) being 5, 10, and 15 mm.

Select a scattering angle of 30 degrees and try to minimize the Gaussian beam effect by choosing the diameter of the probe volume to be larger than the largest drop.

10.5. Estimate the errors for a PTV measurement in a flow with particles of 80 μm and a maximum velocity of 10 m/s. A copper-vapor laser is available with a pulse duration of 30 ns and a pulse-to-pulse jitter (variability of time between pulses) of 2 ns. Assume that the image can be located within an accuracy of 20 percent; i.e., $c = 0.2$ in Equation 10.100.

The following properties of the optical system are given:

magnification	1
laser wavelength	510.6 nm
f-number of lens	8
resolution of recording system	20 μm

Determine the following parameters:

- image diameter,
- a suitable pulse frequency to allow for an image separation of 5 d_I ,
- error due to blur in relation to the image diameter uncertainty,
- uncertainty in velocity measurement.

This page intentionally left blank

Appendix A

Single-Particle Equations

The objective of this appendix is to present a derivation for the governing equations for a single particle or droplet. These equations are fundamental to the development of numerical models for dispersed-phase flows. These derivations result from the application of the Reynolds Transport Theorem which is presented below.

A.1 Reynolds transport theorem

Newton's second law and the first law of thermodynamics are well known for a fluid element of constant mass moving through a flow field. Applying these laws to identifiable fluid elements is the Lagrangian approach to fluid mechanics. However, the most useful and popular approach to describe the dynamic and thermal state of a fluid is the Eulerian approach. In this case the state of the flow is described by the properties of fluid elements at the time they pass a given point (window) in space. The Reynolds transport theorem provides the link between the Lagrangian and Eulerian approaches.

Fundamental to the Reynolds transport theorem is the mathematical description of the mass flux of a fluid. Consider an element of area ΔS of surface S in Figure A.1 through which fluid passes with velocity w_i with respect to the surface. The mass flux is given by

$$\dot{M} = \rho w_i n_i \Delta S \quad (\text{A.1})$$

where n_i is a unit vector normal to the area element. For a closed surface, as shown in Figure A.1, the unit vector has a positive sense if pointing outward from the enclosed volume. Thus the dot product in Equation A.1 represents mass flow *from the control volume* or a mass *efflux*. Integrating the mass flux over the entire surface of the volume gives the net mass efflux from the volume

$$\dot{M} = \int_S \rho w_i n_i dS \quad (\text{A.2})$$

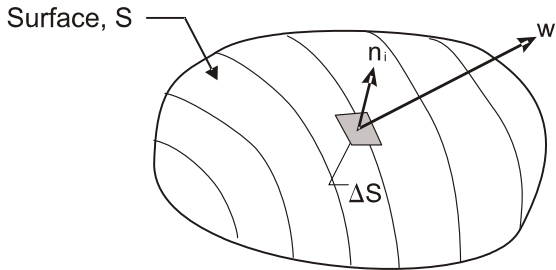


Figure A.1: Fluid velocity vector and unit normal vector at surface element.

The same approach can be used to determine the net efflux of other quantities such as energy or momentum. If B is the extensive property of a fluid and β is the corresponding intensive property, then the net efflux of property B from the volume is

$$\dot{B} = \int_S \rho \beta w_i n_i dS \quad (\text{A.3})$$

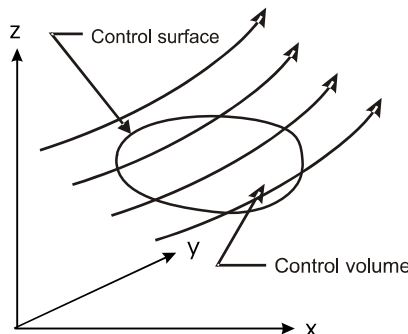


Figure A.2: Streamlines passing through control volume in space.

Consider an arbitrary volume in space through which fluid can pass as shown in Figure A.2. This volume is the control volume (cv) enclosed by the control surface (cs). It can move through space, rotate or change size. Now consider a mass element which moves through the control volume as shown in Figure A.3. This fluid element will be referred to as the *system*. At time t the boundaries of the system are the control surface. At this time the mass of the system is the mass in the control volume. At time $t + \delta t$ the system moves out of the control volume. The mass of the system which has left the volume is δM_{out} while the mass which has entered the volume is δM_{in} . The amount of property B associated with the mass (system) which has left is δB_{out} , while the corresponding amount of B that has entered is δB_{in} .

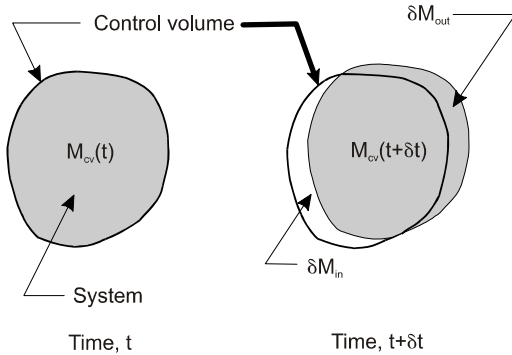


Figure A.3: System moving through a control volume at two successive times.

By definition the rate of change of property B of the system is given by

$$\frac{dB_{sys}}{dt} = \lim_{\delta t \rightarrow 0} \frac{B_{sys}(t + \delta t) - B_{sys}(t)}{\delta t} \quad (\text{A.4})$$

The amount of B of the system at time t corresponds to the amount of B in the control volume at time t because at this instant the system is entirely surrounded by the control surface. Thus

$$B_{sys}(t) = B_{cv}(t) \quad (\text{A.5})$$

At time $t + \delta t$ some mass has left while some mass has entered the control volume. The mass of the system now consists of the mass which has left plus the mass in the control volume minus the mass which has entered. Thus the value of the property B of the system at time $t + \delta t$ is

$$B_{sys}(t + \delta t) = \delta B_{out} + B_{cv}(t + \delta t) - \delta B_{in} \quad (\text{A.6})$$

Substituting the expressions for B_{sys} at t and $t + \delta t$ into Equation (A.4) and rearranging yields

$$\frac{dB_{sys}}{dt} = \lim_{\delta t \rightarrow 0} \left[\frac{B_{cv}(t + \delta t) - B_{cv}(t)}{\delta t} + \frac{\delta B_{out}}{\delta t} - \frac{\delta B_{in}}{\delta t} \right] \quad (\text{A.7})$$

The first two terms are simply the rate of change of the property B in the control volume; that is,

$$\lim_{\delta t \rightarrow 0} \left[\frac{B_{cv}(t + \delta t) - B_{cv}(t)}{\delta t} \right] = \frac{dB_{cv}}{dt} \quad (\text{A.8})$$

The amount of B in the control volume is obtained by integrating the product of the corresponding intensive property β and fluid density over the control volume. Thus

$$\frac{dB_{cv}}{dt} = \frac{d}{dt} \int_{cv} \rho \beta dV \quad (\text{A.9})$$

The other two terms represent the net mass flux of B out of the control volume or, in other words, the net efflux of property B across the control surface. Thus

$$\lim_{\delta t \rightarrow 0} \left[\frac{\delta B_{out}}{\delta t} - \frac{\delta B_{in}}{\delta t} \right] = \int_c \rho \beta w_i n_i dS \quad (\text{A.10})$$

It must be emphasized that the velocity w_i is measured *with respect to the control surface* because the integral is the property flux across the control surface.

Finally the Reynolds transport theorem becomes

$$\frac{dB_{sys}}{dt} = \frac{d}{dt} \int_{cv} \rho \beta dV + \int_{cs} \rho \beta w_i n_i dS \quad (\text{A.11})$$

Thus the rate of change of B of a system is equal to the rate of change of B in the control volume plus the net efflux of B across the control surface. There is no restriction on the control volume. It can be translating, accelerating, rotating or changing in size and the Reynolds transport theorem is still applicable.

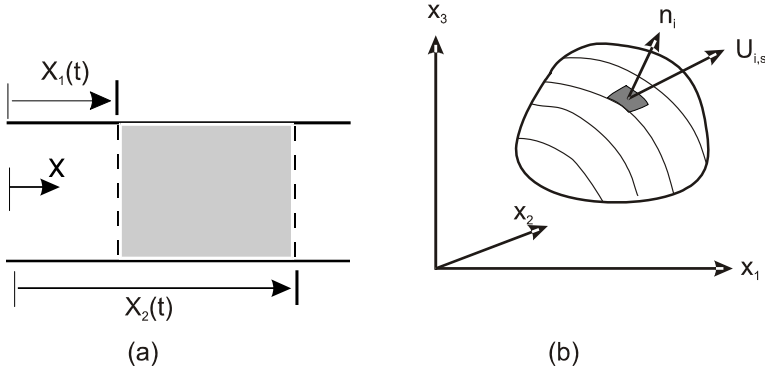


Figure A.4: Translating boundaries in relation to Leibnitz rule for differentiation of an integral: (a) one-dimensional configuration, (b) three-dimensional control surface.

A corollary to the Reynolds transport theorem can be obtained by applying Leibnitz rule for differentiation of an integral; namely,

$$\frac{d}{dt} \int_{X_1(t)}^{X_2(t)} f(x, t) dx = \int_{X_1(t)}^{X_2(t)} \frac{\partial f(x, t)}{\partial t} dx + f(X_1, t) \frac{dX_1}{dt} - f(X_2, t) \frac{dX_2}{dt} \quad (\text{A.12})$$

where X_1 and X_2 are the spatial limits of integration as shown in Figure A.4a. One notes that the integrand has been changed to a partial derivative of the function with respect to time and that the derivatives of the limits, X_1 and X_2 , are taken with respect to time. The time derivative of the limits corresponds

to the speed at which the boundaries move. This theorem can be extended to a function of three space variables in which the integral is taken over a volume enclosed by a surface as shown in Figure A.4b. For consistency, the volume and surface will be the control volume and control surface. Leibnitz rule is

$$\frac{d}{dt} \int_{cv} f(x_i, t) dV = \int_{cv} \frac{\partial f(x_i, t)}{\partial t} dV + \int_{cs} f(x_i, t) U_{i,s} n_i dS \quad (\text{A.13})$$

where $U_{i,s}$ is the velocity of the control surface with respect to the coordinate reference frame.

Applying Leibnitz rule to the Reynolds transport theorem in Equation (A.11), one has

$$\frac{dB_{sys}}{dt} = \int_{cv} \frac{\partial(\rho\beta)}{\partial t} dV + \int_{cs} \rho\beta(w_i + U_{i,s}) n_i dS \quad (\text{A.14})$$

However, the vector sum of the velocity at the control surface and the velocity of the fluid with respect to the control surface yields the velocity of the fluid with respect to the coordinate reference frame.

$$w_i + U_{i,s} = u_i \quad (\text{A.15})$$

Thus the alternate form of the Reynolds transport theorem is

$$\frac{dB_{sys}}{dt} = \int_{cv} \frac{\partial(\rho\beta)}{\partial t} dV + \int_{cs} \rho\beta u_i n_i dS \quad (\text{A.16})$$

In this form the velocity of the fluid at the control surface is the velocity *with respect to the coordinate reference frame*, not the control surface. This form is most useful for deriving the fundamental equations for fluid flow.

The original form of the Reynolds transport theorem will now be applied to the property conservation for particles and droplets conveyed by a fluid.

The fundamental equations for dispersed phase flows are formulated from the equations describing the conservation of mass, momentum and energy for an individual droplet or particle. The resulting equations might be regarded as “Lagrangian” because they apply to moving mass elements and do not describe the change of conditions at a point. The following discussion applies to “particles” or “droplets” although the word “particle” will be used throughout.

Consider the particle shown in Figure A.5. The particle is moving through the fluid with a velocity v_i with respect to an inertial reference frame. Assume also that the particle is spherical in order to avoid the complexities associated with aspherical particles yet still retain the essence of the equations.

The control surface is located adjacent to, and just outside of, the particle surface. It thus lies within the boundary layer of the particle. The transition from particle surface properties to local fluid properties takes place across the boundary layer. As the particle burns, evaporates or condenses, the control surface moves to remain adjacent to and just outside of the particle surface.

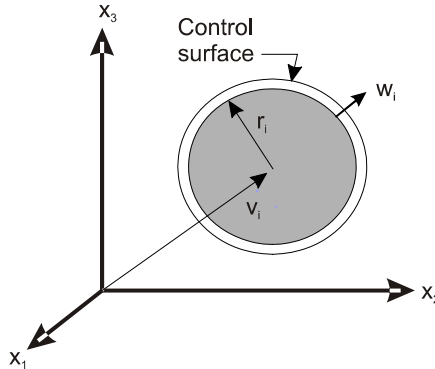


Figure A.5: Moving control surface enclosing particle.

The velocity, w_i , is the velocity through the control surface with respect to the control surface. Thus as the mass of the particle changes, due to evaporation for example, the mass passes through the control surface with a velocity w_i .

A.2 Mass conservation

The equation for mass conservation of a system is

$$\frac{dM}{dt} = 0 \quad (\text{A.17})$$

because, by definition, the mass of a system, M , is constant. The intensive property corresponding to mass is the mass per unit mass or, simply, unity. Thus the Reynolds transport theorem applied to mass conservation is

$$\frac{d}{dt} \int_{cv} \rho_d dV + \int_{cs} \rho_s w_i n_i dS = 0 \quad (\text{A.18})$$

where ρ_d is the material density of the particle¹ and ρ_s is the density of the fluid at the control surface.

The integral of the density over the volume of the particle is simply the instantaneous mass of the particle, m , so the continuity equation can be written as

$$\frac{dm}{dt} = - \int_{cs} \rho_s w_i n_i dS \quad (\text{A.19})$$

If the magnitude of the efflux velocity w_i and fluid density are uniform over the control surface the continuity equation simplifies to

$$\frac{dm}{dt} = -\rho_s w S_d \quad (\text{A.20})$$

¹The subscript “d” represents the dispersed phase.

where w is the magnitude of the efflux velocity vector. Obviously if the particle is evaporating, the efflux velocity is positive and the particle mass decreases with time. On the other hand, condensation gives rise to a negative efflux velocity and the particle mass increases with time. This equation forms the basis for the nondimensional numbers relating to mass transfer discussed in Chapter 4.

A.3 Momentum conservation

A.3.1 Linear momentum

Newton's second law states that the net force acting on a system is equal to the rate of change of momentum of the system, or

$$F_i = \frac{d(MU_i)}{dt} \quad (\text{A.21})$$

In this case the extensive variable is the momentum, MU_i , so the corresponding intensive variable is the velocity, U_i , measured with respect to an inertial reference frame. The application of Reynolds transport theorem for rate of change of momentum yields

$$F_i = \frac{d}{dt} \int_{cv} \rho_d U_i dV + \int_{cs} \rho_s U_{i,s} n_j w_j dS \quad (\text{A.22})$$

where $U_{i,s}$ is the velocity of the fluid at the control surface with respect to the inertial reference frame. This is a vector equation for the direction i .

In general, the particle may be rotating and there may be an internal circulation within the particle (or droplet). However, it will be assumed here that there is no internal motion and the particle is rotating about an axis through its center of mass. The velocity inside the particle is then given by

$$U_i = v_i + \epsilon_{ijk} \omega_j \xi_k \quad (\text{A.23})$$

where v_i is the velocity of the particle's center of mass with respect to an inertial reference frame, ω_i is the particle's rotation vector and ξ_i is the distance from the center of mass. Thus the integral for the momentum in the control volume can be written as

$$\frac{d}{dt} \int_{cv} \rho_d U_i dV = \frac{d}{dt} \int_{cv} \rho_d (v_i + \epsilon_{ijk} \omega_j \xi_k) dV \quad (\text{A.24})$$

Because v_i and ω_i are constant over the interior of the particle, the above equation becomes

$$\frac{d}{dt} \int_{cv} \rho_d U_i dV = \frac{d}{dt} (mv_i) + \frac{d}{dt} \epsilon_{ijk} \omega_j \int_{cv} \xi_k \rho_d dV \quad (\text{A.25})$$

By definition of the center of mass, the integral on the right side is zero so the equation can be reduced to

$$\frac{d}{dt} \int_{cv} \rho_d U_i dV = \frac{d}{dt} (mv_i) = v_i \frac{dm}{dt} + m \frac{dv_i}{dt} \quad (\text{A.26})$$

If the particle is evaporating or condensing, then the velocity of the surface with respect to the center of the particle is

$$\dot{r}n_i + \epsilon_{ijk}\omega_j r_k$$

where \dot{r} is the regression rate of the surface. Thus the velocity of the fluid crossing the control surface with respect to an inertial reference frame is

$$U_{i,s} = v_i + \epsilon_{ijk}\omega_j r_k + (\dot{r} + w)n_i = v_i + \epsilon_{ijk}\omega_j r_k + w'n_i \quad (\text{A.27})$$

where, for convenience, the sum of the regression rate and the efflux velocity, $(\dot{r} + w)n_i$ has been replaced by $w'n_i$.

The net efflux of momentum from the control surface is given by

$$\int_{cs} \rho_s U_{i,s} w_j n_j dS = \int_{cs} \rho_s (v_i + \epsilon_{ijk}\omega_j r_k + w'n_i) w_l n_l dS \quad (\text{A.28})$$

In that v_i is not a function of the surface position, one can write

$$\int_{cs} \rho_s v_i w_j n_j dS = v_i \int_{cs} \rho_s w_j n_j dS \quad (\text{A.29})$$

By using the continuity equation, Equation A.19, the integral is reduced to

$$v_i \int_{cs} \rho_s w_j n_j dS = -v_i \frac{dm}{dt} \quad (\text{A.30})$$

Finally the addition of Equations A.26 and A.30 yields the momentum equation for the particle

$$F_i = m \frac{dv_i}{dt} + \int_{cs} \rho_s w' n_i w_j n_j dS + \epsilon_{ijk}\omega_j \int_{cs} \rho_s r_k w_l n_l dS \quad (\text{A.31})$$

For an evaporating or burning particle, the efflux velocity and regression velocity will be normal to the surface at the surface so the first integral in Equation A.31 becomes

$$\int_{cs} \rho_s w' n_i w_j n_j dS = \int_{cs} \rho_s w' w n_i dS = -T_i \quad (\text{A.32})$$

This term represents the negative thrust, T_i , on the particle due to mass efflux from the surface. For example, if a particle were a flat disk as shown in Figure A.6, and the mass was rejected only from the leeward face, the particle would experience a thrust as evaluated with the above integral. In some instances like a burning coal particle, the mass efflux is not uniform

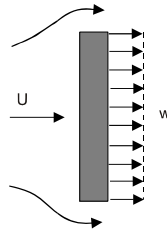


Figure A.6: “Flat disk” particle with mass efflux on leeward side.

over the surface and spurious lateral motions are observed. However, for most applications involving droplet burning or evaporation, the nonuniformity of momentum flux is small compared to the other forces acting on a droplet. If the momentum efflux is uniform over the surface, then

$$\int_{cs} \rho_s w' w n_i dS = \rho_s w w' \int_{cs} n_i dS = 0 \quad (\text{A.33})$$

Also, if the mass flux is uniform over the surface and the particle is spherical, the integral associated with the particle rotation is also zero.

$$\epsilon_{ijk} \omega_j \int_{cs} \rho_s r_k w_l n_\ell dA = \epsilon_{ijk} \omega_j \int_{cs} \rho_s w r n_k dA = 0$$

The momentum equation finally simplifies to

$$m \frac{dv_i}{dt} = F_i \quad (\text{A.34})$$

or, in words, the forces acting on the particle are equal to the product of the instantaneous mass of the particle and the acceleration at the particle’s center of mass.

The forces acting on a particle can be subdivided into two sources: surface forces and body forces.

$$F_i = F_{i,s} + F_{i,b} \quad (\text{A.35})$$

If the particles are in close proximity, there may be additional forces due to particle-particle contact. These are addressed in Chapter 5.

Body forces

Body forces are forces that act on the mass of the particle. The most common is the gravitational force, which is the product of the particle mass and local acceleration due to gravity.

$$F_{i,g} = m g_i \quad (\text{A.36})$$

where g_i is the component of the gravitational acceleration in direction i .

Another body force could be the Coulomb force or the force due to charges in an electric field. This force is the most important in the dynamics of particles in an electrostatic precipitator. The Coulomb force is given by

$$F_{i,c} = -qE_i \quad (\text{A.37})$$

where q is the charge on the particle and E_i is the potential gradient of the electric field. Typically the charge on a particle accumulates on the particle surface and there is a saturation charge beyond which no additional charges can be accommodated on the surface.

Another body force may be due to a magnetic field in which case the force depends on the gradient in the magnetic field and the permeability of the particle mass.

Surface forces

The surface forces are due to pressure and shear stress acting on the surface. The net pressure force is obtained from

$$F_{i,p} = - \int_{cs} p_s n_i dS \quad (\text{A.38})$$

where n_i is the unit outward normal vector from the surface and p_s is the pressure at the surface. The minus sign is needed to provide the pressure force *on the particle*. This pressure force may have components which are in the direction of particle-fluid relative velocity vector (drag) and normal to the vector (lift). The pressure force component in the drag direction is called *form drag*.

The net force due to shear stress is represented by

$$F_{i,\tau} = \int_{cs} \tau_{ij} n_j dS \quad (\text{A.39})$$

where τ_{ij} is the shear stress tensor at the particle surface. The component of this force in the drag direction is the *viscous* or *shear drag*.

The sum of the pressure and shear forces acting on the particle constitutes the surface forces

$$F_i = \int_{cs} (-p_s n_i + \tau_{ij} n_j) dS \quad (\text{A.40})$$

The representation of the surface forces by drag and lift coefficients is discussed in Chapter 4.

The final form for the particle momentum equation is

$$m \frac{dv_i}{dt} + \int_{cs} \rho_s w' w n_i dA = F_{i,b} + F_i \quad (\text{A.41})$$

which reduces to

$$m \frac{dv_i}{dt} = F_{i,b} + F_i \quad (\text{A.42})$$

if the momentum efflux from the surface is uniform.

A.3.2 Moment of momentum

The equation relating the torque applied to a system and the rate of change of angular momentum is

$$T_i = \frac{d}{dt}(M H_i) \quad (\text{A.43})$$

where T_i is the applied torque vector and H_i is the moment of momentum per unit mass of the system.

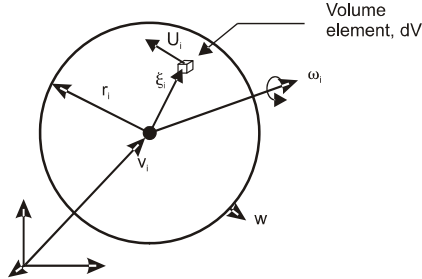


Figure A.7: Rotating, evaporating spherical particle.

A rotating, evaporating spherical particle is shown in Figure A.7. The particle is rotating with an angular velocity of ω_i . A volume element dV is positioned at ξ_i with respect to the center of mass and is moving at a velocity U_i with respect to the reference frame. The velocity of the center of mass with respect to the reference frame is v_i . The radius vector on the sphere is r_i and the velocity of the mass crossing the surface is w . The moment of momentum per unit mass for the volume element is

$$h_i = \epsilon_{ijk} \xi_j U_k \quad (\text{A.44})$$

Applying Reynolds transport theorem to the rotating particle, the rotation equation becomes

$$T_i = \frac{d}{dt} \int_{cv} \rho h_i dV + \int_{cs} \rho_s h_i w_j n_j dS \quad (\text{A.45})$$

The moment of momentum within the control volume is given by

$$\int_{cv} \rho h_i dV = \int_{cv} \rho \epsilon_{ijk} \xi_j U_k dV \quad (\text{A.46})$$

The velocity of the volume element is

$$U_i = v_i + \epsilon_{ijk} \omega_j \xi_k \quad (\text{A.47})$$

and the moment of momentum in the control volume is determined by

$$\int_{cv} \rho h_i dV = \int_{cv} \rho \epsilon_{ijk} \xi_j (v_k + \epsilon_{klm} \omega_l \xi_m) dV \quad (\text{A.48})$$

Because v_i is constant over the volume and by definition of the center of mass,

$$\int_{cv} \rho \epsilon_{ijk} \xi_j v_k dV = \epsilon_{ijk} v_k \int_{cv} \rho \xi_j dV = 0 \quad (\text{A.49})$$

The integral over the second term becomes²

$$\int_{cv} \rho \epsilon_{ijk} \xi_j \epsilon_{klm} \omega_l \xi_m dV = \omega_i \int_{cv} \rho \xi_j \xi_j dV - \omega_j \int_{cv} \rho \xi_j \xi_i dV \quad (\text{A.50})$$

Taking the subscript i as the 1-direction, the equation becomes

$$\begin{aligned} & \omega_1 \int_{cv} \rho \xi_j \xi_j dV - \omega_j \int_{cv} \rho \xi_j \xi_1 dV = \\ & \omega_1 \int_{cv} \rho (\xi_2^2 + \xi_3^2) dV - \omega_2 \int_{cv} \rho \xi_1 \xi_2 dV - \omega_3 \int_{cv} \rho \xi_1 \xi_3 dV \end{aligned} \quad (\text{A.51})$$

The first integral on the right is the moment of inertia, I_1 , about the axis in the 1-direction. If the particle is symmetric about the center or mass (a sphere), the other integrals on the right side vanish and the momentum of inertia is the same about any axis so the first term of Equation A.45 becomes

$$\frac{d}{dt} \int_{cv} \rho h_i dV = \frac{d}{dt} (\omega_i I) \quad (\text{A.52})$$

The net efflux of the moment of momentum through the surface is given by

$$\int_{cs} \rho_s h_i w_j n_j dS = \int_{cs} \rho_s \epsilon_{ijk} r_j (v_k + \epsilon_{klm} \omega_l r_m + n_k w') w dS \quad (\text{A.53})$$

The first integral on the right side is equal to zero,

$$\int_{cs} \rho_s \epsilon_{ijk} r_j v_k w dS = v_k \rho_s w \epsilon_{ijk} \int_{cs} r_j dS = 0 \quad (\text{A.54})$$

provided the particle is spherical and the mass efflux is constant over the surface. The last integral is

$$\int_{cs} \rho_s \epsilon_{ijk} r_j n_k w' w dS = \rho_s w w' r \int_{cs} \epsilon_{ijk} n_j n_k dS = 0 \quad (\text{A.55})$$

²This manipulation follows from the identity from tensor analysis.

$$\epsilon_{ijk} \epsilon_{ilm} = \delta_{jl} \delta_{km} - \delta_{jm} \delta_{kl}$$

if the particle is spherical and the mass flux is uniform.

Part of the integrand in the second integral can be related the moment of inertia associated with the shell of mass adjacent to the surface of the particle

$$\epsilon_{ijk}\epsilon_{klm}r_j\omega_lr_m = \frac{w_i}{\rho_d S} \frac{dI}{dr} \quad (\text{A.56})$$

where S is the surface area. Also at the surface

$$\rho_s w = -\rho_d \frac{dr}{dt} \quad (\text{A.57})$$

The second integral can be evaluated as

$$\int_{cs} \rho_s \epsilon_{ijk}\epsilon_{klm}r_j\omega_lr_m wdS = - \int_{cs} \frac{w_i}{\rho_d S} \frac{dI}{dr} \rho_d \frac{dr}{dt} dS \quad (\text{A.58})$$

$$= -\omega_i \frac{dI}{dt} \quad (\text{A.59})$$

for a spherical particle because $\rho_s wdS$ represents the mass reduction rate at the surface due to mass transfer. Finally, the net efflux of moment of momentum from a spherical, uniformly evaporating droplet is

$$\int_{cs} \rho_s H_i w_j n_j dS = -\omega_i \frac{dI}{dt} \quad (\text{A.60})$$

Incorporating Equations A.52 and A.60 into Equation A.45 yields

$$T_i = I \frac{d\omega_i}{dt} \quad (\text{A.61})$$

as the equation for rotation of a spherical, uniformly evaporating droplet.

The body forces due to gravity do not contribute to the applied torque. Also the forces due to pressure on the surface of a spherical droplet do not contribute to a torque since the force passes through the center of mass (no moment arm). The torque due to the surface shear stress is given by

$$T_i = \int_{cs} \epsilon_{ijk} r_j \tau_{lk} n_l dS \quad (\text{A.62})$$

The evaluation of the torque on a particle is addressed in Chapter 4.

A.4 Energy conservation

The first law of thermodynamics for a system states that the rate of change of energy is equal to the rate at which heat is transferred to the system and the rate at which work is done by the system,

$$\frac{dE}{dt} = \dot{Q} - \dot{W} \quad (\text{A.63})$$

where E , the energy, includes both internal and external (mechanical) energies as well as the energy associated with surface tension.

The internal energy is written as

$$I = Mi \quad (\text{A.64})$$

where i is the internal energy per unit mass (specific internal energy). The external energy is the kinetic energy,

$$KE = M \frac{U_i U_i}{2} \quad (\text{A.65})$$

where U_i is the velocity of the matter with respect to an inertial reference frame. Thus the specific external energy³ is $U_i U_i / 2$. The energy associated with surface tension is the product of the surface area of the particle and the surface tension

$$E_\sigma = S\sigma \quad (\text{A.66})$$

Thus the total energy can be written as

$$E = M(i + \frac{U_i U_i}{2}) + S\sigma \quad (\text{A.67})$$

which, for convenience, will be abbreviated to

$$E = Me + S\sigma \quad (\text{A.68})$$

where e is the sum of the specific internal and kinetic energy.

Application of the Reynolds transport theorem to relate the change of internal and external energies of the system to the change in the control volume and the net efflux through the control surface gives

$$\frac{d(Me)}{dt} = \frac{d}{dt} \int_{cv} \rho_d e dV + \int_{cs} \rho_s e w_i n_i dS \quad (\text{A.69})$$

Thus the first law of thermodynamics applied to the control volume is

$$\dot{Q} - \dot{W} = \frac{d}{dt} \int_{cv} \rho_d e dV + \int_{cs} \rho_s e s w_i n_i dS + \frac{d}{dt}(S\sigma) \quad (\text{A.70})$$

where \dot{Q} and \dot{W} are the heat transfer rate to the system and the rate at which work is done by the system the instant it occupies the control volume.

It is assumed that the particle is neither rotating nor has internal motion. In this case, the velocity of the matter inside the droplet is v_i . The rate of change of energy within the control volume becomes

$$\begin{aligned} \frac{d}{dt} \int_{cv} \rho_d e dV + \frac{d}{dt}(S\sigma) &= \frac{d}{dt} \int_{cv} \rho_d \left(i + \frac{v_i v_i}{2} \right) dV + \sigma \frac{dS}{dt} \\ &= \frac{d}{dt} \left(m \frac{v_i v_i}{2} \right) + \frac{d}{dt}(m\bar{v}) + \frac{2\sigma}{r} \dot{r} S \end{aligned} \quad (\text{A.71})$$

³The energy due to rotation is not included here.

where \bar{i} is the average specific internal energy of the particle and the surface tension is assumed invariant with time.

Differentiation of the kinetic energy term yields two terms

$$\frac{d}{dt}\left(m\frac{v_i v_i}{2}\right) = mv_i \frac{dv_i}{dt} + v^2 \frac{dm}{dt} \quad (\text{A.72})$$

where v is simply the magnitude of the velocity vector v_i . This expression will be utilized later in the final assembly of the terms in the Reynolds transport theorem.

Evaluation of the energy flux term in the Reynolds transport equation requires the energy of the matter crossing the control surface; namely,

$$e_s = i_s + \frac{U_{i,s} U_{i,s}}{2} \quad (\text{A.73})$$

where i_s is the specific internal energy and $U_{i,s}$ is the velocity with respect to an inertial reference frame. This velocity can be expressed as

$$U_{i,s} = v_i + w_i + \dot{r}n_i \quad (\text{A.74})$$

It is convenient to use the sum of the efflux velocity at the surface and the surface regression velocity as a single variable $w'_i = (w + \dot{r})n_i$ as was done in the momentum equation. Thus the specific kinetic energy at the surface is

$$\frac{U_{i,s} U_{i,s}}{2} = \frac{(v_i + w' n_i)(v_i + w' n_i)}{2} = \frac{v^2}{2} + \frac{w'^2}{2} + w' n_i v_i \quad (\text{A.75})$$

Substituting these expressions into the efflux term of the Reynolds transport theorem yields

$$\begin{aligned} \int_{cs} \rho_s e_s w_j n_j dS &= \left(\frac{v^2}{2} + \frac{w'^2}{2}\right) \int_{cs} \rho_s w_j n_j dS + \\ &\quad v_i \int_{cs} \rho_s w' w n_i dS + \int_{cs} i_s \rho_s w_j n_j dS \end{aligned} \quad (\text{A.76})$$

From the continuity equation, Equation A.18, the integral of the mass flux over the surface is equal to $-(dm/dt)$ so the above integral reduces to

$$\begin{aligned} \int_{cs} \rho_s e_s w_j n_j dS &= -\left(\frac{v^2}{2} + \frac{w'^2}{2}\right) \frac{dm}{dt} + \\ &\quad v_i \int_{cs} \rho_s w' w n_i dS + \int_{cs} \rho_s i_s w_j n_j dS \end{aligned} \quad (\text{A.77})$$

Adding Equations A.71 and A.77 gives the rate of change of energy of the system at the instant it is in the control volume

$$\begin{aligned} \frac{dE}{dt} &= mv_i \frac{dv_i}{dt} - \frac{(w')^2}{2} \left(\frac{dm}{dt}\right) + \frac{d}{dt}(m\bar{i}) \\ &\quad + v_i \int_{cs} \rho_s w' w n_i dS + \int_{cs} \rho_s i_s w_j n_j dS + \frac{2\sigma}{r} \dot{r} S \end{aligned} \quad (\text{A.78})$$

This expression must now be equated to the rate of heat transfer to the particle and the rate at which work is done by the particle on the surroundings.

A.4.1 Heat transfer to particle

Heat transfer takes place through two mechanisms: radiation and conduction. Heat transfer due to particle-particle contact is not addressed here.

The radiative heat transfer is the net energy due to absorption and emission. If the droplet or the particle is considered a “grey” body, the net radiative heat transfer to the particle is

$$\dot{Q}_r = 4\pi r^2(\alpha J - \epsilon\sigma T_d^4) \quad (\text{A.79})$$

where α is the absorptivity, ϵ is the emissivity, J is the radiosity and σ is the Stephan-Boltzmann constant. In general, a solution for the radiation field has to be obtained before the local radiosity can be determined.

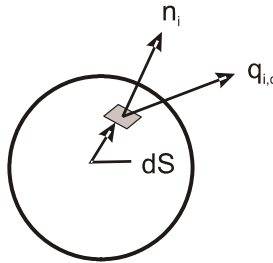


Figure A.8: Conductive heat transfer through area element at particle surface.

The net conductive heat transfer can be evaluated by integrating the heat flux vector, $q_{i,c}$, over the surface as shown in Figure A.8. The net heat transfer due to conduction is

$$\dot{Q}_c = - \int_{cs} q_{i,c} n_i dS \quad (\text{A.80})$$

where the minus sign is needed to give the net heat transfer rate to the droplet.

A.4.2 Work rate of particles on surroundings

Work arises from displacement of both body and surface forces. The work rate due to body forces is simply the negative product of the velocity of the particle and the body force,

$$\dot{W}_b = -F_{i,b}v_i \quad (\text{A.81})$$

The work rate due to pressure forces is the dot product of the pressure force acting on an element of area and the velocity of matter passing through the element

$$d\dot{W}_p = (v_i + w'_i)n_i p_s dS \quad (\text{A.82})$$

where p_s is the pressure at the control surface. By definition the pressure force is acting on the element so the motion of the matter against the pressure

force represents work done by the system. The work per unit time done by the system over the entire control surface is

$$\dot{W}_p = \int_{cs} (v_i + w'_i) n_i p_s dS \quad (\text{A.83})$$

The shear stress force acting on the area element in the i -direction is $\tau_{ij} n_j dS$ where τ_{ij} is the shear stress tensor. The work rate associated with this force and the velocity at the surface is

$$d\dot{W}_s = -(v_i + w'_i) \tau_{ij} n_j dS \quad (\text{A.84})$$

In this case the dot product of the force and the velocity represents work done by the surroundings on the system, hence the negative sign. The total work due to shear stress forces acting on the system is

$$\dot{W}_s = - \int_{cs} (v_i + w'_i) \tau_{ij} n_j dS \quad (\text{A.85})$$

Adding the pressure and shear work rate integrals and realizing the velocity v_i is constant with respect to the integration results in

$$\begin{aligned} \int_{cs} (v_i + w'_i) (n_i p_s - \tau_{ij} n_j) dS &= v_i \int_{cs} (n_i p_s - \tau_{ij} n_j) dS + \\ &\quad \int_{cs} p_s w'_i n_i dS - \int_{cs} w'_i \tau_{ij} n_j dS \end{aligned} \quad (\text{A.86})$$

The first integral on the right represents the surface forces acting on the droplet. Note that this integral is the negative of the integral in Equation A.40 so

$$v_i \int_{cs} (n_i p_s - \tau_{ij} n_j) dS = -v_i F_i \quad (\text{A.87})$$

The second integral on the right of Equation A.86 can be expressed as

$$\begin{aligned} \int_{cs} p_s w'_i n_i dS &= \int_{cs} p_s (w_i + \dot{r} n_i) n_i dS \\ &= \int_{cs} \rho_s \frac{p_s}{\rho_s} w_i n_i dS + \int_{cs} \dot{r} p_s dS \end{aligned} \quad (\text{A.88})$$

The third integral is zero

$$\int_{cs} w'_i \tau_{ij} n_i dS = \int_{cs} w' n_i \tau_{ij} n_j dS = 0 \quad (\text{A.89})$$

because the vector $\tau_{ij} n_j$ lies in the local tangent plane of the surface and the vector n_i is normal to the surface. Hence the dot product of these two vectors is zero.

Combining all the terms (Equations A.78, A.81, A.87 and A.88) to form the energy equation

$$\frac{dE}{dt} = \dot{Q} - \dot{W}$$

results in

$$\begin{aligned} \frac{d}{dt}(mi) + mv_i \frac{dv_i}{dt} - \frac{(w')^2}{2} \frac{dm}{dt} + \frac{2\sigma}{r} \dot{r} S \\ + \int_{cs} i_s \rho_s w_i n_i dS + v_i \int_{cs} \rho_s w' w n_i dS \\ = \dot{Q}_r + \dot{Q}_c + v_i (F_{i,b} + F_i) \\ - \int_{cs} \rho_s \frac{p_s}{\rho_s} w_i n_i dS - \int_{cs} \dot{r} p_s dS \end{aligned} \quad (\text{A.90})$$

This equation can be rewritten as

$$\begin{aligned} \frac{d}{dt}(mi) + v_i \left(m \frac{dv_i}{dt} + \int_{cs} \rho_s w' w n_i dA - F_{i,b} - F_i \right) \\ - \frac{(w')^2}{2} \frac{dm}{dt} + \frac{2\sigma}{r} r S + \int_{cs} \left(i_s + \frac{p_s}{\rho_s} \right) \rho_s w_i n_i dS \\ = \dot{Q}_r + \dot{Q}_c - \int_{cs} \dot{r} p_s dS \end{aligned} \quad (\text{A.91})$$

With reference to the momentum equation for the droplet, Equation A.31, the factor multiplying the v_i in the second term is zero so the energy equation further reduces to

$$\frac{d\bar{m}}{dt} - \frac{w'^2}{2} \frac{dm}{dt} + \int_{cs} h_s \rho_s w_i n_i dS = \dot{Q}_r + \dot{Q}_c - \dot{r} S (\bar{p}_s + \frac{2\sigma}{r}) \quad (\text{A.92})$$

where h_s is the enthalpy of the fluid crossing the control surface and \bar{p}_s is the average pressure on the particle surface. The regression rate has been assumed uniform over the surface. The combination $\bar{p}_s + 2\sigma/r$ is the pressure inside the droplet, p_d .⁴ Thus, the energy equation further simplifies to

$$m \frac{d\bar{m}}{dt} + \bar{m} \frac{dm}{dt} - \frac{w'^2}{2} \frac{dm}{dt} + \int_{cs} h_s \rho_s w_i n_i dS = \dot{Q}_r + \dot{Q}_c - \dot{r} \rho_d \frac{p_d}{\rho_d} S \quad (\text{A.93})$$

The factor $\rho_d \dot{r} A$ is the rate of change of droplet mass dm/dt so the second term on the left side can be combined with the last term on the right side which results in

$$m \frac{d\bar{m}}{dt} = \dot{Q}_r + \dot{Q}_c + \frac{dm}{dt} (\bar{h}_s - \bar{h}_d + \frac{w'^2}{2}) \quad (\text{A.94})$$

where \bar{h}_d is the enthalpy of the particle phase. Usually the kinetic energy associated with the mass efflux velocity is very small compared with the enthalpy difference between phases

$$\bar{h}_s - \bar{h}_d \gg \frac{w'^2}{2}$$

⁴Actually there will be a pressure jump across the surface due to the momentum flux so p_d is not the actual pressure inside the droplet. Under most conditions, this pressure jump is small.

so the conventional form of the particle energy equation is

$$m \frac{d\bar{t}}{dt} = \dot{Q}_r + \dot{Q}_c + \frac{dm}{dt}(\bar{h}_s - \bar{h}_d) \quad (\text{A.95})$$

This equation states that the energy of the particle is controlled by the heat transfer to the particle and the energy associated with the change of phase. For example, if there is no heat transfer to an evaporating droplet, the internal energy (temperature) of the droplet will decrease as mass is evaporated ($dm/dt < 0$) from the surface. The application of this equation is addressed in Chapter 4 and subsequent chapters.

Other equations can be developed for the single particles such as the entropy equation. The development of these equations follows the same approach as used above.

This page intentionally left blank

Appendix B

Volume Averaging

In dealing with a mixture of droplets or particles, it is impractical to solve for the fluid properties at every point in the mixture. Thus one is driven to consider the average properties in a volume containing many particles as discussed in Chapter 6. For example, the concept of bulk density as the mass of the phase per unit volume of mixture is an average property. A formal approach is now sought to express the conservation laws for the continuous phase in terms of average properties.

The approach used here differs from the approach used by Anderson and Jackson (1967) in which a monotone decreasing, differentiable weighting function had to be introduced to ensure the differentiability of the volume averages. The introduction of a weighting function is not required here.

Consider a mixture of fluid and particles enclosed in the spherical volume shown in Figure B.1. The averaging volume (V) is composed of the volume of the continuous phase (V_c) and the volume occupied by the dispersed phase (V_d). The volume has to be large enough such that a small increase in the volume will not affect the value of the average; that is, the same value for bulk density would be obtained if the volume were slightly changed. Still, the volume has to be small compared to the system dimensions or it will not be possible to write differential equations for the conservation laws.

The formalism used for volume averaging can be found in Slattery (1972). Based on the volume over which averages are taken, there are two types of averages to be considered. Let B be some property of the continuous phase. The *phase average* of B is the average over the volume of the continuous phase and is defined as

$$\langle B \rangle = \frac{1}{V_c} \int_{V_c} BdV \quad (\text{B.1})$$

If B were the continuous phase density, ρ_c , then $\langle \rho_c \rangle$ is the average material density of the continuous phase in the volume. Obviously, if the continuous phase density is constant then $\langle \rho_c \rangle = \rho_c$.

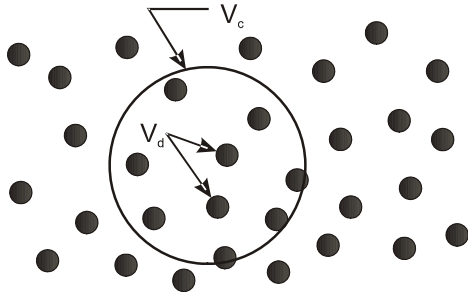


Figure B.1: Particles in averaging volume.

The *volume average* of the local property B is given by

$$\bar{B} = \frac{1}{V} \int_{V_c} B dV \quad (\text{B.2})$$

Once again if B is the continuous phase density, the local volume average density is

$$\bar{\rho}_c = \frac{1}{V} \int_{V_c} \rho_c dV \quad (\text{B.3})$$

The equation for local average density can be rewritten as¹

$$\bar{\rho}_c = \frac{V_c}{V} \frac{1}{V_c} \int_{V_c} \rho_c dV \quad (\text{B.4})$$

The ratio V_c/V is the volume fraction, α_c , of the fluid so the relationship between phase average and local average continuous phase density is given by

$$\bar{\rho}_c = \alpha_c \langle \rho_c \rangle \quad (\text{B.5})$$

A more formal statement regarding the minimum size of the averaging volume is now possible. If the averaging volume is displaced over a distance corresponding to the linear dimension of the volume ($\sim V^{1/3}$), then the phase average properties should not change. This implies that

$$\langle \bar{B} \rangle = \bar{B} \quad (\text{B.6})$$

B.1 Volume average of the gradient operation

All the conservation laws for a flowing fluid involve a gradient term. To form the average of the conservation equations over the averaging volume requires a

¹The local volume average of the density is the same as the bulk density introduced in Chapter 2.

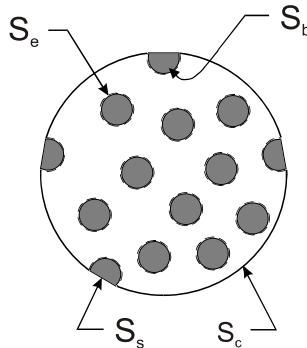


Figure B.2: Definition of surfaces.

relationship for the local volume average of the gradient. The volume average of the gradient over the continuous phase is defined as

$$\overline{\frac{\partial B}{\partial x_i}} = \frac{1}{V} \int_{V_c} \frac{\partial B}{\partial x_i} dV \quad (\text{B.7})$$

We now seek a formal method to interchange the volume and gradient operation.

The following developments are valid for any dispersed-phase flow which may consist of particles (porous or solid) or droplets. For simplicity, the word “particle” will be used for both.

Consider the averaging volume containing particles as shown in Figure B.2. Some of the particles are completely enclosed by the volume, while others (boundary particles) have been severed by the surface enclosing the volume. The portion of the surface through the continuous phase is designated as S_c while the surfaces which sever the particles is S_s . The complete surface of the control volume, S , is equal to

$$S = S_c + S_s$$

The surface surrounding the particles completely inside the volume is S_e while the inside surface of the boundary particles is S_b . The total surface surrounding the particles inside the averaging volume, S_d , is

$$S_d = S_b + S_e$$

Consider an averaging volume which moves through a field of particles as shown in Figure B.3. The center of the averaging volume is located by the vector $c_i(s)$ here s is a parameter. The vector $R_i(s)$ extends from the center to the edge of the volume defined by the S_c and S_b surfaces. The $R_i(s)$ vector shown in the figure terminates at a S_b surface, the interior surface of a boundary particle. Assume that the center of the volume is displaced to

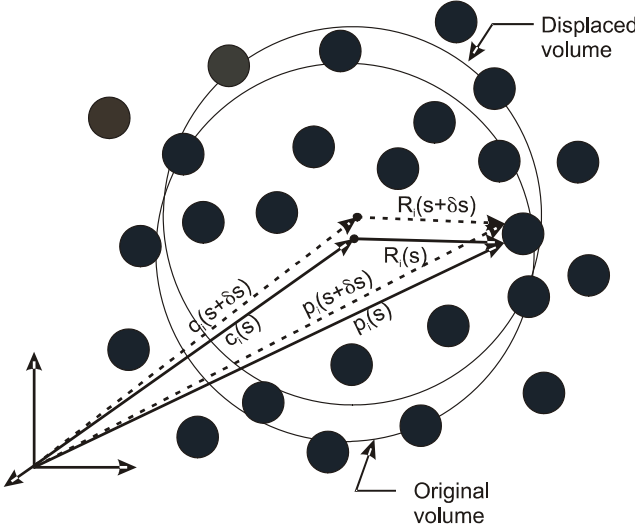


Figure B.3: Displaced averaging volume.

a new location given by $c_i(s + \delta s)$ shown by the dashed line on the figure. During this displacement the dispersed-phase elements remain fixed while the R_i and p_i vectors change as shown.

The details of the vector displacements are shown in Figure B.4. As the volume is displaced, the R_i and p_i vectors move along the surface of the particle so the vector p_i is incremented by an amount δp_i which lies tangent to the particle surface. In the limit as $\delta s \rightarrow 0$

$$\lim_{\delta s \rightarrow 0} \frac{\delta p_i}{\delta s} = \frac{dp_i}{ds}$$

which is a vector tangent to the surface. This applies to all the internal surfaces of all the particles, namely S_d .

The change in the volume average of B as the averaging volume translates with s can be determined by application of Leibnitz rule for the derivative of an integral. The derivative of the integral of B over V_c with respect to s can be expressed as

$$\frac{d}{ds} \int_{V_c} BdV = \int_{V_c} \frac{\partial B}{\partial s} dV + \int_{S_c + S_d} B \frac{dp_i}{ds} \eta_i dS \quad (\text{B.8})$$

where η_i is the unit outward normal vector from the averaging volume. In this case, the vector η_i would be directed into the particles on the S_d surfaces.

The property B is an explicit function of time and position only and not a function of the parameter s so

$$\frac{\partial B}{\partial s} = 0 \quad (\text{B.9})$$

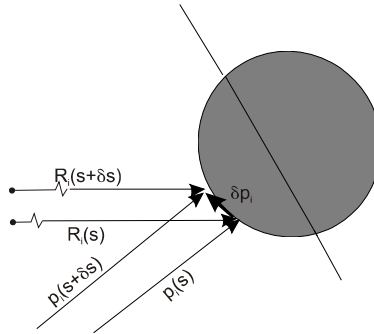


Figure B.4: Details of displaced vectors in neighborhood of particle.

Also, on the surfaces S_d , the dot product of the vector dp_i/ds and η_i is zero since dp_i/ds lies along the tangent to the surfaces S_d . Thus the derivative with respect to s of the integral of B over the continuous-phase volume reduces to

$$\frac{d}{ds} \int_{V_c} B dV = \int_{S_c} B \frac{dp_i}{ds} \eta_i dS \quad (\text{B.10})$$

The path of the center of the control volume is given by the vector function $c_i(s)$. The coordinate of a general point on the surface of the averaging volume, $p_i(s)$, is the vector sum of the center coordinate and the radius, R_i ,

$$p_i(s) = c_i(s) + R_i(s) \quad (\text{B.11})$$

The change of $p_i(s)$ with s on the surfaces S_c is obtained from

$$\frac{dp_i}{ds} = \frac{dc_i}{ds} \quad (\text{B.12})$$

since the vector R_i is constant on this surface as the volume is displaced; that is, the averaging volume neither deforms nor rotates. Because dc_i/ds is not a function of the position on the surface S_c , the integral in Equation B.10 becomes

$$\int_{S_c} B \frac{dp_i}{ds} \eta_i dS = \frac{dc_i}{ds} \int_{S_c} B \eta_i dS \quad (\text{B.13})$$

Also, the derivative with respect to s can be written using the chain rule as

$$\frac{d}{ds} = \frac{dc_i}{ds} \frac{\partial}{\partial x_i} \quad (\text{B.14})$$

Finally, Equation B.8 can be expressed as

$$\frac{dc_i}{ds} \left(\frac{\partial}{\partial x_i} \int_{V_c} B dV - \int_{S_c} B \eta_i dS \right) = 0 \quad (\text{B.15})$$

Since dc_i/ds is not zero,

$$\frac{\partial}{\partial x_i} \int_{V_c} BdV = \int_{S_c} B\eta_i dS \quad (\text{B.16})$$

Applying Green's transformation to the definition of the local volume average of the gradient allows us to write

$$\int_{V_c} \frac{\partial B}{\partial x_i} dV = \int_{S_d+S_c} B\eta_i dS \quad (\text{B.17})$$

where S_d is the surface of all the particles inside the averaging volume including the interior surface of those elements intersected by the surface of the averaging volume. Using Equation B.15 for the surface integral over S_c results in

$$\frac{1}{V} \int_{V_c} \frac{\partial B}{\partial x_i} dV = \frac{1}{V} \frac{\partial}{\partial x_i} \int_{V_c} BdV + \frac{1}{V} \int_{S_d} B\eta_i dS \quad (\text{B.18})$$

or

$$\overline{\frac{\partial B}{\partial x_i}} = \overline{\frac{\partial B}{\partial x_i}} + \frac{1}{V} \int_{S_d} B\eta_i dS \quad (\text{B.19})$$

which is the theorem for the volume average of the gradient. The unit normal vector η_i is defined as "outward" from the continuous phase and "inward" to the dispersed phase. It is more convenient to use a unit normal vector directed outward from the dispersed phase designated here as n_i ($n_i = -\eta_i$) which changes the volume averaging theorem to

$$\overline{\frac{\partial B}{\partial x_i}} = \overline{\frac{\partial B}{\partial x_i}} - \frac{1}{V} \int_{S_d} Bn_i dS \quad (\text{B.20})$$

One notes that the volume average of the gradient is the gradient of the volume average plus an additional term which involves the integral of B over the interface between the dispersed and continuous phases. The property B can be a scalar, vector or second-order tensor field.

B.2 Volume averaging of the time derivative

One must also consider the volume average of the time derivative when applying the volume averaging equations to a dispersed-phase flow.

Consider as before the averaging volume enclosing the particles. The continuous phase is "enclosed" by the surface through the continuous phase, S_c , and the surfaces adjacent to the dispersed phase, S_d . Applying the corollary of the Leibnitz theorem for partial derivatives one has

$$\frac{\partial}{\partial t} \int_{V_c} BdV = \int_{V_c} \frac{\partial B}{\partial t} dV + \int_{S_d+S_c} B \frac{\partial p_i}{\partial t} \eta_i dS \quad (\text{B.21})$$

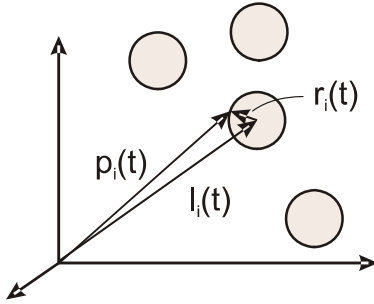


Figure B.5: Vectors locating surface of dispersed phase element “i.”

where p_i is the vector representing the surface enclosing the continuous phase and η_i is the unit normal vector outward from the surfaces (and into the particles). There is no change of the surface S_c with time so

$$\int_{S_c} B \frac{\partial p_i}{\partial t} \eta_i dS = 0 \quad (\text{B.22})$$

Assume the particles are spherical as shown in Figure B.5. The surface of every particle can be described as

$$p_i(t) = l_i(t) + r(t)\eta_i \quad (\text{B.23})$$

where l_i is the location of the center of the particle, r is the radius and n_i is the unit normal vector outward from the element surface. The partial derivative p_i with respect to time is

$$\frac{\partial p_i}{\partial t} = v_i + \dot{r}\eta_i + \epsilon_{ijk}\omega_j r \eta_k \quad (\text{B.24})$$

where v_i is the particle velocity and the vector ω_j is the particle's rotational rate. Thus the derivative of the volume average becomes

$$\frac{\partial}{\partial t} \int_{V_c} B dV = \int_{V_c} \frac{\partial B}{\partial t} dV + \int_{S_d} B(v_i + \dot{r}\eta_j + \epsilon_{ijk}\omega_j r \eta_k) \eta_i dS \quad (\text{B.25})$$

On the particle surfaces $n_i = -\eta_i$ and

$$\epsilon_{ijk}\omega_j r \eta_k n_i = -\epsilon_{ijk}\omega_j r n_k n_i = 0$$

Thus the volume average of the time derivative is given by

$$\overline{\frac{\partial B}{\partial t}} = \frac{\partial \overline{B}}{\partial t} - \frac{1}{V} \int_{S_d} B(v_i + \dot{r}\eta_j) \eta_i dS \quad (\text{B.26})$$

$$= \frac{\partial \overline{B}}{\partial t} - \frac{1}{V} \int_{S_d} B(v_i \eta_i - \dot{r}) dS \quad (\text{B.27})$$

Replacing η_i with $-n_i$ yields the final form for the volume average of the time derivative

$$\overline{\frac{\partial B}{\partial t}} = \frac{\partial \overline{B}}{\partial t} + \frac{1}{V} \int_{S_d} B(v_i n_i + \dot{r}) dS \quad (\text{B.28})$$

This completes the formulation of the equations for volume averaging. The application of these equations to develop the volume-averaged forms of the continuity, momentum and energy equations for fluid-particle mixtures is provided in Appendix C.

Appendix C

Volume-Averaged Equations

The formal volume averaging procedures developed in Appendix B are applied to the continuity, momentum and energy equations of the carrier phase.

C.1 Continuity equation

The continuity equation for the continuous phase is

$$\frac{\partial \rho_c}{\partial t} + \frac{\partial}{\partial x_i} (\rho_c u_i) = 0 \quad (\text{C.1})$$

Taking the local volume average of each term

$$\overline{\frac{\partial \rho_c}{\partial t}} + \overline{\frac{\partial}{\partial x_i} (\rho_c u_i)} = 0 \quad (\text{C.2})$$

and applying the volume-averaging equations gives

$$\frac{\partial \overline{\rho_c}}{\partial t} + \frac{1}{V} \int_{S_d} \rho_c (v_i n_i + \dot{r}) dS + \frac{\partial}{\partial x_i} (\overline{\rho_c u_i}) - \frac{1}{V} \int_{S_d} \rho_c u_i n_i dS = 0 \quad (\text{C.3})$$

At the droplet surface, the velocity of the gas crossing the surface is

$$u_i = v_i + (\dot{r} + w)n_i \quad (\text{C.4})$$

where v_i is the velocity of the particle center and $w n_i$ is the velocity of the gases with respect to the particle surface¹. Substituting this equation into Equation C.3 results in

¹Particle rotation could also be included but the resulting continuity equation will be unchanged.

$$\frac{\partial \overline{\rho_c}}{\partial t} + \frac{\partial}{\partial x_i} (\overline{\rho_c u_i}) = \frac{1}{V} \int_{S_d} \rho_c w dS \quad (C.5)$$

The average density $\overline{\rho_c}$ can be written as $\alpha_c \langle \rho_c \rangle$. The average mass flux is

$$\overline{\rho_c u_i} = \alpha_c \frac{1}{V_c} \int_{V_c} \rho_c u_i dV \quad (C.6)$$

The average velocity \tilde{u}_i is defined such that

$$\tilde{u}_i = \frac{1}{\langle \rho_c \rangle} \frac{1}{V_c} \int_{V_c} \rho_c u_i dV \quad (C.7)$$

which is the *mass-averaged* velocity. For a constant density fluid, the mass-averaged velocity is equal to the local volume average, $\tilde{u}_i = \langle u_i \rangle$. The velocity u_i can be expressed as the sum of the mass-averaged velocity and the deviation therefrom.

$$u_i = \tilde{u}_i + \delta u_i \quad (C.8)$$

Substituting this equation into Equation C.7 shows

$$\int_{V_c} \rho_c \delta u_i dV = 0 \quad (C.9)$$

The integral over the droplet or particle surfaces

$$\frac{1}{V} \int_{S_d} \rho_c w dS = s_{mass} \quad (C.10)$$

is the mass added per unit volume of mixture and identified as the mass source term, s_{mass} .

Thus the continuity equation for the carrier phase becomes

$$\frac{\partial}{\partial t} (\alpha_c \langle \rho_c \rangle) + \frac{\partial}{\partial x_i} (\alpha_c \langle \rho_c \rangle \tilde{u}_i) = s_{mass} \quad (C.11)$$

The mass source term can be evaluated by summing over all the particles inside the control volume or

$$s_{mass} = -\frac{1}{V} \sum_k \dot{m}_k \quad (C.12)$$

where \dot{m}_k is the rate of change of the mass of particle k and the summation is carried out over all droplets inside the control volume. The inclusion of the boundary particles depends on whether the particle centers are inside or outside the boundary of the averaging volume. If all particles evaporate at the same rate, the source term can be expressed as

$$s_{mass} = -n\dot{m} \quad (C.13)$$

where n is the local number density and \dot{m} is the rate at which the particle mass changed.

C.2 Momentum equation

The momentum equation for the carrier phase is

$$\frac{\partial}{\partial t} (\rho_c u_i) + \frac{\partial}{\partial x_j} (\rho_c u_i u_j) = -\frac{\partial p}{\partial x_i} + \frac{\partial \tau_{ij}}{\partial x_j} + \rho_c g_i \quad (\text{C.14})$$

Applying the averaging equation to the time derivative gives

$$\overline{\frac{\partial}{\partial t} (\rho_c u_i)} = \frac{\partial}{\partial t} (\overline{\rho_c u_i}) + \frac{1}{V} \int_{S_d} \rho_c u_i (v_j n_j + \dot{r}) dS \quad (\text{C.15})$$

and averaging the convection term results in

$$\overline{\frac{\partial}{\partial x_j} (\rho_c u_i u_j)} = \frac{\partial}{\partial x_j} (\overline{\rho_c u_i u_j}) - \frac{1}{V} \int_{S_d} \rho_c u_i u_j n_j dS \quad (\text{C.16})$$

Substituting the velocity at the surface, Equation C.4, into the integral over the particle surfaces gives

$$\frac{1}{V} \int_{S_d} \rho_c u_i u_j n_j dS = \frac{1}{V} \int_{S_d} \rho_c u_i [v_j + (\dot{r} + w)n_j] n_j dS$$

Thus the sum of the volume-averaged local and convective accelerations is

$$\begin{aligned} & \overline{\frac{\partial}{\partial t} (\rho_c u_i)} + \overline{\frac{\partial}{\partial x_j} (\rho_c u_i u_j)} \\ &= \frac{\partial}{\partial t} (\overline{\rho_c u_i}) + \frac{\partial}{\partial x_j} (\overline{\rho_c u_i u_j}) - \frac{1}{V} \int_{S_d} \rho_c u_i w dS \\ &= \frac{\partial}{\partial t} (\overline{\rho_c u_i}) + \frac{\partial}{\partial x_j} (\overline{\rho_c u_i u_j}) - \frac{1}{V} \int_{S_d} \rho_c (v_i + w' n_i) w dS \end{aligned} \quad (\text{C.17})$$

where, now, $w' = w + \dot{r}$ which is the velocity of the fluid at the surface with respect to the particle center.

As with the continuity equation, the volume average of the mass flux can be expressed as

$$\overline{\rho_c u_i} = \alpha_c \langle \rho_c u_i \rangle = \alpha_c \langle \rho_c \rangle \tilde{u}_i \quad (\text{C.18})$$

The volume average of the convection term becomes

$$\overline{\rho_c u_i u_j} = \alpha_c \langle \rho_c u_i u_j \rangle \quad (\text{C.19})$$

Using Equations C.8 and C.9, the convection term becomes²

$$\overline{\rho_c u_i u_j} = \alpha_c \langle \rho_c \rangle \tilde{u}_i \tilde{u}_j + \alpha_c \langle \rho_c \delta u_i \delta u_j \rangle \quad (\text{C.20})$$

²In this development, the term $\langle \rho_c \delta u_i \rangle$ is neglected. For a flow with constant continuous phase material density, the equation is correct with $\tilde{u}_i \rightarrow \langle u_i \rangle$ and $\delta u_i = u_i - \langle u_i \rangle$.

where $\delta u_i = \tilde{u}_i - u_i$. The last term, which is due to sub-volume fluctuations, is equivalent to the *Reynolds stress* encountered in a single-phase flow and shall be designated as the *volume-averaged Reynolds stress*. The flow does not have to be turbulent to create this “stress” since fluctuations can be caused by the flow around the particles. However in turbulent flows this “stress” can be significantly larger than the laminar stress.

Expanding the surface integral in Equation C.17 results in

$$\frac{1}{V} \int_{S_d} \rho_c (v_i + w' n_i) w dS = \frac{1}{V} \int_{S_d} \rho_c v_i w dS + \frac{1}{V} \int_{S_d} \rho_c w' w n_i dS \quad (\text{C.21})$$

The second term is the negative “thrust” given by Equation A.32 in Appendix A. If the mass flux over the surface is uniform, this term is zero. The first integral can be evaluated by summing over all the particles in the volume including the boundary particles,

$$\frac{1}{V} \int_{S_d} v_i \rho_c w dS = -\frac{1}{V} \sum_k v_{i,k} \dot{m}_k \quad (\text{C.22})$$

where $v_{i,k}$ is the velocity of particle k . If the evaporation rates and velocities of all the particles in the volume are the same, this source term simplifies to

$$\frac{1}{V} \int_{S_d} v_i \rho_c w dS = -n v_i \dot{m} \quad (\text{C.23})$$

The average of the pressure gradient term in the momentum equation is

$$\overline{\frac{\partial p}{\partial x_i}} = \frac{\partial \bar{p}}{\partial x_i} - \frac{1}{V} \int_{S_d} p n_i dS = \frac{\partial}{\partial x_i} (\alpha_c \langle p \rangle) - \frac{1}{V} \int_{S_d} p n_i dS \quad (\text{C.24})$$

It is convenient to decompose the pressure on the particle surface into the sum of the local average pressure and the deviation therefrom.

$$p = \langle p \rangle + \delta p \quad (\text{C.25})$$

The integral of the pressure over the particles inside the averaging volume is

$$\frac{1}{V} \int_{S_e} p n_i dS = \frac{1}{V} \int_{S_e} \delta p n_i dS \quad (\text{C.26})$$

which is the “form force” (a part of the drag and lift force) on the particles.

A boundary particle, k , is shown in Figure C.1. The integral over the boundary particle is the integral over the portion of the surface inside the averaging volume, $S_{b,k}$. The surface severed by the averaging volume is $S_{s,k}$. Thus for particle k

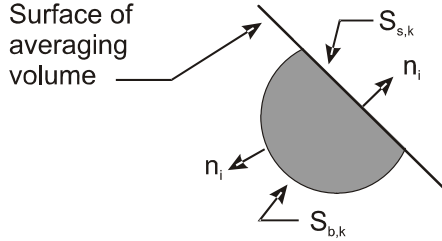


Figure C.1: Surfaces of boundary particle, k , severed by the surface of averaging volume.

$$\begin{aligned} \frac{1}{V} \int_{S_{b,k}} p n_i dS &= \frac{1}{V} \int_{S_{b,k}} (\langle p \rangle + \delta p) n_i dS \\ &= \frac{1}{V} \int_{S_{b,k}} \langle p \rangle n_i dS + \frac{1}{V} \int_{S_{b,k}} \delta p n_i dS \end{aligned} \quad (\text{C.27})$$

where $\langle p \rangle$ is the average pressure at the particle location. Because the combination of $S_{b,k}$ and $S_{s,k}$ form a closed surface

$$\int_{S_{b,k} + S_{s,k}} n_i dS = 0 \quad (\text{C.28})$$

then

$$\frac{1}{V} \int_{S_{b,k}} \langle p \rangle n_i dS = -\frac{1}{V} \int_{S_{s,k}} \langle p \rangle n_i dS \quad (\text{C.29})$$

The integral over all the severed surfaces can be replaced by³

$$\frac{1}{V} \int_{S_s} \langle p \rangle n_i dS = \frac{1}{V} \int_S \alpha_d \langle p \rangle n_i dS = \frac{\partial}{\partial x_i} (\alpha_d \langle p \rangle) \quad (\text{C.30})$$

This term, when combined with Equation C.24, gives the force due to the pressure gradient as $\partial \langle p \rangle / \partial x_i$. Other developments have not included this term and concluded that the force due to the pressure gradient is $\partial (\alpha_c \langle p \rangle) / \partial x_i$ which implies in a constant pressure field that there would be a force due to a gradient in volume fraction. This made no physical sense and a term was arbitrarily added to avoid this problem. The integral of $\delta p n_i$ over the inside surfaces, $S_{b,k}$, is the sum of the “form forces” on the boundary particles.

The same procedure can be carried out with the shear stress term resulting in

$$\overline{\frac{\partial \tau_{ij}}{\partial x_j}} = \frac{\partial}{\partial x_j} (\alpha_c \langle \tau_{ij} \rangle) - \frac{1}{V} \int_{S_d} \delta \tau_{ij} n_i dS \quad (\text{C.31})$$

³The local area of severed surfaces $\sum_k S_{s,k}$ is related to the surface area ΔS by $\alpha_d \Delta S$.

where the last term is the force due to shear on the droplets inside (including boundary droplets) the averaging volume. The integral of the pressure force and the shear stress on all the interior surfaces S_d is equal to the hydrodynamic forces (lift and drag) on the particles in the volume. Thus

$$\frac{1}{V} \int_{S_d} (-\delta p n_i + \delta \tau_{ij} n_j) dS = \frac{1}{V} \sum_k F_{k,i} \quad (\text{C.32})$$

where $F_{k,i}$ is the hydrodynamic force *on* the particle k . If all the particles in the control volume have the same force, the term becomes

$$\frac{1}{V} \sum_k F_{is,k} = nF_i \quad (\text{C.33})$$

This is a momentum source term due to drag-lift interaction between the particles and the carrier phase.

Collecting all the terms, the momentum equation for the carrier phase assumes the form

$$\begin{aligned} \frac{\partial}{\partial t} (\alpha_c \langle \rho_c \rangle \tilde{u}_i) + \frac{\partial}{\partial x_j} (\alpha_c \langle \rho_c \rangle \tilde{u}_i \tilde{u}_j) &= -\frac{1}{V} \sum_k v_{i,k} \dot{m}_k \\ -\frac{\partial}{\partial x_j} (\alpha_c \langle \rho_c \delta u_i \delta u_j \rangle) - \frac{\partial}{\partial x_i} \langle p \rangle + \frac{\partial}{\partial x_j} \langle \tau_{ij} \rangle - \frac{1}{V} \sum_k F_{k,i} + \alpha_c \langle \rho_c \rangle g_i \end{aligned} \quad (\text{C.34})$$

This equation is discussed in Chapter 6.

C.3 Energy equation

The total energy equation includes both the internal and external energies (kinetic energy) of the carrier phase. The energy equation is developed from the first law of thermodynamics

$$\frac{dE}{dt} = \dot{Q} - \dot{W} \quad (\text{C.35})$$

for a system where E is the sum of the internal and external energies, \dot{Q} is the heat transfer rate to the continuous phase and \dot{W} is the rate at which the continuous phase does work on the surroundings. Applying the Reynolds transport equation to the system, the Eulerian form of the energy equation is

$$\begin{aligned} \frac{\partial}{\partial t} \left[\rho_c \left(i_c + \frac{u_i u_i}{2} \right) \right] + \frac{\partial}{\partial x_j} \left[\rho_c u_j \left(i_c + \frac{u_i u_i}{2} \right) \right] \\ = -\frac{\partial q_i}{\partial x_i} - \frac{\partial}{\partial x_i} (p u_i) + \frac{\partial}{\partial x_j} (u_i \tau_{ij}) + \rho_c u_i g_i \end{aligned} \quad (\text{C.36})$$

where i_c is the specific internal energy of the continuous phase and q_i is the rate of heat transfer per unit area. An equation for mechanical energy can

be obtained by multiplying the momentum equation, Equation C.14, by u_i which, after some manipulation reduces to

$$\begin{aligned} & \frac{\partial}{\partial t} \left(\rho_c \frac{u_i u_i}{2} \right) + \frac{\partial}{\partial x_j} \left[\rho_c u_j \left(\frac{u_i u_i}{2} \right) \right] \\ &= -u_i \frac{\partial p}{\partial x_j} + u_i \frac{\partial \tau_{ij}}{\partial x_i} + \rho_c u_i g_i \end{aligned} \quad (\text{C.37})$$

Subtracting the mechanical energy equation from the total energy equation yields the thermal energy equation.

$$\frac{\partial}{\partial t} (\rho_c i_c) + \frac{\partial}{\partial x_j} (\rho_c u_j i_c) = -p \frac{\partial u_i}{\partial x_i} + \frac{\partial u_i}{\partial x_j} \tau_{ij} - \frac{\partial q_i}{\partial x_i} \quad (\text{C.38})$$

The term $\tau_{ij} \partial u_i / \partial x_j$ is the dissipation function which will be designated as Φ and which is equal to

$$\Phi = \mu_c \left[\left(\frac{\partial u_i}{\partial x_j} \right) \left(\frac{\partial u_i}{\partial x_j} + \frac{\partial u_j}{\partial x_i} \right) \right] = \frac{\mu_c}{2} \left(\frac{\partial u_i}{\partial x_j} + \frac{\partial u_j}{\partial x_i} \right) \left(\frac{\partial u_i}{\partial x_j} + \frac{\partial u_j}{\partial x_i} \right) \quad (\text{C.39})$$

and is always positive. The analysis will be based on an incompressible fluid so

$$\frac{\partial u_i}{\partial x_i} = 0$$

Thus the form of the thermal energy equation is

$$\frac{\partial}{\partial t} (\rho_c i) + \frac{\partial}{\partial x_j} (\rho_c u_j i) = \Phi - \frac{\partial q_i}{\partial x_i} \quad (\text{C.40})$$

Executing the volume average of the total energy equation is less cumbersome by taking the volume average of the thermal and mechanical energy equations separately and then adding the two equations to obtain the total energy equation. This approach will be used here by taking first the volume average of the thermal energy equation and then the mechanical energy equation.

C.3.1 Thermal energy equation

The terms in the thermal energy equation are identified as shown

$$\overbrace{\frac{\partial}{\partial t} (\rho_c i_c)}^a + \overbrace{\frac{\partial}{\partial x_j} (\rho_c u_j i_c)}^b = \overbrace{\Phi}^c - \overbrace{\frac{\partial q_i}{\partial x_i}}^d \quad (\text{C.41})$$

Term a

This is the unsteady term. Taking the volume average yields

$$\overline{\frac{\partial}{\partial t} (\rho_c i_c)} = \frac{\partial}{\partial t} \left(\overline{\rho_c i_c} \right) + \frac{1}{V} \int_{S_d} (\dot{r} + v_i n_i) \rho_c i_c dS \quad (\text{C.42})$$

Term b

This term represents the convection of internal energy. Taking the volume average gives

$$\overline{\frac{\partial}{\partial x_j}(\rho_c u_j i_c)} = \frac{\partial}{\partial x_i} (\overline{\rho_c u_j i_c}) - \frac{1}{V} \int_{S_d} \rho_c i_c u_i n_i dS \quad (C.43)$$

The velocity of the fluid at the surface of the particles is

$$u_i = v_i + (\dot{r} + w)n_i$$

so the combination of the two integrals in Equations C.42 and C.43 over the surface reduces to

$$\frac{1}{V} \int_{S_d} (\dot{r} + v_i n_i) \rho_c i dS - \frac{1}{V} \int_{S_d} \rho_c i u_i n_i dS = -\frac{1}{V} \int_{S_d} \rho_c i w dS \quad (C.44)$$

which is the energy flux per unit time due to mass transfer from the particle surface. Summing over all particles in the volume, the integral can be replaced by

$$\frac{1}{V} \int_{S_d} \rho_c i w dS = -\frac{1}{V} \sum_k \dot{m}_k i_{s,k} \quad (C.45)$$

where \dot{m}_k is the mass rate of change and $i_{s,k}$ is the specific internal energy of particle k at the particle surface.

Term c

The volume average of the dissipation term is

$$\overline{\Phi} = \frac{1}{V} \int_V \Phi dV = \alpha_c \langle \Phi \rangle \quad (C.46)$$

Term d

The volume average of the heat transfer term results in

$$\begin{aligned} \overline{\frac{\partial q_i}{\partial x_i}} &= \frac{\partial \bar{q}_i}{\partial x_i} - \frac{1}{V} \int_{S_d} q_i n_i dS \\ &= \frac{\partial (\alpha_c \langle q_i \rangle)}{\partial x_i} - \frac{1}{V} \int_{S_d} q_i n_i dS \end{aligned} \quad (C.47)$$

The heat transfer flux over the surface of a particle from the particle to the fluid can be expressed as the sum of an average value over the surface, $\hat{q}n_i$ and a deviation therefrom, δq_i ,

$$q_i = \hat{q}n_i + \delta q_i, \quad (C.48)$$

where

$$\int_{S_k} \delta q_i n_i dS = 0 \quad (\text{C.49})$$

and S_k is the surface of particle k . The integral over the surfaces of all the interior particles becomes

$$\frac{1}{V} \int_{S_e} (\hat{q} n_i + \delta q_i) n_i dS = \frac{1}{V} \int_{S_e} \hat{q} dS \quad (\text{C.50})$$

which can be expressed as

$$\frac{1}{V} \int_{S_e} \hat{q} dS = -\frac{1}{V} \sum_k \dot{Q}_k \quad (\text{C.51})$$

where \dot{Q}_k is the net heat transfer rate from the fluid to particle k inside the averaging volume. The particles included in the summation over k are completely inside the averaging volume.

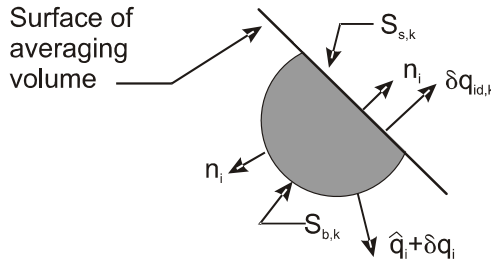


Figure C.2: Heat transfer and surfaces for a boundary particle, k .

The surfaces and heat transfer for boundary particle k are shown in Figure C.2. The heat transfer vector through the severed surface is $\delta q_{id,k}$. The heat transfer from the boundary particle is

$$\int_{S_{b,k}} (\hat{q} n_i + \delta q_i) n_i dS = \hat{q} S_{b,k} + \int_{S_{b,k}} \delta q_i n_i dS \quad (\text{C.52})$$

where the first term on the right is the heat transfer to the fluid from the surface of the boundary particle inside the averaging volume. From Equation C.49

$$\int_{S_{b,k}} \delta q_i n_i dS + n_i \delta q_{id,k} S_{s,k} = 0 \quad (\text{C.53})$$

so the second term is

$$\int_{S_{b,k}} \delta q_i n_i dS = -n_i \delta q_{id,k} S_{s,k} \quad (\text{C.54})$$

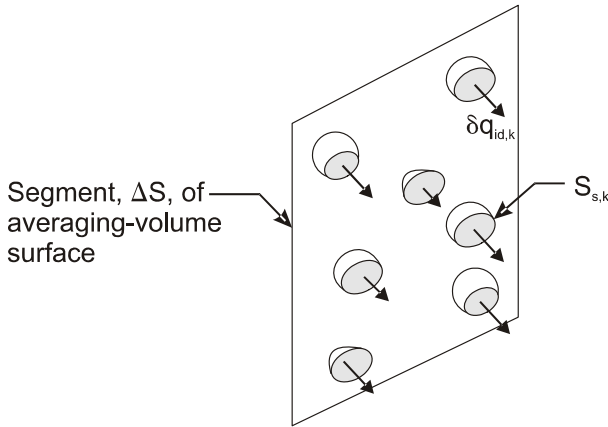


Figure C.3: Heat transfer through severed surfaces of boundary particles intersected by surface segment ΔS .

Boundary particles severed by the surface ΔS of the averaging volume is shown in Figure C.3. There is a heat transfer flux of $\delta q_{id,k}$ through each surface $S_{s,k}$. It is convenient to define an area averaged heat transfer rate

$$\{q_{id}\} = \frac{\sum_k \delta q_{i,d} S_{s,k}}{\sum_k S_{s,k}} \quad (\text{C.55})$$

where the summation is taken over those boundary particles intersected by the local area. However, the sum of the severed areas is related to ΔS by

$$\sum_k S_{s,k} = \alpha_d \Delta S$$

where α_d is the local volume fraction of the particle phase. Then summing over all the severed surfaces of the boundary particles

$$\frac{1}{V} \sum_k n_i \delta q_{i,d} S_{s,k} = \frac{1}{V} \int_S \alpha_d n_i \{q_{id}\} dS = \frac{\partial}{\partial x_i} (\alpha_d \{q_{id}\}) \quad (\text{C.56})$$

Finally the heat transfer term becomes

$$\overline{\frac{\partial q_i}{\partial x_i}} = \frac{\partial}{\partial x_i} (\alpha_c \langle q_i \rangle + \alpha_d \{q_{id}\}) + \frac{1}{V} \sum_k \dot{Q}_k \quad (\text{C.57})$$

where the summation includes all particles, the interior and boundary particles.

For convective heat transfer from the particle k to the carrier phase \dot{Q}_k becomes

$$\dot{Q}_k = 2\pi k'_c (Nu/2)_k D_k (\langle T_c \rangle - T_{d,k}) \quad (C.58)$$

The composite heat transfer through the carrier phase and the particles will be expressed as

$$q_i^{\text{eff}} = \alpha_c \langle q_i \rangle + \alpha_d \{ q_{id} \}. \quad (C.59)$$

or, in terms of a temperature gradient,

$$q_i^{\text{eff}} = -k'_{\text{eff}} \frac{\partial \langle T_c \rangle}{\partial x_i} \quad (C.60)$$

where k'_{eff} is the effective thermal conductivity for the mixture.

Finally the volume-averaged thermal energy equation for the carrier phase is

$$\begin{aligned} & \frac{\partial}{\partial t} (\alpha_c \rho_c \langle i_c \rangle) + \frac{\partial}{\partial x_i} (\alpha_c \rho_c \langle u_i i_c \rangle) \\ &= -\frac{1}{V} \sum_k \dot{m}_k i_{s,k} + \alpha_c \langle \Phi \rangle + \frac{\partial}{\partial x_i} \left(k'_{\text{eff}} \frac{\partial \langle T_c \rangle}{\partial x_i} \right) - \frac{1}{V} \sum_k \dot{Q}_k \end{aligned} \quad (C.61)$$

C.3.2 Mechanical energy equation

The mechanical energy equation for the carrier phase is

$$\begin{aligned} & \frac{\partial}{\partial t} \left[\rho_c \frac{U^2}{2} \right] + \frac{\partial}{\partial x_i} \left[\rho_c u_i \frac{U^2}{2} \right] = \\ & \quad -u_i \frac{\partial}{\partial x_i} p + u_i \frac{\partial}{\partial x_j} \tau_{ji} + \rho_c u_i g_i \end{aligned} \quad (C.62)$$

where $U^2/2 = u_i u_i/2$ or the kinetic energy per unit mass of the carrier phase. Using the incompressible flow condition, the equation can be written as

$$\begin{aligned} & \frac{\partial}{\partial t} \left[\rho_c \frac{U^2}{2} \right] + \frac{\partial}{\partial x_i} \left[\rho_c u_i \frac{U^2}{2} \right] = \\ & \quad -\frac{\partial}{\partial x_i} (u_i p) + \frac{\partial}{\partial x_j} (u_i \tau_{ij}) - \tau_{ij} \frac{\partial u_i}{\partial x_j} + \rho_c u_i g_i \end{aligned} \quad (C.63)$$

The third term on the right side is the dissipation so the equation can be written as

$$\begin{aligned} & \overbrace{\frac{\partial}{\partial t} \left(\rho_c \frac{U^2}{2} \right)}^a + \overbrace{\frac{\partial}{\partial x_j} \left(\rho_c u_j \frac{U^2}{2} \right)}^b = \\ & \quad -\overbrace{\frac{\partial}{\partial x_i} (u_i p)}^c + \overbrace{\frac{\partial}{\partial x_j} (u_i \tau_{ij})}^d - \overbrace{\Phi}^e + \overbrace{\rho_c u_i g_i}^f \end{aligned} \quad (C.64)$$

The volume average of each term is carried out below.

Term a

Applying Equation 28 from Appendix B for volume average of the time derivative results in

$$\overline{\frac{\partial}{\partial t} \left(\rho_c \frac{U^2}{2} \right)} = \frac{\partial}{\partial t} \overline{\left(\rho_c \frac{U^2}{2} \right)} + \frac{1}{V} \int_{S_d} \rho_c (v_i n_i + \dot{r}) \frac{U^2}{2} dS \quad (\text{C.65})$$

The first term on the right can be written as

$$\overline{\left(\rho_c \frac{u_j u_j}{2} \right)} = \alpha_c \rho_c \left\langle \frac{U^2}{2} \right\rangle \quad (\text{C.66})$$

Term b

Applying Equation 20 from Appendix B for the volume average of the spatial derivative yields

$$\begin{aligned} \overline{\frac{\partial}{\partial x_i} \left[\rho_c u_i \frac{U^2}{2} \right]} &= \frac{\partial}{\partial x_i} \overline{\left[\rho_c u_i \frac{U^2}{2} \right]} \\ &\quad - \frac{1}{V} \int_{S_d} \rho_c u_j \frac{U^2}{2} n_j dS \end{aligned} \quad (\text{C.67})$$

The integral over the particle surfaces is obtained by replacing u_i with the velocity at the particle surface, $v_i + (\dot{r} + w)n_i$, so

$$-\frac{1}{V} \int_{S_d} \rho_c u_i \frac{U^2}{2} n_i dS = -\frac{1}{V} \int_{S_d} \rho_c [v_i + (\dot{r} + w)n_i] \frac{U^2}{2} n_i dS \quad (\text{C.68})$$

Adding Equations C.65 and C.67 results in

$$\begin{aligned} &\overline{\frac{\partial}{\partial t} \left(\rho_c \frac{U^2}{2} \right)} + \overline{\frac{\partial}{\partial x_i} \left(\rho_c u_i \frac{U^2}{2} \right)} \\ &= \frac{\partial}{\partial t} \left(\alpha_c \rho_c \left\langle \frac{U^2}{2} \right\rangle \right) + \frac{\partial}{\partial x_i} \left(\alpha_c \rho_c \left\langle u_i \frac{U^2}{2} \right\rangle \right) \\ &\quad - \frac{1}{V} \int_{S_d} \rho_c w \frac{U^2}{2} dS \end{aligned} \quad (\text{C.69})$$

where the last term is identified as the flux of kinetic energy from the particle surfaces. For each particle k

$$\begin{aligned} \int_{S_k} \rho_c w \frac{U^2}{2} dS &= \int_{S_k} \rho_c w_k \frac{(v_{j,k} + w'_k n_j)(v_{j,k} + w'_k n_j)}{2} dS \\ &= \int_{S_k} \rho_c w_k \frac{|v_k|^2 + (w'_k)^2}{2} dS \end{aligned} \quad (\text{C.70})$$

where the cross product is zero from

$$\int_S \rho_c w_k v_{j,k} w'_k n_i dS = \rho_c w_k v_{j,k} w'_k \int_S n_i dS = 0 \quad (\text{C.71})$$

since the surface of each particle is a closed surface. For convenience, $U_s^2/2$ will be used for $\left[|v_k|^2 + (w'_k)^2\right]/2$. Thus, the last term in Equation C.69 is

$$-\frac{1}{V} \int_{S_d} \rho_c w \frac{U^2}{2} dS = \frac{1}{V} \sum_k \dot{m}_k \frac{U_{s,k}^2}{2} \quad (\text{C.72})$$

where \dot{m}_k is the rate of change of mass of particle.

Term c Applying Equation B.20 from Appendix B for volume average of spatial derivatives yields

$$-\overline{\frac{\partial}{\partial x_i}(u_i p)} = -\frac{\partial}{\partial x_i}(\alpha_c \langle u_i p \rangle) + \frac{1}{V} \int_{S_d} p(v_i + w' n_i) n_i dS \quad (\text{C.73})$$

The integral of the pressure over the particle surfaces can be rewritten as

$$\begin{aligned} \frac{1}{V} \int_{S_e} p[v_i + w' n_i] n_i dS &= \frac{1}{V} \int_{S_e} v_i (\langle p \rangle + \delta p) n_i dS + \frac{1}{V} \int_{S_e} p(\dot{r} + w) dS \\ &= \frac{1}{V} \int_{S_e + S_b} v_i \langle p \rangle n_i dS + \frac{1}{V} \int_{S_e} v_i \delta p n_i dS \\ &\quad + \frac{1}{V} \int_{S_e} p(\dot{r} + w) dS \end{aligned} \quad (\text{C.74})$$

where the integral is split up to the sum of the surfaces of the interior particles and the boundary surfaces. For each interior particle

$$\frac{1}{V} \int_S v_i \langle p \rangle n_i dS = \frac{1}{V} v_i \langle p \rangle \int_S n_i dS = 0 \quad (\text{C.75})$$

For each boundary particle k

$$\frac{1}{V} \int_{S_{b,k}} \langle p \rangle v_i n_i dS = -\frac{1}{V} \int_{S_{s,k}} \langle p \rangle v_{i,k} n_i dS \quad (\text{C.76})$$

where $S_{b,k}$ is the surface inside the averaging volume as $S_{s,k}$ is the area of the severed surface and $v_{i,k}$ is the velocity of particle. Since $\langle p \rangle$ and v_i are constant for integration over the severed surface

$$\frac{1}{V} \int_{S_{s,k}} \langle p \rangle v_{i,k} n_i dS = \frac{1}{V} \langle p \rangle v_{i,k} n_i S_{s,k} \quad (\text{C.77})$$

Boundary particles passing through a segment of averaging surface ΔS is shown in Figure C.4. The particle mass flux is the sum of the mass flux for each particle

$$\dot{m}_d = \sum_k \rho_d n_i v_{i,k} S_{s,k} \quad (\text{C.78})$$

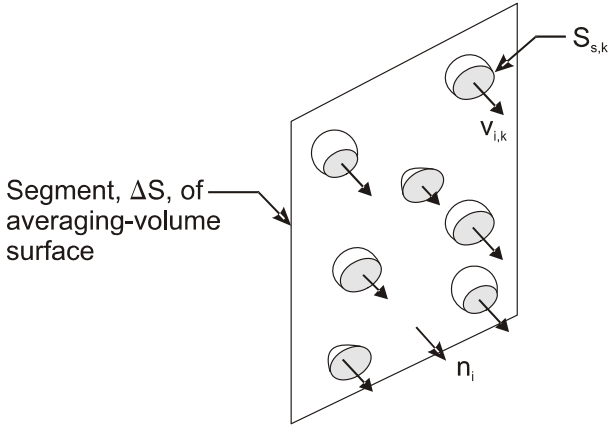


Figure C.4: Boundary particles passing through a segment ΔS of the averaging-volume surface.

The mass flux through the surface can be expressed as

$$\dot{m}_d = \rho_d \tilde{v}_i n_i \alpha_d \Delta S \quad (\text{C.79})$$

where \tilde{v}_i is the mass-averaged particle velocity defined by Equation 6.33 in Chapter 6. Thus the integral over the severed surfaces becomes

$$\frac{1}{V} \int_{S_s} \langle p \rangle v_i \cdot n_i dS = \frac{1}{V} \int_S \alpha_d \langle p \rangle \tilde{v}_i \cdot n_i dS = \frac{\partial}{\partial x_i} (\alpha_d \langle p \rangle \tilde{v}_i) \quad (\text{C.80})$$

The last integral in Equation C.74 is

$$\frac{1}{V} \int_{S_e} p(\dot{r} + w) dS = \frac{1}{V} \sum_k p_s \dot{r}_k S_k - \frac{1}{V} \sum_k \dot{m}_k \left(\frac{p_s}{\rho_c} \right) \quad (\text{C.81})$$

where p_s is the pressure at the particle surface, \dot{r}_k is the rate of radius change and S_k is the surface area of particle k . The product of \dot{r}_k and S_k is the volume rate of change for the particle. Due to acceleration of fluid leaving the particle surface, the surface pressure may be higher than the average pressure. However the approximation is made that $p_s \simeq \langle p \rangle$ so the first sum in Equation C.81 is

$$\frac{1}{V} \sum_k p_s \dot{r}_k S_k = \langle p \rangle \frac{\dot{V}_d}{V} \quad (\text{C.82})$$

where \dot{V}_d is the rate of volume change for dispersed phase in volume V or the rate of change of the dispersed phase volume fraction. This term is the flow work due to the volume change of the dispersed phase.

Summing all the parts term c becomes

$$\begin{aligned} \overline{-\frac{\partial}{\partial x_i}(u_i p)} &= -\frac{\partial}{\partial x_i}(\alpha_c \langle u_i p \rangle) + \frac{\partial}{\partial x_i}(\alpha_d \langle p \rangle \tilde{v}_i) + \frac{1}{V} \int_{S_e} v_i \delta p n_i dS \\ &\quad + \langle p \rangle \frac{\dot{V}_d}{V} - \frac{1}{V} \sum_k \dot{m}_k \left(\frac{p_s}{\rho_c} \right) \end{aligned} \quad (\text{C.83})$$

Term d Taking the volume average of

$$\overline{\frac{\partial}{\partial x_j}(u_i \tau_{ij})} = \frac{\partial}{\partial x_j}(\alpha_c \langle u_i \tau_{ij} \rangle) - \frac{1}{V} \int_{S_d} \tau_{ij}(v_i + w' n_i) n_j dS \quad (\text{C.84})$$

The integral over the surfaces becomes

$$-\frac{1}{V} \int_{S_d} \tau_{ij}(v_i + w' n_i) n_j dS = -\frac{1}{V} \int_{S_d} \tau_{ij} v_i n_j dS - \frac{1}{V} \int_{S_d} \tau_{ij} w' n_i n_j dS \quad (\text{C.85})$$

The last integral is zero because the vector $\tau_{ij} n_j$ is parallel to the particle surface and n_i is normal so the dot product is zero. The first integral is written as

$$-\frac{1}{V} \int_{S_d} ((\langle \tau_{ij} \rangle + \delta \tau_{ij}) v_i n_j dS) = -\frac{1}{V} \int_{S_d} \delta \tau_{ij} v_i n_j dS \quad (\text{C.86})$$

based on the same arguments used for term c. There is no contribution due to the boundary droplet because the vector due to shear stress on the severed surface would be normal to the velocity.

Combining the terms for term d gives

$$\overline{\frac{\partial}{\partial x_j}(u_i \tau_{ij})} = \frac{\partial}{\partial x_j}(\alpha_c \langle u_i \tau_{ij} \rangle) - \frac{1}{V} \int_{S_d} \delta \tau_{ij} v_i n_j dS \quad (\text{C.87})$$

Term e Taking the volume average of term e simply gives

$$\overline{\Phi} = \alpha_c \langle \Phi \rangle \quad (\text{C.88})$$

Term f The volume average of term f is

$$\overline{\rho_c u_i g_i} = \alpha_c \rho_c \langle u_i \rangle g_i \quad (\text{C.89})$$

Before combining all the terms to form the mechanical energy equation, it is convenient to combine two terms in c and d to give the work done by the forces on the particle

$$\frac{1}{V} \int_{S_e} v_i \delta p n_i dS - \frac{1}{V} \int_{S_d} \delta \tau_{ij} v_i n_j dS = \frac{1}{V} \int_{S_e} v_i (\delta p n_i - \delta \tau_{ij} n_j) dS \quad (\text{C.90})$$

For each particle k

$$\int_{S_k} v_i (\delta p n_i - \delta \tau_{ij} n_j) dS = -v_{k,i} F_{k,i} \quad (C.91)$$

where $v_{k,i}$ is the velocity of particle k and $F_{k,i}$ is the surface force in the i direction. For all the particles in the volume

$$\frac{1}{V} \int_{S_e} v_i (\delta p n_i - \delta \tau_{ij} n_j) dS = -\frac{1}{V} \sum_k v_{k,i} F_{k,i} \quad (C.92)$$

which is the work due to the fluid dynamic forces on the particles.

Summing all the terms, the volume-averaged form of the mechanical energy equation is

$$\begin{aligned} & \frac{\partial}{\partial t} \left(\alpha_c \rho_c \left\langle \frac{U^2}{2} \right\rangle \right) + \frac{\partial}{\partial x_i} \left(\alpha_c \rho_c \left\langle u_i \frac{U^2}{2} \right\rangle \right) \\ &= -\frac{\partial}{\partial x_i} (\alpha_c \langle u_i p \rangle) + \frac{\partial}{\partial x_j} (\alpha_c \langle u_i \tau_{ij} \rangle) \\ & \quad + \frac{\partial}{\partial x_i} (\alpha_d \langle p \rangle \tilde{v}_i) + \langle p \rangle \frac{\dot{V}_d}{V} \\ & \quad - \frac{1}{V} \sum_k v_{k,i} F_{k,i} - \frac{1}{V} \sum_k \dot{m}_k \left[\frac{U_{s,k}^2}{2} + \left(\frac{p_s}{\rho_c} \right) \right] \\ & \quad - \alpha_c \langle \Phi \rangle + \alpha_c \rho_c \langle u_i \rangle g_i \end{aligned} \quad (C.93)$$

C.3.3 Total energy equation

The total energy equation is obtained by adding the thermal energy equation, Equation C.61 and Equation C.93. After collecting terms, the final equation is

$$\begin{aligned} & \frac{\partial}{\partial t} \left(\alpha_c \rho_c \left\langle i_c + \frac{U^2}{2} \right\rangle \right) + \frac{\partial}{\partial x_i} \left[\alpha_c \rho_c \left\langle u_i \left(i_c + \frac{p}{\rho_c} + \frac{U^2}{2} \right) \right\rangle \right] \\ &= -\frac{1}{V} \sum_k \dot{m}_k \left[\frac{U_{s,k}^2}{2} + i_{s,k} + \left(\frac{p_s}{\rho_c} \right) \right] \\ & \quad + \frac{\partial}{\partial x_i} (\alpha_d \langle p \rangle \tilde{v}_i) + \langle p \rangle \frac{\dot{V}_d}{V} - \frac{1}{V} \sum_k v_{k,i} F_{k,i} \\ & \quad + \frac{\partial}{\partial x_j} (\alpha_c \langle u_i \tau_{ij} \rangle) + \alpha_c \rho_c \langle u_i \rangle g_i \\ & \quad + \frac{\partial}{\partial x_i} \left(k'_{\text{eff}} \frac{\partial \langle T_c \rangle}{\partial x_i} \right) - \frac{1}{V} \sum_k \dot{Q}_k \end{aligned} \quad (C.94)$$

Appendix D

Turbulence Equations

This appendix presents the development of the volume-averaged form of the turbulence energy, dissipation and Reynolds stress equations.

The equation for the turbulence energy of the continuous phase in a fluid-particle flow is derived using the same procedure as used for single phase flows. The procedure starts with the mechanical energy equation which is obtained by taking the vector product of the velocity with the momentum equation and can be expressed as (Equation 62 in Appendix C)

$$\begin{aligned} & \frac{\partial}{\partial t} \left(\rho_c \frac{u_i u_i}{2} \right) + \frac{\partial}{\partial x_j} \left(\rho_c u_j \frac{u_i u_i}{2} \right) \\ &= -u_i \frac{\partial p}{\partial x_i} + u_i \frac{\partial \tau_{ij}}{\partial x_j} + \rho_c g_i u_i \end{aligned} \quad (\text{D.1})$$

This equation is volume averaged using the relationships developed in Appendix B for the spatial and temporal gradients. The velocities are then decomposed into the sum of a phase average and deviation,

$$u_i = \langle u_i \rangle + \delta u_i$$

Finally the product of the volume-averaged momentum equation, Equation 34 in Appendix C, and the volume-averaged velocity is subtracted from the volume-averaged mechanical energy equation to obtain an equation for the phase-averaged turbulence kinetic energy,

$$k_c = \frac{1}{V_c} \int_{V_c} \frac{\delta u_i \delta u_i}{2} dV = \left\langle \frac{\delta u_i \delta u_i}{2} \right\rangle \quad (\text{D.2})$$

The volume-averaged form of the rate of turbulence energy dissipation is

$$\varepsilon_c = \nu_c \left\langle \frac{\partial \delta u_i}{\partial x_j} \frac{\partial \delta u_i}{\partial x_j} \right\rangle \quad (\text{D.3})$$

The analysis presented here is an extension of the temporal averaging approach for single phase flows (Bernard and Wallace, 2002) in which the dissipation is defined as¹

$$\varepsilon = \overline{\nu_c \frac{\partial u'_i}{\partial x_j} \frac{\partial u'_i}{\partial x_j}} \quad (\text{D.4})$$

where u'_i is the fluctuation velocity and the double overbar indicates time averaging. A transport equation for dissipation is developed by taking the time average of the product of the gradient of the Navier-Stokes equations, the gradient of the fluctuation velocity and twice the kinematic viscosity $\left(\overline{2\nu_c \frac{\partial u'_i}{\partial x_j} \frac{\partial}{\partial x_j} NS_i} \right)$. The notation NS_i is the i component of the Navier-Stokes equation. Arguments are presented for grouping terms together and modeling other terms. The same approach is used for volume averaging, starting with $\overline{(2\nu_c \frac{\partial \delta u_i}{\partial x_j} \frac{\partial}{\partial x_j} NS_i)}$ and using similar arguments for term groupings and modeling.

The volume averaged form of the incompressible Reynolds stress tensor is

$$R_{ij} = \langle \delta u_i \delta u_j \rangle \quad (\text{D.5})$$

A transport equation for the Reynolds stress can be found by combining the products of the velocities and Navier-Stokes equations, $u_i NS_j + u_j NS_i$, taking the volume average and then subtracting the corresponding form of the volume-averaged momentum equation.

The analyses for the turbulence energy, dissipation and Reynolds stress are based on the following assumptions:

1. Constant density fluid.
2. No mass transfer at particle surface.
3. Particles are spherical and not rotating.

The purpose of these assumptions is to simplify the analysis. All these assumptions could be relaxed and the derivation could be carried out in the same fashion but the inclusion of more details would be required. Still the essence of the results would be the same.

D.1 Turbulence energy

The development of the turbulence energy equation first requires the volume-averaged forms of the continuity and momentum equations

¹The double-bar notation is used for time averaging while the single overbar is used to denote volume averaging.

D.1.1 Continuity and momentum equations

For a constant density fluid with no mass transfer, the volume-averaged continuity equation for the carrier phase, Equation 11 in Appendix C can be written as

$$\frac{\partial \alpha_c}{\partial t} + \frac{\partial}{\partial x_i} (\alpha_c \langle u_i \rangle) = 0 \quad (\text{D.6})$$

and the corresponding continuity equation for the mixture is

$$\frac{\partial}{\partial x_i} (\alpha_c \langle u_i \rangle + \alpha_d \tilde{v}_i) = 0 \quad (\text{D.7})$$

where \tilde{v}_i is the mass-averaged velocity of the dispersed phase.

The volume-averaged momentum equation for a constant density fluid with no mass transfer at the particle surface, Equation 34 in Appendix C, is

$$\begin{aligned} & \frac{\partial}{\partial t} (\alpha_c \rho_c \langle u_i \rangle) + \frac{\partial}{\partial x_j} (\alpha_c \rho_c \langle u_i \rangle \langle u_j \rangle) \\ &= -\frac{\partial}{\partial x_j} (\alpha_c \rho_c \langle \delta u_i \delta u_j \rangle) - \frac{\partial}{\partial x_i} \langle p \rangle + \frac{\partial}{\partial x_j} \langle \tau_{ij} \rangle \\ & \quad - \frac{1}{V} \sum_k F_{k,i} + \alpha_c \rho_c g_i \end{aligned} \quad (\text{D.8})$$

where δu_i is the deviation of the local velocity from the phase-averaged velocity. Multiplying through by $\langle u_i \rangle$ and using the continuity equation, the momentum equation can be expressed in the form

$$\begin{aligned} & \frac{\partial}{\partial t} \left(\alpha_c \rho_c \frac{\langle u_i \rangle \langle u_i \rangle}{2} \right) + \frac{\partial}{\partial x_j} \left(\alpha_c \rho_c \langle u_j \rangle \frac{\langle u_i \rangle \langle u_i \rangle}{2} \right) \\ &= -\langle u_i \rangle \frac{\partial}{\partial x_j} (\alpha_c \rho_c \langle \delta u_i \delta u_j \rangle) - \langle u_i \rangle \frac{\partial}{\partial x_i} \langle p \rangle \\ & \quad + \langle u_i \rangle \frac{\partial}{\partial x_j} \langle \tau_{ij} \rangle - \frac{1}{V} \langle u_i \rangle \sum_k F_{k,i} + \alpha_c \rho_c g_i \langle u_i \rangle \end{aligned} \quad (\text{D.9})$$

This equation will ultimately be subtracted from the volume-averaged mechanical energy equation to yield the equation for turbulence kinetic energy.

D.1.2 Mechanical energy equation

The mechanical energy equation, Equation D.1 is rewritten in the form

$$\begin{aligned} & \overbrace{\frac{\partial}{\partial t} \left(\rho_c \frac{u_i u_i}{2} \right)}^a + \overbrace{\frac{\partial}{\partial x_j} \left(\rho_c u_j \frac{u_i u_i}{2} \right)}^b \\ &= -\overbrace{\frac{\partial (p u_i)}{\partial x_i}}^c + \overbrace{\frac{\partial (u_i \tau_{ij})}{\partial x_j}}^d - \overbrace{\tau_{ij} \frac{\partial u_i}{\partial x_j}}^e + \overbrace{\rho_c g_i u_i}^f \end{aligned} \quad (\text{D.10})$$

where the continuity equation, $\partial u_i / \partial x_i = 0$, has been used on the pressure gradient term and differentiation by parts has been applied to the gradient of the shear stress term. All the terms have been designated by letters for ease of identification. The volume average of each term will now be addressed.

Term a, unsteady term

Using Equation B.28, the volume average of the unsteady term is

$$\overline{\frac{\partial}{\partial t}(\rho_c \frac{u_i u_i}{2})} = \frac{\partial}{\partial t}(\alpha_c \rho_c \left\langle \frac{u_i u_i}{2} \right\rangle) + \frac{1}{V} \int_{S_d} \rho_c v_i \frac{u_j u_j}{2} n_i dS \quad (\text{D.11})$$

since the particles are not transferring mass ($\dot{r} = 0$). The phase average of the kinetic energy is

$$\left\langle \frac{u_i u_i}{2} \right\rangle = \left\langle \frac{(\langle u_i \rangle + \delta u_i)(\langle u_i \rangle + \delta u_i)}{2} \right\rangle = \frac{\langle u_i \rangle \langle u_i \rangle}{2} + \left\langle \frac{\delta u_i \delta u_i}{2} \right\rangle \quad (\text{D.12})$$

because $\langle \delta u_i \rangle = 0$. Thus, the first term in Equation D.11 becomes

$$\frac{\partial}{\partial t}(\alpha_c \rho_c \left\langle \frac{u_i u_i}{2} \right\rangle) = \frac{\partial}{\partial t}(\alpha_c \rho_c \frac{\langle u_i \rangle \langle u_i \rangle}{2} + \alpha_c \rho_c k_c) \quad (\text{D.13})$$

so

$$\overline{\frac{\partial}{\partial t}(\rho_c \frac{u_i u_i}{2})} = \frac{\partial}{\partial t}(\alpha_c \rho_c \frac{\langle u_i \rangle \langle u_i \rangle}{2} + \alpha_c \rho_c k_c) + \frac{1}{V} \int_{S_d} \rho_c v_i \frac{u_j u_j}{2} n_i dS \quad (\text{D.14})$$

Term b, convection term

Using Equation 20 from Appendix B, the volume average of the convection term is

$$\overline{\frac{\partial}{\partial x_j} \left(\rho_c u_j \frac{u_i u_i}{2} \right)} = \frac{\partial}{\partial x_j} \left(\alpha_c \rho_c \left\langle u_j \frac{u_i u_i}{2} \right\rangle \right) - \frac{1}{V} \int_{S_d} \rho_c v_i \frac{u_j u_j}{2} n_i dS \quad (\text{D.15})$$

The phase average of the first term on the right is

$$\begin{aligned} \left\langle u_j \frac{u_i u_i}{2} \right\rangle &= \left\langle (\langle u_j \rangle + \delta u_j) \frac{(\langle u_i \rangle + \delta u_i)(\langle u_i \rangle + \delta u_i)}{2} \right\rangle \\ &= \langle u_j \rangle \frac{\langle u_i \rangle \langle u_i \rangle}{2} + \langle u_j \rangle k_c + \langle u_i \rangle \langle \delta u_i \delta u_i \rangle \\ &\quad + \left\langle \delta u_j \frac{\delta u_i \delta u_i}{2} \right\rangle \end{aligned} \quad (\text{D.16})$$

so the advection term becomes

$$\begin{aligned}
 & \overline{\frac{\partial}{\partial x_j} \left(\rho_c u_j \frac{u_i u_i}{2} \right)} \\
 = & \frac{\partial}{\partial x_j} \left(\rho_c \alpha_c \langle u_j \rangle \frac{\langle u_i \rangle \langle u_i \rangle}{2} \right) + \frac{\partial}{\partial x_j} (\rho_c \alpha_c \langle u_j \rangle k_c) \\
 & + \frac{\partial}{\partial x_j} (\rho_c \alpha_c \langle u_i \rangle \langle \delta u_i \delta u_j \rangle) + \frac{\partial}{\partial x_j} \left(\rho_c \alpha_c \left\langle \delta u_j \frac{\delta u_i \delta u_i}{2} \right\rangle \right) \\
 & - \frac{1}{V} \int_{S_d} \rho_c v_i \frac{u_j u_j}{2} n_i dS
 \end{aligned} \tag{D.17}$$

Adding terms a and b together yields

$$\begin{aligned}
 & \overline{\frac{\partial}{\partial t} \left(\rho_c \frac{u_i u_i}{2} \right)} + \overline{\frac{\partial}{\partial x_j} \left(\rho_c u_j \frac{u_i u_i}{2} \right)} \\
 = & \frac{\partial}{\partial t} \left(\alpha_c \rho_c \frac{\langle u_i \rangle \langle u_i \rangle}{2} \right) + \frac{\partial}{\partial x_j} \left(\rho_c \alpha_c \langle u_j \rangle \frac{\langle u_i \rangle \langle u_i \rangle}{2} \right) \\
 & + \frac{\partial}{\partial t} (\alpha_c \rho_c k_c) + \frac{\partial}{\partial x_j} (\rho_c \alpha_c \langle u_j \rangle k_c) \\
 & + \frac{\partial}{\partial x_j} (\rho_c \alpha_c \langle u_i \rangle \langle \delta u_i \delta u_j \rangle) \\
 & + \frac{\partial}{\partial x_j} \left(\rho_c \alpha_c \left\langle \delta u_j \frac{\delta u_i \delta u_i}{2} \right\rangle \right)
 \end{aligned} \tag{D.18}$$

Term c, flow work term

Applying Equation 20 in Appendix B to the flow work term results in

$$\begin{aligned}
 \overline{\frac{\partial (p u_i)}{\partial x_i}} &= \frac{\partial (\alpha_c \langle p u_i \rangle)}{\partial x_i} - \frac{1}{V} \int_{S_d} p u_i n_i dS \\
 &= \frac{\partial}{\partial x_i} (\alpha_c \langle p \rangle \langle u_i \rangle + \alpha_c \langle \delta p \delta u_i \rangle) \\
 &\quad - \frac{1}{V} \int_{S_d} p u_i n_i dS
 \end{aligned} \tag{D.19}$$

The velocity of the fluid on the surface of every particle is v_i so the last term can be expressed as

$$\begin{aligned}
 \frac{1}{V} \int_{S_d} p u_i n_i dS &= \frac{1}{V} \int_{S_d} (\langle p \rangle + \delta p) v_i n_i dS \\
 &= \frac{1}{V} \int_{S_b + S_e} \langle p \rangle v_i n_i dS + \frac{1}{V} \int_{S_d} \delta p v_i n_i dS
 \end{aligned} \tag{D.20}$$

For each internal particle number, k , the local average pressure and velocity are constant so

$$\int_{S_k} \langle p \rangle v_i n_i dS = \langle p \rangle v_i \int_{S_k} n_i dS = 0 \tag{D.21}$$

where S_k is the surface of particle k . Summing over all the surfaces of the internal particles gives

$$\frac{1}{V} \int_{S_e} \langle p \rangle v_i n_i dS = 0 \quad (\text{D.22})$$

The integral over the internal surfaces of the boundary particles is the same as Equation 30 in Appendix C; namely,

$$\frac{1}{V} \int_{S_b} \langle p \rangle v_i n_i dS = -\frac{1}{V} \int_S \alpha_d \langle p \rangle v_i n_i dS = -\frac{\partial}{\partial x_i} (\alpha_d \langle p \rangle \tilde{v}_i) \quad (\text{D.23})$$

Assembling all the parts of the flow work term leads to

$$\overline{\frac{\partial (pu_i)}{\partial x_i}} = \frac{\partial}{\partial x_i} (\alpha_c \langle p \rangle \langle u_i \rangle + \alpha_c \langle \delta p \delta u_i \rangle) - \frac{1}{V} \int_{S_d} \delta p v_i n_i dS + \frac{\partial}{\partial x_i} (\alpha_d \langle p \rangle \tilde{v}_i) \quad (\text{D.24})$$

Using the continuity equation for the mixture, Equation D.7, the equation is reduced to

$$\overline{\frac{\partial (pu_i)}{\partial x_i}} = \alpha_c \langle u_i \rangle \frac{\partial \langle p \rangle}{\partial x_i} + \alpha_d \tilde{v}_i \frac{\partial \langle p \rangle}{\partial x_i} + \frac{\partial}{\partial x_i} (\alpha_c \langle \delta p \delta u_i \rangle) - \frac{1}{V} \int_{S_d} \delta p v_i n_i dS \quad (\text{D.25})$$

Term d, shear work term

Using the equations for the volume average of a derivative from Appendix B, the volume average of term d is

$$\overline{\frac{\partial (u_i \tau_{ij})}{\partial x_j}} = \frac{\partial}{\partial x_j} (\alpha_c \langle \tau_{ij} \rangle \langle u_i \rangle + \alpha_c \langle \delta \tau_{ij} \delta u_i \rangle) - \frac{1}{V} \int_{S_d} u_i \tau_{ij} n_j dS \quad (\text{D.26})$$

Using the same development as used for Equation D.19 for the integral over the particle surfaces, the volume average of term d is reformulated as

$$\begin{aligned} \overline{\frac{\partial (u_i \tau_{ij})}{\partial x_j}} &= \alpha_c \langle u_i \rangle \frac{\partial \langle \tau_{ij} \rangle}{\partial x_j} + \alpha_d \tilde{v}_i \frac{\partial \langle \tau_{ij} \rangle}{\partial x_j} \\ &\quad + \frac{\partial}{\partial x_j} (\alpha_c \langle \delta \tau_{ij} \delta u_i \rangle) - \frac{1}{V} \int_{S_d} \delta \tau_{ij} v_i n_j dS \end{aligned} \quad (\text{D.27})$$

Term e, dissipation term

The dissipation term can be rewritten as

$$\overline{\tau_{ij} \frac{\partial u_i}{\partial x_j}} = \frac{1}{V} \int_{V_c} (\langle \tau_{ij} \rangle + \delta \tau_{ij}) \frac{\partial u_i}{\partial x_j} dV \quad (\text{D.28})$$

The first term becomes

$$\frac{1}{V} \langle \tau_{ij} \rangle \int_{V_c} \frac{\partial u_i}{\partial x_j} dV = \langle \tau_{ij} \rangle \frac{\partial}{\partial x_j} (\alpha_c \langle u_i \rangle) - \frac{1}{V} \langle \tau_{ij} \rangle \int_{S_d} u_i n_j dS \quad (\text{D.29})$$

On all the interior particles, $u_i = v_i$, so the integral of the velocity over all the particles completely inside the volume is zero.

$$\int_{S_e} u_i n_j dS = \sum_k v_{k,i} \int_{S_k} n_j dS = 0 \quad (\text{D.30})$$

The integral over the internal surfaces of the boundary particles is

$$\frac{1}{V} \int_{S_b} v_i n_j dS = -\frac{1}{V} \int_{S_s} v_i n_j dS = -\frac{1}{V} \int_S v_i \alpha_d n_j dS = -\frac{\partial}{\partial x_j} (\alpha_d \tilde{v}_i) \quad (\text{D.31})$$

Thus the volume average of the dissipation term is

$$\overline{\tau_{ij} \frac{\partial u_i}{\partial x_j}} = \langle \tau_{ij} \rangle \frac{\partial}{\partial x_j} (\alpha_c \langle u_i \rangle + \alpha_d \tilde{v}_i) + \frac{1}{V} \int_{V_c} \delta \tau_{ij} \frac{\partial u_i}{\partial x_j} dV \quad (\text{D.32})$$

However, the first term on the right is zero from the mixture continuity equation so

$$\overline{\tau_{ij} \frac{\partial u_i}{\partial x_j}} = \frac{1}{V} \int_{V_c} \delta \tau_{ij} \frac{\partial u_i}{\partial x_j} dV \quad (\text{D.33})$$

The other part of the dissipation term can be rewritten as

$$\frac{1}{V} \int_{V_c} \delta \tau_{ij} \frac{\partial u_i}{\partial x_j} dV = \frac{1}{V} \int_{V_c} \delta \tau_{ij} \frac{\partial (\langle u_i \rangle + \delta u_i)}{\partial x_j} dV \quad (\text{D.34})$$

The first term is zero because

$$\frac{1}{V} \int_{V_c} \delta \tau_{ij} \frac{\partial \langle u_i \rangle}{\partial x_j} dV = \frac{\partial \langle u_i \rangle}{\partial x_j} \frac{1}{V} \int_{V_c} \delta \tau_{ij} dV = 0 \quad (\text{D.35})$$

Finally, the dissipation term is

$$\overline{\tau_{ij} \frac{\partial u_i}{\partial x_j}} = \alpha_c \left\langle \delta \tau_{ij} \frac{\partial \delta u_i}{\partial x_j} \right\rangle = \alpha_c \rho_c \varepsilon_c = \alpha_c \mu_c \left\langle \frac{\partial \delta u_i}{\partial x_j} \left(\frac{\partial \delta u_i}{\partial x_j} + \frac{\partial \delta u_j}{\partial x_i} \right) \right\rangle \quad (\text{D.36})$$

where ε_c is the rate of dissipation. The important term is the first term (Pope, 2000) so the dissipation rate can be expressed as

$$\mu_c \left\langle \frac{\partial \delta u_i}{\partial x_j} \frac{\partial \delta u_i}{\partial x_j} \right\rangle = \rho_c \varepsilon_c \quad (\text{D.37})$$

Term f, body-force work term

The body-force work term becomes simply

$$\overline{\rho_c g_i u_i} = \alpha_c \rho_c g_i \langle u_i \rangle \quad (\text{D.38})$$

D.1.3 Turbulence energy equation

Assembling all the terms together results in

$$\begin{aligned}
& \frac{\partial}{\partial t} \left(\alpha_c \rho_c \frac{\langle u_i \rangle \langle u_i \rangle}{2} \right) + \frac{\partial}{\partial x_j} \left(\rho_c \alpha_c \langle u_j \rangle \frac{\langle u_i \rangle \langle u_i \rangle}{2} \right) + \frac{\partial}{\partial t} (\alpha_c \rho_c k_c) \\
& + \frac{\partial}{\partial x_j} (\rho_c \alpha_c \langle u_j \rangle k_c) + \frac{\partial}{\partial x_j} (\rho_c \alpha_c \langle u_i \rangle \langle \delta u_i \delta u_j \rangle) \\
& + \frac{\partial}{\partial x_j} \left(\rho_c \alpha_c \left\langle \delta u_j \frac{\delta u_i \delta u_i}{2} \right\rangle \right) \\
= & -\alpha_c \langle u_i \rangle \frac{\partial \langle p \rangle}{\partial x_i} - \alpha_d \tilde{v}_i \frac{\partial \langle p \rangle}{\partial x_i} - \frac{\partial}{\partial x_i} (\alpha_c \langle \delta p \delta u_i \rangle) + \frac{1}{V} \int_{S_d} \delta p v_i n_i dS \\
& + \alpha_c \langle u_i \rangle \frac{\partial \langle \tau_{ij} \rangle}{\partial x_j} + \alpha_d \tilde{v}_i \frac{\partial \langle \tau_{ij} \rangle}{\partial x_j} + \frac{\partial}{\partial x_j} (\alpha_c \langle \delta \tau_{ij} \delta u_i \rangle) \\
& - \frac{1}{V} \int_{S_d} \delta \tau_{ij} v_i n_j dS - \alpha_c \rho_c \varepsilon_c + \alpha_c \rho_c g_i \langle u_i \rangle
\end{aligned} \tag{D.39}$$

Subtracting Equation D.9, the product of $\langle u_i \rangle$ and the volume-averaged momentum equation, leaves

$$\begin{aligned}
& \frac{\partial}{\partial t} (\alpha_c \rho_c k_c) + \frac{\partial}{\partial x_j} (\rho_c \alpha_c \langle u_j \rangle k_c) \\
= & -\rho_c \alpha_c \langle \delta u_i \delta u_j \rangle \frac{\partial \langle u_i \rangle}{\partial x_j} \\
& + \frac{\partial}{\partial x_j} \left(-\rho_c \alpha_c \left\langle \delta u_j \frac{\delta u_i \delta u_i}{2} \right\rangle - \frac{\partial}{\partial x_i} (\alpha_c \langle \delta p \delta u_i \rangle) + \alpha_c \langle \delta \tau_{ij} \delta u_i \rangle \right) \\
& + \alpha_d (\langle u_i \rangle - \tilde{v}_i) \left(\frac{\partial \langle p \rangle}{\partial x_i} - \frac{\partial \langle \tau_{ij} \rangle}{\partial x_j} \right) \\
& + \frac{1}{V} \sum_k \langle u_i \rangle F_{k,i} + \frac{1}{V} \int_{S_d} v_i (\delta p n_i - \delta \tau_{ij} n_j) dS - \alpha_c \rho_c \varepsilon_c
\end{aligned} \tag{D.40}$$

The fluid dynamic force on particle k is

$$F_{k,i} = \int_{S_k} (-\delta p n_i + \delta \tau_{ij} n_j) dS \tag{D.41}$$

where S_k is the surface area of particle k . Thus the integral over all the internal particle surfaces becomes

$$\int_{S_d} v_i (\delta p n_i - \delta \tau_{ij} n_j) dS = - \sum_k v_{k,i} F_{k,i} \tag{D.42}$$

where the summation is carried out over all the particles in the averaging volume.

In keeping with the approach used in single-phase flows, the second term on the right is modeled as a diffusion term

$$\begin{aligned} & \frac{\partial}{\partial x_j} \left(-\rho_c \alpha_c \left\langle \delta u_j \frac{\delta u_i \delta u_i}{2} \right\rangle - \frac{\partial}{\partial x_i} (\alpha_c \langle \delta p \delta u_i \rangle) + \alpha_c \langle \delta \tau_{ij} \delta u_i \rangle \right) \\ = & \frac{\partial}{\partial x_j} \left(\rho_c \alpha_c \frac{\nu_T}{\sigma_k} \frac{\partial k_c}{\partial x_j} \right) \end{aligned} \quad (\text{D.43})$$

where ν_T is the turbulence kinematic viscosity and σ_k is an empirical constant for turbulence diffusion.

The final, most general, form of the turbulence energy equation is

$$\begin{aligned} & \frac{\partial}{\partial t} (\alpha_c \rho_c k_c) + \frac{\partial}{\partial x_j} (\rho_c \alpha_c \langle u_j \rangle k_c) \\ = & \frac{\partial}{\partial x_j} \left(\rho_c \alpha_c \frac{\nu_T}{\sigma_k} \frac{\partial k_c}{\partial x_j} \right) && \text{diffusion} \\ & - \rho_c \alpha_c \langle \delta u_i \delta u_j \rangle \frac{\partial \langle u_i \rangle}{\partial x_j} && \text{fluid velocity gradients} \\ & + \alpha_d (\langle u_i \rangle - \tilde{v}_i) \left(\frac{\partial \langle p \rangle}{\partial x_i} - \frac{\partial \langle \tau_{ij} \rangle}{\partial x_j} \right) && \text{pressure and shear gradients} \\ & \frac{1}{V} \sum_k (\langle u_i \rangle - v_{k,i}) F_{k,i} && \text{fluid dynamic forces} \\ & - \alpha_c \rho_c \varepsilon_c && \text{dissipation} \end{aligned} \quad (\text{D.44})$$

If the particle volume fraction approaches zero, $\alpha_d \rightarrow 0$ (and $\alpha_c \rightarrow 1$), the kinetic energy equation for single-phase flow is recovered. In many dilute flow applications the term associated with pressure and shear stress gradients can be neglected.

The hydrodynamic forces on a particle can be written as the sum of the forces due to undisturbed flow (see Chapter 4) and the remaining forces

$$F_{k,i} = -V_k \frac{\partial \langle p \rangle}{\partial x_i} + V_k \frac{\partial \langle \tau_{ij} \rangle}{\partial x_j} + F'_{k,i} \quad (\text{D.45})$$

where V_k is the volume of particle k , then

$$\begin{aligned} & \frac{1}{V} \sum_k (\langle u_i \rangle - v_{k,i}) F_{k,i} \\ = & - \frac{\partial \langle p \rangle}{\partial x_i} \frac{1}{V} \sum_k (\langle u_i \rangle - v_{k,i}) V_k + \frac{\partial \langle \tau_{ij} \rangle}{\partial x_j} \frac{1}{V} \sum_k (\langle u_i \rangle - v_{k,i}) V_k \\ & + \frac{1}{V} \sum_k F'_{k,i} (\langle u_i \rangle - v_{k,i}) \end{aligned} \quad (\text{D.46})$$

The summations associated with the pressure and shear gradient terms give

$$-\frac{\partial \langle p \rangle}{\partial x_i} \frac{1}{V} \sum_k (\langle u_i \rangle - v_{k,i}) V_k = -\alpha_d \frac{\partial \langle p \rangle}{\partial x_i} (\langle u_i \rangle - \tilde{v}_i) \quad (\text{D.47})$$

$$\frac{\partial \langle \tau_{ij} \rangle}{\partial x_j} \frac{1}{V} \sum_k (\langle u_i \rangle - v_{k,i}) V_k = \alpha_d \frac{\partial \langle \tau_{ij} \rangle}{\partial x_j} (\langle u_i \rangle - \tilde{v}_i) \quad (\text{D.48})$$

The turbulence energy equation now becomes

$$\begin{aligned} & \frac{\partial}{\partial t} (\alpha_c \rho_c k_c) + \frac{\partial}{\partial x_j} (\rho_c \alpha_c \langle u_j \rangle k_c) \\ &= \frac{\partial}{\partial x_j} \left(\rho_c \alpha_c \frac{\nu_T}{\sigma_k} \frac{\partial k_c}{\partial x_j} \right) && \text{diffusion} \\ & \quad - \rho_c \alpha_c \langle \delta u_i \delta u_j \rangle \frac{\partial \langle u_i \rangle}{\partial x_j} && \text{fluid velocity gradients} \\ & \quad + \frac{1}{V} \sum_k (\langle u_i \rangle - v_{k,i}) F'_{k,i} && \text{fluid dynamic forces} \\ & \quad - \alpha_c \rho_c \varepsilon_c && \text{dissipation} \end{aligned} \quad (\text{D.49})$$

If the steady state drag is the only significant hydrodynamic force on a particle then the term due to fluid dynamic forces becomes

$$\frac{1}{V} \sum_k (\langle u_i \rangle - v_{k,i}) F'_{k,i} = \frac{1}{V} \sum_k 3\pi \mu D_k f_k (\langle u_i \rangle - v_{k,i})(u_{k,i} - v_{k,i}) \quad (\text{D.50})$$

The fluid and particle velocities can be written as $u_i = \langle u_i \rangle + \delta u_{k,i}$ and $v_{i,k} = \tilde{v}_i + \delta v_{k,i}$ where $\delta u_{k,i}$ is the deviation of the continuous phase velocity and $\delta v_{k,i}$ is the deviation of the particle velocity at the location of particle k . Assuming all the particles are the same size and have the same drag factor, Equation D.50 can be rewritten as

$$\begin{aligned} & \frac{1}{V} \sum_k (\langle u_i \rangle - v_{i,k}) F''_{k,i} \\ &= \alpha_d \rho_d \frac{f}{\tau_V} |\langle u_i \rangle - \tilde{v}_i|^2 + \alpha_d \rho_d \frac{f}{\tau_V} \left(\widehat{\delta v_i \delta v_i} - \widehat{\delta u_i \delta v_i} \right) \end{aligned} \quad (\text{D.51})$$

where τ_V is the particle velocity response time. The notation on the second two terms means

$$\widehat{\delta v_i \delta v_i} = \frac{1}{N} \sum_k \delta v_{k,i} \delta v_{k,i} \quad \text{and} \quad \widehat{\delta u_i \delta v_i} = \frac{1}{N} \sum_k \delta u_{k,i} \delta v_{k,i} \quad (\text{D.52})$$

where the summation is taken over the location of every particle, k , in the averaging volume. Substituting these equations into the general equation

results in

$$\begin{aligned}
 & \frac{\partial}{\partial t} (\alpha_c \rho_c k_c) + \frac{\partial}{\partial x_j} (\rho_c \alpha_c \langle u_j \rangle k_c) \\
 = & \frac{\partial}{\partial x_j} \left(\rho_c \alpha_c \frac{\nu_T}{\sigma_k} \frac{\partial k_c}{\partial x_j} \right) && \text{diffusion of turbulence} \\
 & - \rho_c \alpha_c \langle \delta u_i \delta u_j \rangle \frac{\partial \langle u_i \rangle}{\partial x_j} && \text{generation by gradients} \\
 & + \alpha_d \rho_d \frac{f}{\tau_V} |\langle u_i \rangle - \tilde{v}_i|^2 && \text{generation by particle drag} \\
 & + \alpha_d \rho_d \frac{f}{\tau_V} \left(\widehat{\delta v_i \delta v_i} - \widehat{\delta u_i \delta v_i} \right) && \text{redistribution} \\
 & - \alpha_c \rho_c \varepsilon_c && \text{dissipation} \tag{D.53}
 \end{aligned}$$

The redistribution terms represent the transfer of kinetic energy between phases. Generally this term is small compared to the generation by particle drag.

D.2 Turbulence dissipation

A transport equation for the turbulence dissipation can be developed by taking a gradient of the Navier-Stokes equations and multiplying it by the gradient of the volume deviation velocity and twice the kinematic viscosity $\left(2\nu_c \frac{\partial \delta u_i}{\partial x_j} \frac{\partial}{\partial x_j} N S_i\right)$. Carrying out this manipulation, the following equation is obtained.

$$\begin{aligned}
 & \overline{2\nu_c \frac{\partial \delta u_i}{\partial x_j} \frac{\partial}{\partial x_j} \left(\frac{\partial u_i}{\partial t} \right)} + \overline{2\nu_c \frac{\partial \delta u_i}{\partial x_j} \frac{\partial}{\partial x_j} \left(u_k \frac{\partial u_i}{\partial x_k} \right)} \\
 = & -2 \frac{\nu_c}{\rho_c} \overline{\frac{\partial \delta u_i}{\partial x_j} \frac{\partial}{\partial x_j} \left(\frac{\partial p}{\partial x_i} \right)} + 2\nu_c^2 \overline{\frac{\partial \delta u_i}{\partial x_j} \frac{\partial}{\partial x_j} \left(\frac{\partial^2 u_i}{\partial x_k \partial x_k} \right)} \\
 & + 2 \frac{\nu_c}{\rho_c} \overline{\frac{\partial \delta u_i}{\partial x_j} \frac{\partial}{\partial x_j} (\rho g_i)} \tag{D.54}
 \end{aligned}$$

Decomposing the above equation into phase average $\langle u_i \rangle$ and deviation components δu_i results in

$$\begin{aligned}
& \underbrace{2\nu_c \frac{\partial \delta u_i}{\partial x_j} \frac{\partial}{\partial x_j} \frac{\partial \langle u_i \rangle}{\partial t}}_a + \underbrace{2\nu_c \frac{\partial \delta u_i}{\partial x_j} \frac{\partial}{\partial x_j} \frac{\partial \delta u_i}{\partial t}}_b + \underbrace{2\nu_c \frac{\partial \delta u_i}{\partial x_j} \frac{\partial \langle u_k \rangle}{\partial x_j} \frac{\partial \langle u_i \rangle}{\partial x_k}}_c + \\
& \underbrace{2\nu_c \frac{\partial \delta u_i}{\partial x_j} \langle u_k \rangle \frac{\partial^2 \langle u_i \rangle}{\partial x_j \partial x_k}}_d + \underbrace{2\nu_c \frac{\partial \delta u_i}{\partial x_j} \frac{\partial \delta u_k}{\partial x_j} \frac{\partial \langle u_i \rangle}{\partial x_k}}_e + \underbrace{2\nu_c \frac{\partial \delta u_i}{\partial x_j} \delta u_k \frac{\partial^2 \langle u_i \rangle}{\partial x_j \partial x_k}}_f + \\
& \underbrace{2\nu_c \frac{\partial \delta u_i}{\partial x_j} \frac{\partial \langle u_k \rangle}{\partial x_j} \frac{\partial \delta u_i}{\partial x_k}}_g + \underbrace{2\nu_c \frac{\partial \delta u_i}{\partial x_j} \langle u_k \rangle \frac{\partial^2 \delta u_i}{\partial x_j \partial x_k}}_h + \underbrace{2\nu_c \frac{\partial \delta u_i}{\partial x_j} \frac{\partial \delta u_k}{\partial x_j} \frac{\partial \delta u_i}{\partial x_k}}_i + \\
& \underbrace{2\nu_c \frac{\partial \delta u_i}{\partial x_j} \delta u_k \frac{\partial^2 \delta u_i}{\partial x_j \partial x_k}}_j = \\
& \underbrace{2\frac{\nu_c}{\rho_c} \frac{\partial \delta u_i}{\partial x_j} \frac{\partial}{\partial x_j} \frac{\partial \langle p \rangle}{\partial x_i}}_k - \underbrace{2\frac{\nu_c}{\rho_c} \frac{\partial \delta u_i}{\partial x_j} \frac{\partial}{\partial x_j} \frac{\partial \delta p}{\partial x_i}}_l + \underbrace{2\nu_c^2 \frac{\partial \delta u_i}{\partial x_j} \frac{\partial}{\partial x_j} \left(\frac{\partial^2 \langle u_i \rangle}{\partial x_k \partial x_k} \right)}_m + \\
& \underbrace{2\nu_c^2 \frac{\partial \delta u_i}{\partial x_j} \frac{\partial}{\partial x_j} \left(\frac{\partial^2 \delta u_i}{\partial x_k \partial x_k} \right)}_n + \underbrace{2\frac{\nu_c}{\rho_c} \frac{\partial \delta u_i}{\partial x_j} \frac{\partial}{\partial x_j} (\rho g_i)}_o
\end{aligned} \tag{D.55}$$

Now each term is volume averaged individually using the equations developed in Appendix B.

D.2.1 Volume averaging

In this section, the details involving the volume averaging of each term in Equation D.55 are presented.

Term a

By definition the volume average of term *a* is

$$2\nu_c \overline{\frac{\partial \delta u_i}{\partial x_j} \frac{\partial}{\partial x_j} \frac{\partial \langle u_i \rangle}{\partial t}} = 2\nu_c \frac{1}{V} \int_{V_c} \frac{\partial \delta u_i}{\partial x_j} \frac{\partial}{\partial x_j} \frac{\partial \langle u_i \rangle}{\partial t} dV \tag{D.56}$$

It is now argued that the gradient of the time average of the volume-averaged velocity does vary over the averaging volume so the above equation can be written as

$$2\nu_c \overline{\frac{\partial \delta u_i}{\partial x_j} \frac{\partial}{\partial x_j} \frac{\partial \langle u_i \rangle}{\partial t}} = 2\nu_c \frac{\partial}{\partial x_j} \frac{\partial \langle u_i \rangle}{\partial t} \frac{1}{V} \int_{V_c} \frac{\partial \delta u_i}{\partial x_j} dV \tag{D.57}$$

Applying the identity from Equation 20 of Appendix B to the above integral gives

$$\frac{1}{V} \int_{V_c} \frac{\partial \delta u_i}{\partial x_j} dV = \frac{\partial}{\partial x_j} \frac{1}{V} \int_{V_c} \delta u_i dV - \frac{1}{V} \int_{S_d} \delta u_i n_j dS \quad (\text{D.58})$$

The integration of the velocity deviations over the averaging volume is, by definition, zero. The integration over the surfaces S_d requires further consideration. Volume averaging does not include the details of the boundary layer around the particles, i.e., the change from the surface velocity to the free stream velocity. Thus it is necessary to define the surface S_d as just outside the particle boundary layer where the velocity is the free-stream velocity.

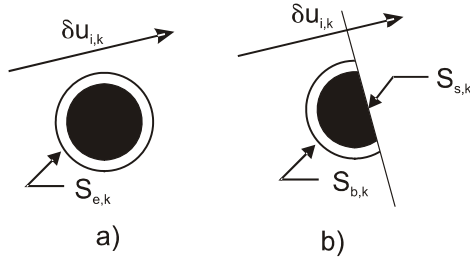


Figure D.1: Integration surfaces for (a) interior particle and (b) boundary particle.

An interior and a boundary particle are shown in Figure D.1. The velocity deviation is the deviation at the location of the particle and does not change with integration over the particle surface. For the interior particle k shown in Figure D.1a, the integral over the surface is

$$\int_{S_{e,k}} \delta u_{i,k} n_j dS = \delta u_{i,k} \int_{S_{d,k}} n_j dS = 0 \quad (\text{D.59})$$

so for all the interior particles

$$\int_{S_e} \delta u_i n_j dS = 0 \quad (\text{D.60})$$

For the boundary particle k shown in Figure D.1b, the integral over the interior surface is

$$\int_{S_{b,k}} \delta u_i n_j dS = \delta u_i n_j S_{s,k} \quad (\text{D.61})$$

because the local $\delta u_{k,i}$ is constant for particle k . Adding the contributions of all the particles intersecting the surface segment ΔS (shown in Figure D.1) gives

$$\sum_k \delta u_{k,i} n_j S_{s,k} = 0 \quad (\text{D.62})$$

because $S_{s,k} > 0$ and the mean of $\delta u_{k,i}$ is, by definition, equal to zero. Thus, for all the boundary particles

$$\int_{S_b} \delta u_i n_j dS = 0 \quad (\text{D.63})$$

The integral over the S_d surface is the sum of the integrals over the S_e and S_b surfaces, so

$$\int_{S_d} \delta u_i n_j dS = \int_{S_e + S_b} \delta u_i n_j dS = 0 \quad (\text{D.64})$$

Finally

$$\frac{1}{V} \int_{V_c} \frac{\partial \delta u_i}{\partial x_j} dV = \overline{\frac{\partial \delta u_i}{\partial x_j}} = 0 \quad (\text{D.65})$$

Substituting Equation D.65 into D.57 shows

$$2\nu_c \overline{\frac{\partial \delta u_i}{\partial x_j} \frac{\partial}{\partial x_j} \frac{\partial \langle u_i \rangle}{\partial t}} = 0 \quad (\text{D.66})$$

Term b

Term b in Equation D.55 can be rewritten as

$$2\nu_c \overline{\frac{\partial \delta u_i}{\partial x_j} \frac{\partial}{\partial x_j} \frac{\partial \delta u_i}{\partial t}} = \overline{\frac{\partial}{\partial t} \nu_c \frac{\partial \delta u_i}{\partial x_j} \frac{\partial \delta u_i}{\partial x_j}} \quad (\text{D.67})$$

Applying the temporal derivative of the volume average, Equation 28 in Appendix B, to the above equation gives

$$\begin{aligned} \overline{\frac{\partial}{\partial t} \nu_c \frac{\partial \delta u_i}{\partial x_j} \frac{\partial \delta u_i}{\partial x_j}} &= \frac{\partial}{\partial t} \left(\alpha_c \left\langle \nu_c \frac{\partial \delta u_i}{\partial x_j} \frac{\partial \delta u_i}{\partial x_j} \right\rangle \right) + \\ &\quad \frac{1}{V} \int_{S_d} \nu_c \overline{\frac{\partial \delta u_i}{\partial x_j} \frac{\partial \delta u_i}{\partial x_j}} v_k n_k dS \end{aligned} \quad (\text{D.68})$$

Substituting the definition of dissipation, Equation (D.3) into the above equation and substituting Equation D.68 into Equation D.67 results in

$$2\nu_c \overline{\frac{\partial \delta u_i}{\partial x_j} \frac{\partial}{\partial x_j} \frac{\partial \delta u_i}{\partial t}} = \frac{\partial}{\partial t} (\alpha_c \varepsilon_c) + \frac{1}{V} \int_{S_d} \nu_c \overline{\frac{\partial \delta u_i}{\partial x_j} \frac{\partial \delta u_i}{\partial x_j}} v_k n_k dS \quad (\text{D.69})$$

Terms c and d

Similar concepts that were used to obtain the volume average of term a can be applied to terms c and d in Equation D.55. The spatial gradients of the volume-averaged velocity can be factored out of the volume integral leaving

$$2\nu_c \overline{\frac{\partial \delta u_i}{\partial x_j} \frac{\partial \langle u_k \rangle}{\partial x_j} \frac{\partial \langle u_i \rangle}{\partial x_k}} = 2\nu_c \overline{\frac{\partial \langle u_k \rangle}{\partial x_j} \frac{\partial \langle u_i \rangle}{\partial x_k} \frac{\partial \delta u_i}{\partial x_j}} \quad (\text{D.70})$$

so based on Equation D.65 term c is

$$2\nu_c \overline{\frac{\partial \delta u_i}{\partial x_j} \frac{\partial \langle u_k \rangle}{\partial x_j} \frac{\partial \langle u_i \rangle}{\partial x_k}} = 0 \quad (\text{D.71})$$

Likewise, term d is found to be

$$2\nu_c \overline{\frac{\partial \delta u_i}{\partial x_j} \langle u_k \rangle \frac{\partial^2 \langle u_i \rangle}{\partial x_j \partial x_k}} = 0 \quad (\text{D.72})$$

Terms e, f and g

In term e the gradient of the volume-averaged velocity can be factored out leaving

$$2\nu_c \overline{\frac{\partial \delta u_i}{\partial x_j} \frac{\partial \delta u_k}{\partial x_k} \frac{\partial \langle u_i \rangle}{\partial x_k}} = 2\nu_c \alpha_c \left\langle \frac{\partial \delta u_i}{\partial x_j} \frac{\partial \delta u_k}{\partial x_j} \right\rangle \frac{\partial \langle u_i \rangle}{\partial x_k} \quad (\text{D.73})$$

Defining the dissipation tensor ε_{ik} as

$$\varepsilon_{ik} = \nu_c \left\langle \frac{\partial \delta u_i}{\partial x_j} \frac{\partial \delta u_k}{\partial x_j} \right\rangle \quad (\text{D.74})$$

this equation can be re-expressed as

$$2\nu_c \overline{\frac{\partial \delta u_i}{\partial x_j} \frac{\partial \delta u_k}{\partial x_j} \frac{\partial \langle u_i \rangle}{\partial x_k}} = 2\alpha_c \varepsilon_{ik} \frac{\partial \langle u_i \rangle}{\partial x_k} \quad (\text{D.75})$$

The volume average of term f is expressed as

$$2\nu_c \overline{\frac{\partial \delta u_i}{\partial x_j} \delta u_k \frac{\partial^2 \langle u_i \rangle}{\partial x_j \partial x_k}} = 2\nu_c \alpha_c \left\langle \delta u_k \frac{\partial \delta u_i}{\partial x_j} \right\rangle \frac{\partial^2 \langle u_i \rangle}{\partial x_j \partial x_k} \quad (\text{D.76})$$

Applying similar methods, the volume average of term g is

$$2\nu_c \overline{\frac{\partial \delta u_i}{\partial x_j} \frac{\partial \langle u_k \rangle}{\partial x_j} \frac{\partial \delta u_i}{\partial x_k}} = 2\nu_c \alpha_c \left\langle \frac{\partial \delta u_i}{\partial x_j} \frac{\partial \delta u_i}{\partial x_k} \right\rangle \frac{\partial \langle u_k \rangle}{\partial x_j} \quad (\text{D.77})$$

Terms h and i

Applying the product rule to term h results in

$$2\nu_c \overline{\frac{\partial \delta u_i}{\partial x_j} \langle u_k \rangle \frac{\partial^2 \delta u_i}{\partial x_j \partial x_k}} = \nu_c \langle u_k \rangle \overline{\frac{\partial}{\partial x_k} \left(\frac{\partial \delta u_i}{\partial x_j} \frac{\partial \delta u_i}{\partial x_j} \right)} \quad (\text{D.78})$$

This term will be combined with term j below.

Term i is simply

$$2\nu_c \overline{\frac{\partial \delta u_i}{\partial x_j} \frac{\partial \delta u_k}{\partial x_j} \frac{\partial \delta u_i}{\partial x_k}} = 2\nu_c \alpha_c \left\langle \frac{\partial \delta u_i}{\partial x_j} \frac{\partial \delta u_k}{\partial x_j} \frac{\partial \delta u_i}{\partial x_k} \right\rangle \quad (\text{D.79})$$

Term j

Similar to the technique used to determine term h , the product rule can be applied to rearrange term j to yield

$$2\nu_c \overline{\frac{\partial \delta u_i}{\partial x_j} \delta u_k \frac{\partial^2 \delta u_i}{\partial x_j \partial x_k}} = \nu_c \overline{\delta u_k \frac{\partial}{\partial x_k} \left(\frac{\partial \delta u_i}{\partial x_j} \frac{\partial \delta u_i}{\partial x_j} \right)} \quad (\text{D.80})$$

Adding terms h and j and using $\langle u_i \rangle + \delta u_i = u_i$ gives

$$2\nu_c \overline{\frac{\partial \delta u_i}{\partial x_j} \langle u_k \rangle \frac{\partial^2 \delta u_i}{\partial x_j \partial x_k}} + 2\nu_c \overline{\frac{\partial \delta u_i}{\partial x_j} \delta u_k \frac{\partial^2 \delta u_i}{\partial x_j \partial x_k}} = \nu_c \overline{\delta u_k \frac{\partial}{\partial x_k} \frac{\partial \delta u_i}{\partial x_j} \frac{\partial \delta u_i}{\partial x_j}} \quad (\text{D.81})$$

Using the incompressible flow condition, $\partial u_i / \partial x_i = 0$, allows one to rewrite the equation as

$$2\nu_c \overline{\frac{\partial \delta u_i}{\partial x_j} \langle u_k \rangle \frac{\partial^2 \delta u_i}{\partial x_j \partial x_k}} + 2\nu_c \overline{\frac{\partial \delta u_i}{\partial x_j} \delta u_k \frac{\partial^2 \delta u_i}{\partial x_j \partial x_k}} = \nu_c \overline{\frac{\partial}{\partial x_k} \left(u_k \frac{\partial \delta u_i}{\partial x_j} \frac{\partial \delta u_i}{\partial x_j} \right)} \quad (\text{D.82})$$

Applying Equation 20 from Appendix B results in

$$\begin{aligned} \nu_c \overline{\frac{\partial}{\partial x_k} \left(u_k \frac{\partial \delta u_i}{\partial x_j} \frac{\partial \delta u_i}{\partial x_j} \right)} &= \nu_c \overline{\frac{\partial}{\partial x_k} \left[\alpha_c \left\langle u_k \left(\frac{\partial \delta u_i}{\partial x_j} \frac{\partial \delta u_i}{\partial x_j} \right) \right\rangle \right]} \\ &\quad - \nu_c \frac{1}{V} \int_{S_d} v_k \frac{\partial \delta u_i}{\partial x_j} \frac{\partial \delta u_i}{\partial x_j} n_k dS \end{aligned} \quad (\text{D.83})$$

When all the terms are assembled, the last term in the above equation will cancel the last term in Equation D.69. Applying $u_i = \langle u_i \rangle + \delta u_i$, the first term on the right side can be rewritten as

$$\begin{aligned} &\nu_c \overline{\frac{\partial}{\partial x_k} \left[\alpha_d \left\langle u_k \left(\frac{\partial \delta u_i}{\partial x_j} \frac{\partial \delta u_i}{\partial x_j} \right) \right\rangle \right]} \\ &= \frac{\partial}{\partial x_k} [\alpha_c \langle u_k \rangle \varepsilon_c] + \nu_c \overline{\frac{\partial}{\partial x_k} \left[\alpha_c \left\langle \delta u_k \left(\frac{\partial \delta u_i}{\partial x_j} \frac{\partial \delta u_i}{\partial x_j} \right) \right\rangle \right]} \end{aligned} \quad (\text{D.84})$$

Finally combining all the terms, the left side of Equation D.54 becomes

$$\begin{aligned} &= 2\nu_c \overline{\frac{\partial \delta u_i}{\partial x_j} \frac{\partial}{\partial x_j} \left(\frac{\partial u_i}{\partial t} \right)} + 2\nu_c \overline{\frac{\partial \delta u_i}{\partial x_j} \frac{\partial}{\partial x_j} \left(u_k \frac{\partial u_i}{\partial x_k} \right)} \\ &= \frac{\partial}{\partial t} (\alpha_c \varepsilon_c) + \frac{\partial}{\partial x_k} [\alpha_c \langle u_k \rangle \varepsilon_c] + \nu_c \overline{\frac{\partial}{\partial x_k} \left[\alpha_c \left\langle \delta u_k \left(\frac{\partial \delta u_i}{\partial x_j} \frac{\partial \delta u_i}{\partial x_j} \right) \right\rangle \right]} \\ &\quad + 2\alpha_c \varepsilon_{ik} \frac{\partial \langle u_i \rangle}{\partial x_k} + 2\nu_c \alpha_c \left\langle \frac{\partial \delta u_i}{\partial x_j} \frac{\partial \delta u_k}{\partial x_j} \right\rangle \frac{\partial \langle u_i \rangle}{\partial x_k} \\ &\quad + 2\nu_c \alpha_c \left\langle \frac{\partial \delta u_i}{\partial x_j} \frac{\partial \delta u_k}{\partial x_j} \frac{\partial \delta u_i}{\partial x_k} \right\rangle + 2\nu_c \alpha_c \left\langle \delta u_k \frac{\partial \delta u_i}{\partial x_j} \right\rangle \frac{\partial^2 \langle u_i \rangle}{\partial x_j \partial x_k} \end{aligned} \quad (\text{D.85})$$

There is a one-to-one correspondence here to the terms obtained by the temporal averaging. The terms on the right side of Equation D.55 will now be addressed.

Term k

The gradient of the volume-averaged pressure can be factored out of the term so this term does not contribute to the dissipation.

$$-2 \frac{\nu_c}{\rho_c} \overline{\frac{\partial \delta u_i}{\partial x_j} \frac{\partial}{\partial x_j} \frac{\partial \langle p \rangle}{\partial x_i}} = -2 \frac{\nu_c}{\rho_c} \overline{\frac{\partial^2 \langle p \rangle}{\partial x_j \partial x_i} \frac{\partial \delta u_i}{\partial x_j}} = 0 \quad (\text{D.86})$$

Term l

Using the product rule and substituting $\delta u_i = u_i - \langle u_i \rangle$, this term can be rewritten as

$$\begin{aligned} & -2 \frac{\nu_c}{\rho_c} \overline{\frac{\partial \delta u_i}{\partial x_j} \frac{\partial}{\partial x_j} \frac{\partial \delta p}{\partial x_i}} \\ = & -2 \frac{\nu_c}{\rho_c} \overline{\frac{\partial}{\partial x_i} \frac{\partial \delta u_i}{\partial x_j} \frac{\partial \delta p}{\partial x_j}} + 2 \frac{\nu_c}{\rho_c} \overline{\frac{\partial^2 u_i}{\partial x_j \partial x_i} \frac{\partial \delta p}{\partial x_j}} - 2 \frac{\nu_c}{\rho_c} \overline{\frac{\partial^2 \langle u_i \rangle}{\partial x_j \partial x_i} \frac{\partial \delta p}{\partial x_j}} \end{aligned} \quad (\text{D.87})$$

The second term on the right is zero based on the assumption of incompressible flow. Applying Equation 20 from Appendix B, the above equation becomes

$$\begin{aligned} & -2 \frac{\nu_c}{\rho_c} \overline{\frac{\partial \delta u_i}{\partial x_j} \frac{\partial}{\partial x_j} \frac{\partial \delta p}{\partial x_i}} \\ = & -2 \frac{\nu_c}{\rho_c} \overline{\frac{\partial}{\partial x_i} \left(\alpha_c \left\langle \frac{\partial \delta u_i}{\partial x_j} \frac{\partial \delta p}{\partial x_j} \right\rangle \right)} - 2 \alpha_c \frac{\nu_c}{\rho_c} \left\langle \frac{\partial^2 \langle u_i \rangle}{\partial x_j \partial x_i} \frac{\partial \delta p}{\partial x_j} \right\rangle \\ & + 2 \frac{\nu_c}{\rho_c} \frac{1}{V} \int_{S_d} \frac{\partial \delta u_i}{\partial x_j} \frac{\partial \delta p}{\partial x_j} n_i dS \end{aligned} \quad (\text{D.88})$$

With Reynolds averaging of single-phase flows, the second term on the right can be set to zero based on the incompressible continuity equation. However, for volume averaging of multiphase flows this is not the case. Order of magnitude analyses indicates that $\partial \langle u_i \rangle / \partial x_i$ scales as the volume fraction of the dispersed phase, α_d , so the term will be insignificant for dilute flows but may be important for dense flows. Thus for dilute flows, the above equation is reduced to

$$\begin{aligned} & -2 \frac{\nu_c}{\rho_c} \overline{\frac{\partial \delta u_i}{\partial x_j} \frac{\partial}{\partial x_j} \frac{\partial \delta p}{\partial x_i}} \\ \approx & -2 \frac{\nu_c}{\rho_c} \overline{\frac{\partial}{\partial x_i} \left(\alpha_c \left\langle \frac{\partial \delta u_i}{\partial x_j} \frac{\partial \delta p}{\partial x_j} \right\rangle \right)} + 2 \frac{\nu_c}{\rho_c} \frac{1}{V} \int_{S_d} \frac{\partial \delta u_i}{\partial x_j} \frac{\partial \delta p}{\partial x_j} n_i dS \end{aligned} \quad (\text{D.89})$$

For dense flows, the second term on the right of Equation D.88 may be added. The term is rewritten as

$$-2 \alpha_c \frac{\nu_c}{\rho_c} \left\langle \frac{\partial^2 \langle u_i \rangle}{\partial x_j \partial x_i} \frac{\partial \delta p}{\partial x_j} \right\rangle = 2 \alpha_c \frac{\nu_c}{\rho_c} \frac{1}{V} \frac{\partial^2 \langle u_i \rangle}{\partial x_j \partial x_i} \int_{S_d} \delta p n_j dS \quad (\text{D.90})$$

The integral of the pressure deviations over the internal particle surfaces is the negative of the form drag on the particle (see Equation C.32). Thus the integral can be approximated by

$$\int_{S_d} \delta p n_j dS \sim -\pi \sum_k f_k D_k \mu_c (u_j - v_j)_k$$

Thus the term becomes

$$-2\alpha_c \frac{\nu_c}{\rho_c} \left\langle \frac{\partial^2 \langle u_i \rangle}{\partial x_j \partial x_i} \frac{\partial \delta p}{\partial x_j} \right\rangle \simeq -C_{\varepsilon 4} \alpha_c \frac{\nu_c^2}{V} \frac{\partial^2 \langle u_i \rangle}{\partial x_j \partial x_i} \sum_k f_k D_k (u_j - v_j)_k \quad (\text{D.91})$$

where the factor 2π has been absorbed into the coefficient $C_{\varepsilon 4}$. This term has not been interpreted nor its utility evaluated.

Terms m and n

In term m , the gradient of the average velocity can be factored out of the volume integral leaving

$$2\nu_c^2 \overline{\frac{\partial \delta u_i}{\partial x_j} \frac{\partial}{\partial x_j} \left(\frac{\partial^2 \langle u_i \rangle}{\partial x_k \partial x_k} \right)} = 2\nu_c^2 \overline{\frac{\partial \delta u_i}{\partial x_j}} \frac{\partial}{\partial x_j} \left(\frac{\partial^2 \langle u_i \rangle}{\partial x_k \partial x_k} \right) \quad (\text{D.92})$$

Applying Equation D.65, term m is equal to zero.

$$2 \frac{\nu_c}{\rho_c} \overline{\frac{\partial \delta u_i}{\partial x_j} \frac{\partial}{\partial x_j} \frac{\partial \langle \tau_{ik} \rangle}{\partial x_k}} = 0 \quad (\text{D.93})$$

Using the product rule term n can be expressed as

$$2\nu_c^2 \overline{\frac{\partial \delta u_i}{\partial x_j} \frac{\partial}{\partial x_k} \frac{\partial^2 \delta u_i}{\partial x_j \partial x_k}} = \nu_c^2 \overline{\frac{\partial^2}{\partial x_k^2} \left(\frac{\partial \delta u_i}{\partial x_j} \frac{\partial \delta u_i}{\partial x_j} \right)} - 2\nu_c^2 \overline{\frac{\partial^2 \delta u_i}{\partial x_k \partial x_j} \frac{\partial^2 \delta u_i}{\partial x_k \partial x_j}} \quad (\text{D.94})$$

which reveals the diffusion of dissipation and dissipation of dissipation terms. Applying Equation 20 in Appendix B twice for the second derivative, term n becomes

$$\begin{aligned} \nu_c^2 \overline{\frac{\partial^2}{\partial x_k^2} \left(\frac{\partial \delta u_i}{\partial x_j} \frac{\partial \delta u_i}{\partial x_j} \right)} &= \nu_c^2 \frac{\partial^2}{\partial x_k^2} \left(\alpha_c \left\langle \frac{\partial \delta u_i}{\partial x_j} \frac{\partial \delta u_i}{\partial x_j} \right\rangle \right) \\ &\quad - \nu_c^2 \frac{1}{V} \int_{S_d} \frac{\partial}{\partial x_k} \left(\frac{\partial \delta u_i}{\partial x_j} \frac{\partial \delta u_i}{\partial x_j} \right) n_k dS \\ &\quad - \nu_c^2 \frac{1}{V} \frac{\partial}{\partial x_k} \int_{S_d} \frac{\partial \delta u_i}{\partial x_j} \frac{\partial \delta u_i}{\partial x_j} n_k dS \\ &\quad - 2\nu_c^2 \alpha_c \left\langle \frac{\partial^2 \delta u_i}{\partial x_k \partial x_j} \frac{\partial^2 \delta u_i}{\partial x_k \partial x_j} \right\rangle \end{aligned} \quad (\text{D.95})$$

Term o

The spatial derivative of the body force term is constant, so it can be factored out of the volume average and

$$2 \frac{\nu_c}{\rho_c} \overline{\frac{\partial \delta u_i}{\partial x_j} \frac{\partial}{\partial x_j} (\rho g_i)} = 2 \frac{\nu_c}{\rho_c} \overline{\frac{\partial \delta u_i}{\partial x_j}} \frac{\partial}{\partial x_j} (\rho g_i) = 0 \quad (\text{D.96})$$

D.2.2 The dissipation transport equation

Collecting all the terms and substituting into Equation D.55 the transport equation for the rate of dissipation becomes

$$\begin{aligned} & \frac{\partial}{\partial t} (\alpha_c \varepsilon_c) + \frac{\partial}{\partial x_k} (\alpha_c \langle u_k \rangle \varepsilon_c) \\ = & -\alpha_c \varepsilon_{ik} \frac{\partial \langle u_i \rangle}{\partial x_k} \quad \text{Production} \\ & -2\nu_c \alpha_c \left\langle \frac{\partial \delta u_i}{\partial x_j} \frac{\partial \delta u_i}{\partial x_k} \right\rangle \frac{\partial \langle u_k \rangle}{\partial x_j} \\ & -2\nu_c \alpha_c \left\langle \delta u_k \frac{\partial \delta u_i}{\partial x_j} \right\rangle \frac{\partial^2 \langle u_i \rangle}{\partial x_j \partial x_k} \\ & -2\nu_c \alpha_c \left\langle \frac{\partial \delta u_i}{\partial x_j} \frac{\partial \delta u_k}{\partial x_j} \frac{\partial \delta u_i}{\partial x_k} \right\rangle \\ & -\nu_c \frac{\partial}{\partial x_k} \left(\alpha_c \left\langle \delta u_k \frac{\partial \delta u_i}{\partial x_j} \frac{\partial \delta u_i}{\partial x_j} \right\rangle \right) \quad \text{Turbulence Transport} \\ & -2 \frac{\nu_c}{\rho_c} \frac{\partial}{\partial x_i} \left(\alpha_c \left\langle \frac{\partial \delta u_i}{\partial x_j} \frac{\partial p}{\partial x_j} \right\rangle \right) \quad \text{Pressure Strain} \\ & + \nu_c \frac{\partial^2}{\partial x_k \partial x_k} (\alpha_c \varepsilon_c) \quad \text{Molecular Diffusion} \\ & -2\nu_c^2 \alpha_c \left\langle \frac{\partial^2 \delta u_i}{\partial x_k \partial x_j} \frac{\partial^2 \delta u_i}{\partial x_k \partial x_j} \right\rangle \quad \text{Dissipation of Dissipation} \\ & -\nu_c^2 \frac{1}{V} \frac{\partial}{\partial x_k} \int_{S_d} \frac{\partial \delta u_i}{\partial x_j} \frac{\partial \delta u_i}{\partial x_j} n_k dS \quad \text{Effect of Particles} \\ & + 2 \frac{\nu_c}{\rho_c V} \frac{1}{V} \int_{S_d} \frac{\partial \delta u_i}{\partial x_j} \frac{\partial \delta p}{\partial x_j} n_i dS \\ & -\nu_c^2 \frac{1}{V} \int_{S_d} \frac{\partial}{\partial x_k} \left(\frac{\partial \delta u_i}{\partial x_j} \frac{\partial \delta u_i}{\partial x_j} \right) n_k dS \end{aligned} \quad (\text{D.97})$$

For dense flows, the term given by Equation D.91 can be added to the right side. This equation reduces to the transport equation based on Reynolds averaging for single-phase flow (Benard and Wallace, 2002) by setting α_c equal to unity and discarding the integrals over the particle surfaces.

The three surface integrals represent the effects of particles on the continuous phase turbulence dissipation. The evaluation of these integrals depends on the flow field around the particle. The relative velocity between the particle and the local velocity is

$$U_i = u_i - v_i \quad (\text{D.98})$$

so the deviation velocity can be expressed as

$$\delta u_i = u_i - \langle u_i \rangle = U_i + v_i - \langle u_i \rangle \quad (\text{D.99})$$

The spatial derivatives of the velocity deviations on the particle surfaces become

$$\frac{\partial \delta u_i}{\partial x_j} |_{S_d} = \frac{\partial U_i}{\partial x_j} |_{S_d} + \frac{\partial v_i}{\partial x_j} |_{S_d} + \frac{\partial \langle u_i \rangle}{\partial x_j} |_{S_d} \quad (\text{D.100})$$

However, v_i and $\langle u_i \rangle$ are constant on each particle surface so

$$\frac{\partial \delta u_i}{\partial x_j} |_{S_d} = \frac{\partial U_i}{\partial x_j} |_{S_d} \quad (\text{D.101})$$

The integral

$$-\nu_c^2 \frac{1}{V} \frac{\partial}{\partial x_k} \int_{S_d} \frac{\partial \delta u_i}{\partial x_j} \frac{\partial \delta u_i}{\partial x_j} n_k dS$$

is identified as the diffusion of dissipation due to the presence of the particles. Assuming the particles are spherical and using spherical coordinates (r, θ, ϕ) the local dissipation at the particle surface ($r = a$) is

$$\frac{\partial \delta u_i}{\partial x_j} \frac{\partial \delta u_i}{\partial x_j} = \frac{\partial U_\theta}{\partial r} \frac{\partial U_\theta}{\partial r} |_{r=a} \quad (\text{D.102})$$

based on axially symmetric flow along the z -axis (no dependence on ϕ) where U_θ is velocity component in the polar direction. For Stokes flow around the particles, the dissipation integral evaluates to zero (Schwarzkopf et al., 2009a).

$$-\nu_c^2 \frac{1}{V} \frac{\partial}{\partial x_k} \int_{S_d} \frac{\partial \delta u_i}{\partial x_j} \frac{\partial \delta u_i}{\partial x_j} n_k dS = 0 \quad (\text{D.103})$$

The integral

$$2 \frac{\nu_c}{\rho_c} \frac{1}{V} \int_{S_d} \frac{\partial \delta u_i}{\partial x_j} \frac{\partial \delta p}{\partial x_j} n_i dS$$

is the pressure-gradient-strain due to the presence of the particles. Using spherical coordinates with an axisymmetric flow this integral for a given particle becomes

$$\begin{aligned} & \int_{S_d} \frac{\partial \delta u_i}{\partial x_j} \frac{\partial \delta p}{\partial x_j} n_i dS \\ &= \int_0^{2\pi} \int_0^\pi \left[\frac{\partial U_r}{\partial r} \frac{\partial \delta p}{\partial r} + \left(\frac{1}{r} \frac{\partial U_r}{\partial \theta} - \frac{U_\theta}{r} \right) \frac{1}{r} \frac{\partial \delta p}{\partial \theta} \right]_{r=a} a^2 \sin \theta d\theta d\phi \end{aligned} \quad (\text{D.104})$$

At the surface of a sphere

$$\frac{\partial U_r}{\partial r} = 0 \quad \frac{\partial U_r}{\partial \theta} = 0 \quad U_\theta = 0 \quad (\text{D.105})$$

so the integral reduces to zero

$$\int_{S_d} \frac{\partial \delta u_i}{\partial x_j} \frac{\partial \delta p}{\partial x_j} n_i dS = 0 \quad (\text{D.106})$$

The last integral

$$-\nu_c^2 \frac{1}{V} \int_{S_d} \frac{\partial}{\partial x_k} \left(\frac{\partial \delta u_i}{\partial x_j} \frac{\partial \delta u_i}{\partial x_j} \right) n_k dS$$

is the production of dissipation due to the presence of the particles. Once again using spherical coordinates with axisymmetric flow, the only non-zero term is the integral associated with the gradient in the r -direction. The integral for particle k becomes

$$\int_{S_k} \frac{\partial}{\partial x_k} \left(\frac{\partial \delta u_i}{\partial x_j} \frac{\partial \delta u_i}{\partial x_j} \right) n_k dS = \int_0^{2\pi} \int_0^\pi 2 \left(\frac{\partial U_\theta}{\partial r} \frac{\partial^2 U_\theta}{\partial r^2} \right)_{r=a} a^2 \sin \theta d\theta d\phi \quad (\text{D.107})$$

Evaluating the above integral assuming Stokes flow and summing over all particles in the averaging volume gives (Schwarzkopf et al., 2009a)

$$-\nu_c^2 \frac{1}{V} \int_{S_d} \frac{\partial}{\partial x_k} \left(\frac{\partial \delta u_i}{\partial x_j} \frac{\partial \delta u_i}{\partial x_j} \right) n_k dS = 72\pi \frac{\nu_c^2}{V} \sum_k \frac{|u_i - v_i|_k^2}{D_k} \quad (\text{D.108})$$

where D_k is the particle diameter. The deviation from Stokes drag can be approximated by the drag factor, f . Also to account for non-Stokesian effects and different turbulence scales, the factor 72π is replaced by an empirical coefficient $C_{\varepsilon 3}$.

Using the same arguments for modeling terms as used for single-phase flows, the transport equation for rate of turbulence dissipation becomes

$$\begin{aligned} & \frac{\partial}{\partial t} (\alpha_c \varepsilon_c) + \frac{\partial}{\partial x_k} (\alpha_c \langle u_k \rangle \varepsilon_c) \\ &= -\alpha_c C'_{\varepsilon 1} \frac{\varepsilon_c}{k_c} R_{ij} \frac{\partial u_i}{\partial x_j} + \frac{\partial}{\partial x_j} \left(\alpha_c \left(\nu_c + \frac{\nu_T}{\sigma_\varepsilon} \right) \frac{\partial \varepsilon_c}{\partial x_j} \right) \\ & \quad - C'_{\varepsilon 2} \alpha_c \frac{\varepsilon_c^2}{k_c} + C_{\varepsilon 3} \frac{\nu_c^2}{V} \sum_k f_k \frac{|u_i - v_i|_k^2}{D_k} \end{aligned} \quad (\text{D.109})$$

where the summation is carried out over all particles in the averaging volume.

D.3 Reynolds stress

The volume-averaged Reynolds stress tensor, which appears in the volume-averaged form of the Navier-Stokes equations, is defined as

$$R_{ij} = \langle \delta u_i \delta u_j \rangle \quad (\text{D.110})$$

In order to complete the set of turbulence equations, a transport equation is needed for the Reynolds stress. This development begins by manipulating the Navier-Stokes equations to yield an equation for the tensor $u_i u_j$. This is done by multiplying the velocity u_i with the j -component of the Navier-Stokes equation (NS_j) and adding the product of u_j and the i -component of the Navier-Stokes equation; namely, $u_i NS_j + u_j NS_i$. The result is

$$\begin{aligned} \frac{\partial(\rho_c u_i u_j)}{\partial t} + \frac{\partial(\rho_c u_i u_j u_k)}{\partial x_k} &= -u_j \frac{\partial p}{\partial x_i} - u_i \frac{\partial p}{\partial x_j} + u_j \frac{\partial \tau_{ik}}{\partial x_k} \\ &\quad + u_i \frac{\partial \tau_{jk}}{\partial x_k} + \rho_c g_i u_j + \rho_c g_j u_i \end{aligned} \quad (\text{D.111})$$

A volume average is then taken and the velocities, pressure and shear stress are then expressed as the sum of a volume-averaged value and a deviation. The volume-averaged momentum equations are also combined in the form $\langle u_i \rangle \langle NS_j \rangle + \langle u_j \rangle \langle NS_i \rangle$ to provide an equation for the tensor $\langle u_i \rangle \langle u_j \rangle$. This equation is subtracted from the volume average of Equation D.111 leaving an equation for the Reynolds stress.

D.3.1 Volume-averaged momentum equations

Carrying out the operation $\langle u_i \rangle \langle NS_j \rangle + \langle u_j \rangle \langle NS_i \rangle$ using Equation D.8 and Equation D.6 leads to

$$\begin{aligned} &\frac{\partial}{\partial t} (\alpha_c \rho_c \langle u_i \rangle \langle u_j \rangle) + \frac{\partial}{\partial x_k} (\alpha_c \rho_c \langle u_k \rangle \langle u_i \rangle \langle u_j \rangle) \\ &= -\langle u_i \rangle \frac{\partial}{\partial x_k} (\alpha_c \rho_c R_{jk}) - \langle u_j \rangle \frac{\partial}{\partial x_k} (\alpha_c \rho_c R_{ik}) \\ &\quad - \langle u_i \rangle \frac{\partial \langle p \rangle}{\partial x_j} - \langle u_j \rangle \frac{\partial \langle p \rangle}{\partial x_i} + \langle u_i \rangle \frac{\partial \langle \tau_{jk} \rangle}{\partial x_k} + \langle u_j \rangle \frac{\partial \langle \tau_{ik} \rangle}{\partial x_k} \\ &\quad - \langle u_i \rangle \sum_k F_{k,j} - \langle u_j \rangle \sum_k F_{k,i} + \alpha_c \rho_c (g_i \langle u_j \rangle + g_j \langle u_i \rangle) \end{aligned} \quad (\text{D.112})$$

D.3.2 Volume average for the Reynolds stress

For purpose of analysis, Equation D.111 is rewritten in the form

$$\begin{aligned}
 & \overbrace{\frac{\partial(\rho_c u_i u_j)}{\partial t} + \frac{\partial(\rho_c u_i u_j u_k)}{\partial x_k}}^a \\
 = & \overbrace{-\frac{\partial}{\partial x_i}(pu_j) - \frac{\partial}{\partial x_j}(pu_i) + p \left(\frac{\partial u_i}{\partial x_j} + \frac{\partial u_j}{\partial x_i} \right)}^b \\
 & \overbrace{+ \frac{\partial}{\partial x_k}(\tau_{ik} u_j) + \frac{\partial}{\partial x_k}(\tau_{jk} u_i) - \tau_{ik} \frac{\partial u_j}{\partial x_k} - \tau_{jk} \frac{\partial u_i}{\partial x_k}}^d \\
 & \overbrace{+ \rho_c g_i u_j + \rho_c g_j u_i}^f
 \end{aligned} \quad (\text{D.113})$$

Each set of terms will be volume averaged according to the equations derived in Appendix B and using many of the relationships developed for the turbulence energy equation.

Set a

The volume average of the time derivative is

$$\overline{\frac{\partial(\rho_c u_i u_j)}{\partial t}} = \frac{\partial}{\partial t} (\alpha_c \langle \rho_c u_i u_j \rangle) + \int_{S_d} \rho_c (u_i u_j) v_k n_k dS \quad (\text{D.114})$$

and the volume average of the spatial derivative becomes

$$\overline{\frac{\partial(\rho_c u_i u_j u_k)}{\partial x_k}} = \frac{\partial}{\partial x_k} (\alpha_c \langle \rho_c u_i u_j u_k \rangle) - \int_{S_d} \rho_c (u_i u_j) v_k n_k dS \quad (\text{D.115})$$

Adding the two equations cancels the integrals over the particle surfaces leaving

$$\begin{aligned}
 & \overline{\frac{\partial(\rho_c u_i u_j)}{\partial t}} + \overline{\frac{\partial(\rho_c u_i u_j u_k)}{\partial x_k}} \\
 = & \frac{\partial}{\partial t} (\alpha_c \langle \rho_c u_i u_j \rangle) + \frac{\partial}{\partial x_k} (\alpha_c \langle \rho_c u_i u_j u_k \rangle)
 \end{aligned} \quad (\text{D.116})$$

Substituting $u_i = \langle u_i \rangle + \delta u_i$ for the velocities, expanding and using the definition $\langle \delta u_i \rangle = 0$ results in

$$\begin{aligned} & \overline{\frac{\partial (\rho_c u_i u_j)}{\partial t}} + \overline{\frac{\partial (\rho_c u_i u_j u_k)}{\partial x_k}} \\ = & \frac{\partial}{\partial t} (\alpha_c \rho_c \langle u_i \rangle \langle u_j \rangle) + \frac{\partial}{\partial t} (\alpha_c \rho_c R_{ij}) + \frac{\partial}{\partial x_k} (\alpha_c \rho_c \langle u_i \rangle \langle u_j \rangle \langle u_k \rangle) \\ & + \frac{\partial}{\partial x_k} (\alpha_c \rho_c \langle \delta u_i \delta u_j \delta u_k \rangle) + \frac{\partial}{\partial x_k} (\alpha_c \rho_c \langle u_k \rangle R_{ij}) \\ & + \frac{\partial}{\partial x_k} (\alpha_c \rho_c \langle u_i \rangle R_{jk}) + \frac{\partial}{\partial x_k} (\alpha_c \rho_c \langle u_j \rangle R_{ik}) \end{aligned} \quad (\text{D.117})$$

Set b

The volume average of the first term in set b is

$$-\overline{\frac{\partial}{\partial x_i} (pu_j)} = -\frac{\partial}{\partial x_i} (\alpha_c \langle pu_j \rangle) + \frac{1}{V} \int_{S_d} p v_j n_i dS \quad (\text{D.118})$$

where v_i is the particle velocity. Expressing the pressure as $\langle p \rangle + \delta p$, the integral over the particle surfaces using Equations D.22 and D.23 is

$$\int_{S_d} p v_j n_i dS = \frac{1}{V} \int_{S_d} \delta p v_j n_i dS - \frac{\partial}{\partial x_i} (\langle p \rangle \alpha_d \tilde{v}_j) \quad (\text{D.119})$$

Also decomposing the velocity u_j into $\langle u_j \rangle + \delta u_j$ the first term on the right side of Equation D.118 becomes

$$-\frac{\partial}{\partial x_i} (\alpha_c \langle pu_j \rangle) = -\frac{\partial}{\partial x_i} (\alpha_c \langle p \rangle \langle u_j \rangle + \langle \delta p \delta u_j \rangle) \quad (\text{D.120})$$

Combining terms

$$\begin{aligned} & -\overline{\frac{\partial}{\partial x_i} (pu_j)} \\ = & -\frac{\partial}{\partial x_i} (\alpha_c \langle p \rangle \langle u_j \rangle + \langle p \rangle \alpha_d \tilde{v}_j) - \frac{\partial}{\partial x_i} (\alpha_c \langle \delta p \delta u_j \rangle) \\ & + \frac{1}{V} \int_{S_d} \delta p v_j n_i dS \end{aligned} \quad (\text{D.121})$$

Performing the same operations for the second term in set b and combining with the above equation leads to the following result for set b.

$$\begin{aligned}
& \overline{-\frac{\partial}{\partial x_i} (pu_j) - \frac{\partial}{\partial x_j} (pu_i)} \\
= & -\frac{\partial}{\partial x_i} [\langle p \rangle (\alpha_c \langle u_j \rangle + \alpha_d \tilde{v}_j)] - \frac{\partial}{\partial x_j} [\langle p \rangle (\alpha_c \langle u_i \rangle + \alpha_d \tilde{v}_i)] \\
& -\frac{\partial}{\partial x_i} (\alpha_c \langle \delta p \delta u_j \rangle) - \frac{\partial}{\partial x_j} (\alpha_c \langle \delta p \delta u_i \rangle) \\
& + \frac{1}{V} \int_{S_d} \delta p v_j n_i dS + \frac{1}{V} \int_{S_d} \delta p v_i n_j dS
\end{aligned} \tag{D.122}$$

Set c

The volume average of the first term in set *c* is

$$\overline{p \left(\frac{\partial u_i}{\partial x_j} \right)} = \langle p \rangle \overline{\left(\frac{\partial u_i}{\partial x_j} \right)} + \overline{\delta p \left(\frac{\partial (\langle u_i \rangle + \delta u_i)}{\partial x_j} \right)} \tag{D.123}$$

Using the relationship from Appendix B for the volume average of a gradient, the first term on the right is

$$\langle p \rangle \overline{\left(\frac{\partial u_i}{\partial x_j} \right)} = \langle p \rangle \frac{\partial}{\partial x_j} (\alpha_c \langle u_i \rangle) - \langle p \rangle \int_{S_d} v_i n_j dS \tag{D.124}$$

The integral over the surfaces of the internal particles is zero leaving the integral over the boundary particles. Using Equation D.31 for the integral over the internal surfaces of the boundary particles gives

$$\langle p \rangle \overline{\frac{\partial u_i}{\partial x_j}} = \langle p \rangle \frac{\partial}{\partial x_j} (\alpha_c \langle u_i \rangle + \alpha_d \tilde{v}_i) \tag{D.125}$$

Also by definition

$$\overline{\delta p \frac{\partial \langle u_i \rangle}{\partial x_j}} = \alpha_c \frac{\partial \langle u_i \rangle}{\partial x_j} \langle \delta p \rangle = 0 \tag{D.126}$$

Thus Equation D.123 becomes

$$\overline{p \frac{\partial u_i}{\partial x_j}} = \alpha_c \left\langle \delta p \frac{\partial \delta u_i}{\partial x_j} \right\rangle + \langle p \rangle \frac{\partial}{\partial x_j} (\alpha_c \langle u_i \rangle + \alpha_d \tilde{v}_i) \tag{D.127}$$

Performing the same operations on the last term in set *c* results in

$$\begin{aligned}
\overline{p \left(\frac{\partial u_i}{\partial x_j} + \frac{\partial u_j}{\partial x_i} \right)} &= \alpha_c \left(\left\langle \delta p \frac{\partial \delta u_i}{\partial x_j} \right\rangle + \left\langle \delta p \frac{\partial \delta u_j}{\partial x_i} \right\rangle \right) \\
&+ \langle p \rangle \frac{\partial}{\partial x_j} (\alpha_c \langle u_i \rangle + \alpha_d \tilde{v}_i) \\
&+ \langle p \rangle \frac{\partial}{\partial x_i} (\alpha_c \langle u_j \rangle + \alpha_d \tilde{v}_j)
\end{aligned} \tag{D.128}$$

Set d

The same procedures can be used for set *d* and used for set *b*. The final result is

$$\begin{aligned}
 & \overline{\frac{\partial}{\partial x_k} (\tau_{ik} u_j) + \frac{\partial}{\partial x_k} (\tau_{jk} u_i)} \\
 = & \frac{\partial}{\partial x_k} [\langle \tau_{ik} \rangle (\alpha_c \langle u_j \rangle + \alpha_d \tilde{v}_j)] + \frac{\partial}{\partial x_k} [\langle \tau_{jk} \rangle (\alpha_c \langle u_i \rangle + \alpha_d \tilde{v}_i)] \\
 & + \frac{\partial}{\partial x_k} (\alpha_c \langle \delta \tau_{ik} \delta u_j \rangle) + \frac{\partial}{\partial x_k} (\alpha_c \langle \delta \tau_{jk} \delta u_i \rangle) \\
 & - \frac{1}{V} \int_{S_d} \delta \tau_{ik} v_j n_k dS - \frac{1}{V} \int_{S_d} \delta \tau_{jk} v_i n_k dS
 \end{aligned} \tag{D.129}$$

Set e

The volume average of the first term in set *e* is

$$-\overline{\tau_{ik} \frac{\partial u_j}{\partial x_k}} = -\langle \tau_{ik} \rangle \overline{\frac{\partial u_j}{\partial x_k}} - \overline{\delta \tau_{ik} \frac{\partial}{\partial x_k} (\langle u_j \rangle + \delta u_j)} \tag{D.130}$$

As with Equation D.125, the first term is

$$-\langle \tau_{ik} \rangle \overline{\frac{\partial u_j}{\partial x_k}} = -\langle \tau_{ik} \rangle \frac{\partial}{\partial x_k} (\alpha_c \langle u_j \rangle + \alpha_d \tilde{v}_j) \tag{D.131}$$

Also, by definition

$$\overline{\delta \tau_{ik} \frac{\partial}{\partial x_k} \langle u_j \rangle} = \alpha_c \frac{\partial}{\partial x_k} \langle u_j \rangle \langle \delta \tau_{ik} \rangle = 0 \tag{D.132}$$

Combining both terms for set *e* gives

$$\begin{aligned}
 & \overline{-\tau_{ik} \frac{\partial u_j}{\partial x_k} - \tau_{jk} \frac{\partial u_i}{\partial x_k}} \\
 = & -\alpha_c \left(\left\langle \delta \tau_{ik} \frac{\partial \delta u_j}{\partial x_k} \right\rangle + \left\langle \delta \tau_{jk} \frac{\partial \delta u_i}{\partial x_k} \right\rangle \right) \\
 & - \langle \tau_{ik} \rangle \frac{\partial}{\partial x_k} (\alpha_c \langle u_j \rangle + \alpha_d \tilde{v}_j) \\
 & - \langle \tau_{jk} \rangle \frac{\partial}{\partial x_k} (\alpha_c \langle u_i \rangle + \alpha_d \tilde{v}_i)
 \end{aligned} \tag{D.133}$$

Set f

The volume average of set *f* is simply

$$\overline{\rho_c g_i u_j + \rho_c g_j u_i} = \alpha_c \rho_c (g_i \langle u_j \rangle + g_j \langle u_i \rangle) \tag{D.134}$$

When combining sets b and d , the following combination appears which corresponds to the product of the particle velocity and hydrodynamic force on the particle

$$\frac{1}{V} \int_{S_d} \delta p v_j n_i dS - \frac{1}{V} \int_{S_d} \delta \tau_{ik} v_j n_k dS = -\frac{1}{V} \sum_k v_{k,j} F_{k,i} \quad (\text{D.135})$$

where $v_{k,j}$ is the velocity of particle k and $F_{k,i}$ is the hydrodynamic force vector and the summation is carried out over all the particles in the averaging volume.

D.3.3 Reynolds stress equation

Combining all the sets of equations, a through f , and subtracting Equation D.112 yields the equation for the Reynolds transport tensor, Equation D.136. This is the general form for the transport equation. The last four terms in the above equation represent the effect of the particles on the Reynolds stress. It can also be seen that when the void fraction approaches unity $\alpha_c \rightarrow 1$ and the effect of particles vanish ($\alpha_d \rightarrow 0$ and $F_{k,i} \rightarrow 0$) and the Reynolds stress equation for single-phase flow is recovered.

$$\begin{aligned} & \frac{\partial}{\partial t} (\alpha_c \rho_c R_{ij}) + \frac{\partial}{\partial x_k} (\alpha_c \rho_c \langle u_k \rangle R_{ij}) \\ = & -\frac{\partial}{\partial x_k} (\alpha_c \rho_c \langle \delta u_i \delta u_j \delta u_k \rangle) - \alpha_c \rho_c R_{jk} \frac{\partial \langle u_i \rangle}{\partial x_k} - \alpha_c \rho_c R_{ik} \frac{\partial \langle u_j \rangle}{\partial x_k} \\ & -\frac{\partial}{\partial x_i} (\alpha_c \langle \delta p \delta u_j \rangle) - \frac{\partial}{\partial x_j} (\alpha_c \langle \delta p \delta u_i \rangle) \\ & + \alpha_c \left(\left\langle \delta p \frac{\partial \delta u_i}{\partial x_j} \right\rangle + \left\langle \delta p \frac{\partial \delta u_j}{\partial x_i} \right\rangle \right) \\ & + \frac{\partial}{\partial x_k} (\alpha_c \langle \delta \tau_{ik} \delta u_j \rangle) + \frac{\partial}{\partial x_k} (\alpha_c \langle \delta \tau_{jk} \delta u_i \rangle) \\ & - \alpha_c \left(\left\langle \delta \tau_{ik} \frac{\partial \delta u_j}{\partial x_k} \right\rangle + \left\langle \delta \tau_{jk} \frac{\partial \delta u_i}{\partial x_k} \right\rangle \right) \\ & + \alpha_d (\langle u_j \rangle - \tilde{v}_j) \left(\frac{\partial \langle p \rangle}{\partial x_i} - \frac{\partial \tau_{ik}}{\partial x_k} \right) + \alpha_d (\langle u_i \rangle - \tilde{v}_i) \left(\frac{\partial \langle p \rangle}{\partial x_j} - \frac{\partial \tau_{jk}}{\partial x_k} \right) \\ & + \frac{1}{V} \sum_k (\langle u_i \rangle - v_{k,i}) F_{k,j} + \frac{1}{V} \sum_k (\langle u_j \rangle - v_{k,j}) F_{k,i} \end{aligned} \quad (\text{D.136})$$

Modeling Terms

There are several terms in Equation D.136 that need closure models. At this point, closure models for dispersed phase flows are not well understood. However, the equations must collapse to the single-phase equation set when the particle volume fraction goes to zero ($\alpha_d \rightarrow 0$). Therefore, as with the

volume averaged $k - \varepsilon$ model, the single-phase models are adopted here and methods for determining the coefficients are discussed in Chapter 7. The production terms (shown below) are in closed form and do not need a model.

$$-\alpha_c \rho_c R_{jk} \frac{\partial \langle u_i \rangle}{\partial x_k} - \alpha_c \rho_c R_{ik} \frac{\partial \langle u_j \rangle}{\partial x_k} \quad (\text{D.137})$$

The transport terms can be approximated using a gradient diffusion model (Daly and Harlow, 1970; Launder, 1989)

$$\begin{aligned} & -\frac{\partial}{\partial x_i} (\alpha_c \langle \delta u_j \delta p \rangle) - \frac{\partial}{\partial x_j} (\alpha_c \langle \delta u_i \delta p \rangle) \\ & + \frac{\partial}{\partial x_k} (\alpha_c \langle \delta u_j \delta \tau_{ik} \rangle) + \frac{\partial}{\partial x_k} (\alpha_c \langle \delta u_i \delta \tau_{jk} \rangle) \\ & - \frac{\partial}{\partial x_k} (\alpha_c \rho_c \langle \delta u_i \delta u_j \delta u_k \rangle) \\ & \approx C'_r \frac{\partial}{\partial x_k} \left(\rho_c R_{km} \frac{k_c}{\varepsilon_c} \frac{\partial R_{ij}}{\partial x_m} \right) \end{aligned} \quad (\text{D.138})$$

where the triple correlation is included. There are a few methods that model the transport terms independent of the triple correlation; however, a simpler approach has been adopted here. The traditional approach to model the pressure strain terms is to separate them into two parts: (1) a slow return to isotropy term ($\Phi_{ij,1}$), and (2) a rapid distortion term ($\Phi_{ij,2}$) such as

$$\alpha_c \left\langle \delta p \left(\frac{\partial \delta u_i}{\partial x_j} + \frac{\partial \delta u_j}{\partial x_i} \right) \right\rangle \approx \alpha_c (\Phi_{ij,1} + \Phi_{ij,2}) \quad (\text{D.139})$$

Although there are several models (Banerjee et al., 2009) proposed to model the above terms, Launder (1989) indicates that, up until 1998, none were particularly persuasive. Historically, the linear model proposed by Rotta (1951) has been used to model the slow return to isotropy. This may be due to its simple form and robustness. The model proposed by Rotta is

$$\Phi_{ij,1} = -C'_{r1} \rho_c \frac{\varepsilon_c}{k_c} \left(R_{ij} - \frac{1}{3} R_{kk} \delta_{ij} \right) \quad (\text{D.140})$$

Again there are several models (Banerjee et al., 2009) developed for the rapid distortion term that are based on realizability constraints. These models are rigorous and complex. A simple model commonly found in the literature is

$$\Phi_{ij,2} = C'_{r2} \left(\alpha_c \rho_c R_{jk} \frac{\partial \langle u_i \rangle}{\partial x_k} + \alpha_c \rho_c R_{ik} \frac{\partial \langle u_j \rangle}{\partial x_k} - \frac{2}{3} \alpha_c \rho_c R_{km} \frac{\partial \langle u_k \rangle}{\partial x_m} \delta_{ij} \right) \quad (\text{D.141})$$

where C'_{r2} may include particle effects. As shown in Launder (1989), an additional rapid distortion term ($\Phi_{ij,3}$) representing the production due to

the effect of the particles should be accounted for. This is further discussed in Chapter 7.

Assuming high Reynolds number flows and local isotropy at the small length scales, the following dissipation tensors can be modeled by the isotropic dissipation scalar such as

$$-\alpha_c \left\langle \delta\tau_{ik} \frac{\partial \delta u_j}{\partial x_k} \right\rangle - \alpha_c \left\langle \delta\tau_{jk} \frac{\partial \delta u_i}{\partial x_k} \right\rangle \approx -\frac{2}{3} \alpha_c \rho_c \varepsilon_c \delta_{ij} \quad (\text{D.142})$$

where the isotropic dissipation scalar is

$$\varepsilon_c = \nu_c \left\langle \frac{\partial \delta u_i}{\partial x_k} \frac{\partial \delta u_i}{\partial x_k} \right\rangle \quad (\text{D.143})$$

The hydrodynamic force acting on the particle can be expressed as the sum of the forces due to undisturbed flow (Equation 4.40) and the remaining forces

$$F_{k,i} = -V_{p,k} \frac{\partial \langle p \rangle}{\partial x_i} + V_{p,k} \frac{\partial \langle \tau_{ij} \rangle}{\partial x_j} + F'_{k,i} \quad (\text{D.144})$$

Substituting this equation for the force on the particle into Equation D.136 using the above models for the other terms results in

$$\begin{aligned} & \frac{\partial}{\partial t} (\alpha_c \rho_c R_{ij}) + \frac{\partial}{\partial x_k} (\alpha_c \rho_c \langle u_k \rangle R_{ij}) \\ = & -\alpha_c \rho_c R_{jk} \frac{\partial \langle u_i \rangle}{\partial x_k} - \alpha_c \rho_c R_{ik} \frac{\partial \langle u_j \rangle}{\partial x_k} \quad \text{Production} \\ & - C'_{r1} \alpha_c \rho_c \frac{\varepsilon_c}{k_c} \left(R_{ij} - \frac{1}{3} R_{kk} \delta_{ij} \right) \quad \text{Return to Isotropy} \\ & + C'_{r2} \alpha_c \rho_c \left(R_{jk} \frac{\partial \langle u_i \rangle}{\partial x_k} + R_{ik} \frac{\partial \langle u_j \rangle}{\partial x_k} - \frac{2}{3} R_{km} \frac{\partial \langle u_k \rangle}{\partial x_m} \delta_{ij} \right) \quad \text{Rapid Distortion} \\ & + C'_r \frac{\partial}{\partial x_k} \left(\alpha_c \rho_c R_{km} \frac{k_c}{\varepsilon_c} \frac{\partial R_{ij}}{\partial x_m} \right) \quad \text{Diffusion} \\ & - \frac{2}{3} \alpha_c \rho_c \varepsilon_c \delta_{ij} \quad \text{Dissipation} \\ & + \frac{1}{V} \sum_k (\langle u_i \rangle - v_{k,i}) F'_{k,j} + \frac{1}{V} \sum_k (\langle u_j \rangle - v_{k,j}) F'_{k,i} \quad \text{Particle forces} \end{aligned} \quad (\text{D.145})$$

where the last two terms are related to production and redistribution terms. In fact, by contracting indices (i.e., setting $i = j$) and multiplying by 1/2, the production and redistribution terms are identical to those shown in Section 1, the turbulent energy equation. The coefficients are discussed in Chapter 7.

If the only significant drag force acting on the particles is the steady state drag then the last term in Equation D.145 can be written as

$$\begin{aligned}
 & \frac{3\pi\mu_c}{V} \sum_k D_k f_k \left[\begin{array}{l} (\langle u_j \rangle - v_{k,j}) (u_{k,i} - v_{k,i}) \\ + (\langle u_i \rangle - v_{k,i}) (u_{k,i} - v_{k,j}) \end{array} \right] \\
 = & 2\alpha_d \rho_d \frac{f}{\tau_V} [(\langle u_i \rangle - \tilde{v}_i) (\langle u_j \rangle - \tilde{v}_j)] \\
 & + 2\alpha_d \rho_d \frac{f}{\tau_V} \left(\widehat{\delta v_i \delta v_j} - \widehat{\delta v_j \delta u_i} \right)
 \end{aligned} \tag{D.146}$$

where the definitions for the summations correspond to those used for Equation D.51.

Appendix E

Brownian Motion

If the size of a particle suspended in a fluid is very small (less than a micron), the motion of the particle is affected by the discrete nature of molecular motion, exhibiting a random motion due to collisions of molecules with the particle as shown in Figure E.1. This is called *Brownian motion* which occurs in both gases and liquids, the amplitude of the fluctuating motion being smaller in a liquid. Since the particle mass is much larger than that of the impacting molecule, the velocity of the particle motion is small compared to the molecular motion. If the particle spatial concentration is not uniform, the particles migrate toward the region of smaller concentration due to *Brownian motion*. The variation of spatial concentration due to one-dimensional Brownian diffusion is shown in Figure E.2. One-dimensional diffusion means that the concentration is a function of time and one spatial coordinate (x).

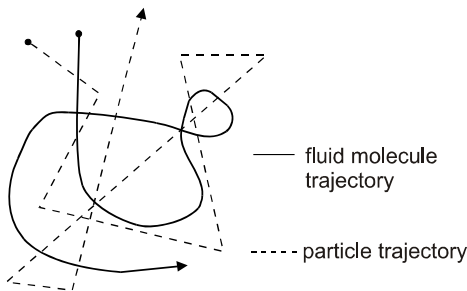


Figure E.1: Particle movement through Brownian motion.

Brownian particle motion can be analyzed using Newton's second law of motion. Particles undergoing Brownian motion are moved by random molecular impact force and resisted by fluid drag. For simplicity, consider one-dimensional motion as shown in Figure E.2. If fluid is assumed to be a gas at rest, the equation of motion of a small particle is given by

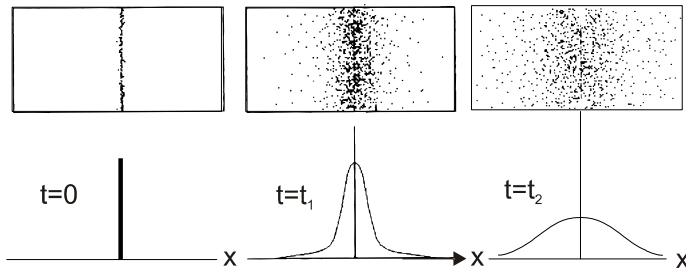


Figure E.2: One-dimensional diffusion from a line source.

$$m \frac{dv}{dt} = F(t) - \frac{1}{B} v \quad (\text{E.1})$$

where m and v are particle mass and velocity, respectively. This is referred to as the *Langevin equation*. The first term on the right side, $F(t)$, is the random impact force due to the molecules and the second term is the Stokes drag force modified for rarefaction effects. The factor B , defined as the *mobility*, is expressed as

$$B = \frac{C_c}{6\pi\mu_c a} \quad (\text{E.2})$$

where C_c is the Cunningham correction factor, μ_c the fluid viscosity and a the particle radius. The Cunningham correction factor, which corrects for rarefied flow effects, is a function of the Knudsen number and is defined in Chapter 4.

Substituting the relation $v = \frac{dx}{dt}$ into Equation E.1 and multiplying both sides by x yields,

$$\frac{1}{2} m \frac{d^2 x^2}{dt^2} - m \left(\frac{dx}{dt} \right)^2 = x F(t) - \frac{1}{2B} \frac{dx^2}{dt} \quad (\text{E.3})$$

Taking the ensemble average of the above equation over many particles and realizing that the average of $x F(t)$ is zero because the random force has no correlation with particle position¹, one obtains

$$\frac{1}{2} m \frac{d^2 \langle x^2 \rangle}{dt^2} + \frac{1}{2B} \frac{d \langle x^2 \rangle}{dt} = m \langle v^2 \rangle \quad (\text{E.4})$$

where $\langle \rangle$ signifies ensemble average. The right side of the above equation is the kinetic energy of particles. With no loss in translation energy with molecular impact, the kinetic energy of the particle motion should equal that

¹In Brownian motion, the response time of the particles is much smaller than the time between molecular impacts. Thus the particles have no “memory” of the previous impact so the particle position and force are uncorrelated.

of the gas which is related to the absolute temperature T of gas through the Boltzman constant k by

$$m\langle v^2 \rangle = kT \quad (\text{E.5})$$

Substituting the above relation into Equation E.4 and integrating results in

$$\frac{d\langle x^2 \rangle}{dt} = 2kBT + C \exp\left(-\frac{t}{mB}\right) \quad (\text{E.6})$$

where C is the constant of integration. The second term of the right side of Equation E.6 becomes negligible after a certain time and the equation simplifies to²

$$\langle x^2 \rangle = 2kBT \cdot t \quad (\text{E.7})$$

Another approach is based on the diffusion or *Fokker-Plank* equation. Again using the one-dimensional formulation for simplicity, the diffusion process is expressed by the equation

$$\frac{\partial P}{\partial t} = D_f \frac{\partial^2 P}{\partial x^2} \quad (\text{E.8})$$

where D_f is the diffusion coefficient and $P(x, t)$ is the probability that a particle which was initially ($t = 0$) located at $x = 0$ reaches position x at time t . The solution to Equation E.8 with the initial condition³ $P(0, 0) = \delta(0)$ and boundary condition $P(\infty, t) = 0$ is

$$P(x, t) = \frac{1}{2\sqrt{\pi D_f t}} \exp\left(-\frac{x^2}{4D_f t}\right) \quad (\text{E.9})$$

The mean value of x^2 , namely $\langle x^2 \rangle$, can be evaluated from

$$\langle x^2 \rangle = \int_{-\infty}^{\infty} x^2 P dx = 2D_f t \quad (\text{E.10})$$

and the mean value of x is

$$\langle x \rangle = \int_{-\infty}^{\infty} x P dx = \sqrt{\frac{4D_f t}{\pi}} \quad (\text{E.11})$$

²This equation was derived by Einstein in 1905.

³ $\delta(0)$ is the Dirac delta function at $x = 0$. Thus all the particles are initially at position $x = 0$ and diffuse away from this point with time.

By comparing Equation E.10 with the Einstein relation in Equation E.7, the diffusion coefficient D_f is found to be

$$D_f = kBT \quad (\text{E.12})$$

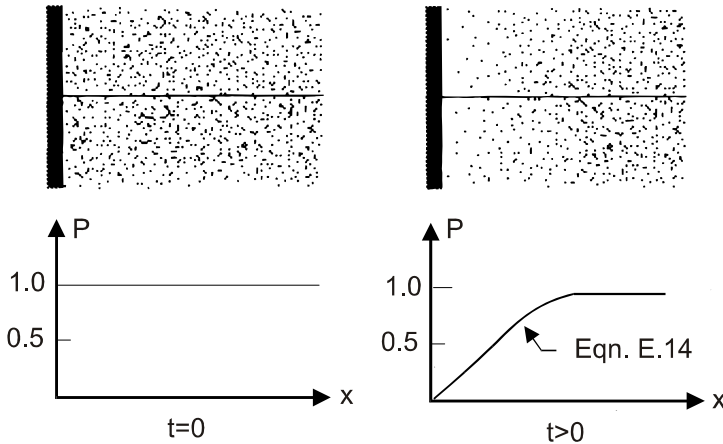


Figure E.3: Particle diffusion in the presence of a wall.

Solutions of the diffusion equation have various forms depending on boundary conditions. The above solution corresponds to particle diffusion into an infinite space with no boundary. If, for example, the space were bounded by a solid wall as shown in Figure E.3, the boundary and initial conditions would be

$$\begin{aligned} P(x, 0) &= 1 && \text{for } x > 0 \\ P(0, t) &= 0 && \text{for } t \geq 0 \end{aligned} \quad (\text{E.13})$$

and the solution to the diffusion equation is

$$P(x, t) = \operatorname{erf} \left\{ \frac{x}{2\sqrt{D_f t}} \right\} \quad (\text{E.14})$$

where $\operatorname{erf}(x)$ is the error function defined by

$$\operatorname{erf}(z) = \frac{2}{\sqrt{\pi}} \int_0^z e^{-\zeta^2} d\zeta$$

The distribution of particle concentration predicted by Equation E.14 is shown in Figure E.3. The boundary condition at the wall signifies that particles impacting the wall are all deposited on the wall (with no re-entrainment) and, thus, the concentration at the wall is zero. The rate of deposition, or

deposition flux, is defined as the number of particles per time per unit area which deposit on the wall. The deposition flux is given by

$$J = -n_0 D_f \left(\frac{\partial P}{\partial x} \right)_{x=0} \quad (\text{E.15})$$

where n_0 is particle concentration far from the wall. The particles diffuse from regions of high concentration to low concentration, so $\frac{\partial P}{\partial x}$ in the above application is negative.

This page intentionally left blank

References

- Abrahamson, J.**, 1975, Collision rates of small particles in a vigorously turbulent fluid, *Chem. Engr. Sci.* 30, 1371.
- Achenbach, E.**, 1972, Experiments on the flow past spheres at very high Reynolds numbers, *J. Fluid Mech.*, 107, 565.
- Adams, M.J. and Edmondson, B.**, 1987, Forces between particles in continuous and discrete liquid media, *Tribology in Particular Technology*, Briscoe, B.J. and Adams, M.J., (Eds.), Adams Hilger, Bristol and Philadelphia, Chap. 2.4.
- Adrian, R.J.**, 1986, Multi-point optical measurements of simultaneous vectors in unsteady flow - A review, *Int. J. Heat and Fluid Flow*, 7, 127.
- Adrian, R.J.**, 1991, Particle-imaging techniques for experimental fluid mechanics. *Ann. Rev. Fluid Mech.*, 23, 261.
- Aizu, Y., Durst, F., Gréhan, G., Onofri, F. and Xu, T.-H.**, 1993, PDA-system without Gaussian beam defects, Third International Congress on Optical Particle Sizing, Yokohama, Japan.
- Albrecht, H-E., Damaschke, N., Borys, M. and Tropea, C.**, 2003, *Laser Doppler and Phase Doppler Measurement Techniques*. Series: Experimental Fluid Mechanics, Springer-Verlag, Berlin.
- Allano, D., Gouesbet, G., Grèhan, G. and Lisiecki, D.**, 1984, Droplet sizing using a top-hat laser beam technique. *J. of Physics D: Applied Physics*, 17, 43.
- Allen, T.**, 1990, *Particle Size Measurements*, Chapman and Hall, London, 4th ed.
- Anderson, D.A., Tannehill, J.C. and Pletcher, R.H.**, 1984, *Computational Fluid Mechanics and Heat Transfer*, Hemisphere Publ. Corp., Bristol, PA.
- Anderson, T.B. and Jackson, R.**, 1967, Fluid mechanical description of fluidized beds, *Ind. & Engr. Chem.*, 6, 527.
- Andrews, M.J. and O'Rourke, P.J.**, 1996, The multiphase particle-in-cell method for dense particulate flows, *Int. J. Multiphase Flow*, 22, 379.
- Auton, T.R., Hunt, J.C.R. and Prud'homme, M.**, 1988, The force exerted on a body in an inviscid unsteady nonuniform rotational flow, *J. Fluid Mech.*, 197, 241.

- Bagchi, P. and Balachandar, S.**, 2002, Shear versus vortex-induced lift force on a rigid sphere at moderate Re , *J. Fluid Mech.*, 473, 379.
- Bagchi, P. and Balachandar, S.**, 2003, Effect of turbulence on the drag and lift of a particle, *Phys. Fluids*, 15, 3496.
- Bagnold, R.A.**, 1954, Experiments on a gravity-free dispersion of large solid spheres in a Newtonian-fluid under shear, *Proc. Roy. Soc., A* 225, 49.
- Bailey, A.B. and Hiatt, J.**, 1972, Sphere drag coefficients for a broad range of Mach and Reynolds numbers, *AIAA J.*, 10, 1436.
- Balachandar, S. and Eaton, J.K.**, 2010, Turbulent dispersed multiphase flow, *Annu. Rev. Fluid Mech.*, 42, 111.
- Banerjee, S., Ertu̇nç, Ö., Köksay, C. and Durst, F.**, 2009, Pressure strain modeling of homogeneous axisymmetric turbulence, *J. of Turb.*, 10, 1.
- Barkla, H.M. and Auchterlonie, L.J.**, 1971, The Magnus or Robins effect on rotating spheres, *J. Fluid Mech.*, 47 (3), 437.
- Barndorff-Nielsen, O.**, 1977, Exponentially decreasing distributions of the logarithm of particle size, *Proc. Res. Soc. Lond. A*, 353, 401.
- Basset, A.B.**, 1888, *Treatise on Hydrodynamics*, Deighton Bell, London.
- Bauckhage, K.**, 1988, The phase-Doppler-difference-method, a new laser-Doppler technique for simultaneous size and velocity measurements. *Part. Part. Syst. Charact.* 5, 16-22.
- Beck, M.S. and Plaskowski, A.**, 1987, *Cross Correlation Flowmeters: Their Design and Application*. Adam Hilger, Bristol.
- Bedford, A., and Fowler, W.**, 2008, *Engineering Mechanics Statics and Dynamics*, Prentice Hall, Upper Saddle River, NJ.
- Bellan, J. and Harstad, K.**, 1987, The details of convective evaporation of dense and dilute clusters of droplets, *Int. J. Heat Mass Transfer*, 30, 1083.
- Benyahia, S., Syamlal, M. and O'Brien, T.J.**, 2005, Evaluation of boundary conditions used to model dilute, turbulent gas/solids flows in pipes, *Powder Tech.*, 156, 62.
- Benyahia, S., Syamlal, M. and O'Brien, T.J.**, 2006, Extension of the Hill-Koch-Ladd drag correlation over all ranges of Reynolds number and solids volume fraction, *Powder Tech.*, 162, 166.
- Berlemon, A., Desjonquieres, P. and Gouesbet, G.**, 1990, Particle Lagrangian simulation in turbulent flows, *Int. J. Multiphase Flows*, 16, 19.
- Bernard, P.S. and Wallace, J.M.**, 2002, *Turbulent Flow: Analysis, Measurement and Prediction*, John Wiley and sons, NJ.
- Berrouk, A.S., Laurence, D., Riley, J.J. and Stock, D.E.**, 2007, Stochastic modeling of inertial particle dispersion by subgrid motion for LES of high Reynolds number pipe flow, *J. Turbulence*, 8, 1.
- Beuvich, Yu. A.**, 1966, Motion resistance of a particle suspended in a turbulent medium, *Fluid Dynamics*, 1, 119.
- Bini, M. and Jones, W.P.**, 2008, Large-eddy simulation of particle-laden turbulent flows, *J. Fluid Mech.*, 614, 207.
- Bird, R.B., Stewart, W.E. and Lightfoot, E.N.**, 1960, *Transport Phenomena*, Wiley & Sons, New York.

- Blei, S. and Sommerfeld, M.**, 2007, CFD in Drying Technology - Spray drying simulation, *Modern Drying Technology*: Volume 1, Computational Tools at Different Scales (eds. E. Tostas and A.S. Majumdar), Wiley-VCH, Weinheim, p. 155.
- Bohnet, M.**, 1973, Staubgehaltsbestimmung in strömenden Gasen. *Chemie-Ing.-Techn.*, 45, 18.
- Börner, Th., Durst, F. and Manero, E.**, 1986, LDV measurements of gas-particle confined jet flow and digital data processing, *Proc. 3rd International Symposium on Applications of Laser Anemometry to Fluid Mechanics*, Paper 4.5.
- Boussinesq, J.**, 1895, *Theorie Analytique de la Chaleur*, L'Ecole Polytechnique, Paris, 2, 224.
- Brock, J.R.**, 1962, On the theory of thermal forces acting on aerosol particles, *J. Colloid Science*, 17, 768.
- Bröder, D. and Sommerfeld, M.**, 2007, Planar shadow image velocimetry for the analysis of the hydrodynamics in bubbly flows. *Meas. Sci. Tech.*, 18, 2513.
- Broßmann, R.**, 1966, Die Lichtstreuung an kleinen Teilchen als Grundlage einer Teilchengrößenbestimmung. Doctoral Thesis, University of Karlsruhe, Faculty of Mechanical and Process Engineering.
- Brucato, A., Grisafi, F. and Montone, G.**, 1998, Particle drag in turbulent fluids, *Chem. Eng. Sci.*, 53, 3295.
- Burton, T.M. and Eaton, J.K.**, 2005, Fully resolved simulations of particle-turbulence interaction, *J. Fluid. Mech.*, 545, 67.
- Cabot, W.H. and Cook, A.W.**, 2006, Reynolds number effects on Rayleigh-Taylor instability with possible implications for type Ia supernovae, *Nature Phys.*, 2, 562.
- Camenen, B.S.**, 2007, Simple and general formula for the settling velocity of particles, *J. Hydraulic Engr.*, 133, 229.
- Chavez, A. and Mayinger, F.**, 1990, Evaluation of pulsed laser holograms of spray droplets using digital image processing. *Proc. 2nd Int. Congress on Optical Particle Sizing*, Arizona, 462-471.
- Chen, C.P. and Wood, P.E.**, 1985, A turbulence closure model for dilute gas-particle flows, *Canadian J. of Chem. Eng.*, 63, 349.
- Cheremisinoff, N.P. and Cheremisinoff, P.N.**, 1984, *Hydrodynamics of Gas-Solid Fluidization*, Gulf Publishing Co., Houston TX.
- Chiang, C.H. and Sirignano, W.A.**, 1993, Interacting, convecting, vaporizing fuel droplets with variable properties. *Int. J. Heat & Mass Trans.*, 36, 875.
- Chigier, N.A., Ungut, A. and Yule, A.J.**, 1979, Particle size and velocity measurements in planes by laser anemometer, *Proc. 17th Symp. (Int.) on Combustion*, 315.
- Chigier, N.A.**, 1983, Drop size and velocity instrumentation, *Prog. Energy Combust. Sci.*, 9, 155.

- Chigier, N.A.**, 1991, Optical imaging of sprays. *Prog. Energy Combust. Sci.*, 17, 211.
- Chigier, N.A.**, 1995, Spray Combustion, *Proc. ASME Fluids Engr. Div.*, FED Vol. 223, 3.
- Chu, C.M. and Churchill, S.W.**, 1955, Numerical solution of problems in multiple scattering of electromagnetic radiation, *J. Phys. Chem.*, 59, 955.
- Ciccone, A.D., Kawall, J.G. and Keffer, J.F.**, 1990, Flow visualization/digital image analysis of saltating particle motions, *Experiments in Fluids*, 9, 65.
- Clamen, A. and Gauvin, W.H.**, 1969, Effects of turbulence on the drag coefficients of spheres in a supercritical flow regime, *AICHE J.*, 15, 184.
- Clift, R. and Gauvin, W.H.**, 1970, The motion of particles in turbulent gas streams, *Proc. Chemeca '70*, 1, 14.
- Clift, R., Grace, J.R. and Weber, M.E.**, 1978, *Bubbles, Drops and Particles*, Academic Press, San Diego, CA.
- Corrsin, S. and Lumley, J.**, 1956, On the equation of motion for a particle in turbulent fluid, *App. Sci. Res.*, 2-3, 114.
- Crowe, C.T.**, 1961, Drag coefficients of inert, burning or evaporating particles accelerating in gas streams, PhD Dissertation, U. of Michigan.
- Crowe, C.T., Babcock, W.R., Willoughby, P.G. and Carlson, R.L.**, 1969, Measurement of particle drag coefficients in flow regimes encountered by particles in a rocket nozzle, United Technology Report 2269-FR.
- Crowe, C.T.**, 1991, The state-of-the-art in the development of numerical models for dispersed phase flows, *Proc. First Intl. Conf. on Multiphase Flows -'91-Tsukuba*, Vol. 3, 49.
- Crowe, C.T.** (ed.), 2006, *Multiphase Flow Handbook*, CRC Press, Boca Raton, FL.
- Crowe, C.T., Babcock, W. and Willoughby, P.G..**, 1973, Drag coefficient for particles in rarefied, low Mach number flows, *Prog. Heat and Mass Trans.*, 6, 419.
- Crowe, C.T., Sharma, M.P. and Stock, D.E..**, 1977, The Particle-Source-in-Cell method for gas droplet flow, *J. Fluid Engr.*, 99, 325.
- Crowe, C.T..**, 1993, Modeling turbulence in multiphase flows, *Proc. 2nd Int. Symp. on Engr. Turbulence Modeling and Measurements*, Elsevier, Amsterdam, 899.
- Crowe, C.T. and Gilliland, I.**, 1998, Turbulence modulation of fluid-particle flows – a basic approach, 3rd Int. Conf. on Multiphase Flows, Lyon, France, June 8-12.
- Crowe, C.T. and Wang, P.**, 2000, Towards a universal model for carrier-phase turbulence in dispersed phase flows, ASME Fluids Eng. Div. Summer Meeting, Boston, MA, June 11-15.
- Csandy, G.T..**, 1963, Turbulent diffusion of heavy particles in the atmosphere, *J. Atmos. Sci.*, 20, 201.
- Cundall, P.A. and Strack, O.D..**, 1979, A discrete numerical model for granular assemblies, *Geotechnique*, 29, 47.

- Czarnecki, J. and Dabros, T.**, 1980, Attenuation of the van der Waals attraction energy in the particle/semi-infinite medium systems due to the roughness of the particle surface, *J. Colloid Interface*, 78, 25.
- Daly, B.J. and Harlow, F.H.**, 1970, Transport equations in turbulence, *Phys. Fluids*, 13, 2634.
- Damaschke, N., Nobach, H., Nonn, Th. I., Semidetnov, N. and Tropea, C.**, 2005, Multi-dimensional particle sizing techniques. *Experiments in Fluids* 39, 336.
- Dandy, D.S. and Dwyer, H.A.**, 1990, A sphere in shear flow at finite Reynolds number: effect of particle lift, drag and heat transfer, *J. Fluid Mech.*, 216, 381.
- DANTEC/Invent, STREU**, 1994, A computational code for the light scattering properties of spherical particles. Instruction Manual.
- Davidson, P.A.**, 2004, *Turbulence: An Introduction for Scientists and Engineers*, Oxford Univ. Press., Oxford, UK.
- Davis, J.M.**, 1949, The aerodynamics of golf balls, *J. Appl. Physics*, 20, 821.
- Denis, S.C.R., Singh, S.N. and Ingham, D.B.**, 1980, The steady flow due to a rotating sphere at low and moderate Reynolds numbers, *J. Fluid Mech.*, 101(2), 257.
- Di Felice, R.**, 1994, The voidage function for fluid-particle interaction systems, *Int. J. Multiphase Flow*, 20, 153.
- Dilber, I. and Mereu, S.**, 1996, Effect of turbulent fluctuations in the numerical simulation of spray dryers, *Num. Meth. for Multiphase Flows*, ASME FED Vol. 236, 291.
- Drew, D.A.**, 1983. Mathematical modeling of two-phase flow, *Ann. Rev. Fluid Mech.*, 15, 266.
- Drobyshevsky, N.I., Zaichik, L.I., Mulkin, R.V. and Strizhov, V.F.**, 2009, Development and application of a diffusion-inertia model for simulation gas-dispersed turbulent flows, *Thermophysics and Aeromechanics*, 16, 521.
- Dukowicz, J.K.**, 1980, A particle-fluid numerical model for liquid sprays, *J. Comput. Phys.*, 33, 229.
- Durst, F. and Zaré, M.**, 1975, Laser-Doppler measurements in two-phase flows. *Proc. of the LDA-Symposium*, University of Denmark.
- Durst, F., Melling, A. and Whitelaw, J.H.**, 1981. *Principles and Practice of Laser-Doppler Anemometry*. 2nd Edition, Academic Press, London.
- Durst, F.**, 1982, Review-combined measurements of particle velocities, size distribution and concentration, *J. of Fluids Eng.*, 104, 284.
- Durst, F., Melling, A. and Whitelaw, J.H.**, 1987, *Theorie und Praxis der Laser-Doppler Anemometrie*, G. Braun, Karlsruhe.
- Eaton, J.K.**, 2006, Turbulence modulation by particles, *Multiphase Flow Handbook* (ed. C.T. Crowe), CRC, Taylor and Francis.

- Eaton, J.K.**, 2009, Two-way coupled turbulence simulations of gas-particle flows using point-particle tracking, *Int. J. Multiphase Flow*, 35, 792.
- Eisenklam, P., Arunachalam, S.A. and Weston, J.A.**, 1967, Evaporation rates and drag resistance of burning drops, *Eleventh (Int.) Symp. on Combustion*, 715.
- Elghobashi, S. and Truesdell, G.C.**, 1992, Direct simulation of particle dispersion in a decaying isotropic turbulence, *J. Fluid Mech.*, 242, 655.
- Elghobashi, S. and Truesdell, G.C.**, 1993, On the 2-way interaction between homogeneous turbulence and dispersed solid particles. 1. Turbulence modification, *Phys. of Fluids A*, 5, 1790.
- Epstein, P.S.**, 1929, Zur Theorie des Radiometers, *Zeit. für Physik*, 54, 537.
- Ergun, S.**, 1952, Fluid flow through packed columns, *Chem. Engr. Prog.*, 48, 89.
- Eswaran, V. and Pope, S.B.**, 1988, Direct numerical simulations of the turbulent mixing of a passive scalar, *Phys. Fluids*, 31, 506.
- Fairweather, M. and Hurn, J-P.**, 2008, Validation of an anisotropic model of turbulent flows containing solid particles applied to gas-solid jets, *Comp. Chem. Engr.*, 32, 590.
- Farmer, W.M.**, 1972, Measurement of particle size, number density and velocity using a laser interferometer. *Applied Optics*, 11, 2603.
- Farmer, W.M.**, 1974, Observation of large particles with a laser interferometer. *Applied Optics*, 13, 610.
- Feng, Z.G. and Michaelides, E.E.**, 1994, Heat transfer from a rigid sphere in a non-uniform flow and temperature field, *Int. J. Heat & Mass Trans.* 37, 2069.
- Feng, Z-G. and Michaelides, E.E.**, 2009, Robust treatment of no slip boundary condition and velocity updating for the lattice-Boltzmann simulation of particulate flows, *Computers and Fluids*, 38, 370.
- Feng, Z.G. and Michaelides, E.E.**, 2009, Application of the immersed boundary method and direct numerical simulation for the heat transfer from particles, ASME FEDSM2009-78493.
- Ferrante, A. and Elghobashi, S.**, 2003, On the physical mechanisms of two-way coupling in particle-laden isotropic turbulence, *Physics of Fluids*, 15, 315.
- Feuillebois, F. and Lasek, A.**, 1978, On the rotational historic term in non-stationary Stokes flow, *J. Mech. & Appl. Math.*, 31, 435.
- Finnie, I.**, 1972, Some observations on the erosion of ductile materials, *Wear*, Vol. 19, 81.
- Fiveland, W.A.**, 1988, Three-dimenisonal radiative heat-transfer solutions by discrete-ordinates method, *J. Thermophysics*, 2, 309.
- Frank, Th., Schade, K.P. and Petrak, D.**, 1993, Numerical simulation and experimental investigation of gas-solid two-phase flow in a horizontal channel, *Int. J. Multiphase Flow*, 19, 187.
- Fritsching, U.**, 2001, *Spraysimulation*, Shaker Verlag, Aachen.

- Frössling, N.**, 1938, Über die Verdüngung fallenden Tropfen, *Gerlands Beitr. Zur Geophysik*, 52, 170.
- Gay, M. and Michaelides, E.E.**, 2003, Effect of the history term on the transient energy equation for sphere, *Int. J. Heat & Mass Trans.*, 46, 1575.
- Germano, M., Piomelli, U. and Moin, P.**, 1991, A dynamic subgrid-scale eddy viscosity model, *Phy. Fluids A*, 3, 1760.
- Gibilario, L.G., Di Felice, R. and Waldram, S.P.**, 1985, Generalized friction factor and drag coefficient correlations for fluid-particle interactions, *Chem. Eng. Sci.*, 40, 1817.
- Gidaspow, D.**, 1994, *Multiphase Flow and Fluidization*, Academic Press, San Diego, CA.
- Gore, R.A. and Crowe, C.T.**, 1989, The effect of particle size on modulating turbulent intensity, *Intl. J. Multiphase Flow*, 15, 279.
- Gosman, A.D., Pun, W.M., Runchal, A.K., Spalding, D.B. and Wolfshtein, M.**, 1969, *Heat and mass transfer in recirculating flows*, Academic Press, London.
- Gosman, A.D. and Ioannides, E.**, 1981, Aspects of computer simulation of liquid-fueled combustors, AIAA Paper 81-0323.
- Govan, A.H., Hewitt, G.F. and Ngan, G.F.**, 1989, Particle motion in a turbulent pipe flow, *Int. J. Multiphase Flow*, 15, 471.
- Grèhan, G. and Gouesbet, G.**, 1986, Simultaneous measurements of velocities and size of particles in flows using a combined system incorporating a top-hat beam technique. *App. Opt.* 25, 3527.
- Grèhan, G., Gouesbet, G., Nagwi, A. and Durst, F.**, 1992, On elimination of the trajectory effects in phase-Doppler systems. *Proc. 5th European Symp. Particle Characterization (PARTEC 92)*, 309.
- Griffiths, W.D. and Boyson, F.**, 1996, Computational fluid dynamics (CFD) and empirical modelling of the performance of a number of cyclone separators, *J. Aerosol Sci.*, 27, 281.
- Hamaker, H.C.**, 1937, The London-Van der Waals' attraction between spheroid particles, *Physica*, 4, 1058.
- Hardalupas, Y., Hishida, K., Maeda, M., Morikita, H., Taylor, A.M.K.P. and Whitelaw, J.H.**, 1994, Shadow Doppler technique for sizing particles of arbitrary shape. *Appl. Optics*, 33, 8417.
- Harris, S.E. and Crighton, D.G.**, 1994, Solitons, solitary waves, and voidage disturbances in gas-fluidized beds, *J. Fluid Mech.*, 266, 243.
- Hassan, Y.A., Blanchat, T.K., Seeley, C.H. and Canaan, R.E.**, 1992, Simultaneous velocity measurements of both components of a two-phase flow using particle image velocimetry. *Int. J. Multiphase Flow*, 18, 371.
- Hedley, A.B., Nuruzzaman, A.S.M. and Martin, G.F.**, 1971, Progress review No. 62 - Combustion of single droplets and simplified spray systems, *J. Inst. Fuel*, 44, 38.
- Henderson, C.B.**, 1976, Drag coefficients of spheres in continuum and rarefied flows, *AIAA Jnl.* 14, 707.

- HermSEN, R.W.**, 1979, Review of particle drag models, JANAF Performance Standardization Subcommittee 12th Meeting Minutes, CPIA, 113.
- Hess, C.F.**, 1984, Non-intrusive optical single-particle counter for measuring the size and velocity of droplets in a spray, *Applied Optics*, 23, 4375.
- Hess, C.F. and Espinosa, V.E.**, 1984, Spray characterization with a nonintrusive technique using absolute scattered light, *Optical Eng.*, 23, 604.
- Hetsroni, G. and Sokolov, M.**, 1971, Distribution of mass, velocity and intensity of turbulence in a two-phase turbulent jet, *J. Appl. Mech.*, 38, 315.
- Hetsroni, G.**, 1989, Particles-turbulence interaction, *Int. J. Multiphase Flow*, 15, 735.
- Hibbeler, R.C.**, 2007, *Engineering Mechanics: Dynamics*, Pearson/-Prentice-Hall, Upper Saddle River, NJ.
- Hill, R.S., Koch, D.B.L. and Ladd, A.J.C.**, 2001a, The first effects of fluid inertia on flows in ordered and random arrays of spheres, *J. Fluid, Mech.*, 448, 213.
- Hill, R.S., Koch, D.B.L. and Ladd, A.J.C.**, 2001b, Moderate Reynolds number flows in ordered and random arrays of spheres, *J. Fluid, Mech.*, 448, 243.
- Hill, S.C. and Smoot, L.D.**, 1993, Comprehensive three dimensional model for the simulation of combustion systems: PCGC-3, *Energy and Fuels*, 7, 874.
- Hinze, J.O.**, 1975, *Turbulence*, McGraw-Hill, New York.
- Hirleman, D.E., Oechsle, V. and Chigier, N.A.**, 1984, Response characteristics of laser diffraction particle size analyzers: Optical sample volume extent and lens effects, *Optical Engineering*, 23, 610.
- Hishida, K. and Maeda, M.**, 1990, Application of laser/phase Doppler anemometry to dispersed two-phase flow. *Part. Part. Syst. Charact.*, 7, 152.
- Hjelmfelt, A.T. and Mockros, L.F.**, 1966, Motion of discrete particles in a turbulent fluid, *App. Sci. Res.*, 16, 149.
- Ho, C.A. and Sommerfeld, M.**, 2002, Modeling of micro-particle agglomeration in turbulent flow, *Chem. Eng. Sci.*, 57, 3073.
- Hölzer, A. and Sommerfeld, M.**, 2008, New simple correlation formula for the drag coefficient of non-spherical particles., *Powder Tech.*, 184, 361.
- Horner, S.F.**, 1965, *Fluid-Dynamic Drag*, published by author, Midland Park, NJ.
- Hosokawa, S., Tomiyama, A., Morimura, M., Fujiwara, S. and Sakaguchi, T.**, 1998, Influences of relative velocity on turbulent intensity in gas-solid two-phase flow in a vertical pipe, 3rd Int. Conf. Multiphase Flow, Lyon, France.
- Huber, N. and Sommerfeld, M.**, 1994, Characterization of the cross-sectional particle concentration distribution in pneumatic conveying systems, *Powder Tech.*, 79, 191.
- Ingebo, R.D.**, 1956, Drag coefficients for droplets and solid spheres in clouds accelerating in airstreams, NACA TN 3762.

- Ishii, M.**, 1975, *Thermo-fluid Dynamic Theory of Two-Phase Flow*, Eyrolles, Paris.
- Jackson, R.**, 1997, Locally averaged equations of motion for a mixture of ideal spherical particles and a Newtonian fluid, *Chem. Eng. Sci.*, 52, 2457.
- Jackson, R.**, 1998, Erratum: Locally averaged..., *Chem. Eng. Sci.*, 53, 1955.
- Jenkins, J.J. and Savage, S.B.**, 1983, A theory for the rapid flow of identical smooth nearly elastic spherical particles, *J. Fluid Mech.*, 130, 187.
- Jin, G., He, G-W., Wang, L-P. and Jian, Z.**, 2010, Subscale fluid velocity timescales as seen by inertial particles in large-eddy simulation of particle-laden turbulence, *Int. J. Multiphase Flow*, 36, 432.
- Johnson, P.C. and Jackson, R.**, 1987, Frictional-collisional constitutive relations for granular materials with application to plane shearing, *J. Fluid Mech.*, 176, 67.
- Jorgensen, S.E. and Johnsen, I.**, 1981 *Principles of Environmental Science and Technology*, Elsevier Scientific Publishing Co., New York, NY.
- Johnson, K.L.**, 1985, *Contact Mechanics*, Cambridge Univ. Press, NY.
- Jurewicz, J.T. and Stock, D.E.**, 1976, Numerical model for turbulent diffusion in gas-particle flows, ASME 76-WA/FE-33.
- Kartushinsky, A.I., Michaelides, E.E. and Zaichik, L.I.**, 2009, Comparison of RANS and PDF methods for air-particle flows, *Int. J. Multiphase Flow*, 35, 914.
- Kavanau, L.L.**, 1955, Heat transfer from spheres to a rarefied gas in subsonic flow, *ASME Trans.*, 77, 617.
- Kenning, V.M. and Crowe, C.T.**, 1997, On the effect of particles on the carrier phase turbulence in gas-particle flows, *Int. J. Multiphase Flows*, 23, 403.
- Kim, J., Moin, P. and Moser, R.**, 1987, Turbulence statistics in fully developed channel flow at low Reynolds number, *J. Fluid Mech.*, 177, 133.
- Kipphan, H.**, 1977, Bestimmung von Transportkenngrößen bei Mehrphasenströmungen mit Hilfe der Korrelationstechnik. *Chem.-Ing.-Techn.*, 49, 695.
- Kliafas, Y., Taylor, A.M.K.P. and Whitelaw, J.H.**, 1990, Errors due to turbidity in particle sizing using laser-Doppler anemometry, *J. Fluid Engineering*, 112, 142.
- Klinzing, G.E.**, 1981, *Gas-Solid Transport*, McGraw-Hill, New York.
- Kolmogorov, A.N.**, 1941, The local structure of turbulence in incompressible viscous fluid for very large Reynolds numbers, *Dokl. Akad. Nauk. SSSR* 30, 299 (English translation can be found in *Proc. R. Soc. London Ser. A*, 434, 9, 1991.)
- Kulick, J.D., Fessler, J.R. and Eaton, J.K.**, 1993, On the interactions between particles and turbulence in a fully developed channel flow in air, Report No. MD-66, Dept. Stanford University.
- Kulick, J.D., Fessler, J.R. and Eaton, J.K.**, 1994, Particle response and turbulence modification in fully-developed channel flow, *J. Fluid Mech.*,

- 277, 109.
- Kussin, J. and Sommerfeld, M.**, 2002, Experimental studies on particle behavior and turbulence modification in horizontal channel flow with different wall roughness, *Exp. in Fluids*, 33, 143.
- Ladd, A.J.C.**, 1994a, Numerical simulations of particle suspensions via a discretized Boltzmann equation Part I. Theoretical foundation, *J. Fluid Mechanics*, 271, 285.
- Ladd, A.J.C.**, 1994b, Numerical simulations of particle suspensions via a discretized Boltzmann equation Part I. Numerical results, *J. Fluid Mechanics*, 271, 311.
- Lain, S., Bröder, D. and Sommerfeld, M.**, 1999, Experimental and numerical studies of the hydrodynamics in a bubble column, *Chem. Eng. Sci.*, 54, 4913.
- Lain, S. and Sommerfeld, M.**, 2008, Euler/Lagrange computations of pneumatic conveying in a horizontal channel with different wall roughness, *Powder Tech.*, 184, 76.
- Lauder, B.E., Reese, G.J. and Rodi, W.**, 1975, Progress in the development of a Reynolds-stress turbulence closure, *J. Fluid Mech.*, 68, 537.
- Lauder, B.E.**, 1989, Second-moment closure: present...and future?, *Int. J. Heat and Fluid Flow*, 10, 282.
- Le, H., Moin, P. and Kim, J.**, 1997, Direct numerical simulation of turbulent flow over a backward-facing step, *J. Fluid Mech.*, 330, 349.
- Leboreiro, J., Joseph, G.G., Hrenya, C.M. and Snider, D.M., Banerjee, S.S. and Galvin, J.E.**, 2008, The influence of binary drag laws on the simulation of species segregation in gas-fluidized beds, *Powder Tech.*, 184, 275.
- Lee, M.M., Hanratty, T.J. and Adrian, R.J.**, 1989, An axial viewing photographic technique to study turbulence characteristics of particles, *Int. J. Multiphase Flow*, 15, 787.
- Lee, S.L. and Durst, F.**, 1982, On the motion of particles in turbulent duct flows, *Int. J. Multiphase Flow*, 8, 125.
- Levy, Y. and Lockwood F.C.**, 1981, Velocity measurements in a particle laden turbulent free jet, *Combustion and Flame*, 40, 333.
- Li, T., Grace, J. and Bi, X.**, 2010, Study of the wall boundary condition in numerical simulations of bubbling fluidized beds, *Powder Tech.*, 203, 447.
- Liljegren, L.M.**, 1996, On modeling particles as point forces in a gas-particle flow, *Numerical Methods for Multiphase Flows*, ASME FED Vol. 236, 173.
- Lischer, J. and Louge, M.Y.**, 1991, Optical fiber measurements of particle concentration in dense suspensions: Calibration and Simulation, *Appl. Optics*, 30, 8.
- Lockwood, F.C., Salooja, A.P. and Syed, S.A.**, 1980, A prediction method for coal-fired furnaces, *Combust. Flame*, 38, 1.
- Longmire, E.K. and Eaton, J.K.**, 1992, Structure of a particle-laden round jet, *Jnl. Fluid Mech.*, 236, 217.

- Longmire, E.K. and Anderson, S.L.**, 1995, Effects of vortices on particle motion in a stagnation zone. *Gas-Particle Flows*, ASME FED, Vol. 228, 89.
- Lu, Q.Q., Fontaine, J.R. and Aubertin, G.**, 1993, Numerical study of the solid particle motion in grid generated turbulence, *Int. J. Heat Mass Transf.*, 36, 79.
- Lun, C.K.K., Savage, S.B. and Chepurng, N.**, 1984, Kinetic theories for granular flow: Inelastic particles in Couette flow and singly inelastic particles in a general flow field, *J. Fluid Mech.*, 140, 223.
- MacColl, J.W.**, 1928, Aerodynamics of a spinning sphere, *J. Roy. Aero. Soc.*, 32, 777.
- Maeda, M., Hishida, K. and Furutani, T.**, 1980, Optical measurements of local gas and particle velocity in an upward flowing dilute gas-solid suspension, *Proc. Polyphase Flow and Transport Technology Conf.*, Century 2-ETC, San Francisco.
- Magnée, A.**, 1995, Generalized law of erosion: application to various alloys and intermetallics, *Wear*, Vol. 181, 500.
- Marble, F.E.**, 1963, Dynamics of a gas containing small, solid particles, *Comb. and Prop.*, 5th AGARD Symp., Braunschwig, GE, 175.
- Masters, K.**, 1972, *Spray Drying: an introduction to principles, operational practice and applications*, Leonard Hill Books, London.
- Matsumoto, S. and Saito, S.**, 1970a, On the mechanism of suspensions in horizontal pneumatic conveying: Monte Carlo simulation based on the irregular bouncing model, *J. Chem. Engr. Japan*, 3, 83.
- Matsumoto, S. and Saito, S.**, 1970b, Monte Carlo simulation of horizontal pneumatic conveying based on the rough wall model, *J. Chem. Engr. Japan*, 3, 223.
- Maxey, M.R. and Riley, J.J.**, 1983, Equation of motion for a small rigid sphere in a nonuniform flow, *Phys. Fluids*, 26(4), 883.
- McKeen, T. and Pugsley, T.**, 2003, Simulation and experimental validation of a freely bubbling bed of FCC catalyst, *Powder Tech.*, 129, 139.
- McLaughlin, J.B.**, 1991, Inertial migration of small sphere in linear shear flows, *J. Fluid Mech.*, 224, 261.
- Mei, R., Lawrence, C.J. and Adrian, R.**, 1991, Unsteady drag on a sphere at finite Reynolds number with small fluctuations in free-stream velocity, *J. Fluid Mech.*, 233, 613.
- Mei, R.**, 1992, An approximate expression for the shear lift on a spherical particle at finite Reynolds number, *Int. J. Multiphase Flow*, 18, 145.
- Michaelides, E.E.**, 2006, *Particles, Bubbles, and Drops: Their Motion, Heat and Mass Transfer*, World Scientific, Singapore, Hackensack, NJ.
- Michaelides, E.E. and Roig, A.**, 2010, A reinterpretation of the Odar and Hamilton data on the unsteady equation of motion of particles, *AICHE J.*, DOI 10.1002/aic.12498.
- Mie, G.**, 1908, Beiträge zur Optik trüber Medien, speziell kolloidaler Metallösungen. *Ann. der Physik*, 25, 377.

- Millikan, R.A.**, 1923, The general law of fall of a small spherical body through a gas, and its bearing upon the nature of molecular reflection from surfaces, *Phys. Rev.*, 22, 1.
- Mindlin, R.D.**, 1949, Compliance of elastic bodies in contact, *J. Appl. Mech. (Trans. ASME)*, 16, 259.
- Mizukami, M., Parthasarathy, R.N. and Faeth, G.M.**, 1992, Particle-generated turbulence in homogeneous dilute dispersed flows, *Int. J. Multiphase Flow*, 18, 397.
- Modarress, D. and Tan, H.**, 1983, LDA signal discrimination in two-phase flows, *Experiments in Fluids*, 1, 129.
- Morikita, H., Hishida, K. and Maeda, M.**, 1994, Simultaneous measurement of velocity and equivalent diameter of non-spherical particles, *Part. Part. Syst. Charact.*, 11, 227.
- Morikita, H. and Taylor, A.M.K.P.**, 1998, Application of shadow Doppler velocimetry to paint spray: potential and limitations in sizing optically inhomogeneous droplets, *Meas. Sci. Tech.*, 9, 221.
- Mugele, R.A. and Evans, H.D.**, 1951, Droplet size distribution in sprays, *Ind. Engr. Chem.* 43, 1317.
- Müller, C.R., Holland, D.J., Sederman, A.J., Scott, S.A., Dennis, J.S. and Gladden, L.F.**, 2008, Granular temperature: comparison of magnetic resonance measurements with Discrete Element Model, *Powder Tech.*, 184, 241.
- Muoio, N.G., Crowe, C.T., Fritsching, U. and Bergmann, D.**, 1996, Effect of thermal coupling on numerical simulations of the spray forming process, *Num. Meth. for Multiphase Flows*, ASME FED Vol. 236, 233.
- Nam, S.**, 1995, Computational prediction of the delivered water flux through fire plumes and comparison with measurements, *ASME HTD* Vol. 321, 97.
- Naot, D., Shavit, A. and Wolfshtein, M.**, 1970, Interactions between components of the turbulent velocity correlation tensor due to pressure fluctuations, *Israel J. Tech.*, 8, 259.
- Naqwi, A.A. and Durst, F.**, 1991, Light scattering applied to LDA and PDA measurements. Part 1: Theory and numerical treatments. *Part. Part. Syst. Charact.*, 8, 245.
- Negus, C.R. and Drain, L.E.**, 1982, Mie calculations of scattered light from a spherical particle traversing a fringe pattern produced by two intersecting laser beams, *J. Phys. D: Applied Physics*, 15, 375, 1982.
- Neve, R.S. and Jaafar, F.B.**, 1982, The effects of turbulence and surface roughness on the drag of spheres in thin jets, *The Aero. J.*, 86, 331.
- Neve, R.S. and Shansonga, T.**, 1989, The effects of turbulence characteristics on sphere drag, *Int. J. Heat and Fluid Flow*, 10, 318.
- Nigmatulin, R.I.**, 1979, Spatial averaging in the mechanics of heterogeneous and dispersed systems, *Int. J. Multiphase Flow*, 5, 353.
- Odar, F. and Hamilton, W.S.**, 1964, Forces on a sphere accelerating in a viscous fluid. *J. Fluid Mech.*, 18, 302.

- Odar, F.**, 1966, Verification of the proposed equation for calculation of the forces on a sphere accelerating in a viscous flow, *J. Fluid Mech.*, 25, 591.
- Oesterlé, B. and Dinh, B.**, 1998, Experiments on the lift of a spinning sphere in a range of intermediate Reynolds numbers, *Exper. in Fluids*, 25, 16.
- Oesterlé, B.**, 2009, On heavy particle dispersion in turbulent shear flows: 3-D analysis of the effects of crossing trajectories, *Boundary-Layer Meteorol.*, 130, 71.
- Ogawa, S.A., Umemura, A. and Oshima, N.**, 1980, On the equations for fluidized granular materials, *Z. Angew. Math. Phys.*, 31, 483.
- O'Rourke, P.J.**, 1981, Collective drop effects on vaporizing liquid sprays, Ph.D. Thesis, Los Alamos, National Lab., NM.
- Oseen, C.W.**, 1927, *Hydrodynamik*, Leipzig.
- Paris, A.D. and Eaton, J.K.**, 2001, Turbulence attenuation in a particle-laden channel flow, Report No. TSD-137, Stanford University.
- Parthasarathy, R. N. and Faeth, G.M.**, 1990, Turbulence modulation in homogeneous dilute particle-laden flows, *J. Fluid Mech.*, 220, 485.
- Pascal, P. and Oesterlé, B.**, 2000, On the dispersion of discrete particles moving in a turbulent shear flow, *Int. J. Multiphase Flow*, 26, 293.
- Patankar, S.V.**, 1980, *Numerical Heat Transfer and Fluid Flow*, McGraw-Hill, New York.
- Patnaik, P.C., Vittal, N. and Pande, P.K.**, 1992, Drag coefficient of a stationary sphere in gradient flow, *J. Hydraulic Research*, 30, 389.
- Perkins, R.J. and Hunt, J.C.R.**, 1989, Particle tracking in turbulent flows. In *Advances in Turbulence*, 2, Springer-Verlag, Berlin, 286.
- Petrak, D. and Hoffmann, A.**, 1985, The properties of a new fiberoptic measuring technique and its application to fluid-solid flows. *Advances in Mechanics*, 8, 59.
- Philip, O.G., Schmidt, W.D. and Hassan, Y.A.**, 1994, Development of a high speed particle image velocimetry technique using fluorescent tracers to study steam bubble collapse, *Nuclear Eng. and Design* 149, 375.
- Pope, S.B.**, 2000, *Turbulent Flows*, Cambridge Univ. Press, NY.
- Prosperetti, A. and Tryggvason, G.**, 2007, *Computational Methods for Multiphase Flow*, Cambridge Univ. Press, NY.
- Putnam, A.**, 1961, Integrable form of droplet drag coefficient, *ARS J.*, 31, 1467.
- Qiu, H.-H. and Sommerfeld, M.**, 1992, A reliable method for determining the measurement volume size and particle mass fluxes using phase-Doppler anemometry. *Experiments in Fluids*, 13, 393.
- Raithby, G.D. and Eckert, E.R.G.**, 1968, The effect of turbulence parameters and support position on the heat transfer from spheres, *Int. J. Heat and Mass Transfer*, 11, 1233.
- Ranz, W.E. and Marshall, W.R.**, 1952, Evaporation from drops - I and II, *Chem. Engr. Prog.* 48, 141 and 173.
- Rao, K.K. and Nott, P.R.**, 2008, *An Introduction to Granular Flow*, Cambridge Univ. Press, NY.

- Reeks, M.W.**, 1977, On the dispersion of small particles suspended in isotropic turbulence fields, *J. Fluid Mech.* 83, 529.
- Reeks, M.W. and McKee, S.**, 1984, The dispersive effects of Basset history forces on particle motion in a turbulent flow, *Phys. Fluids*, 27(7), 1573.
- Renksizbulut, M. and Yuen, M.C.**, 1983, Experimental study of droplet evaporation in a high-temperature air stream, *J. of Heat Transfer*, 105, 384.
- Rensner, D. and Werther, J.**, 1992, Estimation of the effective measuring volume of single fiber reflection probes for solids concentration measurements. *Preprints of the 5th European Symposium Particle Characterization (PARTEC 92)*, 107.
- Rhie, C.M. and Chow, W.L.**, 1983, Numerical study of the turbulent flow past an airfoil with trailing edge separation, *AIAA J.*, 21, 1525.
- Richardson, J.F. and Zaki, W.N.**, 1954, Sedimentation and Fluidization - Part 1, *Trans. Inst. Chem. Engr.*, 32, 35-53.
- Richardson, L.F.**, 1922, *Weather Prediction by Numerical Process*, Cambridge University Press, Cambridge, UK.
- Roberts, D.W.**, 1977, Particle sizing using laser interferometry. *Applied Optics*, 16, 1861.
- Rogers, C.B. and Eaton, J.K.**, 1991, The effect of small particles on fluid turbulence in a flat-plate turbulent boundary layer in air, *Phys. of Fluids*, A3, 928.
- Rotta, J.**, 1951, Statistische Theorie nichthomogener Turbulenz, I. mitteilung, *Zeit. für Physik*, 129, 547 (English translation: Statistical theory of homogeneous turbulence, Part 1, NASA-TT-F-14560, Oct. 1972.)
- Rowe, P.N., Claxton, K.T. and Lewis, J.B.**, 1965, Heat and mass transfer from a single sphere in an extensive flowing fluid, *Trans. Instn. Chem. Engrs.* 43, T14.
- Rubinow, S.I. and Keller, J.B.**, 1961, The transverse force on spinning sphere moving in a viscous fluid, *J. Fluid Mech.*, 11, 447.
- Rudinger, G.**, 1980, Fundamentals of Gas-Particle Flow, *Handbook of Powder Technology*, Vol. 2, Elsevier Scientific Publishing Co., Amsterdam.
- Rudoff, R.R. and Bachalo, W.D.**, 1988, Measurements of droplet drag coefficients in polydispersed turbulent flow field, *AIAA Paper 88-0235*.
- Saffman, M.**, 1987, Optical particle sizing using the phase of LDA signals. Dantec Information, No. 05, 8.
- Saffman, P.G.**, 1965, The lift on a small sphere in a slow shear flow, *J. Fluid Mech.*, 22, 385.
- Saffman, P.G.**, 1968, Corrigendum to "The lift on a small sphere in a slow shear flow", *J. Fluid Mech.*, 31, 624.
- Sankar, S.V. and Bachalo, W.D.**, 1991, Response characteristics of the phase-Doppler particle analyzer for sizing spherical particles larger than the wavelength. *Appl. Optics*, 30, 1487.

- Sato, Y. and Hishida, K.**, 1996, Transport process of turbulent energy in particle-laden turbulent flow, *Int. J. Heat and Fluid Flow*, 17, 202.
- Savage, S.B. and Jeffrey, D.J.**, 1981, The stress tensor in a granular flow at high shear rates, *J. Fluid Mech.*, 110, 457.
- Savolainen, K. and Karvinen, R.**, 1998, The effect of particles on gas turbulence in a vertical upward pipe flow, 3rd Int. Conf. Multiphase Flow, Lyon, France, June 8-12.
- Schaaf, S.A. and Chambré, P.L.**, 1958, Fundamentals of gas dynamics, *High Speed Aerodynamics and Jet Propulsion*, Emmons H.W., (Ed.) , Vol. 3, pp. 687-739, Princeton Univ. Press, Princeton, NJ.
- Schiller L. and Naumann, A.**, 1933, Über die grundlegenden Berechnungen bei der Schwerkraftaufbereitung, *Ver. Deut. Ing.*, 77, 318.
- Schöneborn, P.-R.**, 1975, The interaction between a single particle and an oscillating fluid, *Int. J. Multiphase Flow*, 2, 307-317.
- Schuch, G. and Löffler, F.**, 1978, Über die Abscheidewahrscheinlichkeit von feststoffpartikeln und Tropfen in einer Gasströmung durch Trägheitseffekte, *Verfahrenstechnik*, 12, 302.
- Schwarzkopf, J.D.**, 2008, Turbulence modulation in particle laden flows: The derivation and validation of a dissipation transport equation, Ph.D. Dissertation, Washington State University.
- Schwarzkopf, J.D., Crowe, C.T., and Dutta, P.**, 2009a, A turbulence dissipation model for particle laden flow, *AIChE J.*, 55, 1416.
- Schwarzkopf, J.D., Crowe, C.T., Riley, J.J., Wetchagarun, S. and Dutta, P.**, 2009b, Direct numerical simulation of stationary particles in homogeneous turbulent decay: application of the $k-\varepsilon$ model, *Int. J. Multiphase Flow*, 30, 411.
- Schwarzkopf, J.D., Crowe, C.T. and Dutta, P.**, 2009c, Application of volume-averaged $k - \varepsilon$ model to particle-laden turbulent channel flow, *J. Fluids Engr.*, 131, 101301.
- Shanov, V., Tabakoff, W. and Gunaraj, J.A.**, 1996, Study of CVD coated and uncoated INCO 718 exposed to particulate flow, *Transport Phenomena in Materials Processing and Manufacturing*, ASME HTD-Vol. 336, FED-Vol. 240, 227.
- Sheen, H., Chang, Y. and Chiang, Y.**, 1993, Two dimensional measurements of flow structure in a two-phase vertical pipe flow, *Proc. Natl. Sci. Counc.*, 17, 200.
- Shimizu, A.**, 1993, Numerical prediction of erosion for suspension flow duct, *Gas-Solids Flows - 1993*, ASME FED, Vol. 166, 237.
- Shook, C.A. and Roco, M.C.**, 1991, *Slurry Flow: Principles and Practice*, Butterworth-Heinemann, Boston, MA.
- Shuyan, W., Huilin, L., Xiang, L., Jianzhi, W., Yunhua, Z. and Yunlong, D.**, 2009, Discrete Particle Simulations for flow of binary particle mixture in a bubbling fluidized bed with a transport energy weighted averaging scheme, *Chem. Engr. Sci.*, 64, 1707.

- Siegel, R. and Howell, J.R.**, 1981, *Thermal Radiation Heat Transfer*, McGraw-Hill.
- Sirignano, W.A.**, 1999, *Fluid Dynamics and Transport of Droplets and Sprays*, Cambridge Univ. Press, NY.
- Slattery, C.**, 1972, *Momentum, Energy, and Mass Transfer in Continua*, McGraw-Hill, New York, NY.
- Smagorinsky, J.**, 1963, General circulation experiments with the primitive equations: I. The basic equations. *Mon. Weather Rev.*, 91, 99.
- Smith, P.J., Fletcher, T.J. and Smoot, L.D.**, 1981, Model for pulverized coal-fired reactors, *18th Int. Symp. on Combustion*, 1285.
- Smoot, L.D. and Smith, P.J.**, 1985, *Coal Combustion and Gasification*, Plenum Press, New York.
- Snider, D.M.**, 2001, An incompressible three-dimensional multiphase particle-in-cell model for dense particle flows, *J. Computational Physics*, 170, 523.
- Snider, D.M.**, 2007, Three fundamental granular flow experiments and CFD predictions, *Powder Tech.*, 176, 36.
- Snider, D.M. and Banerjee, S.**, 2010, Heterogeneous gas chemistry in the CFD Eulerian-Lagrangian numerical scheme (ozone decomposition), *Powder Tech.*, 199, 100.
- Sommerfeld, M. and Zivkovic, G.**, 1992, Recent Advances in the simulation of pneumatic conveying through pipe systems, *Computational Methods in Applied Sciences*, Hirsch C., (Ed.) 201.
- Sommerfeld, M. and Tropea, C.**, 1999, Single-point Laser Measurement, Chapter 7 in *Instrumentation for Fluid-Particle Flow* (ed. S.L. Soo), Noyes Publications, 252.
- Sommerfeld, M. and Huber, N.**, 1999, Experimental analysis and modeling of particle-wall collisions, *Int. J. Multiphase Flow*, 25, 1457.
- Sommerfeld, M., Huber, N. and Wächter, P.**, 1993, Particle-wall collisions: Experimental studies and numerical models. *Gas-Solid Flows 1993*, ASME FED 166, 183.
- Sommerfeld, M.**, 2001, Validation of stochastic Lagrangian modeling approach for inter-particle collisions in homogeneous turbulence, *Int. J. Multiphase Flow*, 27, 1829.
- Sommerfeld, M.**, 2007, Application of extended imaging techniques for analyzing elementary processes in multiphase flow. *Multiphase Flow: The Ultimate Measurement Challenge*. (Eds. Cai, X., Wu, Y. Huang, Z.. Wang S., and Wang, M.), AIP Conference Proceedings, Meville, New York, Vol. 914, 20.
- Sommerfeld, M.**, 2010, Modeling particle collisions and agglomeration in gas-particle flows, 7th Int. Conf. on Multiphase Flows, Tampa, FL.
- Sommerfeld, M. and Qiu, H.H.**, 1995, Particle concentration measurements by phase-Doppler anemometry in complex dispersed two-phase flows. *Exper. in Fluids*, 18, 187.

- Soo, S.L., Stukel, J.J. and Hughes, J.M.**, 1969, Measurement of mass flow and density of aerosols in transport. *Environ. Sci. and Tech.*, 3, 386.
- Squires, K.D. and Eaton, J.K.**, 1990, Particle response and turbulence modification in isotropic turbulence, *Phys. Fluids*, A2(7), 1191.
- Squires, K.D. and Eaton, J.K.**, 1991, Preferential concentration of particles by turbulence, *Phys. Fluids* A, 3, 130.
- Stokes, G.G.**, 1851. On the effect of internal friction of fluids on the motion of a pendulum, *Trans. Cambridge Phil. Soc.*, 9, 8.
- Strehlow, R.A.**, 1984, *Combustion fundamentals*, McGraw-Hill, New York.
- Strutt, J.W.**, 1871, On the scattering of light by small particles, *Phil. Mag.*, Ser. 4, 41, 447.
- Swithenbank, J., Beer, J.U., Taylor, D.S., Abbot, D. and McCreath, G.C.**, 1977, A laser diagnostic technique for the measurement of droplet and particle size distribution. *Prog. in Astro. and Aero.*, AIAA, 421.
- Synder, W.H. and Lumley, J.L.**, 1971, Some measurements of particle velocity and auto-correlation functions in a turbulent flow, *J. Fluid Mech.* 48, 41.
- Tabakoff, W.**, 1982, Performance deterioration on turbomachinery with the presence of particles, *Particulate Laden Flows in Turbomachinery*, AIAA /ASME Joint Fluids, Plasma, Thermodynamics and Heat Transfer Conference, 3.
- Taghipour, F., Ellis, N. and Wong, C.**, 2005, Experimental and computational study of gas-solid fluidized bed hydrodynamics, *Chem. Eng. Sci.*, 60, 6857.
- Takeuchi, S., Wang, S. and Rhodes, M.**, 2008, Discrete element simulation of three-dimensional conical-based spouted beds, *Powder Tech.*, 184, 141.
- Talbot, L.**, 1981, Thermophoresis - A review, *Rarefied gas Dynamics, Part 1*, Fisher, S. (Ed.), 74, 467.
- Tanaka, T., Yamagata, K. and Tsuji, Y.**, 1990, Experiment on fluid forces on a rotating sphere and spheroid, *Proc. Second KSME-JSME Fluids Engr. Conf.*, 1, 366.
- Tayali, N.E. and Bates, C.J.**, 1990, Particle sizing techniques in multiphase flows: A review. *Flow Meas. Instrum.*, 1, 77, 1990.
- Taylor, G.I.**, 1921, Diffusion by continuous movements, *Proc. London Math. Soc.* Ser. 2, 196.
- Tchen, C.M.**, 1949, Mean values and correlation problems connected with the motion of small particles suspended in a turbulent fluid, Doctoral Dissertation, Delft, Holland.
- Tokuhiro, A., Maekawa, M., Iizuka, K., Hishida, K. and Maeda, M.**, 1996, The effect of a single bubble on turbulence structure in grid turbulence flow by combined shadow-image and PIV technique. *Proc. of the 8th Int. Symp. on Applications of Laser Techniques to Fluid Mechanics*, Lisbon.
- Torobin, L.B. and Gauvin, W.H.**, 1961, The drag coefficients of single

- spheres moving in steady and accelerated motion in a turbulent fluid, *AICHE J.*, 7, 615.
- Tran-Cong, S., Gay, M. and Michaelides, E.E.**, 2004, Drag coefficient of irregularly shaped particles. *Powder Tech.*, 139, 21.
- Tropea, C.** 1995, Laser Doppler anemometry: Recent developments and future challenges. *Meas. Sci. Techn.*, 6, 605.
- Tropea, C., Xu, T.-H., Onofri, F., Gréhan, G., Haugen, P. and Stieglmeier, M.**, 1996, Dual-mode phase-Doppler anemometer. *Part. Part. Syst. Charact.*, 13, 165.
- Tropea, C.**, 2011, Optical particle characterization in flows, *Ann. Rev. Fluid Mech.*, 43, 399.
- Tsuji, T., Yabumoto, K. and Tanaka, T.**, 2008, Spontaneous structures in three-dimensional bubbling gas-fluidized bed by parallel DEM-CFD coupling simulation, *Powder Tech.*, 184, 132.
- Tsuji, Y., Shen, N-Y. and Morikawa, Y.**, 1989, Numerical simulation of gas-solid flows. I. (Particle-to-wall collisions), Tech. Rpt. of Osaka University, 233.
- Tsuji, Y., Morikawa, Y. and Shiomi, H.**, 1984, LDV measurements of an air-solid two-phase flow in a vertical pipe, *J. Fluid Mech.*, 139, 417.
- Tsuji, Y., Morikawa, Y., Tanaka, T., Nakatsukasa, N. and Nakatani, M.**, 1987, Numerical simulation of gas-solid two-phase flow in a two-dimensional horizontal channel, *Int. J. Multiphase Flow*, 13, 671.
- Tsuji, Y., Shen, N-Y. and Morikawa, Y.**, 1991, Lagrangian simulation of dilute gas-solids flows in a horizontal pipe, *Adv. Powder Tech.*, 2, 63.
- Tsuji, Y., Tanaka, T. and Ishida, T.**, 1992, Lagrangian numerical simulation of plug flow of collisionless particles in a horizontal pipe, *Powder Tech.*, 71, 239.
- Tsuji, Y., Kawaguchi, T. and Tanaka, T.**, 1993, Discrete particle simulation of a two-dimensional fluidized bed, *Powder Tech.* 77, 79.
- Uhlherr, P.H.T. and Sinclair, C.G.**, 1970, The effect of free stream turbulence on the drag coefficient of spheres, *Proc. Chemca '70*, 1, 1.
- Ulmann, M.**, 2008, Interface-resolved direct numerical simulation of vertical particulate channel flow in the turbulent regime, *Phys. Fluids*, 20, 053305 (27 pages).
- Umhauer, H.**, 1983, Particle size distribution analysis by scattered light measurements using an optically defined measuring volume. *J. Aerosol Sci.*, 14, 765.
- Umhauer, H., Löffler-Mang, M., Neumann, P. and Leukel, W.**, 1990, Pulse holography and phase-Doppler technique. A comparison when applied to swirl pressure-jet atomizers. *Particle and Particle Systems Characterization*, 7, 226.
- Valentine, J.R. and Decker, R.A.**, 1994, Application of Lagrangian particle tracking scheme in a body-fitted coordinate system, *Num. Meth. for Multiphase Flows*, ASME FED Vol. 185, 39.

- Van Deemter, J.J. and van der Laan, E.T.**, 1961, Momentum and energy balances for dispersed two-phase flow, *Appl. Sci. Res.* (A), 10, 102.
- Van Dyke, M.**, 1982, *An Album of Fluid Motion*, Parabolic Press, Stanford, CA.
- Van de Hulst, H.C.**, 1981, *Light Scattering by Small Particles*. Dover Publ., Inc., New York.
- Van der Hoef, M.A., Beetsra, R. and Kuipers, J.A.M.**, 2005, Lattice-Boltzmann simulations of low-Reynolds-number flow past mono- and bi-disperse arrays of spheres: Results for permeability and drag force, *J. Fluid Mech.*, 528, 233.
- Van Wachem, B.G.M., Schouten, J.C., Krishna, R. and van den Bleek, C.M.**, 1999, Validation of the Eulerian simulated dynamic behavior of gas-solid fluidized beds, *Chem. Eng. Sci.*, 54, 2141.
- Van Wachem, B.G.M., Shouten, J.C., Bleek, C.M., Krishna, R. and Sinclair, J.L.**, 2001, Comparative analyses of CFD models of dense gas-solid systems, *AICHE J.*, 47, 1035.
- Varaksin, A.Y., Kurosaki, Y., Satch, I., Polezhaev, Y.V. and Polyahov, A.F.**, 1998, Experimental study of the direct influence of small particles on carrier air turbulence intensity for pipe flow, 3rd Int. Conf. Multiphase Flow, Lyon, France, June 8-12.
- Verdurmen, R.E.M., Menn, P., Ritzert, J., Blei, S., Nhamiao, G.C.S., Sonne Sørensen, T., Gunsing, M., Straatsma, J., Verschueren, M., Sineijn, M., Schulte, G., Fritsching, U., Bauckhage, K., Tropea, C., Sommerfeld, M., Watkins, A.P., Yule, A.J. and Schonfeldt, H.**, 2004, *Simulation of agglomeration in spray drying installations: The EDECAD Project*, Drying Tech., 22, 1403.
- Voir, D.J. and Michaelides, E.E.**, 1994, The effect of the history term on the motion of rigid spheres in a viscous fluid, *Int. J. Multiphase Flow*, 20, 547.
- Waddel, H.**, 1933, Sphericity and roundness of rock particles, *J. Geol.*, 41, 310.
- Walsh, M.J.**, 1975, Drag coefficient equations for small particles in high speed flows, *AIAA Jnl.*, 13, 1526.
- Walton, O.R.**, 1993, Numerical simulation of inelastic, frictional, particle-particle interaction, *Particulate two-phase flow*, Roco, M., (Ed.), Butterworth-Heinemann, Boston MA, 884.
- Walton, O.R. and Braun, R.L.**, 1986, Viscosity, granular-temperature, and stress calculations for shearing assemblies of inelastic, frictional disks, *J. Rheology*, 30, 949.
- Wang, L-P. and Stock, D.E.**, 1992, Stochastic trajectory models for turbulent diffusion: Monte Carlo process versus Markoff chains, *Atmos. Environ.*, 26A, 1599.
- Wang, Q. and Squires, K.D.**, 1996, Large eddy simulation of particle-laden turbulent channel flow, *Phys. Fluids*, 8, 1207.
- Warnica, W.D., Renksizbulut, M. and Strong, A.B.**, 1994, Drag

- coefficient of spherical liquid droplets. Part 2: Turbulent gaseous fields, *Exp. Fluids*, 18, 265.
- Weiner B.B.**, 1984, Particle and droplet sizing using Fraunhofer diffraction. in *Modern Methods of Particle Size Analysis* Barth, H. G. (Ed.), J. Wiley, New York, 135.
- Wells, M.R. and Stock, D.E.**, 1983, The effects of crossing trajectories on the dispersion of particles in turbulent flow, *J. Fluid Mech.* 136, 31.
- Wen, C.Y. and Yu, Y.H.**, 1966, Mechanics of Fluidization, *Chem. Engr. Prog. Sump. Series*, 62, 100.
- Wen, F., Kamalu, N., Chung, J.N., Crowe, C.T. and Troutt, T.R.**, 1992, Particle dispersion by vortex structures in plane mixing layers, *J. Fluids Engr.*, 114, 657.
- Werther, J.**, 1999, Measurement techniques in fluidized beds, *Powder Tech.*, 102, 15.
- White, H.J.**, 1963, *Industrial Electrostatic Precipitation*, Addison-Wesley, Reading, PA.
- Wilcox, D.C.**, 2004, *Turbulence Modeling for CFD*, DEC Ind. La Cañada CA.
- Williams, A.**, 1990, *Combustion of liquid fuel sprays*, Butterworths.
- Williams, R.A., Xie, C.G., Dickin, F.J., Simons, S.J.R. and Beck, M.S.**, 1991, Review: Multi-phase flow measurement in powder processing. *Powder Tech.*, 66, 203, 1991.
- Wilson, K.C., Addie, G.R. and Clift R.**, 1992, *Slurry transport using centrifugal pumps*, Elsevier, Amsterdam.
- Xu, T.-H., Durst, F and Tropea, C.**, 1993, The three-parameter log-hyperbolic distribution and its application to particle sizing, *Atom. and Sprays*, 3, 109.
- Xu, T.-H. and Tropea, C.**, 1994, Improving the performance of two-component phase Doppler anemometers, *Meas. Sci. Tech.*, 5, 969.
- Yamamoto, Y., Potthoff, M., Tanaka, T., Kajishima, T. and Tsuji, Y.**, 2001, Large-eddy simulation of turbulent gas-particle flow in a vertical channel: effect of considering inter-particle collisions, *J. Fluid Mech.*, 442, 303.
- Yearling, P.R. and Gould, R.D.**, 1995, Convective heat and mass transfer from a single evaporating water, methanol and ethanol droplet, *ASME FED Vol. 233*, 33.
- Yeoman, M.L., Azzopardi, B.J., White, H.J., Bates, C.J. and Roberts, P.J.**, 1982, Optical development and application of a two-colour LDA system for the simultaneous measurement of particle size and particle velocity. *Engineering Applications of Laser Velocimetry*, 127, ASME Winter Annual Meeting.
- Yuan, Z. and Michaelides, E.E.**, 1992, Turbulence modulation in particulate flows – a theoretical approach, *Int. J. Multiphase Flow*, 18, 779.
- Yuen, M.C. and Chen, L.W.**, 1976, On drag of evaporating liquid droplets, *Comb. Sci. and Tech.*, 14, 147.

- Yuu, S., Yasukouchi, N., Hirosawa, Y. and Jotaki, T.**, 1978, Particle diffusion in a dust laden round jet, *AICHE J.*, 24, 509.
- Yuu, S., Ueno, T. and Umekage, T.**, 2001, Numerical simulation of the high Reynolds number slit nozzle gas-particle jet using subgrid-scale coupling large eddy simulation, *Chem. Engr. Sci.*, 56, 4293.
- Zarin, N.A. and Nicholls, J.A.**, 1971, Sphere drag in solid rockets - non continuum and turbulence effects, *Comb. Sci. and Tech.*, 3, 273.
- Zhang, D.Z. and Prosperetti, A.**, 1994, Ensembled phase-averaged equations for bubbly flows, *Phys. Fluids*, 9, 2956.
- Zhang, Y. and Reese, J.M.**, 2001, Particle-gas turbulence interactions in a kinetic theory approach to granular flows, *Int. J. Multiphase Flow*, 27, 1945.
- Zhang, Y. and Reese, J.M.**, 2003, Gas turbulence modulation in a two-fluid model for gas-solid flows, *AICHE J.*, 49, 3048.
- Zhou, L.X. and Chen, T.**, 2001, Simulation of swirling gas-particle flows using USM and $k-\varepsilon-kp$ two-phase turbulence models, *Powder Technology*, 114, 1.
- Zhou, Q. and Leschziner, M.A.**, 1991, A time-correlated stochastic model for particle dispersion in isotropic turbulence, *Eighth Symp. on Turb. Shear Flows*, Tech. Univ. Munich, 1, 1031.
- Zhu, H.P., Zhou, Z.Y., Yang, R.Y. and Yu, A.B.**, 2008, Discrete particle simulation of particulate systems: A review of major applications and findings, *Chem. Eng. Sci.*, 63, 5728.

This page intentionally left blank

Nomenclature

a	particle radius, radius of curvature [m]
A	projected area [m^2], Hamaker constant [J]
A_i	cross-sectional area at station i [m^2]
Ac	acceleration parameter [-]
B	transfer number [-]
c	speed of sound [m/s], particle circularity [-]
c_d	specific heat of dispersed phase [J/kg-K]
c_p	specific heat of continuous phase at constant pressure [J/kg-K]
C	mass concentration [-]
C_B	coefficient for Basset force equation [-]
C_D	drag coefficient [-]
C_s	thermal slip coefficient [-]
C_S	ratio of lift to Saffman lift force [-], Smagorinsky coefficient
C_{LR}	lift coefficient due to particle rotation [-]
C_t	thermal exchange coefficient [-]
C_{vm}	coefficient for virtual mass force equation [-]
C_μ	coefficient for turbulence effective viscosity [-]
$C_{\varepsilon 1}$	coefficient for production of dissipation [-]
$C_{\varepsilon 2}$	coefficient for dissipation of dissipation [-]
$C_{\varepsilon 3}$	coefficient for particle production of dissipation [-]
d_f	fringe spacing [m]
D	Particle diameter [m]
D_A	surface-equivalent sphere diameter [m]
D_M	median diameter [m]
D_n	volume equivalent sphere diameter [m]
D_T	throat diameter [m]
D_v	diffusion coefficient [m^2/s]
D_ε	diffusion of dissipation [$\text{kg}/\text{m} \cdot \text{s}^3$]
\bar{D}	average diameter [m]
D_{32}	Sauter mean diameter [m]
e	coefficient of restitution [-], charge on a electron [C]
E	energy [J], Youngs modulus [Pa]
E_i	electric field intensity [N/C]
E_0	electric field strength [N/C]

f	drag factor [−], frequency [Hz], friction factor [−]
\hat{f}	focal length [m]
f_i	force per unit volume due to particles $\left[\text{N}/\text{m}^3\right]$
$f(D)$	continuous frequency distribution [−]
$\tilde{f}(D)$	discrete frequency distribution [−]
$\tilde{F}(D)$	discrete cumulative distribution [−]
$F(D)$	continuous cumulative distribution [−]
F_d	drag force [N]
F_i, \mathbf{F}	force vector [N]
$F_{T,i}$	thermophoretic force vector [N]
g_i	gravitational acceleration $\left[\text{m}/\text{s}^2\right]$
g_0	distribution function [−]
$G(x_i)$	filter function [−]
\mathbf{G}	relative velocity vector [m/s]
Ga	Galileo number [−]
h	specific enthalpy [J/kg]
h_L	latent heat [J/kg]
H	heat of combustion [J/kg], shear modulus [Pa]
I	moment of inertia $\left[\text{kg}\cdot\text{m}^2\right]$
I_r	relative turbulence intensity [−], radiation intensity $\left[\text{W}/\text{m}^2\right]$
J	radiosity $\left[\text{W}/\text{m}^2\right]$
\mathbf{J}	impulsive force [N]
k	stiffness [N/m], turbulence kinetic energy $\left[\text{m}^2/\text{s}^2\right]$
k'_{eff}	effective thermal conductivity [W/mK]
k'	thermal conductivity [W/mK]
K_a	absorption coefficient [−]
K_s	scattering coefficient [−]
Kn	Knudsen number [−]
ℓ	interparticle spacing [m], Eulerian length scale [m]
l	length scale [m]
L	volume side dimension [m], characteristic length [m]
m	particle mass (kg), refractive index ratio [−]
M	mass [kg]
\dot{M}	mass flow rate [kg/s]
\mathcal{M}	molecular weight [kg/mole]
n	number density (m^{-3})
N	total number [−]
Nu	Nusselt number [−]
n_i, \mathbf{n}	unit outward normal vector [−]
p	pressure [Pa]
p_A	partial pressure of species A [Pa]

P	perimeter [m]
P_{ij}	pressure strain tensor [Pa]
P_{pl}	yield pressure [Pa]
Pr	Prandtl number [-]
P_ε	production of dissipation $\left[\text{kg}/\text{ms}^3\right]$
q	charge [C]
$\hat{\dot{q}}$	average heat transfer rate over surface $\left[\text{W}/\text{m}^2\right]$
\dot{q}_c	heat flux through the continuous phase $\left[\text{W}/\text{m}^2\right]$
\dot{Q}_d	heat transfer rate to particle [W]
Q_s	scattering efficiency factor [-]
r	radial coordinate [m], particle radius [m]
r_i	radial vector [m]
Re	Reynolds number [-]
Re_G	shear Reynolds number [-]
R_{ij}	volume-averaged Reynolds stress $\left[\text{m}^2/\text{s}^2\right]$
R_E	Eulerian correlation function [-]
R_{xx}	cross-correlation function [-]
s	source per unit volume
S	surface area $[\text{m}^2]$
St	Stokes number [-], Stanton number [-]
Sh	Sherwood number [-]
Sc	Schmidt number [-]
t	time [s]
T	temperature [K]
T_i	torque vector $[\text{N} \cdot \text{m}]$
T_L	Lagrangian time scale [s]
u	continuous phase velocity [m/s]
u_i, \mathbf{u}	continuous phase velocity vector [m/s]
U	free stream velocity [m/s], superficial velocity [m/s]
v	particle velocity [m/s]
v_i, \mathbf{v}	particle velocity vector [m/s]
v_{crit}	critical velocity [m/s]
v_T	terminal velocity [m/s]
V	volume $[\text{m}^3]$
w_i	velocity of gases at particle surface with respect to surface [m/s]
w'_i	velocity of gases at particle surface with respect to droplet center [m/s]
$W(v_i, x_i, t)$	phase space density [-]
\dot{W}	Work rate [W]
x	wetness [-]
x_i	spatial coordinate [m]
z	local loading [-]
Z	overall loading [-]

Greek letters

α	volume fraction [–]
α_c	thermal diffusivity of continuous phase [m^2/s]
β_V	parameter for momentum coupling [Ns/m^4]
γ	dissipation of granular temperature [kg/ms^3]
ϵ	emissivity [–]
ϵ_o	permittivity [–]
ε	dissipation [m^2/s^3]
η	damping coefficient, Kolmogorov length scale [m]
η_i	impact efficiency [–]
Θ	granular temperature [m^2/s^2]
κ	coefficient for conductivity of granular temperature [kg/ms]
λ	mean free path [m], evaporation constant [m^2/s], burning rate [m^2/s]
μ	mean value, viscosity [$\text{N} \cdot \text{s}/\text{m}^2$]
μ_s	solids phase shear viscosity [$\text{N} \cdot \text{s}/\text{m}^2$]
$\overline{\mu}$	viscosity ratio [–]
ν	kinematic viscosity [m^2/s]
ν_s	subgrid kinematic viscosity [m^2/s]
ν_T	turbulent kinematic viscosity [m^2/s]
Π	coupling parameter [–]
ρ	density [kg/m^3], Poisson ratio [–], charge density [C/m^2]
$\overline{\rho}$	bulk density [kg/m^3]
σ	standard deviation, capillary force [N/m], charge density [C/m^2], effective Schmidt number [–], Stephan-Boltzmann constant [$\text{W}/\text{m}^2\text{K}^4$]
σ^2	variance
τ	response time (s), solid stress [N/m^2]
τ_{ij}	shear stress tensor [Pa]
τ_η	Kolmogorov time scale [s]
ϕ	velocity ratio [–], cross-wise sphericity [–], potential function
ψ	elevation angle in PDA [$^\circ$]
Ψ	sphericity [–]
τ	response time [s]
φ	scattering angle in PDA [$^\circ$]
φ_B	Brewster angle [$^\circ$]
φ_R	rainbow angle [$^\circ$]

ω_i, ω	rotational rate vector [rad/s]
ω_A	mass fraction of species A [-]
Ω	rotational rate vector [rad/s]

Subscripts

c	continuous phase, carrier phase
cl	center line
C	collision
d	dispersed phase, droplet phase
e	emitter
m	mass
n	number
p	pressure, computational particle
r	radiation, receiver
s	particle surface
t	tangential
ss	steady state

Operations

$\overline{\overline{}}$	time average
$\overline{}$	volume average, superficial
$\langle \rangle$	phase average, interstitial
$\langle \rangle$	mass average, filtered
$\langle \rangle$	number averaged

Since the publication of the first edition of **Multiphase Flows with Droplets and Particles**, there have been significant advances in science and engineering applications of multiphase flows.

Maintaining the pedagogical approach that made the first edition so popular, this second edition provides a background in this important area of fluid mechanics to those new to the field and a resource to those actively involved in the design and development of multiphase systems.

See what's new in the Second Edition:

- Chapter on the latest developments in carrier-phase turbulence
- Extended chapter on numerical modeling that includes new formulations for turbulence and Reynolds stress models
- Review of the fundamental equations and the validity of the traditional “two-fluid” approach
- Expanded exercises with a solutions manual available

A quick look at the table of contents supplies a snapshot of the breadth and depth of coverage found in this completely revised and updated text. Suitable for a first-year graduate course and a reference for engineers and scientists, the book is clearly written and provides an essential presentation of key topics in the study of gas-particle and gas-droplet flows.



CRC Press

Taylor & Francis Group

an informa business

www.taylorandfrancisgroup.com

6000 Broken Sound Parkway, NW
Suite 300, Boca Raton, FL 33487
711 Third Avenue
New York, NY 10017
2 Park Square, Milton Park
Abingdon, Oxon OX14 4RN, UK

K11877

ISBN: 978-1-4398-4050-4

90000



9 781439 840504

www.crcpress.com